

Computer Applications in Applied Polymer Science

Computer Applications in Applied Polymer Science

Theodore Provder, EDITOR
Glidden Coatings and Resins

Based on a symposium
sponsored by the Division
of Organic Coatings and
Plastics Chemistry
at the 182nd Meeting of
the American Chemical Society,
New York, New York,
August 23–28, 1981.

A C S S Y M P O S I U M S E R I E S **197**

AMERICAN CHEMICAL SOCIETY
WASHINGTON, D. C. 1982



Library of Congress Cataloging in Publication Data

Computer applications in applied polymer science.
(ACS symposium series, ISSN 0097-6156; 197)
Includes bibliographies and index.

1. Plastics—Data processing—Congresses. 2. Coatings—Data processing—Congresses.

I. Provder, Theodore, 1939- . II. American Chemical Society. III. American Chemical Society. Division of Organic Coatings and Plastics Chemistry. IV. Series.

TPI122.C65 1982 667'.9 82-13735
ISBN 0-8412-0733-X ACS MC8 197 1-448 1982

Copyright © 1982

American Chemical Society

All Rights Reserved. The appearance of the code at the bottom of the first page of each article in this volume indicates the copyright owner's consent that reprographic copies of the article may be made for personal or internal use or for the personal or internal use of specific clients. This consent is given on the condition, however, that the copier pay the stated per copy fee through the Copyright Clearance Center, Inc. for copying beyond that permitted by Sections 107 or 108 of the U.S. Copyright Law. This consent does not extend to copying or transmission by any means—graphic or electronic—for any other purpose, such as for general distribution, for advertising or promotional purposes, for creating new collective work, for resale, or for information storage and retrieval systems. The copying fee for each chapter is indicated in the code at the bottom of the first page of the chapter.

The citation of trade names and/or names of manufacturers in this publication is not to be construed as an endorsement or as approval by ACS of the commercial products or services referenced herein; nor should the mere reference herein to any drawing, specification, chemical process, or other data be regarded as a license or as a conveyance of any right or permission, to the holder, reader, or any other person or corporation, to manufacture, reproduce, use, or sell any patented invention or copyrighted work that may in any way be related thereto.

PRINTED IN THE UNITED STATES OF AMERICA

**American Chemical
Society Library**

1155 16th St., N.W.
Washington, D.C. 20036
In Computer Applications in Applied Polymer Science; Provder, T.;
ACS Symposium Series; American Chemical Society: Washington, DC, 1982.

ACS Symposium Series

M. Joan Comstock, *Series Editor*

Advisory Board

David L. Allara

Robert Baker

Donald D. Dollberg

Robert E. Feeney

Brian M. Harney

W. Jeffrey Howe

James D. Idol, Jr.

Herbert D. Kaesz

Marvin Margoshes

Robert Ory

Leon Petrakis

Theodore Provder

Charles N. Satterfield

Dennis Schuetzle

Davis L. Temple, Jr.

Gunter Zweig

FOREWORD

The ACS SYMPOSIUM SERIES was founded in 1974 to provide a medium for publishing symposia quickly in book form. The format of the SERIES parallels that of the continuing ADVANCES IN CHEMISTRY SERIES except that in order to save time the papers are not typeset but are reproduced as they are submitted by the authors in camera-ready form. As a further means of saving time, the papers are not edited or reviewed except by the symposium chairman, who becomes editor of the book. Papers published in the ACS SYMPOSIUM SERIES are original contributions not published elsewhere in whole or major part and include reports of research as well as reviews since symposia may embrace both types of presentation.

PREFACE

THE USE OF COMPUTERS in applied polymer science and technology has been growing at an exponential rate over the last several years. This has been brought about by the continued improvement in cost/performance in medium size and minicomputer systems. The microcomputer explosion over the last five years has significantly accelerated the use of computers in the laboratory by providing the average chemist hands-on moderate computer power at low cost. The microcomputer, more readily, has enabled the polymer scientist and technologist to perform complex calculation, to automate instrumentation for monitoring, data analysis and instrument control, and to develop complex mathematical models for physical and chemical processes.

The topics in this book reflect the growth in the application of computer science and technology to the broad field of polymer science. The book is divided into three main sections. The first section deals with polymerization process modeling and control. The papers in this section cover a variety of polymerization processes, bulk polymerization, solution polymerization, emulsion polymerization, and condensation polymerization including homo- and co-polymerization. The second section covers the field of instrumentation automation for polymer characterization and modeling. The instruments covered in this section include viscometer, capillary rheometer, thermal analysis equipment, torsion pendulum, and dielectric polarization apparatus. The third section is more general in nature and covers various aspects of computer use for mathematical modeling. Some of the topics covered are degradation kinetics, solution properties, water/cosolvent evaporation, emulsification, heat capacity data bank, master plots for vibration damping, and the use of experimental design and analysis.

This book has brought together representative uses of computer science and technology in the field of applied polymer science. It is hoped that this book will spur further activity in this area.

The editor wishes to thank the authors for their effective oral and written communications and the reviewers for their critiques and constructive comments.

THEODORE PROVDER
Glidden Coatings and Resins
Strongsville, OH 44136

May 7, 1982

Control of an Isothermal Polystyrene Reactor

D. C. TIMM, R. E. GILBERT, T. T. KO,¹ and M. R. SIMMONS²

University of Nebraska, Department of Chemical Engineering, Lincoln, NE 68588

Over the past ten years, Timm and co-workers have made an extensive experimental study of the anionic polymerization of styrene initiated by n-butyllithium. As part of that work, descriptive dynamic equations have been derived. Viewed as a control problem, input variables for the system are the flow rates, the input initiator concentration, and the input monomer concentration. The primary outputs are the number average molecular weight and the production rate of polymer. Since there are two outputs and three inputs, the control matrix is not square. In order to deal with this situation, a decoupling matrix is added upstream of the process. Decoupling is accomplished according to a steady-state optimal policy. After decoupling, the non-linear system is simulated on the digital computer and placed under closed loop negative feedback control. Results are presented for proportional and for proportional-plus-integral control.

Polymerization reactions require stringent operating conditions for continuous production of quality resins. In this paper the chain-growth polymerization of styrene initiated with n-butyllithium in the presence of a solvent is described. A perfectly mixed isothermal, constant volume reactor is employed. Coupled kinetic relationships descriptive of the initiator, monomer, polystyryl anion and polymer mass concentration are simulated. Trommsdorff effects (1) are incorporated. Controlled variables include number average molecular weight and production rate of total polymer. Manipulated variables are flow rate, input monomer concentration, and input initiator concentration. The

¹ Current address: Mostek Corporation, Dallas, TX

² Current address: Texas Instruments, Inc., Dallas, TX

controller uncouples the controlled variables so as to produce an optimal operating policy at steady state.

Polymerization Dynamics

Timm and co-workers (2, 3, 4) have developed the following descriptive model for this system. The medium viscosity has a significant effect on the rate of initiation.

$$\begin{aligned}
 \dot{T} &= -QT/V + K_I MI^b && \text{mol polymer/liter/min} \\
 \dot{M} &= Q (M_{in} - M)/V - K_p AM && \text{mol monomer/liter/min} \\
 \dot{I} &= Q (I_{in} - I)/V - K_I MI^b && \text{mol initiator/liter/min} \\
 \dot{W} &= M_o K_i MI^b + M_o K_p MT - QW/V && \text{gm polymer/liter/min} \\
 A &= ((1 + 4K_{eq} T)^{1/2} - 1)/2K_{eq} && \text{mol unassociated polystyryl anion/liter} \\
 \mu &= \mu_o + 2.059 \cdot 10^{-13} W^{3.684} / T^{1.125} && \text{centipoise} \\
 K_p &= K_p^o \mu - .0002 \\
 K_{eq} &= K_{eq}^o \mu - .2025 && (1)
 \end{aligned}$$

A space vector y , an input vector x , and a controlled variable vector c are defined as

$$y = (T, M, I, W)^t \quad x = (Q, I_{in}, M_{in})^t \quad c = (MW, S)^t \quad (2)$$

The number average molecular weight and the production rate in the controlled vector are defined as $MW = W/T$ and $S = QW$.

Direct simulation of these non-linear equations will be described later. For control analysis, however, it is much more convenient to linearize them about a reference steady state. This reference state (see Table I) was one of several experimentally observed states. The linearization is straight-forward. The results are

$$\dot{\hat{y}} + A\hat{y} = B\hat{x} \quad \text{and} \quad \hat{c} = D\hat{y} + E\hat{x} \quad (3)$$

where \hat{y} and \hat{x} represent deviations from the steady-state values of y and x . The matrices A, B, D , and E were determined by Ko (5) and are listed in Table II. Note that the off-diagonal elements of A indicate significant dynamic and steady-state interactions among the state variables.

TABLE I
Steady State Conditions

Q	= .016710	liter/min	A	= .0073289	g mole/liter
I _{in}	= .02009	mol/liter	MW	= 41416.54	gram/g mole
M _{in}	= 3.264	mol/liter	S	= 10.641	gram/min
T	= .015368	mol/liter	K _p	= 12.3287	liter/g mole/min
M	= .35370	mol/liter	K _{eq}	= 149.6674	liter/g mole
I	= .0047221	mol/liter	μ	= 1643.48	centipoise
W	= 636.485	gm/liter			

Process Transfer Function

Taking the Laplace transform of equation 3 and combining to eliminate the state variables gives

$$\hat{c}(s) = \{D(sI + A)^{-1} B + E\} \hat{x}(s) = G_p(s) \hat{x}(s) \quad (4)$$

The term in braces is the process transfer function. Inasmuch as x has three components and c only two, the system is underdetermined--i.e. many combinations of \hat{x} 's will yield the same \hat{c} 's, at least in the steady-state. In this paper a method of selecting the \hat{x} vector which is optimal in the steady-state is described. The method is shown schematically in Figure 1. The input vector \hat{x} is determined by an uncoupling matrix G_m whose inputs come from the feedback controller G_c . A performance function is attached to the \hat{x} vector. The elements of G_m are computed so as to minimize (or maximize) this function in the steady-state.

Optimization

The performance function assumed here is of the general form

$$\hat{H} = \alpha \hat{Q} + \beta \hat{I}_{in} + \gamma \hat{M}_{in} + \delta \hat{Q} \hat{I}_{in} + \epsilon \hat{Q} \hat{M}_{in} \quad (5)$$

Note that H is written as deviation from steady-state and is a function of flow rates and concentrations of input species.

To obtain steady-state step responses, one sets $s = 0$ in the transfer function. The steady-state matrix relating \hat{c} to \hat{x} is, from equation 4, $DA^{-1}B + E$. This matrix is labeled P and its elements p_{ij} are listed in Table II. Referring to Figure 1, the equations represented by the matrix P are

$$\hat{c}_1 = \hat{M}W = p_{11} \hat{Q} + p_{12} \hat{I}_{in} + p_{13} \hat{M}_{in} \quad (6)$$

and

$$\hat{c}_2 = \hat{S} = p_{21} \hat{Q} + p_{22} \hat{I}_{in} + p_{23} \hat{M}_{in}$$

For given values of \hat{c}_1 and \hat{c}_2 (molecular weight and production rate), these relations cannot be solved for the three inputs \hat{Q} , \hat{I}_{in} , and \hat{M}_{in} . However, if the requirement that H be an extremum is included, the following third equation results.

$$\partial \hat{H} / \partial \hat{Q} = \alpha + \beta I'_{in} + \gamma M'_{in} + \hat{Q} \{ \delta I'_{in} + \epsilon M'_{in} \} + \delta \hat{I}_{in} + \epsilon \hat{M}_{in} = 0 \quad (7)$$

where I'_{in} and M'_{in} are constants given by

$$I'_{in} = \frac{p_{13} p_{21} - p_{11} p_{23}}{p_{12} p_{23} - p_{13} p_{22}} \quad \text{and} \quad M'_{in} = \frac{p_{11} p_{22} - p_{12} p_{21}}{p_{12} p_{23} - p_{13} p_{22}}$$

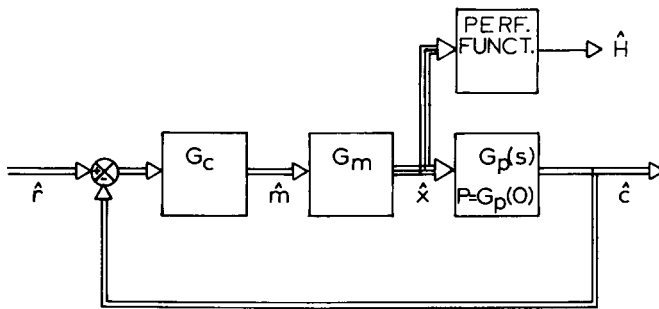


Figure 1. Schematic of closed loop, decoupled control system.

TABLE II

Matrices of the Linearized Equations

$$\begin{aligned}
 A &= \begin{bmatrix} .01097768 & -.0004769625 & 0.01000460 & 0 \\ 1.203198 & .1013335 & 0 & 1.348425 \times 10^{-5} \\ 0 & .0004769625 & 0.2098228 & 0 \\ -453.6174 & -19.75414 & -1.0404784 & .010986185 \end{bmatrix} \\
 B &= \begin{bmatrix} -.01009054 & 0 & 0 \\ 1.91153 & 0 & .01097777 \\ .01009054 & .01097777 & 0 \\ -417.6297 & 0 & -.00088201 \end{bmatrix} \\
 D &= \begin{bmatrix} -2.695 \times 10^6 & 0 & 0 & 65.07071 \\ 0 & 0 & 0 & .016719 \end{bmatrix} \\
 E &= \begin{bmatrix} 0 & 0 & 0 \\ 636.4851 & 0 & 0 \end{bmatrix} \\
 P = DA^{-1}B + E &= \begin{bmatrix} -163671.2 & -592577.3 & 7736.454 \\ 572.3516 & 98.06289 & 3.0314785 \end{bmatrix}
 \end{aligned}$$

Equations 6 and 7 can be solved and placed in the form

$$\begin{aligned}\hat{Q} &= g_{11}c_1 + g_{12}c_2 \\ \hat{I}_{in} &= g_{21}c_1 + g_{22}c_2 \\ \hat{M}_{in} &= g_{31}c_1 + g_{32}c_2\end{aligned}\quad (8)$$

If the system is to be fully decoupled in the steady-state, it is sufficient that \hat{c} and \hat{m} be equal after completion of a step change. This means that \hat{m}_1 and \hat{m}_2 may be substituted for \hat{c}_1 and \hat{c}_2 and, therefore, the elements g_{ij} of relation 8 define G_m in Figure 1. These elements are functions of the coefficients in the performance equation 5.

Systems Simulation

Once the system's interactions have been removed, it can be placed under closed loop control as indicated in Figure 1. For illustrative purposes, a simplified form of equation 7 was selected. For the reference steady-state to be optimal, the first three terms are zero. The coefficient ϵ was further assumed negligible compared to the coefficient δ . Actual plant economics will determine the coefficients of equation 7.

The controller transfer function matrix was chosen to be diagonal--one element to control molecular weight and the other to control production rate. Although the decoupling and optimization analysis was performed on the linearized system, the tests of the system under control were made by simulation of the original set of non-linear equations 1. Simulation was carried out on a large digital computer using IBM's Continuous System Modeling Program (CSMP). A simple proportional controller was chosen for each controlled variable. The results are shown in Figures 2, 3 and 4. In Figure 2 a step change of 2000 units is made in the desired molecular weight while the production rate set point was not changed. In Figure 3 molecular weight was held constant and production rate was changed by 0.5 grams/min. In Figure 4 both quantities were given step changes. In all cases each controller gain was set to 2.0, which gave reasonably tight control with limited oscillations.

It can be seen from the graphs that at steady-state the loops are indeed decoupled. When a change is made in the set point for molecular weight only, the production rate deviates for a brief period, but returns to its original value. The same is true for step changes in the production rate, where it is seen that molecular weight hardly deviates during the transient period. Figure 4 shows that molecular weight and production rate can be varied simultaneously but independently by changes in their respective set points. Figure 5 is a repeat of Figure 4 but with a small amount of integral action ($T_i = 100$ min.) added to each controller so that there is no steady state offset.

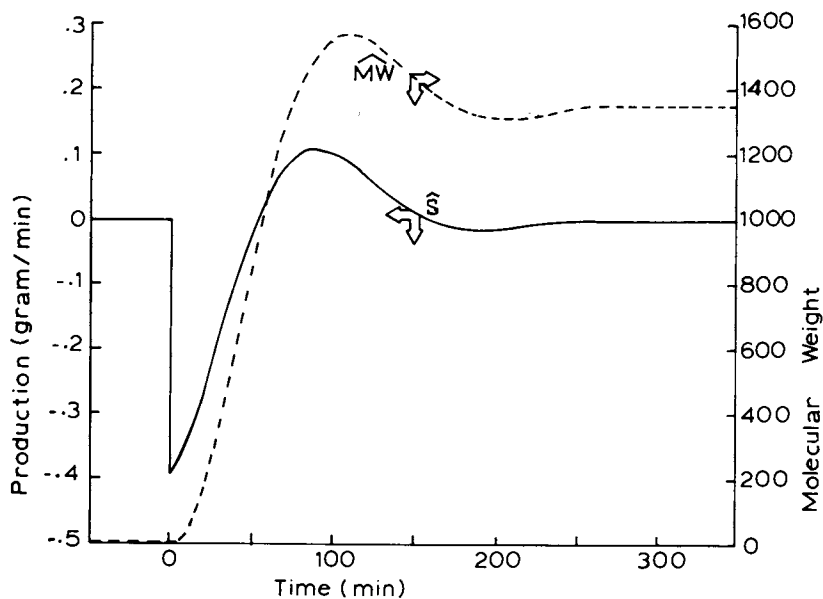


Figure 2. Dynamics for MW set point change—proportional control. Key: —, \hat{S} and ---, MW. $G_c = 2(1 + 0.01/s)I$; $\hat{r} = (2000, 0.5)^t$.

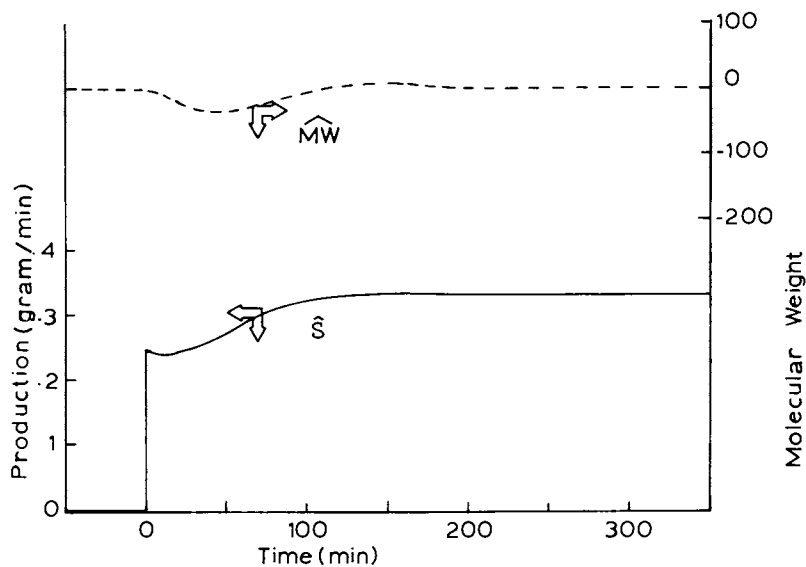


Figure 3. Dynamics for production rate set point change—proportional control. Key: —, \hat{S} and ---, MW. $G_c = 2I$; $\hat{r} = (0, 0.5)^t$.

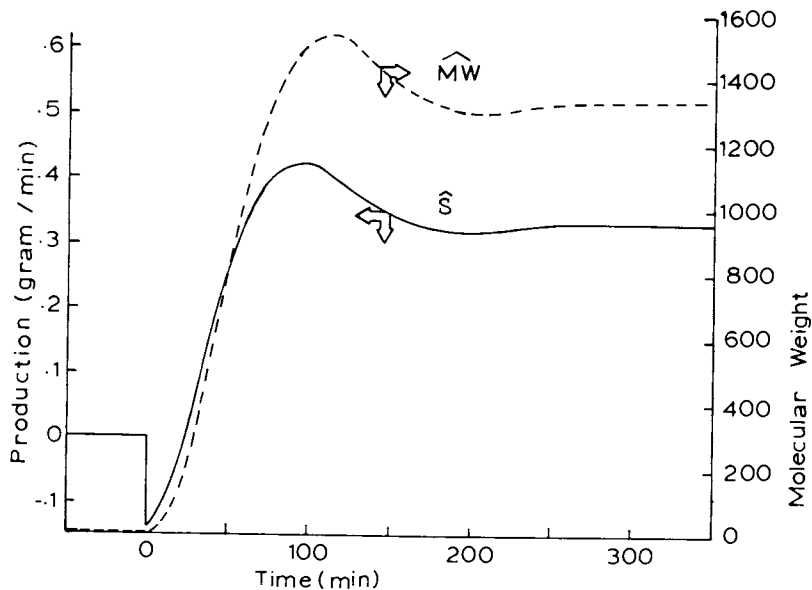


Figure 4. Dynamics for changes in both set points—proportional control. Key: —, \hat{S} and ---, \hat{MW} . $G_c = 2I$; $\hat{r} = (2000, 0.5)^t$.

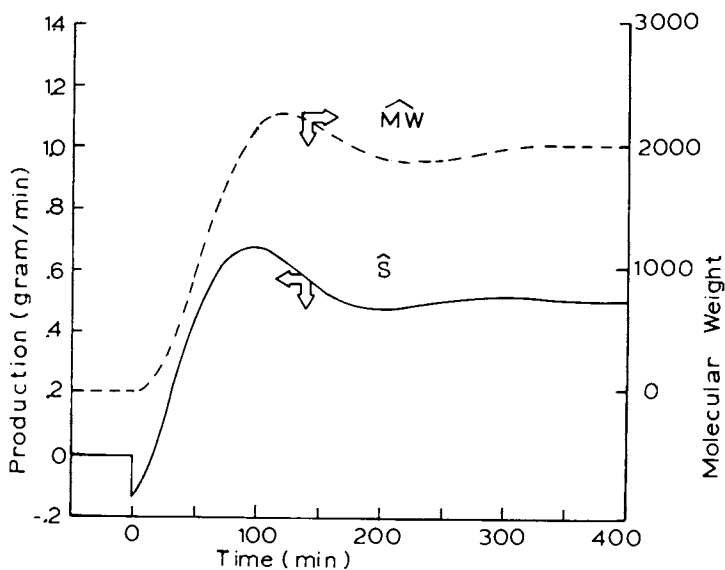


Figure 5. Dynamics for changes in both set points—proportional plus integral control. Key: —, \hat{S} and ---, \hat{MW} . $G_c = 2(1 + 0.01/s)I$; $\hat{r} = (2000, 0.5)^t$.

Discussion

A highly non-linear polymerization reactor can be controlled satisfactorily using controller designs based on the linearized case. Steady-state decoupling of outputs appears to be adequate under the conditions studied. It has also been shown that when the decoupling matrix is not square, some form of optimization technique can be used to provide "best" values of the input parameters.

Future studies are aimed at simple dynamic decoupling so that transient swings of the "non-changing" parameters can be reduced.

Literature Cited

1. Trommsdorff, E., Kohle, H., and Legally, P., MaKromol. Chem. 1947, 1, 169.
2. Timm, D.C., and Rachow, J.W., Adv Chem. Series, 1974, 122.
3. Timm, D.C., and Kubicek, L.F., Chem. Engr. Sci., 1974, 2145.
4. Timm, D.C., Kuang, C., Palsetia, V.K., and Yu, T.S., ACS Symp. Series, 1978, 104, 375.
5. Ko, T.T., Programming The MMD-1 Microcomputer, 1980, unpublished M.S. Thesis, University of Nebraska-Lincoln, Lincoln, Nebraska.

RECEIVED April 27, 1982.

Simulation of the Kinetics of Styrene Polymerization

L. A. CUTTER and T. D. DREXLER

United States Steel Corporation, Research Center, Monroeville, PA 15146

A mathematical model for styrene polymerization, based on free-radical kinetics, accounts for changes in termination coefficient with increasing conversion by an empirical function of viscosity at the polymerization temperature. Solution of the differential equations results in an expression that calculates the weight fraction of polymer of selected chain lengths. Conversions, and number, weight, and Z molecular-weight averages are also predicted as a function of time. The model was tested on peroxide-initiated suspension polymerizations and also on batch and continuous thermally initiated bulk polymerizations.

0097-6156/82/0197-0013\$06.00/0
© 1982 American Chemical Society

Bamford et al.(1) have presented the basic kinetics for free-radical polymerization of styrene, and Hamielec et al.,(2) employing Bamford's nomenclature, developed differential equations that are the starting point for the mathematical model.

The rates (in moles/litre sec) of the component reactions in the overall free-radical chain scheme are as follows:

$$\text{The rate of initiation, } I = 2 \cdot f \cdot k_d \cdot I_n + k_{ti} \cdot M^x$$

where

f = the efficiency of the initiator in starting reaction chains.

k_d = rate coefficient for decomposition of the initiator, sec^{-1}

I_n = initiator concentration in moles/litre

M = monomer concentration in moles/litre

x = exponent for thermal initiation, assumed = 3.

The rate of chain propagation of a radical of chain length

$$r = k_p \cdot M \cdot R_r^0$$

k_p = rate coefficient for propagation litre/mole sec.

R_r^{0P} = concentration of radicals of chain length r moles/litre.

The rate of termination of radicals of chain length

$$r = k_{tc} \cdot R_r^0 \cdot R^0 \text{ (Termination is assumed to be by combination only).}$$

k_{tc} = rate coefficient for termination litre/mole sec.

R^0 = total concentration of free radicals mole/litre.

The rates of chain transfer are:

$$\text{To solvent} = k_{fs} \cdot R_r^0 \cdot S$$

$$\text{To monomer} = k_f \cdot R_r^0 \cdot M$$

k_{fs} = rate coefficient for chain transfer to solvent, litre/mole sec.

S = solvent concentration, moles/litre.

k_f = rate coefficient for chain transfer to monomer, litre/mole sec.

The differential equations used in this model are the same as those presented by Hamielec.(2) The rate of change of concentration of radicals of chain length one (R_1^0) is given by

$$\frac{dR_1^0}{dt} = I - k_p \cdot M \cdot R_1^0 + (k_{fs} \cdot S + k_f \cdot M) \cdot (R^0 - R_1^0) - k_{tc} R_1^0 \cdot R^0 \quad (1)$$

The rate of change for R_2^0 and longer chains is

$$\frac{dR_r^0}{dt} = k_p \cdot M \cdot R_{r-1}^0 - k_p \cdot M \cdot R_r^0 - (k_{fs} \cdot S + k_f \cdot M) \cdot R_r^0 - k_{tc} \cdot R_r^0 \cdot R^0 \quad (2)$$

The overall rate of change of radical is

$$\frac{dR^0}{dt} = \sum_{r=1}^{\infty} \frac{dR_r^0}{dt} = I - k_{tc} \cdot (R^0)^2 \quad (3)$$

The rate of monomer consumption (polymerization rate) is given by

$$-\frac{dM}{dt} = I + k_p \cdot M \cdot R^0 + k_f \cdot M \cdot R^0 \quad (4)$$

The rate of formation of dead polymer of chain length r is

$$\frac{dP_r}{dt} = (k_{fs} \cdot S + k_f \cdot M) R_r^0 + 1/2 \cdot k_{tc} \cdot \sum_{n=1}^{r-1} R_n^0 \cdot R_{r-n}^0 \quad (5)$$

If the rate of formation of radical, I , is taken as a constant for a short period of time, Equation 3 can be integrated directly for this short period to give

$$R^0 = \sqrt{\frac{I}{k_{tc}}} \cdot \tanh\left(\sqrt{I \cdot k_{tc}} \cdot t\right) \quad (6)$$

For the polymerization of styrene, $\sqrt{I \cdot k_{tc}}$ is about 0.1 so that within a few seconds of reaction time $\tanh\left(\sqrt{I \cdot k_{tc}} \cdot t\right) \approx 1$ and for all practical purposes

$$R^0 = \sqrt{\frac{I}{k_{tc}}} \quad (7)$$

Equation 4 can be integrated by the consideration that for long chains I is negligible compared with $k_p M R^0$. The result is

$$M = M_0 \cdot e^{-\int_0^t (k_p + k_f) \cdot R^0 \cdot dt} \quad (8)$$

A further simplification can be made because $\frac{dR_r^0}{dt}$ is very nearly equal to zero, giving rise to a pseudo steady state. Under this condition the derivatives can be eliminated from Equations 1 and 2, making them algebraic. These equations give a recurring relationship between R_r^0 and R_{r-1}^0 .

$$R_1^0 = R^0 \left(\frac{k_{fs} \cdot S + k_f \cdot M + \sqrt{I \cdot k_{tc}}}{k_p \cdot M + k_{fs} \cdot S + k_f \cdot M + \sqrt{I \cdot k_{tc}}} \right) \quad (9)$$

$$R_r^0 = R_{r-1}^0 \left(\frac{k_p \cdot M}{k_p \cdot M + k_{fs} \cdot S + k_f \cdot M + \sqrt{I \cdot k_{tc}}} \right) \quad (10)$$

Now let

$$\zeta = \frac{k_p \cdot M}{k_p \cdot M + k_{fs} \cdot S + k_f \cdot M + \sqrt{I \cdot k_{tc}}} \quad (11)$$

where ζ is the probability factor for the probability that a free radical will propagate rather than enter a termination reaction.

With this definition, Equation 10 can be written

$$R_r^0 = R_{r-1}^0 \cdot \zeta \quad (12)$$

and Equation 9 becomes

$$R_1^0 = R^0 \cdot (1-\zeta) \quad (13)$$

Equations 12 and 13 can be manipulated to give

$$R_r^0 = R^0 \cdot (1-\zeta) \cdot \zeta^{r-1} \quad (14)$$

With the use of Equation 14, Equation 5 can be written

$$\frac{dP_r}{dt} = \left(k_{fs} \cdot S + k_f \cdot M \right) \cdot R^0 \cdot (1-\zeta) \cdot \zeta^{r-1} \quad (15)$$

$$+ 1/2 \cdot k_{tc} \cdot R^{02} \cdot (r-1) \cdot (1-\zeta)^2 \cdot \zeta^{r-2}$$

If Equation 15 is integrated and summed over all the species, we get

$$\sum_{r=1}^{\infty} P_r = \int_0^t \left[\left(k_{fs} \cdot S + k_f \cdot M \right) R^0 + 1/2 \cdot k_{tc} \cdot R^{02} \right] dt \quad (16)$$

ζ does not appear in Equation 16 because the sum of the geometric

$$\text{series} \left(\sum_{r=1}^{\infty} \zeta^{r-1} = \frac{1}{1-\zeta} \right) \text{ and } \left(\sum_{r=1}^{\infty} (r-1) \cdot \zeta^{r-2} = \frac{1}{(1-\zeta)^2} \right)$$

causes the ζ to cancel out on summation.

Other values of interest are the number weight, and z average chain lengths which can be calculated by

$$\bar{M}_n = \frac{\sum_{r=1}^{\infty} r \cdot P_r}{\sum_{r=1}^{\infty} P_r} \quad (17)$$

$$\bar{M}_w = \frac{\sum_{r=1}^{\infty} r^2 \cdot P_r}{\sum_{r=1}^{\infty} r \cdot P_r} \quad (18)$$

$$\bar{M}_z = \frac{\sum_{r=1}^{\infty} r^3 \cdot P_r}{\sum_{r=1}^{\infty} r^2 \cdot P_r} \quad (19)$$

Expressions for the summations necessary to calculate these averages can be developed in the same way as Equation 16

$$\sum_{r=1}^{\infty} r \cdot P_r = \int_0^t \left[\frac{(k_{fs} \cdot S + k_f \cdot M) \cdot R^0}{(1-\zeta)} + \frac{k_{tc} \cdot R^{02}}{2(1-\zeta)} \right] dt \quad (20)$$

$$\sum_{r=1}^{\infty} r^2 \cdot P_r = \int_0^t \left[\frac{(k_{fs} \cdot S + k_f \cdot M) \cdot R^0 \cdot (1 + \zeta)}{(1-\zeta)^2} + \frac{k_{tc} \cdot R^{02} \cdot (2 + \zeta)}{2(1-\zeta)^2} \right] dt \quad (21)$$

$$\sum_{r=1}^{\infty} r^3 \cdot P_r = \int_0^t \left[\frac{(k_{fs} \cdot S + k_f \cdot M) \cdot R^0 \cdot (1 + 4\zeta + \zeta^2)}{(1-\zeta)^3} + \frac{k_{tc} \cdot R^{02} \cdot (4 + 7\zeta + \zeta^2)}{2(1-\zeta)^3} \right] dt \quad (22)$$

The weight fraction of polymers of given chain length can be calculated from

$$W_r = \frac{r \cdot P_r}{M_0 - M} \quad (23)$$

This ratio can be obtained for selected chain lengths by integrating Equation 15.

Computer Model

A digital-computer program was written to solve the equations and calculate the conversion at any time in a batch polymerization. Polymerization rates, instantaneous and cumulative molecular-weight distributions, and molecular-weight averages are also calculated at this time.

Numerical integration is performed as indicated in the previous section on Equations 8, 15, 20, 21, and 22 at constant temperature over time intervals selected by the user. Up to 10 step changes in temperature can be made in the course of a batch polymerization. Provision is made for up to five initiators (primarily for suspension polymerization); in addition thermally initiated polymerization can be calculated with or without initiators.

For initial testing of the model, values of the rate coefficients were taken from the literature; modifications were made to better fit the data as shown in Table I.

As noted by earlier investigators, a correction must be applied to the termination coefficient k_{tc} to allow for the decrease in termination rate caused by the reduction in rates of diffusion of the polymer radicals as conversion and viscosity increase. An empirical correction function was developed to correct k_{tc} for the increased viscosity at higher conversions.

$$K_{tc} \text{ (corrected)} = K_{tc} \frac{1 + c_2 \cdot \exp(\log_{10} \eta - c_1)}{1 + \exp(\log_{10} \eta - c_1)}$$

where

η = zero-shear viscosity in poises

c_1 = constant = 4

c_2 = constant = e^{-5}

At low conversions and viscosities $K_{tc} \text{ (corrected)} = K_{tc}$ the expression $1 + \exp(\log_{10} \eta - 4)$ in the denominator is the main correction to K_{tc} to make K_{tc} decrease to conform to the experimental data. Making the expression $1 + \exp(\log_{10} \eta - c_1)$ minimizes the effect of viscosity at low conversions, where viscosity is changing rapidly, but has a relatively small effect on the rates and molecular weights. The correction term in the numerator was included to moderate the effect of the denominator at very high viscosities and conversions.

The zero-shear viscosity was calculated by Hoffman (3) adapting the generalized equation of Berry and Fox (4)

Table I
Rate Coefficients for Polymerization of Styrene

Rate Coefficient	Symbol	Literature Value	Model Value	Reference
Propagation	k_p	$1.051 \times 10^7 \text{ exp } (-3557/T)$	$1.051 \times 10^7 \text{ exp } (-3557/T)$	2
Termination by combination	k_{tc}	$1.255 \times 10^9 \text{ exp } (-844/T)$	$1.255 \times 10^9 \text{ exp } (-844/T)$	2
Chain transfer to monomer	k_f	$2.31 \times 10^6 \text{ exp } (-6377/T)$	$2.14 \times 10^7 \text{ exp } (-6952/T)$	2
Initiator decomposition	k_d			
Benzoyl peroxide		$1.073 \times 10^{14} \text{ exp } (-14895/T)$	$1.712 \times 10^{15} \text{ exp } (-15924/T)$	8
t-Butyl perbenzoate		$2.25 \times 10^{15} \text{ exp } (-17500/T)$	$6.00 \times 10^{14} \text{ exp } (-17275/T)$	8
Chain transfer to				
Ethylbenzene	k_{fs}	$0.3115 \text{ exp } (-2775/T)$	$0.3115 \text{ exp } (-2775/T)$	9
Initiator efficiency	f			
Benzoyl peroxide		0.60	0.525	10
t-butyl perbenzoate		None	0.525	
Thermal initiation	k_{ti}	$1.23 \times 10^{10} \text{ exp } (-18600/T)$	$1.99 \times 10^6 \text{ exp } (-14842/T)$	11
Exponent		3.0	3.0	11

$$\log \eta - a \log(\rho \bar{M}_w) - 4.32(a - 1) - 7.5 + C$$

where η is the polymer (shear rate independent) viscosity in poises, ρ is the polymer concentration, \bar{M}_w is the weight average molecular weight of the polymer, and a is equal to 3.4 if $\rho \bar{M}_w$ is greater than 21,000 and equal to 1.0 if $\rho \bar{M}_w$ is less than 21,000. The parameter C is a parameter accounting for the temperature dependence of viscosity.

$$1/C = \alpha(T - T_0)$$

where α and T_0 are experimental parameters unique to each polymer and T is the temperature in degrees Kelvin.

The equations are independent of the nature of the solvent except where the solvent tends to promote polymer aggregation or phase separation.

$$\alpha = 5.6 \times 10^{-4} - 7.3 \log \rho$$

$$T_0 = 89.2 - 47.0 \rho + 491 \rho^2 - 229 \rho^3$$

These expressions are analytical representations of Berry's data (5), the expression for α somewhat modified to conform to experimental values for 8 percent polystyrene in toluene.

Experimental

Batch, peroxide-initiated, suspension polymerizations were run in stirred pilot plant reactors. Conversion and molecular weight (GPC) data on a typical suspension formulation run in a 15 gallon reactor are presented in Table II and compared with computer predictions. (The heatup from 90 to 122°C was approximately linear between 8 and 9 hours.)

Final conversion and molecular weight are predicted well, but intermediate conversions and molecular weights are predicted less accurately (both high under this set of conditions).

Data on a thermal batch bulk polymerization at 150°C (run in a two-litre bench-scale reactor) are presented in Table III and compared with computer predictions. Here, the computer prediction of molecular weight is good (almost independent of conversion) while the predicted conversions are slightly low. Comparison of the model predictions with thermal polymerization data of Hui and Hamielec (6) and Husain and Hamielec (7) also indicate that the

Table II

Peroxide-Initiated Suspension Polymerization-
Comparison of Computer Predictions With Pilot-Plant Results

Formulation (parts by weight)

Styrene 100

Benzoyl Peroxide 0.148

t butyl perbenzoate 0.04

Time, hours	Temperature, °C	Predicted Values			Experimental Values		
		Conversion, %	\bar{M}_N	\bar{M}_W	Conversion, %	\bar{M}_N	\bar{M}_W
0	60	0.0			0.0		
1	90	7.9	84500	141000	6.4	66800	125800
2	90	24.6	79000	127000	21.7	70500	125700
3	90	36.3	85800	140000	31.0	75900	137600
4	90	47.2	97000	175000	36.8	82100	158100
5	90	63.4	118000	279000	45.3	95700	182400
6	90	79.7	138000	378000	55.5	106500	216700
7	90	87.1	147000	408000	63.5	145100	322200
8	90	90.8	151000	406000	76.1	136100	421000
9	122						
11	122	99.90	143000	408000	99.96	127200	407200

Table III

Batch Thermal Polymerization

Pure styrene at 150°C

Time, hr.	Predicted			Experimental		
	Conversion, %	\bar{M}_N	\bar{M}_W	Conversion, %	\bar{M}_N	\bar{M}_W
0	0	-	-	0	-	-
0.08	4.3			3		
0.50	21.6			31		
0.83	31.3	116000	222000	38	122800	244000
1.25	41.3			56		
1.75	51.7			60		
2.17	60.0			74		
2.50	66.2	126000	248000	76	115600	248900

predicted conversion rates are low for thermal polymerization over the temperature range 100-230°C.

Continuous bulk, thermal polymerizations were run in a 5.1 cm jacketed pipe loop reactor with a total length at 230 cm as diagrammed in Figure 1. A gear pump circulated the high viscosity polymerization mixture at 3.8 litres per minute. The reactor was fed from one of two reservoirs by a diaphragm pump. It was operated full at all times, with the product overflowing through a back-pressure control valve before cooling and collection. The reactor was started up batchwise, until a desired conversion was obtained, then the feed was started and allowed to continue until the solids remained steady for at least one residence time. The rate of conversion per hour was calculated as follows

$$\text{Rate \% / hr} = \frac{\text{Conversion \%}}{\text{Residence time hours}}$$

In Table IV rates and molecular weights obtained under these conditions approximating steady state are compared with rates of conversion and instantaneous molecular weights from the mathematical model of the batch process, at conversions for which experimental data were available. Quite good agreement is obtained. Temperature (140 to 160°C) is the primary variable affecting both rate and molecular weight. In addition, rate is affected by conversion and the presence of ethylbenzene, and molecular weight is affected by ethylbenzene but only very slightly by conversion.

Summary

The computer program simulates the batch polymerization of styrene and has been applied to the relatively low temperature peroxide-initiated polymerization typical of suspension processes and to higher temperature bulk, thermal conditions. It has been useful in the design of new suspension processes and for more general process analysis.

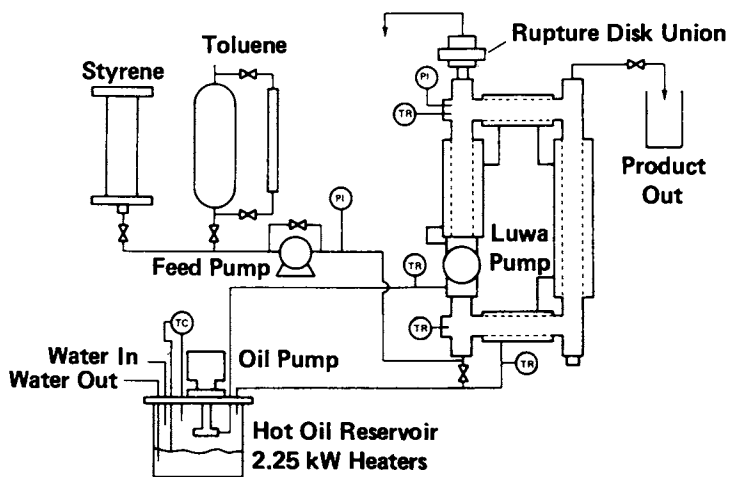


Figure 1. Continuous loop reactor.

Table IV
 Continuous Bulk Thermal Polymerization of Styrene-
 Comparison of Computer Prediction With Experimental Data

Temperature, °C	Ethylbenzene,		Mineral Oil,		Conversion, %	Predicted Values			Experimental Values		
	%	%	%	%		Rate, %/hr	\bar{M}_N	\bar{M}_W	Rate, %/hr	\bar{M}_N	\bar{M}_W
140	0	0	0	0	52	13.9	173000	341000	16.3	164100	344800
140	0	0	0	0	64	13.8	183000	365000	13.7	156200	338900
150	0	0	0	0	50	20.2	137000	272000	26.0	135600	298100
150	0	0	0	0	70	17.9	151000	302000	15.3	131600	281100
150	6	6	0	0	51	15.5	125000	248000	19.3	132000	272200
150	6	6	0	0	66.6	12.5	130000	259000	10.8	105900	233400
160	0	0	0	0	53	29.0	112000	221000	38.8	109100	236300
160	0	0	0	0	67	24.6	122000	246000	21.0	102900	235700
160	6	6	0	0	69	15.8	106000	212000	13.6	82800	190100
160	6	6	0	0	65	17.6	106000	211000	15.6	88800	200700
160	6	6	3	3	67	17.0	106000	212000	18.0	89900	193000

Acknowledgments

The material in this paper is intended for general information only. Any use of this material in relation to any specific application should be based on independent examination and verification of its unrestricted availability for such use, and a determination of suitability for the applicability by professionally qualified personnel. No license under any United States Steel Corporation patents or other proprietary interest is implied by the publication of this paper. Those making use thereof or relying upon the material assume all risk and liability arising from such use or reliance.

Literature Cited

1. Bamford, C. H.; Barb, W. G.; Jenkins, A. D.; Onyon, P. F., "The Kinetics of Vinyl Polymerization by Radical Mechanics," Butterworths; London, 1958.
2. Hamielec, A. E.; Hodgins, J. W.; Tebbens, K. A.I.Ch.E Journal 1967, 13, 1087.
3. Hoffman, R. D. USS Research Memorandum, Nov. 22, 1974.
4. Berry, G. C. and Fox, T. G., Adv. Polymer Sci. 1968, 5, 261-357.
5. Berry, G. C., J. Phys. Chem. 1966, 70, 1194.
6. Hui, A. W., and Hamielec, A. E., J. Appl. Polymer Sci. 1972, 16, 749-769.
7. Husain, A., and Hamielec, A. E., J. Appl. Polymer Sci. 1978, 22, 1207-1223.
8. Masson, J. C.; in "Polymer Handbook;" Wiley; New York, 1966; p. II-88.
9. Young, L. J.; Brandrup, G.; Brandrup, J. in "Polymer Handbook;" Wiley; New York, 1966, p. II-88.
10. Flory, P. J., "Principles of Polymer Chemistry;" Cornell University Press: Ithaca, NY, 1953; p. 118.
11. Platt, A. E.; Boyer, R. F. in "Encyclopedia of Polymer Science and Technology;" Wiley; New York, 1970; p. 162.

RECEIVED May 4, 1982.

Computational Aspects of Free Radical Polymerization Kinetics with Chain Length Dependent Termination

S. K. SOH and D. C. SUNDBERG

University of New Hampshire, Department of Chemical Engineering, Durham, NH 03824

It is well known that the polymerization rate and the molecular weight distribution of vinyl polymers can change markedly during the course of polymerization and that these changes are due to the influence of self diffusion upon the termination reaction. This phenomenon is commonly referred to as the gel effect and in order to explain the polymerization behavior during this period of the reaction, the consideration of chain length dependence of the termination reaction has been previously suggested. Benson and North (1), O'Driscoll (2), Ito (3) and Yasakawa (4) have published the results of their computations based upon different functional forms of the chain length dependence. However, it is difficult if not impossible to generalize these methods. The purpose of this paper is to propose a general theory applicable to vinyl polymerizations in which the monomer and polymer are mutually soluble, and which will allow the prediction of the reaction rate and molecular weight distribution for any chosen functional form of the termination rate constant. This theory is suitable for computer computations and can deal with both disproportionation and recombination modes of termination and may include chain transfer reactions.

Quantitative Development

The termination reaction in vinyl polymerization obviously involves the movement and interaction of macroradicals of all

0097-6156/82/0197-0027\$06.00/0
© 1982 American Chemical Society

possible chain lengths. The ease of movement of these chains may be dependent upon chain length and thus the apparent termination rate constant may have chain length dependency. However, once one accepts the possibility of chain length dependent termination reactions, one is immediately faced with the problem of defining the relationship between the termination rate constant between radicals of different lengths, i and j ,

$$k_{tij} \equiv \text{function of } i \text{ and } j \quad (1)$$

It is natural that this mixing rule be expressed as some function of the rate constants for termination between radicals of equal length, k_{tii} and k_{tjj} ,

$$k_{tij} = \text{function of } (k_{tii} \text{ and } k_{tjj}) \quad (2)$$

It is worthwhile to examine the forms of eq'n (2) suggested by the existing models of chain length dependent termination reactions. O'Driscoll (2) and Yasakawa (4) assumed a geometrical mixing rule expressed as,

$$k_{tij} = (k_{tii} k_{tjj})^{1/2} \quad (3)$$

This form predicts that k_{tij} approaches zero when either k_{tii} or k_{tjj} approaches zero. Considering that the beginning of the gel effect is the result of translational diffusion controlled termination (1), it is reasonable to assume that k_{tii} may become very small if the translational diffusivity of the i -mer approaches zero. However, if i -mer radicals whose $k_{tii} \approx 0$ are mixed with j -mer radicals whose $k_{tjj} \neq 0$, it must be realized that there can be termination due to the mobility of the j -mer. Equation (3) would predict no reaction and on this basis the authors do not accept the geometric mixing rule as having general applicability.

Ito's recent paper (3) and the "Ball and Chain Model" of Benson and North (1) assumed the following form;

$$k_{tij} = 1/2 (k_{tii} + k_{tjj}) \quad (4)$$

where the factor of 1/2 is necessary to assure proper representation when $i=j$. The present authors have chosen to work with the arithmetic mixing rule expressed by eq'n (4) because it is analogous to the arithmetic mixing rule used to express binary diffusion coefficients in terms of the appropriate self diffusion coefficients.

Polymerization Kinetics

The instantaneous reaction rate in bulk polymerization can be expressed as

$$R_p = k_p [M] (R_t / \bar{k}_t)^{1/2} \quad (5)$$

where \bar{k}_t is the average value of k_t for all termination reactions occurring at that instant. The average termination rate constant must be able to express the total termination rate,

$$R_t = \bar{k}_t [R\cdot]^2 \quad (6)$$

and the total termination rate must simply be the sum of the termination rate of each chain length, r_i , or

$$R_t = \sum_{i=1}^{\infty} r_i \quad (7)$$

The r_i 's will be described by

$$r_i = \sum_{j=1}^{\infty} k_{tij} [R\cdot]_i [R\cdot]_j + k_{tii} [R\cdot]_i^2 \quad (8)$$

Furthermore, in terms of the mole fractions of radicals (X_i) of chain length i , defined as

$$X_i \equiv [R\cdot]_i / \sum_{i=1}^{\infty} [R\cdot]_i = [R\cdot]_i / [R\cdot] \quad (9)$$

eq'n (8) can be rewritten as

$$r_i = [R\cdot]^2 \left\{ \sum_{j=1}^{\infty} k_{tij} X_i X_j + k_{tii} X_i^2 \right\} \quad (10)$$

Combining eq's (4)-(10) one finds that after some algebra

$$\bar{k}_t = \sum_{i=1}^{\infty} k_{tii} X_i \quad (11)$$

The term X_i needs to be explained in terms of normal polymerization variables and is developed as follows. The probability that a propagation step takes place in preference to termination or chain transfer is expressed as $p(i)$,

$$p(i) = k_p [M] / \{k_p [M] + 1/2 (k_{tii} + \bar{k}_t) [R\cdot] + k_{tr,M} [M] + k_{tr,S} [S]\} \quad (12)$$

where the second term in the denominator expresses the rate of termination of an i -mer radical with all other possible macro-radicals, and the last two terms describe chain transfer to monomer and solvent, respectively. The probability, $P(i)$, that a primary radical survives to become a macro-radical of length i is the appropriate multiple of the $p(i)$'s,

$$P(i) = \prod_{i=1}^i p(i) \quad (13)$$

Now X_i can be expressed as (5),

$$X_i = P(i) / \sum_{n=1}^{\infty} P(n) \quad (14)$$

Combining eq's (11) and (14),

$$\bar{k}_t = \sum_{i=1}^{\infty} k_{tii} P(i) / \sum_{n=1}^{\infty} P(n) \quad (15)$$

Thus far we have placed no restrictions on the form of k_{tii} . However, it becomes useful at this point to define k_{tii} as a function of both chain length and polymer to monomer ratio, the latter conveniently described as the fractional conversion. We will limit further discussion to the conditions under which k_{tii} may be described by a conversion dependency which is not related to chain length and a chain length dependency which may be related to conversion. We choose to write this as

$$k_{t_{ii}} = k_{t_{vif}} f(i/i_c) \quad (16)$$

where $k_{t_{vif}}$ is a function of conversion but not chain length, and i_c (an arbitrary critical chain length) may be a function of conversion. As the conversion dependency of $k_{t_{vif}}$ and i_c are left arbitrary, the kinetic relationships which follow are still very general and will be valid for vinyl polymerizations. However, since increasing chain length will cause a decrease in the termination rate constant, we envision that the chain length dependent function $f(i/i_c)$ will have the general behavior shown in Figure 1. Here i/i_c has been replaced with the dimensionless variable y .

The combination of eq's (15) and (16) yields

$$Z \equiv \bar{k}_t / k_{t_{vif}} = \int_0^\infty f(y) P(y) dy / \int_0^\infty P(y) dy \quad (17)$$

The parameter Z is a dimensionless number with a value of unity when \bar{k}_t has no chain length dependency.

The common psuedo steady state assumption was employed here,

$$R_i = R_t = \bar{k}_t [R\cdot]^2$$

in order to obtain $[R\cdot]$ as $(R_i / \bar{k}_t)^{1/2}$. This allows eq'n (12) to be written as

$$1/p(i) = 1 + \gamma f(i) / (2i_c \sqrt{Z}) + \gamma \sqrt{Z} / 2i_c + \beta / i_c \quad (18)$$

where

$$\gamma \equiv i_c (R_i k_{t_{vif}})^{1/2} / (k_p [M]) \quad (19)$$

$$\beta \equiv C_M i_c + C_S i_c [S] / [M] \quad (20)$$

Combining eq's (13) and (18) it can be shown (5, 6) that,

$$P(y) = \exp \{ -(\beta + \gamma \sqrt{Z} / 2) y - \gamma / (2\sqrt{Z}) \int_0^y f(y) dy \} \quad (21)$$

This probability of a primary radical surviving to become a

macroradical of length y will of course decrease as y increases. But with chain length dependent termination this decrease should be less dramatic than without it. This is shown conceptually in Figure 2.

At this point the general description of the average termination rate constant is complete and is embodied in eq's (17) and (19)-(21). It will be noted that eq's. (17) and (21) are interdependent and must be solved simultaneously by trial and error. This first requires that one choose a functional form of $f(y)$ so that its integral can be determined for use in eq'n. (21). Then a value of Z is guessed and $P(y)$ is calculated for arbitrary values of γ and β . This allows Z to be computed from eq'n. (17) and its value is then compared with the one guessed. The procedure is repeated until convergence is obtained. Since these values of $P(y)$ and Z are obtained for arbitrary values of γ and β , a master plot can be constructed and used in a very general fashion. Such a master plot is shown in Figure 3 for a choice of $f(y) = 1$ for $y \leq 1$ and $f(y) = y^{-2.4}$ for $y > 1$ (5, 6). This clearly shows the effect of chain transfer (β) and conversion (γ) upon Z , that portion of the termination rate constant dependent upon chain length. These curves can easily be put in numerical form and stored in computer memory for use in calculating reaction rates and molecular weights.

Molecular Weight Development

The probability of formation of dead polymer chains of length i is denoted as $N_d(i)$ and $N_r(i)$ where the subscripts d and r refer to disproportionation and recombination, respectively.

$$N_d(i) = (C_M + C_S [S]/[M]) [R\cdot] X_i + [R\cdot]^2 \sum_{j=1}^{\infty} k_{t ij} X_i X_j \quad (22)$$

$$N_r(i) = (C_M + C_S [S]/[M]) [R\cdot] X_i + [R\cdot]^2 \sum_{j=1}^{i-1} k_{t jk} X_j X_q \quad (23)$$

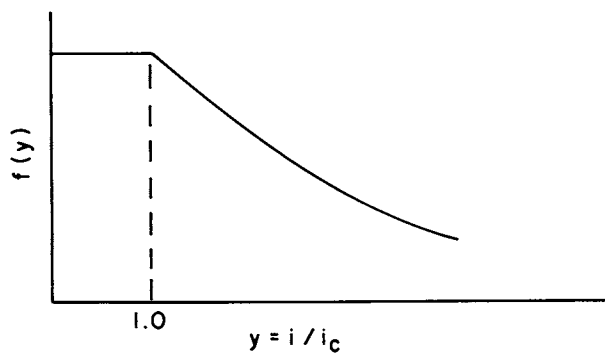


Figure 1. Chain length dependence function.

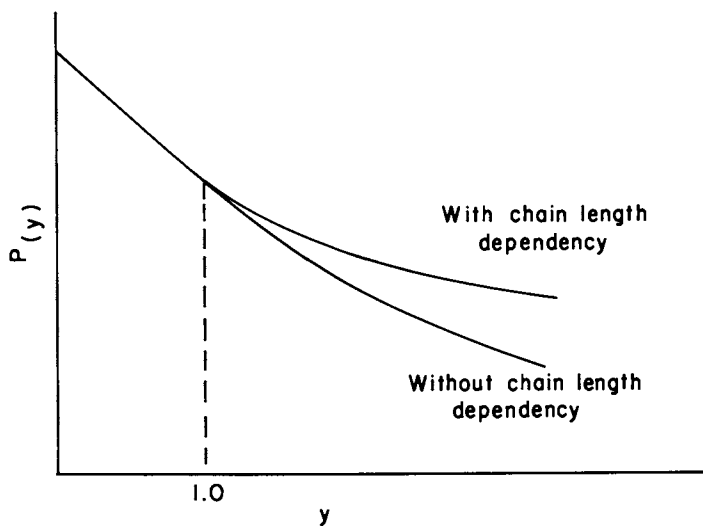


Figure 2. Variation of $P(y)$ with chain length.

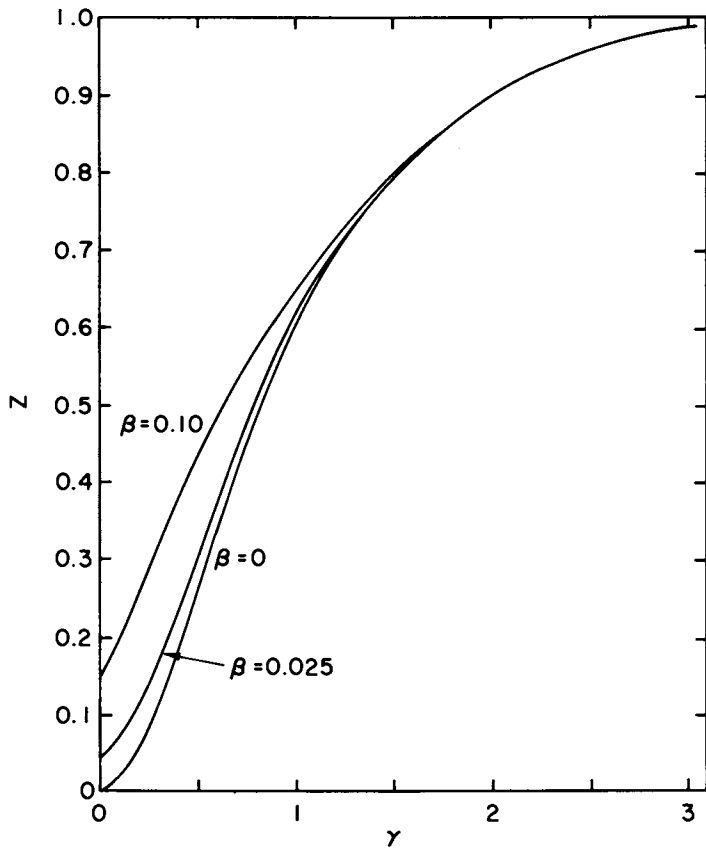


Figure 3. Master plot for Z.

where $q=i-j$ and where the first term represents the contribution from chain transfer and the second term that from termination. The first term in each equation denotes chain transfer and the second denotes termination. In terms of the continuous variable y and using the relationships developed earlier, eq's (22) and (23) become

$$i_c N_d (y) = [\beta + \gamma\{Z + f(y)\} / 2\sqrt{Z}] P(y) \quad (24)$$

$$i_c N_r (y) = \beta P(y) + \gamma(\beta + \gamma\sqrt{Z}) / (2\sqrt{Z}) \int_0^{y/2} [f(t) + f(y-t)] P(t) P(y-t) dt \quad (25)$$

To generate a series of molecular weight averages from the above equations, it is necessary to define the i -th moments of $N(y)$, $P(y)$, and $f(y) P(y)$ as

$$N_i^m \equiv \int_0^\infty y^i N_m (y) dy \quad (26)$$

$$P_i = \int_0^\infty y^i P(y) dy \quad (27)$$

$$F_i \equiv \int_0^\infty y^i f(y) P(y) dy \quad (28)$$

where m can be d or r . Equation (24) or (25) can be substituted into eq'n (26) to give

$$i_c N_i^d = (\beta + \gamma\sqrt{Z}/2) P_i + (\gamma/2\sqrt{Z}) F_i \quad (29)$$

$$i_c N_i^r = \beta P_i + (\gamma/2\sqrt{Z}) (\beta + \gamma\sqrt{Z}) \sum_{j=0}^i \binom{i}{j} F_j P_{i-j} \quad (30)$$

where

$$\binom{i}{j} = i! / (j!(i-j)!)$$

With some algebra, F_i of equation (28) can be expressed as P_i .

$$F_i = (2\sqrt{Z}/\gamma) \{iP_{i-1} - (\beta + \gamma\sqrt{Z}/2) P_i\}, \quad (i \geq 1) \quad (31)$$

$$F_0 = Z/(\beta + \gamma\sqrt{Z})$$

Equations (29)-(31) show that only P_i need to be evaluated for any particular distribution function $f(y)$ to evaluate N_m^i , which is necessary to evaluate molecular weight averages.

The number average degree of polymerization x_n^d or x_n^r can be obtained as

$$x_n^d/i_c = N_1^d/N_0^d = 1/(\beta + \gamma\sqrt{Z}) \quad (32)$$

$$x_n^r/i_c = N_1^r/N_0^r = 1/(\beta + \gamma\sqrt{Z}/2) \quad (33)$$

It should be noted here that eq's (32) and (33) are identical to the more familiar forms

$$1/x_n^d = C_M + C_S [S]/[M] + 1/v \quad (34)$$

$$1/x_n^r = C_M + C_S [S]/[M] + 1/2v \quad (35)$$

where

$$v = k_p [M]/(\bar{k}_t R_i)^{1/2}$$

Equations (34) and (35) show that the number average molecular weight is not affected by the chain length dependence except via \bar{k}_t , which is not unexpected as the same result was shown some time ago by North (1). However, this provides an important criteria that other investigators have not considered. That is if the \bar{k}_t functionality is determined empirically by fitting time-conversion data, then no additional information can be obtained from the number average molecular weight data, as the latter must (by definition) be predicted by the \bar{k}_t dependency obtained from the rate data. It is only the weight average and higher averages ($z, z+1, \text{etc.}$) which contain independent information about the chain length dependency of \bar{k}_t . Thus any proposed model should be

compared to the higher order molecular weight averages to test the validity of the assumptions regarding chain length dependency. It is in this regard that the authors became convinced of the chain length dependency of the termination reactions in vinyl polymerizations because all previous predictions of the higher order molecular weight averages based on chain length independency have failed to fit the experimental data.

As the number average molecular weight is the same for different distribution functions if they yield same average termination rate constant, it is advantageous to define the molecular weight indices, ℓ_i 's, as the ratio of *i*th order molecular weight average to the number average molecular weight M_n ,

$$\ell_i = M_i / M_n \quad (36)$$

For termination by disproportionation, the indices (ℓ_i^d 's) are readily expressed in terms of the moments P_i 's, but for the case of recombination with chain transfer to monomer, it is much simpler to express the ℓ_i^r 's in terms of ℓ_i^d 's. These expressions are given in Table 1. The expressions in this table show that in order to evaluate the molecular weight development for any mode of termination, only the indices for disproportionation are necessary. Since the molecular weight indices are completely determined by $P(y)$ and Z , master plots can also be constructed for the ℓ_i 's. Those for ℓ_w and ℓ_z are shown in Figures 4 and 5, respectively, for the same choice of $f(y)$ as depicted in Figure 3. We think that it is of interest to note that the instantaneous molecular weight distribution indices may change significantly during the reaction (changing values of γ), and that for the form of $f(y)$ used here they deviate markedly from the Schulz-Flory distribution (the latter having $\ell_w^d = 2.0$ and $\ell_z^d = 3.0$).

Equations (17), (21), (32), (33) and those of Table 1 completely determine the instantaneous polymerization kinetics and molecular weight averages. Simple relationships are available

Table 1
Indices of the Molecular Weight Distribution

Molecular Weight Index	Disproportionation	Mode of Termination	Recombination
$\lambda_w \equiv M_w/M_n$	$2(\beta+\gamma\sqrt{Z})^2 P_1$		$f_1 f_0 \ell_w^d$
$\lambda_z \equiv M_z/M_n$	$3/2(\beta+\gamma\sqrt{Z}) P_2/P_1$		$3(f_1/f_2)(2\ell_z^d + \ell_w^d/2 - f_1 \ell_w^d \ell_z^d)$
$\lambda_{z+1} \equiv M_{z+1}/M_n$	$4/3(\beta+\gamma\sqrt{Z}) P_3/P_2$		$4f_1 \ell_z^d (f_2 \ell_{z+1}^d + \ell_w^d [1 - (\ell_w^d + \ell_z^d) / 2]) / \ell_z^d (2 - f_1 \ell_w^d + \ell_w^d / 2)$
$\lambda_{z+i} \equiv M_{z+i}/M_n$	$(\frac{i+3}{i+2})(\beta+\gamma\sqrt{Z}) P_{2+i}/P_{1+i}$		

$$f_1 \equiv N_0^I = (\beta+\gamma\sqrt{Z}/2) / (\beta+\gamma\sqrt{Z}) = M_n^I/M_n^d$$

$$f_2 \equiv 2 - f_1 \ell_w^d / 2$$

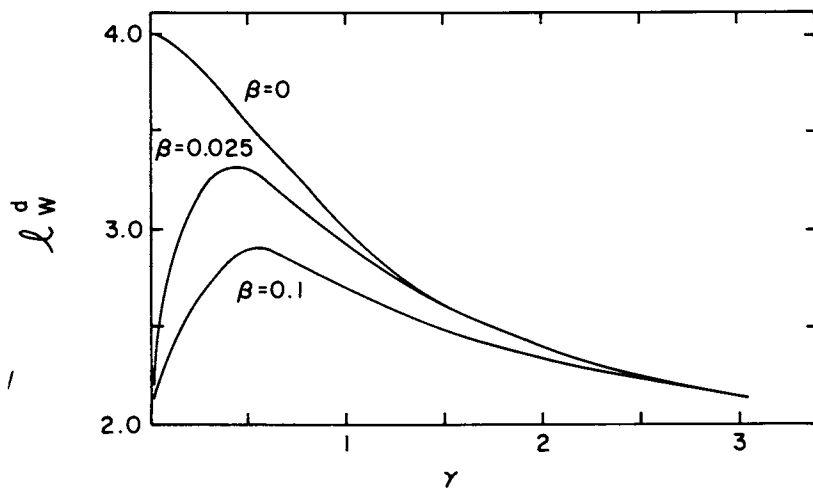


Figure 4. Master plot for l_w^d .

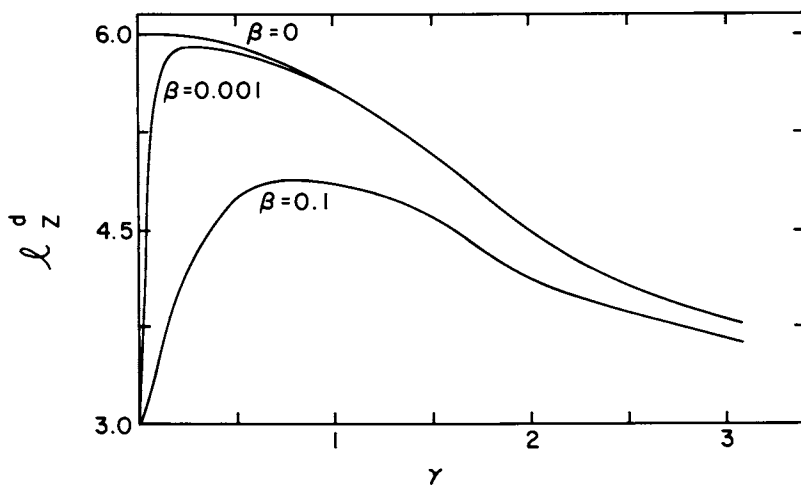


Figure 5. Master plot for l_z^d .

to relate the cumulative values to the instantaneous values (5). Given the functional form of $f(y)$, the indices Z and ℓ_i 's need to be calculated only once and can be used for any polymerization system. The conversion dependency of $k_{t\text{vf}}$ and i_c must be specified, but the choice is arbitrary. Thus there are only two dimensionless parameters, β and γ , which determine the entire polymerization behavior.

Although it is beyond the scope of this paper to delve very deeply into application of the model, it may be useful to show in a limited fashion the type results that are attainable. Figures 6 and 7 show the comparison of molecular weight data for methyl methacrylate (7) and ethyl methacrylate (8) and the respective model predictions. The details of the simulations are given elsewhere (6). These figures show how dramatic the changes in molecular weight can be and the capability of a particular form of the chain length dependent model in predicting those changes.

Conclusions

A general method of computing the polymerization kinetics and molecular weight development for systems experiencing the gel effect and resultant chain length dependent termination reactions has been established. The generality of this procedure allows for arbitrary choices of both the chain length and conversion dependencies of the termination rate constant. This method has been applied to a wide variety of polymerization systems to test a particular form of the chain length and conversion dependency (5, 6). Remarkable success has been achieved for such diverse systems as methyl methacrylate, ethyl acrylate, vinyl acetate, styrene, ethyl methacrylate and propyl acrylate.

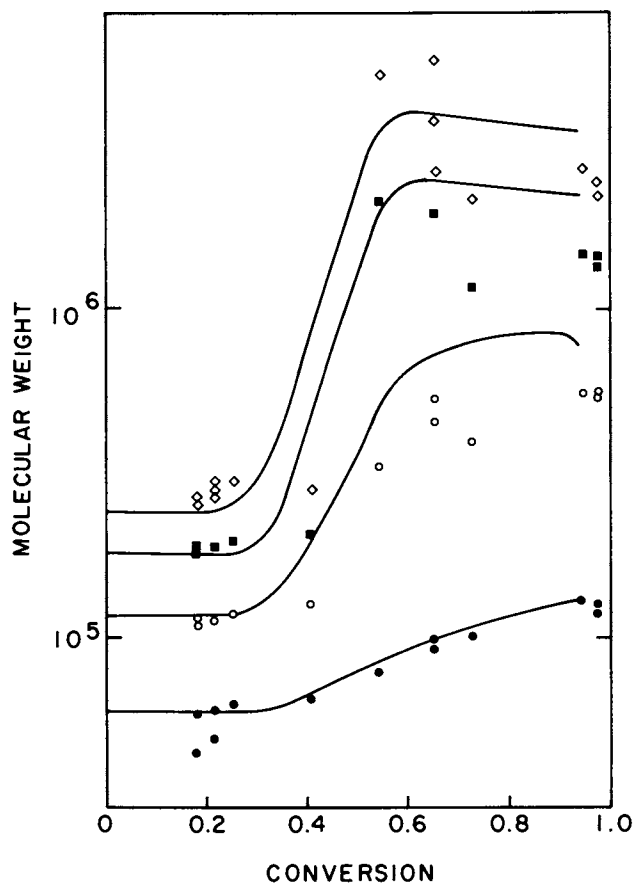


Figure 6. Molecular weight data (7) and model predictions for poly(methyl methacrylate). Key: ●, M_n ; ○, M_w ; ■, M_z ; ◇, M_{z+1} .

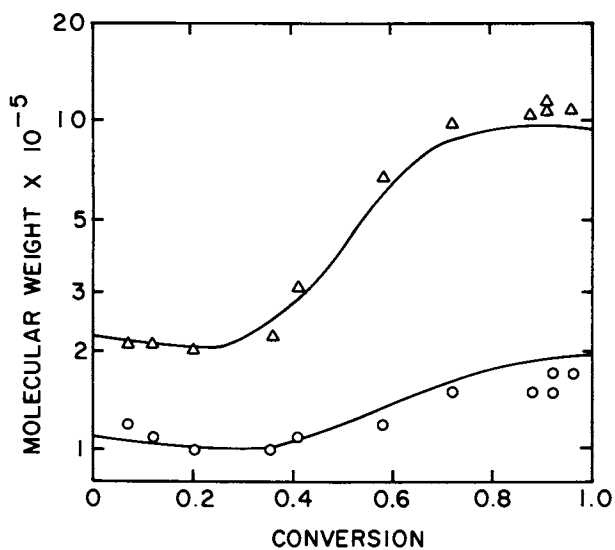


Figure 7. Molecular weight data (8) and model predictions for poly(ethyl methacrylate). Key: \circ , M_n ; \triangle , M_w .

Literature Cited

1. S.W. Benson and A.M. North, *J. Am. Chem. Soc.* 81, 1339 (1959), 84, 935 (1962).
2. J.N. Cardenas and K.F. O'Driscoll, *J. Polymer Sci. Polymer Chem. Ed.*, 14, 883 (1976), 15, 1883 (1977).
3. K. Ito, *J. Polymer Sci., Polymer Chemistry Ed.*, 12, 1991 (1974), 15, 1759 (1977), 18, 701 (1980), *Polymer J.*, 11, 795 (1979).
4. T. Yasakawa and K. Murakami, *Polymer*, 21, 1423 (1980).
5. S.K. Soh, Ph.D. Thesis, Univ. of New Hampshire, Durham, NH 03824 (1981).
6. S.K. Soh and D.C. Sundberg, accepted for publication in *J. Polymer Sci., Polymer Chem. Ed.* (1982).
7. S.T. Balke and A.E. Hamielec, *J. Appl. Polymer Sci.*, 17, 905 (1973).
8. J.N. Cardenas and K.F. O'Driscoll, *J. Polymer Sci., Polymer Chem. Ed.*, 15, 2097 (1977).

RECEIVED May 4, 1982.

Analysis of Molecular Weight Distribution Using Multicomponent Models

EPHRAIM BROYER

Allied Corporation, Corporate Research & Development, Morristown, NJ 07960

RICHARD F. ABBOTT

Allied Corporation, Allied Fibers & Plastics, Baton Rouge, LA 70805

The analysis of molecular weight distribution is an important tool in polymerization and is used widely in quality control, development of new grades, polymerization reaction engineering and in assessing the effects of processing on properties. In this work, a polymer is considered as a blend of defined components. Each component is described by a molecular weight distribution model. In this study the models of Flory, Schulz-Zimm and Wesslau were used. A computer program was written, which calculates the weight fraction of each component and the parameters defining its distribution. Characterization of molecular weight distribution is transformed, therefore, to a non-linear regression analysis, which can be solved by any number of different techniques. The components of the blend can be related to catalyst activity or to operating conditions of the polymerization reactors. The method was used to analyze GPC curves of HDPE samples. Good description of the distribution was obtained with 2-5 components. The Wesslau model requires the smallest number of components to define a molecular weight distribution for HDPE.

The importance of molecular weight distribution in studies of polymerization, polymer processing and the physical and mechanical properties of polymers creates a need for mathematical description of the distribution. Several models are commonly used (Flory [1], Schulz-Zimm

0097-6156/82/0197-0045\$06.00/0

© 1982 American Chemical Society

[2], Wesslau [3] and Tung [4]). Often these simple models do not describe adequately the measured distribution of Commercial polymers. Theoretical derivations for the blending of two components with known distributions have been reported [5]. These studies concentrated on the effect of the parameters on the MWD of the blend.

This work originated from the need to reproduce mathematically the MWD as measured by GPC. The proposed method describes a polymer as a blend of components; each of them is defined by its parameters and weight fraction. It provides the information needed in the development and engineering of a polymerization process and can be related to operating conditions and catalyst performance.

MULTI-COMPONENT MODELS

A polymer in this study is assumed to be a blend of several components. Each component is defined by its weight fraction and a MWD, which is described by a model. A general equation for the weight fraction of molecules of size P (P - degree of polymerization) is given by

$$W(P) = \sum_1^N g_i w_i(\bar{C}_i, P) \quad (1)$$

where

$$\sum_1^N g_i = 1 \quad (2)$$

N is the number of components in the blend and g_i is the weight fraction of the i^{th} component. w_i is the equation describing the MWD of the i^{th} component calculated for molecules of size P, with parameters given by the vector \bar{C} . Equation 2 is a mass balance for the system. Use of a linear combination of the models leads to a simple evaluation of the molecular weight averages of the system. In this study the MWDs of the components are described by the models proposed by Flory, Schulz and Zimm, and Wesslau. A brief description of each model and its characteristics is given. The equations of the average molecular weights of the blends are also presented.

Flory Distribution Model

The Flory distribution is a random distribution useful in several modes of polymerization. This distribution results from addition polymerization reactions when the only significant processes that interrupt macromolecular growth are either or both of chain transfer (to any species but the polymer) or termination by disproportionation. Likewise, this molecular weight distribution describes linear condensation polymerization when equal reactivity is assumed for all ends only when the reaction involves an equilibrium between polymerization and depolymerization. The model describes the distribution with one parameter which is the number average molecular weight. The distribution equation is:

$$W(P) = y^2 P \exp(-yP) \quad (3)$$

where

$$y = \frac{1}{P_n} = \frac{2}{P_w} = \frac{3}{P_z} \quad (4)$$

y is the reciprocal of the number average degree of polymerization. The indices n, w, and z are for the number, weights, and z molecular weight averages. The simplicity of the Flory distribution (1 parameter), the constant ratio between the averages, and its theoretical derivation are the main reasons for its use. In a blend of N components, each defined by a Flory distribution, the weight fraction of molecules of size P is given by:

$$W(P) = \sum_1^N g_i y_i^2 P \exp(-y_i P) \quad (5)$$

Equation 5 results from combining Equations 3 and 1. A molecular weight distribution is defined, according to this scheme, by (2N-1) parameters. The reduction of one parameter results from imposing the constraint of Equation 2.

Schulz-Zimm Distribution Model

This is a specific case of the generalized exponential distribution. It was derived to describe polymerization with a constant rate of initiation and termination by second order interaction with

American Chemical
Society Library

the monomer. It provides description for vinyl and condensation polymers. It is a two parameter model given by:

$$W(P) = \frac{Y^{a+1} P^a}{\Gamma(a+1)} \exp(-YP) \quad (6)$$

where

$$Y = \frac{a}{P_n} = \frac{a+1}{P_w} = \frac{a+2}{P_z} \quad (7)$$

The reciprocal of a measures the breadth of the distribution and Γ is the gamma function. Although this model provides an adequate fit for the distribution curves, the calculated parameters may lead to erroneous molecular weight averages.

If a polymer is considered as a blend of components, the distribution equation is:

$$W(P) = \frac{N \sum_i g_i Y_i^{a_i+1} P^{a_i}}{\Gamma(a_i+1)} \exp(-Y_i P) \quad (8)$$

(3N-1) parameters must be determined to describe the MWD.

Wesslau Distribution Model

This is a specific case of the generalized logarithmic distribution. It is a log-normal distribution which allows one to cover a wide range of molecular weights. The weight fraction of the logarithm of the molecular size is assumed to be normally distributed. The distribution is defined by two parameters and is given by:

$$W(P) = \frac{1}{\beta P \sqrt{\pi}} \exp \left\{ - \left[\frac{\ln(P/P_0)}{\beta} \right]^2 \right\} \quad (9)$$

where

$$P_0 = \frac{P_n}{\exp(-\beta^2/4)} = \frac{P_w}{\exp(\beta^2/4)} = \frac{P_z}{\exp(3\beta^2/4)} \quad (10)$$

P_0 is the median value of the distribution, that is, one half of the values of P are less than P_0 , and it is the standard deviation of $\ln P$. A constant ratio of $\exp(\beta^2/2)$ is observed between the molecular weight averages. The peak of the MWD is located at $P_n^{3/2}/P_w^{1/2}$. In case the polymer is considered to be a blend, the weight distribution is given by:

$$W(P) = \sum_1^N \frac{g_i}{\beta_i P \sqrt{\pi}} \exp \left\{ - \left[\frac{\ln(P/P_{0i})}{\beta_i} \right]^2 \right\} \quad (11)$$

As with the Schulz-Zimm model, one needs to evaluate $(3N-1)$ parameters to characterize a blend. A graph of the blend cumulative distribution on probability log paper will result in a curve composed of several straight segments.

Average Molecular Weights

Evaluation of the number, weight and Z molecular weight averages of the blend is done after these molecular averages are calculated for each component. Equations 4, 7, and 10 provide relations between the parameters of the models and the molecular averages of the components. The molecular weight averages of the blend are calculated according to addition rules and are a function only of the molecular averages and the weight fraction of each component.

The number average molecular weight is:

$$\bar{M}_n = \left[\sum_1^N g_i / M_{ni} \right]^{-1} \quad (12)$$

The weight average molecular weight is:

$$\bar{M}_w = \sum_1^N g_i M_{wi} \quad (13)$$

The Z average molecular weight is:

$$\bar{M}_z = \sum_1^N g_i M_{wi} M_{zi} / \bar{M}_w \quad (14)$$

CALCULATION OF THE PARAMETERS

Molecular weight distribution is usually measured by GPC or other fractionation techniques. The accuracy of fraction separation depends on factors like the length of the column, flow rate and concentration. A common GPC measurement describes a distribution by 20-30 fractions.

Evaluation of the parameters in equations 5, 8 and 11 can be done by:

A. Integration of these equations and comparison with a cumulative distribution or the differential distribution as provided by the normalized GPC chromatogram.

B. Differentiation of the cumulative distribution to weight fractions of one unit of degree of polymerization, and directly compare them with equations 5, 8 and 11.

In both methods, a non-linear regression procedure is needed to evaluate the parameters. The use of the integration procedure may require long computation times, especially if a model cannot be integrated analytically. We, therefore, decided to use the differential form of the distribution and numerically differentiated the cumulative distributions. The cumulative distribution was piece-wise interpolated and for each fraction the differential was calculated as the weight fraction of molecules of size P . The differentiating procedure is described schematically in Figure 1. Differentiating by such a numerical technique is done once for each GPC reading. The fitting of these data points is tested with the various models. Numerical differentiating through this interpolation procedure provides adequate accuracy, but other interpolation procedures may be used.

The main purpose of this work was to reproduce the whole MWD and the objective function of the non-linear regression was to minimize the sum of relative errors. Determination of each basic model starts with one component and the number of components is increased until an acceptable fit is obtained between the computed curve and measured one. Agreement has to be reached also between the values of the computed and experimental molecular averages.

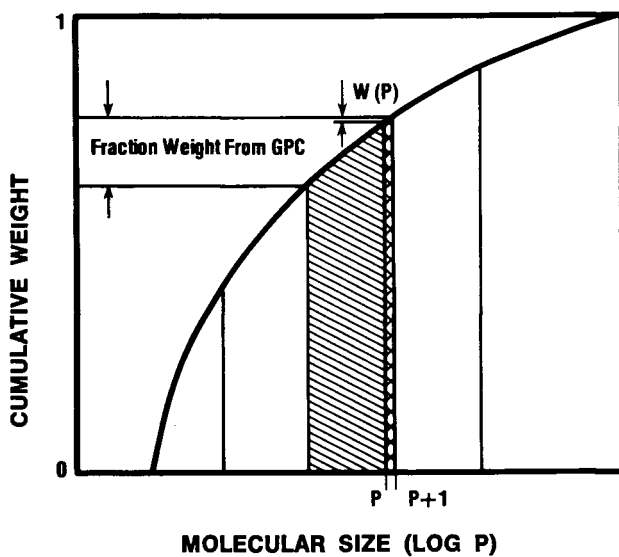


Figure 1. Schematic description of the calculation of the differential weight fraction.

ANALYSIS OF THE GPC OF HDPE

The chromatograms of three samples of high density polyethylene were analysed according to the procedures outlined in the previous sections. The parameters calculated for each model are listed on the respective graphs.

Sample 1 is a polymer with a relatively narrow molecular weight distribution which was characterized by 115 fractions. Its weight average $M_w = 6.22 \times 10^4$, and its dispersity is given by $M_w/M_n = 2.68$ and $M_z/M_w = 3.07$. All the multicomponents models give adequate fit to the molecular weight averages, but the Wesslau models provide it with the least number of components. Figures 2-5 are plots of several reproduction attempts with the tested models. The Wesslau model, which is considered as the best description for MWD of Ziegler type polymerization, provided the best reproduction of the distribution curve. A one component Wesslau model (Figure 2) provides good agreement with the molecular weight averages, but there are large deviations between the estimates and the measurements. A two component Wesslau model (Figure 3) provides excellent fit to the MWD curve and the averages. The addition of the component of high molecular weight (only 1% weight) and small changes in the parameters of the main component resulted in this excellent fit. The Schulz-Zimm (Figure 4) or the Flory models (Figure 5) do not provide a good fit to the MWD with the same number of components.

HDPE Sample 2 is a polymer with a wide MWD, where $M_w = 7.34 \times 10^4$, $M_w/M_n = 6.33$ and $M_z/M_w = 15.9$. The last dispersity ratio is large because of the tail of high molecular weight fractions. A 3 component Flory model (Figure 6) describes well the high molecular weight tail but the reproduction of the MWD is not satisfactory. 2 component Schulz-Zimm model (Figure 7) does not adequately reproduce the distribution. Figure 8 describes the results of a 2 component Wesslau model. Although a one component model provides good fit to most of the MWD, the high molecular weight tail (which

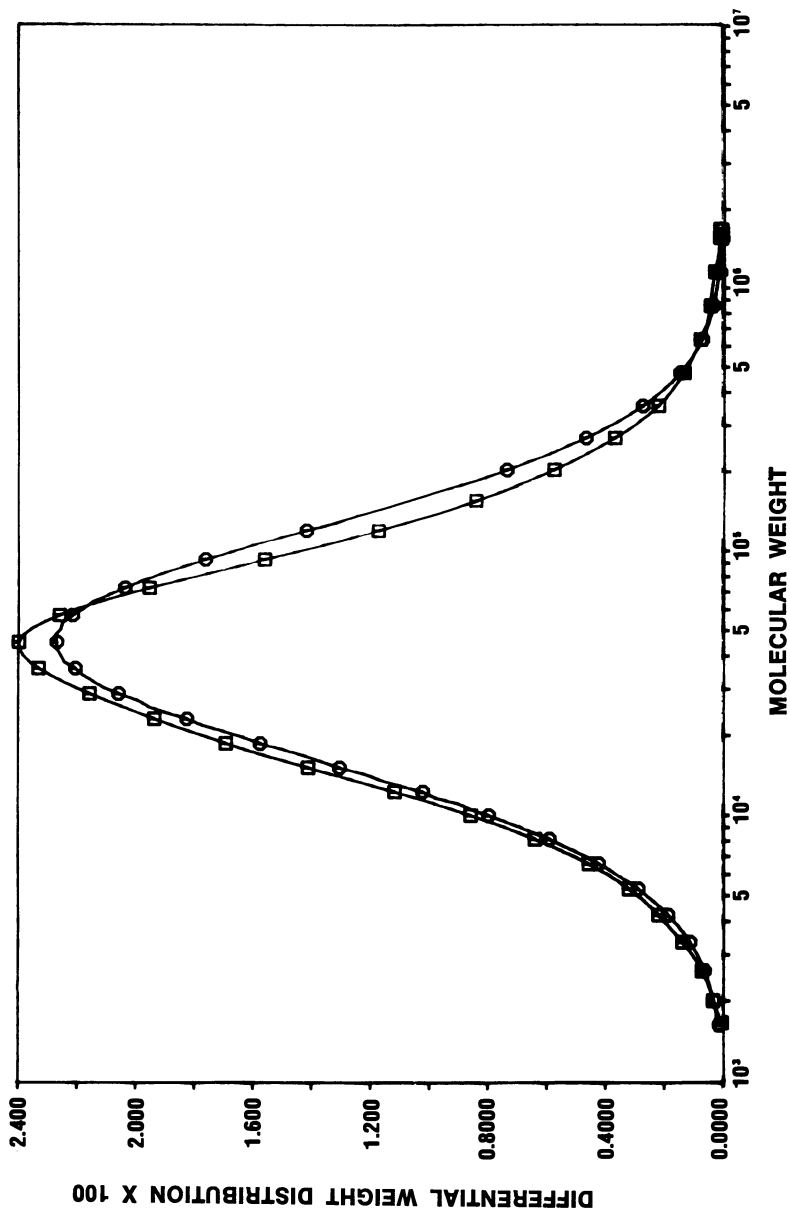


Figure 2. Analysis of MWD of polyethylene sample 1 by 1-component Wesslau model. Key: \square , experiment and \circ , model. $\beta = 1.42$, $M_0 = 3.93 \times 10^4$.

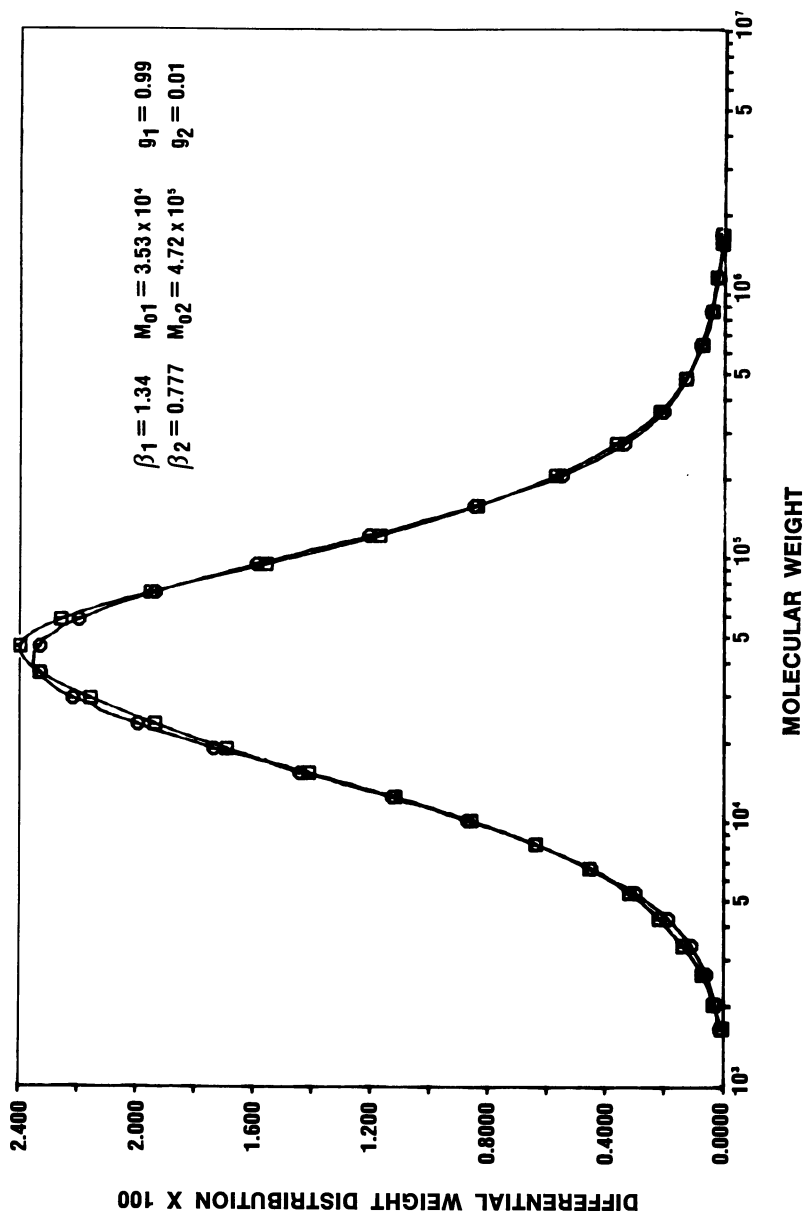


Figure 3. Analysis of MWD of polyethylene sample 1 by 2-component Weibull model. Key: \square , experiment and \circ , model.

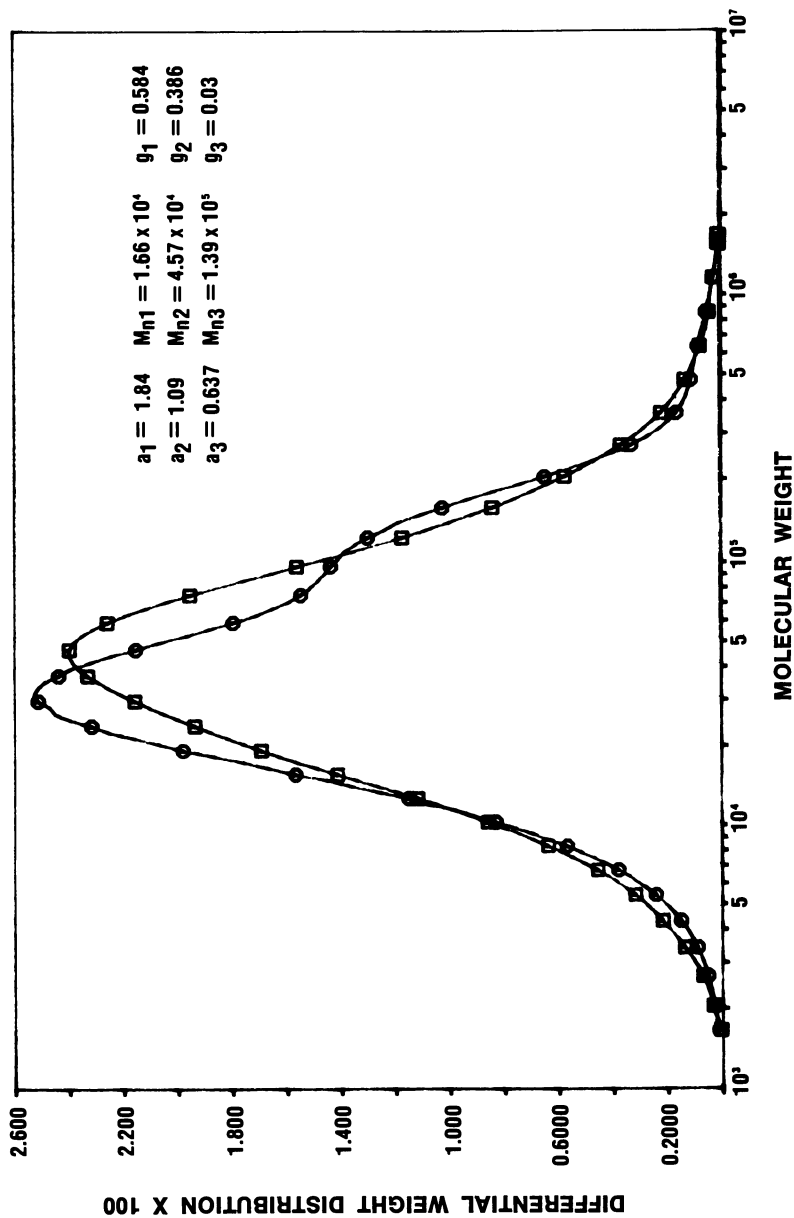


Figure 4. Analysis of MWD of polyethylene sample 1 by 3-component Schulz-Zimm model. Key: □, experiment and ○, model.

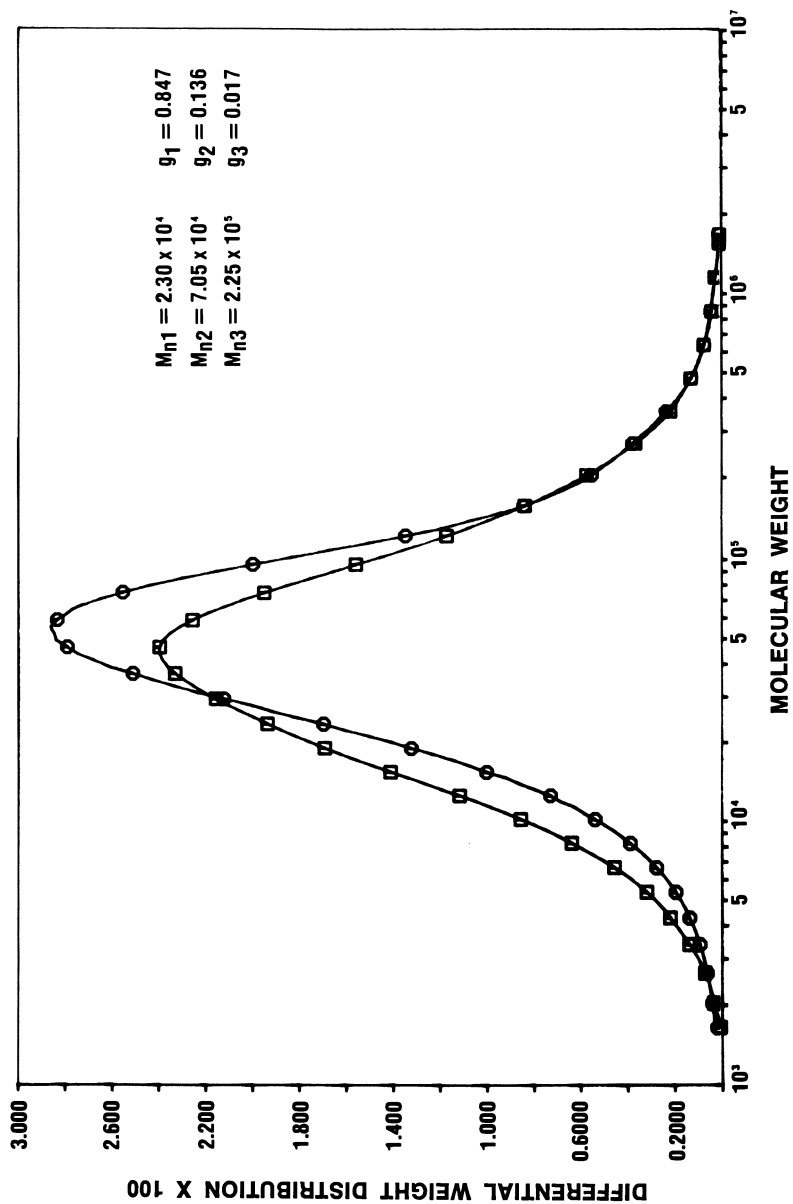


Figure 5. Analysis of MWD of polyethylene sample 1 by 3-component Flory model. Key: □, experiment and ○, model.

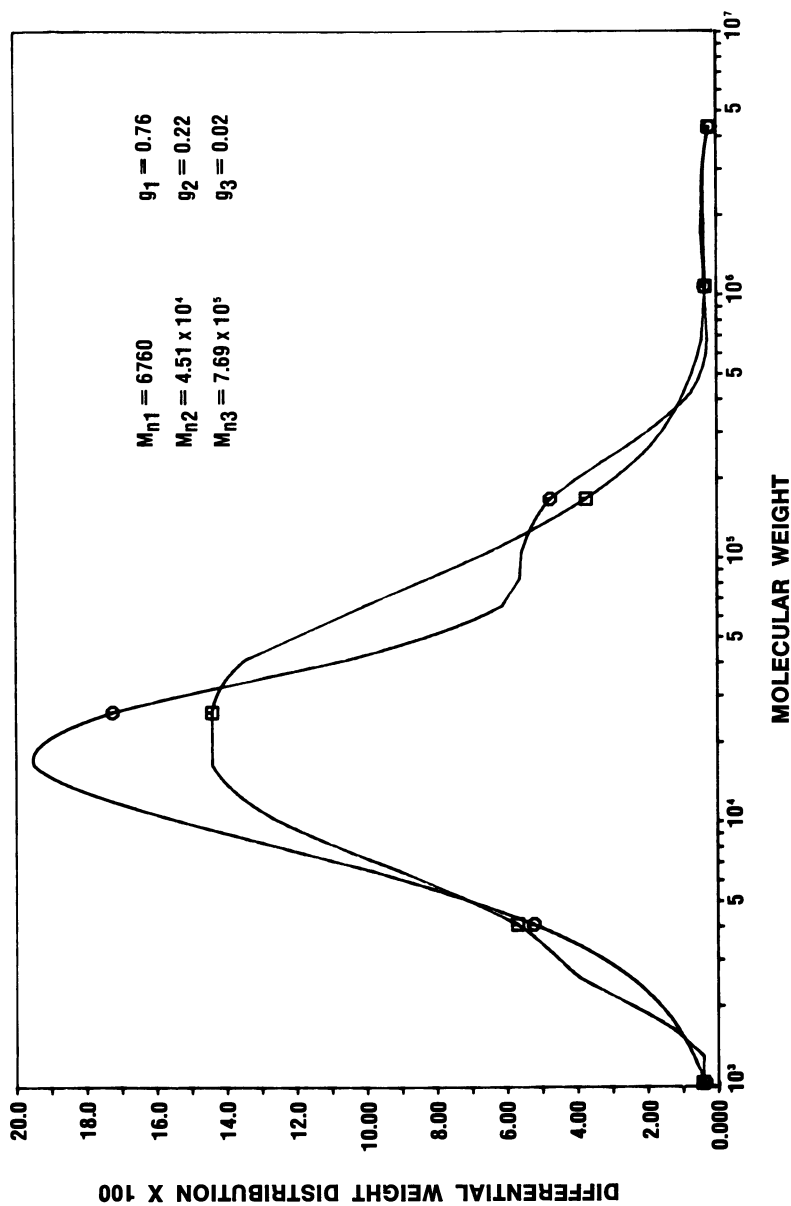


Figure 6. Analysis of MWD of polyethylene sample 2 by 3-component Flory model. Key: \square , experiment and \circ , model.

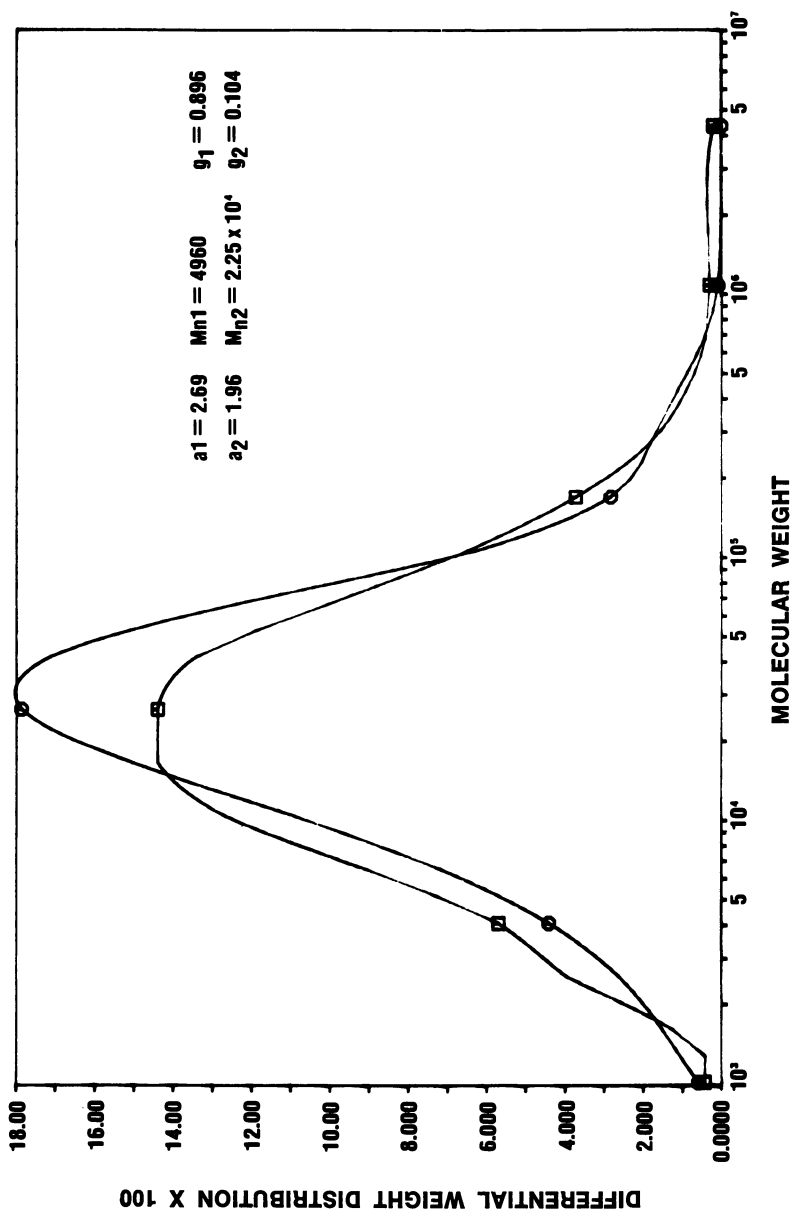


Figure 7. Analysis of MWD of polyethylene sample 2 by 2-component Schulz-Zimm model. Key: □, experiment and ○, model.

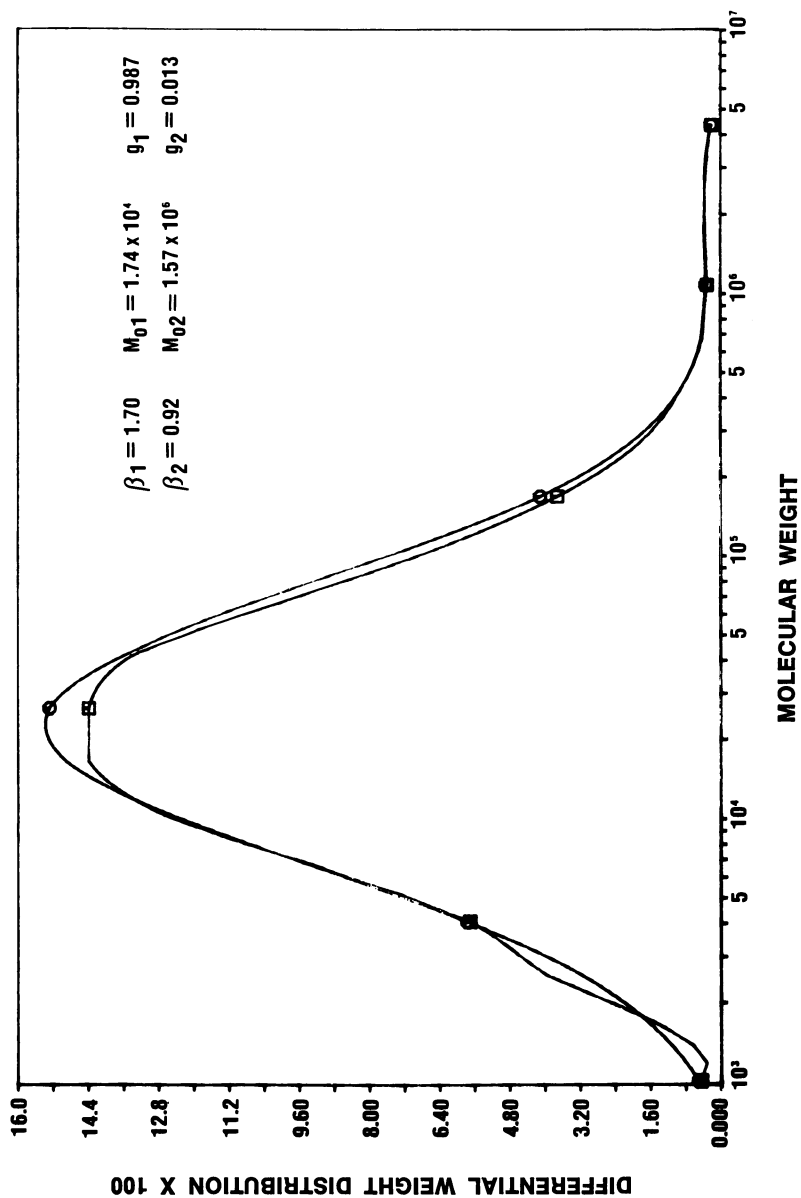


Figure 8. Analysis of MWD of polyethylene sample 2 by 2-component Weslau model. Key: □, experiment and ○, model.

affects the rheology of the polymer) is not adequately accounted for. Addition of 1.3% of the high molecular weight fraction improves the reproduction of the MWD remarkably.

HDPE Sample 3 is a polymer with a bimodal distribution, characterized by $M_w = 3.10 \times 10^5$ and dispersity defined by $M_w/M_n = 39.3$ and $M_z/M_w = 6$. The bimodal shape affects considerably the rheological and the mechanical properties of the distribution and a good reproduction of the distribution is therefore essential. Vast differences are found between averages calculated from the GPC and the regressed parameters. Examination of Figures 9-11 shows, however, that acceptable fit was obtained between the multi component models and the experiments. The 3 component Flory model (Figure 9) and the 2 component Schulz-Zim model (Figure 10) give only a fair fit. The 2 component Wesslaw model (Figure 11) provides; however, very good reproduction of the MWD.

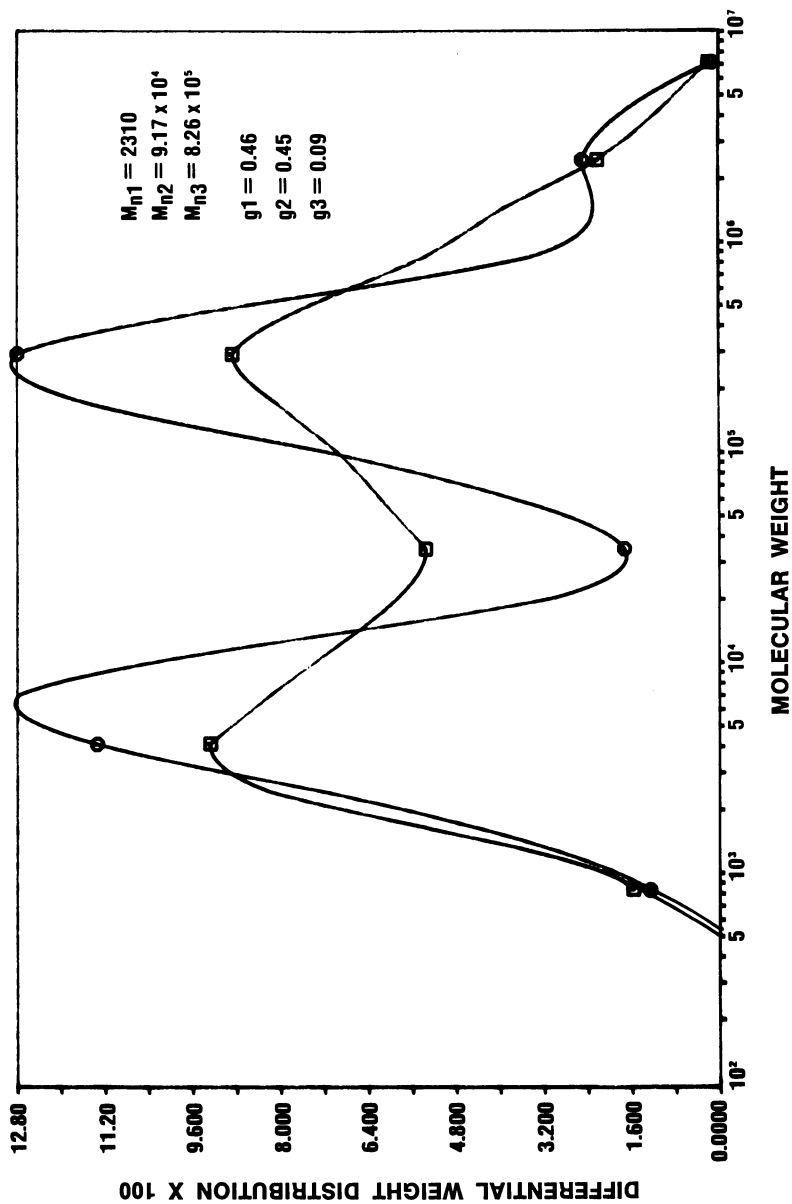


Figure 9. Analysis of MWD of polyethylene sample 3 by 3-component Flory model. Key: \square , experiment and \circ , model.

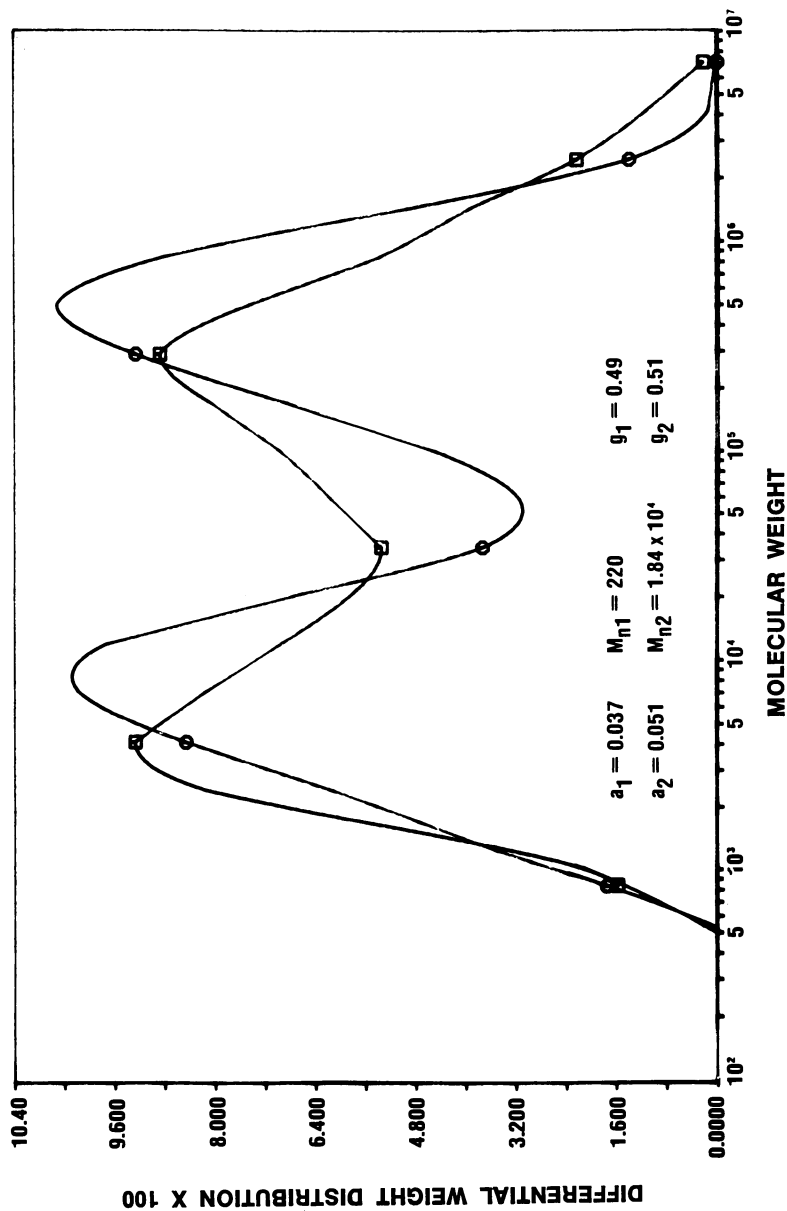


Figure 10. Analysis of MWD of polyethylene sample 3 by 2-component Schulz-Zimm model. Key: □, experiment and ○, model.

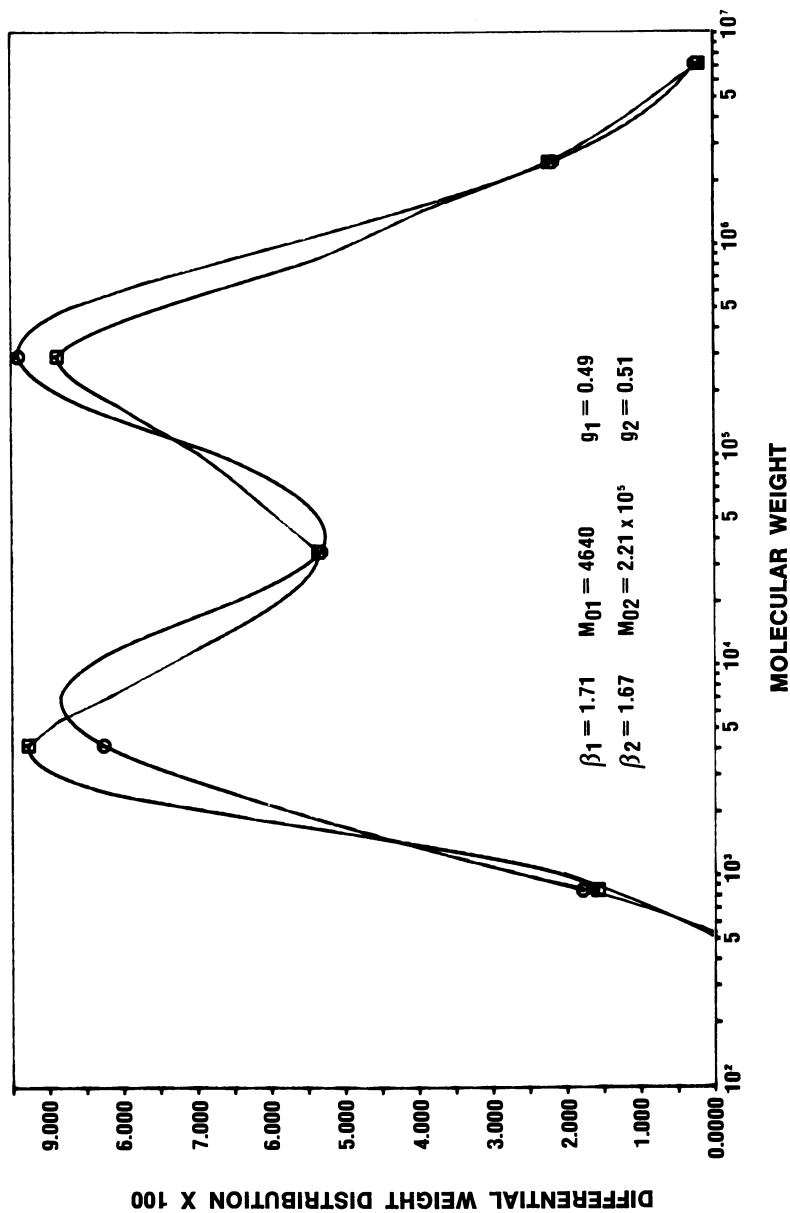


Figure 11. Analysis of MWD of polyethylene sample 3 by 2-component Weibull model. Key: \square , experiment and \circ , model.

Acknowledgment

The authors are grateful to H. D. Oltmann and A. M. Kotliar for their valuable advice.

Literature Cited

1. P.J. Flory, Principles of Polymer Chemistry, Cornell University Press, Ithaca New York, (1953).
2. G.V. Schulz, Z Physik. Chem., B43, 25 (1939).
3. H. Wesslau, Makromol. Chem., 20, 111 (1956).
4. L.H. Tung, J. Polym. Sci., 20, 495 (1956).
5. A.M. Kotliar, J. Polym. Sci., A2, 1057 (1964).

RECEIVED May 4, 1982.

Use of Continuous System Modeling Program (CSMP) to Simulate Polymerization, Polycondensation, and Polymer Modification Reactions

H. JAMES HARWOOD, ANDRZEJ DWORAK¹, TING KEN L. NYEU,
and SHEN-NAN TONG²

University of Akron, Institute of Polymer Science, Akron, OH 44325

A brief introduction to IBM's CSMP (Continuous System Modeling Program) is provided. This program is a powerful, easily used tool for numerically integrating complex systems of differential equations, such as are often encountered in considerations of dynamic processes involving polymers. This paper illustrates its application to problems encountered in studies on polymer modification reactions, polymer epimerization reactions, p-cresol-formaldehyde condensation reactions, and monomer-promoted polyaddition reactions. A 23-statement CSMP program was written, for example, to duplicate the predictor-corrector program of Bauer for simulating irreversible polymer modification reactions. By adding only about ten additional statements to this program, a program for simulating reversible polymer modification and epimerization reactions was derived. Use of CSMP to generate plotted output and to evaluate kinetic parameters are also illustrated.

Polymerization, polycondensation and polymer modification reactions are dynamic processes that are often represented by sets of differential equations. Analytical integration of such equations is often difficult or impossible and the solutions that are obtained often have complex forms that provide limited insight concerning the nature of the processes. This has been particular-

¹ Institute of Polymer Chemistry, Polish Academy of Sciences, Zabrze, Poland.

² Union Industrial Research Laboratories, Industrial Technology Research Institute, Hsin-chu, Taiwan, R.O.C.

0097-6156/82/0197-0065\$06.25/0

© 1982 American Chemical Society

ly true for polymer modification reactions. Numerical integration of the differential equations by the Runge-Kutta or predictor-corrector methods provides numerical information that is useful for studying these processes and equivalent information can be obtained by Monte Carlo simulations. Unfortunately these approaches require extensive computer programming. This difficulty can be overcome, however, if a continuous system simulation language such as IBM's CSMP language is used for the programming. It is possible for chemists with only a rudimentary knowledge of FORTRAN (or BASIC) to use CSMP. The programming required to simulate most polymerization, polycondensation or polymer-modification reactions is only slightly more than is required to define the differential equations involved. This will be illustrated for a number of examples in the remainder of this paper.

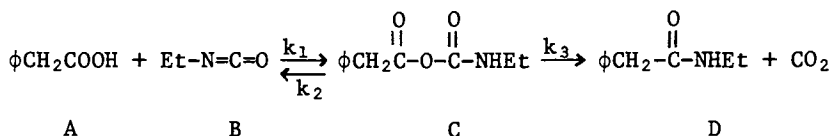
CSMP Language

A number of continuous system languages (CSSL, MIMIC, SL-1, DSL-90, LEANS, MIDAS) have been written for use with digital computers to obtain the performance of an analog or analog-digital hybrid computer. These have been used very effectively for calculations and simulations involving dynamic systems such as are encountered in mechanical, electrical, aeronautical and chemical engineering, in process control, and in chemical or biochemical kinetic studies. A particularly powerful language in this class is the IBM product CSMP (Continuous System Modeling Program) (1). This language utilizes function and structure statements that correspond to devices normally found in analog computers (integrators, differentiators, function generators, delays, limiters, pulse generators, logic functions, etc.). Differential equations and other functions are written in standard FORTRAN language. Integrations are done by methods selected by the programmer, the fifth order predictor-corrector Milne or fourth order Runge-Kutta methods being among the possible options. The statement for calculating $x = a + \int_0^t (bt+ct^2)dt$ is written simply as $X = \text{INTGRL}(A,B*T + C*T**2)$, for example.

Functions describing dynamic aspects of a system are calculated together at each time interval and the CSMP compiler sorts the functions into a logical sequence. The SORT capability of CSMP can be overridden to enable conventional FORTRAN programming to occur in certain sections. The full range of FORTRAN programming is possible, including the use of the Scientific Subroutine Package. This makes it possible to use CSMP for parameter optimization or evaluation (2). Output instructions in CSMP are very simple. PRINT and PRTPLOT statements require only a listing of the items of interest and the PREPARE statement can be used to write output on an external device for processing by user developed plotting routines. Other features of CSMP will become evident in the programming to be described below, but the CSMP User's Manual should be consulted for information about all the capabilities of CSMP.

A Simple Kinetic Problem

During studies on the mechanism of N-carboxy anhydride polymerization, it became desirable to simulate the following reaction.



Because of the relative simplicity of this system, we will consider its simulation by CSMP in detail, to acquaint the reader with the general features of CSMP programming. The following system of differential equations describes the above reaction sequence.

$$\frac{d(\text{A})}{dt} = -k_1(\text{A})(\text{B}) + k_2\text{C}$$

$$\frac{d(\text{B})}{dt} = -k_1(\text{A})(\text{B}) + k_2\text{C}$$

$$\frac{d(\text{C})}{dt} = -(k_2 + k_3)(\text{C}) + k_1(\text{A})(\text{B})$$

$$\frac{d(\text{D})}{dt} = k_3\text{C}$$

Program A can be used to simulate this reaction.

PROGRAM A

```

TITLE ISOCYANATE-ACID REACTION SIMULATION
PARAMETER K1=1.00E-04,K2=1.00E-04,K3=10.0E-04
INCON A=0.8000, B=0.8000, C=0, D=0
DYNAMIC
      DADT=-K1*A*B+K2*C
      DBDT=-K1*A*B+K2*C
      DCDT=K1*A*B-K2*C-K3*C
      DDDT=K3*C
      A=INTGRL(0.8000,DADT)
      B=INTGRL(0.8000,DBDT)
      C=INTGRL(0.0,DCDT)
      D=INTGRL(0.0,DDDT)
TIMER FINTIM=2000.,OUTDEL=5
FINISH D=0.8000
PRIPLOT A,C,D
PRINT A,C,D
PREPARE A,B,C,D
LABEL NCAMODEL KINETICS
END
STOP

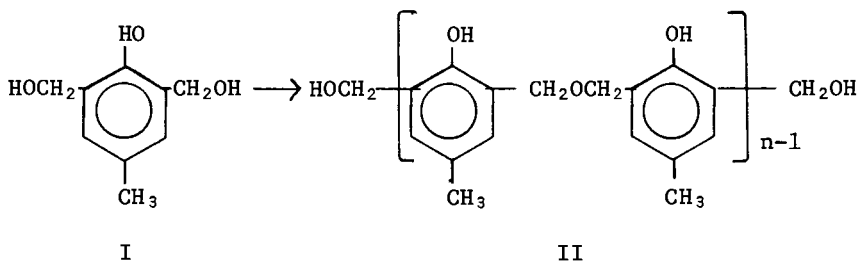
```

The TITLE and LABEL statements are simply used to provide headings for the program output and could be omitted. The PARAMETER and INCON statements illustrate one way of providing data to the program. Thus, the PARAMETER statement provides values of the rate constants, k_1 , k_2 and k_3 and the INCON statement provides initial reactant concentrations.

The DYNAMIC part of the program contains definitions of the differentials DADT, DBDT, DCDT and DDDT as well as instructions to integrate them [i.e., $A = \text{INTGRL}(0.2476, \text{DADT})$]. The TIMER statement indicates that the calculation should be done for 2000 time units (e.g., seconds) and the output should be provided every 5 time units. However, the FINISH statement requests that the calculation stops when the concentration of D reaches 0.2476. The PRINT statement provides a listing of A, C and D concentrations as a function of time. Figure 1 shows a partial listing of the output generated by this statement. The PRTPLOT statement provides the same information, except that the printer generated plots of species concentrations are provided as a function of time. Figure 2 shows a partial listing of the output provided by this statement. The PREPARE statement writes A, B, C and D concentrations and TIME on an external device for use by a separate plotting routine. Figure 3 shows the plot generated by this data and the plotting routine shown in Figure 4. The plotting program reads T(time), A, B, C and D values, provided via the PREPARE option, from device 8 and then constructs plotted lines from them. Experimental data, read from device 5, are plotted as symbols.

This example shows how simple it can be to write a CSMP program. It would have required only a few more statements to have included the possibility that C is also in equilibrium with two symmetrical anhydrides, one of which can decarboxylate to form a disubstituted area. DeTar's program (3) REMECH could also have been used for these calculations. Although we have no experience with this program, it seems that it would be at least as difficult to prepare input for REMECH as it would be to simply write a program in CSMP.

Resole Polycondensation



By use of 300 MHz pmr spectroscopy, it is possible to measure the concentrations of monomer (I), dimer (II, $n = 2$), trimer

ISOCYANATE-ACID REACTION SIMULATION

TIME		A	C	D
0.0		8.0000E-01	0.0	0.0
5.0000E-01	00	7.9968E-01	3.1899E-04	7.9832E-07
1.0000E-01	01	7.9936E-01	6.3598E-04	3.1866E-06
1.5000E-01	01	7.9904E-01	9.5098E-04	7.1548E-06
2.0000E-01	01	7.9872E-01	1.2640E-03	1.2693E-05
2.5000E-01	01	7.9840E-01	1.5750E-03	1.9791E-05
3.0000E-01	01	7.9809E-01	1.8841E-03	2.8440E-05
3.5000E-01	01	7.9777E-01	2.1913E-03	3.8629E-05
4.0000E-01	01	7.9745E-01	2.4965E-03	5.0350E-05
4.5000E-01	01	7.9714E-01	2.7997E-03	6.3591E-05
5.0000E-01	01	7.9682E-01	3.1011E-03	7.8344E-05
5.5000E-01	01	7.9650E-01	3.4005E-03	9.4599E-05
6.0000E-01	01	7.9619E-01	3.6981E-03	1.1235E-04
6.5000E-01	01	7.9587E-01	3.9938E-03	1.3158E-04
7.0000E-01	01	7.9556E-01	4.2876E-03	1.5228E-04
7.5000E-01	01	7.9524E-01	4.5795E-03	1.7445E-04
8.0000E-01	01	7.9493E-01	4.8696E-03	1.9807E-04
8.5000E-01	01	7.9462E-01	5.1579E-03	2.2314E-04
9.0000E-01	01	7.9430E-01	5.4443E-03	2.4965E-04

Figure 1. Typical output resulting from the PRINT statement in CSMP programs.

NCAMODEL KINETICS

TIME	C	MINIMUM 0.0	MAXIMUM 4.2764E=02
0.0	0.0	+	I
5.0000E 00	3.1899E-04	+	
1.0000E 01	6.3598E-04	+	
1.5000E 01	9.5098E-04	-+	
2.0000E 01	1.2640E-03	-+	
2.5000E 01	1.5750E-03	++	
3.0000E 01	1.8841E-03	---+	
3.5000E 01	2.1913E-03	---+	
4.0000E 01	2.4965E-03	---+	
4.5000E 01	2.7997E-03	----+	
5.0000E 01	3.1011E-03	----+	
5.5000E 01	3.4005E-03	----+	
6.0000E 01	3.6981E-03	----+	
6.5000E 01	3.9938E-03	----+	
7.0000E 01	4.2876E-03	----+	
7.5000E 01	4.5795E-03	----+	
8.0000E 01	4.8696E-03	----+	
8.5000E 01	5.1579E-03	----+	
9.0000E 01	5.4443E-03	----+	
9.5000E 01	5.7289E-03	----+	
1.0000E 02	6.0117E-03	----+	
1.0500E 02	6.2927E-03	----+	
1.1000E 02	6.5719E-03	----+	
1.1500E 02	6.8493E-03	----+	
1.2000E 02	7.1250E-03	----+	
1.2500E 02	7.3989E-03	----+	
1.3000E 02	7.6711E-03	----+	
1.3500E 02	7.9415E-03	----+	
1.4000E 02	8.2102E-03	----+	
1.4500E 02	8.4772E-03	----+	
1.5000E 02	8.7425E-03	----+	
1.5500E 02	9.0060E-03	----+	
1.6000E 02	9.2679E-03	----+	
1.6500E 02	9.5281E-03	----+	
1.7000E 02	9.7867E-03	----+	
1.7500E 02	1.0044E-02	----+	
1.8000E 02	1.0299E-02	----+	
1.8500E 02	1.0552E-02	----+	
1.9000E 02	1.0804E-02	----+	
1.9500E 02	1.1055E-02	----+	
2.0000E 02	1.1303E-02	----+	
2.0500E 02	1.1550E-02	----+	
2.1000E 02	1.1796E-02	----+	
2.1500E 02	1.2040E-02	----+	
2.2000E 02	1.2282E-02	----+	
2.2500E 02	1.2523E-02	----+	
2.3000E 02	1.2762E-02	----+	
2.3500E 02	1.3000E-02	----+	
2.4000E 02	1.3236E-02	----+	
2.4500E 02	1.3471E-02	----+	
2.5000E 02	1.3704E-02	----+	

C VERSUS TIME

Figure 2. Typical output resulting from the PRTPLOT statement in CSMP programs.

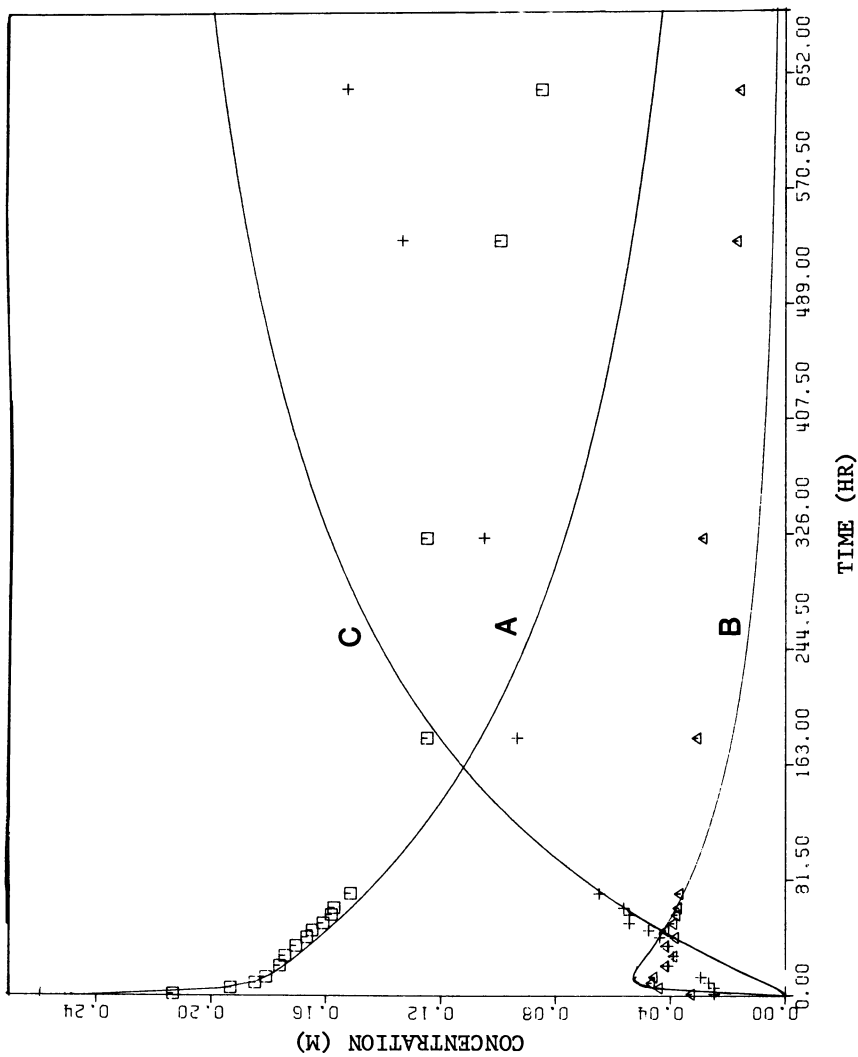


Figure 3. A typical plot generated by the program listed in Figure 4, based on CSMP results provided by a CSMP PREPARE statement. Parameters: $K1 = 0.32$, $K2 = 0.18$, $K3 = 0.020$.

```

DIMENSION TIME(2002),AA(2002),BB(2002),CC(2002),
          DD(2002)
INTEGER RC
DATA TT/'ENDS'/
C SKIPFIRST 11 RECORDS ON TAPE
DO 10 I=1,11
10 READ (8)
C READ A RECORD
RC=0
20 READ (8,END=99) T,A,B,C,D
C TEST FOR 'END' CHARACTERS
IF (T.EQ.TT) GO TO 99
RC=RC+1
TIME(RC)=T
AA(RC)=A
BB(RC)=B
CC(RC)=C
DD(RC)=D
GO TO 20
99 TIME(RC+1)=0.
TIME(RC+2)=62.5
AA(RC+1)=0
AA(RC+2)=0.08
BB(RC+1)=0
BB(RC+2)=0.08
CC(RC+1)=0
CC(RC+2)=0.08
DD(RC+1)=0
DD(RC+2)=0.08
CALL PLOTS
CALL PLOT (5.0,1.0,-3)
CALL AXIS (0.0,0.0,'TIME',-4,32.,0.0,TIME(RC+1),
          TIME(RC+2))
CALL AXIS (0.0,0.0,'CONCENTRATIONS',14,10.0,90.0,AA
          (RC+1),AA(RC+2))
CALL LINE(TIME,AA,RC,1,0,0)
CALL NEWPEN(2)
CALL LINE(TIME,CC,RC,1,0,0)
CALL NEWPEN(3)
CALL LINE(TIME,DD,RC,1,0,0)
CALL NEWPEN(1)
READ(5,16) N
READ(5,15)(TIME(I),AA(I),CC(I),DD(I),I=1,N)
DO 18 I = 1,N
TIME(I) = TIME(I)*0.016
AA(I) = AA(I)*12.5
CC(I) = CC(I)*12.5
18 DD(I) = DD(I)*12.5
DO 17 I = 1,N
CALL SYMBOL(TIME(I),AA(I),0.1,0,0,0,-1)
CALL SYMBOL(TIME(I),CC(I),0.1,2,0,0,-1)
17 CALL SYMBOL(TIME(I),DD(I),0.1,3,0,0,-1)
15 FORMAT(4F10.5)
16 FORMAT(I2)
CALL PLOT (10.0,0.0,999)
STOP
END

```

Figure 4. A program for plotting the output provided by a CSMP PREPARE statement.

(II, $n = 3$) and higher species (II, $n > 3$) present in condensates of 2,6-dimethylol-4-methylphenol (I). Simulation of this condensation process is complicated because of the large number of reactions possible among the various intermediates. For data collected below conversions of 70 percent (methylol groups consumed), it is sufficient to consider only octamers and smaller species to be present in significant concentration. Separate rate constants can be used for reaction of monomer with monomer (k_1), monomer with condensed species (k_2) and condensed species with condensed species (k_3). Using A_n to represent the concentrations of individual species ($A_1 =$ monomer, $A_2 =$ dimer, etc.), differential equations of the following form can be written for the various species.

$$\frac{d(A_1)}{dt} = -2k_1(A_1)^2 - k_2(A_1)(A_2) - k_2(A_1)(A_3) - \dots - k_2(A_1)(A_8)$$

$$\frac{d(A_2)}{dt} = k_1(A_1)^2 - k_2(A_1)(A_2) - 2k_3(A_2)^2 - k_3(A_2)(A_3) - \dots - k_3(A_2)(A_8)$$

$$\frac{d(A_4)}{dt} = k_2(A_1)(A_3) + k_3(A_2)^2 - k_2(A_4)(A_1) - k_3(A_4)(A_2) - k_3(A_4)(A_3) - 2k_3(A_4)^2 - k_3(A_4)(A_5) - \dots - k_3(A_4)(A_8)$$

Program B defines the eight differential equations needed to simulate this condensation reaction, arranges for their simultaneous integration and specifies that A_n concentrations be printed at appropriate times. The quantity SUMAN was used to make the programming more compact. The statement defining this quantity can be placed anywhere in the DYNAMIC part of the program. Although it should logically be evaluated before any of the differentials are evaluated, the CSMP compiler looks after this matter. By comparing the results of this simulation with experimental data it was possible to show that k_1 , k_2 and k_3 have relative values of 1.0, 1.5 and 2.0 in this system. This result is attributed to activation of methylol groups toward condensation by hydrogen-bonding with neighboring phenolic groups. It seems that only one methylol group can be activated at a time in the monomer. Figure 5 compares observed and calculated results for this reaction.

Use of CSMP for Parameter Evaluation

CSMP programs can be called as subroutines by optimization programs such as Chandler's STEPIT program (4). This enables one to evaluate parameters by optimizing fits of calculated results to experimental data. This was the approach taken to evaluate k_1 , k_2 and k_3 in the previous example.

To adapt Program B for use with STEPIT it was necessary to convert it to Program C. The labeled COMMON (COMMON/ONE...) statement was used to place variables required by STEPIT in COMMON

PROGRAM B

```

TITLE SIMULATION OF RESOLE POLYCONDENSATION
INITIAL
PARAMETER K1=7.92E-2,K2=1.58E-1,K3=3.17E-1
INCON A1=0.054,A2=0.,A3=0.,A4=0.,A5=0.,A6=0.,A7=0.,A8=0.
DYNAMIC
DAIDT=-2*K1*A1*A1-K2*A1*SUMAN
DA2DT=K1*A1*A1-K2*A1*A2-K3*A2*(A2+SUMAN)
DA3DT=K2*A1*(A2-A3)-K3*A3*(A3+SUMAN)
DA4DT=K2*A1*(A3-A4)+K3*A2*A2-K3*A4*(A4+SUMAN)
DA5DT=K2*A1*(A4-A5)+K3*A2*A3-K3*A5*(A5+SUMAN)
DA6DT=K2*A1*(A5-A6)+K3*(A2*A4+A3*A3)-K3*A6*(A6+SUMAN)
DA7DT=K2*A1*(A6-A7)+K3*(A2*A5+A3*A4)-K3*A7*(A7+SUMAN)
DA8DT=K2*A1*(A7-A8)+K3*(A2*A6+A3*A5+A4*A4)-K3*A8*(A8+SUMAN)
A1=INTGRL(0.054,DAIDT)
A2=INTGRL(0.0,DA2DT)
A3=INTGRL(0.0,DA3DT)
A4=INTGRL(0.0,DA4DT)
A5=INTGRL(0.0,DA5DT)
A6=INTGRL(0.0,DA6DT)
A7=INTGRL(0.0,DA7DT)
A8=INTGRL(0.0,DA8DT)
SUMAN=A2+A3+A4+A5+A6+A7+A8
TIMER DELT=1.,FINTIM=1000.,OUTDEL=5.,PRDEL=5.
FINISH A1=0.030
PRINT A1,A2,A3,A4,A5,A6,A7,A8
END
STOP
END JOB

```

with the CSMP program. The METHOD statement selected a fixed step Runge-Kutta method rather than a variable step method. The RENAME statement was necessary to avoid confusion between DELMIN variables used by the STEPIT and CSMP programs. The FIXED statement was required to define INTEGER variables defined in the COMMON statement and used in the PROCEDURE segment later in the program. The AFGEN statements are used to define a function of a variable versus TIME. In this instance they defined experimental values of monomer (XA1), dimer (XA2) and larger (XA3) condensate concentrations at various times. The values of the rate constants K1, K2 and K3 are provided as input to the CSMP routine by STEPIT, via the X(1), X(2) and X(3) values in COMMON/ONE/. The PROCEDURE statement and the statements that fall between it and the ENDPRO statement constitute a small FORTRAN routine that is processed at each time interval to determine if the time value corresponds to any of those values for which there is experimental data, and, if so, to calculate the sum of the squares of the differences between observed (XA1, XA2, XA3) and calculated (A1, A2, A9) species

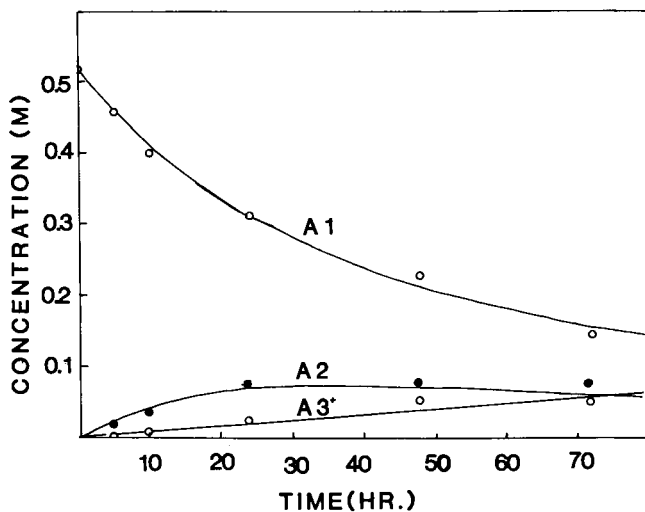


Figure 5. Concentrations of monomer (A1), dimer (A2) and larger species (A3^{*}) during the self-condensation of 2,4-dimethylol-4-methylphenol (0.52 M) in pyridine at 100°C. The solid curves were calculated with Program B. Parameters: $K_1 = 0.023$, $K_2 = 0.036$, $K_3 = 0.062$. These rate constants were obtained by use of STEPIT in conjunction with Programs C and D.

concentrations and to add these to CHISQ. At the end of a simulation run, the value of CHISQ provides a measure of how well the rate constants are able to reproduce the observed results. This value is returned to STEPIT, via COMMON, which then adjusts these rate constants to reduce CHISQ and thereby obtain a satisfactory fit.

PROGRAM C

```

/      COMMON/ONE/X(27),XMAX(27),XMIN(27),DELTAX(27),DELMIN(27),
/      1MASK(27),NV,NTRACE,MATRIX
METHOD RKSFX
RENAME DELMIN=DLMIN
FIXED  NV,NTRACE,MATRIX,I,J,K
INCON CHISQ=0.
TITLE SIMULATION OF RESOLE POLYCONDENSATION
      AFGEN XA1=5.,.88,10.,.77,24.,.60,48.,.445
      AFGEN XA2=5.,.04,10.,.07,24.,.14,48.,.15
      AFGEN XA3=5.,.01,10.,.02,24.,.05,48.,.11
DYNAMIC
      K1 = X(1)
      K2 = X(2)
      K3 = X(3)
DA1DT=-2*K1*A1*A1-K2*A1*SUMAN
DA2DT=K1*A1*A1-K2*A1*A2-K3*A2*(A2+SUMAN)
DA3DT=K2*A1*(A2-A3)-K3*A3*(A3+SUMAN)
DA4DT=K2*A1*(A3-A4)+K3*A2*A2-K3*A4*(A4+SUMAN)
DA5DT=K2*A1*(A4-A5)+K3*A2*A3-K3*A5*(A5+SUMAN)
DA6DT=K2*A1*(A5-A6)+K3*(A2*A4+A3*A3)-K3*A6*(A6+SUMAN)
DA7DT=K2*A1*(A6-A7)+K3*(A2*A5+A3*A4)-K3*A7*(A7+SUMAN)
DA8DT=K2*A1*(A7-A8)+K3*(A2*A6+A3*A5+A4*A4)-K3*A8*(A8+SUMAN)
A1=INTGRL(0.52,DA1DT)
A2=INTGRL(0.0,DA2DT)
A3=INTGRL(0.0,DA3DT)
A4=INTGRL(0.0,DA4DT)
A5=INTGRL(0.0,DA5DT)
A6=INTGRL(0.0,DA6DT)
A7=INTGRL(0.0,DA7DT)
A8=INTGRL(0.0,DA8DT)
SUMAN=A2+A3+A4+A5+A6+A7+A8
A9=SUMAN-A2
TIMER FINTIM=80.,DELT=1.
PROCEDURE CHISQ = FUNCT(A1,XA1,A2,XA2,A9,XA3,TIME,KEEP)
      IF(KEEP.NE.1) GO TO 1
      IF(TIME.EQ.5) GO TO 2
      IF(TIME.EQ.10.) GO TO 2
      IF(TIME.EQ.24.) GO TO 2
      IF(TIME.EQ.48.) GO TO 2
      GO TO 1
      2 CHISQ=CHISQ + (AFGEN(XA1,TIME)*0.52 - A1)**2 + ...
      (AFGEN(XA2,TIME)*0.52-A2)**2 + (AFGEN(XA3,TIME)*0.52-A9)**2
      1 CONTINUE
ENDPRO
TERMINAL
END
STOP

```

Minor changes must also be introduced into STEPIT to use it with CSMP programs. Since this is a very large program, and since

the changes are rather minor, instructions for doing this are provided in outline form in Figure 6. The program must be identified as SUBROUTINE MAIN to make it the controlling program and to override the controlling program (MAINEX) usually used by CSMP. The COMMON statement, as used here, is specific to CSMP. It requests the CSMP compiler to create an unlabeled COMMON region that contains variables and constants used by CSMP and by Program C. One of these (CHISQ) is required for STEPIT. The labeled COMMON (COMMON/ONE/...) statement is identical to the labeled COMMON statement in Program C and, except for the ERR(27,3) specification that is now handled by a DIMENSION statement, it replaces the unlabeled COMMON statement present in the original version of STEPIT. INITLZ and INTRAN are CSMP subroutines that must be called to initialize a CSMP job and to provide for the processing of the CSMP program written by the user (Program C in this case). STEPIT normally makes frequent calls to a user written Subroutine FUNK that evaluates CHISQ, which is the parameter that indicates how well calculated and observed values agree. In our case FUNK is Program C. By calling RKS instead of FUNK, Program C is executed using the fourth order, Runge-Kutta integration method. Other integration methods could be used instead, by calling other integration routines (eq. MILNE, SIMP, RECT, TRAPZ, ADAMS, etc.) instead of RKS. In any case, the eleven calls to FUNK by STEPIT are replaced by CALL RKS and a RETURN statement is added to complete the necessary modifications. The above describes a "bare bones" set of instructions for adapting STEPIT for usage with CSMP. If use of PRTPLOT statements in the user written CSMP program are contemplated, additional modification of STEPIT will be necessary. This is described in the CSMP System Manual.

STEPIT requires as input, initial parameter values (X), limits on their maximum (XMAX) and minimum (XMIN) size, initial increments to be used for varying parameter values (DELTA), the accuracy desired for each variable (DELMIN), the number of parameters to be evaluated (NV) and various control constants (MASK, NTRACE, MATRIX). These are provided by use of a BLOCK DATA subroutine, an example of which is provided as Program D.

PROGRAM D

```
BLOCK DATA
COMMON/ONE/X,XMAX,XMIN,DELTA,DELMIN,MASK,NV,NTRACE,MATRIX
REAL X(27)/0.02,0.02,0.02,0.02,24*0./,XMAX(27)/0.2,0.2,0.2,24*0./,
1XMIN(27)/27*0./,DELMIN(27)/0.001,0.001,0.001,24*0./,
2DELTA(27)/27*0.010/,MASK(27)/27*0./
INTEGER NV/3/,NTRACE/1/,MATRIX/0/
END
```

The combination of the modified STEPIT program with Programs C and D yielded the fit of experimental and calculated results shown in Figure 5. This required 88 simulation runs and consumed 6.75 sec. of CPU time on an IBM 370/158 Model 3 computer.


```

SUBROUTINE MAIN
COMMON
COMMON/ONE/ X(27),XMAX(27),XMIN(27),
1DELTA(27),DELMIN(27),MASK(27),NV,
2NTRACE,MATRIX
DIMENSION ERR(27,3)
CALL  INITLZ
CALL  INTRAN
,
,
,
CALL  FUNK  →  { CHISQ = 0.0
,              { CALL RKS
,
,
CALL  FUNK  →  { CHISQ = 0.0
,              { CALL RKS
,
,
,
      ETC. FOR A TOTAL OF 11 CALLS TO FUNK
,
,
,
RETURN
END

```

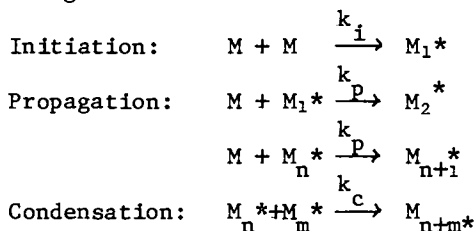
Figure 6. Outline of changes necessary to modify STEPIT for usage with CSMP programs.

Although it was a frustrating experience to learn how to merge STEPIT with CSMP, we are now able to use the combination routinely for parameter evaluations and with very little programming effort. Hopefully, the information provided in this section will enable the reader to also take advantage of this powerful combination.

Self-Promoted Polyaddition with Condensation

The thermal polymerization of styrene (5), the alkali catalyzed polymerization of lactams (6) and (as some would have it) (7) the strong base initiated polymerization of N-carboxy anhydrides (NCA's) (8) are examples of polymerizations in which monomer generates the species responsible for polymerization. The maximum D.P. possible in such polymerizations is approximately the square root of the ratio of rate constants for propagation and for generation of propagating species. This point alone is sufficient to remove NCA-polymerizations from this class of reactions. However, condensation reactions can accompany NCA-polymerizations proceeding by the "activated monomer" mechanism and it was of interest to determine what effect they would have on polymer molecular weight. It is not possible to integrate the equations involved when self-condensation is superimposed on self-promoted polyaddition, but CSMP programming enables this situation to be simulated without difficulty.

A mechanism for self-promoted polyaddition with condensation can be formulated in the following general way, where M represents monomer and M* an activated species capable of propagating or condensing.



The following differential equations described changes in monomer and growing species concentrations with time:

$$\frac{d(M)}{dt} = - 2k_i(M)^2 - k_p(M^*)(M) \quad ; \quad (M^*) = \Sigma(M_n^*)$$

$$\frac{d(M^*)}{dt} = k_i(M)^2 - k_c(M^*)^2$$

The D.P. and conversion obtained at time t can be calculated from the above expressions, if the initial monomer concentration $(M_0)=1$,

as follows:

$$D.P.(t) = \frac{1 - \int_0^t d(M)/dt}{\int_0^t d(M^*)/dt}$$

$$\text{Conversion} = 1 - \int_0^t d(M)/dt - \int_0^t d(M^*)/dt$$

Program E is a CSMP program based on the above considerations. It provides conversion (CONV), monomer concentration (A=M), activated species concentration (B=M*) and D.P. as a function of time. As in Program C, a PROCEDURE is used. This group of statements (enclosed in a block) is processed as an ordered group to yield DADT and DBDT values at each time increment. The PROCEDURE used here provides the logic necessary to simulate the process after monomer has been completely consumed. Figure 7 shows some results obtained using Program E. It can be seen that when $k_p/k_i=100$ and $k_c \sim k_p$ or k_i , the variation of D.P. with conversion is similar to that obtained in a pure condensation process. Only when $k_c \sim 500$ times larger than k_p does the D.P. vs. conversion plot resemble that of a polyaddition process. The actual model required to simulate the "activated monomer" mechanism of NCA polymerization is slightly more complicated than that covered here, but it leads to the same conclusion: The "activated monomer" mechanism of NCA polymerization must be basically a condensation process if high molecular weight products are to be obtained. These results strengthen our opinion that the "activated monomer" mechanism is untenable.

PROGRAM E

TITLE MONOMER PROMOTED POLYMERIZATION WITH POLYCONDENSATION

PARAMETER KI=0.005,KP=0.1,KC=0.1

INCON A=1.0,B=1.E-06,P=0.,CONV=1,E-06

DYNAMIC

```
PROCEDURE DADT, DBDT = FUNCT(KI,KP,KC,A,B)
```

```
  IF (A.LT.0.0) GO TO 1
  DADT = -2.0*KI*A*A - KP*A*B
  DBDT = KI*A*A - KC*B*B
  GO TO 2
1  DADT = 0.
  DBDT = - KC*B*B
2  CONTINUE
```

```
ENDPRO
```

```
  A = INTGRL(1.0,DADT)
  B = INTGRL(1.E-06,DBDT)
  DP = (1.0-A)/B
  P = (1.0 - A)
  CONV = 1. - ( A + B )
```

```
FINISH CONV = 0.999
TIMER FINTIM=4000.,PRDEL=10.
```

```
PRINT P,A,B,DP,CONV
```

```
END
```

```
STOP
```

```
END JOB
```

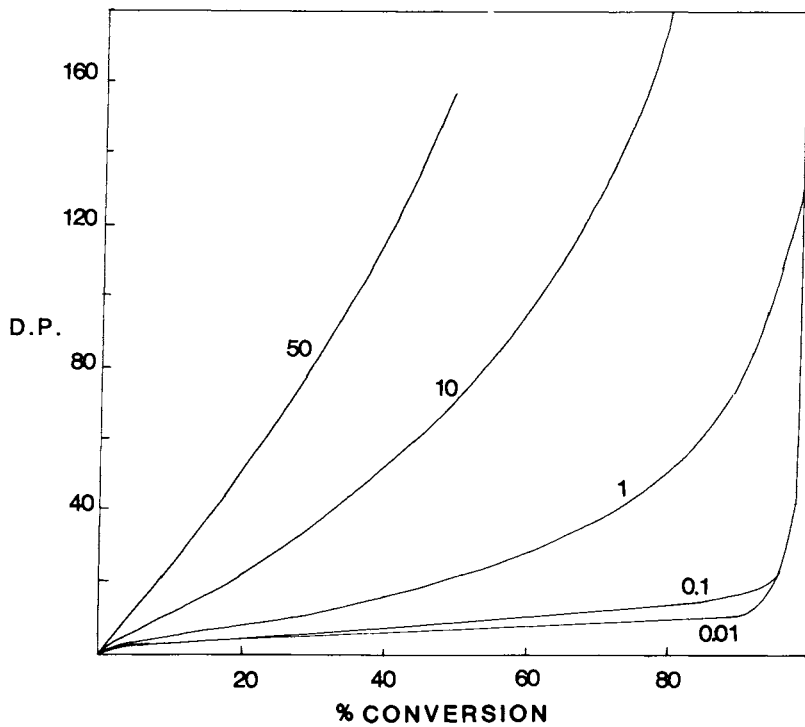
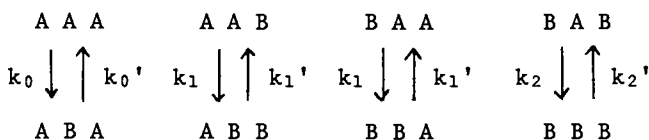


Figure 7. Variation of degree of polymerization (D.P.) with conversion for monomer-promoted polyaddition with condensation. The curves are calculated for $k_i = 0.001$, $k_p = 0.1$, and for $k_c = 0.01 - 50$, as indicated in the figure.

Polymer Modification Reactions

A large amount of theoretical work has been done on the problem of treating the kinetics of polymer modification reactions (9,10). In addition to the kinetics, the distributions of monomer units among the products of such reactions and the compositional heterogeneity of the products are of interest. The problem of treating irreversible polymer reactions is essentially solved, (11) but the solution is awkward to utilize. Very effective approximations have been developed that enable polymer modification reactions to be simulated (12) numerically. The reader is referred to Bauer's paper (11) for a lucid description of how this can be done. His predictor-corrector program for calculating monomer triad distributions in modified polymers can be duplicated with a 25 statement CSMP program but we present here a more general program that simulates reversible polymer modification reactions. Rate constants for the interconversion of A- and B- units in an A-B copolymer are defined as follows:



Program F can be used to calculate the relative concentrations of monomer triads in a modified polymer as a function of time or copolymer composition, or at equilibrium. The rate constants k_0' , k_1' and k_2' are represented by K01, K11 and K21. Following the DYNAMIC statement are six expressions that describe the changes in triad concentrations with time due to the downward reactions (involving k_0 , k_1 and k_2) in the above scheme. The expressions appear in sequential order for AAA, (AAB+BAA), BAB, ABA, (ABB+BBA) and BBB triads. They correspond exactly to Equations 8-10 and 12-14 in Bauer's paper and would be used directly for simulation of an irreversible process. To treat a reversible process, it is necessary to add six additional expressions for changes in triad concentrations due to the upward reactions (involving k_0' , k_1' and k_2') depicted in the above scheme. Following these are six expressions for the net changes in triad concentrations with time and then six statements for integrating these expressions simultaneously. (The expressions for the net triad differentials should actually be incorporated into the INTGRL statements). The remainder of the programming is straight-forward: triad concentrations are summed to obtain monomer concentrations and output of monomer and triad concentrations is requested as a function of time. With the aid of this program we have been able to calculate monomer and triad concentrations as a function of time and at equilibrium that are in excellent agreement with theoretical values or with the results of Monte Carlo simulations. By replacing the

print statement in Program F by the following programming, the program can be used to calculate triad stereosequence distributions for partially and completely epimerized stereoregular polymers.

```
MM=AAA+BBB
MR=AAB+ABB
RR=ABA+BAB
M=MM+MR/2.
PRINT M,MM,MR,RR
```

PROGRAM F

```
TITLE REVERSIBLE POLYMER MODIFICATION REACTIONS
/ CALL ERRSET(209,100,=1,1)
INITIAL
INCON AAA=1.,AAB=0.,ABB=0.,ABA=0.,BAB=0.,BBB=0.
PARAMETER AA=1.0,BB=0.0,CC=0.0,DD=0.0,EE=0.0,FF=0.0
PARAMETER KO=1.E-3,K1=1.E-3,K2=1.E-3,KO1=1.E-3,K11=1.E-3,K21=1.E-3
DYNAMIC
A=(-KO)*AAA-(2.*KO*AAA+K1*AAB)*AAA/(AAA+AAB/2.)
B=(-K1)*AAB+(2.*KO*AAA+K1*AAB)*(AAA-AAB/2.)/(AAA+AAB/2.)
C=(-K2)*BAB+(2.*KO*AAA+K1*AAB)*(AAB/2.)/(AAA+AAB/2.)
D=KO*AAA-(K1*AAB+2.*K2*BAB)*ABA/(ABA+ABB/2.)
E=K1*AAB+(K1*AAB+2.*K2*BAB)*(ABA-ABB/2.)/(ABA+ABB/2.)
F=K2*BAB+(K1*AAB+2.*K2*BAB)*(ABB/2.)/(ABA+ABB/2.)
A1=KO1*ABA+(K11*ABB+2.*K01*ABA)*(AAB/2.)/(BAB+AAB/2.)
B1=K11*ABB+(K11*ABB+2.*K01*ABA)*(BAB-AAB/2.)/(BAB+AAB/2.)
C1=K21*BBB-(K11*ABB+2.*K01*ABA)*BAB/(BAB+AAB/2.)
D1=(-K01)*ABA+(2.*K21*BBB+K11*ABB)*(ABB/2.)/(BBB+ABB/2.)
E1=(-K11)*ABB+(2.*K21*BBB+K11*ABB)*(BBB-ABB/2.)/(BBB+ABB/2.)
F1=(-K21)*BBB-(2.*K21*BBB+K11*ABB)*BBB/(BBB+ABB/2.)
DAAADT=A+A1
DAABDT=B+B1
DBABDT=C+C1
DABADT=D+D1
DABBDT=E+E1
DBBBDT=F+F1
AAA=INTGRL(AA,DAAADT)
AAB=INTGRL(BB,DAABDT)
BAB=INTGRL(CC,DBABDT)
ABA=INTGRL(DD,DABADT)
ABB=INTGRL(EE,DABBDT)
BBB=INTGRL(FF,DBBBDT)
CONV = ABA + ABB + BBB
PRINT CONV,AAA,AAB,BAB,ABA,ABB,BBB
TIMER FINTIM=9000.,PRDEL=20.
END
ENDJOB
```

Summary

The examples discussed herein show that very simple, easily written CSMP programs can be used to treat complex kinetic problems that are encountered in studies on polymerization, polycondensations and polymer modification reactions. It is obvious that CSMP is also applicable to problems involving polymer processing or the dynamic behavior of polymers in solution or bulk. Polymer scientists would be well advised to become familiar with this valuable program. It would also seem important to use CSMP in the classroom. We hope that the instructions and examples provided herein will help others to use CSMP programming effectively and with minimum difficulty.

Other Languages Similar to CSMP

A reviewer has kindly provided references to other programs for solving differential equations by numerical methods (13-21). These will be useful to individuals that do not have IBM equipment but would like to do calculations of the sort outlined above. The general topic has been discussed (13). Sebastian, et al. (14) discuss DPS (Dynamic Process Simulator) and provide references to descriptions of MIMIC (15), ACSL (16), ISIS (17), BEDSOCS (18), DSL/77 (19), DARE (20) and PMSP (21). References to other programs can be found in papers that accompany reference 2 and in other Proceedings of Conferences on Applications of Continuous System Simulation. Because of the simplicity and power of system simulation programs such as are discussed herein, one could expect that every major computer producer would have available software with the capability of CSMP.

Acknowledgements

This work was supported in part by the National Science Foundation (DMR-80-10709). One of us (H.J.H.) is grateful to Dr. K. E. Cox, who introduced him to CSMP more than ten years ago. He would also like to acknowledge discussions concerning CSMP programming with Mr. Roy Cain of the Firestone Tire and Rubber Company. The authors are grateful to Mr. Frank G. Tompkins, III of the University of Akron Computer Center for developing the plotting routine listed in Figure 3. Finally, we wish to acknowledge the receipt of a Fulbright Fellowship by one of us (A.D.).

Literature Cited

1. "System/360 Continuous System Modeling Program Users Manual", IBM Application Program GH 20-0367-4, IBM Corporation, Technical Publications Dept., White Plains, N. Y. 10604, 1972.
2. Herbold, R.J. Proceedings of Conference on Applications of Continuous System Simulations, AFIPS Press, 210 Summit Ave., Montvale, N.J. 07645, June 1969, pp 73-82.

3. Detar, D.F. "Computer Programs in Chemistry, Volume 2", W. A. Benjamin, Inc., N.Y., 1969, Chapters 3-9.
4. Chandler, J.P., Subroutine STEPIT Program 66.1, Quantum Chemistry Program Exchange, Indiana University, Bloomington, Indiana.
5. Pryor, W.A.; Coco, J.H. Macromolecules 1970, 3, 500.
6. Reimschuessel, H.K. in "Ring Opening Polymerization"; Frisch, K.C.; Reegen, S.L. Eds.; M. Dekker, New York, 1969, Chapter 7, pp 313-323.
7. Goodman, M.; Peggion, E.; Szwarc, M.; Bamford, C.H.; Macromolecules 1977, 10, 1299.
8. Sekiguchi, H. Pure and Appl. Chem. 1981, 53, 1689.
9. Plate, N.A.; Noah, O.V. Adv. Polym. Sci. 1979, 31, 134.
10. Boucher, E.A. Prog. Polym. Sci. 1978, 6, 63.
11. Plate, N.A.; Litmanovich, D.; Noah, O.V.; Toom, A.L.; Vasilyev, N.B. J. Polym. Sci., Polym. Chem. Ed. 1974, 12, 2165.
12. Bauer, B.J. Macromolecules 1979, 12, 704.
13. Mah, R.; Seider, W. "Foundations of Computer Aided Chemical Process Design, Volume 1," Engineering Foundation, New York, N. Y., 1981, pg. 403.
14. Sebastian, D.J.G.; Noble, R.G.; Thambynayagam, R.K.M.; Wood, R.K. Proceedings of 2nd. World Congress on Chemical Engineering, Montreal 1981, pg. 473.
15. "MIMIC - A Digital Simulation Language Reference Manual, Pub. No. 44610400, Rev. D.", Control Data Corporation, Minneapolis, Minn., 1970.
16. "Advanced Continuous Simulation Language (ASCL), User Guide/ Reference Manual", Mitchell and Gauthier Associates, Inc., Concord, Mass., 1976.
17. Anon., Proceedings of the 1978 VKSC Conference on Computer Simulation, IPC Science and Technology Press, Guildford, 1978.
18. Ord-Smith, R.J.; Stephenson, J. "Computer Simulation of Continuous Systems", Cambridge, 1975.
19. Colloquium on "Standards for Dynamic Simulation Languages", Digest No. 1980/17, Institution for Electrical Engineers, London, 1980.
20. Korn, D.A.; Wait, J.V. "Digital Continuous System Simulation", Prentice Hall, Inc., Englewood Cliffs, N. J., 1978.
21. Anon., "An Introduction to the CEGB Plant Modeling System Program (PMSP)", Computer, No. 14, CEGB, London, 1977.

RECEIVED May 4, 1982.

Modeling and Control of Copolymerization Reactors

LUIS H. GARCIA-RUBIO¹, J. F. MACGREGOR, and A. E. HAMIELEC

McMaster University, Chemical Engineering Department,
Hamilton, Ontario, L8S 4L7, Canada

Three factors are important in the development and implementation of successful control strategies for copolymerization reactors: the availability of kinetic models which adequately describe the rate of polymerization and the properties of the resulting polymer as functions of the process variables, the availability of on-line instrumentation which enables rapid characterization of the copolymer throughout the reaction, and the availability of process data which allow for the constraints of the process to be built into the control strategy. This paper discusses the limitations of reported control strategies for copolymerization reactors from the viewpoint of the state-of-the-art of kinetic modeling and copolymer characterization. The critical stages in this process where considerable research effort is required are emphasized.

Copolymers and copolymerization reactions have been extensively studied for the last 50 years. However, the complexity of the kinetics and the difficulties encountered in the characterization of the reaction products have long obscured details of the reaction kinetics as well as characteristics of the resulting products.

Copolymer properties are known to be a function of the molecular weight distribution (MWD), the copolymer composition distribution (CCD) and in some cases the sequence length distribution (SLD). The optimal design, operation and control of reactors to produce high quality copolymers with efficient production rates requires:

- ▶ the availability of suitable detectors to monitor conversion, MWD, CCD, SLD or at least some of the leading moments of those distributions.
- ▶ the availability of dynamic models to predict polymerization rates and copolymer properties, to design polymer reactors, and to assist in the implementation of control strategies.

This paper, which is divided into three sections, critically reviews the state-of-the-art of free-radical copolymerization kinetics, characterization, reactor design, operation and control from the view point of their possible implementation to industrial processes.

In Section 1, a sufficiently detailed review of the copolymerization theory is presented. The fundamental assumptions made in development of mathematical models capable of describing copolymerization processes are presented and discussed in view of recent studies. In Section 2, the traditional polymer characterization techniques as applied to copolymers are reviewed. Copolymer

¹ Current address: Xerox Research Center of Canada, 2660 Speakman Drive, Mississauga, Ontario, L5K 2L1, Canada.

composition analysis techniques, molecular weight and sequence length determination techniques are discussed. Finally, in Section 3, a brief review of the reported attempts to implement the existing theory to the design and control of copolymerization reactors is presented.

The areas where additional research is required are highlighted throughout.

Part 1 - Kinetics and Modeling of Copolymerization Reactions

Early in the study of free radical copolymerization, it was recognized that the three fundamental steps of initiation, propagation and termination present in homopolymerization are also present in copolymerization reactions. It has also been recognized that the different chemical nature of the reacting monomers can influence the termination and, particularly, the propagation reactions (4). Depending on the polar and steric characteristics of the reacting monomers, it can be speculated that subsequent propagation steps may depend on the ultimate, penultimate or even remote units along the propagating chain. In other words, propagation and termination reactions may be functions of the microstructure of the propagating chain. In this event, a more comprehensive set of reactions are required to describe the copolymerization process. For example, in the case of penultimate effects, being important, eight reactions are necessary to describe the propagation step.

In addition to sequence effects, the importance of equilibrium copolymerization has been considered (5-7). If depropagation reactions become important, 16 reactions would be required only to describe the propagation step, which implies that at least 16 rate constants are to be estimated or evaluated experimentally. The basic reaction scheme proposed in the 1940s has been expanded in more recent years to include almost every possible reaction that can take place during a copolymerization. However, the usefulness of such complicated schemes is limited not only by the tractability of the resulting equations, but primarily by the feasibility of experimentally identifying the controlling steps in the reactions and estimating the corresponding parameters.

Copolymerization Models. In order to describe completely the course of a copolymerization, it is necessary to know the monomer feed, polymer composition, molecular weight and sequence length as functions of conversion and time. For the accepted copolymerization schemes, the available models can be divided into three categories:

- (i) Average Properties Models,
- (ii) Statistical Models
- (iii) Comprehensive or Distributed Properties Models.

Average Properties Models. The average properties' models include those which have been developed based on the overall copolymer composition and conversion. Among the early ones is the linear or pseudo-first order reactions developed by Wall (1). Mayo and Lewis (2), Skeist (7) and Walling (8) derived a general formulation for binary copolymerizations, a selectivity equation known as the "Copolymerization Equation" which has the form:

$$F_1 = \frac{r_1 f_1^2 + f_1 (1-f_1)}{(r_1 + r_2 - 2) f_1^2 + 2 (1-r_2) f_1 + r_2} \quad (1)$$

where F_1 and f_1 are the mole fraction of monomer 1 in the copolymer and the mol fraction of monomer 1 in the monomer mixture r_1 and r_2 are the reactivity ratios defined as:

$$r_1 = \frac{K_{paa}}{K_{pab}} \quad ; \quad r_2 = \frac{K_{pbb}}{K_{pba}}$$

A selectivity equation including penultimate effects was derived by Merz (4) and later corrected and generalized by Ham (9) to include the effects of remote units along the propagating chain.

Equation 1 was integrated with respect to composition by Meyer and Lowry (9) to the well-known equation:

$$C_M = 1 - \left(\frac{f_1}{f_{10}} \right)^\alpha \left(\frac{1-f_1}{1-f_{10}} \right)^\beta \left(\frac{f_{10}-\delta}{f_1-\delta} \right)^\gamma \quad (2)$$

$$\alpha = \frac{r_2}{1-r_2} \quad ; \quad \beta = \frac{r_1}{1-r_1} \quad , \quad \gamma = \frac{1-r_1r_2}{(1-r_1)(1-r_2)}$$

$$\delta = \frac{1-r_2}{2-r_1-r_2}$$

f_{10} is the mol fraction of monomer 1 in the monomer mixture at time 0.

From equation (2), it is possible to derive expressions for the differential and cumulative overall composition distributions (10).

$$g(f_1) = \frac{dC_M}{dF_1} \quad (3)$$

$$G(F_1) = \int_{F_{10}}^{F_1} g(F_1') dF_1' = \frac{C_M}{C_{MF}} \quad (4)$$

where C_M is the molar conversion when the instantaneous copolymer produced has a mol fraction F_1 . C_{MF} is the terminal conversion.

Equations 1 to 4 describe the copolymerization composition behaviour based on the following assumptions:

- (i) Only ultimate group effects are important.

- (ii) The Stationary State Hypothesis is valid. (SSH)
- (iii) The Long Chain Approximation is valid. (LCA)
- (iv) The stationarity condition is applicable (i.e. in the limit, as the number of monomer units in the chain approaches infinity, the number of A-B links equals the number of B-A links).

These assumptions and equations 1 - 4 have been shown valid for a number of monomer systems (11, 12).

The integration of the rate equations with respect to time and, therefore, the description of the molecular weight behaviour has been more difficult. The reason for this has been that the dependence of the initiation and termination rates on the microstructure and concentration of the chains along the conversion path is largely unknown. Although some simplifying assumptions have been attempted, clearly, no satisfactory solution has yet been obtained. The early work of Walling (8) and Melville, Nobel, and Watson (13) on the formulation of the rate expressions was followed by De Butts (14) who integrated the equations under the assumption of constant initiation rate, no gel effect and bimolecular termination. O'Driscoll and Knorr (15) developed a convenient integration procedure for the total conversion of monomer versus time.

$$\ln(1-C_M) = (m K_{pbb} - K_{pba}) \int_0^t [R\cdot] dt \quad (5)$$

$$m = \frac{K_{paa} - K_{pba}}{K_{pab} - K_{pbb}}$$

where the rate or conversion clearly depends on the total radical concentration $[R\cdot]$. Mecklenburg (16), using the same approach as De Butts, integrated the rate expressions to a simpler form. Miyata (17) considered pseudo first-order reaction rates and derived the corresponding molecular weight expressions. More recently, Lin et al (18) derived a model for the azeotropic polymerization of styrene/acrylonitrile in toluene. By polymerizing at low conversions and, therefore, eliminating the gel effect, and by using a constant ratio of monomers throughout the reaction, the rate expressions were greatly simplified. Expressions for the MWD were also derived. However, five adjustable parameters were fitted to a limited amount of data.

Statistical Models. Due to the difficulties involved in calculating the composition distributions by purely deterministic techniques, statistical methods have been developed from which not only the CCD can be obtained but also the sequence length distribution. These methods view the chain growth as a stochastic process having possible states resulting from the kinetic mechanisms. Early work on this approach was reported by Merz, Alfrey and Goldfinger (4) who derived the copolymerization equation and the SLD for the ultimate effect case. Alfrey Bohrer and Mark (19) and Ham (9) formalized this approach.

Consider the following probabilities:

P_{aa} = probability that a growing chain terminated in A adds another A.

- P_{ab} = probability that a chain terminated in A adds a B.
 P_{bb} = probability that a growing chain terminated in B adds another B.
 P_{ba} = probability that a chain terminated in B adds an A.

from equations 1 to 5

$$P_{aa} = \frac{r_1 f_1}{r_1 f_1 + (1-f_1)} \quad (6)$$

$$P_{ab} = \frac{1-f_1}{r_1 f_1 + 1-f_1} \quad (7)$$

$$P_{bb} = \frac{r_2(1-f_1)}{r_1(1-f_1) + f_1} \quad (8)$$

$$P_{ba} = \frac{f_1}{f_1 + r_2(1-f_1)} \quad (9)$$

$$\text{and } P_{ab} + P_{aa} = 1; P_{ab} + P_{ba} = 1; P_{ba} + P_{bb} = 1 \quad (10)$$

the probability of finding exactly nA units in a growing chain is:

$$A_n = P_{aa}^{n-1} P_{ab}$$

where A_n is also the fraction of all A sequences with length n replacing the value of the probabilities:

$$A_n = \frac{\alpha^{n-1}}{(\alpha + 1)^n} \quad (11)$$

$$\text{where } \alpha = \frac{r_1 f_1}{1-f_1}$$

Similarly for B sequences:

$$B_n = \frac{\beta^{n-1}}{(\beta + 1)^n} \quad (12)$$

$$\text{where } \beta = \frac{r_2(1-f_1)}{f_1}$$

The average sequence lengths can be readily determined from the mean of the distributions:

$$\bar{N}_A = \sum_{n=1}^{\infty} n A_n = 1 + \alpha \quad (13)$$

$$\bar{N}_B = \sum_{n=1}^{\infty} n B_n = 1 + \beta \quad (14)$$

Equations 11 through 14 are instantaneous values. The ultimate chain length will be a weighted composite of these values.

$$\bar{A}_n = \int_0^{X_a} A_n dx_a = \int_0^{C_M} A_n(f_1, r_1) F_1 dx \quad (15)$$

$$\bar{B}_n = \int_0^{X_b} B_n dx_b = \int_0^{C_M} B_n(f_1, r_2) (1-F_1) dx \quad (16)$$

Clearly, this approach is straightforward only for ultimate group or terminal group copolymerization. If more than penultimate effects are required, the equations become unwieldy. Using the concepts and mathematics of Markovian processes, Ham (9) generalized an extended form of the selectivity equation. Later, Price (20, 21) formalized the theory of Markov chains as applied to

copolymers. The development of NMR techniques for polymer characterization (22, 23) has fostered the application of statistical models to sequence length and stereoregularity analysis.

Statistical models have built in the same assumptions that are made in the development of deterministic models. The compactness of their formulation is what makes them extremely useful in the analysis of sequence lengths and complex copolymerizations.

Comprehensive Models. This class of detailed deterministic models for copolymerization are able to describe the MWD and the CCD as functions of the polymerization rate and the relative rate of addition of the monomers to the propagating chain. Simha and Branson (3) published a very extensive and rather complete treatment of the copolymerization reactions under the usual assumptions of free radical polymerization kinetics, namely, ultimate effects SSH, LCA and the absence of gel effect. They did consider, however, the possible variation of the rate constants with respect to composition. Unfortunately, some of their results are stated in such complex formulations that they are difficult to apply directly (10). Stockmeyer (24) simplified the model proposed by Simha and analyzed some limiting cases. More recently, Ray et al (10) completed the work of Simha and Branson by including chain transfer reactions, a correction factor for the gel effect and proposing an algorithm for the numerical calculation of the equations. Such comprehensive models have not been experimentally verified.

Recent experimental results on styrene-acrylonitrile copolymers (12) indicate that, the fundamental reactions of initiation (Figure 1), propagation (Figure 2) and termination (Figure 3) appear to be function of both the terminal group and the environment surrounding the growing chains. Furthermore, $^1\text{H-NMR}$ analysis of these materials suggests that copolymers with varying degree of stereoregularity are formed at different stages along the conversion path, thereby complicating further the modelling of these already difficult systems. Clearly, extensive verification and reformulation of existing models is required before they can be generalized. The progress made in the analysis of copolymers, particularly using chromatography (Figure 4) certainly opens the possibility of such verifications (25).

The Problem of Parameter Estimation in Copolymerization Equations

In order to assess the validity of any of the models reviewed, it is necessary to estimate their parameters, a problem that is closely related to the measurement of some fundamental copolymer properties such as the MWD, SLD, CCD or some of their leading moments. Such measurements are rather difficult and error prone. The complexity of the problem of estimating parameters and discriminating among different models or mechanisms is further increased by the non-linear nature of the models and the large number of parameters required. For example, based on the data of Fordyce and Chapin (26), Ham (9) concluded that the deviations observed in the composition behaviour of styrene/acrylonitrile copolymers was due to the effect of penultimate groups on the propagation reaction (4 parameters versus 2 in the ultimate group effect). However, the confidence region for the reactivity ratios obtained by Tidwell and Mortimer (27) from the same data indicate that the differences observed may be due to experimental error, or at least, that there is no significant evidence to differentiate ultimate from penultimate effects. With the relatively recent development of high resolution NMR (^1H , C^{13}) and size exclusion chromatography (SEC), it appears possible to obtain sufficient

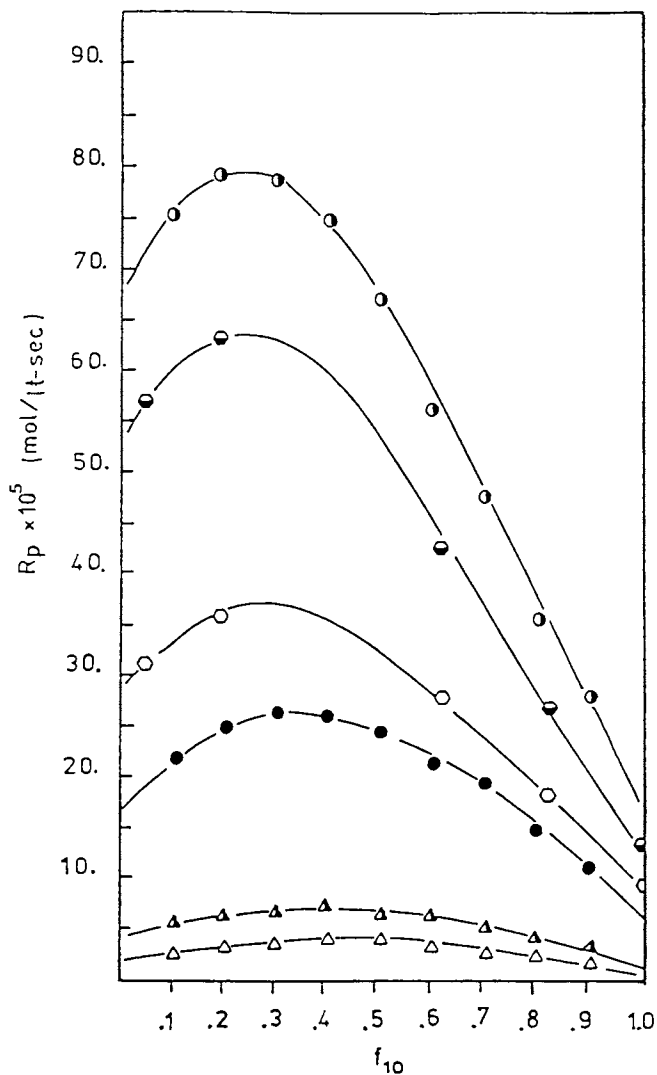


Figure 1. Initial polymerization rates of styrene acrylonitrile bulk polymerization as function of the monomer feed at \circ , 60°C and $[I]_0 = 0.05$ M; \bullet , 60°C and $[I]_0 = 0.032$ M; \square , 60°C and $[I]_0 = 0.016$ M; \bullet , 60°C and $[I]_0 = 0.010$ M; Δ , 40°C and $[I]_0 = 0.050$ M; \triangle , 40°C and $[I]_0 = 0.010$ M. Data from Ref. 12.

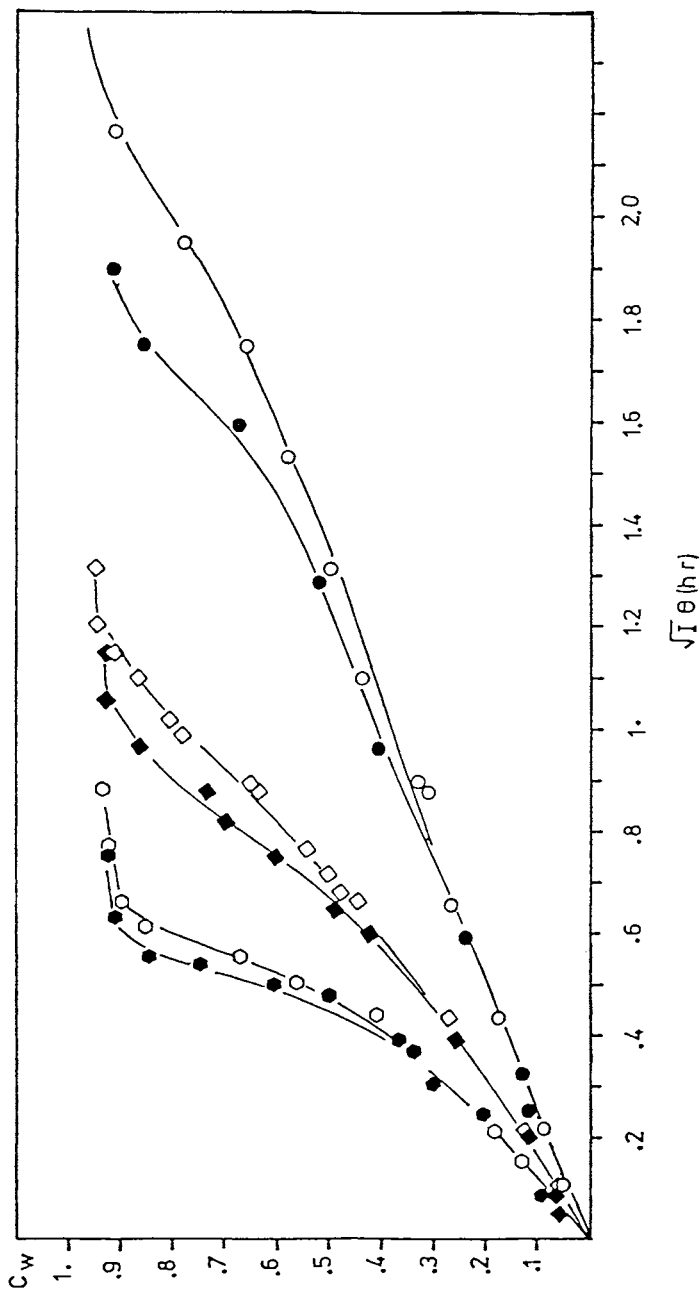


Figure 2. Square root dependence of the initiator concentration for SAN copolymerization at 60°C. Key: \circ , $f_{10} = 0.90$, $[I]_0 = 0.05$ M; \bullet , $f_{10} = 0.90$, $[I]_0 = 0.01$ M; \diamond , $f_{10} = 0.70$, $[I]_0 = 0.05$ M; \blacklozenge , $f_{10} = 0.70$, $[I]_0 = 0.01$ M; \square , $f_{10} = 0.50$, $[I]_0 = 0.05$ M; \blacksquare , $f_{10} = 0.50$, $[I]_0 = 0.01$ M. Data from Ref. 12.

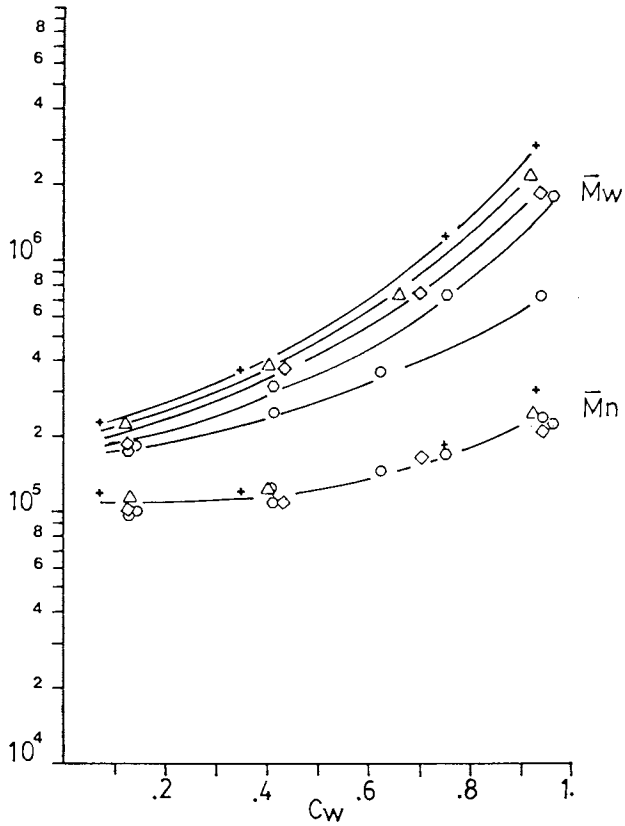


Figure 3. Molecular weight averages for SAN copolymerization at 60°C and $[I]_0 = 0.05$ M (12). Key for f_{10} values: ○, 90; ◻, 80; ◊, 70; △, 60; +, 50. Data from Ref. 12.

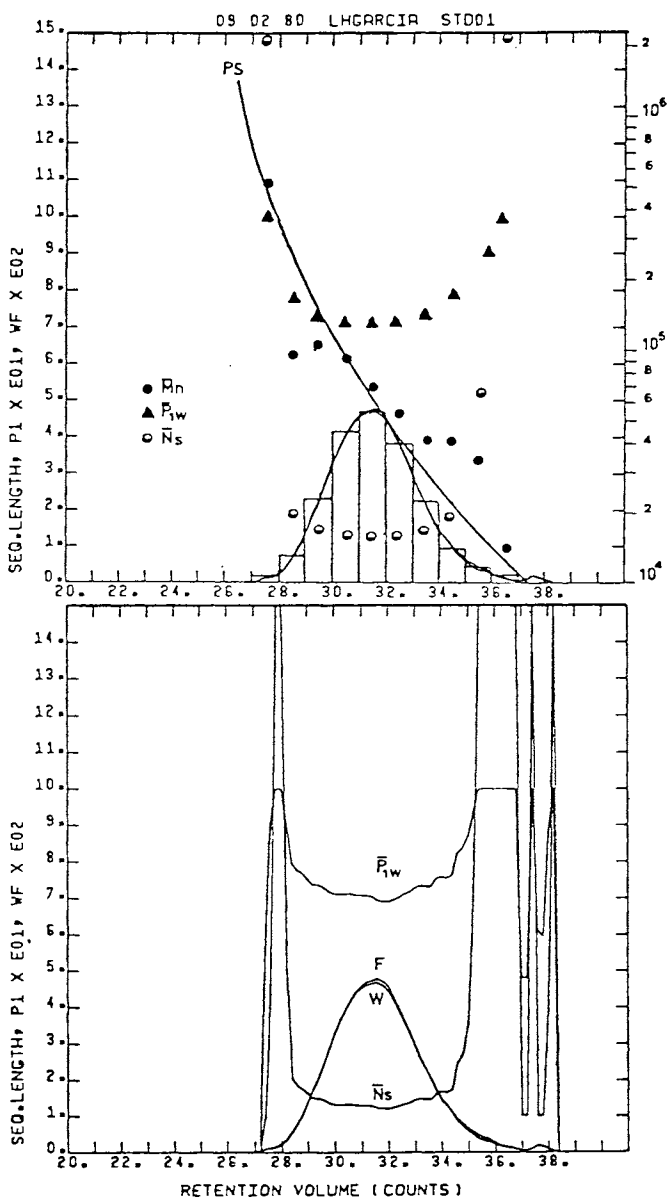


Figure 4. SEC characterization of SAN copolymer standard. Overall weight average molecular weight = 99,900 (light scattering). Overall number average molecular weight = 67,800 (osmometry). Overall weight fraction of styrene in the copolymer = 0.768. \bar{M}_n , \bar{N}_s and \bar{P}_{1w} are the number average molecular weight, average styrene sequence length, and the weight fraction of styrene in the copolymer as function of retention volume. Key: upper, off-line analysis of indicated fractions and lower, continuous detector trace.

experimental evidence to discriminate among copolymer models. Until now, the major emphasis has been on copolymerization equations based on ultimate group effects (equations 1, 2, 11, 12).

The traditional methods for the estimation of reactivity ratios (28, 29) and their more recent offsprings (30-32) are based on the transformation of equation 1 into one of the following forms:

$$r_2 = \frac{F_1^2}{f_1} r_1 + F_1 \left(\frac{1}{f_1} - 1 \right) \quad (17)$$

$$F_1 \left(1 - \frac{1}{f_1} \right) = -r_2 + \frac{F_1^2}{f_1} r_1 \quad (18)$$

$$\frac{1-f_1}{F_1} = -r_1 + \frac{f_1}{F_1^2} r_2 \quad (19)$$

r_1 and r_2 are then estimated graphically or by least squares. The use of equations 17 to 19 for the estimation of reactivity ratios have two shortcomings, one statistical in nature and the other experimental. Experimentally it may be very difficult in some cases to fulfill the conditions for the validity of equation 2, namely, negligible change in the residual monomer composition. Statistically, Tidwell and Mortimer (27) have shown that the use of linear least squares in equations 17 to 19 result in improper weights being applied to the observations. Behnken (33) and Tidwell and Mortimer (27) analyzed the effect of the experimental error when equations 18 to 19 are used and proposed the use of non-linear least squares as being statistically more desirable. However, even this approach ignores the measurement errors in the "independent" variable f_1 . This has led to the application of error in variables methods (EVM) (34-38). The use of these techniques which take into account the presence of error in all variables have been applied to the estimation of reactivity ratios. Yamada, Itahashi and Otsu (39) used the integrated form of the copolymerization equation expressed in terms of conversion and mol fractions of the feed and copolymer composition within a weighted least squares method equivalent to the error propagation method (Box 34). Van der Meer, Linssen and German (40) apply an EVM approach in which the observations are represented as coming from some true (but unknown) values contaminated with error. The true values (nuisance parameters) have to be estimated in addition to the reactivity ratios. Patino-Leal (38) and Reilly and Patino-Leal (41) RPL have described a method in which the true values of the observations are eliminated by obtaining a marginal posterior probability density function for r_1 and r_2 from the joint posterior probability density function of r_1 , r_2 and all the true values of the observations. In their estimation scheme, the model is linearized at each stage about the best estimates of the true values of the responses and the maximum a posteriori estimates of r_1 and r_2 are obtained conditional on this linearization. An outer loop iteration on the point linearization is then carried out. If the linearization is done always about the measured responses, this method transforms into an equivalent error propagation-weighted least squares (34, 39).

Errors in variables' methods are particularly suited for parameter estimation of copolymerization models not only because they provide a better estimation in general but also, because it is relatively easy to incorporate error structures due to the different techniques used in measuring copolymer properties (i.e. spectroscopy, chromatography, calorimetry etc.). The error structure for a variety of characterization techniques has already been identified and used in conjunction with EVM for the estimation of the reactivity ratios for styrene acrylonitrile copolymers (12).

Recent Advances in Copolymerization Theory

In the study of copolymers and copolymerization systems, the sophistication in model calculation has outstripped the experimentalist. Recalling that there are very few independent measures available with a commensurate error of two to fifteen percent, there would appear to be little hope to experimentally verify the many equations available. With the development of new and powerful analytical tools such as C^{13} NMR, FTIR, HPLC etc. and recent success in the interpretation and modelling of the gel effect phenomena (42), new interest has been generated in verifying the copolymerization equations and the effect of predicted properties on the performance of the final product.

Microstructure Heterogeneity and Copolymer Properties. It is well known that deviations on the structure and the composition of polymer blends and copolymers (heterogeneity) has an effect on the quality of the final product (43). Although significant effort has been devoted to the study of polymer blends (44), very little has been clarified in terms of the effects of heterogeneity on the properties of chemically heterogeneous statistical copolymers. Some sensitive properties such as solubility, glass transition temperature, phase separation and molecular size have been extensively studied as functions of the polymer microstructure or the copolymer composition (45-47) but data on heterogeneous or high conversion copolymers is rather scarce. Hendy (48) studied the mechanical properties of acrylonitrile/styrene copolymers and found that heterogeneous copolymers were useless as thermoplastics. Stejskal, Kratochvil and Hrouz (49) studied the mechanical properties of copolymer blends with variances in composition equivalent to those attainable in copolymerizations at high conversions and found no effect of the heterogeneity on the mechanical properties. Samanta (50) in a very comprehensive investigation studied the properties of styrene- α methyl styrene copolymers. No significant effects on the mechanical properties due to heterogeneity were reported other than a dependence on the terminal unit for the rate of thermal degradation. In addition to the properties discussed, the microstructure of the copolymer molecules is known to have an effect on the measurements traditionally used to determine compositions and molecular weights (12). These effects are particularly important, since the bulk properties of the copolymers are often correlated with measurements which may not be adequate.

Based on the controversial experimental evidence available, it is evident that the effects of microstructure and heterogeneity should be evaluated for every system. Such evaluation can greatly simplify the modelling of these systems or at least justify a semi-empirical approach which, thus far, has not been attempted.

On the Validity of the Copolymerization Equations. Tests on the validity of the copolymerization equation in its differential (1) or integrated form (2) have been, in general, limited to relatively low conversions ($X < 20\%$). Most of the deviations observed have been attributed to experimental error or to penultimate (or more

remote) group effects on the propagating chain. The rationale behind experimentation at low conversions has been to approximate the region in which the assumptions of negligible monomer composition changes and insignificant gel effect are valid. Although the reactivity ratios are sensitive to changes in copolymer and/or residual monomer composition, very precise measurements are required. Recently, Johnson, Karmo and Smith (51) using NMR, UV spectroscopy and gas-liquid chromatography studied styrene/methyl methacrylate (St-MMA) copolymers produced in butyl stearate (poor solvent), bulk and benzene (good solvent). Their measurements show deviations from the predicted cumulative copolymer compositions. These deviations coincide with the onset of the gel effect, increasing in magnitude as the conversion proceeds and as the quality of the solvent decreases. Point estimates of the reactivity ratios at high conversions show up to 50% deviation from low conversion estimates. Dionisio and O'Driscoll (52) experimentally verified the observations of Johnson, Karmo and Smith for the bulk copolymerization and by analyzing the rate behaviour concluded that penultimate group effects, depropagation and charge transfer complex formation are unlikely to have caused the observed rate and composition behaviour. Therefore, based on the new evidence, the question of the validity of the integrated form of copolymerization equation has arisen. On the other hand, Garcia-Rubio (12) found no evidence of varying reactivity ratios for low and high conversion SAN copolymerizations. The integrated form of the copolymerization equation gave a reasonable fit of the data over a wide range of conversions and compositions (see for example Figure 6).

Gel Effect Interpretation and Termination Reactions. In bulk solution and emulsion polymerizations, dramatic physical changes occur during the course of the reaction. These changes often affect significantly the rate behaviour and the properties of the final product. It has been recognized that diffusion-controlled reactions such as termination reactions are primarily affected and considerable effort has been devoted in recent years to the understanding and modelling of polymerizations at high conversions (53, 54). These efforts have crystallized in a model (42) based on the free volume theory for polymer solutions which has successfully predicted conversion and molecular weight histories for styrene, MMA, and vinyl chloride polymerizations. One of the main features of the free-volume model is that the additional parameters required are expressed in terms of measurable quantities such as limiting conversions and glass transition temperatures which can be determined independently from the rate histories. The modelling and interpretation of the gel effect and diffusion-controlled reactions in copolymerizations is still at a very early stage. Efforts by Atherton and North (55), Russo and Munari (56) and Chiang and Rudin (57) point to two main causes for the slow development of this area.

1. lack of sufficient rate data,
2. lack of molecular weight data.

The success reported with the limited data available can be easily attributed to the number of parameters involved, having at the present no justification for the use of a particular model other than its parsimony.

Discussion

So far, we have reviewed the existing copolymerization theory. It is evident at this point, that in order to elucidate the copolymerization kinetics, extensive and systematic experimentation is required to provide data on the initiation, termination

and propagation rates. The major stumbling block in the acquisition of experimental data has been, besides the normal difficulties associated with polymer experimentation, the lack of efficient characterization techniques which can yield reliable quantitative information on the MWD, CCD and SLD or at least some of their leading moments. Such information is of primary importance in the elucidation of copolymerization kinetics. It is, therefore, felt that a major experimental effort aimed to the study of copolymerization kinetics and to the development of characterization techniques is clearly justified.

Part 2 Copolymer Characterization

Throughout the study of copolymerization systems, the joint molecular weight distribution (MWD), copolymer composition distribution (CCD) and sequence length distribution (SLD), have been identified as the fundamental properties stemming directly from the synthesis conditions. Therefore, considerable effort has been spent in the development of techniques which yield information on the distributions or some of their moments (Table 1). All of the techniques listed in Table 1 with the exception of size exclusion chromatography (SEC) yield information only on average copolymer properties. In order to obtain information on the distributions themselves, fractionation of the copolymer samples with respect to composition and/or molecular weight is required. Size exclusion chromatography provides a very efficient way of fractionating polymer samples with respect to molecular size. It has, therefore, become one of the most useful techniques available for polymer characterization. SEC is also amenable to on-line control applications; therefore, the applications of SEC to copolymers will be emphasized.

Copolymer Composition

During the study of copolymerization reactions, there are basically two approaches for the determination of the copolymer composition:

1. composition analysis on the residual monomer,
2. composition analysis on the copolymer.

Residual Monomer Analysis. For the composition analysis of either the residual monomer or the copolymer, it is necessary to separate the monomer from the polymer since both contain the same functional groups. This was a serious limitation for the analysis of the residual monomer (significant composition changes may occur during manipulation), until the development of gas (GC), Gas-liquid (GLC) and high-pressure liquid chromatography (HPLC). In these techniques, the separation of monomer from the polymer takes place in the columns, thus providing very good accuracy in relatively short analysis times. The optimal conditions for the analysis (i.e. mobile phase, stationary phase, temperature, detectors etc.) are not always straightforward, but once the technique has been developed, the analysis is fast and simple. Gas chromatography has been used,

for example, by Van der Meer, Linssen and German (40) in the analysis of vinyl acetate-vinyl propionate copolymerization. Johnson, Karmo and Smith (51) studied the validity of the integral form of the copolymerization equation for styrene-methyl methacrylate using gas chromatography. An error of $\pm 2\%$ in composition was reported for the copolymer compositions obtained from GC measurements. Balke and Patel (58) used HPLC for the analysis of styrene n-butyl methacrylate copolymerizations for which very good reproducibility is reported.

Table 1

Copolymer Characterization Techniques

Sequence Length	Composition	Molecular Weight
	Chemical Analysis	End Group Analysis (\bar{M}_n)
	Melt Viscometry	Osmometry (\bar{M}_n)
NMR		
^1H	Elemental Analysis	Viscometry (\bar{M}_v \bar{M}_w)
^{13}C	Spectroscopy	Sedimentation (\bar{M}_w \bar{M}_s)
	UV IR	
IR	Refractometry	Light Scattering (\bar{M}_w)
	NMR	
	TLC	
	GC	
	SEC	
	(fractionation)	

More recently, Garcia-Rubio (12) investigated the styrene acrylonitrile copolymerization kinetics using gas chromatography and, although some difficulties were reported with the monomer extraction process at high conversion, in general very good descriptions of the copolymerization reaction were obtained in terms of the residual monomer composition (Figures 5, 6).

Copolymer Analysis. Even though the overall copolymer composition can be determined by residual monomer analysis, it still is necessary to have reliable quantitative techniques for copolymer composition measurements on the actual copolymer, mainly because concentration detectors for SEC or HPLC are sensitive to composition and because the conversion histories are not always available. Some of the techniques used to determine copolymer composition are melt viscometry (46), chemical analysis, elemental analysis, infrared spectroscopy (IR), Nuclear Magnetic Resonance (NMR), ultra-violet spectroscopy (UV), etc. Melt viscometry, chemical and elemental analysis are general techniques that can be applied to almost any polymer. The spectroscopic techniques can be applied depending on the ability of the functional groups present to absorb at specific wavelengths.

Spectrometric Analysis. Spectroscopy has been extensively used for polymer and copolymer analysis. (59-69). The kind of information available from different spectroscopic techniques as well as the instrumentation required depends on the region of the electromagnetic spectrum in which absorption is taking place. Recent investigations (63) on the use of spectrophotometers for copolymer analysis have shown that the response from spectrophotometers is sometimes sensitive to the microstructure of the polymer molecules and that calibration of spectrophotometers with absolute measurements on the microstructure (i.e. NMR) may be necessary in order to obtain reliable quantitative information on concentration and copolymer composition determinations.

Molecular Weight Determination

Molecular weight determination methods can be classified (66) as: Absolute, Equivalent and Relative. Absolute methods allow the molecular weight to be calculated directly from measured quantities. Knowledge of the physical and chemical structure of the molecules is not required. Absolute techniques include: colligative methods (osmometry, ebulliometry, cryoscopy etc.), light scattering and equilibrium sedimentation. Some methods yield simple, others mixed averages of the molecular weights.

Equivalent methods always require some knowledge of the chemical structure of the molecules before molecular weights can be calculated from measured data. With end group analysis, for example, it is necessary to know both the nature and the number per molecule of end groups.

Relative methods, on the other hand, measure properties that depend on the chemical and physical structure of the macromolecule. Intrinsic viscosity fractionation and SEC methods are examples of this category in which the measurements are functions of the constitution and configuration of the macromolecule in solution. Relative methods must always be calibrated against an absolute method.

This classification cannot always be rigorously applied, for example, in the molecular weight determination by absolute methods of polyelectrolytes or highly-polar polymers, allowance must be made for the interactions caused by the

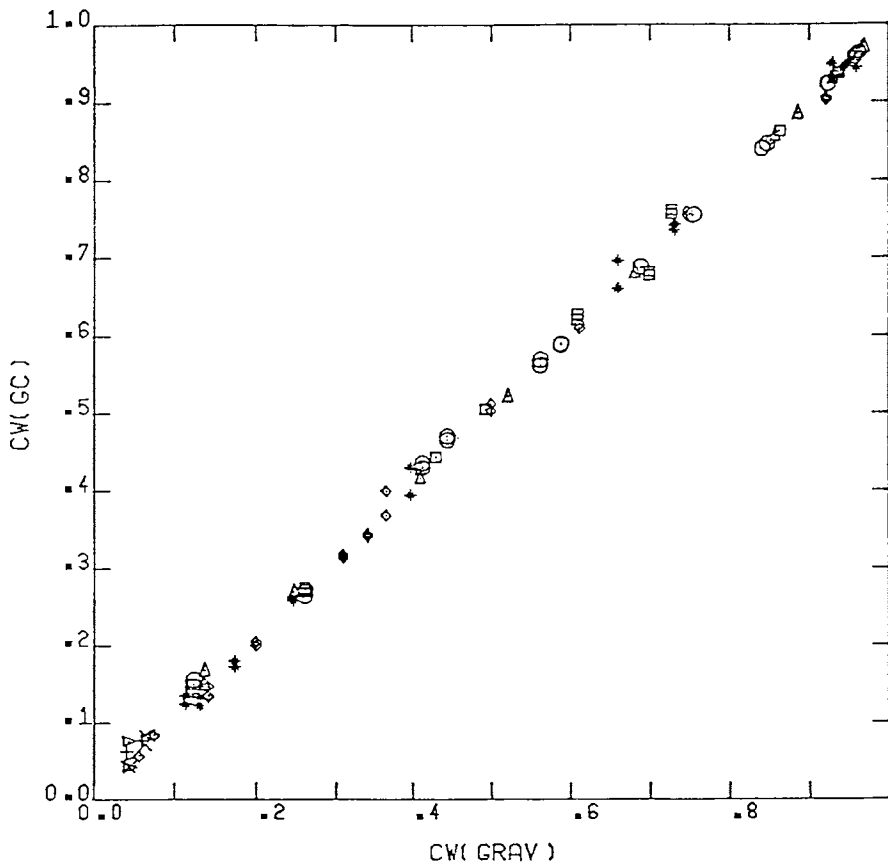


Figure 5. Comparison of conversion histories obtained gravimetrically and by gas chromatography. $T = 60^{\circ}\text{C}$, $[I] = 0.01 \text{ g mol/L}$. Key to feed compositions: Δ , 0.90; \circ , 0.80; \square , 0.70; $*$, 0.60; \diamond , 0.50; $+$, 0.40; ∇ , 0.30; \times , 0.20; and Δ , 0.10. Data from Ref. 12.

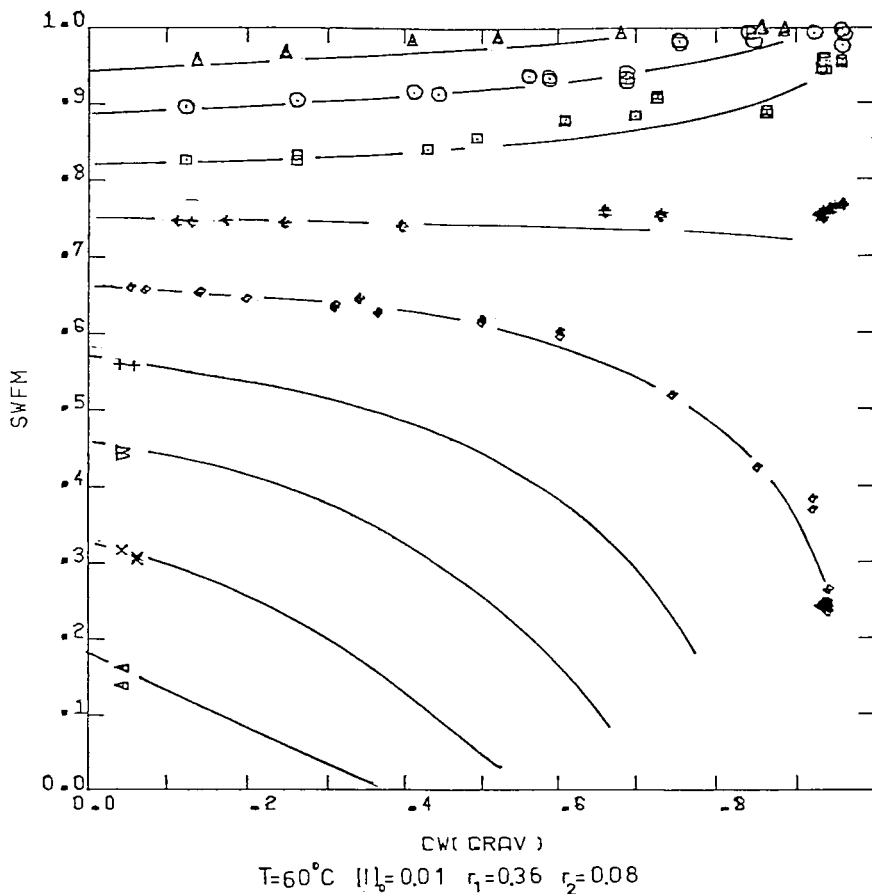


Figure 6. Agreement between experimental and calculated styrene acrylonitrile copolymerization data. Conditions: $T = 60^{\circ}\text{C}$; reactivity ratios, $r_1 = 0.36$ and $r_2 = 0.08$. Key to feed compositions: Δ , 0.90; \circ , 0.80; \square , 0.70; $*$, 0.60; \diamond , 0.50; $+$, 0.40; ∇ , 0.30; \times , 0.20; \triangle , 0.10. Data from Ref. 12.

chemical nature and the properties in solution of such materials. The two most widely-used techniques for average molecular weight determination are: Osmometry and Light Scattering.

Osmometry. When a solution is separated from the pure solvent at isothermal conditions by means of a membrane permeable only to the solvent molecules, the osmotic pressure of the solution is defined as the excess pressure which must be placed on it in order to prevent any diffusion of solvent through the membrane. The cause of osmosis is diffusion which arises from a difference in chemical potential. At the same temperature and pressure, the solvent is at a lower chemical potential in the solution than in its own pure liquid, and there is a tendency for it to pass through the membrane in the direction of pure solvent to solution.

Based on the thermodynamics of ideal solutions, it can be shown that for monodispersed solutes:

$$\lim_{c \rightarrow 0} \frac{\pi}{c} = \frac{RT}{M}$$

$$c \rightarrow 0$$

$$\pi_{c=0} = \frac{cRT}{M} \quad (20)$$

where π is the osmotic pressure, c the concentration of the solute, R the gas constant, T the temperature and M the molecular weight.

for polydispersed solutes assuming additive osmotic pressures:

$$\pi_{c=0} = RT \frac{\sum c_i}{M_n} \quad (21)$$

for solutions of non-associating, non-electrolytes at finite concentrations, (π) can be expressed as an ascending series of positive powers of solute concentration (virial equation form).

$$\pi = RT \left(A_1 c + A_2 c^2 + A_3 c^3 + \dots \right)$$

$$\text{or} \quad (22)$$

$$\frac{\pi}{c} = RT \left(\frac{1}{M_n} + A_2 c + A_3 c^2 + \dots \right)$$

where \bar{M}_n is the number average molecular weight and A_i are virial coefficients.

There are two important features of this technique that are relevant for copolymer applications:

- i. It does not depend on the composition or molecular microstructure.
- ii. Most of the interaction effects (polymer-polymer, solvent-polymer, polymer membrane etc.) as well as deviations from ideal membranes can, in general, be identified and accounted for (66).

Osmometry has been applied to a variety of copolymer systems such as vinyl-chloride-vinyl acetate (67, 68), acrylonitrile vinyl-ether copolymers (69) styrene-acrylonitrile (70), styrene-maleic anhydride (71) and for a series of styrene copolymers (72).

Light Scattering. Light scattering provides one of the most important methods for determining the molecular weights and dimensions of polymers, but unfortunately, its application to copolymers is not straightforward. This method measures the light scattered at an angle to the incident light. Incident light of intensity I_0 on passing through a scattering medium will have its intensity diminished to the amount I_s . From the electromagnetic theory of light, it can be shown that (73):

$$R_\theta = kc \bar{M}_w \quad (23)$$

where R_θ is the Rayleigh ratio and \bar{M}_w is the weight average molecular weight.

The molecular weight estimated from equation 23 is a function of the copolymer composition through the refractive index increments. $(dn/dc)_{c=0}$. By assuming a linear dependence of (dn/dc) with respect to composition, Bushuk and Benoit (74) derived an expression for the weight average molecular weight of copolymers as functions of the refractive index increments

$$\bar{M}_{wapp} = \bar{M}_w + 2P \left(\frac{\nu_A - \nu_B}{\nu_0} \right) + Q \left(\frac{\nu_A - \nu_B}{\nu_0} \right)^2 \quad (24)$$

were:

$$\nu_A = \left(\frac{dn}{dc} \right)_A \quad \nu_0 = \left(\frac{dn}{dc} \right)_{copol.} \quad \nu_B = \left(\frac{dn}{dc} \right)_B \quad (25)$$

P and Q are known as the "heterogeneity parameters" and are a measure of the polydispersity of chain composition. Using equation 24 together with equation 23 in the form:

$$R_\theta = kc \bar{M}_{wapp} \quad (26)$$

for several refractive index increments, \bar{M}_w , P and Q can be experimentally determined. This technique has been successfully applied to mixtures of polymers, block and graft copolymers (75). However, for random copolymer, very few results agree with the theory. Among these, Shimura et al (76) and Baumann Lange (70) which reported results for styrene-acrylonitrile copolymers. For most cases reported (see Benoit 75), the values of P and Q obtained were much greater than could be accounted for on the basis of copolymerization theory i.e. measurements from sedimentation equilibrium in a density gradient (77) compare well with copolymerization theory, whilst there is a factor of about 10^3 between these results and those from light scattering. Recently, Spatorico (78) reviewed the applications of light scattering to copolymers and concluded that it is disappointingly insensitive to low molecular weight copolymers and that the errors involved and its stringent requirements in terms of refractive indices make it unsuitable for routine analysis. Nevertheless, this method is useful since, other than sedimentation equilibrium in a density gradient, there is no simple method of analyzing the polydispersity in copolymer composition.

Copolymer Fractionation. In order to use any of the relative methods of polymer molecular weight analysis well characterized (normally by light scattering and osmometry), narrow molecular weight standards are required. Such standards are, in some cases, produced anionically like polystyrene and polybutadiene or by fractionation via size exclusion or by fractional precipitation of broad MWD polymers. Precipitation or phase separation techniques have been extensively used in homopolymer analysis (79, 80) for copolymers. However, phase separations are complicated by the presence of different chemical species in the polymer molecule. Therefore, the selection of conditions that warrant uniform molecular weight or composition fractions are difficult to obtain. Cross-fractionation techniques have been used in the analysis of styrene-methyl methacrylate copolymers by Teramachi and Kato (81). Low conversion copolymers were fractionated by composition and molecular weight. The joint chain length composition distribution thus found was reported in agreement with Stockmeyer's formulation for termination by combination. Baumann and Lange (70, 82) studied styrene/acrylonitrile copolymers (SAN) by fractionation from CHCl_3 and then by Osmometry and Light Scattering. The light scattering results do not follow the Theory for Azeotropes ($P = Q = 0$ in eq. 26). However, by averaging the results, molecular weight-intrinsic viscosity relationships were obtained. More recently, Tavel and Shaller (83) studied SAN copolymers (with AN content up to 13% by weight) by fractionation with respect to chemical composition. Liquid phase pairs were used with up to 4 components.

Although phase separation techniques have been shown to be useful in copolymer analysis, the amount of work required restricts considerably their application.

Sequence Length Determination

With the development of polymer structural characterizations using spectroscopy, there has been a considerable effort directed to measurements of tacticity, sequence distributions and number average sequence lengths (59-65). Two methods have been traditionally used for microstructure analysis from polymer solutions. Vibrational spectroscopy (infrared) and Nuclear Magnetic Resonance (NMR). Neither of these techniques is absolute. The assignment of absorption bands requires the use of model compounds or standards of known structure.

Infrared Spectroscopy. An infrared absorption spectrum originates from molecular vibrations which cause a change in the dipole moment of the molecule. Such a spectrum, therefore, reflects the structure of the molecule, especially the masses of the constituent atoms and the intramolecular forces acting between them. The interpretation of infrared data obtained from polymer spectra particularly from solutions should be approached with care. Shifts due to solvent interactions, hydrogen bonding etc., can markedly affect the infrared spectrum. However, by considering sufficiently dilute solutions, the contributions from neighbouring groups other than the adjacent ones can be neglected and the spectra of polymers can be considered as a superposition of spectral characteristics of almost independently vibrating units. It is necessary to account only for conformational splitting and, in the case of copolymers, for the deviations in the coupling between immediately-neighbouring units of different chemical structure (A-B links). Using this approximation, the spectral behaviour of triad sequences has been studied for a number of copolymers (63). Although the vibrational spectra of copolymers generally differ appreciably from the summation spectra of homopolymers, it has been possible for some limited cases to deduce quantitative sequence information from such data. In general, the interpretation of vibrational spectra is rather difficult. NMR spectra can be used effectively for this purpose provided the resonances can be correctly assigned.

Nuclear Magnetic Resonance. The successful study of polymers in solution by high resolution NMR spectroscopy started with the pioneering work on the sequence structure of poly methyl methacrylate in 1960. Since then, an ever-increasing number of investigations have been carried out ranging from the elucidation of the statistics of homopolymer and copolymer structure to the study of conformation, relaxation and adsorption properties of polymers. The aspects of sequence length determination and tacticity have received considerable attention (Klesper 84, for example, reports more than 500 entries). Therefore, a detailed review will not be attempted. (For a detailed description of the NMR Theory and statistics of polymer structure, see Bovey 59, Randall 23, and Klesper 84).

Size Exclusion Chromatography

Size Exclusion Chromatography (SEC) is probably the most powerful technique available for characterizing polymeric materials. The chromatogram, depending on the amount of dispersion, approximately corresponds to the molecular size distribution (MWD) in shape. Under ideal conditions, polymeric species are separated according to the hydrodynamic volumes of the molecules in solution (85). The molecules undergo size separation and dispersion throughout their transit through the columns (86). Once corrections for dispersion have been applied the MWD can be calculated from the corrected chromatogram and a suitable calibration curve. The basic equations follow:

The calibration curve as a function of retention volume can be represented as:

$$M = Q(v) \quad (27)$$

The chromatogram $F(v)$ can be represented by the convolution of the true distribution $w(y)$ and the spreading function $G(v,y)$ (Tung's Equation).

$$F(v) = \int_0^{\infty} w(y) G(v,y) dy \quad (28)$$

The columns are normally calibrated for molecular weight (eq. 27) and axial dispersion (parameters of $G(v,y)$). The solution of equation 28 in terms of $w(y)$ then allows for the complete MWD estimation. Some complications may arise, however, due to interactions between the packing material, the polymer and the solvent which will tend to increase the dispersion or decrease the resolution, depending on whether adsorption or exclusion are taking place. These problems are compounded when narrow standards are not available and interactions are not likely to be properly identified. This, unfortunately, is the case for copolymers in general. Polymer/solvent/packing interactions are particularly important when techniques such as the Universal Calibration ($[\eta]M$ vs V) are used. Anomalous molecular weight-retention volume behaviour has been observed over the years for polymers of varying polarity in a number of mobile phase/substrate systems. It is only recently that systematic studies on the effect of such interactions on the molecular weight interpretation are being reported. Dubin, Koontz and Wright (87), studied the elution behaviour of polymers with wide range of polarities in DMF/LiBr and a variety of substrates. Styragel and silanized glass were reported as having affinity for non-polar polymers. Consequently, application of polystyrene curves to SEC analysis of more polar polymers with these substrates led to over-estimation of the molecular weights. Ideal SEC behaviour was found for a number of polymers on untreated glass surfaces. However, polymers with strong hydrogen bonding functionality appear to be susceptible to marked adsorption in DMF/glass systems. Berek et al (88) and Bakos et al (89) studied polystyrene standards in a variety of solvents of different thermodynamic quality with Porasil as stationary phase. A number of interesting observations, which have direct bearing on copolymer analysis, were drawn from their results:

- i. Adsorption is a function of the thermodynamic quality and the selectivity of the solvent.
- ii. The partition of the polymer solute between the mobile and stationary phases is a function of the molecular weight.
- iii. The universal calibration procedure based on the hydrodynamic volume of the polymer molecules is directly applicable only for systems for which adsorption/partition is approximately the same.

Campos, Soria and Figuerelo (90, 91) studied the polymer retention mechanism in GPC on active gels using pure and mixed eluents and narrow PS standards. The effect of different eluents on the exclusion volume, total permeation volume and shifts on the universal calibration curve ($M.[\eta]$ vs. RV) were analyzed as a function of the thermodynamic quality of the solvent and the solvent strength. The effective radius of the gel pores (or conversely the hydrodynamic volume) was found to be a joint function of the solvent strength and its thermodynamic quality. This was explained in terms of the formation of a layer of a quasi-stationary phase of eluent interacting with the substrate. The solvent with greater affinity for the substrate will be more concentrated in the neighbourhood of the gel. Depending on the thermodynamic quality of the solvent and the compatibility of the solute with the packing material, the partition coefficient will increase to the point of complete adsorption or decrease to total exclusion. Using Bakos and Campos concepts, Balke and Patel (58) were able to fractionate styrene-*n*-butyl methacrylate copolymers composition-wise from mixtures of

THF/n-heptane. These remarkable results, although not yet quantitative, indicate not only an alternative to composition analysis but also, the magnitude of the effects that could be present due to polymer/solvent/gel interactions. It is obvious that, if reliable copolymer molecular weight results are to be obtained by SEC, the conditions that guarantee exclusively size or composition fractionation must be met. Experimental investigation of these conditions (25) coupled with elucidation of the effects of the copolymer microstructure on the SEC detectors (65) has led to the characterization of SAN copolymers for which sequence length, composition and molecular weight have been measured as functions of the molecular size (Figure 4).

Discussion

It is evident, at this point, that significant discrepancies exist in the literature regarding the effect of the molecular weight, composition and sequence length on the response of the concentration detectors, the abnormalities observed in the absolute molecular weight characterization techniques and on the hydrodynamic and solubility properties of the macromolecules, which in turn, have significant bearing on the chromatographic separation by composition and molecular size. It is noteworthy that a significant number of studies have been done over a limited range of molecular weights and compositions. Therefore, a complete description of the copolymer properties and their interactions has very seldom been presented. As a consequence, a general methodology for copolymer analysis has not yet been developed. From the information available in the literature, three stages in the copolymer characterization problem have been identified (12, 25, 65):

- i. production and characterization of composition and molecular weight standards,
- ii. investigation of the effects of the composition and microstructure on the concentration detectors (i.e. selection of concentration and/or composition detectors),
- iii. investigation of the microstructure effects on the hydrodynamic and solution properties of the copolymers (calibration and interpretation of chromatographic results).

The problem of copolymer characterization becomes more acute when on-line process measurements are required. Most of the process instrumentation available yields measurements which are functions of the molecular weight, copolymer composition and, in some cases, of the microstructure of the polymer molecules. Such is the case for on-line viscosimeters, densitometers, torque meters etc. Clearly, the development of copolymer characterization techniques in general and on-line instrumentation in particular requires extensive development.

Part 3 Reactor Design and the Control of Copolymerization Reactors

Given the limitations of the kinetic models and the analytical methods, the design, analysis and control of copolymerization reactors has been centered around the problem of maintaining uniform composition and avoiding runaway reactions (i.e. the problem of heat transfer). The effect of mixing in different reactor configurations has been analyzed extensively using the selectivity equations and first order or pseudo first order rate expressions (16). Continuous reactor trains operating at steady-state conditions, or semi-batch systems with adequate mixing and controlled feed of one of the monomers have been proposed to address the problem of uniform composition. In most instances, the molecular weight of the copolymer has been fixed by the temperature and initiator level

selected. However, since the monomer composition will also affect the molecular weight, semi-batch composition control policies will usually lead to broader molecular weight distributions.

Temperature control policies have also been suggested to diminish the composition spread in batch reactors (92, 94). However, the low sensitivity of the reactivity ratios to temperature (Figure 7), the poor heat transfer characteristics of reacting polymer mixtures (slow response times) and the considerable excursions in temperature (and, therefore, molecular weights) required to maintain adequate uniformity in composition make the application of these temperature control policies unrealistic.

Conclusions

It is evident that, in order to elucidate the copolymerization kinetics, extensive and systematic experimentation is required to provide data on the initiation, termination and propagation rates. The major stumbling block in the acquisition of experimental data has been, besides the normal difficulties associated with polymer experimentation, the lack of efficient characterization techniques which can yield reliable quantitative information on the MWD, CCD, and SLD or at least some of their leading moments. Such information is of primary importance in the elucidation of copolymerization kinetics. It is, therefore, felt that a major effort aimed at the study of copolymerization kinetics and at the development of characterization techniques is clearly justified.

An important point to remember in the operation and control of copolymerization reactors is that these systems are inherently multivariable in nature. Therefore, strategies aimed at controlling one variable are often not practical because they lead to unacceptable variations in the other properties. Control of properties like sequence lengths and certainly multivariable strategies for composition, molecular weights and sequence lengths have not yet been addressed. It may be then concluded that only upon verifying some of the existing copolymerization models or modifying them appropriately for a given system, and upon obtaining efficient estimates of their parameters from experimental data will it be possible to develop efficient multivariable control strategies for the important copolymer properties.

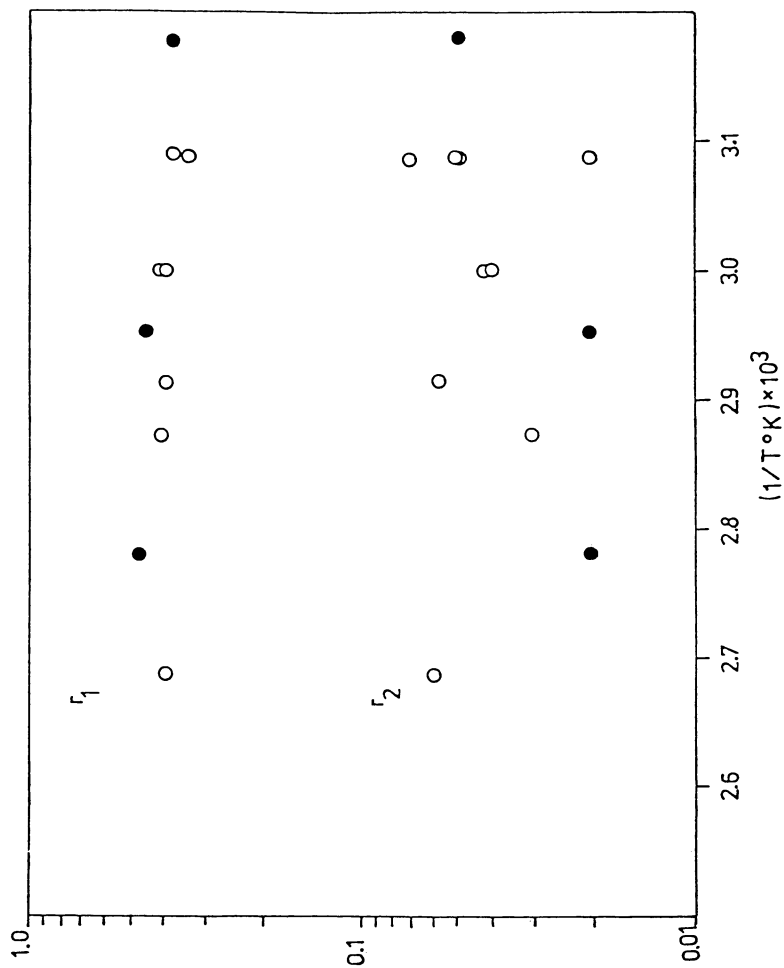


Figure 7. Arrhenius plot of the reactivity ratios for styrene acrylonitrile bulk copolymerization. Literature data.

Literature Cited

1. Wall, F.T., J. Am. Chem. Soc. 1941, 63, 1862
2. Lewis, F.M., Mayo, F.R., J. Am. Chem. Soc. 1944, 66, 1594
3. Simha, R. and Branson, H., J. Chem. Phys. 1944, 12, No. 6, 253
4. Merz, E., Alfrey, T. Jr. and Goldfinger, G., J. Polymer Sci. 1946, 1, 75
5. Durgaryan, A.A., Vysokomol Soyed 1966, 8, No. 6, 867
6. Lowry, G.G., J. Polym. Sci. 1960, 42, 463
7. Skeist, I., J. Am. Chem. Soc. 1946, 68, 1781
8. Walling, C., J. Am. Chem. Soc. 1949, 71, 1930
9. Ham, G., "Copolymerization Interscience", 1965
10. Ray, W.H., Douglas, T.L., Godsolve, E.W., Macromolecules 1971, 4, No. 2, 166
11. Brandrup, J. and Immergut, E.H., "Polymer Handbook", Interscience (1975)
12. Garcia-Rubio, Luis H., "Ph.D. Thesis", McMaster University, Hamilton, Ontario, Canada, 1981
13. Melville, H.W., Noble, B., and Watson, W.F., J. Polym. Sci. 1947, 2 (2), 229
14. de Butts, E.H., J. Am. Chem. Soc. 1950, 72, 411
15. O'Driscoll, K.F., P. Knorr, Macromolecules 1968, 1, 367
16. Mecklenburg, J.C., Can. J. of Chem. Eng. 1970, 48
17. Miyata, T. and F. Nakashio, J. Chem. Eng. of Japan 1975, 8, No. 6
18. Lin, C.C., Chiu, W.Y. and Wang, C.T., J. App. Polym. Sci. 1979, 23, 1203
19. Alfrey T. Jr., J.J. Bohrer and H. Mark (1952), "Copolymerization, High Polymer Series", Vol. VIII, Interscience, New York (1952)
20. Price, F.P., J. Chem. Phys. 36, 209, (1962)
21. Price, F.P., "Markow Chains and Monte Carlo Calculations in Polymer Science" (G. Lowry ed.), Dekker, New York (1970)
22. Bovey, F.A., "Polymer Conformation and Configuration", Academic Press, New York (1969)
23. Randall, J.C., "Polymer Sequence Determination", Academic Press (1977)
24. Stockmeyer, W.N., J. Chem. Phys. 1945, 13, 199
25. Garcia-Rubio, Luis H., J.F. MacGregor and A.E. Hamielec, "181 ACS National Meeting", Atlanta, Ga., March-April 1981
26. Fordyce, R.G., E.C. Chapin, J. Am. Chem. Soc. 1947, 69
27. Tidwell, P.W. and G.A. Mortimer, J. Macromol. Sci. 1970 C4, 281
28. Mayo, F.R. and F.M. Lewis, J. Am. Chem. Soc. 1944, 66, 1599
29. Finneman, M. and S.D. Ross, J. Polym. Sci. 1950, 5, 259
30. Tosi, C., Europ. Polym. J. 1973, 9, 357
31. Braun, D., W. Brendelin and G. Mott, Europ. Polym. J. 1973, 9, 1007
32. Kellen, T. and F. Tudos, J. Macromol. Sci. Chem. 1975, A9, 1
33. Behnken, P.W., J. Polym. Sci. A 1964, 2, 645
34. Box, M.J., Technometrics 1970, 12 (2), 219
35. Britt, H.I. and R.H. Luecke, Technometrics 1973, 15 (2), 233
36. Sutton, T.L. and J.F. MacGregor, Can. J. Chem. Eng. 1977, 55, 602
37. Anderson, T.F., D.S. Abrams and E.A. Greens, AIChE Journal 1978, 24
38. Patino-Leal, H., Reilly, P.M. and K.F. O'Driscoll, J. Polym. Sci. C 1980, 219
39. Yamada, B., M. Itahashi and T. Otsu, J. Polym. Sci. 1978, 16, 1719
40. Van der Meer, R., H.N. Linssen and A.L. German, J. Polym. Sci. 1978, 16, 2915
41. Reilly, P.M., H. Patino-Leal, Technometrics (to be published)

42. Marten, L. and A.E. Hamielec, "Polymerization Reactors and Processes", Am. Chem. Soc. Symposium Ser. 1978, 104, Am. Chem. Soc. Washington, D.C., 43
43. Nielsen, L.E., J. Am. Chem. Soc. 1953, 75, 1453
44. Paul, D.R., "S. Newman Eds., Polymer Blends", Academic Press (1978)
45. Barton, J.M., J. Polymer Sci. C 1970, 30, 573
46. Johnston, N.W. Rev. Macromol. Chem., 1976, C14 (2)
47. Seymour, R.B., Polymer 18 (1977)
48. Hendy, B.N., Adv. in Chem. 1975, Series No. 142, 115
49. Stejskal, J., P. Kratochvil and J. Hrouz, J. Polym. Sci. 1979, 257, 931
50. Samanta, M.C., "Ph.D. "Thesis", University of Waterloo, Waterloo, Ontario, Canada (1978)
51. Johnson, M., T.S. Karmo and R.R. Smith, Europ. Polym. J. 1978, 14, 409
52. Dionisio, J.M. and K.F. O'Driscoll, J. Polym. Sci. Polym. Letters Ed. 1980, 70, 701
53. Friis, N. and A.E. Hamielec, J. Polym. Sci. Chem. Ed., 12, 1974, 251
54. Cardenas, J. and K.E. O'Driscoll, J. Polym. Sci., Polym. Chem. ed. 14, 883 (1976); 15, 1883, 2097 (1977)
55. Atherton, J.N. and A.M. North, Trans. Faraday Soc., 1962, 58, 2049,
56. Russo, S. and S. Munary, J. Macromol. Sci. Chem. 1968, A2, 1321
57. Chiang, S.S.M. and A. Rudin, J. Macromol. Sci. Chem., 1975, A9(2), 237
58. Balke, S.T. and R. Patel, "29th Canadian Chemical Engineering Conference", Sarnia, Ontario, September 1979
59. Bovey, F.A., "High Resolution NMR of Macromolecules", Academic Press (1972)
60. Slonim, I. Ya, and A.N. Lyubimov, "The NMR of Polymers", Plenum Press, New York (1970)
61. Carrol, B. ed., "Physical Methods in Macromol. Chemistry 1", Marcel Dekker (1969)
62. Hummel, D.O., "Infrared Spectra of Polymers", Polymer Reviews, 14, (1966)
63. Henniker, J.C., "Infrared Spectrometry of Industrial Polymers", Academic Press, (1967)
64. Hummel, D.O. ed., "Polymer Spectroscopy", Verlag Chemie (1974)
65. Garcia-Rubio, Luis H., A.E. Hamielec and J.F. MacGregor, "182 National ACS Meeting", New York, August 1981.
66. Elias, H.G., "Macromolecules I", Plenum Press, New York (1977)
67. Chen, H.R. and L.P. Blanchard, J. App. Polym. Sci., 1972, 16, 603
68. Janca, J., L. Mekvickova and M. Kolinsky, J. App. Polym. Sci. 1978, 22, 2661
69. Kenyon, A.S. and A.E. Mottus, "App. Polym. Symposium No. 25", (1974)
70. Bauman, H. and H. Lange, Angew. Makromol. Chem. 1969, 9, 16
71. Chow, C.D., J. App. Polym. Sci., 1976, 20, 1619
72. Jordan, E., J. Polym. Sci., 1968, 6
73. Huglin, M.B. ed., "Light Scattering from Polymer Solutions", Academic Press (1972)
74. Bushuk, W. and H. Benoit, Can. J. of Chem. 1958, 36, 1616
75. Benoit, H. and D. Froelich in, "Light Scattering from Polymer Solutions" (M.B. Huglin ed.) Academic press (1972)
76. Shimura, Y., I. Mita and H. Kambe, J. Polym. Sci. Polymer Letters Ed. 2, 1964, 403
77. Lamprecht, J., "Ph.D. Thesis", Strasbourg (1970)

78. Spatorico, A.L. and B. Coulter, J. App. Polym. Sci., 1973, 11
79. Guzman, G.M., "Fractionation of High Polymers Prog. High Polym." 1, 1961, 113
80. Cantow, M.J.R. ed., "Polymer Fractionation", Academic Press, New York (1967)
81. Teramachi, S. and Y. Kato, "Macromolecules", 1970, 4 (1), 54
82. Lange, H., H. Baumann, Angew Makromol. Chem. 1970, 14, 25
83. Tavel, P.V. and J. Schaller, Makromol. Chem. 1978, 179, 677
84. Klesper, E., "Polymer Spectroscopy (D.O. Hummel Ed.)", Verlag Chemie (1974)
85. Grubisic, Z., P. Rempp and H. Benoit, J. Polym. Sci. 1967, B5, 753
86. Friis, N., A.E. Hamielec, Adv. in Chrom. 1975, 13
87. Dubin, P., S. Koontz and K. Wright, J. Polym. Sci. 1977, 15, 2047
88. Berek, D., D. Bakos and L. Soltes, Makromol. Chem. 176, 391, (1975)
89. Bakos, E., T. Bleha, A. Ozima and D. Berek, J. App. Polym. Sci. 1979, 23, 2233
90. Campos, A., V. Soria and J. Figueruelo, Makromol. Chem. 1979, 180, 1961
91. Figuerelo, J., V. Saria, A. Campos, J. of Liq. Chrom. 3 (3), 1980, 367
92. Ray, W.H. and C.E. Gall, "Macromolecules 1", 367 (1968)
93. Hicks, J., A. Nolan and W.H. Ray, Cdn. J. Chem. Eng. 1967, 47, 590
94. Tirrell, M. and K. Gromley, presented at the "73rd Annual AIChE Meeting", San Francisco, 1980.

RECEIVED May 28, 1982.

Copolymerization Reaction Engineering

Controlled and Uncontrolled Semi-batch Solution Copolymerization of Styrene with Methyl Acrylate

A. F. JOHNSON, B. KHALIGH, and J. RAMSAY

University of Bradford, Schools of Polymer Science and Control Engineering,
Bradford BD7 1DP West Yorkshire, England

Model-reference feed-forward control strategies have been developed for the synthesis of compositionally homogeneous copolymer from free-radically initiated binary copolymerisation reactions where (i) the co-reactants have greatly different reactivities (ii) the reactions are taken to high monomer conversions and (iii) the reactions are carried out in solution in a semi-batch isothermal reactor. The control strategy aims at maintaining a constant molar ratio of coreactants in the reactor through the combined and repeated application at regular time intervals of the mathematical models of batch and semi-batch copolymerisation processes. The models provide a flow rate profile which has been used to generate set-points for a computer controlled semi-batch experimental reactor. In this work the reactor conditions are adjusted by the addition of the more reactive monomer only. The control policy has been shown to be largely successful in the case of the copolymerisation of styrene with methyl acrylate when initiated by azo-bis-iso-butyronitrile in toluene solution.

Many aspects of homopolymerisation reaction engineering have been studied in recent years (1-4). Much attention has been given the nature of the dependence of the polymer molecular weight (MW) and molecular weight distribution (MWD) on the operating conditions of the polymerisation reactor.

0097-6156/82/0197-0117\$06.00/0

© 1982 American Chemical Society

Alongside the growth of understanding of the complex inter-relationship between the reaction and reactor dynamics there has been rapid increase in the application of computers for polymerisation reactor control (5).

In contrast to the requirements for homopolymerisation processes, the parameters needed to fully describe copolymerisation processes are more numerous. Molecular features such as the copolymer composition, composition distribution and chain sequence structure and their variation with conversion are compounded with those of copolymer MW and MWD. To understand copolymerisation processes, it is desirable to decouple as many of these molecular parameters as possible and study the influence of polymerisation reactor conditions on each. As yet there have been relatively few reports on the detailed behaviour of copolymerisation reactors (6-9). This work forms part of a wider range of investigations which are being carried out in our laboratories of control methods for the production of speciality polymers.

It is common for the monomers taking part in copolymerisation reactions to be of different reactivities which leads to a drift in copolymer composition with conversion. The instantaneous copolymer composition can be related to the instantaneous composition of the monomer feed through r_1 and r_2 , the monomer reactivity ratios (10) as shown in Equation (1).

$$F_1 = \frac{r_1 f_1^2 + f_1 f_2}{r_1 f_1^2 + 2f_1 f_2 + r_2 f_2^2} \quad (1)$$

Here F_1 and F_2 are the instantaneous mole fractions of monomers 1 and 2 in the polymer respectively and f_1 and f_2 are the instantaneous mole fraction of monomer 1 and 2 in the feed respectively. The reactivity ratios are a function of the reaction temperature. Equation (1) demonstrates that the instantaneous composition of the copolymer depends upon the ratio of monomers in the reaction mixture and the temperature. Variations in the composition of the feed with conversion, or temperature changes during polymerisation, will cause changes in the overall composition of the product.

Methods of achieving uniform composition copolymers from various polymerisation processes have been described. Hanson and Zimmerman (11) used a continuous recycle reactor to produce copolymers of a known and predictable homogeneous composition at relatively high percentage conversion. Hatate et al (12) studied a continuous copolymerisation in stirred tank reactors and considered the effect of micro-mixing on the copolymer

composition. Hanna (13) has devised a method for the rapid calculation of monomer addition to a semi-batch copolymerisation reactor to compensate for the loss of the more reactive monomer. Reaville and Fallwell (14) refined and extended Hanna's approach. They used graphical methods of integration of the model equations and, as such, their technique is time consuming and inflexible. Ray and Gall (15) described a method of controlling the copolymer composition in a batch reactor by employing temperature as the control variable. Tirrell and Gromley (16) have taken Ray and Gall's approach and have used an optimum temperature profile for an experimental reactor in an effort to minimise the copolymer composition drift.

All the methods mentioned above use a mathematical model of the copolymerisation process in one way or another to arrive at a control policy for the production of compositionally homogeneous products. In this work use is made of a dynamic model of the process to control the feed rate of the more reactive monomer to a semi-batch reactor. Feedback from the process comes from an off-line model. The method is a general one and can be readily extended to accommodate feedback loops using on-line measurement devices with an experimental reactor.

The Control Policy

In order to develop the control strategy Equation (1) can be modified and represented in terms of the monomer ratio $\rho = [A]/[B]$ where [A] and [B] are the instantaneous molar concentrations of the monomers A and B.

$$F_1 = \frac{r_1 \rho^2 + \rho}{r_1 \rho^2 + 2\rho + r_2} \quad (2)$$

It is clear that if the value of ρ can be held constant during the course of reaction the instantaneous (therefore, the mean) copolymer composition will remain constant.

If the initial conditions of the reaction mixture are V^0 (volume), A^0 and B^0 (moles of monomers A and B respectively) and ρ^0 (monomer ratio) then after a time interval (Δt), the conditions within the reactor change to $V(\Delta t)$, $A_0(\Delta t)$ and $B(\Delta t)$. If there is no volume change during polymerisation then $V(\Delta t) = V^0$. Should the two monomers be consumed at the same rate then ρ remains constant. However, since one of the monomers is usually more reactive than the other,

$$\rho(\Delta t) \neq \rho^0$$

If monomer A is more reactive than monomer B then

$$\rho(\Delta t) < \rho^0$$

consequently $A_0(\Delta t) - B(\Delta t) \cdot \rho^0 < 0$ (3)

The inequality, Equation 3, can be made into an equality by the addition of the quantity n_A which is computed as

$$n_A(0) = A_0(\Delta t) - B(\Delta t) \cdot \rho^0 \quad (4)$$

It is apparent that $n_A(0)$ is the amount of monomer A which must be added during the time interval ($0 \rightarrow \Delta t$) so that at the end of the interval $\rho(\Delta t) = \rho^0$.

If A is added in a continuous stream to the reactor in a solution of concentration $[A_f]$ then the necessary flow rate may be obtained from

$$F_A(0) = n_A(0) / \{[A_f] \Delta t\} \quad (5)$$

assuming that the flow rate F_A is constant over the interval. The new initial conditions for the reactor at time $t = \Delta t$ are

$$V(\Delta t) = F_A(0) \Delta t + V^0$$

$$A_1(\Delta t) \text{ and } B(\Delta t) \text{ moles of monomers}$$

From these new conditions the reaction in the batch reactor can be advanced to time $t = 2\Delta t$. At this time the entire procedure for computing the new feed flow-rate has to be repeated. Since no correction for the consumption of B has been made, the amount of B present must decrease as the reaction proceeds. As a result, progressively less of monomer A has to be added to keep ρ constant. When A is feed to the reactor not as pure monomer, but in solution the increase in volume caused by the added solvent will reduce the concentrations of the reactants and have a consequential effect on the overall rate of polymerisation.

The control scheme presented can be described superficially as a predictor-corrector action. The prediction is done by the batch reactor model, which in turn provides the necessary

control action to correct for drift in the monomer composition in the semi-batch reactor model. The switch between batch and semi-batch models at time intervals Δt can be continued until some desired boundary condition is satisfied.

Mathematical Model

The models are required to give accurate information concerning the consumption of the two monomers during copolymerisation. The modelling techniques used here are extensions of well established methods for homopolymerisation reactions. The construction of the models may be summarised briefly as follows:

The species M_k ($k = 1, 2, \dots, S$) present in the reaction mixture is assumed to have a molecular weight w_k (g mole^{-1}), density d_k (g cm^{-3}), molar enthalpy u_k (cal mole^{-1}), and molar specific heat at constant pressure C_{pK} ($\text{cal mole}^{-1} \text{C}^{-1}$) and of initial molar concentration $[M_k^0]$ (mole l^{-1}). The reaction volume is V^0 (l) and temperature T^0 ($^{\circ}\text{C}$). For species M_{kj}^f ($j = 1, 2, \dots, N$) of molar concentration $[M_{kj}^f]$, density d_k , molecular weight w_k , molar enthalpy u_k , and molar specific heat C_{pK} are in the feeds to the reactor of flow rates F_j (l sec^{-1}) and temperature T_j^f .

The species M_k undergo R reactions whose stoichiometries are

$$\sum_{i=1}^R c_{ik} M_k = 0 \quad k = (1, \dots, S)$$

The stoichiometric coefficient c_{ik} is greater than zero if M_k is a product of the i -th reaction, is negative if M_k is a reactant and is zero if M_k plays no part in the i -th reaction.

If the volume change of the reaction mixture due to reaction is assumed to be negligible relative to that caused by the inflow of materials into the reactor, then

$$\frac{dV}{dt} = \sum_{j=1}^N F_j \quad V(t=0) = V^0$$

The molar enthalpy u_k is a function of temperature, which vanishes at the reference temperature T_R (i.e., 25°C).

The molar balance for the species M_k is then

$$\frac{d}{dt} \{V[M_k]\} = \sum_{j=1}^N F_j [M_{kj}^f] + V \sum_{i=1}^R c_{ik} r_i, \quad [M_k](t=0) = [M_k^0]$$

where r_i is the rate of the i -th reaction.

The energy balance (heat balance) for the system is then

$$\frac{d}{dt} \left\{ V \sum_{k=1}^S [M_k] u_k(T) \right\} = \sum_{j=1}^N \sum_{k=1}^S F_j [M_{kj}^f] u_k(T_j^f) - V \sum_{i=1}^R (\Delta H_i) r_i + Q$$

where (ΔH_i) is the heat of the i -th reaction and Q is the rate of heat removal or addition to the process. Using the relationship between the enthalpy and specific heat at constant pressure it follows that

$$\frac{dT}{dt} = \frac{\sum_{j=1}^N \sum_{k=1}^S (T_j^f - T) F_j [M_{kj}^f] C_{pk} - V \sum_{i=1}^R (\Delta H_i^T) r_i + Q}{\sum_{k=1}^S V [M_k] C_{pk}}$$

$$T(t=0) = T^0$$

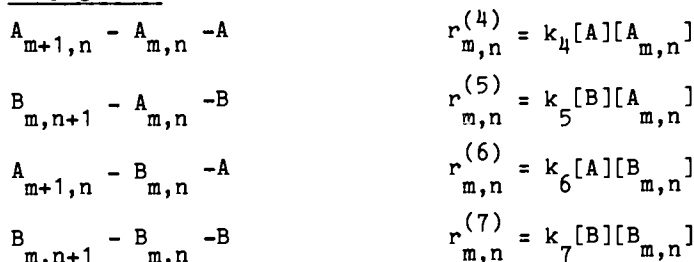
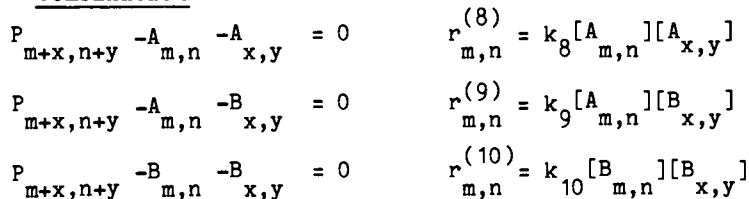
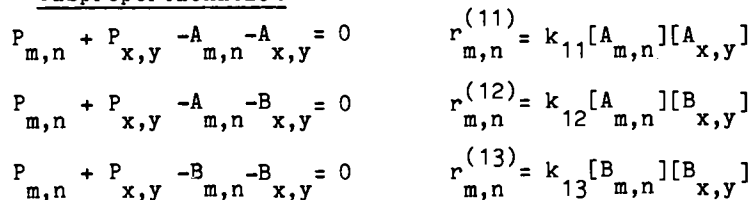
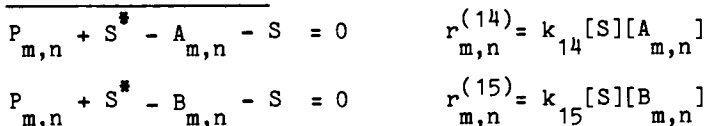
The model equations developed for the semi-batch reaction process can be modified for the batch process by ignoring the inflow of material and energy terms.

The above logic has been applied to the copolymerisation equations given in Table I. A detailed derivation of the copolymerisation model and a summary of the constants used in the model have been described elsewhere (17).

The value of ρ for the free running operation of the system is obtained from the batch model equations and deviations from the desired value are used to calculate the required monomer feed volume flow-rate for the semi-batch polymerisation process.

A solution of the semi-batch reactor model equations yields the results that would be expected from a real reactor. If the control action has been effective, ρ should remain constant. Any error in the computation of the exact amount of the required

Table I. Copolymerization Reaction Scheme

InitiationPropagationTerminationCombinationDisproportionationTransfer to Solvent

monomer will be reflected in the value of ρ at the end of the semi-batch operation interval. This error will have to be corrected in the next or subsequent intervals. However, if any of the following is singly or collectively true then a new ρ will be established and maintained in the reactor (i) the mathematical models do not accurately represent the true behaviour of the system, (ii) or the process experiences disturbances, (iii) or the kinetic data used in the construction of the model are in error. The result will be the production of a compositionally uniform copolymer but one of differing in composition from that desired.

Experimental

Experimental System The copolymerisation of styrene with methyl acrylate in toluene using azo-bis-iso-butyronitrile (AIBN) was selected as the model experimental system because the overall rate of reaction is relatively fast, copolymer analysis is relatively simple using a variety of techniques and the appropriate kinetic and physical constants are available in the literature. This monomer combination also has suitable reactivity ratios ($r_1 = 0.76$ and $r_2 = 0.175$ at 80°C), (18) making control action essential for many different values if compositionally homogeneous polymers are to be prepared at higher conversions in a semi-batch reactor.

Materials. Styrene, methyl acrylate, toluene and AIBN were purified by standard techniques (19).

Reactor and Reactor Conditions. A 5-litre glass reactor (15 cm diameter) fitted with four stainless steel baffles (10 cm x 1.5 cm) immersed in a thermostatted oil bath at 80°C (reflux temperature of methyl acrylate) was used for polymerisation. Stirring was by means of a marine type impeller (6 cm diameter and pitch 45°). The overall reaction rate was sufficiently slow to ensure isothermal conditions. Additions of solutions of the more reactive monomer (styrene, of molar concentration 0.8) to the reactor were made using a computer controlled positive displacement pump (Precision Metering Ltd.) with four long-stroke pump heads, 90° out of phase to minimise pulsation of the flow.

Sample Analysis. (i) Conversion. Measured samples (≈ 20 ml) were taken from the reactor at regular intervals (30 min), and polymerisation quenched by rapid cooling and the addition of a small quantity of t-butyl catechol. The polymer was isolated by rotary evaporation at reduced pressure to remove residual monomer and then reprecipitated several times from acetone solution with aqueous methanol. The product was finally dried under vacuum. Polymer yields were obtained by weighing.

(ii) Composition. (a) UV-Spectroscopy. The copolymers had an absorption at 269 nm in chloroform solution which obeyed Beer's Law and is characteristic of the repeat units from the styrene monomer ($\lambda_{\max} = 269 \text{ nm}$, $\epsilon = 1.7 \text{ mole cm}^{-2}$). Measurements were made with a Unicam SP800A spectrophotometer and 1 cm quartz cells.

(b) Hnmr measurements. The proton magnetic spectra of the products were obtained using a Jeol-100 Mhz instrument. The relative amounts of phenyl ($\tau = 3.68$) and methyl ($\tau = 1.79-1.81$) protons were used to determine the average composition of copolymers.

(iii) Molecular Weight. A Waters Associates gel permeation chromatograph fitted with a model 6000A pump, U6K injector and UV, IR and RI detectors was used for the estimation of molecular weights, molecular weight distribution and copolymer composition. Both analytical and preparative gel columns (Polymer Laboratories Ltd) were employed. Analyses were carried out at 25 °C in THF and the column sets were calibrated with monodisperse polystyrene standards (Polymer Laboratories Ltd).

(iv) Computers and Computer Software. Computer simulation programs were written in FORTRAN for a HP2100A computer. The control algorithm were implemented on an ARGUS 700E process control computer using ICOL a real time control language developed at Bradford University (20).

Results and Discussion

(a) Computer Simulation -Batch Reactor. The object of these investigations was to gain an insight into the behaviour of the process in the open-loop mode of operation. The process divides into two distinctive stages. In the first, styrene copolymerises with methyl acrylate while in the second the homopolymerisation of methyl acrylate takes place after all the styrene has been consumed (see Figure 1). During the course of the copolymerisation ρ decreased from its initial value of 0.25 to zero (Figure 2). As a result the average copolymer composition changed from 0.4 to 0.2 (see Figure 3). The variations in the number average degree of polymerisation (NADP) and the weight average degree (WADP) are shown in Figure 4 while Figure 5 shows the changes in the dispersity index of the material produced as the reaction proceeds.

(b) Computer Simulation -Controlled Semi-Batch Reactor. Batch reactor studies showed that styrene was the more reactive monomer. The feed flow rate profile calculated by means of the control algorithm to compensate for its loss is shown in Figure 6. The effect of the feed flow rate profile was to keep ρ and

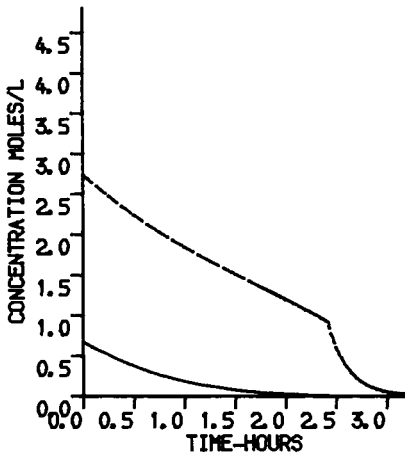


Figure 1. Monomer concentrations with reaction time in a batch reactor. Key: ---, MA; —, ST.

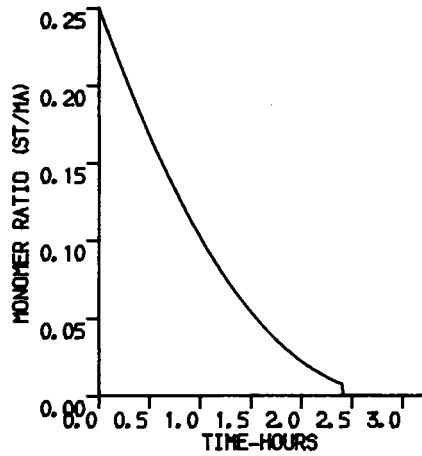


Figure 2. Variation of monomer ratio with reaction time in a batch reactor.

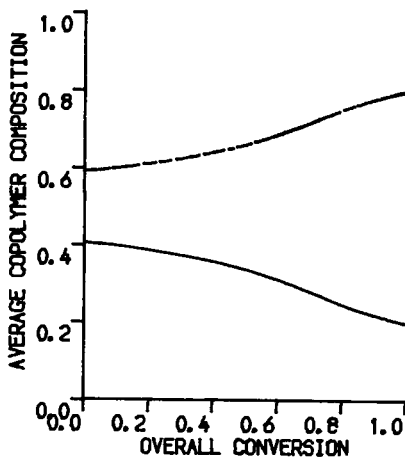


Figure 3. Average copolymer composition with conversion in a batch reactor. Key: ---, MA; —, ST.

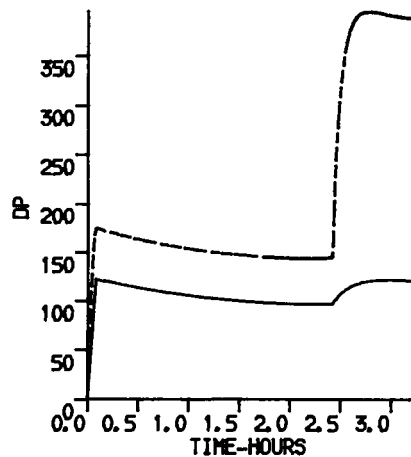


Figure 4. Degree of polymerization with reaction time in a batch reactor. Key: ---, WADP; —, NADP.

the average copolymer composition constant throughout the course of reaction. The NADP and WADP are shown in Figure 7 while Figure 8 shows the average polydispersity index of the material as the reaction proceeds.

In another study step changes in ρ were made during a run. In order to simulate a real experiment the maximum flow rate delivery of the feed pump was constrained to a realistic value. Figure 9 shows the step change in ρ while Figure 10 shows the behaviour of the feed pump under the restriction imposed upon it. The corresponding variations in the average copolymer composition are shown in Figure 11. Figures 12 and 13 indicate that the NADP, the WADP, and the dispersity index are unaffected by changes in the monomer ratio. It is apparent that the control action has effectively made the process follow the desired set point changes without affecting the MW and the MWD of the copolymer.

To investigate the effects of sudden changes in the reaction temperature, an initial temperature of 60 °C was chosen which was increased stepwise to 80 °C during a run. Figure 14 shows the response of the reaction rate to this change. Figures 15 and 16 show the effects of this change on the feed flow-rate and on the monomer ratio, while Figure 17 shows the effect on the average copolymer composition. It is clear that the effects of reaction temperature changes have been effectively suppressed. However, Figure 18 demonstrates that a reduction in the MW has occurred, as would be expected.

(c) Reactor Experiments. In a typical experiment the aim was to produce a homogeneous copolymer having a 0.4 mole fraction of styrene at high monomer conversion. It can be seen from Equation (1) that in order to achieve this objective it was necessary to maintain a constant ratio of monomer concentrations with a mole fraction of styrene of 0.2. The results of this experiment can be compared with a batch copolymerisation which was allowed to proceed without any control action other than to pump pure solvent into the reactor to produce a rate of change of volume in the reaction mixture comparable to that for the semi-batch controlled experiment. To compare experimental results under various conditions the copolymer composition, the primary parameter of interest was measured, although other parameters have been checked, e.g., the solids content of the reaction mixture. Figure 19 shows the experimental observations of copolymer composition with reaction time while Figure 20 depicts the solids content of the reactor with reaction time (at 4 hours conversion of monomers was approximately 75%). It can be seen that the copolymer composition remained essentially constant with time in the controlled experiment within the limits of accuracy of the measurement of composition but changed dramatically in the uncontrolled experiment. Similar results have been obtained for different mole fractions of styrene in

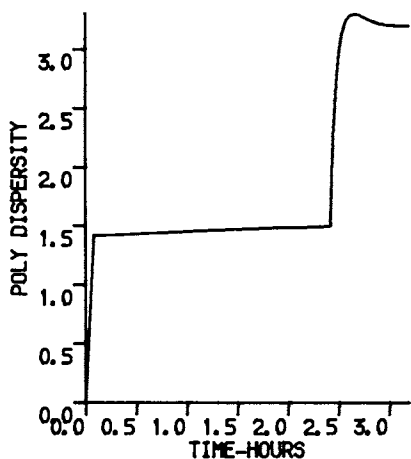


Figure 5. Polydispersity index with reaction time in a batch reactor.

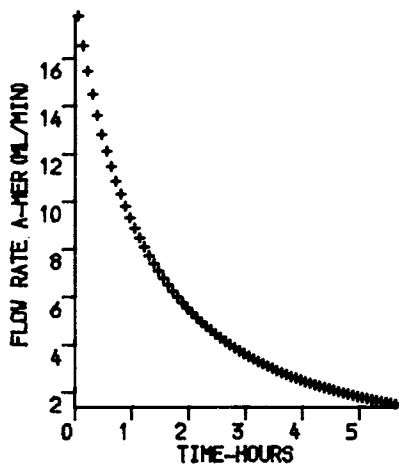


Figure 6. Feed flow-rate profile with time to a semi-batch reactor.

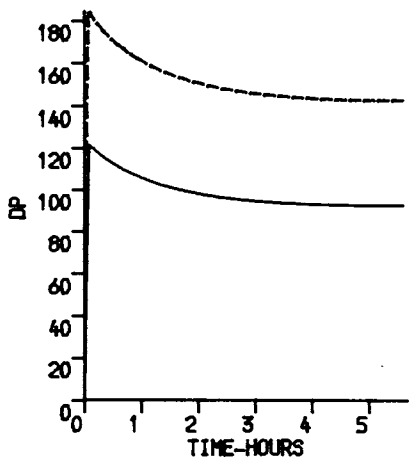


Figure 7. Degree of polymerization with reaction time in a controlled semi-batch reactor. Key: ---, WADP; —, NADP.

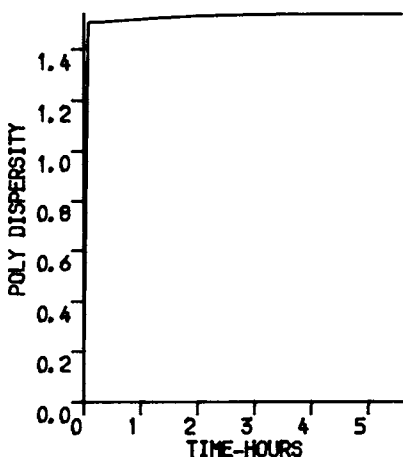


Figure 8. Polydispersity index with reaction time in a controlled semi-batch reactor.

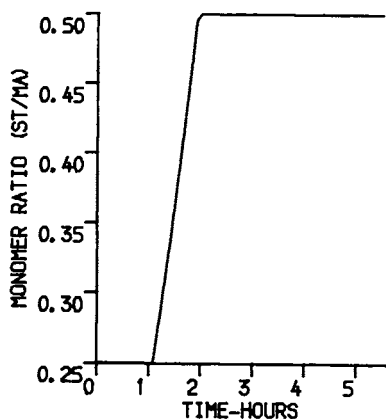


Figure 9. Dynamic response to a step change in monomer ratio in a controlled semi-batch reactor.

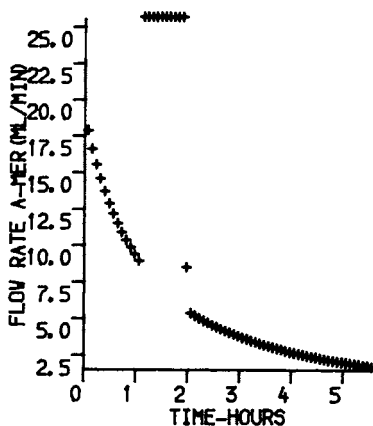


Figure 10. Dynamic feed flow-rate profile in response to step change in monomer ratio in a controlled semi-batch reactor.

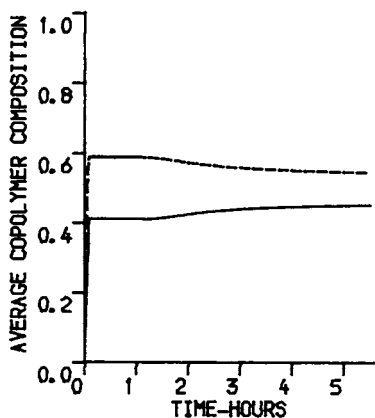


Figure 11. Average copolymer composition with time in response to step change in monomer ratio in a controlled semi-batch reactor. Key: ---, MA; —, ST.

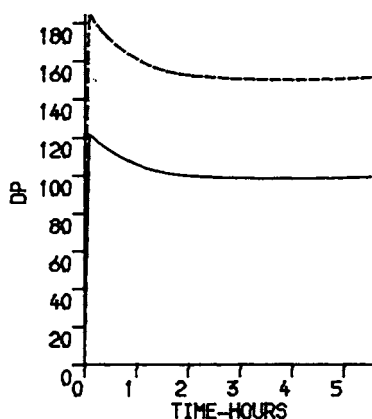


Figure 12. Degree of polymerization with time in response to step change in monomer ratio in a controlled semi-batch reactor. Key: ---, WADP; —, NADP.

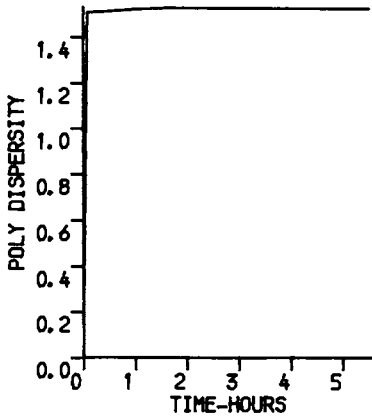


Figure 13. Polydispersity index change with time in response to step change in monomer ratio in a controlled semi-batch reactor.

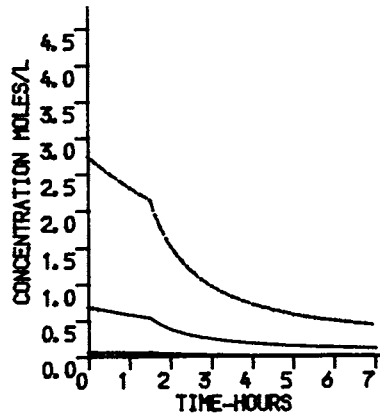


Figure 14. Change in monomer concentrations with time in response to step change in reaction temperature (60°C to 80°C). Key: ---, MA; —, ST.

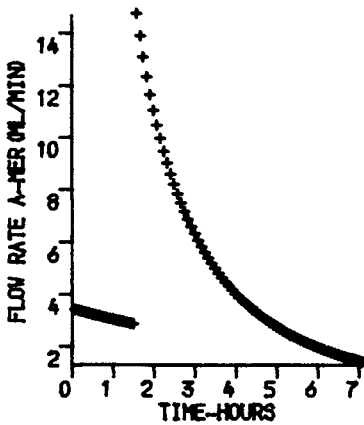


Figure 15. Flow rate change in response to step change in reaction temperature (60°C to 80°C) in controlled semi-batch reactor.

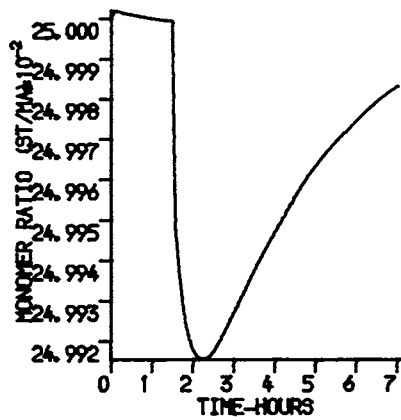


Figure 16. Monomer ratio change with time in response to step change in temperature in controlled semi-batch reactor.

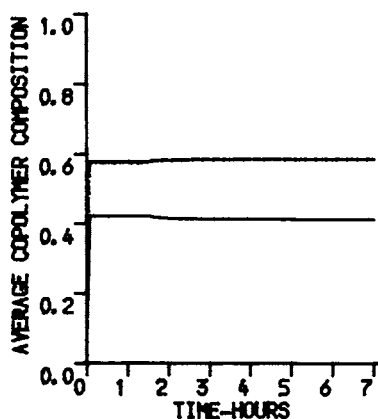


Figure 17. Average copolymer composition with time in response to step change in reaction temperature in controlled semi-batch reactor.

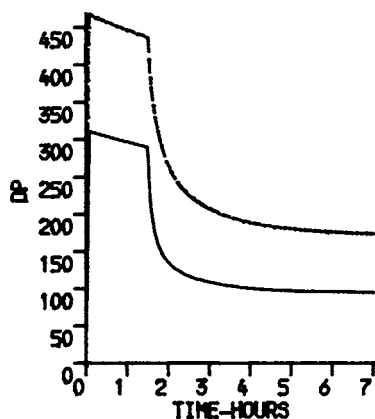


Figure 18. Degree of polymerization with time in response to step change in reaction temperature in controlled semi-batch reactor. Key: ---, WADP; —, NADP.

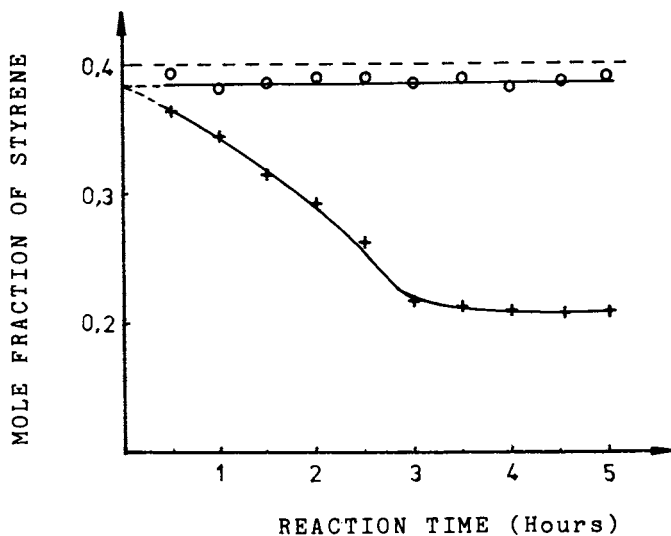


Figure 19. Comparison of experimentally measured amounts of styrene in copolymer produced in a controlled (○) and uncontrolled (+) semi-batch reactor with reaction time.

the copolymer. Experiments have also been carried out at the azeotropic point for this system. At the azeotropic composition it is possible to decouple the effects of polymer composition drift from molecular weight changes as a result of depletion of the monomers and the initiator in a batch process. This should also be the case for a controlled semi-batch reactor. The results for high conversion polymerisations conducted at the azeotropic point will be presented in a subsequent report. The calculated molecular weights (based on GPC measurements carried out using polystyrene standards) are presented in Table II (a) and II (b).

The major limitations of the feed forward control strategy presented here are that (i) it is only as good as the fundamental data which are used in the models and (ii) it can only be used for systems which conform to the conventionally accepted mode of behaviour of free radical chain polymerisation in solution. However, the same approach can be used with the appropriate models for any copolymerisation process. The range of application can be increased by making an arbitrary assessment of the parameters necessary for the control models and/or by introducing a feedback loop which incorporates some state measurement device, e.g., an in-line gas chromatograph for measurement of residual monomers concentrations. Such a scheme is shown in Figure 21.

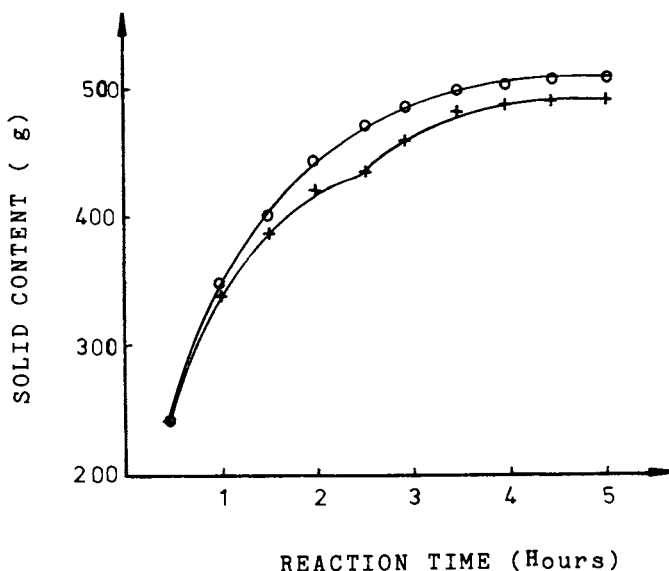


Figure 20. Solid content in a controlled (O) and uncontrolled (+) experimental semi-batch reactor with reaction time.

Table II

Variation of copolymer characteristics with reaction time in:

a) Uncontrolled semi-batch process

Reaction time (Hours)	M_w (g-mole ⁻¹)	M_n (g-mole ⁻¹)	Dispersity Index
0.5	10600	6320	1.68
1.0	9620	5600	1.72
1.5	9390	5420	1.73
2.0	9140	4870	1.88
2.5	9980	5660	1.76
3.0	11000	6990	1.58
3.5	10000	5330	1.89
4.0	9670	5000	1.94

b) Controlled semi-batch process

Reaction time (Hours)	M_w (g-mole ⁻¹)	M_n (g-mole ⁻¹)	Dispersity Index
0.5	11800	7110	1.66
1.0	11000	6530	1.68
1.5	8920	5210	1.71
2.0	9.50	5190	1.76
2.5	9720	5770	1.68
3.0	8810	5050	1.74
3.5	8150	4770	1.71
4.0	10700	6330	1.69

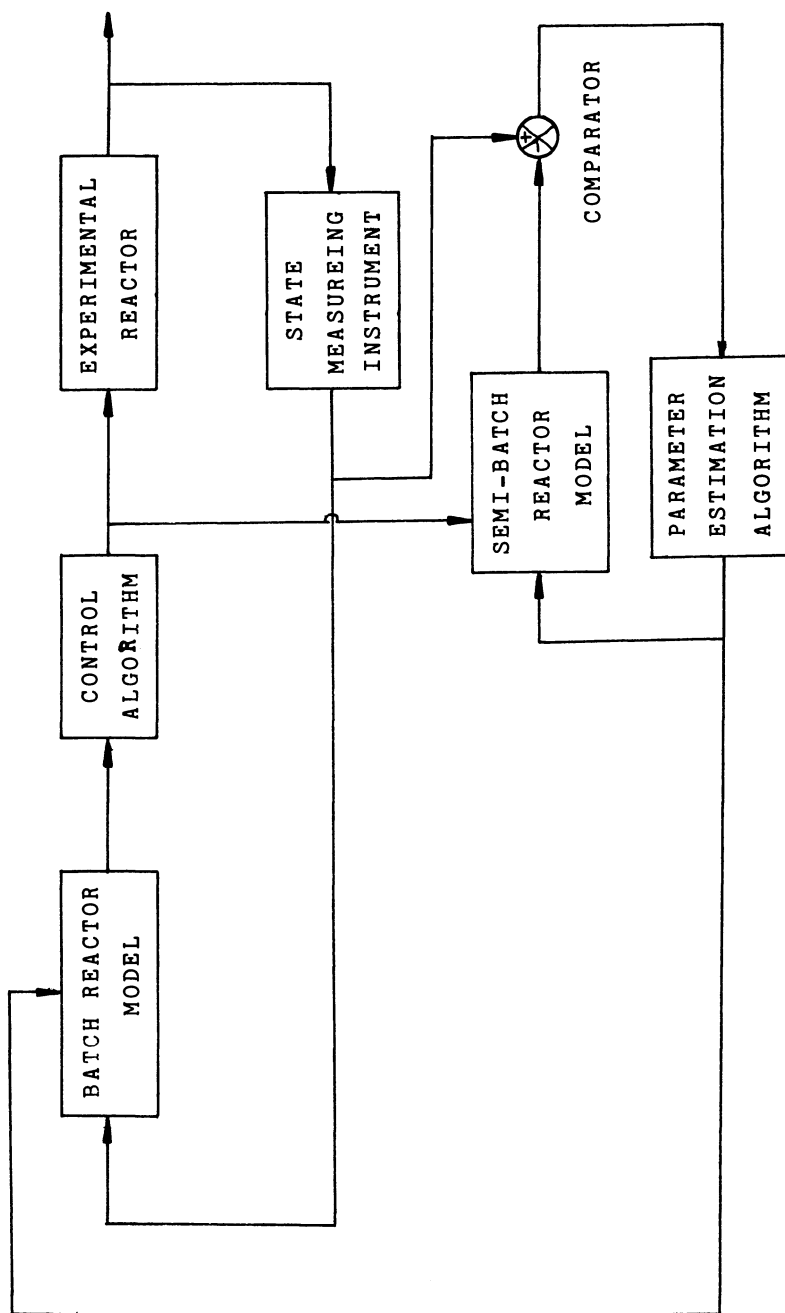


Figure 21. Model reference adaptive control scheme.

Acknowledgements

The authors wish to express their gratitude to the Science and Engineering Research Council for a Research Grant which has made our reactor studies possible.

Literature Cited

1. Imoto, T.; Int. Chem. Eng. 1972, 12(3), 546-53.
2. Fan, L.T.; Shastry, J.S.; J. Polymer Sci. Macromolecular Reviews 1973, 7, 155-87.
3. Ray, W.H.; Laurence R.L.; "Polymerisation Reaction Engineering", Chapter 9 of "Chemical Reactor Theory. A Review ", Lapidus L. and Amundson N.R. , 1977, Prentice Hall, 532-82 .
4. Gerrens, H.; 4th/Eurp. Symp. Chem. Reaction Eng., 1976, Heidelberg Germany , 585-615 .
5. Hoogendoorn, K. ; Nap, C.; ISA, 1975, 129-36.
6. Szabo, T.T. ; Nauman, E.B.; AIChE J., 1969, 15(4), 575-80.
7. Mecklenburgh, J.C.; Can. J. Chem. Eng., 1970, 48, 279-85.
8. Nauman, E.B.; J. Macromol. Sci. Revs. Macromol. Chem. 1974, C10(1), 75-112.
9. O'Driscoll, K.F. ; Knorr, R.; Macromolecules, 1969, 2(5), 507-15.
10. Ham, G.E., Ed., "Copolymerisation", Interscience, 1964, New York.
11. Hanson, A.W. ; Zimmerman, R.L.; Ind. Eng. Chem., 1957, 49, 1803.
12. Hatate, Y.; Nakashio, F.; Sakai, W.; J. Chem. Eng. of Japan, 1971, 48, 348-54.
13. Hanna, R.J.; Ind. Eng. Chem., 1957, 49(2), 208-9.
14. Reaville, E.T.; Fallwell Jnr., W.F.; Official Digest, 1964, June, 625-47.
15. Ray, W.H. ; Gall, C.E.; Macromolecules , 1969, 2(4), 425.
16. Tirrell, M. ; Gromley, K.; Chem. Eng. Sci., 1981, -36-, 367.
17. Johnson, A. F.; Khaligh, B.; Ramsay, J.; Int. J. of Modelling and Simulation , 1981, 1(4), 313-17.
18. Brandrup, J. ; Immergut, F.H.; "Polymer Handbook", 2ed., 1975, Wiley Interscience.
19. Termachi, S.; et al.; Macromolecules, 1978, 11(6), 1206-10.
20. Butts, B.; "Real Time Extended Basic: User Manual", 1978, Postgraduate School of Control Engineering University Of Bradford .

RECEIVED May 4, 1982.

Programs for Calculating Structural Features of Terpolymers

YASUTO KODAIRA and H. JAMES HARWOOD

The University of Akron, Institute of Polymer Science, Akron, OH 44325

Two computer programs are described for calculating structural aspects (composition, dyad-, triad-, tetrad-, and pentad-distributions, number and weight monomer sequence distributions, monomer centered triad- and pentad-fractions) of terpolymers prepared in either low or high conversion. The programs are applicable for either terminal (1st order Markoffian) or penultimate (2nd order Markoffian) terpolymerization system. Calculation methods employed in preparing the programs are discussed.

The chemical and physical properties of terpolymers are influenced by their compositions and by the way the monomer units are arranged along their chains. It is important to be able to calculate the relative amounts of structural features present in terpolymers that arise from differences in monomer unit arrangements. For terpolymers prepared in conversions low enough that the composition of the monomer mixture does not change during the course of their preparation, structural features can be calculated easily from the proportions of monomers present in the polymerization mixture and from kinetic constants (reactivity ratios) appropriate for the terpolymerization system. When the composition of the monomer mixture changes during the reaction, due to some monomers being consumed faster than others, numerical integration is necessary to calculate average values for the relative amounts of structural features present. The computer is practically indispensable for such calculations. Because of the large number of structural features that are present in terpolymers, it is advisable to use a computer for such calculations even when the composition of the monomer mixture does not change during the process.

Shown below is a representative portion of a terpolymer chain derived from monomers A, B and C. The structural features of interest are: the relative amounts A-, B- and C-monomer units; the relative amounts of AA-, (BA+AB)-(CA+AC)-, BB-, (BC+CB)- and CC-pairs (dyad distributions); the relative amounts of groups of

0097-6156/82/0197-0137\$06.00/0
© 1982 American Chemical Society

three (triad distributions), four (tetrad distributions), five (pentad distributions) or more (n-add distributions) monomer units; the percentage of monomer units of a given type in particular environments (triad, pentad or n-add fractions); and the number and weight distributions of monomer sequences of various lengths. These various features are also illustrated below.

	~ A - B - C - A - A - B - B - A - C - B - C - C - A ~									
Dyads	AB	CA	AB	BA	CB	CC				
		BC	AA	BB	AC	BC	CA			
Triads	ABC		AAB	BAC		BCC				
		BCA	ABB	ACB		CCA				
		CAA	BBA		CBC					
Tetrads	ABCA		ABBA		CBCC					
		BCAA	BBAC		BCCA					
		CAAB	BACB							
		AABB	ACBC							
A-Sequences	~A		AA		A					A ~
B-Sequences		B		BB		B				
C-Sequences			C			C	CC			

We have previously reviewed (1,2) the methods used to calculate structural features of copolymers and terpolymers from monomer reactivity ratios, monomer feed compositions and conversions, and have written a program for calculating structural features of copolymers from either terminal model or penultimate model reactivity ratios (3). This program has been distributed widely and is in general use. A listing of an instructive program for calculating structural features of instantaneous terpolymers from monomer feed compositions and terminal model reactivity ratios was appended to one of our earlier reviews (1). Our reviews (1,2) cite other examples of programming terpolymer composition and/or structure calculations, either by stochastic or Monte-Carlo methods. In the present paper, we describe two general programs for calculating structural features of terpolymers from monomer feed compositions, conversions, and either penultimate or terminal model reactivity ratios. Program A is completely self-contained and will accommodate a penultimate effect with one monomer. Program B calls a matrix multiplication subroutine (GMPRD from the IBM Scientific Subroutine Package, or VMULFF from the IMSL Library) (4), but is completely general; penultimate effects can be associated with all three monomers in this case. The programs provide monomer concentrations, dyad through pentad distributions, triad and pentad fractions, as well as the number and weight distribution of A-, B- and C-sequences of monomer units.

General Method

The development of these programs followed the general procedure outlined previously (1). This involved the following steps:

1. Propagation reactions involved in the polymerization system under study are written, along with appropriate rate expressions. Appropriate reactivity ratios are defined.

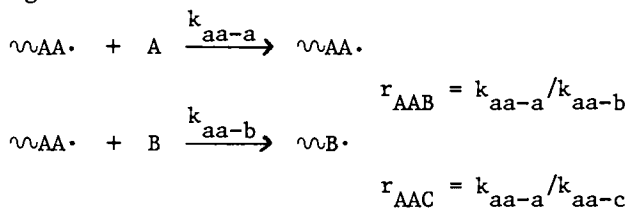
2. Conditional probabilities for monomer or sequence placements are calculated from monomer feed concentrations and reactivity ratios, using expressions derived from the rate expressions written in the first step. The conditions employed in defining these probabilities correspond to the types of propagating species (e.g., $\sim A\cdot$, $\sim BA\cdot$) identified in the first step.

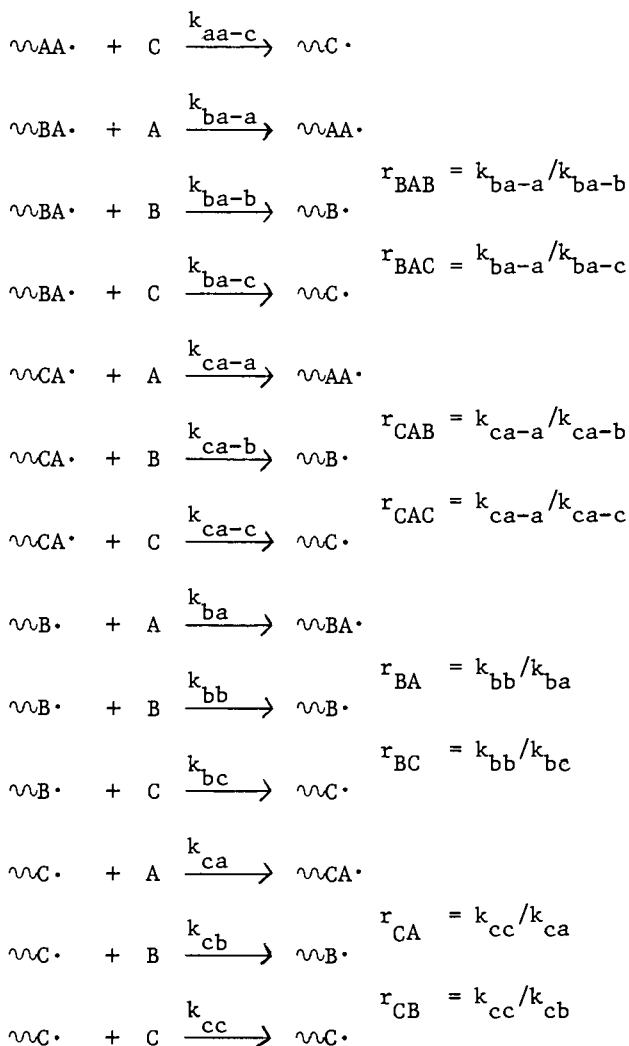
3. Unconditional probabilities for monomer or sequence placements are calculated from the conditional probabilities. This may be accomplished by writing stationary relationships (necessary n-add relationships) involving conditional and unconditional probabilities, followed by solving such relationships simultaneously for the conditional probabilities. While this can be done algebraically, it is simpler to do this by conducting operations on a matrix constructed from the conditional probabilities. The procedure described by Price (5) can provide an algebraic solution if desired, but it can be the basis of a program that provides numerical results. The matrix multiplication method (1), provides numerical results only, but it seems to be the preferred approach when the polymerization system is complex.

4. Unconditional probabilities of sequences smaller than those evaluated in step three, if any, are calculated by addition of unconditional probabilities evaluated in step three. Unconditional probabilities of sequences larger than those evaluated in step three are calculated by multiplication of appropriate conditional and unconditional probabilities.

Program A

This program was written to calculate structural features of terpolymers prepared via the following propagation reactions from radicals $AA\cdot$, $BA\cdot$, $CA\cdot$, $B\cdot$ and $C\cdot$ and from monomers A, B and C. Reactivity ratios utilized by this program are also defined in the following scheme:





On the basis of the above, it is clear that unconditional probabilities of AA, BA, CA, B and C need to be evaluated to provide a basis for other calculations. These probabilities will be designated $P(\text{AA})$, $P(\text{BA})$, etc. The conditional probabilities necessary for this evaluation are designated $P(\text{J/I})$, where I and J are the initial and final species involved in a propagation step. These are calculated by considering the kinetic expressions written above. For example, in calculating $P(\text{AA}/\text{AA})$, one must compare the rate of $\sim\text{AA}\cdot$ radicals adding monomer A to the rate of $\sim\text{AA}\cdot$ radicals adding monomers A, B or C (A_f , B_f and C_f represent the concentrations of monomers A, B and C in the polymerization mixture)

$$\begin{aligned}
 P(\text{AA}/\text{AA}) &= \frac{k_{\text{aa-a}} (\sim\text{AA}\cdot) A_f}{k_{\text{aa-a}} (\sim\text{AA}\cdot) A_f + k_{\text{aa-b}} (\sim\text{AA}\cdot) B_f + k_{\text{aa-c}} (\sim\text{AA}\cdot) C_f} \\
 &= \frac{1}{1 + \frac{k_{\text{aa-b}} B_f}{k_{\text{aa-a}} A_f} + \frac{k_{\text{aa-c}} C_f}{k_{\text{aa-a}} A_f}} \\
 &= 1 / (1 + B_f / r_{\text{AAB}} A_f + C_f / r_{\text{AAC}} A_f)
 \end{aligned}$$

Similarly,

$$P(\text{B}/\text{AA}) = (B_f / r_{\text{AAB}} A_f) / (1 + B_f / r_{\text{AAB}} A_f + C_f / r_{\text{AAC}} A_f)$$

$$P(\text{C}/\text{AA}) = 1 - P(\text{AA}/\text{AA}) - P(\text{B}/\text{AA})$$

etc.

The transition matrix involving these probabilities is as follows:

	AA	BA	CA	B	(Initial State)
AA	P(AA/AA)	P(AA/BA)	P(AA/CA)	0	0
BA	0	0	0	P(BA/B)	0
CA	0	0	0	0	P(CA/C)
B	P(B/AA)	P(B/BA)	P(B/CA)	P(B/B)	P(B/C)
C	P(C/AA)	P(C/BA)	P(C/CA)	P(C/B)	P(C/C)
↑					
(Final State)					

Evaluation of P(AA), P(BA), P(CA), P(B) and P(C) from this matrix by the method of Price (5) yielded the following results, where λ is the normalization factor required to make the sum of these quantities total 1.0. (λ amounts to the reciprocal of the sum of the expressions that are multiplied by λ in the equations given below)

$$\begin{aligned}
 P(\text{AA}) = \lambda * [&(1 - P(\text{B}/\text{B})) * P(\text{CA}/\text{C}) * P(\text{AA}/\text{CA}) - P(\text{BA}/\text{B}) * P(\text{CA}/\text{C}) * (P(\text{B}/\text{BA}) * \\
 &P(\text{AA}/\text{CA}) - P(\text{B}/\text{CA}) * P(\text{AA}/\text{BA})) + P(\text{BA}/\text{B}) * P(\text{B}/\text{C}) * P(\text{AA}/\text{BA})]
 \end{aligned}$$

$$\begin{aligned}
 P(\text{B}) = \lambda * [&(1 - P(\text{AA}/\text{AA})) * (P(\text{B}/\text{C}) + P(\text{CA}/\text{C}) * P(\text{B}/\text{CA})) + P(\text{AA}/\text{CA}) * \\
 &P(\text{CA}/\text{C}) * P(\text{B}/\text{AA})]
 \end{aligned}$$

$$P(C) = \lambda * [(P(AA/AA) - 1) * (P(B/B) - 1 + P(BA/B) * P(B/BA)) - P(AA/BA) * P(B/AA) * P(BA/B)]$$

$$P(BA) = \lambda * P(B) * P(BA/B)$$

$$P(CA) = \lambda * P(C) * P(CA/C)$$

The remaining monomer and dyad concentrations can be calculated from the above quantities and appropriate probabilities.

$$P(A) = P(AA) + P(BA) + P(CA)$$

$$P(AB) = P(AA) * P(B/AA) + P(BA) * P(B/BA) + P(CA) * P(B/CA)$$

$$P(AC) = P(AA) * P(C/AA) + P(BA) * P(C/BA) + P(CA) * P(C/CA)$$

$$P(BB) = P(B) * P(B/B)$$

$$P(BC) = P(B) * P(C/B)$$

$$P(CB) = P(C) * P(B/C)$$

$$P(CC) = P(C) * P(C/C)$$

By following this general approach, n-add distributions (probabilities) up to pentads (B-centered pentads only at the present time) are calculated, viz.,

$$P(AAB) = P(AA) * P(AB/AA)$$

$$P(BBA) = P(B) * P(B/B) * P(BA/B)$$

$$P(CBBAC) = P(C) * P(B/C) * P(B/B) * P(BA/B) * P(C/BA)$$

Since a large number of n-add distributions are involved in the calculations, the program reports complete distributions only for dyads and triads. Collected distributions are reported for dyads, and tetrads. These quantities are of greater interest than the individual n-add distributions, since the properties of the central portions of unsymmetrical sequences are usually the same as those of the reversed sequences (e.g., the central units in $ABC\bar{C}CB$ and $B\bar{C}CBA$ sequences usually have identical chemical and physical properties.) Collected n-add distributions are thus calculated by adding appropriate n-add distributions. Examples of such calculations are shown below, where P' (n-add) defines a collected n-add distribution.

$$P'(AA) = P(AA)$$

$$P'(AB) = P(AB)+P(BA)$$

$$P'(CAAB) = P(CAAB)+P(BAAC)$$

Triad fractions (individual and collected) and B-centered pentad fractions (collected) are also provided by the program. These correspond to the fractions of monomer units residing in particular environments in the polymer. For example, f_{CAB}^* designates the fraction of A-units centered in CAB triads. Such quantities are calculated by dividing appropriate n-add distributions by monomer probabilities, viz.,

$$f_{CAB}^* = P(CAB)/P(A)$$

Obviously, collected triad and pentad fractions are of greater general interest than individual fractions.

Number (N.D.) and weight (W.D.) distributions of A-, B- and C- monomer sequences are also calculated.

$$N.D.(A)_1 = 1 - (P(BA)*P(AA/BA)+P(CA)*P(AA/CA))/(P(BA)*P(CA))$$

$$N.D.(A)_{n>1} = (P(BA)*P(AA/BA)+P(CA)*P(AA/CA))*(1-P(AA/AA))* \\ P(AA/AA)^{n-2}/(P(BA)+P(CA))$$

$$N.D.(B)_n = P(B/B)^{n-1}*(1-P(B/B))$$

$$N.D.(C)_n = P(C/C)^{n-1}*(1-P(C/C))$$

$$W.D.(A)_n = (n*N.D.(A)_n)/(1+(P(BA)*P(AA/BA)+P(CA)*P(AA/CA))/ \\ ((P(BA)+P(CA))*(1-P(AA/AA))))$$

$$W.D.(B)_n = n* P(B/B)^{n-1}*(1-P(B/B))^2$$

$$W.D.(C)_n = n* P(C/C)^{n-1}*(1-P(C/C))^2$$

Calculations at high conversion - The quantities discussed above are calculated at regular conversion increments and are integrated using the trapezoidal method as is described in several of our earlier papers (1,3). Average values of n-add distributions, etc., are then reported for conversions specified by the user. As an option the program will also provide information about the concentrations of unreacted monomers at various conversions.

Typical output from this program is shown in Figure 1. This output is for a calculation involving only terminal model reactivity ratios, which is an option of the program.


```

SAMPLE INPUT FOR PROGRAM A
REACTIVITY RATIOS
RA= 0.50000      RBA= 0.50000
RB= 0.50000      RAB= 0.20000
RC= 0.50000      RAC= 0.20000
RD= 0.50000      RBC= 0.20000

MOL. WEIGHTS OF FEED MONOMERS
MWF= 100.00000  MWE= 125.00000  CMW= 150.00000

FEED MONOMER IN MOLE PER CENT
A = 10.00000    B = 25.00000    C = 65.00000

CONVERSION INCREMENT= 0.00100

WEIGHT PER CENT CONVERSION=22.99901

TERMPOLYMER COMPOSITION
AE 0.19152      BE 0.34263      CE 0.50576

DIAD DISTRIBUTIONS
AAE 0.00501    ABE 0.02564      AC 0.12097
BAE 0.04508    BBE 0.05876      BC 0.23799
CAE 0.13077    CBE 0.25823      CC 0.14681

TRIAD DISTRIBUTIONS
AAE 0.0017     ABE 0.00085     AAC 0.00399
BAE 0.00152   HBE 0.00777     BAC 0.03659
CAE 0.00332   CBE 0.01702     CAC 0.08038

BAE 0.00144   ABE 0.00441     ABE 0.01779
BAE 0.00789   HBE 0.01009     HBE 0.04079
CBE 0.00455   CBE 0.00427     CBE 0.17941

ACE 0.02414   ACB 0.06179     ACC 0.03506
UCA 0.06741   HCB 0.12152     HCB 0.06906
CCE 0.02930   CCB 0.07492     CCE 0.04269

TRIAD FRACTIONS
AAE 0.00100    ABE 0.01005     ACA 0.04768
AAE 0.00100    ABE 0.01280     ACB 0.12217
AAE 0.00503    ACB 0.05197     ACC 0.06933
BAE 0.01701    HBA 0.02301     BBA 0.09374
BAE 0.01124    HBE 0.02645     HBE 0.29027
BAE 0.00155    HCE 0.11405     HCE 0.13654
CAE 0.00191    CBA 0.10085     CCA 0.05774
CAE 0.11224    CBE 0.12919     CCB 0.14913
CAE 0.53319    CCE 0.52363     CCE 0.08441

COLLECTED TETRAD DISTRIBUTIONS
AAAA 0.00001   ABBA 0.00059     ACCA 0.00698
AAAC 0.00024   ABBC 0.00899     ACCC 0.01966
AAAB 0.00024   ABBC 0.00174     BCCB 0.03524
AAAB 0.00034   ABBC 0.00211     ACCB 0.03164
BAAC 0.00177   JBBC 0.01460     BCCE 0.04185
CAAC 0.00225   CBBC 0.00373     CCCC 0.01124

COLLECTED DIAD DISTRIBUTIONS
AA= 0.00501    BB= 0.05876
AB= 0.07152    BC= 0.49652
AC= 0.22170    CC= 0.14681

COLLECTED TRIAD FRACTIONS
AAA= 0.00109   ABA= 0.01005
AAB= 0.01561   ABB= 0.03587
AAC= 0.04824   ABC= 0.12276
BAB= 0.05124   BBA= 0.02985
BAC= 0.09361   BBC= 0.24824
CAC= 0.53018   CBC= 0.52363
ACA= 0.04768
ACB= 0.12152
ACC= 0.06906
BCB= 0.03524
BCA= 0.03164
BCC= 0.04185
CCC= 0.08441

```

Figure 1. Sample output from Program A. Continued on next page.

```

AAAA = 0.000023  AACAE = 0.00159  ABACA = 0.01193
AAAH = 0.00041  AACHE = 0.00301  ABCEB = 0.02536
AABC = 0.00173  AACCF = 0.00212  ABCC = 0.01515
BAHA = 0.00167  BAAAE = 0.01139  BBCHA = 0.04168
BAAB = 0.00217  BAAHE = 0.02671
BABAC = 0.01154  BACAE = 0.01552  BBCC = 0.02464
CABA = 0.00563  CACAE = 0.03525  CBCHA = 0.07863
CABH = 0.00421  CACH = 0.02398  CBCEB = 0.17601
CABC = 0.00934  CACC = 0.04663  CBCC = 0.10418

COLLECTED B-CENTERED PENTAD FRACTIONS
AABAA = 0.00001  ABBAE = 0.00030  ACBCA = 0.02496
AABBE = 0.00016  ABBAH = 0.00195  ACBCB = 0.11302
AABAC = 0.00049  ABHAC = 0.00451  ACBC = 0.06654
BABA = 0.00052  BUHRE = 0.00087  BCBCB = 0.12579
BABAC = 0.00356  BBHAC = 0.00732  BCBC = 0.14908
CABAC = 0.00531  CBHAC = 0.01539  CBBC = 0.04422

AABBA = 0.00012  ABACA = 0.00114  ABBCA = 0.00594
AAHBE = 0.00021  AADUE = 0.00245  ABBCB = 0.01272
AABBE = 0.00087  AADUC = 0.00146  ABBC = 0.00758
BABBA = 0.00092  BABCA = 0.00724  BBBCA = 0.00940
BABBE = 0.00134  BABUE = 0.01608  BBHCB = 0.02088
BAHBE = 0.00564  BAHCC = 0.00948  BBHCC = 0.01232
CABBA = 0.00253  CABCA = 0.02615  CBBCA = 0.03936
CABBE = 0.00462  CAHCC = 0.05548  CBBCB = 0.08803
CABCE = 0.01473  CABCC = 0.03329  CBBC = 0.05201

NUMBER DISTRIBUTION OF SEQUENCES
A-SEQ.  H-SEQ.  C-SEQ.
1  0.96705  0.70993  0.08655
2  0.03197  0.14202  0.23529
3  0.00105  0.02417  0.06055
4  0.00003  0.00419  0.01387
5  0.00000  0.00072  0.00598
6  0.00000  0.00012  0.00062
7  0.00000  0.00002  0.00012
8  0.00000  0.00000  0.00002
9  0.00000  0.00000  0.00000
10 0.00000  0.00000  0.00000
REST 0.00000  0.00000  0.00000

WEIGHT DISTRIBUTION OF SEQUENCES
A-SEQ.  B-SEQ.  C-SEQ.
1  0.95164  0.08655  0.50414
2  0.00306  0.23529  0.29206
3  0.00014  0.06055  0.12712
4  0.00001  0.01387  0.04927
5  0.00000  0.00598  0.01793
6  0.00000  0.00062  0.00628
7  0.00000  0.00012  0.00214
8  0.00000  0.00002  0.00072
9  0.00000  0.00000  0.00024
10 0.00000  0.00000  0.00008
REST 0.00000  0.00000  0.00003

COMPUTATION COMPLETED

```

Figure 1. Continued. Sample output from Program A.

Program B

This program functions in essentially the same manner as Program A, except it can accept as input 18 reactivity ratios, corresponding to a situation where all monomers exhibit penultimate effects. As is also the case in Program A, terminal model reactivity ratios can be used, however. The programming involves the calculation of 27 conditional probabilities. These probabilities are calculated in the same way that $P(AA/AA)$, $P(AA/BA)$ and $P(AA/CA)$ are calculated in the case of Program A.

Figure 2 shows the 9x9 transition matrix that is constructed from these conditional probabilities. It should be noted that all initial and final states are dyads in this case. Since it would be difficult to use Price's cofactor method (5) with such a large matrix, the matrix multiplication method we have described previously (1) was used to evaluate unconditional dyad probabilities (e.g., $P(AB)$, $P(CC)$, etc.). Thus, repeated multiplication of the transition matrix by itself causes it to converge to the matrix shown in Figure 3, which contains unconditional dyad probabilities as its elements. These are then added to obtain monomer probabilities, viz.,

$$P(A) = P(AA) + P(AB) + P(AC)$$

$$P(B) = P(AB) + P(BB) + P(CB)$$

$$P(C) = P(AC) + P(BC) + P(CC)$$

Triad and higher n-add probabilities are calculated by multiplying appropriate unconditional and conditional probabilities. A few examples are shown below.

$$P(AAA) = P(AA)*P(AA/AA)$$

$$P(AAB) = P(AA)*P(AB/AA)$$

$$P(BAA) = P(BA)*P(AA/BA)$$

$$P(AABC) = P(AA)*P(AB/AA)*P(BC/AB)$$

$$P(BABC) = P(BA)*P(AB/BA)*P(BC/AB) = P(BAB)*P(BC/AB)$$

$$P(BACBC) = P(BA)*P(AC/BA)*P(CB/AC)*P(BC/CB)$$

Triad and pentad fractions are calculated in the usual way, viz.,

$$f_{AAB}^* = P(AAB)/P(B)$$

$$f_{BACBC}^* = P(BACBC)/P(C)$$

(FINAL STATE)	(INITIAL STATE) [†]								
	AA	BA	CA	AB	BB	CB	AC	BC	CC
AA	P(AA/AA)	P(AA/BA)	P(AA/CA)	0	0	0	0	0	0
BA	0	0	0	P(BA/AB)	P(BA/BB)	P(BA/CB)	0	0	0
CA	0	0	0	0	0	0	P(CA/AC)	P(CA/BC)	P(CA/CC)
AB	P(AB/AA)	P(AB/BA)	P(AB/CA)	0	0	0	0	0	0
BB	0	0	0	P(BB/AB)	P(BB/BB)	P(BB/CB)	0	0	0
CB	0	0	0	0	0	0	P(CB/AC)	P(CB/BC)	P(CB/CC)
AC	P(AC/AA)	P(AC/BA)	P(AC/CA)	0	0	0	0	0	0
BC	0	0	0	P(BC/AB)	P(BC/BB)	P(BC/CB)	0	0	0
CC	0	0	0	0	0	0	P(CC/AC)	P(CC/BC)	P(CC/CC)

Figure 2. Matrix of conditional probabilities (transition matrix) used in Program B.

American Chemical
Society Library
1155 16th St., N.W.

P(AA)	P(AA)	P(AA)	P(AA)	P(AA)	P(AA)	P(AA)	P(AA)	P(AA)
P(BA)	P(BA)	P(BA)	P(BA)	P(BA)	P(BA)	P(BA)	P(BA)	P(BA)
P(CA)	P(CA)	P(CA)	P(CA)	P(CA)	P(CA)	P(CA)	P(CA)	P(CA)
P(AB)	P(AB)	P(AB)	P(AB)	P(AB)	P(AB)	P(AB)	P(AB)	P(AB)
P(BB)	P(BB)	P(BB)	P(BB)	P(BB)	P(BB)	P(BB)	P(BB)	P(BB)
P(CB)	P(CB)	P(CB)	P(CB)	P(CB)	P(CB)	P(CB)	P(CB)	P(CB)
P(AC)	P(AC)	P(AC)	P(AC)	P(AC)	P(AC)	P(AC)	P(AC)	P(AC)
P(BC)	P(BC)	P(BC)	P(BC)	P(BC)	P(BC)	P(BC)	P(BC)	P(BC)
P(CC)	P(CC)	P(CC)	P(CC)	P(CC)	P(CC)	P(CC)	P(CC)	P(CC)

Figure 3. Limiting product matrix obtained by repeatedly squaring the matrix of conditional probabilities depicted in Figure 2.

As in the case of Program A, collected n-add distributions and collected n-add fractions are provided in some cases.

Number and weight distributions of A-, B- or C-monomer sequences are also calculated, using the same approach employed in Program A. Program B is being extended to provide A- as well as B-centered pentad distributions and fractions. As is also the case in Program A, trapezoidal integration is used to provide average values of structural features of polymers prepared in conversions specified by the user. Segments of Program B have been used in calculate sequence distributions in styrene-methyl methacrylate copolymers derived from styrene-methacrylic anhydride copolymers (6).

Summary

The two programs described in this paper should be sufficient to handle most problems that will be encountered in studies on terpolymers or terpolymerization. They have been used for monomer conversions in excess of 95 percent. Monomer concentrations are continuously monitored during the integration process and the process is terminated if any monomer concentration falls below 10^{-5} mole percent. Programs A and B require 18,682 and 19,940 bytes of core storage, respectively, and require 36.4 and 15.5 seconds of CPU time for compilation using an IBM 370/158 Model 3 computer and a FORTRAN H compiler. For the same problem Program A runs approximately 73 percent faster than Program B, execution times being of the order of seconds. These programs do not provide for the possibility that some of the monomer units may be enchaind in head-tail rather than tail to head fashion, but with minor revision they could be used to perform calculations for copolymers in which this possibility exists for one of the monomer units. They could also be used for a homopolymerization process in which the monomer can be enchaind in three different ways in the polymer, as is the case in polybutadienes. The programs are not suitable for reversible terpolymerizations or for situations where monomer complexes participate in the polymerizations, however. By suitable modification these programs can be used for calculating the structures of copolymers formed under conditions where monomer-monomer complexes participate in the copolymerization process (1). Copies of either of these programs and instructions for their use are available from the authors.

Acknowledgments

This work was supported in part by a grant (DMR-75-19372) from the National Science Foundation. The authors are grateful to the Asahi Chemical Industry Co., Ltd. for granting and supporting an academic leave for one of them.

Literature Cited

1. Harwood, H.J.; Kodaira, Y.; Neumann, D.L. in "Computers in Polymer Sciences", Mattson, J.S.; Mark, Jr., H.B.; MacDonald, Jr., H.C., Eds., M. Dekker, Inc., New York, 1977, Chapter 2.
2. Harwood, H.J. in "Data Processing in Chemistry", Hippe, Z., Ed., Elsevier, in press.
3. Harwood, H.J. J. Polymer Sci., Part C, 1968, 25, 37.
4. IBM System/360 Scientific Subroutine Package, Version III, Programmer's Manual, Application Program GH-20-0205-4, pg. 99.
5. Price, F.P. J. Chem. Phys., 1962, 36, 209.
6. Neumann, D.L.; Harwood, H.J. Am. Chem. Soc., Div. Polym. Chem., Preprints, 1981, 22, 13.

RECEIVED May 4, 1982.

UV Spectrophotometers as Detectors for Size Exclusion Chromatography of Styrene-Acrylonitrile (SAN) Copolymers

LUIS H. GARCIA-RUBIO¹, A. E. HAMIELEC, and J. F. MACGREGOR

McMaster University, Chemical Engineering Department,
Hamilton, L8S 4L7 Ontario, Canada

The application of UV spectrophotometers to the analysis of styrene containing copolymers has been extensively reported in the literature. However, hypochromic effects and band shifts which result in deviations from Beer's Law have limited the use of UV detectors as mass or composition detectors in size exclusion chromatography applications. Deviations from Beer's Law for low conversion styrene-acrylonitrile copolymers in tetrahydrofuran have been experimentally investigated and compared with results previously reported in the literature. The behaviour of the extinction coefficient as a function of the copolymer composition is discussed in view of the information obtained from infrared and nuclear magnetic resonance measurements on the same polymers. As a result of this investigation, a quantitative correlation of the extinction coefficients of styrene-acrylonitrile copolymers with the length of the styrene sequences has been obtained which, in turn, allows for the use of UV spectrophotometers as sequence length detectors.

Traditionally, spectrophotometers have been used in liquid and size exclusion chromatography applications as detectors for the measurement of concentrations and compositions. Three regions of the electromagnetic spectrum are generally used for mass detection. The ultraviolet (50-4000 Å), the visible (4000-7000 Å), and the infrared (7 μm-500 μm). In the visible region, polymer molecules generally do not absorb but quantitative changes in the refractive index (RI) of the solution are normally observed. Therefore, refractometers are used as standard SEC detectors. UV spectrophotometers have high sensitivity for aromatic and carbonyl bands and, because they monitor specific functional groups, are rarely influenced by environmental factors such as temperature pressure, etc. UV specificity is limited because not every compound absorbs in the UV region. It has been, nevertheless, successfully applied to strongly-absorbing solute bands in regions of high solvent transparency. Although infrared analysis of copolymers has been extensively used (1), it is with the development of new and powerful techniques (infrared lasers, Fourier Transformed Infrared (FTIR), Multiple Scan IR (MIR) etc.) that the infrared analysis of SEC effluents has become a useful technique. IR spectroscopy is more general than RI or UV since almost every organic molecule will show some form of absorption in the IR Region.

¹ Current address: Xerox Research Center of Canada, 2660 Speakman Drive, Mississauga, Ontario, L5K 2L1, Canada.

In the use of spectrophotometers as mass detectors, two fundamental assumptions are made.

- i. The intensity of an absorption band is related to the concentration of the substance or functional group that absorbs the incident radiation. If the concentrations are small, Beer's Law is assumed valid (i.e. there exists a linear relationship between the absorption and the concentration).

$$A_{\lambda_i} = \log \frac{I_0}{I_{\lambda_i}} = \epsilon_{\lambda_i} l c_i \quad (1)$$

- ii. The absorption spectrum of mixtures is in general additive, i.e. the sum of the individual spectra of the components.

$$A_{\lambda_T} = \sum_{i=1}^N A_{\lambda_i} \quad (2)$$

where N is the number of components

Similar assumptions are used for refractive index measurements.

$$\Delta n_i = \left(\frac{dn}{dc} \right)_i c_i \quad (3)$$

$$\Delta n_T = \sum_{i=1}^N \Delta n_i \quad (4)$$

It is obvious, that if the different functional groups present in a copolymer molecule absorb at different wavelengths, the composition and the polymer concentration can be readily obtained. Based on these premises UV, IR and RI are used for copolymer analysis. However, there have been indications over the years that the assumptions of linearity and additivity may not always be valid. Extensive studies on the refractive index of polymers in solution by Barrall, Cantow and Johnson (2), have shown that the specific refractive index increment (dn/dc) is a function of the molecular weight. The linearity of (dn/dc) with respect to composition has been verified for a number of systems mainly block copolymers (3, 4). It has not, however, been sufficiently tested for random copolymers (5) and, therefore, its validity in general cannot be assumed. Fluorescence studies by Vala, Hoebig and Rice (6) have shown that there is a difference between the absorption spectra of isotactic and atactic polystyrene in the region between 2,000 Å and 2,500 Å. The UV absorption behaviour of styrene copolymers has been investigated by O'Driscoll et al (7), Brussau and Stein (8) and Gallo and Russo (9). Deviations from Beer's Law of up to 60% are consistently reported. The set of results put forward by the above authors indicates that the assumptions of linearity (Eq. 1 and 3) and additivity (Eq. 2 and 4) should be verified for each particular polymer system. It is the purpose of this paper to discuss the use of

spectrophotometers and refractometers as SEC detectors for the analysis of styrene acrylonitrile copolymers. Particular emphasis is placed on U.V. spectrophotometers from which it is shown, that average styrene sequence lengths can be obtained.

Materials

Styrene acrylonitrile copolymers were synthesized by bulk free radical polymerization at 60°C and 40°C over a wide range of initial monomer compositions (10). Copolymer compositions were determined by gas chromatography and verified by H¹ NMR spectroscopy. The narrow MWD polystyrene standards (Pressure Chemicals) and the SAN copolymers were purified prior to the analysis by dissolution in THF and precipitation from absolute methanol.

Infrared and Near Infrared Spectroscopy

The sensitivity of infrared measurements to composition has been studied by Wolfram and Grasselli (11). Significant shifts of the position of the C=N stretching band (~2,240 cm⁻¹) of SAN copolymers of different composition are reported (Table I) but no significant changes in the intensity of the bands were observed. More recently, Mirabella (12) investigated the effect of the molecular weight on the infrared absorptivity of polystyrene standards at two frequencies 1,450 cm⁻¹ and 1,493 cm⁻¹. Some changes in absorptivity were observed at 1,493 cm⁻¹ but were attributed to end group effects. The band at 1,450 cm⁻¹ gave no indication of any effect due to differences in molecular weights.

TABLE I

Infrared Analysis of SAN Copolymer

%St	$\gamma_{C \equiv N}$ (cm ⁻¹)	T _g °C
0	2242	90
15	2240	104
60	2237	99
75	2236	97

A necessary step in the use of spectroscopy data is the assignment of absorption bands to specific functional groups or to properties known to be present in the molecules. Extensive encyclopaedic work has led to the identification of domains of absorption modes within the infrared region. Using these as reference (13), identification of some of the absorption bands for SAN copolymers in the fundamental vibrations region is possible. The assignment of polymer absorption bands on the near infrared region has not been, unfortunately, as extensively documented. However, a sufficient number of bands can be assigned, based on the works of Foster, Row and Griskey (14) and Crandall and Jagtap (15), to investigate the effect of composition on the absorption behaviour of SAN copolymers (16).

Experimental. IR measurements were done in a Beckman IR-5 spectrophotometer either on films or solutions. Films were prepared from 10% w/v or CH_2Cl_2 polymer solutions. Solution measurements were done in a 0.01 mm path length NaCl cell. THF, DMF or CHCl_3 were the solvents normally used. Near infrared spectra were recorded from a Beckman DK-A spectrophotometer. 10 mm path length silica cells were used. Relatively high concentrations (5% w/v) of polymer in CHCl_3 were used in this preliminary evaluation. Measurements were done at room temperature in all cases. Table II describes the copolymers used in the evaluation of the IR region.

Results and Discussion. The application of infrared spectroscopy to the analysis of SAN copolymers in solution has two limitations: the poor solubility of the polymers, which constrains the analysis to those regions where the solvents are transparent and the poor sensitivity of the infrared at low concentrations. This last problem is more severe when the characteristic absorption bands have medium or weak intensities (typically $-\text{C}\equiv\text{N}$ stretching). Of particular interest are the bands between 3-7 μm , some of which can be detected in a variety of solvents and provide information on the AN/St ratio. The bands at 13 and 14 μm are very strong and amenable to detection particularly in SEC applications. These bands contain information on the styrene concentration and the molecular structure (Hummel 1974).

Figure 1 and Table III show the absorption behaviour of copolymers obtained at low conversions (homogeneous) and high conversion (heterogeneous). Clearly, the $-\text{C}\equiv\text{N}$ stretching band is sensitive to the changes in molecular structure induced by the change in the polymerization environment throughout the course of the reaction (i.e. composition, viscosity). The effect seems to be the greater, the smaller the acrylonitrile content. These observations are consistent with the near IR measurements at 2.83 μm (Figure 3). In the case of the $-\text{C}=\text{N}$ stretching, not only changes in intensity are observed with increasing acrylonitrile content, but also shifts in the position of the band can also be correlated with changes in composition as reported by Wolfram and Grasselli (11). Figure 2 shows the band shifts observed for low conversion copolymers. Other absorption bands up to 12.5 μm are not as sensitive to the acrylonitrile content and can be used for mass or composition detection. The absorption bands beyond 12.5 μm require more analysis before a definite statement can be made with regard to their sensitivity and information content.

A summary of the near infrared absorption is presented in Figure 3 and Table IV.

Refractive Index Measurements

Refractive index and specific refractive index increments $\rightarrow(\nu = \text{dn}/\text{dc})$ of polymers in solution have been studied extensively in connection with light scattering measurements and size exclusion chromatography applications to polymer characterization for which refractometers are used as standard concentration detectors. Contrary to the observations made in the infrared region (12), refractive index increments have been shown to be a function of the molecular weight of the polymers (2) and, in some cases, of the copolymer composition (17). Therefore, the assumptions of linearity and additivity (Eq. 1 to 4) have to be verified for each particular polymer system. In the case of styrene/acrylonitrile copolymers, there is an additional uncertainty due to the

Table II
SAN Copolymers Used in Infrared and Near Infrared Studies

Low Conversion <10%			Complete Conversion		
Sample	f_{10}	P_1	Sample	f_{10}	P_1
R-01-09	.950	.92	R-01-09A	.950	.950
R-01-08	.800	.74	R-01-08A	.800	.803
R-01-07	.743	.69	R-01-07A	.743	.743
R-01-06	.904	.82	R-01-06A	.904	.904
R-01-05	.800	.73	R-01-05A	.800	.801
R-01-04	.613	.55	R-01-04A	.613	.643
R-01-03	.412	.55	R-01-03A	.412	insoluble

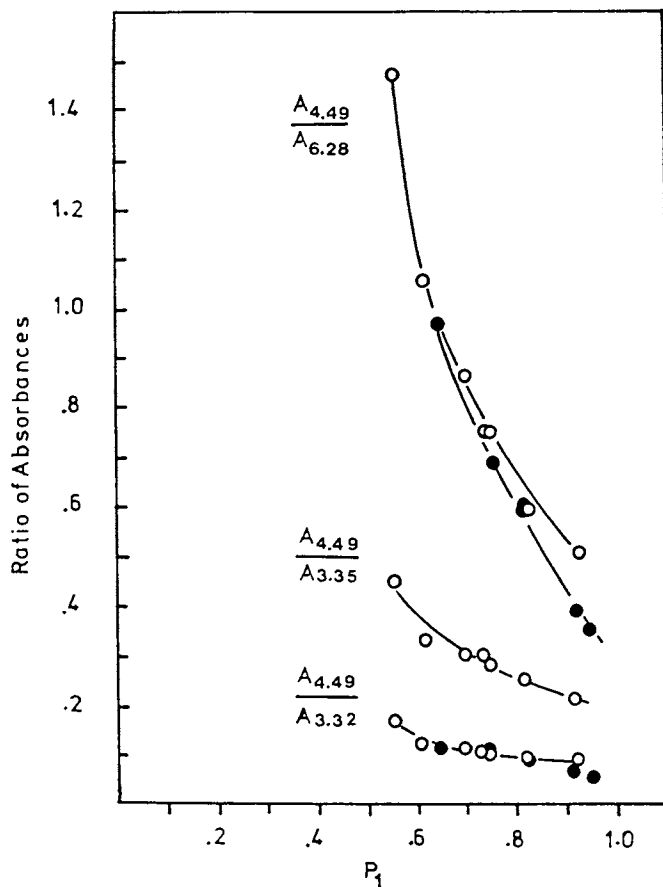


Figure 1. IR absorption ratios for \circ , low conversion and \bullet , high conversion copolymers.

Table III
Infrared Absorption

Sample R-01	Composition P ₁	Wave Length μm								
		2.38	2.78	3.52	3.45	4.28	4.49	6.28	6.72	6.92
09	.92	.126	.074	.561	.229	.184	.051	.10	.261	.250
08	.740	.126	.075	.594	.218	.181	.063	.084	.240	.251
07	.69	.130	.072	.602	.233	.175	.072	.084	.248	.272
06	.82	.128	.073	.585	.222	.174	.056	.094	.246	.255
05	.73	.131	.075	.602	.215	.184	.065	.086	.233	.252
04	.605	.137	.076	.640	.235	.184	.078	.074	.222	.248
03	.55	.132	.076	.561	.215	.181	.097	.066	.215	.252
09A	.95	.108	.066	.530	.231	.171	.034	.097	.256	.24
08A	.803	.128	.073	.572	.226	.174	.056	.094	.252	.252
07A	.743	.126	.073	.594	.213	.180	.061	.089	.233	.244
06A	.904	.126	.073	.606	.232	.177	.041	.105	.256	.258
05A	.801	.131	.076	.622	.223	.184	.056	.092	.256	.260
04A	.643	.133	.078	.648	.215	.184	.073	.084	.237	.256
09A	.95	.130	.077	.588	.229	.187	.041	.102	.264	.252

A - High Conversion Copolymers

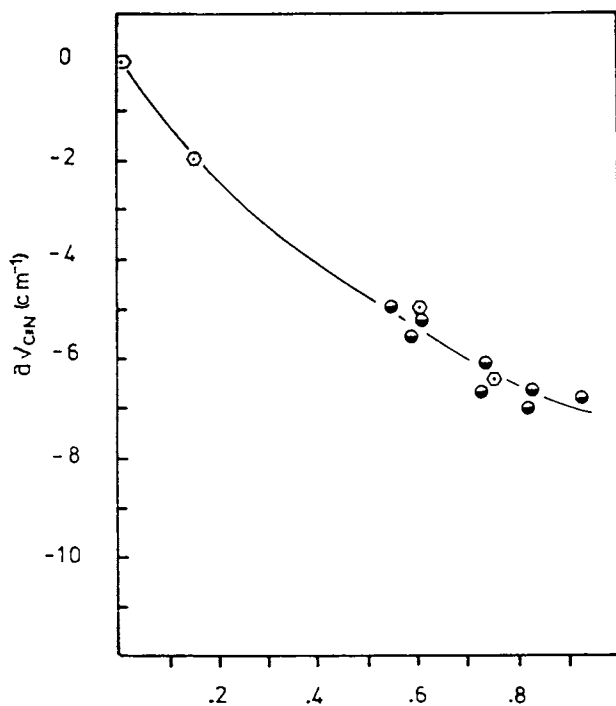


Figure 2. IR shifts of the $-\text{C}\equiv\text{N}$ stretching band as function of composition P_1 styrene mol fraction in the copolymer. Key: \circ , data of Grasselli (1973) and \bullet , this work.

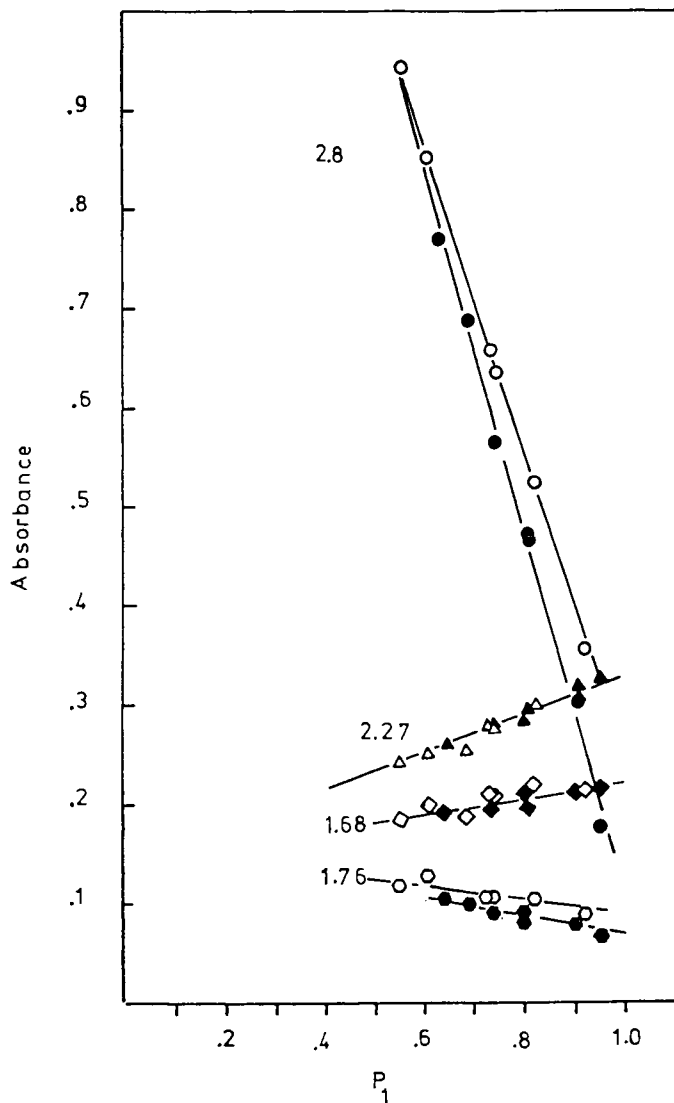


Figure 3. Near IR absorption as function of composition P_1 —styrene mol fraction in the copolymer. Open symbols indicate low conversion and solid symbols indicate high conversion. Key to wavelength (μm): \circ \bullet , 2.8; \triangle \blacktriangle , 2.27; \diamond \blacklozenge , 1.68; \circ \bullet , 1.76.

Table IV
Near Infrared Absorption

Sample R-01	P ₁	Wavelength (μm)								
		1.68	1.76	2.27	2.30	2.47	2.48	2.8	2.83	3.1
09	.92	.215	.093	.305	.229	.839	.870	.352	.357	.1871
08	.74	.208	.111	.276	.264	.745	.790	.456	.638	.229
07	.69	.184	.101	.252	.268	.703	.740	.438	.688	.229
06	.82	.222	.108	.305	.260	.824	.839	.532	.523	.208
05	.73	.211	.108	.280	.268	.756	.783	.495	.658	.237
04	.605	.200	.132	.252	.323	.721	.745	.585	.854	.292
03	.55	.185	.120	.240	.314	.757	.810	.683	.948	.280
09A	.95	.216	.0783	.326	.204	.886	.903	.288	.175	.164
08A	.803	.197	.086	.284	.233	.801	.818	.379	.171	.237
07A	.743	.197	.094	.277	.244	.780	.801	.456	.567	.215
06A	.904	.215	.084	.319	.222	.854	.893	.330	.301	.174
05A	.801	.211	.092	.294	.229	.796	.824	.403	.466	.208
04A	.643	.194	.108	.260	.269	.733	.757	.602	.770	.252

A - High Conversion Copolymers

limited solubility of acrylonitrile-rich copolymers in solvents which are transparent in the ultraviolet region.

Experimental. The differential refractive indexes of polymer solutions were measured at 25°C with a Waters Scientific R-403 differential refractometer connected on-line with a size exclusion chromatograph. The refractometer was calibrated to refractive index units (Riu) with benzene/carbon tetrachloride solutions. The rationale behind using the refractometer on-line with the chromatograph is the elimination of impurities in the sample (water, residual monomer etc.) which affect the refractive index measurements particularly at low polymer concentrations and to calibrate the detectors at the flow conditions at which they were normally operated. Polymer solutions of several concentrations (0.015–0.0025 wt %) were injected repeatedly to verify the reproducibility of the measurements, which was typically $\Delta n \pm 0.5 \times 10^{-6}$ for replicates on the same solutions.

Results and Discussion. The specific refractive index increments defined as:

$$\nu = \left(\frac{dn}{dc} \right)_{t,\lambda} = \lim_{c \rightarrow 0} \frac{\Delta n}{c} \quad (5)$$

where

$$\Delta n = \nu \cdot c + kc^2 \quad (6)$$

were estimated directly using equation 6 and measurements of refractive index differences of polymer solutions at several concentrations. Equation 6 was used instead of the standard linearized equation ($\Delta n/c$) in order to maintain the error structure in both Δn and the concentrations (10). The 95% confidence intervals for the values of ν were, on the average: $\nu \pm 0.003$ (Riu/g/cc) for replicates on the same sample. The pooled standard deviation for all samples is $\pm 2.0\%$ or ± 0.004 (Riu/g/cc).

A number of narrow polystyrene standards (Waters Scientific) were examined in order to quantify the dependence of the specific refractive index increments in THF on the molecular weight of the polymer. The results shown in Figure 4 agree quite well with those reported by Schulz and Baumann (18). The values of ν increase slightly with molecular weight up to approximately 20,000 and then remain constant within the experimental error. Partial specific volumes \bar{v}_1 were estimated using the equation

$$\nu = \frac{r_{1-} (\bar{v}_1) \left[\frac{n_o^2 - 1}{n_o^2 + 2} \right]}{\frac{2}{3} n_o \left[1 - \frac{n_o^2 - 1}{n_o^2 + 2} \right]^2} \quad (7)$$

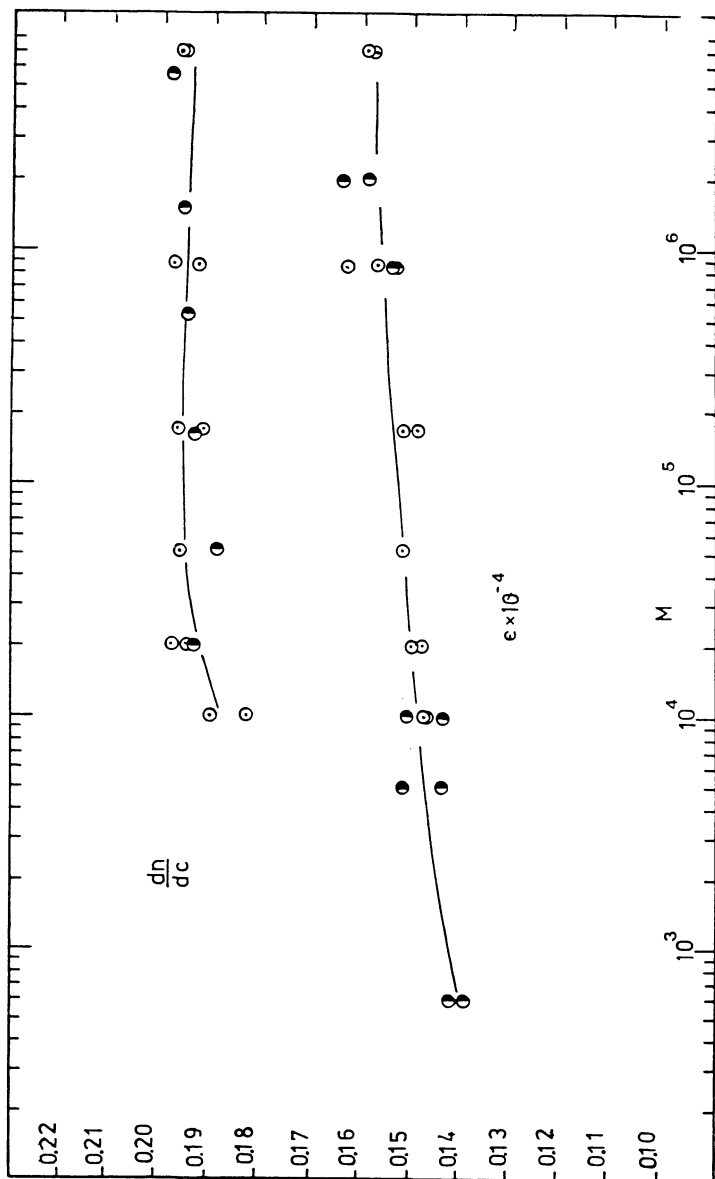


Figure 4. Specific refractive index increments (dn/dc , data of Schultz and Bauman, 1968) and extinction coefficients ($\epsilon \times 10^{-4}$, this work) of polystyrene standards as function of the molecular weight. Key: \bullet , total copolymer measurements; \circ , data obtained with the SEC.

where

$$r_1 = v_1 \frac{n_1^2 - 1}{n_1^2 + 2}$$

n_0 is the refractive index of the solvent, n_1 , the refractive index of the polymer, v_1 is the specific volume of the polymer and \bar{v}_1 the partial specific volume of the polymer in solution.

Equation 7 was derived independently by Machtle and Fisher (17) and Lorimer (19) assuming additivity of the specific refractivities (Equation 8) and the validity of the Lorenz-Lorenz equation (9) respectively.

$$R = \sum_{i=1}^q P_i r_i \quad (8)$$

$$v_1 \frac{n^2 - 1}{n^2 + 2} = \sum_{i=1}^q v_i (n_i^2 - 1) / (n_i^2 + 2) \quad (9)$$

R total specific refractivity

P_i mass fraction of component i

v_i total specific volume

The results obtained with equation 7 are summarized in Table V. The specific volume of the polymer at infinite dilution is considerably smaller than the specific volume of the solid substance ($v_1 = 0.948 \text{ cm}^3/\text{g}$) in agreement with values reported elsewhere (4).

Specific refractive indexes of SAN copolymers at several compositions were also measured in THF. Low conversion copolymers were initially investigated to correlate the effect of the composition on the refractive index increments (Fig. 5). All measured points lie on a straight line within the experimental error indicating that the assumption of additivity appears to be valid for both ν and \bar{v}_1 .

$$\bar{v}_1 = \sum_{i=1}^q P_{iw} (\bar{v}_1)_i \quad (10)$$

$$\nu = \sum_{i=1}^q P_{iw} (\nu)_i \quad (11)$$

Table V
Refractive Index Increments and Extinction Coefficient
of Polystyrene Standards

Sample	Mw x 10 ⁻³	ν	$\bar{\nu}_1$	$\epsilon \times 10^{-4}$	$\epsilon \times 10^{-4}$
		Riu/g/cc	cc/g	$\frac{A_U \cdot \text{cm}^2}{g}$	$\frac{A_U \cdot \text{cm}^2}{g}$
PS02	.60	--	--	.14	--
PS03	5.00	--	--	.1478	--
PS04	10.30	.1870	.89505	.143	.1454
PS05	19.85	.1955	.8766	--	.1495
PS06	51.00	.1961	.8753	--	.1512
PS08	173.00	.1942	.8794	--	.1497
	411.00	--	--	.1538	--
PS12	867.00	.1970	.8734	.1537	.1574
	1800.00	--	--	.1556	--
	2145.00	--	--	.1608	--
PS16	7100.00	.1965	.8745	--	.1590
Mean		.1944	.8790	.1506	.1520
-		-.038	-0.006	-.071	-.044
+		+.0135	-0.018	+.067	+.046

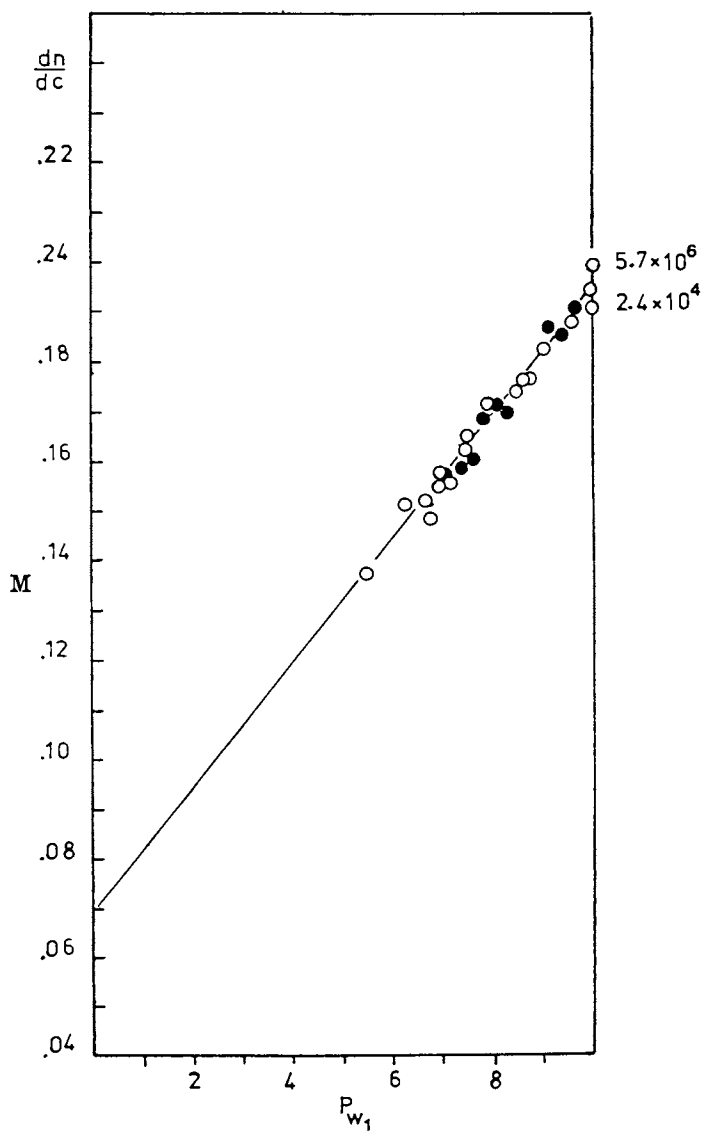


Figure 5. Specific refractive index increments of SAN copolymers. Key: \circ , low conversion; \bullet , high conversion. MW of polystyrene standards indicated on right hand axis.

Polymers obtained at intermediate and high conversions with varying degrees of composition heterogeneity were also investigated (Fig. 5). No significant deviations were observed. The scatter present in the data could be attributed to errors associated with the composition and to differences in molecular weights. The specific refractive indexes ν_i in equation 11 were estimated in a slightly different form:

$$\nu = \nu_1 - (\nu_1 - \nu^*) \frac{1 - P_{1w}}{1 - P_{1w}^*} \quad (12)$$

where P_{1w}^* and ν^* were chosen as the azeotrope's composition and refractive index increment. Equation 11 was transformed using Equation 12 to minimize the uncertainties associated with the extrapolation required to estimate the refractive index increment for polyacrylonitrile in THF. (Polyacrylonitrile is insoluble in THF). In the final estimation of ν^* , all the PS and SAN results were used. The estimated values are: $\nu_1 = .1928$ and $\nu^* = .1619$ both with a 95% confidence region of ± 0.003 . The value of the increment for polyacrylonitrile calculated from Equation 12 is $\nu_2 = .069$ which is approximately half the value predicted by Equation 7 assuming that $\bar{\nu}_1 = \nu_1$. Partial specific volumes for the copolymers were calculated using Equation 7. Unfortunately, the magnitude of the experimental error makes it difficult to draw conclusions on the behaviour of the volume of copolymer molecules in solution. The results obtained from refractive index measurements have been summarized in Figure 6 and Tables 6 and 7.

Ultraviolet Spectroscopy

The qualitative and quantitative study of chromophores with ultraviolet light has undergone intensive development in classic organic chemistry and now constitutes routine analysis in many cases. (Chromophore groups are groups capable of undergoing electronic transitions between their different electron levels when energy corresponding to the ultraviolet wave lengths is applied to them. Typically these are conjugated systems such as dienes, phenyl groups etc.) Ultraviolet analysis applications to polymers have been centered, primarily, on polymers and copolymers containing styrene or styrene derivatives, where the group or chromophore responsible for the ultraviolet absorption is the phenyl ring in the styrene units. Recent studies on the absorption behaviour of styrene containing polymers have shown significant deviations from the standard assumptions of linearity (Beer's Law) and additivity. These deviations have been attributed to the microstructure of the polymer chains and in some cases to the conformation of the molecules in solution. Clearly, if these observations can be verified for styrene/acrylonitrile copolymers, ultraviolet (UV) detectors could be used to monitor sequence length, tacticity or molecular conformation as functions of the molecular size in size exclusion chromatography applications. In view of the importance of these measurements, a review of the most relevant reports is included in this section.

Literature Review. The early reports on the difference in absorption behaviour of polystyrenes in solution are due to Vala and Rice (6). These authors attributed the hypochromism (decrease in absorption intensity) observed in some of the absorption bands when the spectra of isotactic and atactic polystyrenes are compared to the conformation of the polymer molecules in solution. Hypochromic

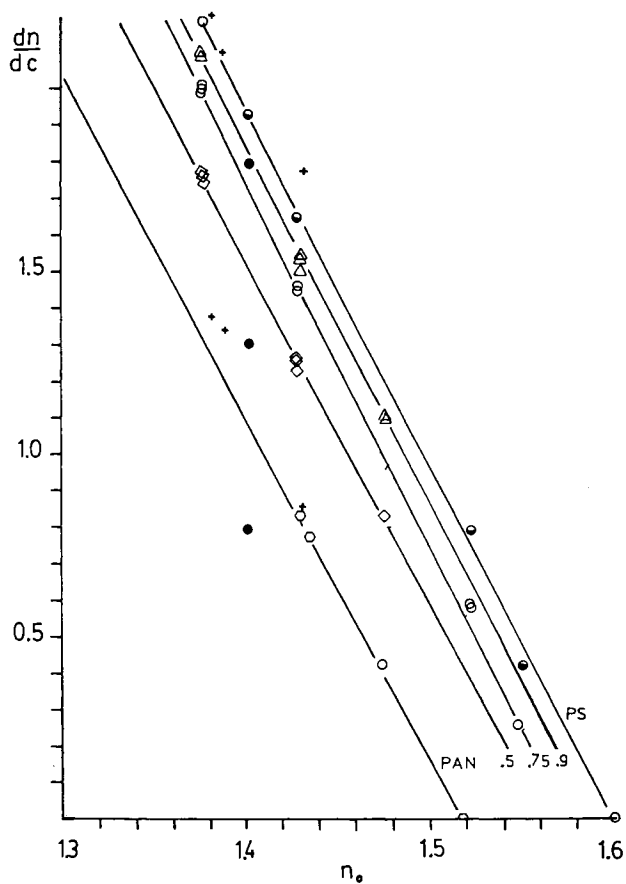


Figure 6. Summary of refractive index increment data as function of the refractive index of the solvent (n_s) \odot , Data from Baumann and Lange, Blanks and Shah, Kambe, and this work. See Ref. 10 for further explanation.

Table VI
Refractive Index Increments of Low Conversion Copolymer

Sample	P_{1w}	ν $\frac{\text{Riu-cm}^3}{\text{g}}$	\bar{v}_1 cm^3/g
R-01-09	.958	.1887	.8780
R-02-02	.873	.1759	.8844
R-02-04	.837	.1754	.8756
R-02-06	.799	.1710	.8748
R-02-08	.735	.1573	.8870
R-02-10	.690	.1538	.8823
R-02-01A	.677	.1532	.8800
R-04-01	.550	.1377	.8789
R-04-02	.620	.1513	.8686
R-04-03	.670	.1547	.8749
R-04-04	.685	.1578	.8722
R-04-05	.724	.1555	.8879
R-04-06	.750	.1622	.8805
R-04-07	.788	.1686	.8770
R-04-08	.840	.1734	.8808
R-04-09	.896	.1825	.8764

Table VII
Summary of Refractive Index Increments
and Partial Specific Volumes for
Low and High Conversion Copolymers

Sample	P_{1w}	$\nu \frac{\text{Riu-cm}^3}{\text{g}}$	$v_1 \frac{\text{cm}^3}{\text{g}}$
R-01-09	.958	.1887	.8799
R-01-09-A	.974	.1895	.8825
R-02-02	.873	.1759	.8844
R-02-11	.867	.1763	.8819
R-02-16	.876	.1756	.8859
R-02-41	.916	.1868	.8725
R-02-51	.941	.1850	.8833
R-02-04	.837	.1754	.8756
R-02-17	.832	.1688	.8886
R-02-32	.852	.1749	.8808
R-02-47	.879	.1747	.8863
R-02-06	.799	.1710	.8748
R-02-13	.784	.1678	.8776
R-02-43	.814	.1699	.8813
R-02-53	.814	.1705	.8780
R-02-08	.735	.1573	.8870
R-02-14	.731	.1560	.8887
R-02-19	.748	.1577	.8897
R-02-49	.746	.1586	.8872
R-02-10	.690	.1538	.8823
R-02-15	.701	.1546	.8835
R-02-01A	.677	.1532	.8800
SAN Std.	.77	.1599	.8909

effects were also observed by O'Driscoll, Wertz and Husar (7) in the analysis of styrene methyl methacrylate (SMMA) copolymers. The hypochromicity was attributed to the interaction of phenyl groups on adjacent monomer units and correlated with the calculated fraction of dyads.

Brussau and Stein (8) investigated the effect of the sequence length on the UV absorption of styrene containing copolymers such as styrene maleic anhydride (SMA), styrene butadiene (SB) and styrene acrylonitrile at several wave lengths in chloroform and THF. Their experimental results indicate that the response of the UV detector appears to be a function of the styrene sequences. Therefore, UV spectrophotometers were regarded as not being effective for concentration detection in chromatography applications to copolymer analysis. Stutzel, Miyamoto and Cantow (20) also investigated SMMA copolymers in THF and dioxane solutions at several temperatures. From their experimental results, they concluded that it is unlikely that the hypochromic effects are due to differences in conformation, but rather, that the differences in absorption are due to the sequential arrangement of the monomer units in the chain in agreement with O'Driscoll's and Brussau's conclusions. The average extinction coefficient for the copolymer was expressed as a function of the probabilities of the three styrene-centered triads:

$$\bar{\epsilon} = f_{SSS} \epsilon_{SSS} + f_{MSS} \epsilon_{MSS} + f_{MSM} \epsilon_{MSM} \quad (13)$$

where $\bar{\epsilon}$ is the observed average extinction coefficient. ϵ_{ijk} are the styrene-centered triad extinction coefficients and f_{isj} are the styrene-centered normalized triad probabilities. Stutzel and Miyamoto suggest that the extinction coefficient ϵ_{SSS} can be approximated by that of polystyrene, whereas ϵ_{MSM} can be estimated from alternating copolymers. Stutzel's arguments have been strongly contradicted by the experimental evidence presented by Gallo and Russo (9), who studied the hypochromism of SMMA copolymers in solution as functions of the solvent's dielectric constant. Their results can be summarized as follows:

- ▶ the hypochromic effects are present for copolymers and non-existent for mechanical mixtures of polystyrene and methyl methacrylate;
- ▶ the percent hypochromism and the composition at which it appears are functions of the dielectric constant of the solvent;
- ▶ solvents with high dielectric constant show smaller hypochromic effects.

The above evidence indicates that hypochromism in SMMA copolymers is related to the conformation of the copolymer molecules in solution. Unfortunately, although it is known that the conformation of the molecules in solution is a function of the microstructure, the relationship between sequence length, tacticity and conformation has not been quantified. More recently, Gruber and Knell (21) investigated the absorption behaviour of styrene/butyl acrylate and styrene/n-butyl acrylate copolymers at a wave length of 269 nm in chloroform. These authors concluded, in agreement with O'Driscoll, Brussau and Stutzel, that the differences observed between the expected behaviour of the extinction coefficients and the experimental values obtained could be explained in terms of the interaction between neighbouring aromatic nuclei (London forces). In other words, that the extinction coefficient of styrene containing copolymers is a function of the length of the styrene sequences in the copolymer.

Whether the lengthening of the styrene sequences is directly responsible for the anomalous behaviour of styrene containing copolymers or whether it is due to a change in tacticity and/or conformation proceeding hand-in-hand with it, cannot be decided on the basis of the experimental evidence thus far reported in the literature. The general consensus favours the hypothesis that recognizes the

length of the styrene sequences as being the most important factor in explaining the observed deviations from Beer's Law.

Experimental. Absorbances of selected polymer and copolymer samples were measured with a Waters 440 ultraviolet absorbance detector equipped with a 254 nm filter, and a Beckman 25 ultraviolet/visible spectrophotometer. The Water's instrument was used on-line with the size exclusion chromatograph (16). The Beckman 25 was used to calibrate and standardize the Water's 440 UV detector. THF was used as standard solvent. The extinction coefficients were estimated from absorbance measurements at several polymer concentrations. The standard deviation for the absorbance measurements was typically $\pm .001$ Au for replicates on the same sample. All measurements were done at room temperature.

Results and Discussion. As a first step in the analysis of the absorption behaviour of SAN copolymers, the effects of tacticity and molecular weight on the extinction coefficients of well-characterized polystyrene samples were investigated.

The spectra of isotactic and atactic polystyrenes are shown in Figure 7. The spectra are quite similar except for the bands at ~ 258 nm and ~ 262 nm which show differences in intensity i.e. the ratio A_{258}/A_{262} increases for isotactic polystyrene. This ratio also increases with acrylonitrile content (Figure 8) indicating some degree of tacticity in agreement with the H^1 NMR results (10, 22) and with the conclusions of Gallo and Russo.

The absorption behaviour of narrow polystyrene standards as a function of the molecular weight is shown in Figure 4. The extinction coefficient increases slightly ($\sim 12\%$) over the molecular weight range $600-7.1 \times 10^6$. The reason for such increase is unknown. It can be speculated, however, that the increase in extinction coefficient with molecular weight is due to an increase in scattered light as the molecular dimensions approach the wavelength of the incident light. The extinction coefficients of selected polystyrene standards as functions of the molecular weight are reported in Table V. An average value of $\epsilon_{ps} = 0.152 \times 10^4$ (Au.cm²/mol) or on molar basis $\epsilon_{ps} = 0.158 \times 10^6$ (Au.cm²/gms) was used for comparison with the extinction coefficient of SAN copolymers.

The assumptions of linearity (Beer's Law) and additivity (Equations 1 and 2) can be stated for UV absorption as follows:

$$A_{\lambda} = \epsilon_{\lambda} \cdot l \cdot c \quad (14)$$

and for multicomponents

$$\bar{A}_{\lambda} = \sum_{i=1}^n A_{i\lambda} = l \cdot \sum_{i=1}^n \epsilon_{i\lambda} \cdot c_i \quad (15)$$

where $A_{i\lambda}$ is the absorbance of the i th component at the wavelength λ , l is the cell's path length, $\epsilon_{i\lambda}$ the extinction coefficient of the i th component and c_i is the concentration of the i th component. For copolymers ($n=2$) equation 15 can be written as:

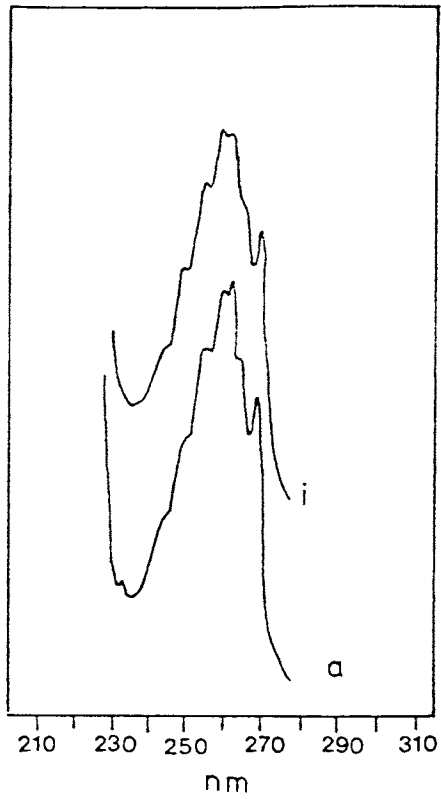


Figure 7. UV spectra of a, atactic and i, isotactic polystyrenes in THF wavelength (nm).

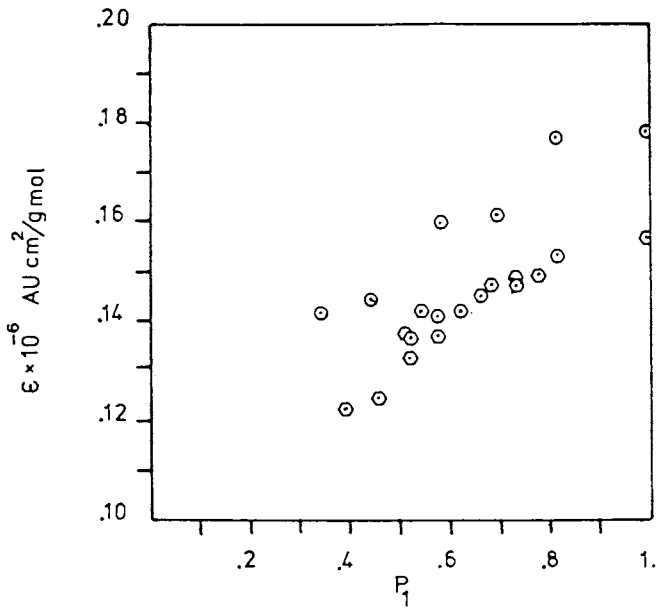


Figure 8. Molar extinction coefficients of low conversion SAN copolymers in THF at 25°C, 254 nm.

$$\bar{A}_\lambda = l \cdot c \cdot (\epsilon_{1\lambda} \cdot P_1 + \epsilon_{2\lambda} \cdot (1-P_1)) \quad (16)$$

where c is the copolymer concentration (gmol/cm^3) and P_1 is the mole fraction of monomer 1 in the copolymer. If only one of the monomers absorb at a given wave length, equation 16 can be simplified to

$$\bar{A}_\lambda = l \cdot c \cdot \epsilon_{1\lambda} P_1 \quad (17)$$

a standard assumption made in the UV analysis of styrene containing copolymers is that, the only chromophore present in the copolymer molecules is the phenyl group in the styryl units (see references cited in Literature Review). This assumption is justified on the basis that the nitrile group absorbs significantly only at wave lengths <230 nm, far from the selected wave length of 254 nm. Based on the assumption of selective UV styryl absorption, the extinction coefficients of low conversion SAN copolymers were estimated and compared with those reported by Brussau and Stein. Table VIII and Figure 8 summarize the extinction coefficients at 254 nm. Although the actual values do not agree, the normalized extinction coefficients (with respect to polystyrene) agree very well within the experimental error (Figure 9). Comparison of the normalized coefficients at several wave lengths (Figure 9) show the same trends across the spectrum, indicating that only the magnitude of the deviations is wave length dependent. Under these conditions, UV spectrophotometers cannot be used directly to determine the composition of styrene acrylonitrile copolymers. However, if it is further assumed that the conformation effects are due to microstructure configurations, there is justification in correlating the extinction coefficient with the sequence length of the styrene units. The normalized extinction coefficient correlates linearly with the styrene average sequence length \bar{N}_S or with the normalized styrene/acrylonitrile dyad probability (Figure 10 and Table IX) in agreement with O'Driscoll observations for St-MMA. Replacing these linear relations into equation 17 an equation relating absorption to styrene concentration ($c \cdot P_1$) and average sequence length (\bar{N}_S) can be obtained

$$\bar{A}_\lambda = l \cdot c \cdot P_1 \cdot \epsilon_{ps\lambda} \cdot \left(1 - \frac{\beta_\lambda}{\bar{N}_S}\right) \quad (18)$$

clearly, by measuring the copolymer absorption at least two wave lengths both the styrene concentration and average sequence length can be estimated either directly (measurements at two wave lengths) or in the least squares sense by measuring the absorption at more than 2 wave lengths.

The effect of the average sequence length on the absorption behaviour of SAN copolymers can be explained as a decrease in the absorption intensity of the styryl units due to the electron withdrawing characteristics of neighbouring nitrile groups. If this effect propagates through two or more styrene units, then it is possible to use the approach suggested by Stutzel (Equation 13).

If multiple UV detectors or stop flow techniques are used in size exclusion chromatography, equation 18 would allow the calculation of composition and sequence length across the chromatogram. This, in fact, has been shown to be the case for SAN copolymers of varying degrees of heterogeneity (16). The parameters β_λ (Table IX) obtained from off-line measurements, in conjunction with the Universal calibration curve, were used to characterize the copolymers shown in Figures 11-13 for which the average copolymer composition, the average styrene sequence length and the number average molecular weight have been measured as functions of the molecular size (10).

Table VIII
Extinction Coefficients for Low Conversion SAN Copolymers
254 nm in THF at 25°C

Sample	Composition		$\epsilon_w \times 10^{-4}$ Au.cm ² /g	$\epsilon \times 10^{-6}$ Au.cm ² /g.mol	ϵ_1/ϵ_{ps}
	Mole	Weight			
S100*	1.00	1.000	.1700	.1770	1.00
SA-90-10*	.821	.90	.1700	.1684	.951
SA-81-18*	.696	.818	.1550	.1614	0.912
SA-73-27*	.579	.730	.1540	.1604	0.906
SA-61-39*	.446	.612	.1390	.1448	0.818
SA-50-50*	.340	.503	.1360	.1416	0.80
PS**	1.000	1.000	.1506	.1568	1.0
R-04-01	.384	.550	.1186	.1235	.788
R-04-02	.454	.620	.1197	.1247	.795
R-04-03	.509	.670	.1331	.1386	.884
R-04-04	.526	.685	.1317	.1372	.874
R-04-05	.572	.724	.1356	.1412	.900
R-04-06	.605	.750	.1367	.1424	.908
R-04-07	.654	.788	.1393	.1451	.925
R-04-08	.728	.840	.1417	.1476	.941
R-04-09	.815	.896	.1477	.1538	.981
R-02-01A	.518	.678	.1273	.1326	.845
R-02-10	.531	.690	.1375	.1432	.913
R-02-08	.586	.735	.1323	.1378	.879
R-02-06	.670	.799	.1419	.1478	.942
R-02-04	.723	.837	.1422	.1481	.944
R-02-02	.778	.873	.1435	.1494	.953

* Data from Brussau and Stein (1970)

** Average Value from Table V

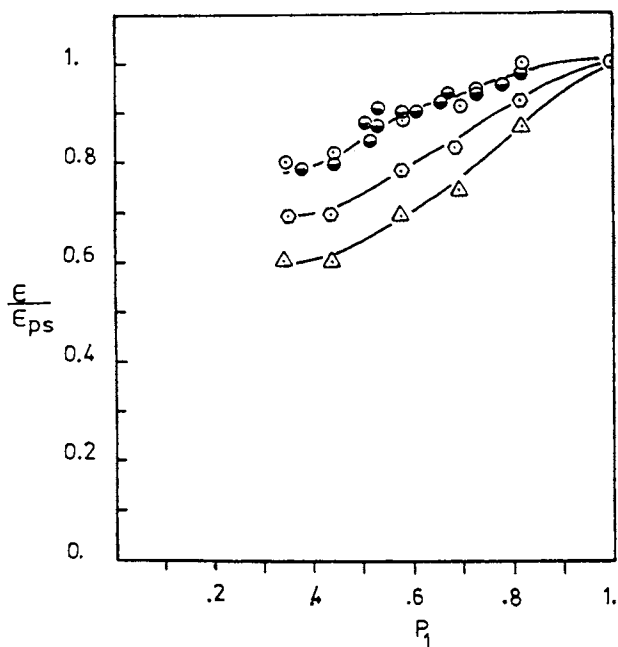


Figure 9. Normalized extinction coefficients for SAN copolymers in THF at 25°C. Data of Brussau and Stein (1970): ○, 254 nm; ◻, 261 nm; and △, 269 nm. Data from this work: ●, 254 nm.

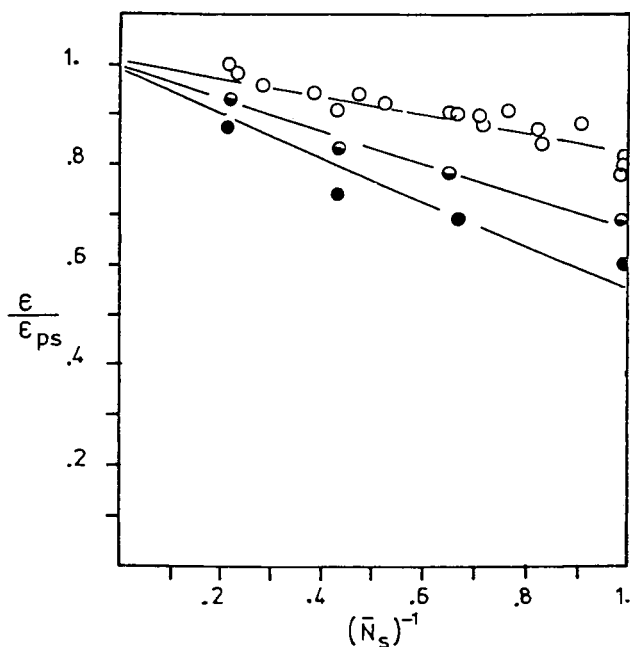


Figure 10. Correlation between extinction coefficient and average sequence length. Data of Brussau and Stein (1970): ●, 269 nm and ●, 261 nm. Data from this work: ○, 254 nm.

Table IX

Correlation Between Molar Extinction
Coefficient and Average Sequence Length
THF (25°C)

254 nm	$\frac{\epsilon}{\epsilon_{ps}} = 1 - 0.1831 \frac{1}{\bar{N}_s}$	Correlation = -0.952
261 nm	$\frac{\epsilon}{\epsilon_{ps}} = 1 - 0.3081 \frac{1}{\bar{N}_s}$	Correlation = -0.995
269 nm	$\frac{\epsilon}{\epsilon_{ps}} = 1 - 0.4075 \frac{1}{\bar{N}_s}$	Correlation = -0.985

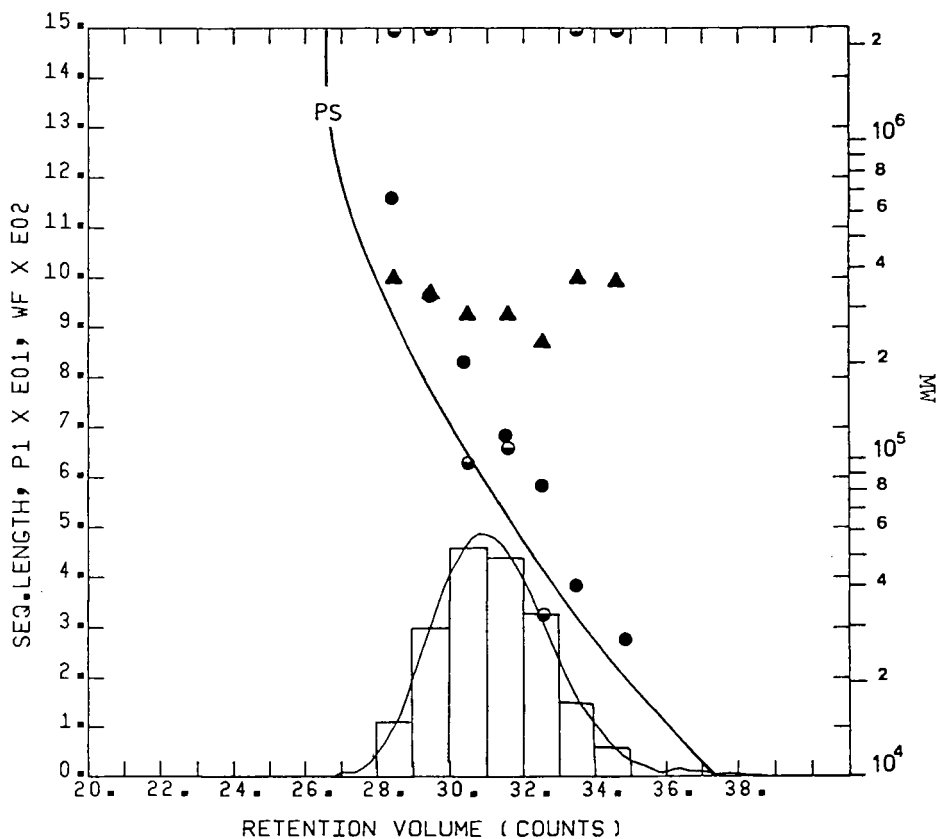


Figure 11. Copolymer composition (\bar{P}_{1w}), average styrene sequence length (\bar{N}_s) and number average molecular weight as function of the retention volume. Molar feed composition is 0.90. PS is the polystyrene calibration curve. Key: ●, \bar{M}_n ; ▲, \bar{P}_{1w} ; and ●, \bar{N}_s .

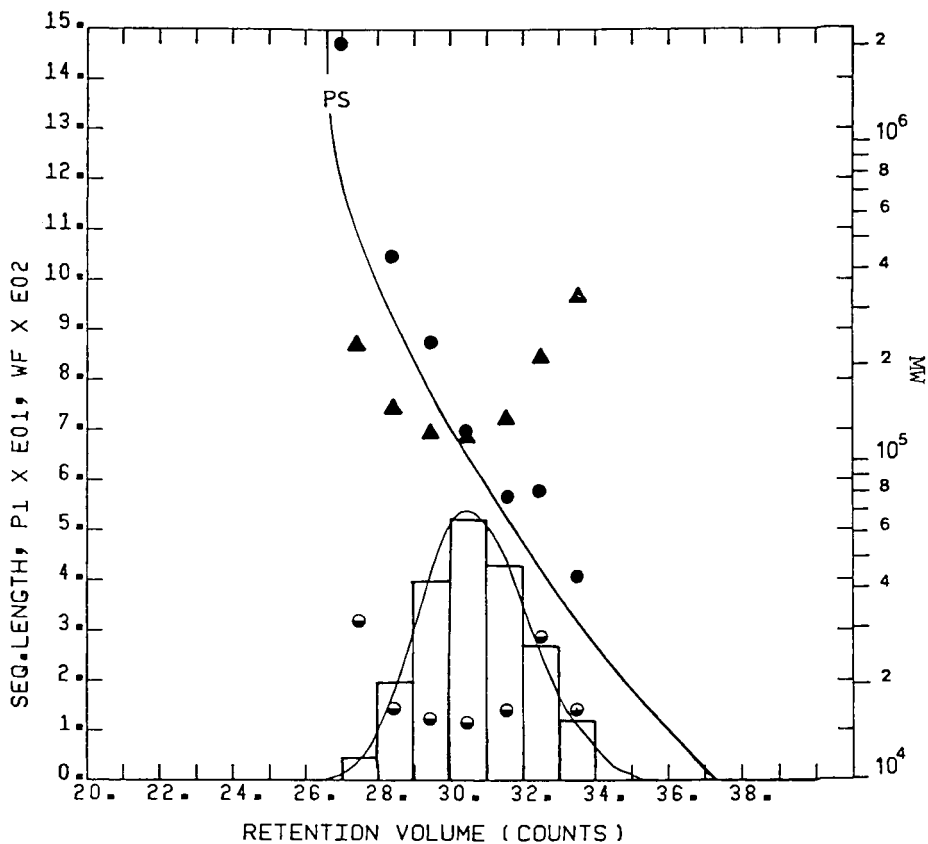


Figure 12. Copolymer composition (\bar{P}_{1w}), average styrene sequence length (\bar{N}_s) and number average molecular weight as function of the retention volume. Molar feed composition is 0.50. PS is the polystyrene calibration curve. Key: ●, \bar{M}_n ; ▲, \bar{P}_{1w} ; and ○, \bar{N}_s .

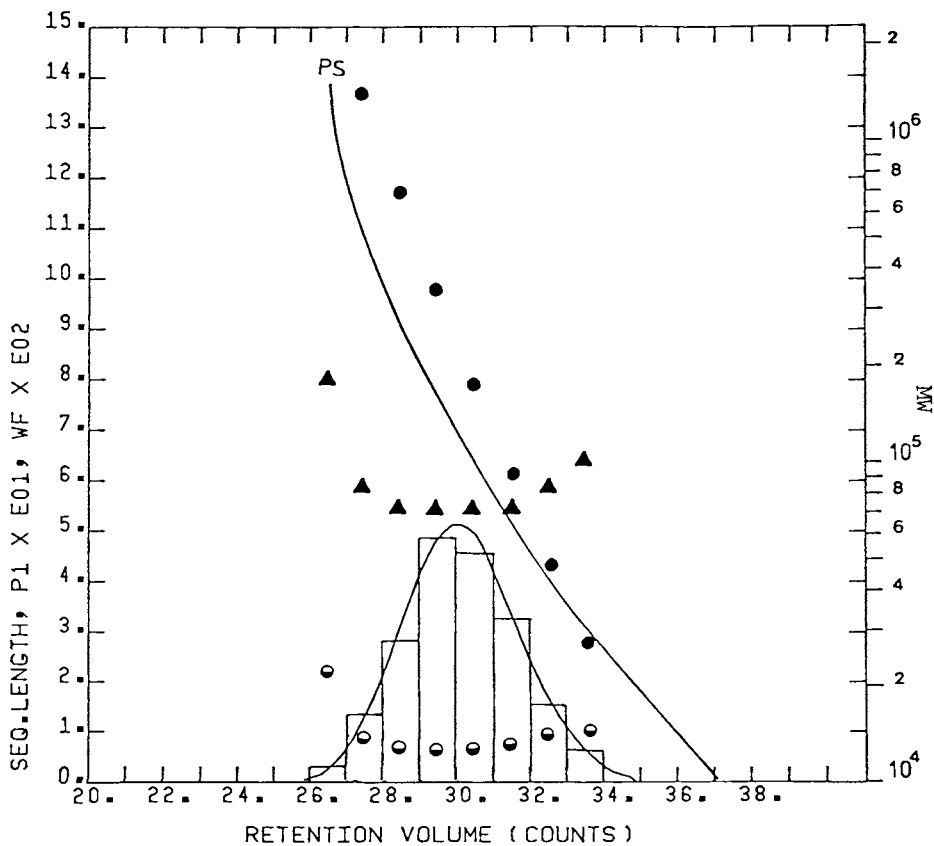


Figure 13. Copolymer composition (\bar{P}_{1w}), average styrene sequence length (\bar{N}_s), and number average molecular weight as function of the retention volume. Molar feed composition is 0.10. PS is the polystyrene calibration curve. Key: ●, \bar{M}_n ; ▲, \bar{P}_{1w} ; and ⊙, \bar{N}_s .

Conclusions

It has been shown that the absorption spectra of copolymers reflect the structure of the molecules, especially the masses of the constituent atoms and the intramolecular forces acting between them. It is, therefore, expected that some level of interaction between responses due to mass and those due to configuration and other environmental factors will always be present to some extent. Therefore, the linearity and additivity of the spectrophotometer response should always be verified. The use of these interactions for the elucidation of polymer microstructure as functions of the molecular weight appears to be very promising in view of the results thus far presented. The use of multiple wave length detectors, multiple detectors or stop-flow techniques are evidently the most appropriate for microstructure analysis in size exclusion chromatography applications. Of all the detectors investigated the differential refractometer and the UV spectrophotometer are the most sensitive for the analysis of styrene acrylonitrile copolymers. The infrared and near infrared spectra, although very sensitive to microstructure are difficult to measure from dilute solutions. Modern instrumentation is recommended to investigate further the potential of these two regions, particularly the near infrared where very little work has been done. The results thus far obtained in the characterization of styrene acrylonitrile copolymers are very encouraging since they show that rather complete copolymer characterizations can be obtained by simple measurements and adequate selection of the detection system.

List of Symbols

A	absorbance in absorption units (Au)
c	concentration in g/cm ³ or g mol/cm ³
f ₁₀	styrene feed composition
k	virial coefficients
l	cell path length cm
n	refractive index (Riu)
$\frac{dn}{dc}$	specific refractive index increments Riu.cm ³ /g
Δn	refractive index difference
N	average sequence length
P _i	mass fraction of component i in the copolymer
P _{wi}	weight fraction of component i in the copolymer
t	temperature
v	specific volume cm ³ /g
v	partial specific volume

Greek Symbols

β	fitting coefficient
γ	frequency ⁻¹
ν	alternate symbol for dn/dc
ϵ	extinction coefficient in Au.cm ² /g or Au.cm ² /g mol

Subscripts

i	component or concentration
T	total
o	solvent
w	weight basis
s	styrene
M	methyl methacrylate
ps	polystyrene
1	styrene

Units

Au	absorbance units
nm	nanometers
μm	micrometer
g	grams
Riu	refractive index units

Literature Cited

1. Henniker, J.C., Infrared Spectrometry of Industrial Polymers, 1967, Academic Press.
2. Barral, E.M., Cantow, H.J. and Johnson, J.F., J. App. Polym. Sci. 1968, 12, 1373.

3. Brandrup, J. and Immergut, E.H., Polymer Handbook, 1975, Interscience.
4. Huglin, M.B. ed., Light Scattering from Polymer Solutions 1972, Academic Press.
5. Benoit, H. and Froelich, D., Light Scattering from Polymer Solutions, (M.B. Huglin ed.), 1972, Academic Press.
6. Vala, M.T., Haebig and Rice, S.A., J. Chem. Phys. 1965, 43, No. 3, 886.
7. O'Driscoll, K.F., Wertz, W. and Husar, A., J. Polym. Sci. 1967, A1 5, 2159.
8. Brussau, R.J. and Stein, D.J., Angew. Makromol. Chem. 1970, 12, 59.
9. Gallo, B.M. and Russo, S., J. Macromol. Sci. Chem. 1974, A8, 33, 521.
10. Garcia-Rubio, L.H., Ph.D. Thesis 1981, McMaster University.
11. Wolfram, L.E. and Grasselli, J.G., Polymer Preprints 1973, 14, No. 2, 640.
12. Mirabella, J.R., J. App. Polym. Sci. (to be published).
13. Conley, R.T., Infrared Spectroscopy 1972, Allyn & Bacon Inc., Boston.
14. Foster, G.N., Row, S. and Griskey, R.G., J. App. Polym. Sci. 1964, 8, 1357.
15. Crandall, E.W., Jagtap, A., J. App. Polym. Sci. 1977, 21, 449.
16. Garcia-Rubio, L.H., Hamielec, A.E., and MacGregor, J.F., ACS Meeting 1981, Atlanta, Georgia.
17. Machtle, W. and Fisher, H., Die Angew Makromol. Chem. 1969, 7, 147.
18. Schulz, G.V. and Baumann, H., Makromol. Chem. 1968, 114, 122.
19. Lorimer, J.W., Polymer 1972, 13, 46.
20. Stutzel, B.T., Miyamoto and Cantow, H.J., IVPAC Int. Symp. Makromol. 1972, Helsinki, 337.
21. Gruber, E. and Knell, W., Makromol. Chem. 1978, 179, 733.
22. Whicher, S., Ph.D. Thesis in progress, McMaster University.

RECEIVED May 28, 1982.

Computerized Quantitative Analysis of Copolymers by IR Spectroscopy

E. G. BARTICK¹, J. C. CORBETT, and G. L. McCLURE²

Perkin-Elmer Corporation, Norwalk, CT 06856

The use of a commercially available software package (QUANT) is described in the analysis of copolymer films by computer assisted infrared spectroscopy. Important features of the software are illustrated by the example of analysis of vinyl acetate/vinyl chloride copolymers. Critical aspects of method development are explained and error sources are examined. Calibration is reported with a correlation coefficient of 0.9998. It is observed from the error analysis data on replicate samples that errors associated with sample preparation are significantly larger than those related to measurement and evaluation of the spectra.

Rapid, accurate analysis of copolymer products is critical to the efficiency and economy of modern industrial copolymer production. Infrared spectroscopy is a well established technique for both qualitative and quantitative analysis of polymeric materials (1, 2). However, the coupling of relatively low-cost data handling hardware and software to a microprocessor-controlled infrared spectrophotometer is a relatively recent development. This coupling considerably enhances the level of performance one can expect from quantitative infrared spectroscopy. The result is that such systems greatly reduce the effort, expense, and time required for a given analysis and simultaneously provide improved accuracy, reliability, and precision. This paper will describe a recently developed, commercially available software system which will be referred to hereafter as QUANT. In the course of application research with the QUANT software a wide variety of copolymer systems

¹ Current address: Raybestos Manhattan, Corporate Materials Laboratory, 75 E. Main Street, Stratford, CT 06497

² To whom all correspondence should be addressed

have been successfully analyzed. Indeed, the techniques and principles described in this paper are generally applicable. They may be adapted to suit the analysis of many copolymer systems. However, for the purpose of illustrating particular features of the QUANT software, the present discussion will be restricted to the analysis of vinyl chloride/vinyl acetate copolymer samples.

Experimental

Copolymer materials were purchased from Scientific Polymer Products, Inc., Ontario, New York. Samples were prepared from vinyl chloride/vinyl acetate bulk copolymers by evaporating solutions of the polymers (in 2-butanone (MEK)) on potassium bromide windows. Spectra of the resulting films were obtained on a Perkin-Elmer Model 683 ratio recording double-beam infrared spectrophotometer. The instrument was set to operate with the wide slit program and a times 4 multiplier (noise filter). The resulting spectral data contained a signal-to-noise ratio of approximately 3000:1. All instrument operations and data collection were controlled by a Perkin-Elmer Infrared Data Station. Spectra were recorded and stored on a microflop disk by means of a general purpose spectroscopic manipulation software system called PECDS. Quantitative evaluation was performed subsequently on the collected spectral data using analytical methods created with programs of the QUANT software system for the Infrared Data Station. Evaluation procedures investigated included peak height and peak area techniques. Absorbance ratios were related to concentration ratios by calibration with standards ranging from 2% to 17% vinyl acetate in the copolymer. Multiple samples of a nominal 13% vinyl acetate concentration were run for evaluation by the software as an indicator of the precision of the analysis.

Vinyl acetate concentrations were calculated on the basis of the carbonyl band with a maximum absorbance at 1738 cm^{-1} and a baseline absorbance derived from linear interpolation between absorbance values at 1850 and 1650 cm^{-1} . Vinyl chloride concentrations were calculated on the basis of the net absorbance of the C-Cl band with a maximum absorbance at 691 cm^{-1} with respect to a baseline drawn horizontally from the absorbance at 750 cm^{-1} . Peak area for the vinyl acetate carbonyl absorption was evaluated between 1752 and 1723 cm^{-1} . Peak area for vinyl chloride was evaluated between 750 and 658 cm^{-1} .

Results and Discussion

Description of Software. The QUANT software package is composed of three major programs, SINGLE, RATIO, and MULT. Each of these programs is designed for optimum performance for particular types of quantitative applications. SINGLE is

designed for analysis of single component systems with samples of defined pathlength, and appropriately will be excluded from this discussion. RATIO is designed for two component systems of determined or indeterminate pathlength. MULT is designed for simultaneous analysis of two to ten components and includes matrix techniques in the data processing. A fundamental hypothesis of the RATIO software is that bands can be found attributable to each of the components, and that these bands are not significantly overlapped by bands of the other respective component. It furthermore assumes that, by proper choice of baseline frequencies, the proper amount of background absorbance may be subtracted from the peak absorbance in the vicinity of the band such that the net absorbance measured for a particular component is related to the concentration of that component by a first order dependence only. This implies that the equation of the calibration function for each component must be expressed as in equation 1 (a and b) instead of equation 2(a and b), and that the plots of the calibration functions for each of the individual components would pass through the origin.

$$a) A_1 = (C_1 k_1)X \qquad b) A_2 = (C_2 k_2)X \qquad (1)$$

$$b) A_1 = (C_1 k_1 + b_1)X \qquad b) A_2 = (C_2 k_2 + b_2)X \qquad (2)$$

A_1 and A_2 are the observed absorbances at the analytical wavenumbers ν_1 and ν_2 . C_1 and C_2 represent the concentrations of components 1 and 2. X is the common pathlength. b_1 and b_2 are the effective absorbances which result from particular choices in baselines that would be measured at wavenumbers ν_1 and ν_2 if the concentration of components 1 and 2 were extrapolated to zero concentration. k_1 and k_2 are proportionality constants. If the baselines are chosen correctly then the ratio of net absorbance A_1 to net absorbance A_2 becomes what is shown in equation 3.

$$A_1/A_2 = (k_1/k_2)(C_1/C_2)(X/X) = k(C_1/C_2) \qquad (3)$$

If the analogous ratio is formed with equations 2a and 2b the result is equation 4.

$$A_1/A_2 = \frac{C_1 k_1 + b_1}{(C_2 k_2 + b_2)X} X = \frac{C_1 k_1 + b_1}{C_2 k_2 + b_2} \qquad (4)$$

An unfavorable situation arises if baselines for the bands are not chosen such that the intercepts b_1 and b_2 are not close to zero. Then the absorbance ratio A_1/A_2 is not a linear function of concentration ratio C_1/C_2 . Then the advantages associated with linear equations are no longer available for purposes of calibration of standards and calculation of unknowns. The RATIO software functions on the basis that the absorbance ratio is a

linear function in order to take advantage of the linear least squares technique to process the data. Therefore, it is important that baselines be chosen carefully so that b_1 and b_2 are negligibly small.

The RATIO software can deal with overlap of the bands if only one of the bands is overlapped. The situation of single overlap is observed in the vinyl chloride/vinyl acetate system. As can be seen in Figures 1, 2 and 3, the carbonyl band of vinyl acetate at 1737 cm^{-1} is essentially free of overlap by bands attributable to vinyl chloride (3). However, the vinyl chloride band at 691 cm^{-1} is overlapped to some extent by weak absorptions of vinyl acetate in the $600\text{ to }700\text{ cm}^{-1}$ region. If baselines are chosen such that intercepts are small the absorbances of the bands at 1738 and 691 cm^{-1} should be a linear combination of terms such as shown in equations 5 and 6.

$$A_{1738} = (k_1 C_{VA})X \quad (5)$$

$$A_{691} = (k_2 C_{VC} + k_3 C_{VA})X \quad (6)$$

If the absorbance ratio is formed by dividing equation 6 by equation 5 the result is equation 7.

$$A_{691}/A_{1738} = \frac{k_2 C_{VC} + k_3 C_{VA}}{k_1 C_{VA}} = (k_2/k_1)(C_{VC}/C_{VA}) + (k_3/k_1) \quad (7)$$

Equation 7 demonstrates that an absorbance ratio can be obtained which is a linear function of concentration ratio even if one of the bands included in the evaluation is overlapped by bands of the other component.

Method Construction and Calibration. The flow of the RATIO program (and the MULT program as well) follows the logical sequence of method construction, calibration of standards and calculation of unknowns. A method table for the RATIO software is shown in Table I. It is apparent that the essential content of the method table is the list of instrument parameters in line 2 and the set of wavenumber values in the center of the table. This set of wavenumber values includes directions for the start, end and data interval for scanning the primary and reference bands as well as the positions of baseline points and peak maxima for the band evaluation. The RATIO software includes provision for evaluation by peak height and peak area. Both of these evaluation types were investigated for the vinyl chloride/vinyl acetate system. The greatest advantage to peak area evaluation with copolymers will be found when changing composition leads to significant differences in crystallinity of the product. One observes in such cases that the width of the band at half height fluctuates with changing composition and peak

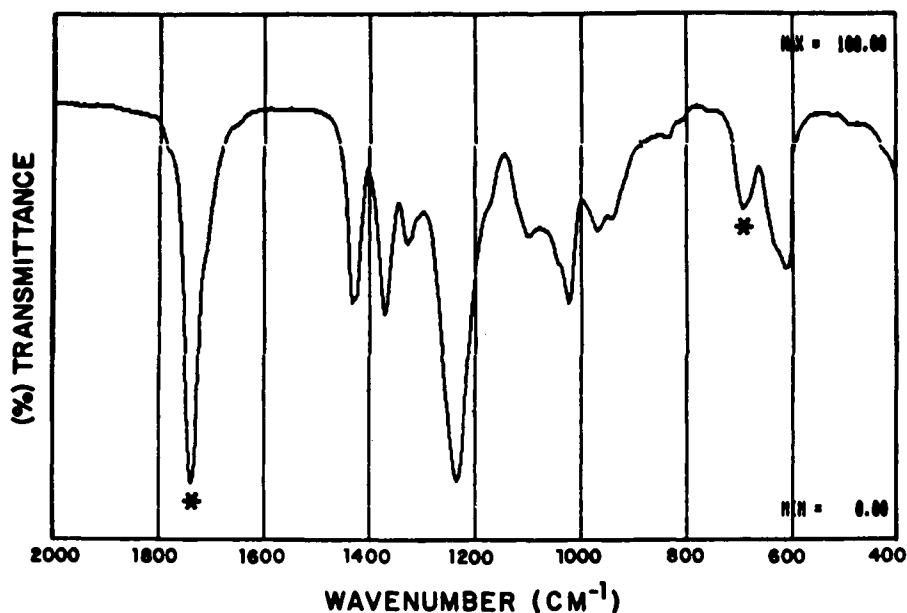


Figure 1. IR spectrum. Vinyl chloride/vinyl acetate copolymer cast on KBr.

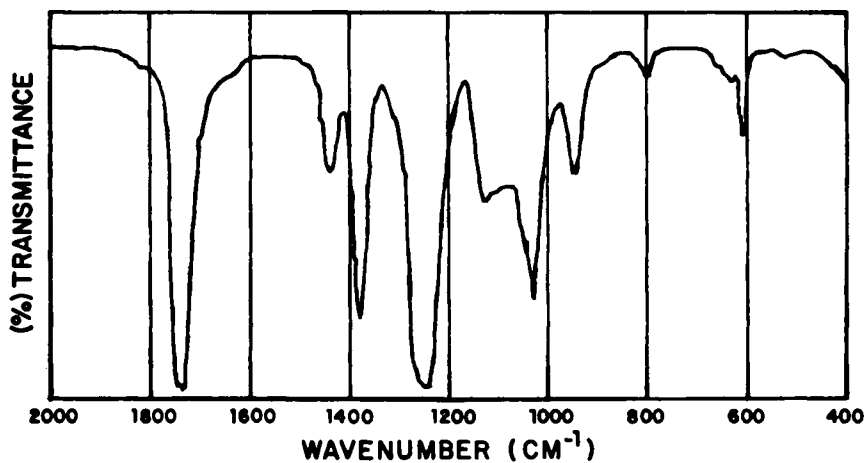


Figure 2. IR spectrum. Poly(vinyl acetate) pressed on KBr.

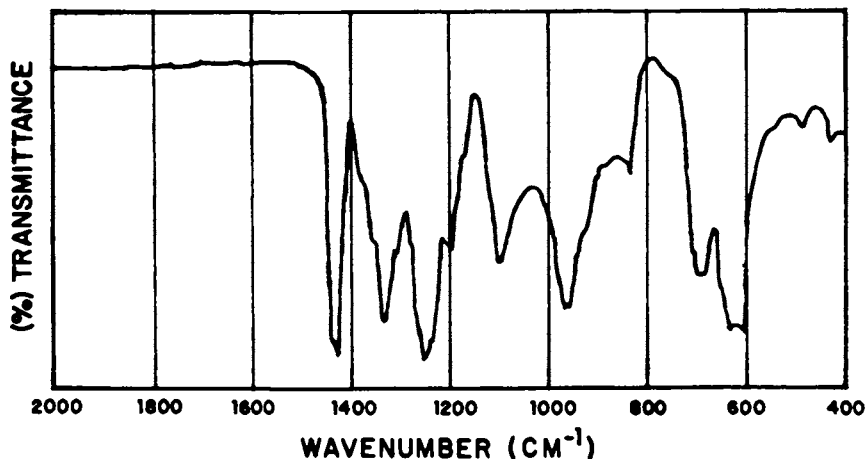


Figure 3. IR spectrum. Poly(vinyl chloride) pressed on KBr.

Table I

Identification VINYL CHLORIDE/VINYL ACETATE

Name VCVAX 81/06/01

Instrument 683 Slit W Multiplier 4 Mode DB

EVALUATION TYPE 12

PRIMARY BAND:

Data Region:	Start	800	End	500	Int	1.00	Total Points	301
Pk-Height	Base1	750	Pkmax	691			Base 2	0
Pk-Area	Base1	750	Lim1	E750	Lim2	E658	Base 2	0

REFERENCE BAND:

Data Region:	Start	1900	End	1600	Int	1.00	Total Points	301
Pk-Height		1850	Pkmax	1738			Base 2	1650
Pk-Area		1850	Lim1	E1752	Lim2	E1723	Base 2	1650

Special Instructions: Vinyl Acetate carbonyl band is to be used with the reference band. Samples are films cast from MEK solutions.

height no longer represents a reliable quantitative parameter because a narrow band associated with a crystalline phase at high concentrations may decrease to a broad lump as the concentration and crystallinity decrease. This behavior is distinctly evident for systems such as ethylene/propylene copolymers. However, it is not an issue in the vinyl chloride/vinyl acetate copolymer system involved in this study, at least within the range of comonomer proportions investigated.

For peak area evaluation it is often desirable to exclude the wings of a band from the evaluation because the wings contain relatively less absorbance signal compared to the center slice of the band. Each point in the spectrum represents a data value derived from a certain amount of absorbance contribution and a certain amount of noise contribution. The noise contribution in the peak wings remains relatively constant even though the absorbance signal of the band is greatly diminished from the peak value. Consequently, absorbance area evaluations, which are derived from a summation of digitized absorbance values, accumulate very little incremental signal in the wings even though noise accumulates consistently with increasing summation range.

The RATIO method table (Table I) includes provision for specifying upper and lower limits of integration for both primary and reference bands with the peak area evaluation procedure. The practical limits of the integration can be determined empirically by evaluating a set of spectra stored on microfloppy disks with varying limits set in the appropriate locations in the method table. Optimum limits can be determined from the calibration plots and related error parameters. The calibration plots shown in Figures 4 and 5 indicate that both evaluation procedures, peak height and peak area provide essentially the same level of precision for the linear least squares fit of the data. The error index and correlation coefficients listed on each table are both indicators of the relative scatter in the data from the least squares fit line. The correlation coefficient is calculated as traditionally defined in statistics. Error index is calculated as an average relative standard deviation. The error index is obtained by treating the spectra of standards as though they were unknown samples and comparing the original concentration data used for the least squares deviation with the concentration values one would obtain from the calibration and the absorbance data. The set of concentration differences form the basis for the error index calculation. The values for both peak height and peak area amount to around 2%. This value is quite acceptable considering that the concentration ratios used to develop the calibration parameters were based on the nominal values for the vinyl acetate concentrations in the commercial products obtained from the supplier. The vinyl acetate/vinyl chloride copolymers used in the analysis were stated to contain

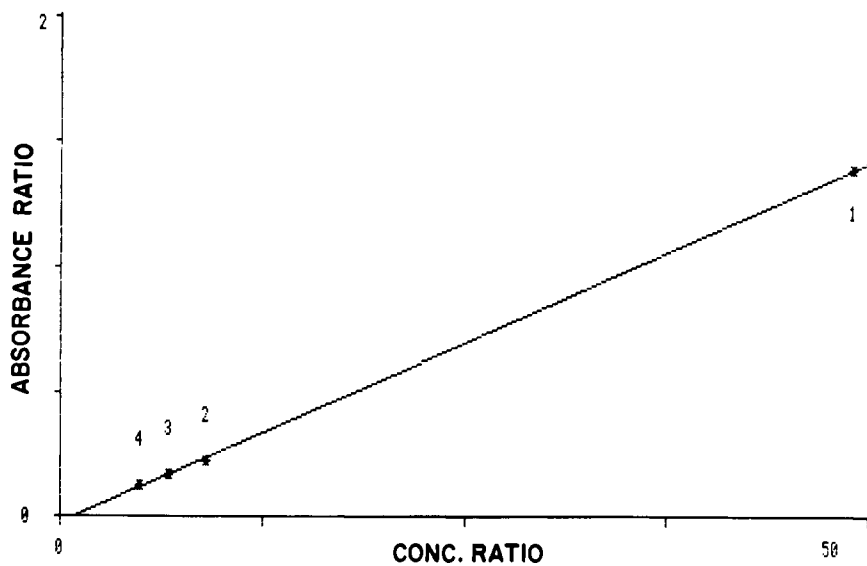


Figure 4. Peak height band ratio calibration plot: slope, 0.02867; intercept, -0.0230 ; error index (%), 1.92; correlation coefficient, 0.999833.

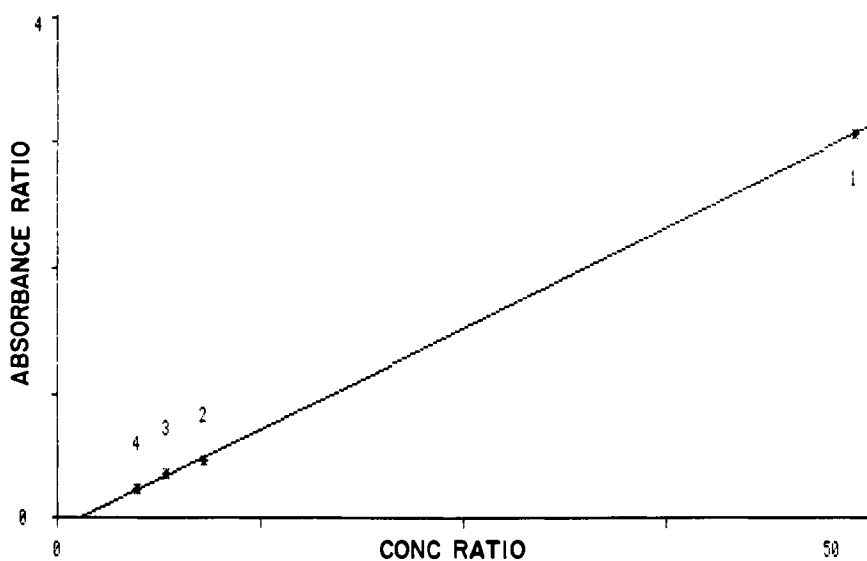


Figure 5. Area band ratio calibration plot: slope, 0.0643; intercept, -0.0920 ; error index (%), 2.11; correlation coefficient, 0.999797.

2, 10, 13, and 17% vinyl acetate. However, the manufacturer has indicated that these concentrations could fluctuate within a range of 2 to 3% vinyl acetate.

Comparison of MULT and RATIO. The MULT software resembles the RATIO software in terms of the general flow of the quantitation process involved in the steps of method specification, calibration by standards and evaluation of unknowns. However, there are two main philosophical differences between MULT and RATIO that determine the relative suitability of either program for a particular application. The obvious difference is that RATIO is designed for only two components. The MULT software allows for simultaneous analysis of two to ten components with no restrictions on overlap except that peaks selected for evaluation must not be coincident. If the path-length of the sample is indeterminate, as with cast films, the further requirement must be made in MULT that a peak of at least one of the components must not be overlapped significantly by any of the other components. MULT accomplishes the analysis of all components with matrix algebra while RATIO calculates concentrations on the basis of a single linear calibration function. MULT assumes additivity of all absorbance contributions from all components to produce the observed absorbance values. In contrast, RATIO uses a subtractive approach which allows a variety of baseline techniques to be used to subtract absorbance contributions to a band from all sources other than the component associated with the particular analytical band under investigation. A further ramification of the differences in approach is that in the RATIO software the spectrum of the entire band is used for evaluation, while in the MULT software the absorbance values are read only at designated individual frequencies. For a two component polymer system, the MULT software requires measurement of absorbance at only one chosen wavenumber for each of the analytical bands. Absorbance should also be measured at one additional wavenumber selected to represent a baseline reference point. More baseline frequencies may be used depending on the requirements of a particular application. The advantage of the fixed frequency measurements of the MULT software is that higher signal-to-noise measurements can be obtained in a shorter length of time than if the full band is scanned. The advantage of the scanning approach used in the RATIO software is that the peak maximum and baseline absorbance minimum may be tracked by the software if the band position shifts with changing composition of a copolymer system. Such a shift is observed for the $C \equiv N$ band in the acrylonitrile-styrene copolymer system. However, no significant band shift was observed in the vinyl acetate/vinyl chloride copolymer.

Sample Preparation. An important source of error which must be considered with cast film analysis is that associated with

actual preparation of the films. Clearly, cast films must be uniformly thick, evenly laminated to the salt crystal support and completely dried of solvent, else spectra will contain anomalous absorbance contributions which will reduce the precision of the analysis (4, 5).

Assessment of Results. Table II contains the analytical data on five different cast films of the vinyl acetate/vinyl chloride copolymers with a nominal 13% vinyl acetate concentration. The samples have been evaluated with the peak height and peak area procedures of the RATIO software as well as with the indeterminate path modification of the MULT software. The results obtained with the MULT software are not significantly different from the results obtained from either peak height or peak area evaluation with the RATIO software. Furthermore, the data in Table II indicate that the values for each film tend to agree more closely for all three evaluation techniques than do the values for all films for any one of the evaluation techniques. The relative standard deviation in the analytical values for a particular sample (3 evaluation techniques) range from 0.18% to 1.3%. The average value is 0.53%. This value is an order of magnitude smaller than the average of the relative standard deviations of the five samples for any of the evaluation techniques (6.0%). This data suggests that the random error in the analysis stems in large part from difficulties in preparing uniform samples rather than in the evaluation of the data.

Conclusions. In presenting a critical analysis of the sources of error, Harris outlined five basic steps in quantitative analysis: 1) Problem definition, 2) System isolation, 3) Sample manipulation, 4) Measurement, and 5) Data evaluation (6). It was pointed out that contributions to total error would be expected to arise in each step. The software system described in this work is principally concerned with step 5, providing a convenient way to evaluate infrared data in a rapid, systematic manner, such that error in evaluation is minimized. Advances in microprocessor electronics in recent years have facilitated both design and construction of instruments such that instrument error (step 4) can be quite low with modern double beam, ratio recording infrared spectrophotometers. If the errors in steps 4 and 5 are minimized, one is led back to step 3 in the list of error sources, sample manipulation. As seen from the data in this paper, sample preparation difficulties can constitute the largest source of variation in analysis of polymer products. In many laboratories, preparation of cast films is regarded as a trade secret or a black art. Casting films may be one of the more difficult sampling techniques of quantitative infrared. However, the dominance of error contributions associated with sample preparation can be observed even in more straight-forward sampling techniques such as solution phase analysis in fixed pathlength cells.

Table II

Analysis of 5 Samples of a Nominal 13% Concentration of Vinyl Acetate in the Copolymers (Data as % Concentration)

	<u>Ratio Peak Height</u>	<u>Ratio Area Slice</u>	<u>MULT</u>	<u>R.S.D.1(%)</u>
1	14.48	14.38	14.12	1.30
2	14.15	14.06	14.13	0.26
3	12.54	12.58	12.54	0.19
4	12.38	12.47	12.55	0.70
5	13.97	13.95	13.92	0.18
Average	13.50	13.49	13.45	0.53
R.S.D.2(%)	6.5	5.9	5.5	

R.S.D.1 = Relative standard deviation of evaluation techniques for each sample.

R.S.D.2 = Relative standard deviation of five samples for each evaluation technique.

The significant point is that the improvement in infrared spectrophotometers, data handling hardware, and software have made the errors in sample handling more obvious and distinguishable. A software system which evaluates each spectrum in a completely reproducible manner is clearly a critically important component of an optimum analytical system. Data handling hardware and software provide the best way to achieve effective use of newer infrared instruments which have ordinate reproducibilities specified to be below 0.1% transmission. It is apparent with such analytical systems that sample handling errors which give rise to spectral effects on the order of 1% transmission become a significant burden on the overall performance of the analysis. Nevertheless, there is a positive and ironic side to this situation. The very same equipment which makes the sample handling errors so distinct also serves as a most suitable avenue for pursuing a systematic study of the problem with an aim toward minimizing these errors.

Literature Cited

1. Hummel, D.O. "Atlas of Polymer and Plastic Analysis"; Vol. 1, Berlag Chemie International, New York and Weinheim, 1978.
2. Vandeberg, J.T.; Anderson, D.G.; Duffer, J.K.; Julian, J.M.; Scott, R.W.; Sutliff R.M.; Vaickus, M.J. "An Infrared Spectroscopy Atlas for the Coatings Industry"; Federation of Societies for Coatings Technology: Philadelphia, 1980.
3. Zeller, M.V.; Pattacini, S.C. "The Infrared Grating Spectra of Polymers, Infrared Applications Study No. 13", Perkin-Elmer Corp., Norwalk, CT. 1973.
4. Jones, R.N. J. Am. Chem. Soc. 1952, 74, 2681-2683.
5. Hirschfeld, T. Anal. Chem., 1979, 51, 495-499.
6. Harris, W.E. Talanta, 1978, 25, 325-329.

RECEIVED May 4, 1982.

Modeling the Equilibrium Swelling of Latex Particles with Monomers

C. M. TSENG, M. S. EL-AASSER, and J. W. VANDERHOFF

Lehigh University, Emulsion Polymers Institute and Departments of Chemical Engineering and Chemistry, Bethlehem, PA 18015

The dependence of the swelling ratio on latex particle size and interfacial tension was studied on two polymer latex systems : polystyrene swollen with styrene in the presence of anionic, nonionic, and polymeric surfactants; and polymethyl methacrylate swollen with methyl methacrylate in the presence of anionic surfactants. The equilibrium swelling ratio was obtained by extracting monomer from swollen latex particles with iso-octane, and then determining the monomer concentration in the extract with a UV detector. The particle-water interfacial tension at equilibrium swelling was estimated by the drop volume method. Comparison of the experimental data with Morton's theory defined a monomer-polymer interaction parameter of 0.35 and a corresponding semi-empirical equation describing the swelling of polystyrene latexes with styrene . A monomer-polymer interaction parameter of 0.45 and a semi-empirical equation was obtained for the swelling of polymethyl methacrylate latexes with methyl methacrylate. A generalized model which takes into account the effect of water dissolved in the swollen particles as well as in the monomer phase is presented. Comparison of the swelling data with the theoretical curves from this model is shown.

The equilibrium concentration of monomer in latex particles during polymerization is an important parameter in kinetic studies of emulsion polymerization. Morton et al. (1) derived a theory for the equilibrium swelling of latex particles with solvent (monomer). In this treatment, the free energy of mixing, which favors swelling, is counterbalanced by the change in interfacial energy due to the increase in the particle surface area. Monomer-to-polymer equilibrium swelling ratios in the range of 3-6 are predicted thermodynamically and achieved experimentally. The

0097-6156/82/0197-0197\$09.25/0
© 1982 American Chemical Society

theory has been applied by several authors to obtain monomer-polymer interaction parameters and particle-water interfacial tensions from swelling results (2). Unfortunately, some of the results are not consistent, e.g., the interaction parameter χ_{mp} ranged from 0.30 to 0.43 for polystyrene latexes swollen with styrene at room temperature, and a value of 0.55-0.58 was obtained for methyl methacrylate-polymethyl methacrylate, in contrast to the observation that methyl methacrylate is a good solvent for its polymer (2).

The thermodynamics governing the swelling of latex particles has received much attention in recent years. Ugelstad et al. (3) demonstrated using thermodynamics treatment and experiments, that the incorporation of a low-molecular-weight water-insoluble compound into latex particles allows them to swell the particles to a much greater extent. Therefore, latexes of large particle size can be grown by seeded emulsion polymerization in fewer steps. Guillot (4) applied a thermodynamic approach to the modeling of emulsion copolymerization processes to give a better understanding of the distribution of comonomers in the different phases and their changes with conversion, which are required for controlling the copolymerization processes.

This paper compares the swelling of monodisperse polystyrene and polymethyl methacrylate latexes with their monomers and the estimated particle-water interfacial tensions with the theoretical curves from Morton's equation. A new model which takes into account the effect of water dissolved in the swollen particles and in the monomer phase on the swelling of relatively hydrophilic systems is presented.

Theory

Model I. When the swollen particle is in equilibrium with the free monomer phase, the following condition exists, according to Morton et al. (1) :

$$\Delta \bar{F} = \Delta \bar{F}_m + \Delta \bar{F}_t = 0 \quad (1)$$

where $\Delta \bar{F}$ is the partial molar free energy of monomer, $\Delta \bar{F}_m$ the contribution from the energy of mixing, and $\Delta \bar{F}_t$ the contribution of the interfacial energy.

Expressing the energy of mixing in terms of the Flory-Huggins equation and the interfacial energy in terms of the Gibbs-Thomson equation gives :

$$[\ln(1-v_p) + (1-(1/j))v_p + \chi_{mp}v_p^2] + 2\bar{V}_m\gamma/rRT = 0 \quad (2)$$

where v_p is volume fraction of polymer in the particle, j the number-average degree of polymerization of the polymer, \bar{V}_m the partial-molar volume of monomer, γ the particle-water interfacial tension, r the particle radius at equilibrium, R the gas constant, and T the absolute temperature.

Gardon (2) suggested using the original radius r_0 instead of the radius at equilibrium r ($r=r_0/v_p^{1/3}$) to avoid confusion :

$$[\ln(1-v_p) + (1-(1/j))v_p + \chi_{mp} v_p^2] + (2\bar{V}_m \gamma / r_0 RT) v_p^{1/3} = 0 \quad (3)$$

Model II. Some monomers have high monomer-water mutual solubilities compared to styrene (Table I) (5). For the swelling of these systems, neglect of the effect of water dissolved in swollen particles as well as in the monomer phase could lead to significant errors. Therefore, free energy terms describing the water-monomer and water-polymer interactions should be included in the equilibrium equations to cover a wide range of monomers.

By treating the free energy of mixing with Flory's ternary polymer solution approach (6), the following equations were obtained for the equilibrium of monomer and water inside and outside the particles :

$$\ln v_m + (1-v_m) - v_w L - v_p / j + (\chi_{wm} L v_w + \chi_{mp} v_p)(v_w + v_p) - \chi_{wp} L v_w v_p + (2\bar{V}_m \gamma / r_0 RT) v_p^{1/3} = \ln a_m \quad (4)$$

$$\ln v_w + (1-v_w) - v_m / L - v_p / j L + (\chi_{wm} v_m + \chi_{wp} v_p)(v_m + v_p) - \chi_{mp} v_m v_p / L + (2\bar{V}_w \gamma / r_0 RT) v_p^{1/3} = \ln a_w \quad (5)$$

Most of the symbols have the same meaning as in equations (2) and (3) with the subscripts m and w denoting monomer and water. Here, L represents \bar{V}_m / \bar{V}_w ; a_m is the activity of monomer in the separate monomer phase, which can be estimated from the solubility of water in monomer; a_w is the activity of water in the aqueous phase, which, for simplicity, can be approximated as unity.

In this model, two more interaction parameters χ_{wm} and χ_{wp} have been introduced; and their values must be calculated in order to make theoretical predictions. The value of χ_{wm} can be calculated from the monomer-water mutual solubilities by using equations (4) and (5) with $v_p=0$. Since solubility data for water-polymer systems are lacking, χ_{wp} can be estimated from the solubility parameters (7) using the equation :

$$\chi_{12} = \bar{V}_1 (\delta_2 - \delta_1)^2 / RT - z \Delta w_s / k \quad (6)$$

where δ is the solubility parameter and the constant entropic contribution, $-z \Delta w_s / k$, typically has values in the range 0.2 - 0.5. For the methyl methacrylate-polymethyl methacrylate system, χ_{wm} is 3.6 as estimated from water-monomer mutual solubilities. Since the solubility parameter of water is 23.4 and that of polymethyl methacrylate is 9.5 (8), a possible range for χ_{wp} is 3.6 - 5.8.

Theoretical curves for Model I or Model II were obtained by solving equation (3) or equations (4) and (5), respectively. An iteration method was used with the aid of a DEC-20 computer. The calculated volume swelling ratio (v_m/v_m^0) was then plotted against the interfacial energy term ($r_o RT/2\bar{V}_m \gamma^R$).

Experimental

The polystyrene latexes used in these swelling studies were Dow monodisperse standards : 0.19 μ m (LS-1102-A), 0.40 μ m (LS-1103-A), and 0.60 μ m (LS-1115-B). The polymethyl methacrylate latexes were prepared by bottle polymerization using potassium persulfate initiator and various concentrations of Aerosol MA and Aerosol AY emulsifiers (American Cyanamid). The particle sizes of the polystyrene latexes were determined by electron microscopy and those of the polymethyl methacrylate latexes using the Brice-Phoenix light scattering photometer by the forward angle ratio method. The latexes were used without cleaning. Surfactants added for swelling studies include sodium dodecyl sulfate (Eastman Kodak), Aerosol MA (American Cyanamid), Triton X-100 (Rohm & Haas) and polyvinyl pyrrolidone K-30 (GAF).

The swelling ratios were determined using the procedure of Vanderhoff et al. (9). Excess monomer was mixed with diluted latex and added surfactant. After swelling, the latex was mildly centrifuged to remove the excess monomer. Iso-octane was then used to extract monomer from the swollen latex particles. The concentration of monomer in the extracted solution was then determined using a UV detector (Instrumentation Specialties Co. model 1840) by absorption spectra at 245nm.

The interfacial tension between a swollen particle and the aqueous phase can be approximated by the interfacial tension between the monomer phase and the swollen latex dispersion. The latter was measured by the drop volume method. The swollen latex dispersion was dropped into the monomer phase using a microsyringe with a thin-wall needle the end of which had been filed flat. The drop volume and density data were then converted to interfacial tension.

Results and Discussion

Swelling of polystyrene latex particles with styrene. The swelling ratios and the corresponding interfacial tensions for the different-size latexes with added anionic surfactants Aerosol MA and sodium dodecyl sulfate are listed in Table II. Those values obtained with added nonionic surfactant Triton X-100 and polymeric surfactant polyvinyl pyrrolidone are listed in Table III. Figure 1 compares theoretical curves from Model I with all of the experimental data. It is found that a curve corresponding to $\chi_{mp} = 0.35$ fits the data best. Therefore, a semi-empirical

Table I
Monomer-Water Mutual Solubilities
at Room Temperature (5)

Monomer	Solubility	
	Monomer in Water (g/100g)	Water in Monomer (g/100g)
Styrene	0.032	0.07
Butyl acrylate	0.2	0.7
Methyl methacrylate	1.5	1.15
Ethyl acrylate	1.5	1.5
Vinyl acetate	2.5	0.1
Methyl acrylate	5.0	2.5
Acrylonitrile	7.4	3.1

Table II
Swelling of Polystyrene Latexes with Styrene
in the Presence of Anionic Surfactants

r_0 (μm)	Surfactant Conc. (% on polymer)	γ (dyne/cm)	Swelling Ratio (v_m/v_p)	$r_0 RT/2\bar{V}_m \gamma$
0.095	AMA, 6.0	28.7	3.02	36
0.095	SDS, 6.0	23.2	3.04	45
0.20	AMA, 6.0	28.1	4.31	78
0.20	SDS, 6.0	21.4	4.77	102
0.30	AMA, 6.0	26.6	5.73	122
0.30	SDS, 6.0	19.5	6.66	168
0.30	AMA, 1.4	30.6	5.14	107
0.20	AMA, 1.4	31.2	4.76	70
0.095	AMA, 1.4	31.6	2.77	33

AMA = Aerosol MA, SDS = Sodium Dodecyl Sulfate

Table III
Swelling of Polystyrene Latexes with Styrene in
the Presence of Nonionic and Polymeric Surfactants

r_0 (μm)	Surfactant Conc. (% on polymer)	γ (dyne/cm)	Swelling Ratio (v_m/v_p)	$r_0^{RT/2\bar{V}_m\gamma}$
0.30	Triton, 6.0	27.9	5.00	117
0.095	Triton, 6.0	27.4	3.35	38
0.20	Triton, 1.5	33.9	4.18	64
0.095	Triton, 1.5	33.6	2.96	31
0.30	PVP, 1.9	35.0	5.68	93
0.20	PVP, 1.9	33.6	4.59	65
0.095	PVP, 4.5	31.4	3.30	33
0.30	PVP, 7.5	21.1	7.46	155
0.20	PVP, 7.5	19.7	4.23	111
0.095	PVP, 7.5	20.1	3.84	52

Triton = Triton X-100, PVP = Polyvinyl pyrrolidone

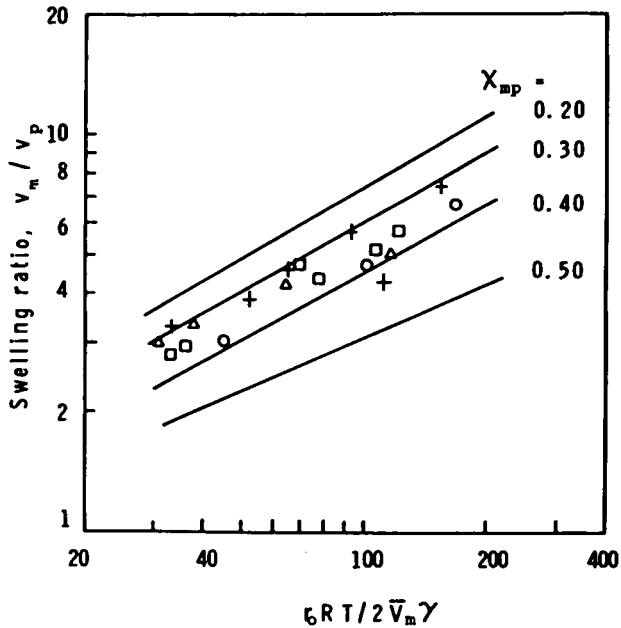


Figure 1. Swelling of polystyrene latexes with styrene: comparison of experimental data with theoretical curves from Model I. Key: \square , AMA; \circ , SDS; \triangle , Triton; $+$, PVP.

equation can be derived from these results :

$$v_m/v_p = 0.339 (r_o RT/2\bar{V}_m \gamma)^{0.594} \quad (7)$$

or

$$v_m/v_p = 84.9 (r_o/\gamma)^{0.594} \quad \text{at room temp.} \quad (8)$$

(r_o in μm , γ in dyne/cm)

These data have also been used to fit theoretical curves from Model II. Since the solubility of water in styrene is quite low, and χ_{wp} is quite close to χ_{wm} , the effect of the interaction terms involving water are negligible. The theoretical curves from Model II are essentially the same as those from Model I with same value of χ_{mp} .

Swelling of polymethyl methacrylate latex particles with methyl methacrylate. Table IV lists the swelling ratios and interfacial tensions for the different-size polymethyl methacrylate latexes with added Aerosol MA and sodium dodecyl sulfate emulsifiers. Comparison of the data with the theoretical curves from Model I (Figure 2) defines an apparent interaction parameter χ_{mp} of 0.45 and the semi-empirical equation :

$$v_m/v_p = 0.361 (r_o RT/2\bar{V}_m \gamma)^{0.512} \quad (9)$$

or

$$v_m/v_p = 43.9 (r_o/\gamma)^{0.512} \quad \text{at room temp.} \quad (10)$$

These experimental data are fitted equally well by Model II by using several pair combinations of the interaction parameters χ_{mp} and χ_{wp} . Figures 3 - 6 show the experimental data compared to theoretical curves from Model II with the following pairs of the interaction parameters χ_{mp} and χ_{wp} : 0.42,4.5; 0.38,5.0; 0.33,5.5; 0.29,5.8. It should be pointed out that Model II gives the same result as Model I when $\chi_{wp} = \chi_{wm} = 3.6$ and $\chi_{mp} = 0.45$. These data, however, are not sufficient to determine which pairs of parameters are closest to the actual values. Determination of the interaction parameters by other methods might help clarify this point.

In summary, the thermodynamic Model I based on Morton's theory has been used to successfully fit experimental data and obtain semi-empirical equations for the swelling of polystyrene and polymethyl methacrylate latexes. The semi-empirical equations offer a quick method for estimating swelling ratio from particle size and interfacial tension. The generalized form of Model II might prove to be more suitable for describing the swelling phenomena of relatively hydrophilic systems .

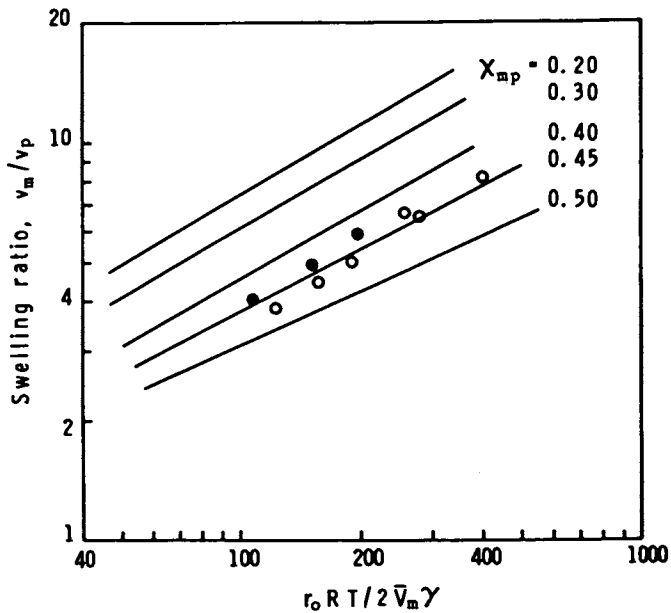


Figure 2. Swelling of poly(methyl methacrylate) latexes with methyl methacrylate: comparison of experimental data with theoretical curves from Model I. Key: ●, AMA; ○, SDS.

Table IV
Swelling of Polymethyl Methacrylate Latexes with
Methyl Methacrylate in the Presence of Anionic Surfactants

r_o (μm)	Surfactant Conc. (% on polymer)	γ (dyne/cm)	Swelling Ratio (v_m/v_p)	$r_o RT / 2 \bar{V}_m \gamma$
0.097	AMA, 1.1	10.5	4.11	109
0.097	SDS, 1.1	9.2	3.88	124
0.097	SDS, 3.2	7.2	4.63	159
0.16	AMA, 1.1	12.3	5.04	152
0.16	SDS, 1.1	9.8	5.12	191
0.16	SDS, 3.2	6.6	6.91	283
0.20	AMA, 1.1	12.1	5.96	197
0.20	SDS, 1.1	9.4	5.89	256
0.20	SDS, 3.2	6.0	8.35	402

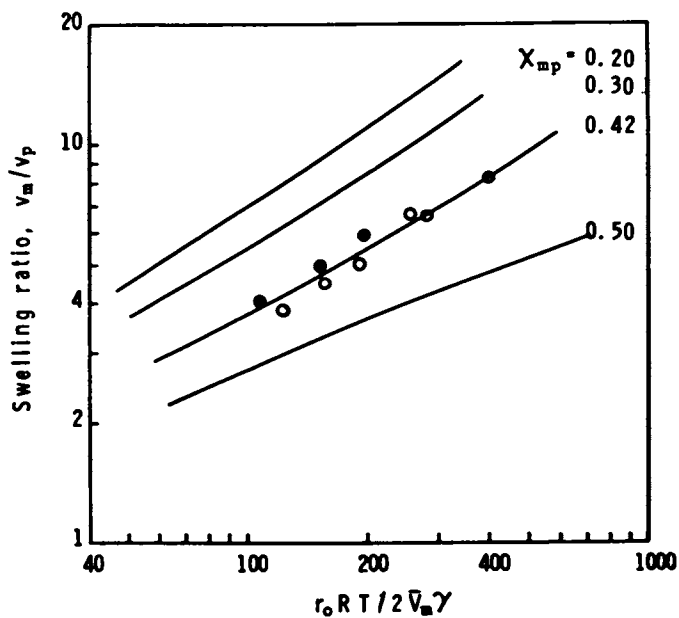


Figure 3. Swelling of poly(methyl methacrylate) latexes with methyl methacrylate: comparison of experimental data with theoretical curves from Model II for $\chi_{wp} = 4.5$. Key: ●, AMA; ○, SDS.

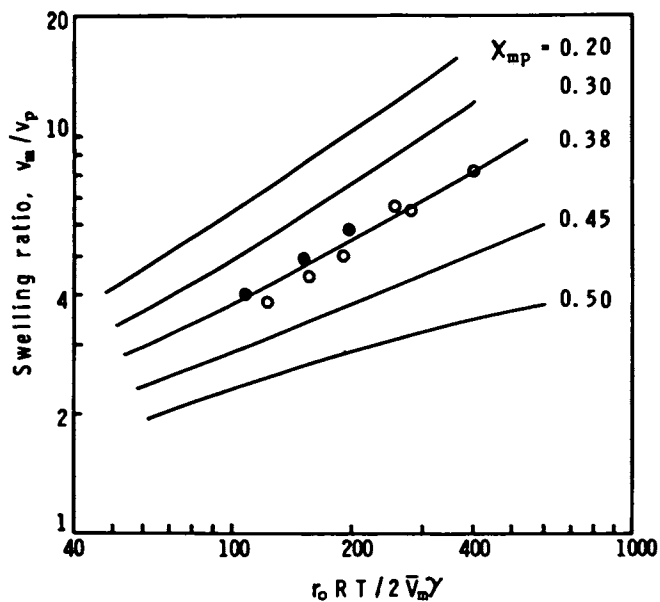


Figure 4. Swelling of poly(methyl methacrylate) latexes with methyl methacrylate: comparison of experimental data with theoretical curves from Model II for $\chi_{wp} = 5.0$. Key: ●, AMA; ○, SDS.

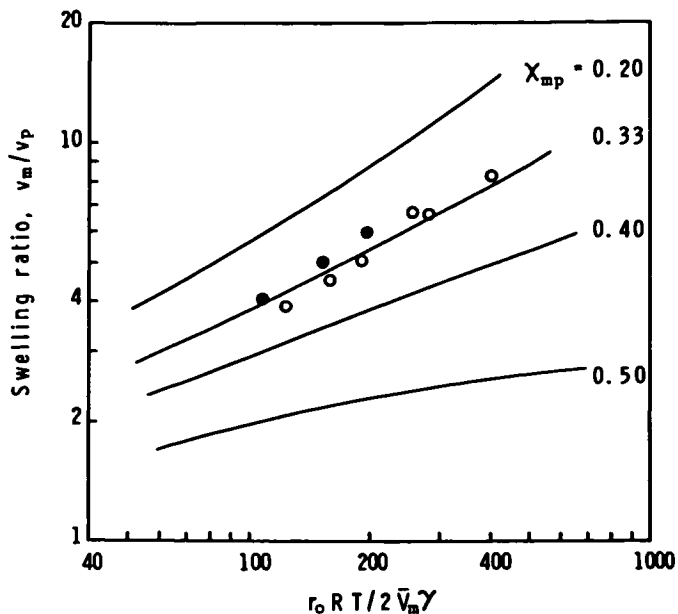


Figure 5. Swelling of poly(methyl methacrylate) latexes with methyl methacrylate: comparison of experimental data with theoretical curves from Model II for $\chi_{wp} = 5.5$. Key: ●, AMA; ○, SDS.

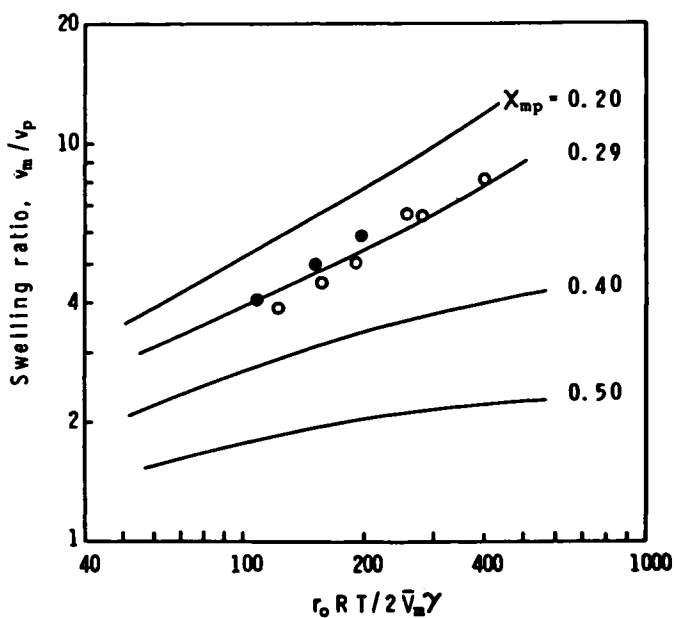


Figure 6. Swelling of poly(methyl methacrylate) latexes with methyl methacrylate: comparison of experimental data with theoretical curves from Model II for $\chi_{wp} = 5.8$. Key: ●, AMA; ○, SDS.

Acknowledgement

The authors would like to thank the National Aeronautics and Space Administration for partial financial support of this work. The help of James Capraro, Thomas Booth and Carmen Gabriel in obtaining some of the swelling data is gratefully acknowledged.

Literature Cited

1. Morton, M.; Kaizerman, S.; Altier, M. W. J. Colloid Sci. 1954, 9, 300.
2. Gardon, J. L. J. Polymer Sci. Part A-1 1968, 6, 2859.
3. Ugelstad, J.; Mørk, P. C.; Kaggerud, K. H.; Ellingsen, T.; Berse, A. Adv. Coll. Int. Sci. 1980, 13, 101.
4. Guillot, J. Makromol. Chem., Rapid Commun. 1980, 1, 697.
5. Leonard, E. C. "Vinyl and Diene Monomers" Part I-III, John Wiley & Sons, N.Y. 1970-1971.
6. Flory, P. J. "Principles of Polymer Chemistry", Cornell University Press, Ithaca, N.Y. 1953; p 549.
7. Orwoll, R. A. Rubber Chem. Tech. 1977, 50, 451.
8. Burrell, H. Interchem. Rev. 1955, 14, 31.
9. Vanderhoff, J. W.; Bradford, E. B.; Tarkowski, H. L.; Wilkinson, B. W.; J. Polymer Sci. 1961, 50, 265.

RECEIVED May 4, 1982.

Continuous Poly(vinyl Acetate) Emulsion Polymerization Reactors

Dynamic Modeling of Molecular Weight and Particle Size Development and Application to Optimal Multiple Reactor System Design

M. POLLOCK, J. F. MacGREGOR, and A. E. HAMIELEC

McMaster University, Department of Chemical Engineering,
Hamilton, Ontario, L8S 4L7, Canada

The unsteady-state emulsion polymerization model of Kiparissides et al [1,2] and Chiang and Thompson [3] for predicting conversion, number of particles and particle size averages in continuous flow stirred tank reactors is extended to predict the long chain branching and molecular weight averages for poly(vinyl acetate). Sustained oscillations in these polymer properties, as well as in the particle properties, are predicted with this model. The extended model is used to show that by changing the continuous stirred tank reactor configuration, the oscillation phenomenon can be eliminated. Furthermore, it is shown that by using this new design, one can produce essentially the same latex product at much higher conversions or a better product (with fewer long chain branches) at the same conversion. In both cases, less initiator and soap are used than in the conventional configuration.

During the production of lattices in continuous flow stirred tank reactors (CSTR's), oscillations are often observed in all the important polymer and particle properties (e.g. conversion, particle size, molecular weight). According to the model developed by Kiparissides et al [1,2], these oscillations are due to the periodic formation and depletion of soap micelles which lead to short periods of rapid particle nucleation followed by long periods where no nucleation occurs. These oscillations can lead to particle agglomeration during the periods of rapid particle generation due to inadequate soap coverage of the polymer particles, and to excessive long chain branching during the high conversion portion of the oscillations. Although large quantities of soap can eliminate the oscillations, this is undesirable from a cost standpoint as well as from a product contamination point of view.

0097-6156/82/0197-0209\$06.00/0

© 1982 American Chemical Society

The dynamic model developed by Kiparissides et al [1,2] and subsequently modified by Chiang and Thompson [3] can predict the conversion, number of particles, particle diameters, etc., for the continuous emulsion polymerization of vinyl acetate. In this paper, the model is extended to predict molecular weight averages and long chain branching as well.

The extended model is then used to design a new continuous stirred tank reactor configuration which eliminates the oscillations and which offers substantial improvements in product quality, productivity and operating costs.

Model Development

Details of the particle property model may be found in Kiparissides et al [1,2] and Chiang and Thompson [3]. Following an approach used by Dickinson [4] and Gorber [5], the development was based on an age distribution analysis in which the classes of particles born between any time, τ and $\tau+d\tau$, were followed through the reactor. The result was a series of differential equations in the total particle size properties (diameter, area and volume), the number of particles, conversion and the initiator and emulsifier levels in the reactor.

In order to incorporate the molecular weight averages and long chain branching effects, a similar approach has been taken. Following the development of Hamielec [6], expressions for the moments of the molecular weight distribution for the class of particles born between times τ and $\tau+d\tau$ were developed.

The development takes into account transfer to monomer, transfer to polymer, and terminal double bond polymerization. For the vinyl acetate system where transfer to monomer is high, the generation of radicals by transfer to monomer is much greater than the generation of radicals by initiation, so that essentially all radicals present have terminal double bonds; hence, effectively all dead polymer molecules also have a terminal double bond. Thus, for vinyl acetate polymerization, the terminal double bond polymerization can be significant, and has been built into the development. The equations for the moments of the molecular weight distribution and the average number of branches per polymer molecule are as follows:

$$\frac{d}{dt}[Q_0(t,\tau)v(t,\tau)] = K_p M_p Y_0(t,\tau) \left[C_m - \frac{K}{v(t,\tau)} \left(\frac{Q_0(t,\tau)v(t,\tau)}{M_p} \right) \right] \quad (1)$$

$$\begin{aligned} \frac{d}{dt}[Q_0(t,\tau)B_N(t,\tau)v(t,\tau)] = & K_p M_p \frac{Y_0(t,\tau)}{v(t,\tau)} [C_p Q_1(t,\tau)v(t,\tau) \\ & + KQ_0(t,\tau)v(t,\tau)] \quad (2) \end{aligned}$$

$$\frac{d}{dt}[Q_1(t,\tau)v(t,\tau)] = K_p M_p Y_o(t,\tau) \quad (3)$$

$$\begin{aligned} \frac{d}{dt}[Q_2(t,\tau)v(t,\tau)] = & K_p M_p \frac{Y_o(t,\tau)}{v(t,\tau)} [v(t,\tau) + 2 \left(\frac{1 + KQ_1(t,\tau)/M_p}{C_m + C_p Q_1(t,\tau)/M_p} \right) \\ & * [v(t,\tau) + \frac{C_p Q_2(t,\tau)v(t,\tau)}{M_p} + \frac{KQ_1(t,\tau)v(t,\tau)}{M_p}] \quad (4) \end{aligned}$$

$$\text{where } Q_n(t,\tau) = \sum_{r=1}^{\infty} r^n P_r(t,\tau)$$

i.e. $Q_o(t,\tau)$, $Q_1(t,\tau)$, $Q_2(t,\tau)$ = moments of polymer molecular weight distribution for particles born between τ and $\tau+d\tau$ at time t (mole/R)

$B_N(t,\tau)$ = branch points per polymer particle for particle born between τ and $\tau+d\tau$ at time t

$v(t,\tau)$ = volume of particle born between τ and $\tau+d\tau$ at time t

$Y_o(t,\tau)$ = number of radicals in a particle born between τ and $\tau+d\tau$ at time t

K_p = propagation rate constant

M_p = concentration of monomer in the polymer particle

$C_m = K_{fm}/K_p$ (K_{fm} = rate constant for transfer to monomer)

$C_p = K_{fp}/K_p$ (K_{fp} = rate constant for transfer to polymer)

$K = K_p^*/K_p$ (K_p^* = rate constant for terminal double bond polymerization)

If the property balances above for any given property $p(t,\tau)$ of the class of particles born between τ and $\tau+d\tau$ are expressed as:

$$\frac{dp(t,\tau)}{dt} = f(t,\tau) \quad (5a)$$

then the total property $P(t)$ obtained by summing over all classes of particles is given by:

$$\frac{dP(t)}{dt} = \frac{P_{IN}(t)-P(t)}{\theta} + f(t) p_o(t,t) + \int_0^t \frac{dp(t,\tau)}{dt} n(t,\tau) d\tau \quad (5b)$$

where $f(t)$ is the particle generation rate at time t , $p_o(t,t)$ is the value of $p(t,\tau)$ at birth, $n(t,\tau)d\tau$ are the number of particles born between τ and $\tau+d\tau$ and θ is the residence time of the reactor.

Using this, the following differential equations have been obtained for the overall molecular weight moments and the average number of long chain branches per polymer molecule.

$$\frac{d Q_o^1(t)}{dt} = \frac{\Delta Q_o^1(t)}{\theta} + K_p M_p Y_{AVE} (C_m V_p(t) - \frac{K Q_o^1(t)}{M_p}) \quad (6)$$

$$\frac{d(Q_o B_n)^1(t)}{dt} = \frac{(\Delta Q_o B_n)^1(t)}{\theta} + K_p M_p Y_{AVE} \left(\frac{C_p Q_1^1(t)}{M_p} + \frac{K Q_o^1(t)}{M_p} \right) \quad (7)$$

$$\frac{d Q_1^1(t)}{dt} = \frac{\Delta Q_1^1(t)}{\theta} + K_p M_p Y_{AVE} V_p(t) \quad (8)$$

$$\begin{aligned} \frac{d Q_2^1(t)}{dt} = & \frac{\Delta Q_2^1(t)}{\theta} + K_p M_p Y_{AVE} [V_p(t) + 2 *RATIO* (V_p(t) + \\ & + \frac{C_p Q_2^1(t)}{M_p} + \frac{K Q_1^1(t)}{M_p})] \end{aligned} \quad (9)$$

$$RATIO = \frac{(1 + K \bar{Q}_1 / M_p)}{(C_m + C_p \bar{Q}_1 / M_p)} \quad (10)$$

where

$$\begin{aligned} Q_o^1(t), Q_1^1(t), Q_2^1(t), (Q_o B_n)^1(t) = & (Q_o V_p)_{total}(t), (Q_1 V_p)_{total}(t), \\ & (Q_2 V_p)_{total}(t), (Q_o B_n V_p)_{total}(t) \end{aligned}$$

respectively

$$\text{and } \Delta Q_n^1(t) = Q_{IN_n}^1(t) - Q_n^1(t) = \text{difference between input and output}$$

$$\text{and } M_N(t) = (Q_1^1(t) / Q_o^1(t)) * MW_{VA}$$

$$M_W(t) = (Q_2^1(t) / Q_1^1(t)) * MW_{VA}$$

$$MW_{VA} = \text{molecular weight of vinyl acetate monomer}$$

In order to carry out the integration as a set of ordinary differential equations, several assumptions were made: that M_p (which is a function of conversion and hence time) was independent of the class of particles being considered; that $RATIO$ was constant for all classes over any given period of integration; and that the number of radicals and number of polymer molecules in any given volume was constant. Thus the following substitutions were made:

$$\frac{Y_o(t, \tau)}{v(t, \tau)} = \text{constant} = \frac{Y_{o_TOT}(t)}{V_p(t)} = Y_{AVE} \quad (11a)$$

$$Q_1(t, \tau) = \text{constant} = \frac{Q_1^1(t)}{V_p(t)} = \bar{Q}_1 \quad (11b)$$

In order to integrate the equations, it was also necessary to obtain an expression for $Y_{o_TOT}(t)$, which was available from the original model by integrating the expression for $\bar{q}(t, \tau)$ over all classes. The final result was:

$$Y_{o_TOT}(t) = \lambda \xi(t) A(t) \left(\frac{N_A d_p}{K_p d_m} \right) \left(\frac{1 - \Phi(t)}{\Phi(t)} \right) \quad (12)$$

$$\text{where } \lambda = \left(\frac{K_p \rho_{MON}}{N_{AVAG} \rho_{POLY}} \right) \left(\frac{K_p f K_d m}{12 \pi D_w \delta K_{fm}} \right)^{1/2}$$

$$\xi = \left(\frac{\Phi(t)}{1 - \Phi(t)} \right) \left(\frac{I_w(t) (1 - e^{-t/\theta})}{A(t)} \right)^{1/2}$$

with $A(t)$ = total particle area
 D_w = monomer diffusion coefficient in water
 $I_w(t)$ = initiator concentration in water phase
 m = monomer partition coefficient
 δ = lumped diffusion coefficient
 $\Phi(t)$ = monomer volume fraction in polymer phase.

The above equations (6) through (12) for the molecular weight and branching averages can be combined with the previous model for conversion and particle properties to provide a comprehensive model of the system. This model is used in the following section to redesign the reactor configuration.

Discussion

The usual industrial system for the production of polymer lattices by emulsion polymerization consists of a series of nearly equal sized CSTR's in which all feed streams enter the first reactor. The first reactor in such a case is illustrated as the "base case" in Figure 1. Also shown in Figure 1 is a newly designed reactor configuration in which a very small initial CSTR has been added and to which most of the initiator and soap but only part of the monomer/water streams are fed. The remaining water, monomer and soap are bypassed and fed to the second large reactor. The logic behind the design is that all the generation of particles can be entirely accomplished in the first very small reactor by running under conditions of high soap and initiator concentrations, and the subsequent reactors used only for particle growth. In this way one achieves either a steady-state generation of particles in the first reactor, or else a very rapid periodic generation which has no destabilizing effect on the much larger downstream reactors. In effect, the small early reactor therefore becomes a continuous seeding reactor.

It would also be possible to use a tubular seed generation reactor as suggested by Greene, Gonzales and Poehlein [7], although the improved mixing characteristics of the CSTR would seem to be preferable. In either case, control of the proper split of monomer and water between this first and the second reactor is essential to achieve the desired number of particles. Nomura and Harada [8] have also noted that relative monomer to water split in the first few reactors would alter the number of particles produced and that a certain split would maximize this number.

A comparison between the single CSTR and the same reactor with a seeding CSTR reactor is shown in Figures 2 and 3. With the seeding reactor present, all property oscillations are eliminated, while maintaining essentially the same productivity and quality (conversion and particle size distribution).

Another advantage of the new reactor configuration is that the soap levels needed downstream in the reactor train can be set by latex stability criteria rather than by soap required to generate sufficient number of particles. The maximum amount of emulsifier required in any reactor system should be based on the need to give adequate coverage of the polymer particles to ensure particle stability (typically 70 to 80% coverage) rather than on the need to generate an adequate number of particles. With the new reactor configuration, soap flow into the system is chosen to give adequate surface coverage and small particle stability in downstream reactors. The required generation rate of particles in reactor 1 is obtained by artificially controlling the emulsifier level in that reactor by regulating the split of the diluting water/monomer stream between the first and second reactors. Of course, any variation in either emulsifier or initiator flow into

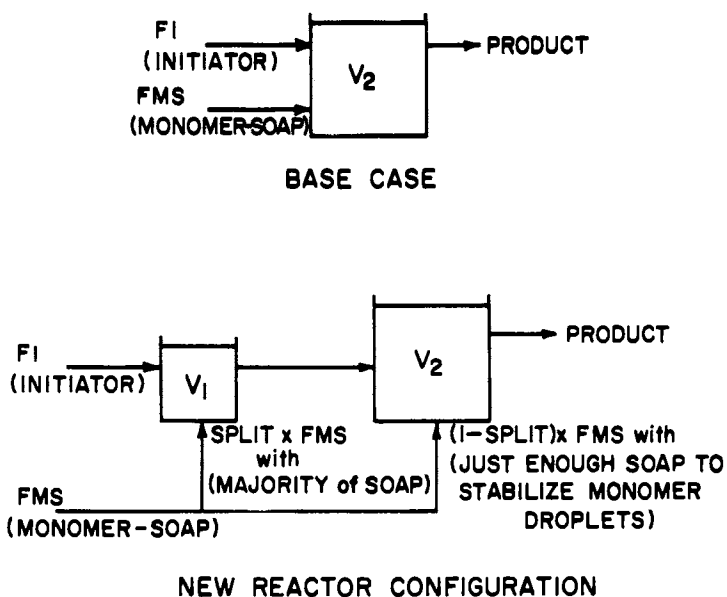


Figure 1. Comparison of reactor configurations: single CSTR (Base Case) versus same size CSTR with small seeding reactor (New Reactor Configuration).

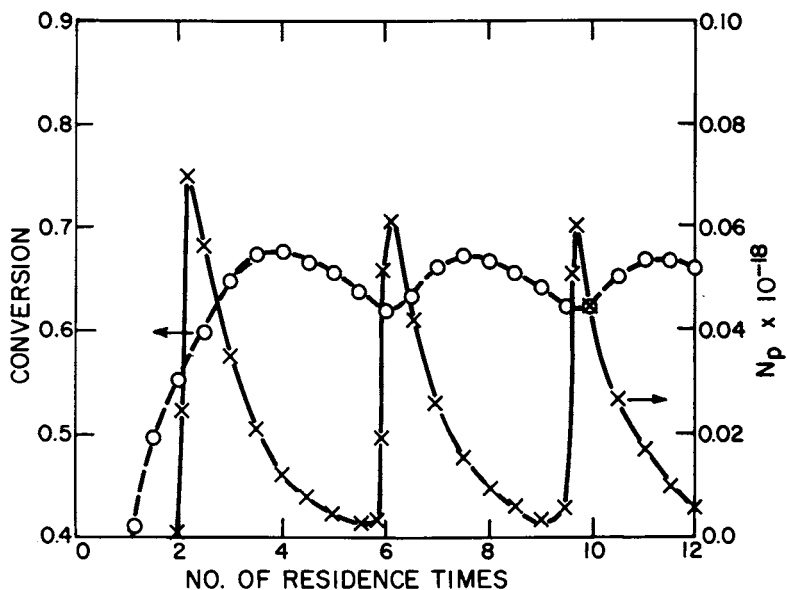


Figure 2a. Conversion (○) and number of particles, N_p (×), versus number of residence times for a single CSTR. Conditions: $\theta = 3600$ s, $[I] = 0.01$ mol/L, $[S] = 0.01$ mol/L.

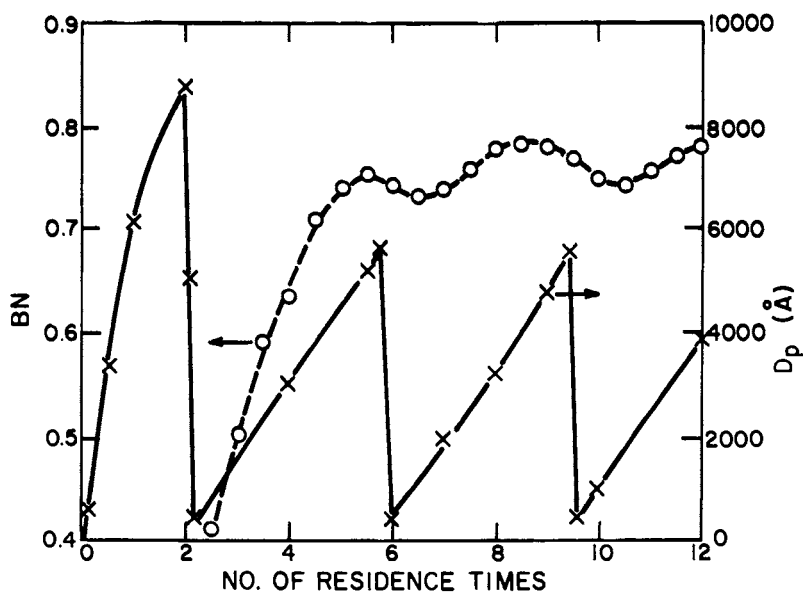


Figure 2b. Average number of branch points per polymer molecule, B_N (○), and number average particle diameter, D_p (×), versus number of residence times for a single CSTR. Conditions: $\theta = 3600$ s, $[I] = 0.01$ mol/L, $[S] = 0.01$ mol/L.

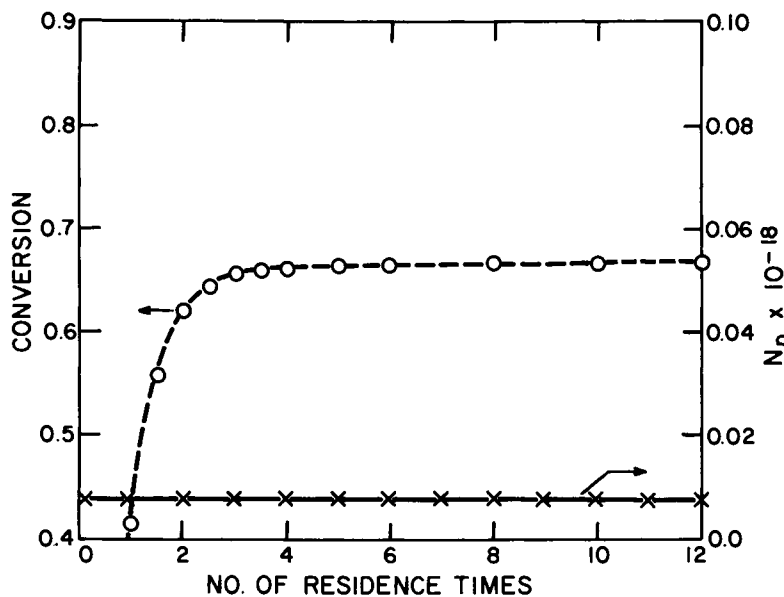


Figure 3a. Conversion (○) and number of particles, N_p (×), versus number of residence times for the new configuration. Conditions: $\theta_1 = 300$ s, $\theta_2 = 3600$ s, split = 0.2, $[I] = 0.005$ mol/L, $[S] = 0.0075$ mol/L in the product.

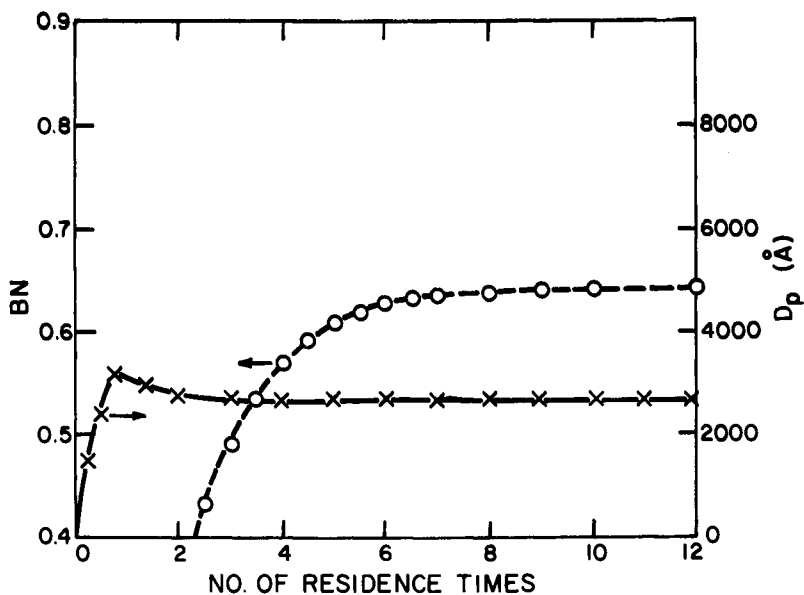


Figure 3b. Average number of branch points, B_N (○), and number average particle diameter, D_p (×), versus number of residence times for the new configuration. Conditions: $\theta_1 = 300$ s, $\theta_2 = 3600$ s, split = 0.2, $[I] = .005$ mol/L, $[S] = 0.0075$ mol/L in the product.

the particle-generation reactor would also change the concentration of particles in the train. Therefore, a suitable process control system should be used to monitor and control particle generation by making small manipulations in the split.

The new configuration yields approximately 80% particle coverage by soap at all times while in the single reactor case, the coverage drops to only 55% immediately after each particle generation period for the example shown in Figures 2 and 3, which is a potentially unstable situation and could lead to agglomeration.

TABLE I: Comparison of Polymer Latex Properties of the Product for a Single CSTR (Base Case) Versus the New Reactor Configuration (Case I and Case II) Where I = Potassium Persulphate and S = Sodium Lauryl Sulphate.

	[I] (mol/l)	[S] (mol/l)	X	M_N ($\times 10^{-5}$)	M_W ($\times 10^{-6}$)	B_N	N_P ($\times 10^{-18}$)	D_P (\AA)	D_W/D_N
BASE									
CASE (single CSTR)	.01	.01	.62	5.89	2.19	.74	.003	400	1.03
			TO	TO	TO	TO	TO	TO	TO
			.67	6.02	2.26	.78	.06	6000	2.97
			(RANGE OF OSCILLATIONS)					AVE	AVE
							= 2700	= 1.21	
CASE I	.005	.0075	.66	5.58	1.91	.67	.009	2800	1.19
CASE II	.005	.01	.71	5.79	2.09	.72	.009	2700	1.18

Table I shows the results for two cases of the new system as well as the base case where no seeding is present. Case I illustrates that for roughly the same conversion and average diameter, the average number of long chain branches per molecule can be reduced by 10% thereby yielding a more processable product in terms of reduced viscosity and die swell, or better adhesive properties.

Case II illustrates that for the same diameter and molecular weight values, approximately 6% higher conversion can be obtained in the new configuration, as well as having stable operation. In both cases the split is set at 20% into the first reactor.

The new reactor configuration is also much more flexible than the conventional one from a control viewpoint. Rather than having to manipulate emulsifier and initiator feeds to control the particle properties and conversion, the major manipulated variables are physical ones, namely the split of feed between the first and second reactor, or the residence time of the small first reactor. While small variations in the initiator flow might also

be needed, the soap flow would usually remain constant as discussed previously.

In addition, both Case I and II show that these results can be achieved with lower initiator and possibly lower soap concentrations. This leads to lower raw material costs, as well as reducing the contamination of the final latex product.

One problem in the conventional system is the presence of impurities. Small amounts of impurities such as oxygen in the water and stabilizer (e.g. MEHQ) in the monomer can inhibit the reaction by reacting with the radicals, and can cause problems in the nucleation of new polymer particles. Impurities can cause a very significant reduction in particle generation thus giving off-spec product and loss in productivity which cannot be overcome with higher initiator flows. This necessitates purifying large quantities of raw materials to remove these impurities. However, in the new design, all nucleation takes place in the seed reactor. Due to the bypass, there is a smaller proportion of the total feed entering the nucleation stage in the reactor system, and there is therefore a much smaller degree of purification required in the new system. The smaller feed streams to the seed CSTR reactor are all that require purification rather than the total feeds in the conventional system. This can represent a significant decrease in the operating cost of the reactor train. Impurities in the bypass stream can be easily countered by increases in initiator. This is due to the fact that the effect of impurities is minimized downstream because the required high particle concentration is already present from the nucleation stage in reactor 1.

For certain applications, a lower bulk latex viscosity is desired. For constant solids, it is possible to lower viscosity by producing a broader particle size distribution. One possibility for producing this broader distribution is to set the concentrations and reactor volumes to produce the diameter in the desired range, then use a controlled cycling of the degree of bypass (either sinusoidal or perhaps in a stepwise fashion) to produce a broader particle size distribution. In this sense, it is possible to broaden the particle size distribution by introducing controlled oscillations into the system, but still produce diameters in some desired range. It should thus be possible to obtain a PSD broader than say with a single CSTR.

In summary, the major advantage of this new system is the stability of the latex product properties, and the reduction of the danger of catastrophic agglomeration. Soap levels can readily be set to give stable latex particles and yet generate any required particle concentration. The new system is also more flexible in its ability to be controlled to produce a desired latex product. It should also prove to be less expensive and more flexible than the alternative of seeding the reactors with seed particles generated apriori in batch reactors.

Furthermore, costs can be reduced by use of less initiator and emulsifier in most cases, plus reduction in raw material

purification costs. While narrow-particle size distributions are produced by this system, it may also be possible to broaden the distribution by cycling the bypass to produce controlled variations in the particle diameter.

Literature Cited

- 1) Kiparissides, C., MacGregor J.F. and Hamielec, A.E., J. Appl. Poly. Sci., 23, pp. 401-418, 1979.
- 2) Kiparissides, C., MacGregor, J.F. and Hamielec, A.E., Can. J. Chem. Eng., 58, pp. 401-418, 1980 (a,b,c).
- 3) Chiang A. and Thompson, R.W., Amer. Inst. Chem. Eng. J., 25, pp. 552-554, 1979.
- 4) Dickinson, R.F., Ph.D. Thesis, University of Waterloo, Waterloo, Ontario, 1976.
- 5) Gorber, D.M., Ph.D. Thesis, University of Waterloo, Waterloo, Ontario, 1973.
- 6) Hamielec, A.E., Course Notes, Part I, An Intensive Short Course on Polymer Production Technology, McMaster University, Hamilton, Ontario, Canada, June 1977.
- 7) Greene, R.K., Gonzalez, R.A. and Poehlein, G.W., ACS Symposium Series 24, pp. 341-358, 1976.
- 8) Nomura, M. and Harada, M., ACS Symposium Series 165, pp. 121-144, 1981.

RECEIVED May 4, 1982.

An Automated Ferranti-Shirley Viscometer

A. F. KAH, M. E. KOEHLER, T. F. NIEMANN, T. PROVIDER, and R. R. ELEY

SCM Corporation, Glidden Coatings and Resins Division,
Dwight P. Joyce Research Center, Strongsville, OH 44136

A Ferranti-Shirley cone-plate viscometer was interfaced to a minicomputer system by means of a microcomputer. The microcomputer collects data from the instrument corresponding to shear rate, shear stress and temperature. Data are transmitted to the minicomputer for storage, analysis and the generation of reports and plots. Four types of analyses are performed:

- 1) Casson analysis of shear stress vs. shear rate for a linear ramp of shear rate with time yields viscosity vs. shear rate and the Casson "infinite shear rate" viscosity.
- 2) Analysis of shear stress at constant shear rate yields an average viscosity and changes in viscosity with time due to effects such as shear thinning, viscous heating and thermoset curing.
- 3) Analysis of spring relaxation data yields viscosity vs. shear rate information at low shear rates.
- 4) A step shear rate experiment which studies the build-up of structure at low shear rate after the sample has been "sheared out" at a high shear rate.

Benefits derived from automation include time savings, improved record keeping and reporting, and a better understanding of the instrument operating characteristics and performance.

0097-6156/82/0197-0223\$06.00/0

© 1982 American Chemical Society

The Ferranti-Shirley Viscometer is a cone-plate type instrument which can be used in a variety of operating modes. Its durability and the wide temperature range accessible with this instrument have made it a valuable tool in the characterization of polymers and coatings. The main drawback in using this instrument for large numbers of samples has been that the time required to manually calculate, tabulate and plot the data obtained from the graphical output frequently exceeds the time required to make the experimental runs themselves.

Data Acquisition System

Automation of the viscometer was achieved by interfacing the instrument to a microcomputer for data acquisition. Data are then transferred via a serial line to a minicomputer system for storage, analysis, report generation and plotting. Details of the mini-microcomputer system and its organization and operation have been reported elsewhere (1).

The microcomputer system chosen is based on the Pro-Log 8821 processor card which uses the Intel 8080A microprocessor. In addition, this card contains 1k bytes of RAM memory and sockets for up to 4k bytes of EPROM memory containing the programs used in data collection and communication. The system also contains 32k bytes of RAM memory for data storage. Analog to digital conversion is accomplished using an Analog Devices RTI 1220-12 card which contains an 8 channel differential input multiplexed 12-bit A/D converter.

The following functions are implemented on two circuit cards designed in our laboratory. Serial I/O for communication with the minicomputer is implemented using a UART. Parallel I/O is used for status lights and communication with TTL compatible instrumentation and is implemented using a Motorola 6821 peripheral interface adapter. The Intel 8214 priority interrupt control chip is used to provide eight priority levels of vectored interrupts. A real-time programmable clock is implemented using the Intel 8253 chip controlled by a crystal time base. The clock is used to control the data acquisition rate.

The microcomputer is interfaced to a Digital Equipment Corporation PDP 11/34 minicomputer system with 68 Mbytes of disk storage, two serial printers, a Gould 5005 electrostatic printer/plotter, magnetic tape storage and several hard and softcopy terminals located throughout the facility. The minicomputer operates in a general time-sharing mode using the RSX11-M operating system. The function of the minicomputer is to provide bulk storage, computational power in a high level language (FORTRAN), and graphic and alphanumeric hard-copy output in the form of reports and plots. Also available on the minicomputer are program packages for statistical analysis and data base management.

Automated Instrument Analysis Process

There are four stages in an automated instrument analysis. These are shown schematically in Figure 1. In the first stage, the instrument operator initiates the experiment by means of a dialog program on the minicomputer. An example of the dialog for the Ferranti-Shirley operation is shown in Figure 2. The program asks a series of questions regarding the sample identification and the experimental parameters required for data collection and analysis. This includes instrument settings and data collection rates for spring and rpm data and for the temperature. A maximum run time for the selected data collection rates is calculated based on memory capacity. Values are checked for errors by comparing the entered values to allowed values or ranges for each parameter. Default values are displayed based on the parameters entered for the previous run and may be changed if desired. This simplifies the entry when several runs are made under the same or similar conditions. When the dialog is complete the minicomputer sends all of the input data to the microcomputer. The microcomputer acknowledges that it has received the data and turns on a status light at the instrument indicating that it is ready.

The second stage is data acquisition. This stage is initiated when the operator starts the instrument. For the Ferranti-Shirley operation data is collected on two analog channels corresponding to the motor speed (tachometer output) and to the torque (spring displacement). The analog signals from the instrument are conditioned and scaled before passing them to the A/D converter. This is accomplished by means of instrumentation amplifiers followed by low pass active filters which are implemented on printed circuit boards designed in our laboratory.

The voltage levels of the signals output from the instrument are highly dependent on the resistive loading designed to be applied by the recorder supplied with the instrument. To avoid difficulties caused by differences in loading when the data collection unit or the recorder are connected or disconnected from the circuit, the signals are loaded at a constant level at the inputs of the instrumentation amplifiers and the output of the active filter, which is capable of driving as low as a 1k ohm load, then feeds the signal to both the microcomputer and to the reactor.

The temperature is input as a BCD number from a digital thermometer which converts the thermocouple voltage to temperature (degrees C) to the nearest 0.1 degree. The digital thermometer is controlled by the microcomputer to convert at the desired rate at up to one conversion per second. During the third stage the microcomputer transmits the data it has collected and stored in its memory to the minicomputer. The minicomputer stores this data in data files on one of the disks.

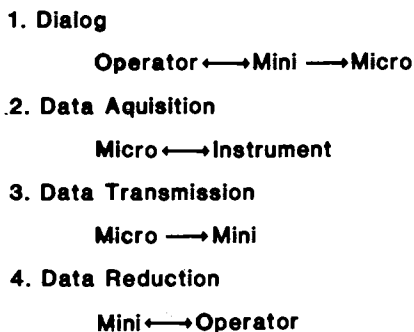


Figure 1. Steps in an Automated Instrument Operation.

```

DIA 35
INSTRUMENT NO. 31 - FERRANTI-SHIRLEY
JOB 5462
Initials...MEK
Sample ID....LATEX A

Analysis type...1
Cone...LT-100
Springs... 1275
Thermocouple position...A
Motor speed...A
Gear...L
Scale multiplier... 1
Sweep time... 20
Springs & RPM data rates (pts/sec)... 2.00
Temperature data rate (pts/min)... 60.00

Maximum run time based on Temperature rate... 16.7 min

Use default values (Y or N)? Y

OK
>

```

Figure 2. Dialog for Ferranti-Shirley Operation.

The fourth stage is the final data analysis and takes place in the minicomputer. This data reduction is done by FORTRAN programs. Reports and plots are generated at this time.

Data Analysis Methods

Voltages corresponding to the tachometer output and spring displacement are converted to angular velocity, ω , and angular displacement, θ in units of radians/second and radians respectively. Shear stress, τ , is calculated from the equation

$$\tau = \frac{3 T}{2\pi R^3} \quad (1)$$

where R is the radius of the cone in cm and T is the torque calculated from the relation

$$T = \kappa\theta \quad (2)$$

where κ is the spring constant in dyne-cm/radian.

For analyses where the motor is used to drive the cone the shear rate, $\dot{\gamma}$, is calculated from the equation

$$\dot{\gamma} = \frac{\omega r}{c} \quad (3)$$

where c is the cone-plate gap at radius r and the term ωr represents the linear velocity at that radius. Since ω and c are both linearly dependent on r , the ratio ω/c is not a function of the radius. Furthermore, since

$$\frac{c}{r} = \tan \alpha \sim \alpha \quad (4)$$

where α is the cone angle, for a small angle α expressed in radians, equation (3) can be simplified further to yield

$$\dot{\gamma} = \frac{\omega}{\alpha} \quad (5)$$

which enables us to calculate the shear rate from the angular velocity and the cone angle.

Three types of analyses are currently incorporated in the analysis program. A fourth type of analysis is being developed and will be included also. These are as follows:

1. Casson analysis (2): For this case, shear stress and shear rate begin at zero. The shear rate ramps linearly to a maximum and returns to zero. The upward and downward sloping portions of the curve are analyzed separately. Those

portions of the data at the beginning, turnaround and end of the curve may be edited out at the operators discretion by entering the limits in rpm.

A form of the Casson Equation

$$\tau^{1/2} = \eta_{\infty}^{1/2} \dot{\gamma}^{1/2} + \tau_0^{1/2} \quad (6)$$

is used to calculate the yield stress, τ_0 , and the Casson "infinite shear rate viscosity", η_{∞} , by means of a linear least squares fit of the square root of shear stress vs. the square root of shear rate which gives $\eta_{\infty}^{1/2}$ as the slope and $\tau_0^{1/2}$ as the intercept. A report detailing the identification information, experimental conditions and the results of the analysis is produced, as shown in Figure 3. Plots of shear rate vs. shear stress shown in Figure 4; square root of shear rate vs. square root of shear stress shown in Figure 5; viscosity vs. shear rate shown in Figure 6; and temperature vs. time can be generated. Results from several experiments can be coplotted as is shown in Figure 6.

2. Viscosity at constant RPM: In this case, shear stress is recorded as a function of time at constant shear rate. Shear stress may be nearly constant or may drop (e.g., shear thinning or viscous heating) or rise (e.g. thermoset curing). An average shear rate is determined and the viscosity is calculated using this average. Viscosity minima and maxima are reported. The operator may edit the data by entering the limits in minutes. For edited data, a least squares fit of the logarithm of the viscosity vs. time is found.

Plots of viscosity vs. time shown in Figure 7; log viscosity vs. time shown in Figure 8; and temperature vs. time shown in Figure 9 can be generated and results from several experiments coplotted. This type of analysis is also used to calibrate the effective cone angle by making measurements on standard Newtonian fluids and back-calculating the value of effective cone angle.

3. Spring relaxation: In this case, the torque spring is compressed and held in place by means of a ratchet and lever. The cone is then released and allowed to turn in the fluid as the spring unwinds. Shear stress data are collected as a function of time. The data are analyzed from the point of maximum shear rate, which occurs shortly after the spring is released, up to a time selected by the operator. Values at less than 5% of spring compression are automatically rejected due to torque nonlinearities.

The object of this experiment is to obtain viscosity as a function of shear rate, $\eta(\dot{\gamma})$, at low shear rates. The shear rate, $\dot{\gamma}$ is defined in equation (5) as a function of

```

FERRANTI-SHIRLEY VISCOMETER
SHEAR STRESS VS. SHEAR RATE

AC-64-633-10      HOOD & TROUGH

-----
      JOB NUMBER      3498
      RUN NUMBER      1
      OPERATOR        RAZ
      DATE            09-APR-81
      TIME            09:11:31

-----
---- CASSON ANALYSIS          UP          DOWN
      VISCOSITY        0.3731          0.3864
      ARITHMETIC AVERAGE 0.3798 POISE

      SLOPE            0.6109          0.6216
      INTERCEPT      13.4218          12.1505
      CORRELATION      0.9999          0.9999
      POINTS USED      139             162

---- TEMPERATURE (C) ON THERMOCOUPLE A
      HIGH              25.1            25.1
      LOW                24.9            24.9
      AVERAGE          24.97           25.07

---- EXPERIMENTAL CONDITIONS
      LT-100           CONE
      3.50             CONE RADIUS (CM)
      1275             SPRING
      60               SWEEP TIME (SECONDS)
      534.8            MAXIMUM RPM
      7134.1           MAXIMUM SHEAR RATE (1/SEC)
      224.34           RATE DERIVATIVE (RPM/SEC)
      200              DATA INTERVAL (MILLISEC)

---- CALIBRATION VALUES
      223872.8         SPRING FACTOR (DYNE-CM/RAD)
      0.785000E-02     EFFECTIVE CONE ANGLE (RAD)

```

Figure 3. Sample report from Program FRANTI.

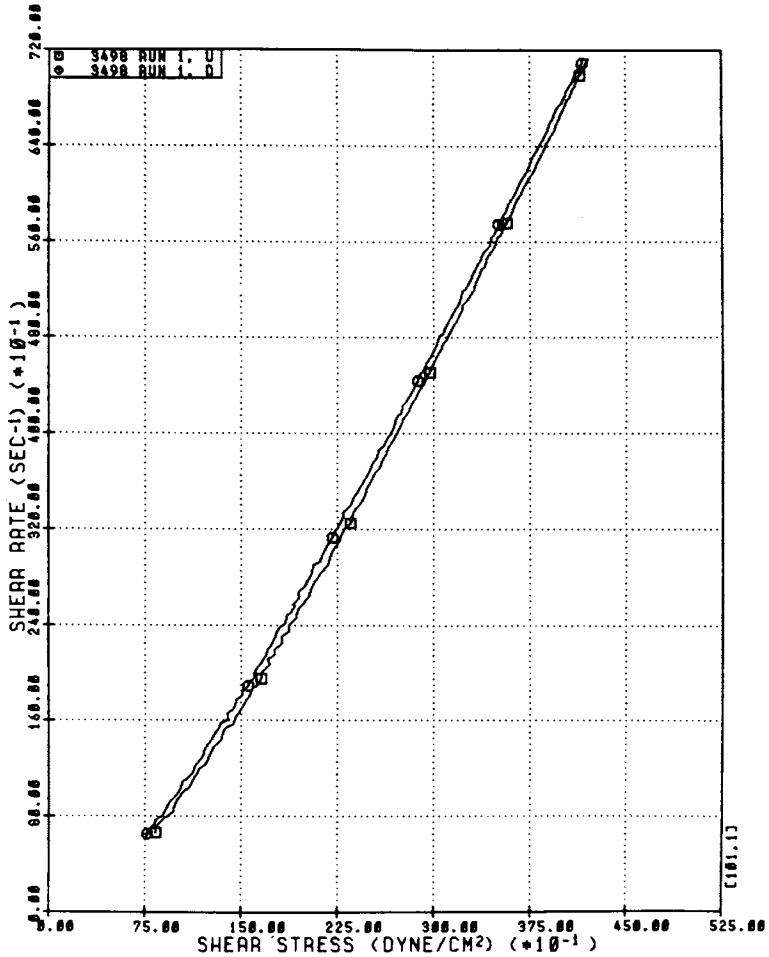


Figure 4. Plot of shear rate vs. shear stress for Casson analysis. Key: \square , 3498 Run 1, U; \circ , 3498 Run 1, D.

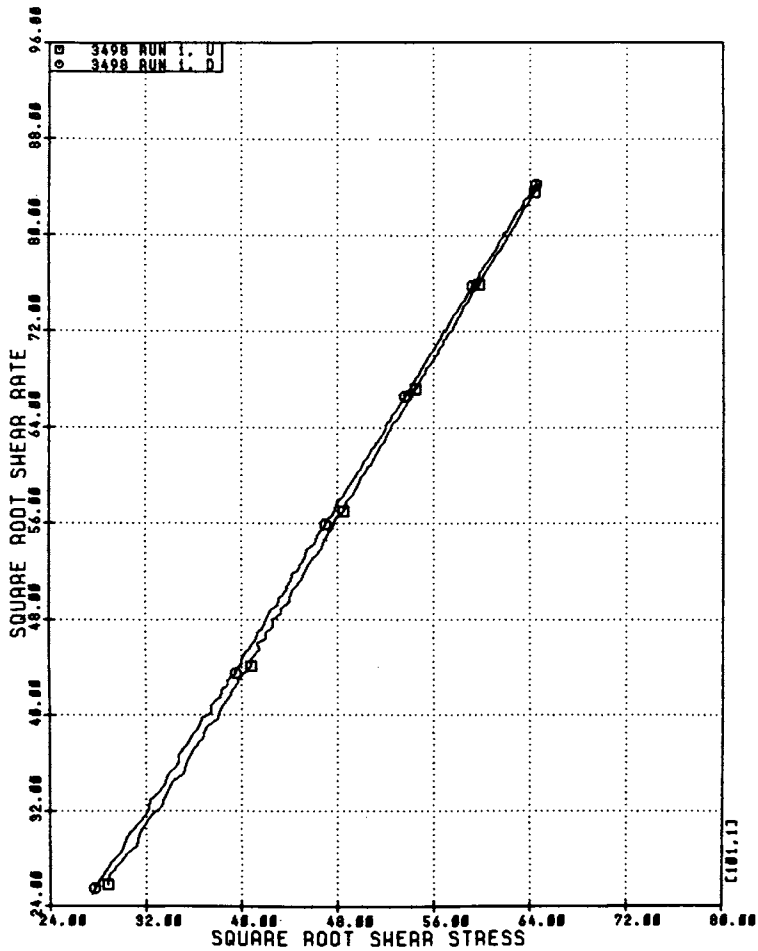


Figure 5. Casson plot. Key: \square , 3498 Run 1, U; \odot , 3498 Run 1, D.

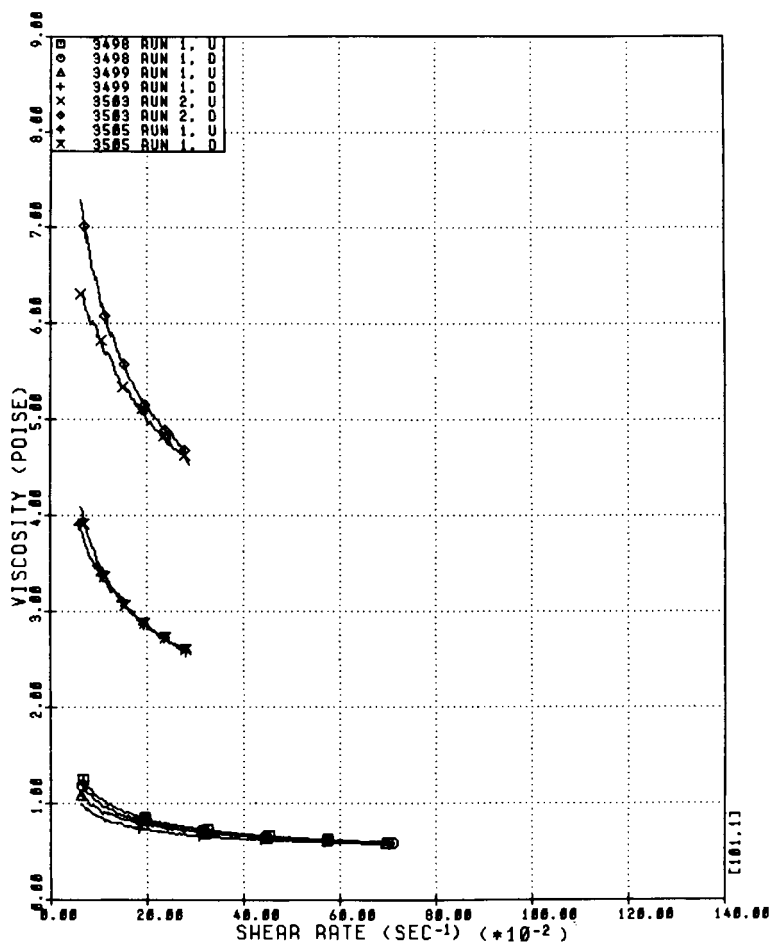


Figure 6. Plot of viscosity vs. shear rate for Casson analysis. Key: □, 3498 Run 1, U; ○, 3498 Run 1, D; △, 3499 Run 1, U; +, 3499 Run 1, D; ×, 3503 Run 2, U; ◇, 3503 Run 2, D; ↑, 3505 Run 1, U; ↘, 3505 Run 1, D.

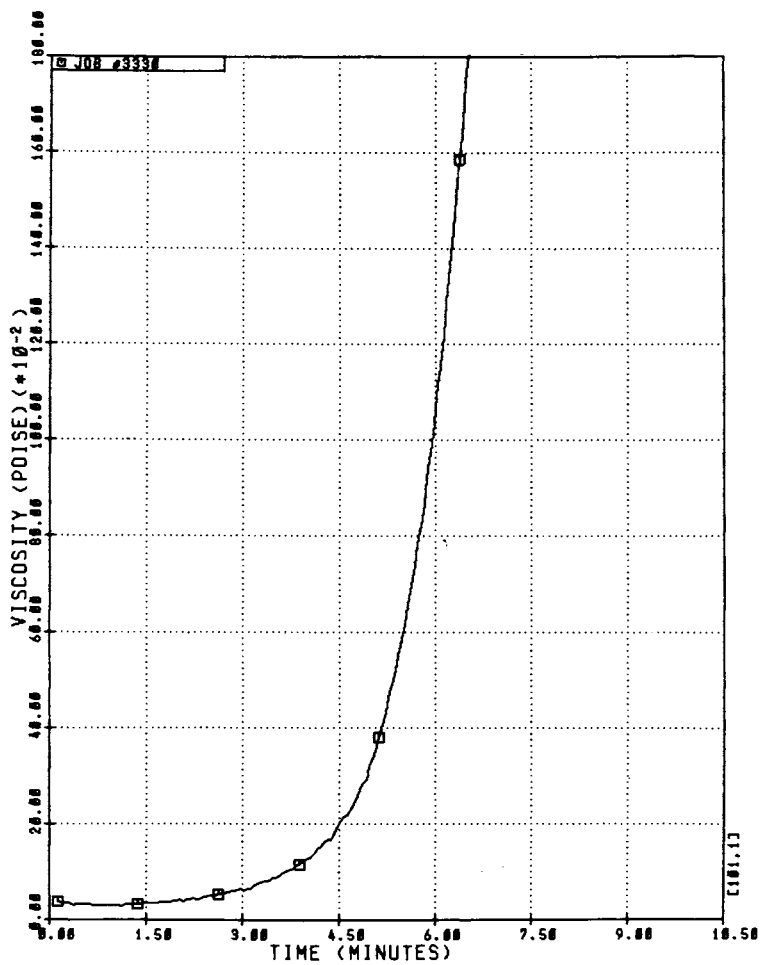


Figure 7. Plot of viscosity vs. time for a curing system. Job # 3330.

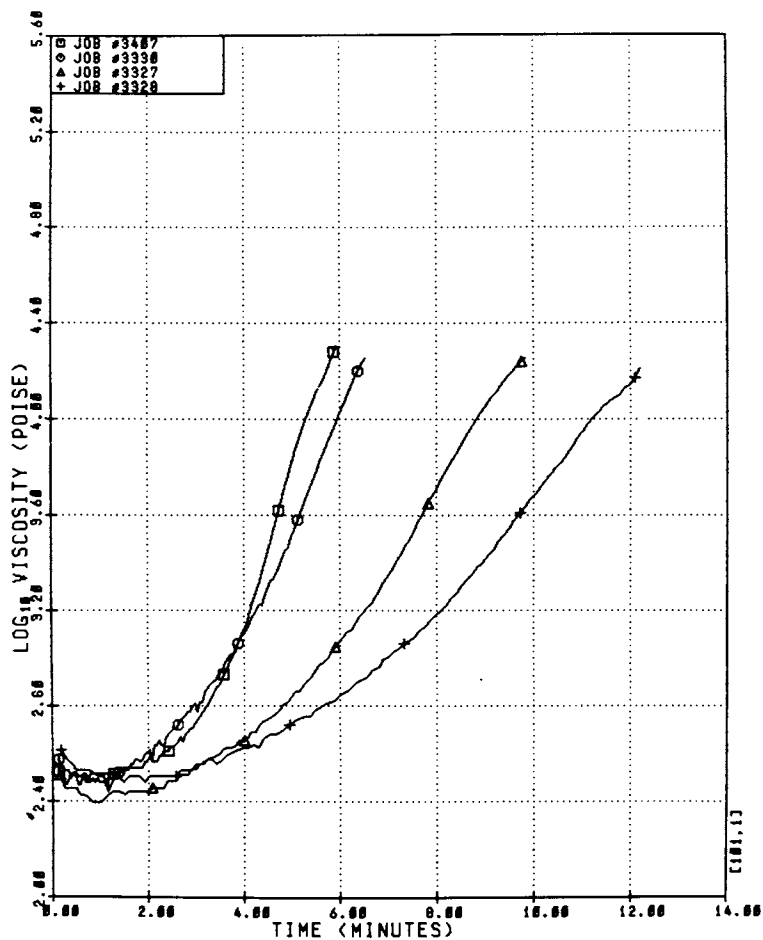


Figure 8. Plot of \log_{10} viscosity vs. time for curing systems. Key: \square , 3407; \circ , 3330; \triangle , 3327; $+$, 3328.

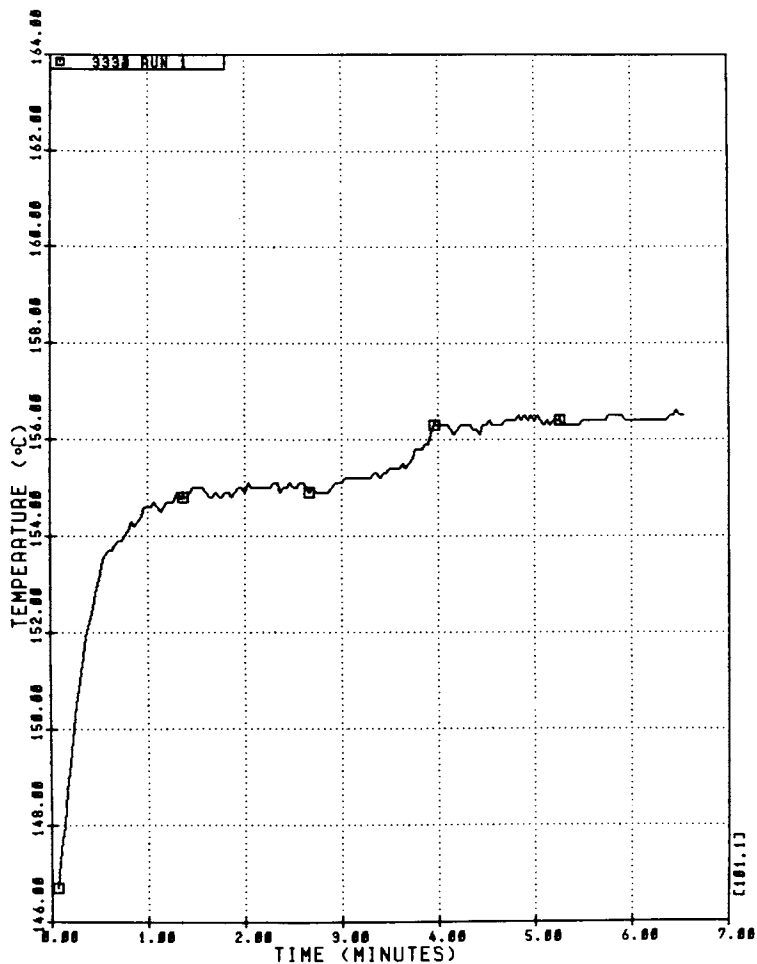


Figure 9. Plot of temperature vs. time for a cure study. Job # 3330 Run 1.

angular velocity, ω , which can be expressed as

$$\omega = \frac{d\theta}{dt} \quad (7)$$

where θ is the angular displacement measured by the torque transducer potentiometer. The time dependent shear rate $\dot{\gamma}(t)$ is then defined as

$$\dot{\gamma}(t) = \left(\frac{d\theta}{dt} \right) \frac{1}{\alpha} \quad (8)$$

The time dependence of the shear stress can be shown by rewriting equation (1) in the form

$$\tau(t) = \frac{3T}{2\pi R^3} \theta(t) \quad (9)$$

The result is that the viscosity as a function of shear rate can be written as

$$\eta(\dot{\gamma}) = \frac{\tau(t)}{\dot{\gamma}(t)} = k \left(\frac{\theta}{d\theta/dt} \right) \quad (10)$$

where $\tau(t)$ is determined from the angular displacement at time t , $\dot{\gamma}(t)$ is determined from the rate of change of the angular displacement with time, and k is a combination of constants including cone angle, cone radius, spring constant etc. To avoid problems with noise, which is amplified by fact that $\dot{\gamma}$ is proportional to the derivative of the displacement divided by the displacement, an analytically smooth data curve is obtained by a polynomial fit to the shear stress-time data and the calculated curve is differentiated by means of the Savitsky-Golay method to obtain the shear rate and viscosity (3,4). Plots of log shear stress vs. time shown in Figure 10; viscosity vs. shear rate for the polynomial fit curve shown in Figure 11a; and viscosity vs. shear rate experimental curve shown in Figure 11b can be generated.

4. Shear Rate Step: This method is under development and will be included in the analysis program. The experiment consists of shearing out a thixotropic material at a relatively high shear rate and then stepping the rate of rotation back to a very low level and measuring the rate of increase in viscosity corresponding to the recovery of structure. The Ferranti-Shirley motor speed control was modified by the

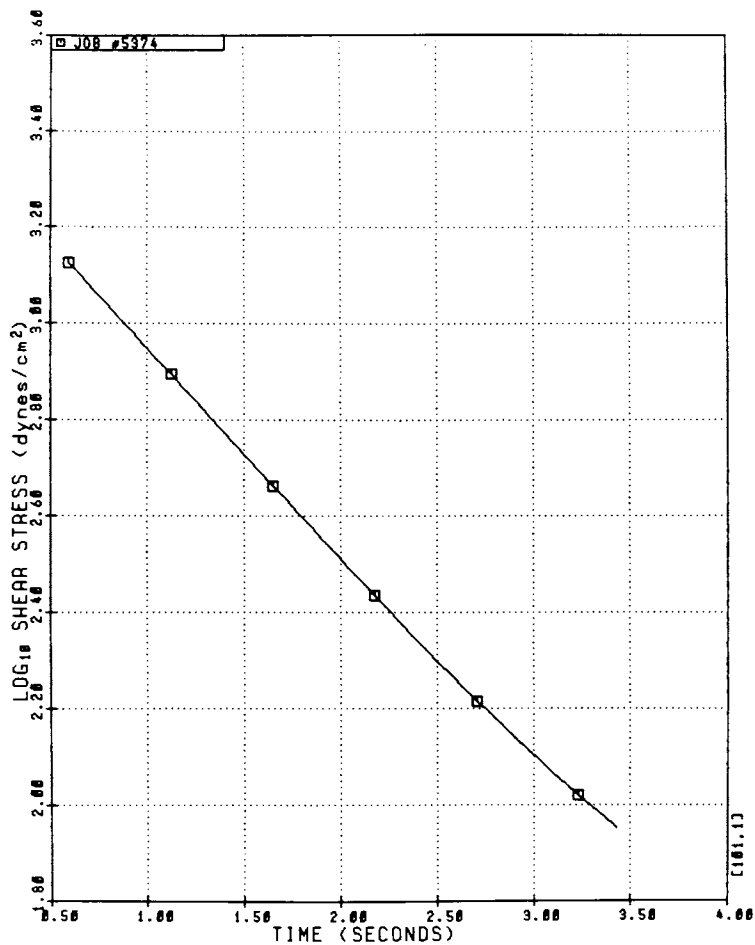


Figure 10. Plot of \log_{10} shear stress vs. time for spring relaxation experiment. Job # 5374.

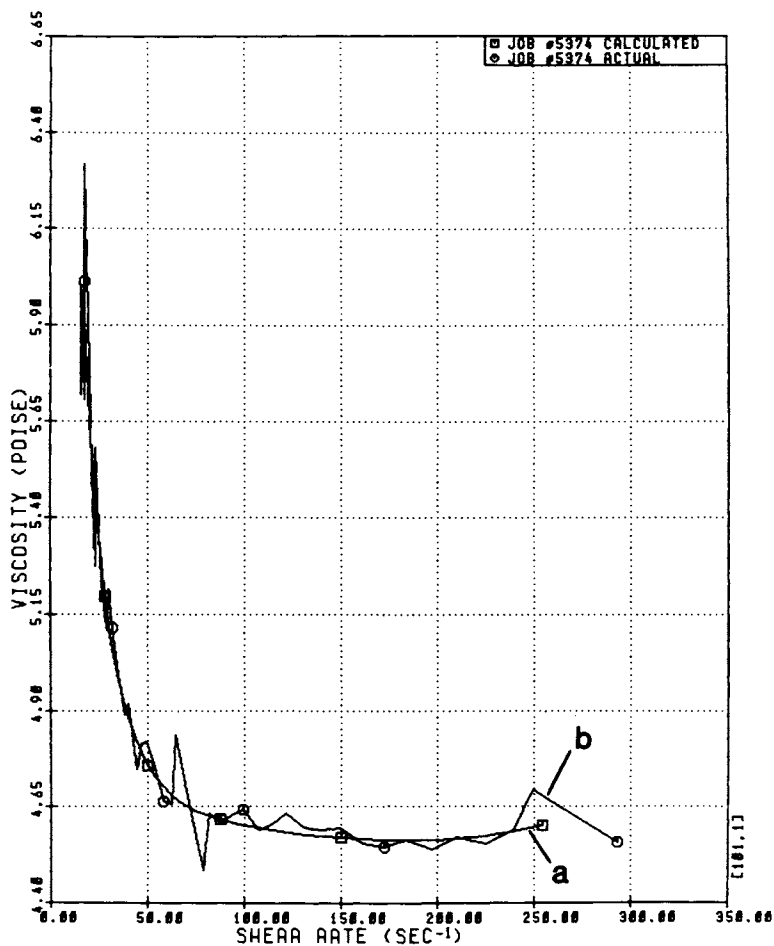


Figure 11. Plot of viscosity vs. shear rate for spring relaxation experiment. Job # 5374. Key: \square , fit curve; \circ , actual data.

addition of a second ten-turn potentiometer with counting dial and a selector switch to rapidly change between the speeds selected on the two dials. The data is analyzed by fitting an exponential function to the recovery curve and calculating a time-constant parameter which characterizes the rate of recovery. A report and a plot of the experimental and fitted viscosity vs. time curves as shown in Figure 12 are generated.

Conclusions

Benefits have been realized from the automation of the Ferranti-Shirley in several areas. First, a significant amount of time has been saved in performing the experiment and in analyzing the data. This has also allowed time for more extensive or varied approaches to the characterization of the samples. Secondly, record-keeping is more complete and accurate. This has simplified accurate reproduction of experimental conditions and has aided in surveying and reporting results. Lastly, automation has made it practical to investigate some problematic areas of viscometer performance and has helped to discern subtle or long term variability in the operating characteristics of the instrument.

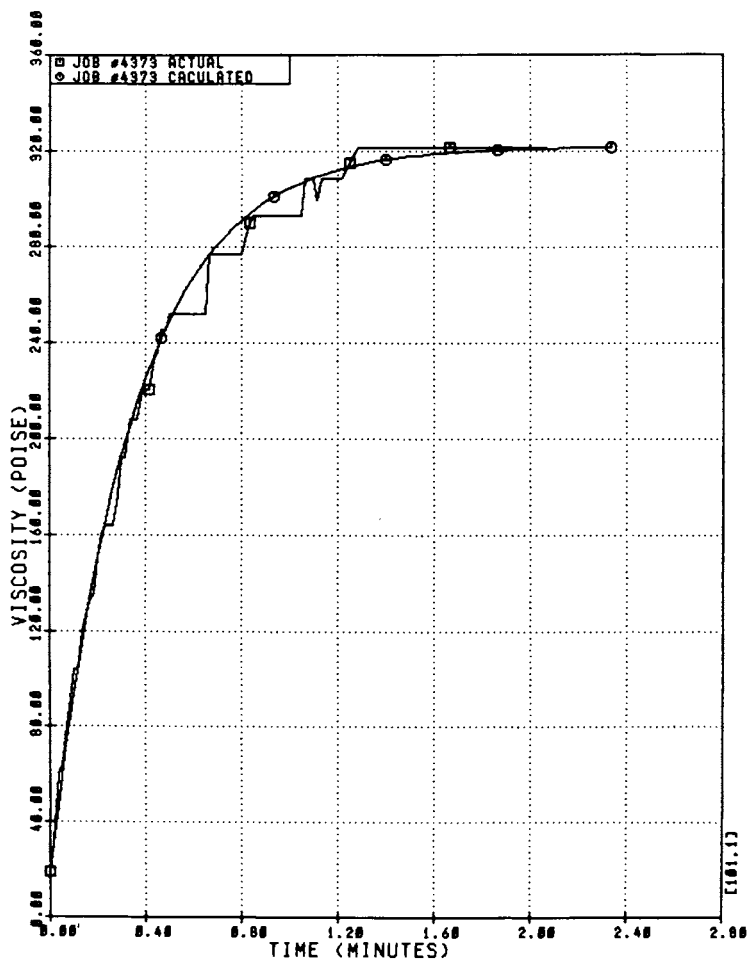


Figure 12. Plot of viscosity vs. time for step shear rate experiment. Thixotropic recovery. Job # 4373. Key: \square , actual data; \odot , fit curve.

Acknowledgement

The authors acknowledge the assistance of Dr. John J. Stansbrey with the numerical methods used in the treatment of data.

Literature Cited

1. Niemann, T. F.; Koehler M. E.; Provder, T. "Microcomputers Used as Laboratory Instrument Controllers and Intelligent Interfaces to a Minicomputer Timesharing System"; in "Personal Computers in Chemistry", Lykos P. Ed.; John Wiley and Sons: New York, 1981.
2. Casson, N. "Rheology of Disperse Systems"; Mill, C. C., Ed.; Pergamon Press: New York, 1959; Chapter 5.
3. Savitsky, A.; Golay, M. J. E. Anal. Chem. 1964, 36, 1627.
4. Stienier, J.; Termonia, Y.; DeTourt, J. Anal. Chem. 1972, 44, 1906.

RECEIVED May 4, 1982.

Automated Capillary Rheometer Measurement and Analysis

T. P. DUNTON

General Electric Company, Polymer Systems Technology, Plastics Business Operations, Pittsfield, MA 01201

S. D. FOSS

General Electric Company, Materials Laboratory, Power Transformer Department, Pittsfield, MA 01201

In order to facilitate rapid melt viscosity measurement and data analysis a modified Göttfert capillary rheometer has been interfaced to a Hewlett-Packard data acquisition system. All test parameters (temperature, barrel pressure, etc) are monitored automatically and the data is stored on magnetic tape. After testing is complete, raw data is entered into an analysis program used to compute tables and draw plots of shear stress, shear rate, and apparent viscosity. Examples of the application of this system to commercial polymers are discussed.

The capillary rheometer is a valuable tool for predicting the processability of thermoplastic resins. This is done by measuring melt viscosities at shear rates and temperatures commonly encountered in extrusion and injection molding. This procedure is difficult and time consuming due to the complex nature of rheological measurements and analyses. An automated system for acquisition and analyses of capillary rheometer data has been developed to speed up and simplify this important analytical technique.

Melt viscosity measurements involve monitoring the pressures produced when molten polymer is forced through a capillary at various shear rates. Viscosities are calculated from capillary rheometer data using the following equations

Volumetric Flow Rate

$$Q = S \times A$$

where Q is the volumetric flow rate, S is the piston velocity and A is the piston cross-sectional area.

0097-6156/82/0197-0243\$06.00/0

© 1982 American Chemical Society

Apparent Shear Rate

$$\dot{\gamma}_w = \frac{4 Q}{\pi R^3}$$

where $\dot{\gamma}_w$ is the shear rate at the wall of the capillary and R is the capillary radius.

Shear Stress

$$\tau_w = \frac{R P}{2 L}$$

where τ_w is the shear stress at the wall, P is the melt pressure, and L is the capillary length.

Apparent Melt Viscosity

$$\eta = \frac{\tau_w}{\dot{\gamma}_w} = \frac{\text{shear stress}}{\text{shear rate}}$$

All variables in these equations are fixed except for piston velocity and melt pressure which are measured experimentally. An HP 3052A data acquisition system is used to acquire raw data from a Göttfert capillary rheometer and to calculate and plot viscosity data.

EQUIPMENT CONSIDERATIONS

To calculate shear stress, shear rate and melt viscosity, the melt pressure and piston velocity must be monitored. The former is measured using a 0 to 20,000 psi pressure transducer mounted in the rheometer barrel just above the capillary. A linear potentiometer is used to monitor piston position during the test. Utilizing the piston displacement data and the HP real time clock, the piston velocity is calculated.

The HP 3052A data acquisition system consists of a 9825A calculator with a real time clock, a multichannel scanner, a high speed digital volt meter and a printer/plotter for display purposes. The system software consists of a monitoring program and an analysis program written in HPL.

DATA ACQUISITION ALGORITHM

Operator interaction with the data acquisition system occurs in the manner shown in Figure 1. The user specifies a time interval, usually several seconds, over which the computer will calculate piston velocity and melt pressure. With the system described above the time interval must be on the whole second since this is the resolution of the real time clock.

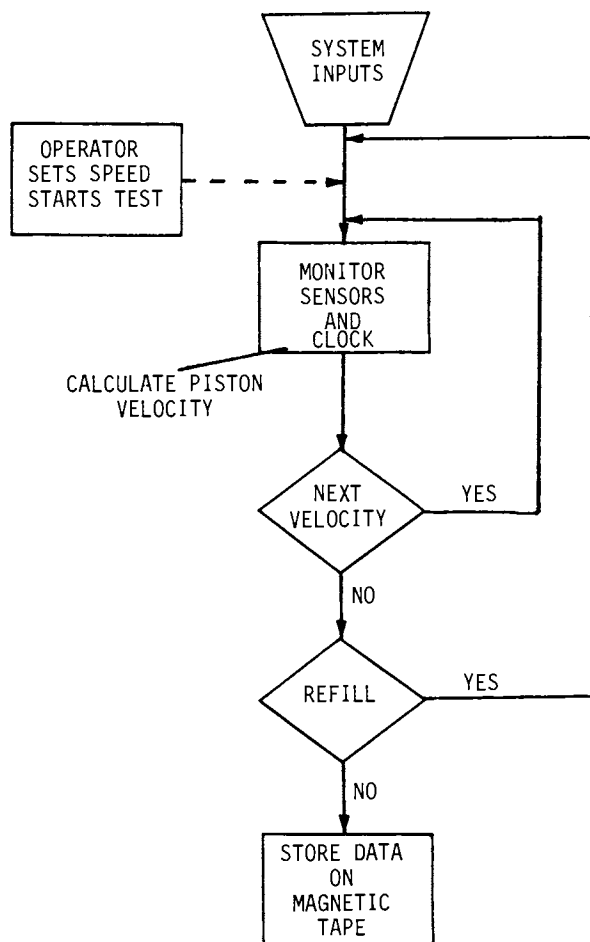


Figure 1. Data acquisition algorithm.

When the test is started and computer monitoring initiated, piston velocity and melt pressure are continuously calculated for each time interval using the following equations:

Piston Velocity

$$S = ((R_1 - R_0) \times F_p) / T$$

where S is the piston velocity (cm/sec), R_0 is the potentiometer reading (ohms) at the start of the interval, R_1 is the potentiometer reading at the end of the interval, F_p is a calibration factor (cm/ohm) for the potentiometer, and T is the time interval.

Melt Pressure

$$P = V \times F_t$$

where P is the melt pressure (PSI), V is the transducer signal (volts) and F_t is the transducer calibration factor (PSI/volt). Only data for the three most recent time intervals are stored in working memory. The computer signals the operator when data have been taken for three intervals. At this time if the melt pressure has leveled off satisfactorily, the operator stops the piston movement. The pressure drop signals the computer to stop taking data. The piston velocity and melt pressure data for the interval, (of the three most recent), with the highest melt pressure reading are taken to be the raw data for that test.

The operator can continue testing or exit as the experiment dictates. This allows for maximum flexibility.

MELT VISCOSITY ANALYSIS AND DISPLAY ALGORITHM

The algorithm shown in Figure 2 demonstrates the flexibility of this program. Data is entered either manually or from magnetic tape. Plot scaling is done automatically or is operator designated. Corrections to the data are optional.

RESULTS AND DISCUSSION

Significant savings in data acquisition and analysis time have resulted from the automation of our rheometer. Piston velocities are now determined rapidly and more accurately than previously had been possible. Preliminary data is quickly and easily plotted thus aiding the decisions on further experimentation.

Viscosity calculations are done in seconds and corrections such as the Rabinowitsch correction shown below are conveniently used.

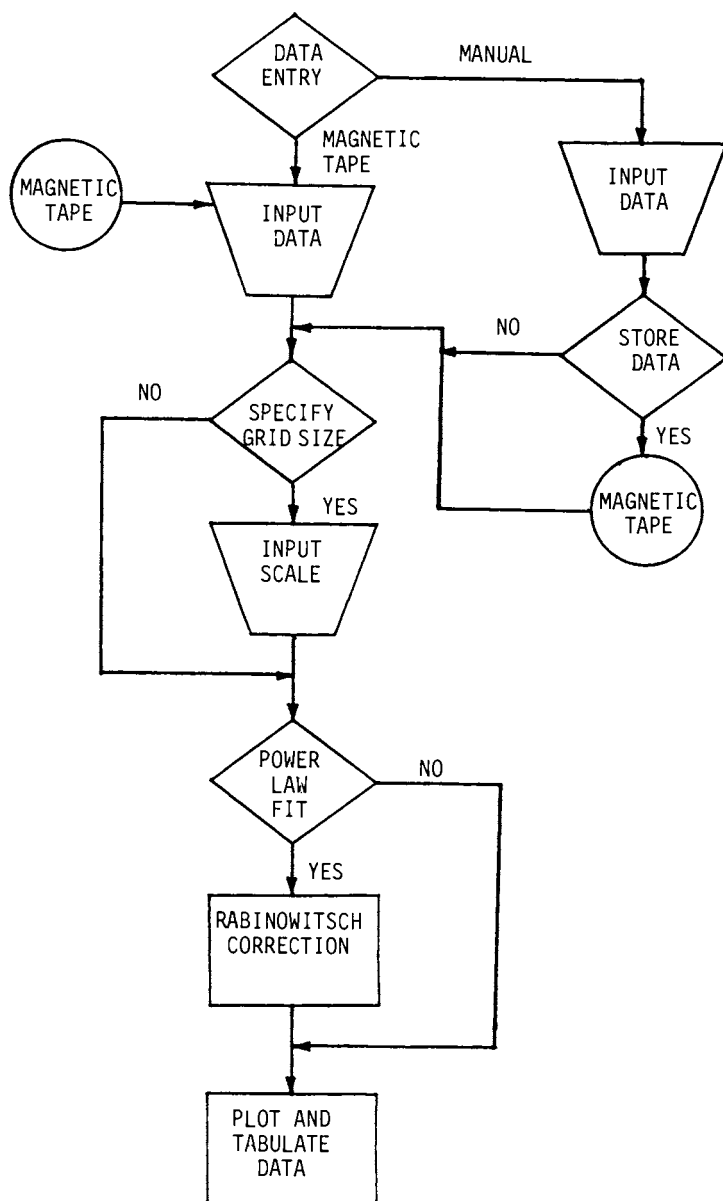


Figure 2. Melt viscosity analysis and display algorithm.

American Chemical
Society Library
1155 16th St., N.W.

$$\dot{\gamma} = \frac{4 Q}{\pi R^3} \left(\frac{3\eta + 1}{4\eta} \right)$$

$$\text{with } \eta = \frac{d \log \tau}{d \log \dot{\gamma}}$$

where η is the power law index for rate of shear at the wall in non-Newtonian fluids. An example of the application of this correction is shown in Figure 3. The viscosity data for a commercial polycarbonate resin is shown plotted with and without the Rabinowitsch correction. As can be seen from the figure, there is a significant shift in viscosity values when the correction is applied.

A very important advantage gained by the rheologist using this system is the ability to rapidly compare up to six viscosity curves on one plot to aid in data interpretation. The viscosity data for several different molecular weight grades of commercial polycarbonate resin are shown in Figure 4. From this plot the relative processability of these materials can easily be determined by comparing their viscosities at the shear rates used in processing.

The ease of operation of this system makes it possible for even inexperienced personnel to quickly learn to use it successfully. Thus rheological data with sophisticated analyses can be easily obtained with a minimum of operator training.

Through automation we now have a flexible, efficient, easy to operate system for obtaining rheological data.

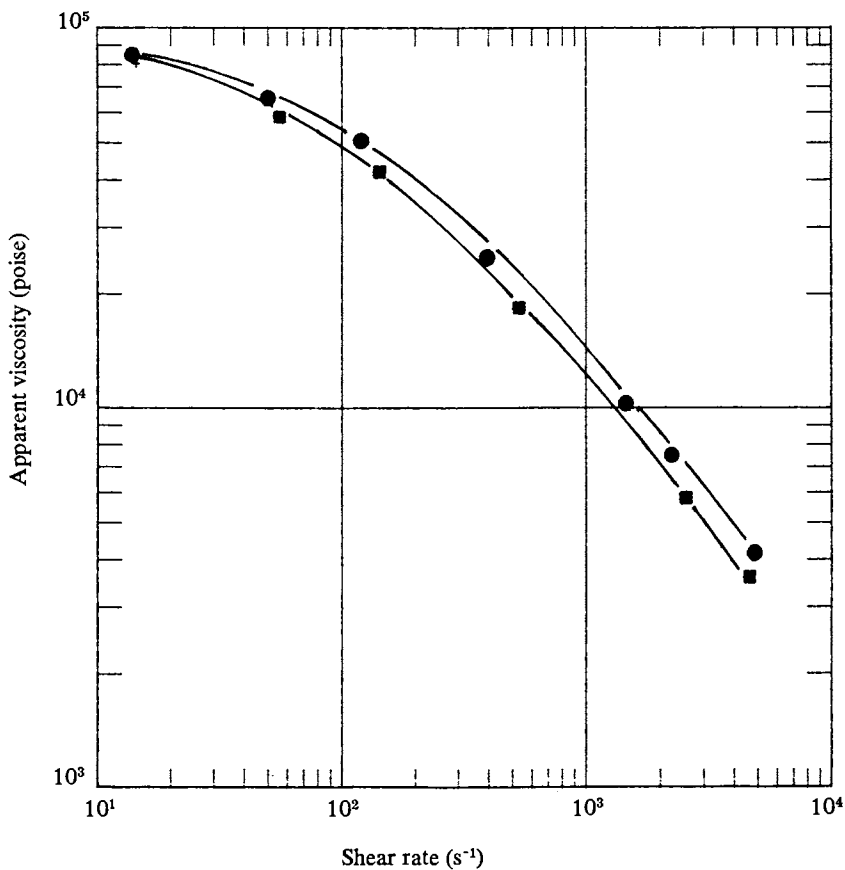


Figure 3. Viscosity data for a commercial polycarbonate resin, LEXAN 135-111, at 250°C. Key: ●, apparent viscosity; ■, Rabinowitsch corrected viscosity.

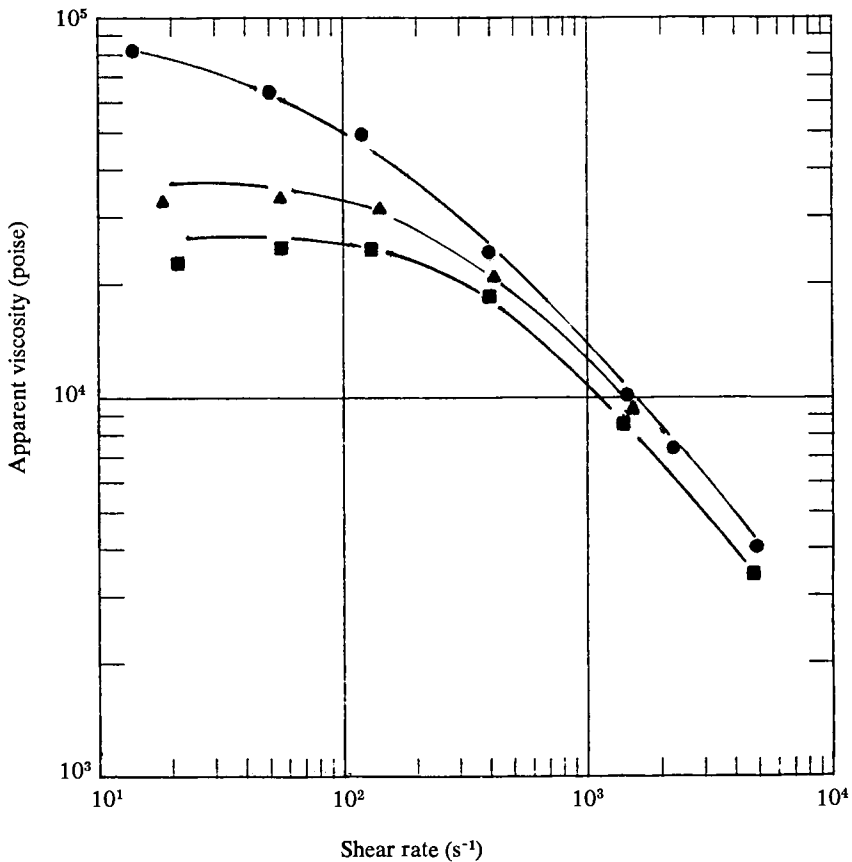


Figure 4. Viscosity data for several different molecular weight grades of commercial polycarbonate resin at 250°C. Key: ●, LEXAN 135-111; ▲, LEXAN 145-111; ■, LEXAN 125-111.

Acknowledgments

The authors wish to thank Carl H. Hansen for his assistance in this project.

Literature Cited

1. Nielsen, Lawrence E., Polymer Rheology, Marcel Dekker, New York, NY (1977).
2. Merz, E. H. and Colwell, R. E., ASTM Bulletin No. 232, September, 1958.

RECEIVED May 4, 1982.

Computer Simulation of Nip Flow in Roll Coating

D. J. COYLE, C. W. MACOSKO, and L. E. SCRIVEN

University of Minnesota, Department of Chemical Engineering & Materials Science,
Minneapolis, MN 55455

The Galerkin finite element method is successfully applied to flow in a relatively simple element of roll coating; symmetric film-splitting in the nip region between smooth, rigid, counterrotating rolls. The calculated flow fields are solutions of the momentum and continuity equations together with appropriate boundary conditions at the liquid/gas interface. The computer code for the analysis accommodates effects of inertia, gravity, and shear-thinning rheology. The predicted locations of the line of film-splitting agree with available experimental data. Pressure profiles are also computed. For capillary number ($N_{Ca} = \mu V / \sigma$) less than about 0.3, there is a pair of counterrotating eddies directly under the meniscus of the splitting film. Shear-thinning behavior by the liquid enlarges the eddies and moderates the pressure gradient in the nip region.

A common method for applying a thin uniform film of a viscous liquid onto a solid substrate is roll coating, one version of which is depicted in Figure 1. In all such coating operations, it is desirable to maximize the speed of coating while maintaining a high degree of uniformity in the coated film. Thus a basic goal in coating flow research is to understand the flow patterns and the mechanisms by which nonuniformities in the final film come about. Another goal is to furnish the design engineer a means to calculate accurate theoretical predictions of how such coating devices will perform. Such theoretical simulation can be extremely effective for the design and improvement of coating equipment.

In roll coating arrangements of the sort shown in Figure 1, liquid is carried by the pick-up roll into the nip region between it and the applicator roll. Beyond the nip the liquid is, in effect, stretched and split into two films, each carried off

0097-6156/82/0197-0251\$06.00/0

© 1982 American Chemical Society

by one of the two rolls. It is the behavior in this region, from nip to split, that determines the flow rate, the film thickness on each roll, the forces exerted on the rolls, and whether or not the final coated film will be uniform. The same is true of the nip flow between the applicator roll and the web carried on the back-up roll when the rolls turn as shown. More often in practice, however, this second nip flow is between co-rotating rolls, which are commonly referred to as "reverse-rolls."

In both cases, an accurate theoretical description of the flow has yet to be developed. This paper deals only with the configuration illustrated in Figure 2, where the rolls are of equal radii and their surfaces are moving with equal speed and in the same direction at the nip. These restrictions bring in a symmetry that allows one to argue that the domain of the simulation can be halved, as shown. Once this simpler configuration has been analyzed, the theory can and is being extended to cases where the convenient symmetry is lacking — and then to cases of reverse-roll coating, which differs somewhat in the type of deformation the liquid suffers, but more importantly in that a wetting line, or dynamic contact line is present near the nip.

Certain aspects of the flow analyzed here have been examined before. Pitts and Greiller (1) presented one of the earliest experimental and theoretical analyses: they solved approximately the biharmonic equation of creeping Newtonian flow in the film-splitting region on the assumption of a parabolic free surface shape. Williamson (2) used a finite difference scheme to solve the biharmonic equation and employed a sixth-degree polynomial to represent the free surface. Greener and Middleman (3) put forward a simple lubrication model which agrees well with their film-thickness data, but relies on approximate, probably quite oversimplified, boundary conditions at the stagnation line where the film splits. While these earlier models can be useful in some situations, they all approximate the boundary conditions at the free surface and are not capable of describing the flow field accurately. In addition, they are all limited to creeping motion, i.e. to low Reynolds number flow in which the inertia of the liquid is negligible, which is not necessarily a valid approximation for high-speed coating operations.

In order to simulate roll coating accurately over all the ranges of parameters of practical relevance, one would need — for a Newtonian liquid — to solve the full Navier-Stokes equation system including the correct boundary conditions. Owing to the shape of the meniscus and to the nonlinear effects of its freeness and of liquid inertia, this cannot be done by conventional mathematical methods. However, computer-aided techniques employing Galerkin's weighted-residual method with finite element basis functions proves very effective. This approach to solving viscous free surface flow problems, such as those that arise in coating operations, has been recently applied to rimming flow (4), extrusion coating (5,6), slide coating (7), and curtain

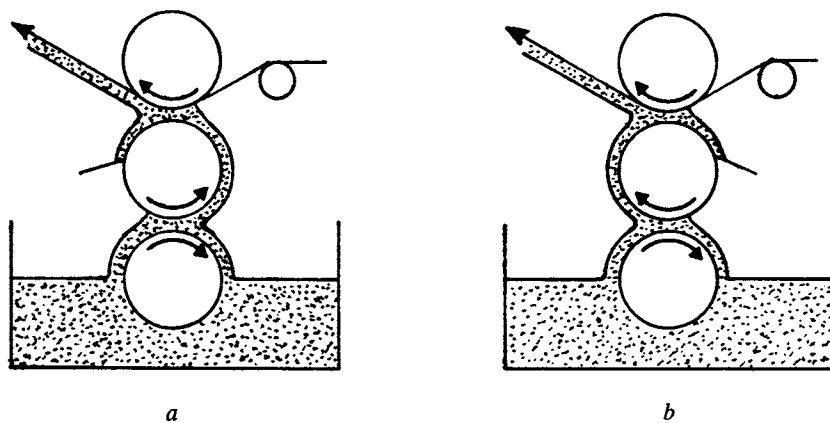


Figure 1. Typical forward (a) and reverse (b) roll coating operations.

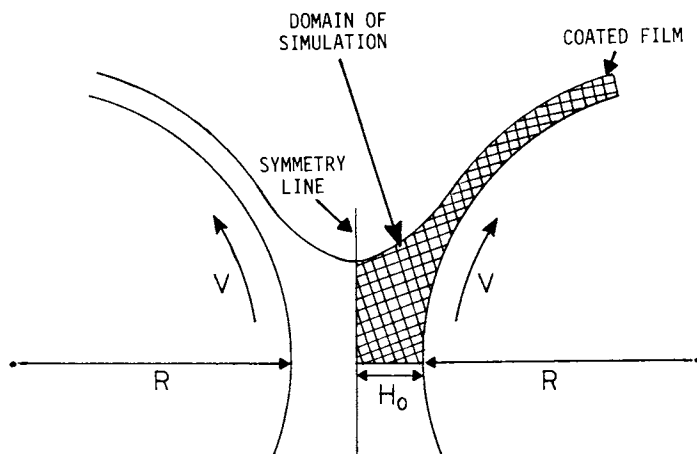


Figure 2. Definition sketch for symmetric film-splitting analysis.

coating (8). In order to determine appropriate boundary conditions on the simpler equations of the lubrication approximation at the liquid/gas interface where the film splits in roll coating and similar operations, Ruschak (9) recently applied the method of matched asymptotic expansions along with the finite element method to examine the flow between rolls. His analysis, however, appears to be restricted to the limit of virtually parallel roll surfaces at the film-splitting region.

Thus the objective here is a generally applicable simulation of steady, two-dimensional, incompressible flow between rigid rolls with film splitting. The results reported are solutions of the full Navier-Stokes system including the physically required boundary conditions. The analysis is also extended to a shear-thinning fluid. The solutions consist of velocity and pressure fields, free surface position and shape, and the sensitivities of these variables to parameter variations, valuable information not readily available from the conventional approach (10). The rate-of-strain, vorticity, and stress fields are also available from the solutions reported here although they are not portrayed. Moreover, the stability of the flow states represented by the solutions can also be found by additional finite element techniques (11), and the results of doing so will be reported in the future.

Finite Element Formulation

Particular advantages of the finite element method for viscous free surface flow problems are: physical boundary conditions enter into the equations in a natural way that is particularly advantageous in the case of free boundaries; complex shapes and curved boundaries are readily handled; locally steep gradients can be resolved by increasing the number of elements in the appropriate region of the flow; and a full functional representation of the solution is obtained.

Within the flowing liquid, mass and momentum must be conserved: for steady, incompressible flow these requirements in dimensionless form are

$$\nabla \cdot \underline{u} = 0 \quad (1)$$

$$-\nabla \cdot \underline{\underline{T}} + N_{Re} \nabla \cdot \underline{\underline{u}} \underline{\underline{u}} - N_g \underline{\underline{f}} = 0 \quad (2)$$

where $N_{Re} \equiv H_0 V \rho / \mu$ is the Reynolds number, the ratio of inertial to viscous forces; $N_g \equiv \rho g H_0^2 / \mu V$ is the gravity number, the ratio of gravity to viscous forces; $\underline{\underline{T}}$ is the total stress tensor (pressure and viscous stress), and $\underline{\underline{f}}$ is a unit vector in the direction in which gravity acts. The location of the free surface that forms part of the boundary is also unknown, but wherever it locates no liquid can flow through it; hence at the free surface

$$\underline{\underline{n}} \cdot \underline{\underline{u}} = 0 \quad (3)$$

At the inlet to the finite element domain, the flow is parallel so the equations of the lubrication approximation are used to specify the inlet velocity profile. These equations are integrated from $-\infty$ to the inlet, generating an equation relating the flow rate to the inlet pressure. The remaining boundary conditions are as shown in Figure 3. The only complexity here is that the fluid traction, $\underline{n} \cdot \underline{T}$, at the free surface has to be specified as a boundary condition on the momentum equation. A force balance there gives, in dimensionless form,

$$\underline{n} \cdot \underline{T} = \frac{1}{N_{Ca}} \frac{d\underline{t}}{ds} + \underline{n} p_a \quad (4)$$

where $N_{Ca} \equiv \mu v / \sigma$ is the capillary number, the ratio of viscous to surface tension forces, and $d\underline{t}/ds$ is the curvature of the free surface (rate of change of the unit tangent vector with respect to arc length along the meniscus). Equation (4) simply states that the total normal stress exerted on the gas/liquid interface must equal the capillary pressure added to the ambient gas pressure, p_a . When the effect of surface tension is negligible, $N_{Ca} \rightarrow \infty$ and the capillary pressure term can be struck. Edge effects are here regarded as negligible and so the solutions sought are two-dimensional flows.

In Galerkin's method, the unknown velocity components, pressure, and free surface location are expanded in a suitable set of basis functions, ϕ^i and ψ^i :

$$\begin{aligned} u(x,y) &= \sum u_i \phi^i\{\xi(x,y), \eta(x,y)\} \\ v(x,y) &= \sum v_i \phi^i\{\xi(x,y), \eta(x,y)\} \\ p(x,y) &= \sum p_i \psi^i\{\xi(x,y), \eta(x,y)\} \\ h(s) &= \sum h_i \phi^i\{\xi(x,y)\} \end{aligned} \quad (5)$$

Here the coefficients u_i , v_i , p_i , and h_i remain to be determined; ξ and η are coordinates in the subdomains into which the actual flow domain is mapped in order to accommodate the complicated shape of its complete boundary.

Next, the weak forms of the mass and momentum conservation equations (1) and (2) are written using these same basis functions as weighting functions:

$$\begin{aligned} M_i &= \int_A \phi^i (-\nabla \cdot \underline{T} + N_{Re} \nabla \cdot \underline{uu} - N_g \underline{f}) dA \\ &= \int_A (\nabla \phi^i \cdot \underline{T} + N_{Re} \nabla \cdot \underline{uu} - N_g \underline{f}) dA - \int_{\partial A} \phi^i \underline{n} \cdot \underline{T} ds = 0 \end{aligned} \quad (6)$$

$$C_i = \int_A \psi^i \nabla \cdot \underline{u} dA = 0 \quad (7)$$

$$K_i = \int_{F.S.} \phi^i \underline{n} \cdot \underline{u} ds = 0 \quad (8)$$

Finite element basis functions are employed, each of which is a simple polynomial on a small subdomain and zero everywhere else. Because these functions are so designed that each takes on the value of unity at just one node and is zero at all other nodes, the coefficients in the expansions, equations (5), are also the values of the unknown variables at the nodes.

The results reported below were obtained with conventional "mixed interpolation" on isoparametric rectangles (12), using nine-node biquadratic basis functions ϕ^i for the velocity components and four-node bilinear basis functions ψ^i for the pressure. The free surface shape was represented by the isoparametric map, the position being determined by the coefficients h_i in the general "free-spine" representation recently devised by Kistler (13).

A typical subdivision of the flow domain into finite elements used in this investigation is shown in Figure 4. The entire mesh is shifted with the free surface position so that no element becomes severely deformed (and so certain inaccuracies are avoided), and the nodes remain concentrated in the region where the flow changes most rapidly.

Equations (6), (7), (8) represent a large set of nonlinear algebraic equations which are solved by Newton's method. This method converges quadratically — a great advantage — over the entire range of parameter values so far examined. The local nature of the basis functions drastically reduces the work required to evaluate the Galerkin integrals, which must be done numerically, and it gives the Jacobian matrix in Newton's method a banded structure that lessens the computational work required in the matrix solution procedure.

The nonlinear algebraic equations represented by equations (6), (7), (8) were generated and solved on a CDC CYBER 74 computer. Solutions typically took 4-5 iterations to converge to an order of 10^{-8} , and for the 440 equations cited in Figure 4 each iteration took approximately 7 seconds.

Results for Newtonian Fluid

In a Newtonian fluid, the stress is a linear, homogeneous, isotropic function of the rate-of-strain part of the velocity gradient. Inserting this constitutive equation into equations (6) - (8) closes the set of equations for nodal velocities and pressures and for free surface locations. This set can then be solved in the manner described above. Figure 5 shows the computed flow field for parameter values representative of operation

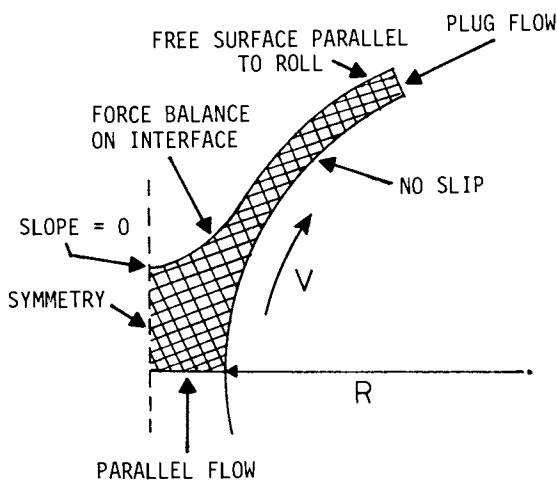


Figure 3. Boundary conditions for symmetric film-splitting.

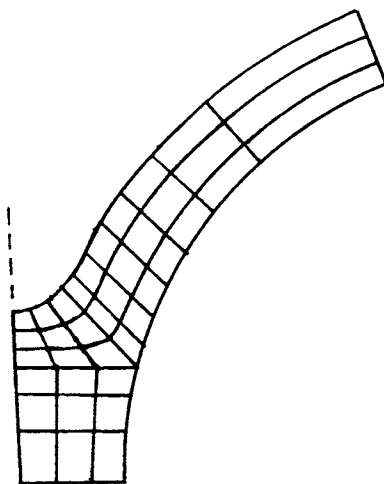


Figure 4. Typical subdivision of the flow domain into finite elements: 39 elements and 440 equations.

of the authors' laboratory two-roll apparatus. The most striking feature is the pair of large, relatively slowly circulating eddies, one on each side of the symmetry plane, located just under the stagnation line at which the film splits. Figure 6 shows how the eddies shrink and finally disappear as the capillary number is increased, i.e. as the viscous normal stress overwhelms the capillary pressure at and near the central stagnation line. When the eddies are absent, there is only the central stagnation line; but as they grow, three stagnation lines move away from the central one: one down the symmetry plane and one to each side on the free surface.

These results show clearly how a lubrication analysis fails. The lubrication approximation requires nearly straight streamlines and is entirely inappropriate for the recirculatory flow when the eddies are present. And when eddies are present the film does not split at the first stagnation point downstream of the nip, as assumed in some lubrication analyses (3), but rather the second. When the capillary number is high enough that the eddies are absent, liquid inertial effects that are neglected in the lubrication approximation may become appreciable.

Figure 7 reveals that the free surface position and shape are quite sensitive to the competition between viscous normal stress and the curvature-dependent capillary pressure. As the ratio of the former to the latter, i.e. $Ca \equiv \mu v / \sigma$, rises, the meniscus recedes toward the nip and curves more sharply. The sample results in Figures 5-10 are for cases in which the effects of gravity and liquid inertia are negligible. The computer program used here is constructed to include these effects as it solves equations (6) - (8); comprehensive case studies and complete portraits of velocity, pressure, stress, and vorticity fields will be reported elsewhere (14).

As with any theoretical prediction, the calculation itself must be validated, and the prediction has to be held up against as closely comparable an experiment as is available. Comprehensive validation of the present calculations will be detailed elsewhere. As for experiments, unfortunately few details of the flow field are fully described in the literature. Pitts and Greiller (1) detected the eddies, but did not indicate over what parameter ranges eddies were or were not present. They did, however, measure where the film splits in a number of experiments. The theoretical predictions calculated by the Galerkin finite element method compare well with their data, as shown in Figure 8. Careful measurements over a wider range of parameters are needed. The agreement over Pitts and Greiller's range is encouraging because the theory shows (Figure 7) the position of the free surface is quite sensitive to varying parameters, more so than flow rate or film thickness, which can be measured as well.

Loading of the rolls and the possibility of cavitation downstream of the nip depend on the pressure profile, which is difficult to measure. It is readily predicted with the Galerkin

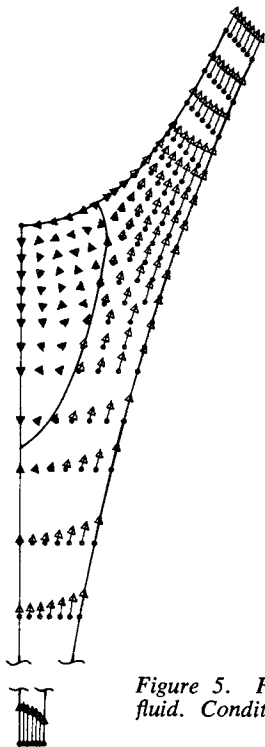


Figure 5. Flow field for a Newtonian fluid. Conditions: $N_{Ca} = 0.1$, $N_{Re} = 0$, $N_g = 0$.

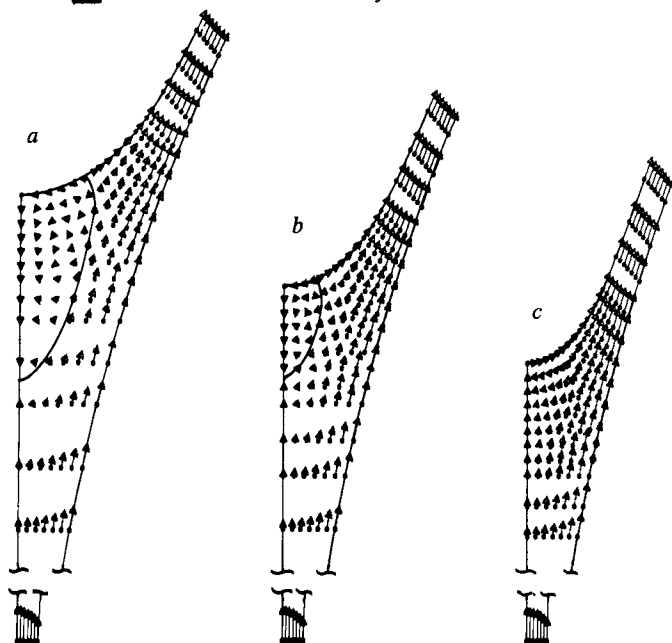


Figure 6. Effect of N_{Ca} on flow field. Key for N_{Ca} : a, 0.1; b, 0.2; c, 0.5.

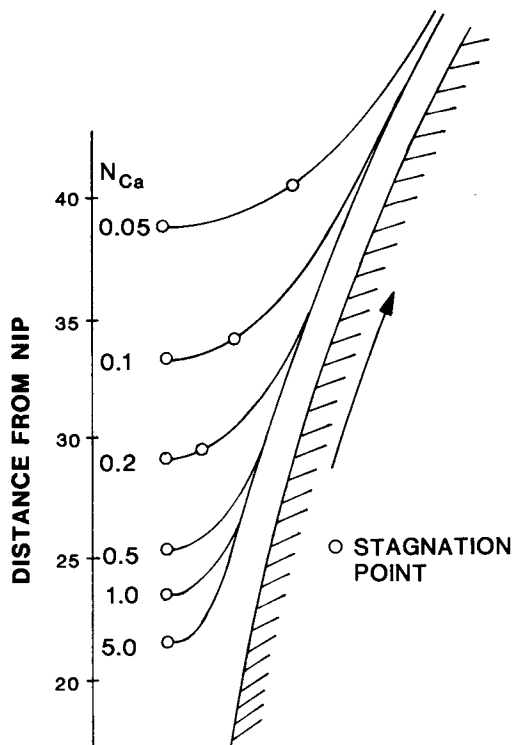


Figure 7. Free surface profiles as a function of N_{Ca} . Conditions: $N_{Re} = 0$, $N_g = 0$.

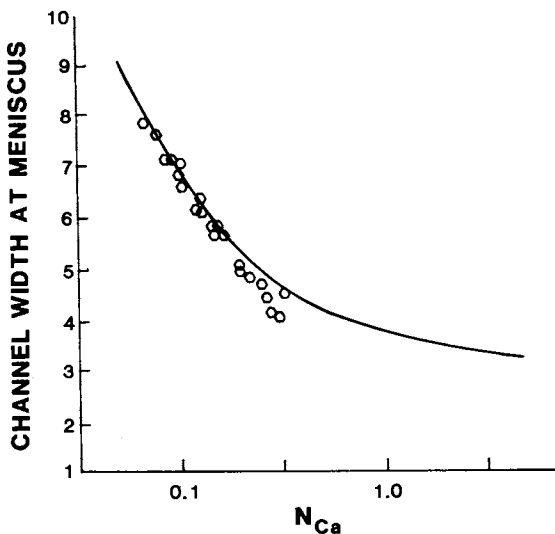


Figure 8. Comparison of theoretical calculation of film-split location (—) with experiments of Pitts and Greiller (1) (\circ).

finite element method, as shown in Figure 9. The profiles, which are for a nip completely flooded upstream at atmospheric pressure, illustrate how the pressure variation increases as the capillary number is increased at vanishing Reynolds number. Shear stress distribution on the rolls is readily predicted as well.

Results for shear-thinning fluids

Many important coating processes are of liquids that are not Newtonian, and so the effects of non-Newtonian rheology on flow between rolls is of great interest. The code used here has been applied to the simplest non-Newtonian model, namely the purely viscous, shear-thinning fluid. Viscoelasticity, though also important, is more difficult to treat and is not considered here.

One of the better models available for fitting non-Newtonian viscosity (η) as a function of shear rate is that of Carreau (15):

$$\frac{\eta - \eta_{\infty}}{\eta_0 - \eta_{\infty}} = \{1 - (\lambda\dot{\gamma})^2\}^{\frac{n-1}{2}} \quad (10)$$

where λ and n are empirical constants. This model has a Newtonian plateau, $\eta = \eta_0$, at low shear rates and a "power law" region of shear-thinning at higher shear rates. This viscosity function makes the stress a nonlinear function of the rate of strain but does not change the functional relationships in the equations. Inasmuch as the unknown free surface and the inertial terms are already nonlinear, the Galerkin finite element code is almost the same as for a Newtonian fluid; nonlinear terms representing viscous stress replace linear ones. The method of solving the equation set remains unchanged.

Some preliminary results are shown in Figure 10, and reveal that shear-thinning behavior causes the film to split further downstream of the nip and to develop larger eddies. The shear-thinning also reduces substantially the magnitudes of the maximum and minimum pressures in the nip region, as though the flow were being lubricated by the low-viscosity zones that develop where the shear rate is higher. A more detailed analysis is in progress.

Summary

Computer-aided analysis employing the Galerkin finite element method provides the means of making accurate theoretical predictions of complicated viscous free surface flows without resorting to simplifying assumptions, which are generally quite restrictive. The approach has been successfully applied to flow in a relatively simple element of roll coating, symmetric film splitting in the nip region between smooth, rigid cylindrical rolls of equal radii turning at equal speed slow enough that inertial effects are insignificant. The predicted locations of the

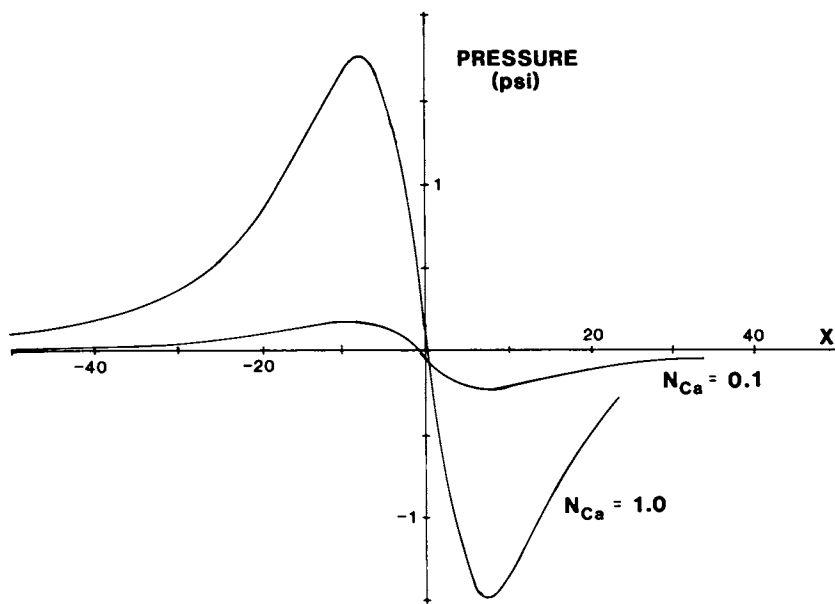


Figure 9. Pressure profiles as a function of N_{Ca} . Conditions: $N_{Re} = 0$, $N_g = 0$, $\mu = 10$ poise, $\sigma = 60$ dyne/cm.

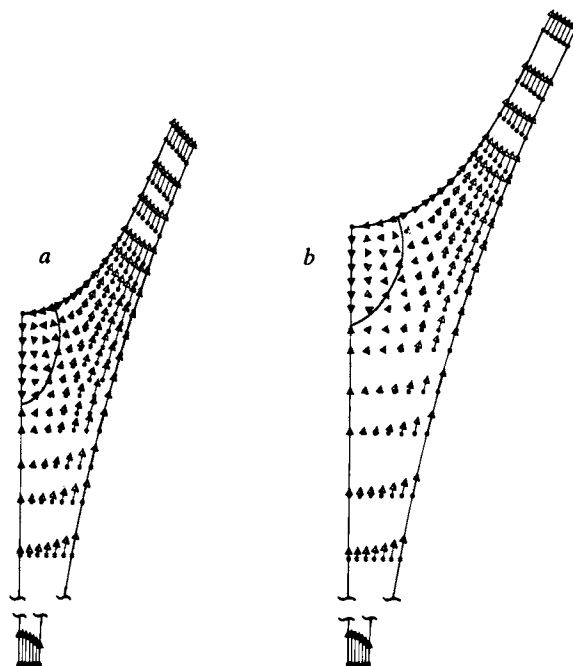


Figure 10. Effect of shear thinning rheology on the flow field ($\lambda \equiv \lambda^*V/H_0$, λ^* in s). Key: a, Newtonian; b, shear-thinning ($\lambda = 10$, $n = 0.5$).

line of film splitting agree with available experiments. The computer code for the analysis also accommodates effects of inertia, gravity, and shear-thinning rheology and has been extended to handle unsymmetric flow regimes. The variables that can be computed include pressure and shear stress profiles and forces on the rolls. The most interesting feature of the symmetric flow analyzed in this paper is the appearance and growth of a pair of counterrotating eddies immediately upstream of the central stagnation line on the liquid/gas interface where the flow splits. As surface tension σ increases relative to viscosity μ and flow speed V , the meniscus of the splitting film moves outwards, i.e. downstream, from the nip. The eddies appear when capillary number, $N_{Ca} \equiv \mu V / \sigma$, reaches a value around 0.3. Such closed recirculation zones would be deleterious were the liquid to react and degrade with time, for instance. Shear-thinning behavior by the liquid enlarges the eddies (and also moderates the pressure gradient in the nip region) in the case studied; comprehensive case studies and flow portraits will be reported elsewhere (14).

Further work is being directed to computer-aided analysis of (1) flow in other roll configurations, especially roll-wall combinations and reverse-roll coating; (2) stability of the flow to meniscus nonuniformity — "ribbing," for example; and (3) effects of viscoelasticity.

Acknowledgements

The authors would like to thank S. F. Kistler for many valuable discussions regarding finite element free surface techniques, as well as H. Saito of Fuji Photo Film Co., Ltd., and N. E. Bixler, for their advice and support. This research was funded by the 3M Company, the National Science Foundation, and the University of Minnesota Computer Center.

Literature Cited

1. Pitts, E.; Greiller, J. *J. Fluid Mech.* 1961, 16, 595.
2. Williamson, A. S. *J. Fluid Mech.* 1972, 52, 539.
3. Greener, J.; Middleman, S. *I. & E.C. Fund.* 1979, 18, 35.
4. Orr, F. M.; Scriven, L. E. *J. Fluid Mech.* 1978, 84, 145.
5. Silliman, W. J. Ph.D. Thesis, University of Minnesota, Minneapolis, MN, 1979.
6. Saito, H.; Scriven, L. E. *J. Comp. Phys.* 1980, 42, 53.
7. Saito, H.; personal communication.
8. Kistler, S. F.; Scriven, L. E., presented at AIChE Annual Meeting, 8-12 November, 1981, New Orleans.
9. Ruschak, K. J. Submitted to *J. Fluid Mech.* 1981.
10. Brown, R. A.; Scriven, L. E.; Silliman, W. J. in "Nonlinear Problems in Dynamics," SIAM. Philadelphia, 1980.
11. Bixler, N. E.; Scriven, L. E., presented at AIChE Annual Spring Meeting, February 1982, Orlando.

12. Zienkiewicz, O. C. "The Finite Element Method," McGraw-Hill, London, 1977.
13. Kistler, S. F.; Scriven, L. E., presented at AIChE Annual Spring Meeting, February 1982, Orlando.
14. Coyle, D. J.; Scriven, L. E.; Macosko, C. W., to be submitted for AIChE Annual Meeting, November 1982, Los Angeles.
15. Bird, R. B.; Armstrong, R. C.; Hassager, O. "Dynamics of Polymeric Liquids," John Wiley and Sons, New York, 1977; p. 210.

RECEIVED May 4, 1982.

Finite Element Modeling of Nonisothermal Polymer Flows

DAVID ROYLANCE

Massachusetts Institute of Technology, Department of Materials Science and Engineering, Cambridge, MA 02139

This paper describes a finite element formulation designed to simulate polymer melt flows in which both conductive and convective heat transfer may be important, and illustrates the numerical model by means of computer experiments using Newtonian extruder drag flow and entry flow as trial problems. Fluid incompressibility is enforced by a penalty treatment of the element pressures, and the thermal convective transport is modeled by conventional Galerkin and optimal upwind treatments.

Process development for polymer melt flow operations has in the past been largely empirical, due in part to the difficulty of obtaining closed-form solutions to the governing equations which satisfy the complicated boundary conditions encountered in actual equipment. The finite element method promises a significant advance in our capability to obtain numerical solutions to these processing problems, in that it is able to generate approximate solutions for irregularly shaped boundaries. In an earlier paper (1) this author described the utility of "penalty" finite elements in predicting the velocity and stress fields developed in melt processing, and this paper will describe the extension of this method to include coupled heat transport effects. It is hoped that such a capability will help the process designer avoid such processing problems as thermomechanical degradation or improperly sized equipment, and further to process materials so as to produce optimal microstructures and properties.

Formulation

The analyses to be reported here were obtained by means of isoparametric penalty elements developed at M.I.T. and incorporated within the finite element analysis program FEAP listed in the text by Zienkiewicz (2). The element formulation will be des-

0097-6156/82/0197-0265\$06.00/0
© 1982 American Chemical Society

cribed briefly here, and the reader new to finite element methodology is referred to standard texts on the subject (2,3) for a more extensive discussion of the various concepts. The description here will be that for plane flow problems, but the concepts are readily extended to axisymmetric and three-dimensional formulations as well.

The solution domain of the problem is discretized as an assemblage of elements along whose boundaries are located nodes at which velocities \underline{u}_i and temperatures T_i are sought. (The i subscript ranges over the element nodes, and underlining indicates a vector or matrix quantity.) The nodal values of the x and y components of velocity and the temperature are listed in a vector \underline{a}_i :

$$\underline{a}_i^T = (u_i, v_i, T_i) = (\underline{u}_i, T_i)$$

The values of velocity and temperature at an arbitrary position within an element can be approximated by interpolating among the nodal values:

$$\underline{u}(x,y) = N_i(x,y) \underline{u}_i$$

$$T(x,y) = N_i(x,y) T_i$$

The interpolation functions $N_i(x,y)$ are obtained from standardized subroutines and can be selected to provide linear, quadratic, or higher-order interpolation among the nodal values. This interpolation is a central concept in finite element analyses, in that the actual variation of the unknowns within an element is replaced by a low-order polynomial interpolation.

The rate-of-deformation tensor \underline{V} can be obtained from the velocity field as:

$$\underline{V}^T = (\partial u/\partial x, \partial v/\partial y, \partial v/\partial x + \partial u/\partial y)$$

$$\underline{V} = \underline{L} \underline{u} = \underline{L} N_i \underline{u}_i = \underline{B}_i \underline{u}_i$$

$$\underline{L} = \begin{bmatrix} \partial/\partial x & 0 \\ 0 & \partial/\partial y \\ \partial/\partial y & \partial/\partial x \end{bmatrix} \quad \underline{B}_i = \begin{bmatrix} N_{i,x} & 0 \\ 0 & N_{i,y} \\ N_{i,y} & N_{i,x} \end{bmatrix}$$

In the case of Newtonian fluids of viscosity μ , the deviatoric stresses $\underline{\tau}$ can be obtained from \underline{V} as:

$$\underline{\tau}^T = (\tau_{xx}, \tau_{yy}, \tau_{xy})$$

$$\underline{\tau} = \underline{D} \underline{V}$$

$$\underline{D} = \mu \begin{bmatrix} 2 & 0 & 0 \\ 0 & 2 & 0 \\ 0 & 0 & 1 \end{bmatrix}$$

The hydrostatic stress p can be obtained by considering the volumetric dilation V_v :

$$V_v = \nabla^T \underline{u} = \underline{m}^T \underline{B}_i \underline{u}_i$$

$$\nabla^T = (\partial/\partial x, \partial/\partial y), \quad \underline{m}^T = (1, 1, 0)$$

$$p = \lambda V_v = \lambda \underline{m}^T \underline{B}_i \underline{u}_i$$

Here λ is comparable to the fluid bulk modulus, and in the case of incompressible fluids can be regarded as a parameter which "penalizes" fluid compressibility. By appropriate choice of λ (generally λ is chosen as $10^7 \mu$ (4)), incompressibility can be enforced to whatever degree is desired. The total stress $\underline{\sigma}$ is then:

$$\underline{\sigma} = \underline{\tau} + \underline{m}p$$

The nodal unknowns \underline{a}_i are to be chosen so as to satisfy the governing equations in an integral sense; this can be done by using a Galerkin weighted residual formulation of the conservation equations for momentum and energy transport:

$$\int_{N_i} N_i^T (\underline{L}^T \underline{\sigma}) \, d\Omega = 0$$

$$\int_{N_i} N_i^T (\nabla^T k \nabla T + Q) \, d\Omega = 0$$

Here Ω is the element area, Q is the internal heat generation, k is the thermal conductivity, and the weighting functions N_i are the same functions used for interpolation. Using Green's theorem on the above integrals and substituting the interpolated expressions for $\underline{\sigma}$ and T , one obtains the matrix equation:

$$\underline{K} \underline{a} = \underline{f}$$

where

$$\underline{K} = \begin{bmatrix} K^\lambda + K^u & 0 \\ 0 & K^T \end{bmatrix} \quad \underline{f} = \begin{Bmatrix} f^u \\ f^T \end{Bmatrix}$$

$$K_{jk}^{\lambda} = \int (\underline{m}^T \underline{B}_j)^T \lambda (\underline{m}^T \underline{B}) \, d\Omega$$

$$K_{jk}^{\mu} = \int \underline{B}_j^T \underline{DB}_k \, d\Omega$$

$$K_{jk}^T = \int (\underline{V}^T \underline{N}_j)_k \underline{V} \underline{N}_k \, d\Omega$$

$$f^u = \int N_i \underline{t}^* \, d\Gamma$$

$$f^T = \int N_i Q \, d\Omega$$

The jk subscripts identify the influence of the velocity (or temperature) of the k th node on the force (or thermal flux) at the j th node, and the \underline{t}^* refers to tractions applied to the element boundary Γ . In these analyses Q is taken as arising only from viscous dissipation:

$$Q = \underline{\tau}^T \underline{V}$$

The FEAP code is configured to cycle through each element in turn, evaluating the various K 's and f 's by Gauss-Legendre numerical integration and adding each element's stiffness or loading to the global arrays relating all of the problem's nodal unknowns (the a 's) to the loading terms (the f 's). In the analyses to be presented below, four-node linear or eight-node parabolic quadrilateral elements were used in conjunction with 2×2 numerical integration on the K^{μ} and K^T terms. "Selective reduced integration" was used to evaluate the K^{λ} terms; this reduced integration order is necessary to prevent the large λ parameter from driving the \underline{a} vector to zero (2,4).

Iteration must be used if the coefficients in the formulation (the μ , k , Q) depend on the final solution for \underline{a} . In the solutions to be given below, the μ and k are taken as constant, and the velocity and temperature fields are coupled only through the Q term. Here only two iterations are necessary: the velocities and viscous dissipation are computed correctly in the first iteration, and the thermal values in the second.

Although momentum convection is generally negligible for polymer melt flows (Reynolds' numbers on the order of 10^{-5}), thermal convection may be significant. The ratio of convective to conductive transport is given approximately by the Peclet number Pe :

$$Pe = U h \rho c_p / k$$

Here U and h are a characteristic velocity and length, while ρ and c_p are the fluid density and specific heat. Using typical values

for down-channel extruder drag flow of low density polyethylene (5), for instance, one computes $Pe \approx 5000$.

Thermal convection can be incorporated in the finite element analysis by adding to the K^T terms the quantity

$$K_{jk}^c = \int N_j \rho c_p \underline{u}^T \nabla N_k \, d\Omega$$

Incorporation of this term is straightforward, since the velocities \underline{u} are known after the first iteration. The convective terms are unsymmetric, however, which requires using less efficient storage and solution schemes than are possible for symmetric systems. Even more seriously, inclusion of convective transport effects tends to produce numerical instability in the computed results, as will be illustrated below.

Down-channel Extruder Flow

The capabilities of the coupled flow-heat transfer model will be illustrated first by means of a simulation of down-channel extruder flow, which may be modeled by the usual unwound-channel approximation as a straight rectangular channel containing fluid which is being dragged downstream by a plate covering the channel top (1,5). This is the well-known Couette flow problem, and is useful as a model problem both by virtue of its relevance to extruder flow and by the availability of theoretical solutions against which the numerical results may be checked. Figure 1 shows the normalized velocity and temperature distributions across the channel height, where the drawn curves are the theoretical predictions and the open symbols are the numerical values obtained using a 4 x 4 mesh of eight-noded parabolic elements. The theoretical temperature variation is given as

$$T^* = (Br/2)y^* (1-y^*)$$

Here y^* is the height from the root of the channel normalized on the total channel height, $T^* = (T-T_w)/T_w$ is the temperature relative to the wall temperature, and $Br = \mu V^2/K$ is a Brinkman number which provides an indicator of the importance of viscous dissipation relative to heat conduction. The numerical results of Figure 1 were obtained with $Br = 8$.

Figure 2 displays the results of a simulation of a slightly more complicated extension of the problem of figure 1. Here the root and barrel temperatures are different, and the flow is retarded by the presence of a pressure gradient which is positive in the downstream direction. This simulation is more typical of extruder operation, in which the barrel but not the screw is heated and the constriction at the die produces a pressure gradient.

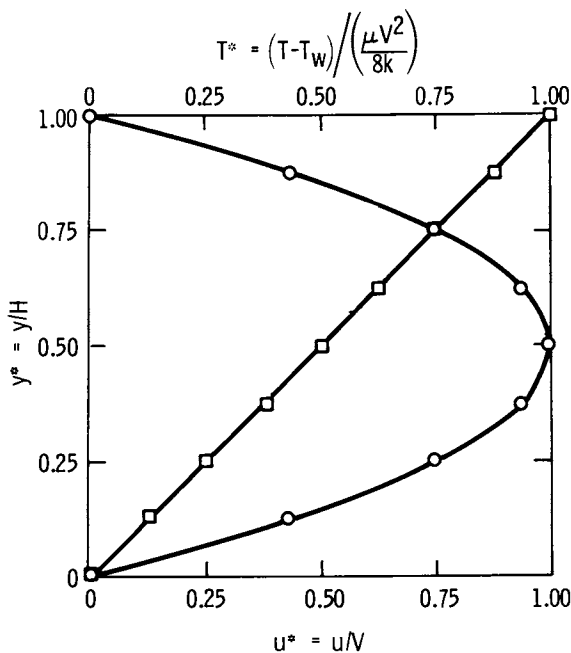


Figure 1. Normalized velocity and temperature distributions in Couette flow.
Key: \square , u^* vs. y^* ; \circ , T^* vs. y^* .

$$u^* = u/V \quad T^* = (T - T_w) / (\mu V^2 / 8k) \quad y^* = y/H$$

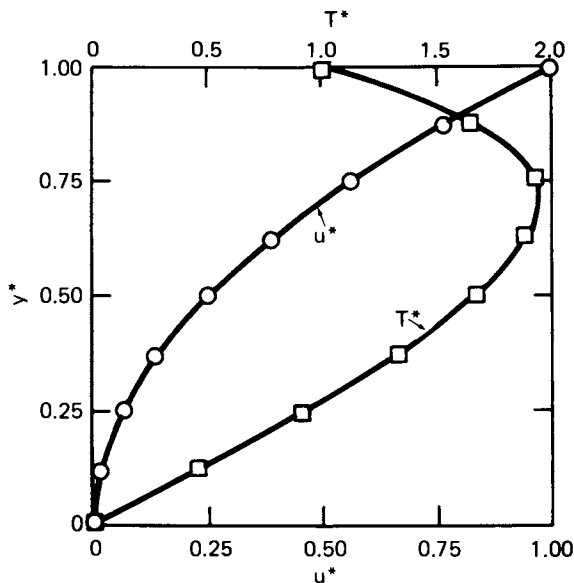


Figure 2. Couette flow with imposed pressure gradient and different root and barrel temperatures. Key: \circ , u^* vs. y^* ; \square , T^* vs. y^* .

Entry Flow

Entry flow is a much-studied problem which provides a more demanding test of numerical codes than does the viscometric Couette flow problem described above. Theoretical and numerical aspects of this flow have been reviewed recently by Boger (6), and comparison with these other results provide a check of at least the flow aspects of the model. A reservoir-to-capillary size ratio of 4:1 was selected, since the flow results become independent of size ratio at this value or larger. Figure 3 shows the grid of 100 four-node linear elements used to model the upper symmetric half of this problem (273 degrees of freedom), and the portion of the velocity field near the throat. A fully-developed Poiseuille velocity distribution was imposed on the entrance to the reservoir. The velocity distribution in the capillary becomes stable within a few diameters of the entrance, but the field is perturbed far upstream. Figure 4 shows the streamlines developed from the flow field by contour integration along vertical lines through the grid, and normalized so as to be zero along the boundaries and unity along the centerline. These streamlines are identical with published experimental and numerical results, although the grid used here was not intended to be fine enough to capture the weak recirculation which develops in the stagnant corner of the reservoir.

Figure 5 shows the contours of shear stress near the throat, normalized on the theoretical value expected at the capillary wall. The shear contours are in agreement with the isochromatic fringes seen in birefringence photography of entry flow (7), which is an example of a possible experimental verification of the flow model.

Although certain grids using the penalty formulation are known to develop a pathology known as "checkerboarding" in which the computed pressures oscillate from element to element (4), this grid is free of that troublesome (but fixable) result. Figure 6 shows the profile of computed pressures along the elements adjacent to the centerline, normalized on the value expected in the reservoir in the absence of entry or exit pressure losses. As is well known, the development of the flow field at the entrance to the capillary produces an additional pressure drop which must be accounted for in capillary viscometry by means of a "capillary correction factor." The correction factor, defined as the entrance pressure drop ΔP_{ent} divided by twice the capillary wall shear stress, is given by Boger as 0.589 based on the numerical and experimental work of several workers. The value computed from the data of figure 6 is 0.594, which is within 1% of Boger's value.

As described above, the temperature field is computed using the finite element formulation of the heat conduction equation, with the viscous heat generation being computed from the stress and velocity fields obtained during the first iteration of the problem. The temperature contours, normalized on the maximum centerline temperature $T_c = \mu v^2 / 3K$ expected for capillary Poiseuille

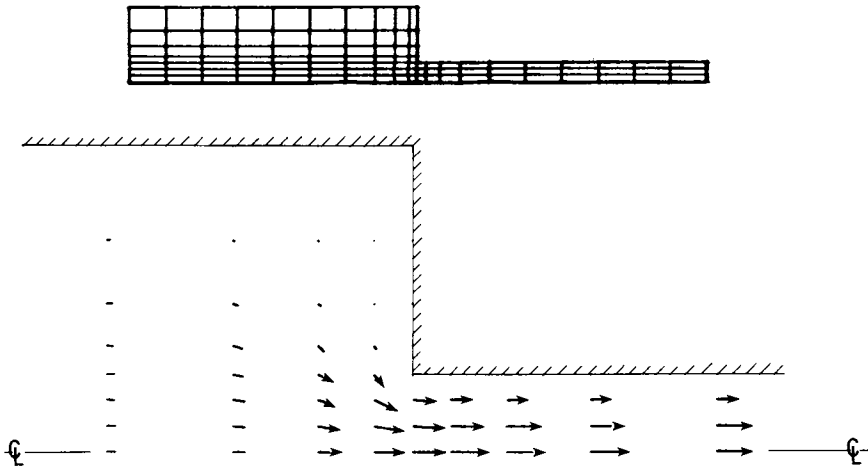


Figure 3. Finite element mesh and computed velocity field for 4:1 entry flow.

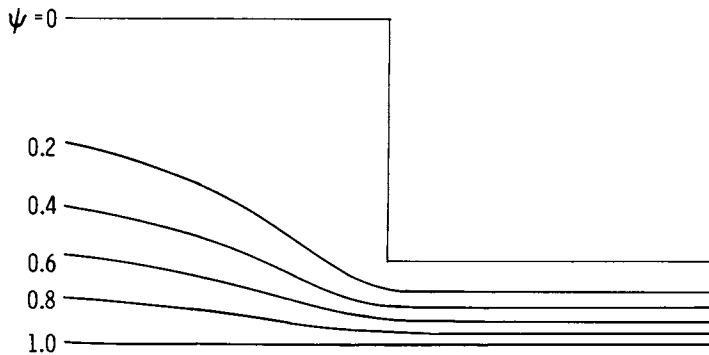


Figure 4. Entry flow streamlines.

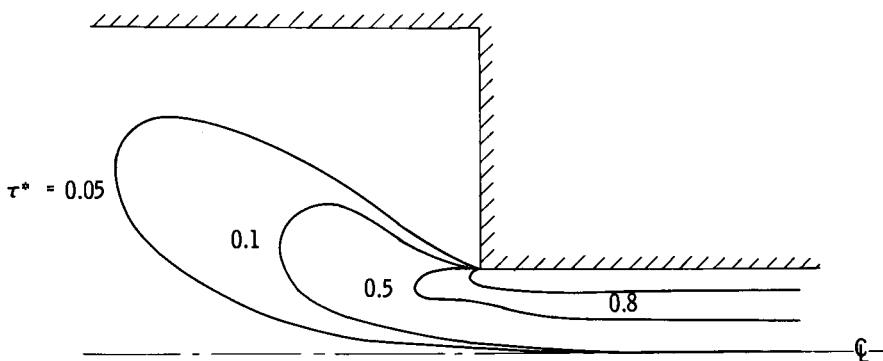


Figure 5. Shear stress contours for 4:1 entry flow.

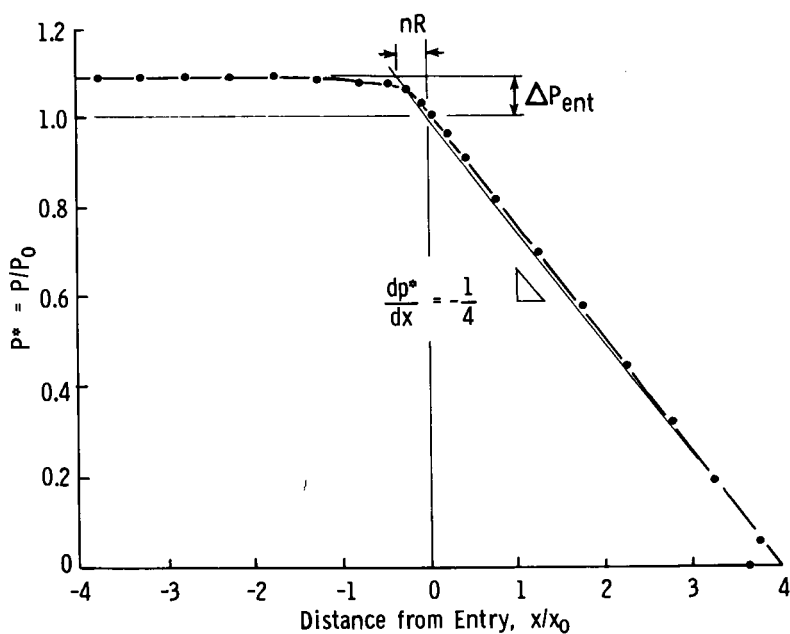


Figure 6. Normalized pressures along centerline.

flow, are shown in Figure 7. A hot spot is noted just upstream of the entrance, due to the combination of increased dissipation and greater distance from the cooler boundaries at this position. This hot spot leads to higher temperatures both upstream and downstream than would have been expected in simple Poiseuille flow, due to conductive heat transfer from the hot region.

The temperature map of Figure 7 is for $Pe = 0$, the case for which convective terms are not included in the heat transport calculations. Whereas all convective terms vanish identically in the Couette flow described in the previous section, convective terms are present in the entry flow problem, and these might be expected to be significant for many real problems in the flow of polymer melts through dies. Figure 8 shows the profile of temperatures along the centerline for several values of Peclet number (Pe based on the capillary half-height and the maximum velocity). It is seen that increasing convective transport serves to carry the cooler upstream particles downstream so as to diminish both the magnitude of the hot spot and its ability to conduct heat upstream. As Pe increases, the influence of the entrance region is compressed into a smaller and smaller boundary layer at the throat, leading to numerical difficulties associated with the inability of the fixed mesh to capture effects which occur in the smaller region. At $Pe = 10$, the values computed by the conventional Galerkin process (solid lines) suffer from noticeable instability, and by $Pe = 100$ the Galerkin solution has degenerated completely to meaningless values.

The instability associated with convection analyses has plagued both finite difference and finite element analyses, and in recent years several ad hoc treatments have been proposed for obtaining stable and nonoscillatory results in the presence of strong convective terms. One of the most popular of these treatments is "upwinding," in which the upstream portion of the interpolation is weighted more heavily in an attempt to smooth out the high local downstream gradients which cause the problem in convective flows. The dotted lines in Figure 8 were obtained using a convenient "optimal" upwinding formulation suggested by Hughes (4), in which the upwind weighting is obtained simply by relocating the integration point at which the element shape functions are evaluated. The position of the upwind point is determined for each element based on its local Peclet number, so that optimum results may be obtained. Figure 8 shows that the upwind solution for $Pe = 10$ is considerably smoother than the Galerkin result, and that the results for $Pe = 100$ in which the upstream temperatures are carried well into the capillary are captured in a smooth and reasonable manner. The reader is cautioned, however, that the use of these upwinding procedures is still controversial, and is directed to a provocative paper by Gresho and Lee (8) in which the drawbacks of this approach are detailed.

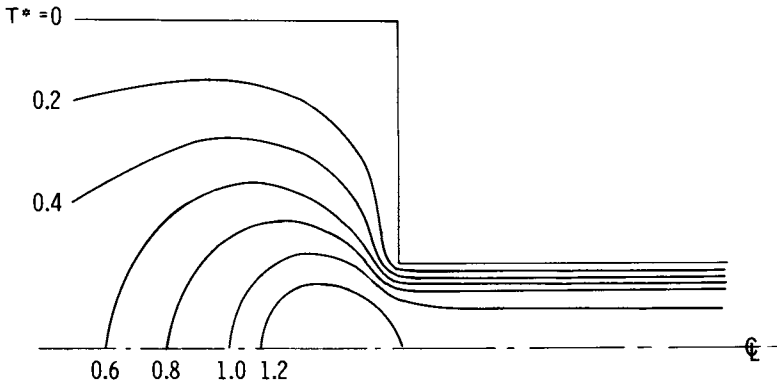


Figure 7. Temperature contours for 4:1 entry flow, $Pe = 0$.

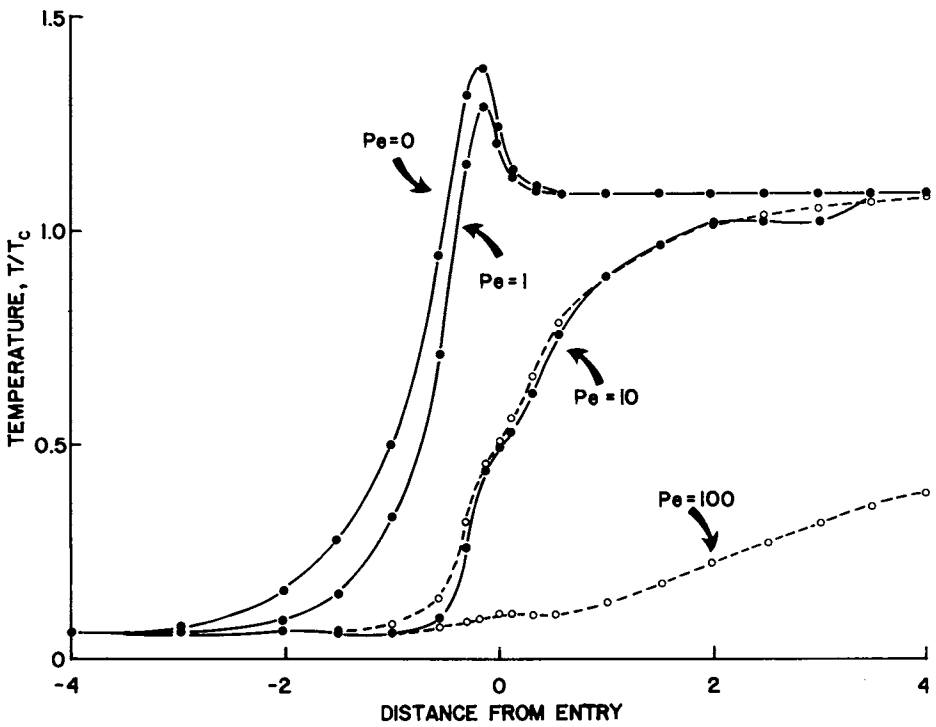


Figure 8. Centerline temperatures at various Peclet numbers. Key: ●, Galerkin; ○, upwind.

Conclusion

This paper has described an analytical tool which can predict velocities, stresses, and temperatures in nonisothermal flow situations of the sort encountered in many polymer melt processing operations. Such a model cannot be expected to replace the experience and intuition which provide the basis for most process design today, but it is hoped that this inexpensive and easily implemented model can provide a means by which the process designer's intuition might be expanded. Properly used, it can be a valuable additional tool at the process designer's disposal.

Development of this model is continuing in our laboratory, and among the aspects still under development are capabilities for transient flows, reactive fluids, free surfaces, and wall slip. Although incorporation of fluid elasticity is desired due to its importance in many polymer melt flows, such a development has proven elusive to a number of well qualified groups in the past several years. At present, it seems prudent to let the theoretical aspects of elastic effects be developed further before attempting their incorporation in a general process model.

Acknowledgements

The author gratefully acknowledges the support of this work by the Army Materials and Mechanics Research Center, and by the National Aeronautics and Space Administration through M.I.T.'s Materials Processing Center.

Literature Cited

1. Roylance, D. Polym. Eng. Sci. 1980, 20, 1029-34.
2. Zienkiewicz, O.C. "The Finite Element Method"; McGraw-Hill: London, 1977.
3. Segerlind, L.J. "Applied Finite Element Analysis"; John Wiley: New York, 1976.
4. Hughes, T.R.J.; Liu, W.K.; Brooks, A. J. Comp. Physics 1979, 30, 1-60.
5. Tadmor, Z.; Klein, I. "Engineering Principles of Plasticating Extrusion"; Van Nostrand Reinhold: New York, 1970.
6. Boger, D.V. "Circular Entry Flows of Inelastic and Viscoelastic Fluids"; to appear in "Advances in Transport Process"; Wiley International.
7. Han, P. "Rheology in Polymer Processing"; Academic Press: New York, 1976; pp 98-105.
8. Gresho, P.M.; Lee, R.L. Computers and Fluids 1981, 9, 223-253.

RECEIVED May 4, 1982.

Measurement of Polarization in Thermoplastic Elastomers with Application to Morphology Studies

M. A. VALLANCE and S. L. COOPER

University of Wisconsin—Madison, Department of Chemical Engineering,
Madison, WI 53706

The measurement of electrical polarization is proposed for studying morphological heterogeneities down to the nanometer size range in segmented copolymers such as segmented polyurethanes. The technique relies on measurement of frequency-dependent, electric polarizations related to frequency-dependent, electric-field redistribution in microdomains of unequal permittivity and conductivity. Due to the low overall conductivities of typical polymers, the polarizations usually become significant at subaudio frequencies. The construction of two processor-aided dielectric spectrometers designed for use in the frequency range 10^{-4} to 10^{+2} Hz are described. Spectra for segmented polyether-polyurethanes and a polyether-polyester are compared to an adjustable model of the polarization process. From these comparisons and DSC results, a correlation between intradomain ordering and lamellar morphology is seen in such polymers. There appears to be a relation between the asymmetry of the polarizations' frequency dependence and the character of the diffuse transition zones between dissimilar microdomains.

Segmented polyurethanes and related thermoplastic elastomers are block copolymers with $(AB)_n$ chemical architecture where A and B are segments of dissimilar homopolymers. These copolymers are synthesized in one or two steps by condensation. As an example, a typical segmented polyurethane might be formed by reacting excess diisocyanate with a polyol "soft" segment which in turn could be reacted with a diol chain extender to form the "hard" segments. The resulting polymer is composed of many segments (n averages 10 to 100), while the individual segment lengths are broadly distributed about a relatively short average length (number average segment molecular weights typically range 500

0097-6156/82/0197-0277\$06.00/0
© 1982 American Chemical Society

to 5,000). In almost all cases thermodynamic forces drive the system towards segregation of A and B segments. However, the chemical architecture constrains the microdomains so formed to have dimensions on the order of 10 nm. The resulting "micro-composite" morphology exhibits elastomeric properties if the use temperature is selected intermediate to the solid-melt or glass transition temperatures of the two phases. In this case the rigid, hard-segment rich domains act as virtual crosslinks and filler particles for the viscous, soft-segment rich phase.

Thermodynamic treatments of block copolymer morphology, such as those of Helfand (1,2,3) and Meier (4), which are based on anionically polymerized, monodisperse segment AB and ABA type block copolymers, are not applicable in the present case. The large number of short segments in each molecule, the possibility of crystallinity in one or both phases, and the likelihood of metastable morphologies work together to preclude the analytical approaches presently available.

The most direct experimental technique for observing the morphology is transmission electron microscopy. Although several micrographs of segmented polyurethane morphologies are recorded in the literature showing nodular textures of reasonable periodicity (5,6,7), a recent mathematical analysis has shown that in all probability these textures are defocus artifacts (8). A recent study of an OsO₄ stained, solution-cast, semicrystalline, segmented polyurethane has produced micrographs which show more detail (9). Nonetheless, lack of contrast and the difficulty of producing sufficiently thin foils with representative morphologies render TEM unsuitable for general use.

Measurement of small-angle x-ray scattering (SAXS) has recently gained in stature for use in morphological investigations. This technique provides information regarding the periodicity and magnitude of electron density fluctuations. The technique has been used on segmented polyurethanes and related polymers to study domain spacing, phase purity, and the width of the transition zone between dissimilar domains (10,11,12).

In the present study we have used a relatively new technique to study the morphology of these systems. Application of an alternating electric field to a multiphase morphology results in a frequency-dependent electric-field distribution due to the different permittivities and conductivities of dissimilar phases. Measured permittivity increases with decreasing frequency $\nu = \omega/2\pi$, approaching a low frequency limit ϵ_0 as the field distribution transits from permittivity dominated to conductivity dominated. For most simple two-phase geometries the frequency dependence of the polarization approaches a simple overdamped resonance:

$$\hat{\epsilon}(\omega) = \epsilon'(\omega) - j\epsilon''(\omega) = \epsilon_\infty + (\epsilon_0 - \epsilon_\infty)/(1 + j\omega/\omega_m) \quad (1)$$

where $\hat{\epsilon}$ is the complex permittivity of which ϵ' and ϵ'' are the

real and imaginary parts. The parameters ϵ_{∞} and ω_m are the high frequency limit of ϵ' and the "damped resonant frequency". The imaginary component ϵ'' vanishes in the high and low frequency limits while peaking at $\omega = \omega_m$. If equation (1) is solved for ϵ'' in terms of ϵ' , whereby ω dependence can be eliminated, it is seen that the equation has the form of a semicircle. As will be shown ϵ_0 , ϵ_{∞} , and ω_m are in part determined by morphology so that experimental determination of these quantities will provide certain morphological insights. A complication is the divergence of most real spectra from the dependence of equation (1). A discussion of a possible source of the divergence is included in the discussion of measured spectra.

Interfacial polarizations have been recorded for many multi-phase solid-state polymer systems: semicrystalline polyamides and polyurethanes (13), segmented polyurethanes (14), segmented polyesters (15,16), polyethylene oxide-polystyrene diblock copolymers (17), and styrene-butadiene-styrene triblock systems (18). In general, due to the low conductivities of polymeric solids, the polarizations are found at subaudio frequencies, where standard bridge experiments do not operate. In order to study these polarizations two processor-controlled dielectric spectrometers have been designed to operate in this frequency range. One uses low-frequency, A.C. excitation in conjunction with cross-correlation analysis while the other uses step excitation with Laplace-transform analysis. The remainder of this paper includes descriptions of the apparatus, a theoretical context in which to view the measured spectra, and the presentation and analysis of some experimental data.

Dielectric Spectrometers

Dielectric spectroscopy can be carried out by observing a material's steady-state response to an oscillating electric field or by observing the transient response to a single event such as a step change in field. The simplest sample geometry in either case is that of the dielectric in a parallel-plate capacitor. Edge effects are minimized by the use of a three-terminal, guard-ring configuration. Typical disk-shaped samples measure 1.5 cm in diameter and 0.01 cm in thickness. The experiment is set up so that the sample resides in a vacuum or a desiccated nitrogen atmosphere, thus minimizing water regain in hygroscopic polymer systems. Good practice dictates the application of integral metallic, usually gold, coatings to the flat surfaces of the sample. This provides for low-impedance electrical contact.

The apparatus used, with slight modifications, is the same for both experiments. The processor is a DEC LSI 11/3 with 64K bytes of RAM. Communication with the processor is done using a CRT terminal. A pair of double-density, flexible-disk drivers are used for storage of software and data. Other system components include a 1 MHz programmable timer, 12-bit A/D and

D/A converters, and a digital plotter. A Nicolet Explorer III digital oscilloscope capable of high-speed data acquisition is interfaced to the processor via 45 TTL lines which provide high speed data transfer in both directions. The oscilloscope is used principally for high frequency (10^{-2} to 10^{+3} Hz) testing and served only as back-up in the present cases. For transducing currents in the nano- to picoampere range a Keithly 427 current amplifier is used with adjustable rise time down to 10 μ s.

Steady-State Experiment. A simple harmonic signal in the frequency range 20 Hz and down is synthesized by stepping the output at a D/A converter at equally spaced intervals up to 5,000 times per cycle. The amplitude is selected up to 10 volts. The resulting signal, which is somewhat notchy, is smoothed by low pass filtering (fourth-order Butterworth). Figure 1 is a schematic of the experiment. The filtered signal is applied to the sample cell while the sample's current response is monitored at the guarded measurement electrode. Because of the low-level currents involved, shielded cable and shock mounting are used throughout the system. Remaining noise can be eliminated by selection of a suitably high rise time on the current amplifier. Proportional voltage output of the current amplifier and the filtered driving signal are simultaneously sampled over one complete cycle at up to 5,000 equally spaced intervals once steady state response is attained. The volume-average electric field $f(\omega t)$ and the volume-average current density through the sample $i(\omega t)$ can be represented as

$$f(\omega t) = F \cos(\omega t + \alpha) \quad (2)$$

$$i(\omega t) = I \cos(\omega t + \beta) \quad (3)$$

Cross correlation is used to calculate F, I, and $\beta - \alpha$ while simultaneously providing digital filtering of higher harmonics (19).

$$F \exp(-j\alpha) = (1/\pi) \int_0^{2\pi} f(\omega t) \exp(j\omega t) d(\omega t) \quad (4)$$

$$I \exp(-j\beta) = (1/\pi) \int_0^{2\pi} i(\omega t) \exp(j\omega t) d(\omega t) \quad (5)$$

The algorithms for these integrations are

$$F \exp(-j\alpha) \approx (2/n) \sum_{k=1}^n f_k \exp(j\omega t_k) \quad (6)$$

$$\text{Iexp}(-j\beta) \approx (2/n) \sum_{k=1}^n i_k \exp(j\omega t_k) \quad (7)$$

where f_k and i_k are the field and current density measurements at time t_k when n samples have been converted over one cycle. Systematic instrumental phase shifts and amplitude distortions are compensated by subsequent repetition of the experiment with the sample cell replaced by a loss-free, precision, adjustable capacitor. The complex permittivity $\hat{\epsilon}$ is easily calculated from the relation (20) (Generalized complex permittivity $\hat{\eta}$ should formally replace complex permittivity $\hat{\epsilon}$ in this expression, as will be explained in the next section):

$$\hat{\epsilon} = \epsilon' - j\epsilon'' = -(jI/\omega F)\exp[j(\beta-\alpha)] \quad (8)$$

The experiment must be repeated at every frequency of interest. Experimental accuracy and resolution are better than 0.25% in $|\hat{\epsilon}|$ and 0.001 radians in $\delta = \arctan(\epsilon''/\epsilon')$ over most of the range down to 10^{-4} Hz.

Transient Response Experiment. The transient response experiment is shown schematically in Figure 2. The sample is charged by a signal from the D/A converter with amplitude up to 10 volts through a TTL-activated reed switch. Charging continues until current through the sample reaches a steady value, indicative of the steady electrical conductivity of the polymer. Subsequently, at time zero, the reed switch is reversed, causing the polarized sample to discharge in a closed loop. At some time after zero, t_1 , A/D conversions of the current amplifier output are commenced, and are made to occur at increasing intervals in a logarithmic progression until such time t_n as the current response has decayed substantially to zero. The A/D converter, which is range programmable (10, 5, 2 or 1 volts), is programmed to operate in an autoranging mode, increasing its dynamic resolution by a factor of 10. In spite of this, the broad range of current magnitudes to be measured, 8 logarithmic decades, dictates that the experiment should be repeated several times, each time resetting the amplification and rise time of the current amplifier to optimize the circuit for measurements in a given time interval. The several data sets can then be recombined for subsequent data analysis. The complex permittivity $\hat{\epsilon}$ at any frequency can be calculated by Laplace transform (or half-space Fourier transform) (20):

$$\hat{\epsilon} = \epsilon' - j\epsilon'' = \mathcal{L}_{j\omega} [i(t)/F] = \int_0^{\infty} [i(t)/F] \exp(-j\omega t) dt \quad (9)$$

where $i(t)$ is the transient, volume-average, current density response through the dielectric and F is the applied volume-

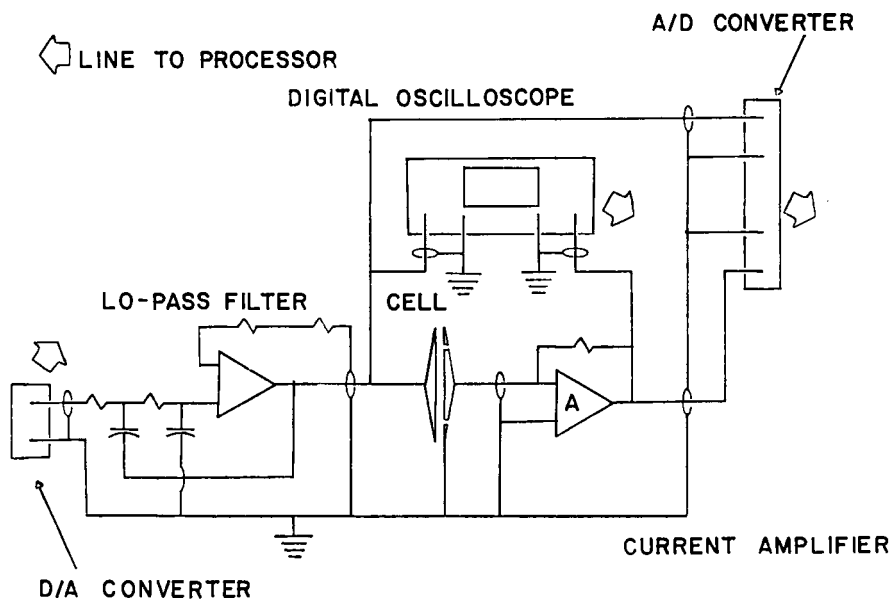


Figure 1. Electrical schematic for the steady-state response dielectric spectrometer.

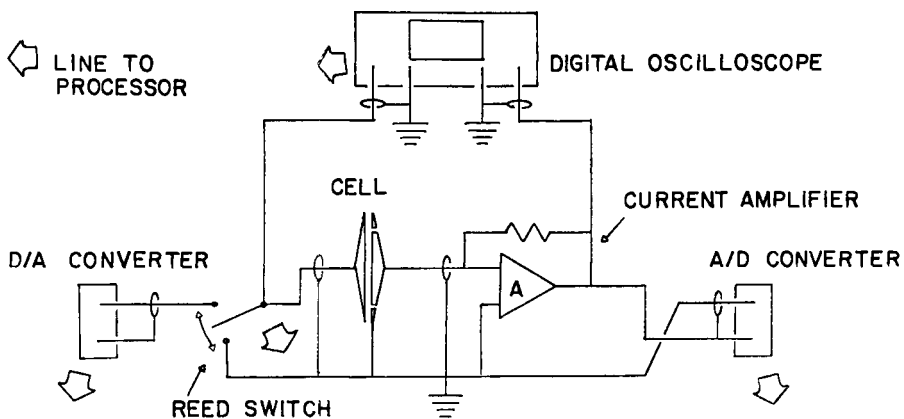


Figure 2. Electrical schematic for the transient response dielectric spectrometer.

average electric field during charging. The same response data are used to calculate $\hat{\epsilon}$ at all frequencies of interest. Since data are taken over a finite interval t_1 to t_n , and not 0 to ∞ , certain approximations must be made. By assuming that $i(t) = 0$ for $t > t_n$ and by choosing all ω values so as to keep ωt_1 small (for instance, less than 0.1):

$$\begin{aligned} \hat{\epsilon} &= \int_0^{t_1} [i(t)/F] \exp(-j\omega t) dt + \int_{t_1}^{t_n} [i(t)/F] \exp(-j\omega t) dt + \int_{t_n}^{\infty} [i(t)/F] \exp(-j\omega t) dt \\ &\approx \int_0^{t_1} [i(t)/F] (1-j\omega t) dt + \int_{t_1}^{t_n} [i(t)/F] \exp(-j\omega t) dt \\ &\approx (k' - j\omega k'') + \int_{t_1}^{t_n} [i(t)/F] \exp(-j\omega t) dt \end{aligned} \quad (10)$$

The positive constants k' and k'' can be evaluated if $\hat{\epsilon}$ can be independently evaluated at some frequency ω_r :

$$\hat{\epsilon}(\omega_r) \approx (k' - j\omega_r k'') + \int_{t_1}^{t_n} [i(t)/F] \exp(-j\omega_r t) dt \quad (11)$$

To evaluate the integral in equation (10) a suitable shape function must be used to approximate $i(t)$ which is known only at discrete times. A polynomial of degree one is chosen, so that on the interval $t_k \leq t \leq t_{k+1}$:

$$i(t) \approx [i_{k+1}(t-t_k) + i_k(t_{k+1}-t)]/[t_{k+1}-t_k] \quad (12)$$

Although it is tempting to choose a polynomial shape function of higher degree as did North, *et al.* (14), such a procedure should be avoided. Contributions from noise and conversion round-off error lead to large distortions when such functions are substituted into equation (10), particularly at low frequencies. The level of numerical error introduced by the use of equation (12) can always be reduced by selecting more closely spaced sampling times. For the present study, a sampling rate of approximately 14 per time decade was chosen. The convenience of data acquisition available with the transient experiment must be balanced against the necessity of introducing several nontrivial approximations and the need for auxiliary test data. Another drawback of this approach is that while instrumental artifacts can be minimized by wise choice of circuit parameters, they cannot

be systematically eliminated as is the case with the steady-state approach. A comparison of the two techniques on real polymer systems has shown them to be in excellent agreement (21,22), although the transient experiment used in that case was somewhat different from the one described here.

Analytical Modeling of Interfacial Polarization

There are a number of models for polarization of heterogeneous systems, many of which are reviewed by van Beek (23). Brown has derived an exact, though unwieldy, series solution using point probability functions (24). For comparison to spectra for the thermoplastic elastomers of interest here, the most useful model seems to be the one derived by Sillars (25) and, in a slightly different form, by Fricke (26). The model assumes a distribution of geometrically similar ellipsoids with major radii, r_1 , r_2 and r_3 which are randomly oriented and randomly distributed in a dissimilar matrix phase. Only non-specific interactions between neighboring ellipsoids are included in the model. This model includes no contribution from the polarization of mobile charge carriers trapped on the interfacial surfaces. The interfaces in multiphase segmented copolymers are diffuse. Furthermore, in the case of the purified polymer systems being studied, there is no evidence for a differentiable trapping mechanism in the interfacial regions. The frequency-dependent complex permittivity $\hat{\epsilon}$ is calculated from (26):

$$\hat{\epsilon} - j\hat{\sigma}/\omega = \hat{\eta}_1 \left\{ 1 + (v_2/3)(\hat{\eta}_2 - \hat{\eta}_1) \sum_{k=1}^3 [\hat{\eta}_1 + A_k v_k (\hat{\eta}_2 - \hat{\eta}_1)]^{-1} \right\} \quad (13)$$

where $\hat{\eta}_i = \epsilon_i - j\sigma_i/\omega$, the subscript i referring to the first (matrix) or second (ellipsoidal) phase. Respectively, ϵ_i , σ_i and v_i are the permittivity, conductivity, and volume fraction of the i th phase. The A_k are given by:

$$A_k = (r_1 r_2 r_3 / 2) \int_0^{\infty} ds / \{ (s+r_k^2) [(s+r_1^2)(s+r_2^2)(s+r_3^2)]^{1/2} \} \quad (14)$$

The left side of equation (13) includes the complex conductivity $\hat{\sigma}$. Due to the frequency-dependent redistribution of electric field in the frequency range of the polarization, the measurable conductivity of the multiphase medium also changes with frequency. Generally the conductivity term in the left balance of equation (13) is negligible at higher frequencies, but becomes important for small ω , where $\hat{\sigma}$ approaches a real, limiting value, indicative of D.C. conductivity. The two spectrometers of the last section actually measure $\hat{\eta} = \hat{\epsilon} - j\hat{\sigma}/\omega$, the generalized complex permittivity, so that straightforward comparisons between model calculations and experimental spectra are possible.

Equation (13) predicts three superimposed polarizations of the type in equation (1) associated with the three principal axes of the ellipsoidal interfaces. The frequency dependence is given by:

$$\omega_{m,k} = [\sigma_1 + A_k v_1 (\sigma_2 - \sigma_1)] / [\epsilon_1 + A_k v_1 (\epsilon_2 - \epsilon_1)] \quad (15)$$

Due to mesophase symmetries and/or order of magnitude strength differences between the three polarizations, model calculations often predict polarizations with frequency dependencies close to that of equation (1).

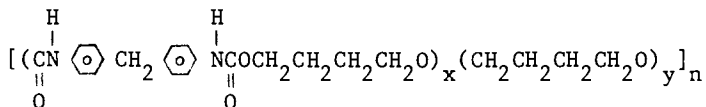
As has been mentioned for thermoplastic elastomers at their use temperatures, one phase is rubbery while the other is glassy. Saito, *et al.* (27) have shown that the conductivity of a polymer above its glass transition temperature T_g increases orders of magnitude with heating over a few tens of degrees. On the other hand, glassy polymers exhibit a very low, temperature-independent conductivity. It seems prudent then to assume the hard phase conductivity negligible in equation (13) as it always appears in a difference expression with the soft phase conductivity; this assumption leads to considerable simplification. In the polymer systems to be used for this study the hard phase occupies a considerably smaller volume fraction than the soft phase, and is therefore chosen to be the ellipsoidal phase. To the extent that both phases may be continuous, this modelling approach must be viewed as an approximate treatment. Since the approach is at best an approximate one, little will be lost by assuming the hard particles to possess spheroidal symmetry ($r_1 = r_2$).

Equation (13) with the above considerations was used to draw the curves in Figure 3. The unitless relative permittivities e_0 , e_∞ , e_1 and e_2 are obtained by normalizing the absolute quantities by the permittivity of vacuum: $e = \epsilon/\epsilon_v$. Spheroidal symmetry is assumed about the c axis in the figure. Several features, of Figure 3 are worth noting: (a) the e_0/e_∞ (polarization strength) curves, which are plotted for constant e_2/e_1 as a function of axial ratio, all have a minimum for the case of spherical inclusions; (b) the strength of the polarization increases with increasing hard domain permittivity; and (c) in the case where inclusions tend to be flake-like in shape extremely large polarization strengths are realized. The use of this model in the interpretation of real data is demonstrated in the next section.

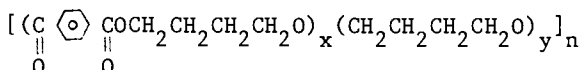
Interpretation of Polymer Spectra

Two comparison studies are discussed in this section: the first involves spectra measured with the steady-state, A.C. spectrometer while the second study involves data measured with the transient response spectrometer.

A Polyester and a Polyurethane. A segmented polyether-polyurethane sample (UET46-1) was synthesized in one step from 4-4' diphenyl methane diisocyanate, 1-4 butanediol and poly(tetramethylene ether)glycol:



A segmented polyether-polyester (H49) was synthesized via melt transesterification from 1-4 dimethyl terephthalate, 1-4 butanediol and poly(tetramethylene ether)glycol:



Both polymers have polyether (PTMO) segment number average molecular weights $\langle M \rangle$ near 1,000. UET46-1 is 46% by weight polyurethane and H49^y is 49% polyester. Since the hard domains are rich in polyester or polyurethane segments and the viscous domains are dominated by polyether segments, the common notation of hard and soft segments pertaining to polyester (or polyurethane) and polyether segments, respectively, is adopted. Prior to molding, both samples were purified by being dissolved in organic solvents and subsequently precipitated by the slow addition of non-solvents. After vacuum drying, test samples were compression molded at 225°C for 5 minutes followed by quenching in air. Samples were subsequently annealed at 125°C in vacuum for at least 24 hours followed by high-vacuum desiccation, application of gold electrodes and a 150-hour, 24°, stabilization period in vacuum.

From the similarities in chemical architecture of these two polymers, as well as from their similar processing histories, some degree of morphological equivalence is expected. Both polymers possess two-phase morphologies as demonstrated by differential scanning calorimetry (DSC). At sub-ambient temperatures the DSC spectra show glass transitions, thought to be soft-phase phenomena. Above room temperature both systems demonstrate endothermic processes related to disruption of hard phases. These events are summarized in Table 1.

The glass transitions of these two systems are shifted to temperatures well above that of the PTMO homopolymer (-88°C) due to hard and soft segment mixing in the soft phase and due to constraints on the mobility of the short soft segments, which are terminated by hard segments residing in either phase. The endotherms occur far below the melting temperatures of the respective hard segment homopolymers (222°C for the polyester and 228°C for the polyurethane). The cause may be equilibrium melting point depression due to the small segment size (28,29), or it may be

Table I

Chemical Architecture and Thermal Properties
(DSC, 20°C/min) for H49 and UET46-1

	H49	UET46-1
PTMO weight fraction	0.51	0.54
$\langle M_y \rangle$	1,000	1,000
glass transition (°C)	-65	-54
endotherm (°C)	189	163

that lattice strains associated with imperfect crystallinity are influencing crystalline stability. A major difference between the two systems is that while H49 is opaque, UET46-1 is transparent. The opaqueness of H49 is due to the presence of light-scattering spherulites (30). If UET46-1 has a spherulitic morphology, the spherulites must be relatively small in size or possess an isotropic refractive index similar to that of the amorphous phase of the polymer.

Figures 4 and 5 show the $\hat{\epsilon}(\omega)$ spectra for these two systems as measured at 24°C. Both systems exhibit polarizations of very large strength ($e_0/e_\infty > 3$) over narrow, subaudio frequency ranges. The two polarizations occur at frequencies (ω_m) separated by 1.5 logarithmic decades. The temperature difference between the glass transition and the test temperature (24°C) is 89° for H49 and 78° for UET46-1. As described in the previous section, this difference can lead to large differences in $s_1 = \sigma_1/\epsilon_v$ (units of inverse time) and corresponding difference in the $\omega_{m,i}$. Simplifying equation (15) under the present assumptions:

$$\omega_{m,i} = s_1 \{ (1 - A_{i,v_1}) / [e_1 + A_{i,v_1}(e_2 - e_1)] \} \quad (16)$$

reveals a linear relation between the $\omega_{m,i}$ and s_1 . The large value of e_0/e_∞ , when compared to Figure 3, is seen to indicate the presence of flake-like, hard-phase domains. Thus the process can be interpreted as due to the presence of lamellar crystalline (or paracrystalline) and amorphous domains.

The complex permittivity plots in Figure 6 show high frequency (low e') divergence from the classical semicircular shape. The shapes are Cole-Davidson arcs (31), indicative of two, or more, superimposed simple polarizations (equation (1)). In order to use equation (13) a computer adaptation of the graphical method of Fong and Smyth (32) was used to resolve the observed polarizations into two simple ones, resulting in an excellent correlation. Attempts to fit the morphological parameters in equation (13) to the parameters of the resolved experimental spectra, making use of the method of steepest

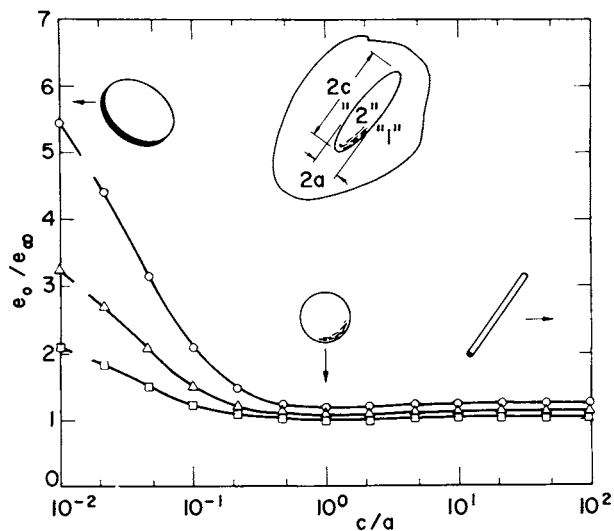


Figure 3. Calculated dielectric polarization strengths from Equation 13. Curves are plotted for several e_2/e_1 ratios as a function of phase 2 domain shapes. Key to e_2/e_1 ratios: \circ , 2.0; \triangle , 1.0; \square , 0.5. For all curves $s_2 = 0$, $r_1 = r_2 = a$, $r_3 = c$, and $v_2 = 0.10$.

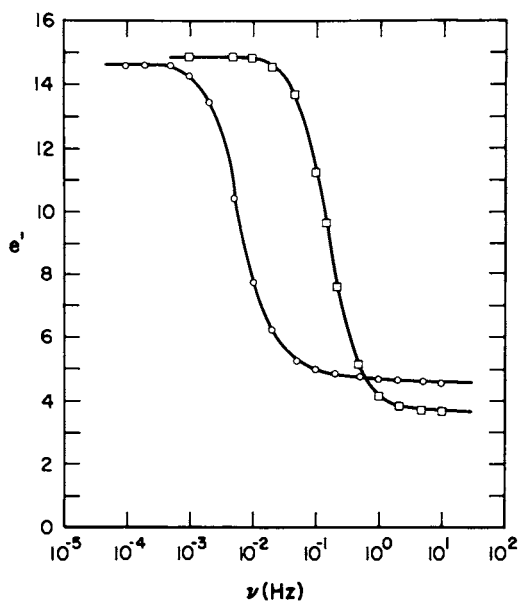


Figure 4. Measured e' spectra at 24°C for \circ , a segmented polyether-polyurethane (UET46-1) and \square , a segmented polyether-polyester (H49). Measurements were made with the steady-state response dielectric spectrometer.

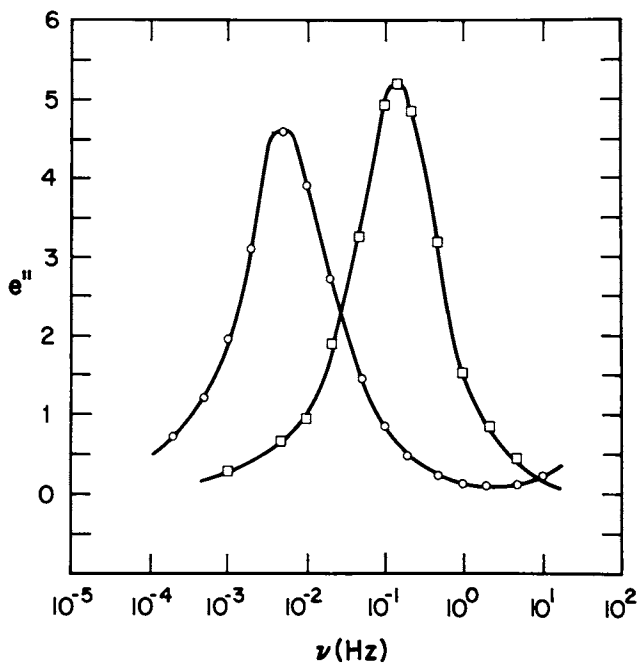


Figure 5. Measured e'' spectra at 24°C for \circ , a segmented polyether-polyurethane (UET46-1) and \square , a segmented polyether-polyester (H49). Measurements were made with the steady-state response dielectric spectrometer.

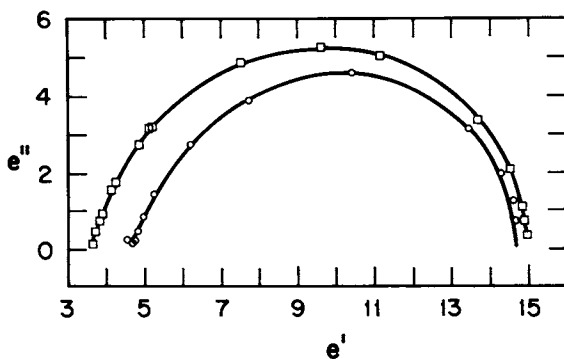


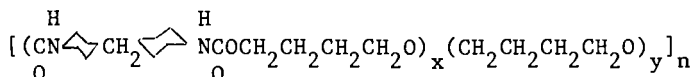
Figure 6. Measured complex permittivity maps at 24°C for \circ , a segmented polyether-polyurethane (UET46-1) and \square , a segmented polyether-polyester (H49). Measurements were made with the steady-state response dielectric spectrometer.

descent for solving the simultaneous, non-linear, algebraic equations, have shown that there are no physically admissible solutions.

The model represented by equation (13) is a highly idealized one, so that its inability to describe the real spectra precisely is not surprising. One modification of the model which might serve to explain the measured spectra is the inclusion of a finite-thickness interface between dissimilar domains with intermediate conductivity. In its simplest form the interface can be approximated as a third, homogeneous phase. For a multi-layer laminate, with the layers perpendicular to the applied field, $\hat{\epsilon}(\omega)$ can be calculated, by generalizing Maxwell's approach (33), as a function of ϵ_i , s_i and v_i for $i = 1, 2$ and 3 . This model has been used to generate the ϵ'' - ϵ' plots in Figure 7; each plot represents a different choice of s_3/s_1 . Although the choices of $v_1 = 0.6$ (soft phase), $v_2 = 0.1$ (hard phase) and $v_3 = 0.3$ (interfacial zone) are arbitrary, such fractions are realistic estimates for the thermoplastic elastomers under study. As the ratio increases from 0 to 1, the plot changes from two separate simple polarizations to a Cole-Davidson arc to one large semicircle. The application of such an approach to morphological studies requires use of a more general multiphase model, which is presently under study.

Although no exact correlation between experiment and model was produced by this exercise, it has been shown that the two polymers studied exhibit phase-separated morphologies that are similar in nature to the extent that they are subject to nearly identical polarizations. The large polarizations measured can only be explained by high interfacial areas, congruent with semicrystalline lamellar morphologies. Finally, the divergence of the observed polarizations from those predicted by the two-phase model is quite likely due to the existence of finite-thickness, transition zones between dissimilar domains.

Two Polyurethanes. Dielectric spectroscopy was performed on two polyurethanes of different architecture using the transient-response spectrometer. One polymer (UET48-1) differs from UET46-1 of the last section primarily in hard segment weight fraction, which is 48% for UET48-1. The second material (HET49-1) is 49% hard segment and differs from UET48-1 in that all rings are saturated:



Samples were purified by swelling in a Soxhlet extractor followed by drying in vacuum. Disks were compression molded at 250°C for 5 minutes followed by air quenching of the mold. Two samples were subsequently annealed at 80° in vacuum for 36 hours followed by slow-cooling to the test temperature 24°. UET48-1

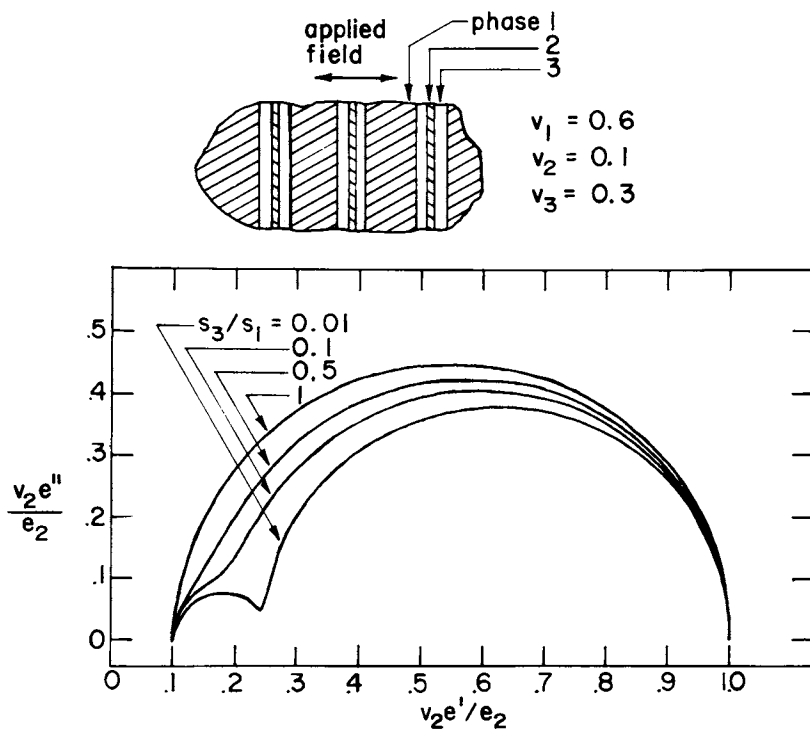


Figure 7. Calculated complex permittivity maps for a three-phase multilayered laminate for different ratios of conductivity in the third (transition zone) and first (soft) phases. For all curves $s_2/s_1 = 0$ and $e_1 = e_2 = e_3$. For $s_3 = s_1$ the first and third phases are equivalent and the resulting arc is a semicircle.

was tested in the annealed and unannealed states. Samples were desiccated in high vacuum where gold electrodes were subsequently applied. All samples were subjected to a 150-hour, 24°C, stabilization period prior to testing at 24°C.

Figure 8 shows the three decay functions which are actually the normalized depolarization currents i/F . The depolarizations for the UET48-1 systems occur over a longer period (100 to 700 s) than that for HET49-1 (~30 s), and the UET48-1 depolarization currents are higher in magnitude. Figure 9 shows the transformed e' spectra; the e'' spectra are not shown. A General Radio 1620-A bridge assembly was used to evaluate k' and k'' as well as to provide the high frequency ($10^2 - 10^4$ Hz) data. The two UET48-1 samples show large polarizations of similar strength and shape although the polarization for the annealed polymer is shifted about 0.7 logarithmic decades higher in frequency. HET49-1 shows only slight polarization in this frequency regime, as seen in Figures 8 and 9. The HET49-1 spectrum flattens out at about 0.1 Hz. The frequency shift caused by annealing UET48-1 is related to higher soft phase conductivity, which in turn results from depression of the glass transition due to annealing. Such a change would necessarily cause a frequency shift, though it need not cause a change in polarization strength. The lack of a large distinct polarization in HET49-1 is suggestive of a non-lamellar morphology. Crystallization of HET49-1 is hampered by the presence of three distinct configurational isomers in the diisocyanate used to form this polymer. In fact a 20°/min DSC scan reveals a two-phase morphology with endothermic disruption of the hard phase occurring at 78°C, indicating a lack of strong ordering in those domains. Thus there appears to be a correlation between the formation of hard segment crystallinity and lamellar morphology in these short-block segmented copolymers. This is not to say that lamellar morphologies occur only for semicrystalline polymers. In totally amorphous AB and ABA block copolymers, such as polystyrene-polybutadiene diblocks, lamellar morphologies can also form, depending on relative fractions of the two blocks and casting parameters.

Summary

Large polarizations are seen to occur in multiphase polymer systems, principally due to the different conductivities in the dissimilar microdomains. Due to the low overall conductivities of these polymers, the polarizations occur at low, often subaudio, frequencies. In order to study these processes two computer-aided dielectric spectrometers have been developed. They differ in the type of excitation used: A.C. versus step. Each spectrometer has certain advantages in terms of accuracy, resolution and convenience. Analytical modelling is used to compare measured spectra to proposed morphologies. Although

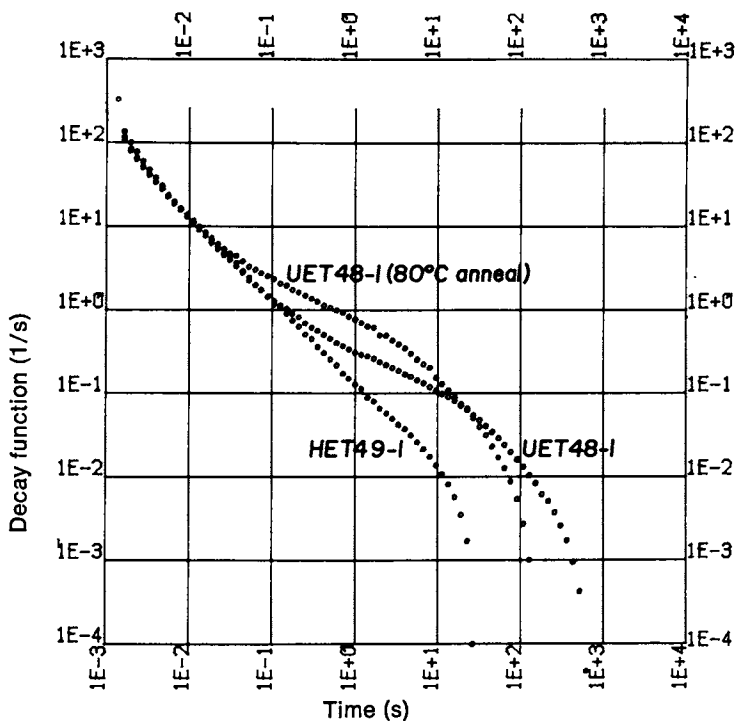


Figure 8. Measured polarization decay functions at 24°C for three segmented polyether-polyurethanes. HET49-1 is tested after annealing at 80°C followed by stabilization at 24°C . UET48-1 is tested with and without annealing. The decay function is the depolarization current density normalized by the electric field value used for polarizing.

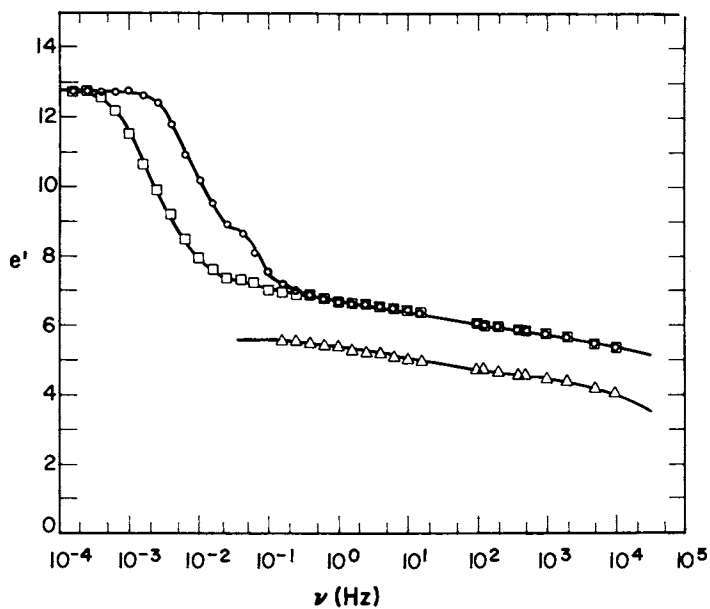


Figure 9. Transformed e' spectra at 24°C for three segmented polyether-polyurethanes. Key: \circ , UET48-1 (80°C anneal); \square , UET48-1; and \triangle , HET49-1 (80°C anneal).

precise fits of models to experimental spectra is difficult for complex morphologies, the experiment can lead to useful morphological insights, particularly in comparative studies.

Acknowledgement

The authors wish to acknowledge partial support of this research by Grant # DMR 81-06888 of the Polymers Section of NSF's Division of Materials Research. The authors also wish to thank International Harvester for providing a fellowship to Michael A. Vallance for work on this project.

Literature Cited

1. Helfand, E.; Macromolecules 1975, 8, 552.
2. Helfand, E.; Wasserman, Z. R. Macromolecules 1976, 9, 879.
3. Helfand, E.; Wasserman, Z. R. Macromolecules 1978, 11, 961.
4. Meier, D. J.; "The Solid State of Polymers" (Eds. Geil, P. H.; Baer, E.; Wada, Y.), Marcel Dekker, New York, 1974.
5. Wilkes, G. L.; Samuels, S. L.; Crystal, R. J. J. Macromol. Sci., Phys. 1974, 10, 203.
6. Koutsky, J. A.; Hein, N. V.; Cooper, S. L. J. Polym. Sci., Polym. Letters 1970, 8, 353.
7. Cella, R. J. J. Polym. Sci., Part C 1973, 42, 727.
8. Roche, E. J.; Thomas, E. L. Polymer 1981, 22, 333.
9. Fridman, I. D.; Thomas, E. L. Polymer 1980, 21, 388.
10. Clough, S. B.; Schneider, N. S.; King, A. O. J. Macromol. Sci., Phys. 1968, 4, 641.
11. Chang, Y. J. P.; Wilkes, G. L. J. Polym. Sci., Polym. Phys. 1975, 13, 455.
12. Bonart, R.; Müller, E. H. J. Macromol. Sci., Phys. 1974, 10, 177.
13. Hiroto, S.; Saito, S.; Nakajima, T. Kolloid Z.Z. Polym. 1966, 213, 109.
14. Dev, S. B.; North, A. M.; Reid, J. C. "Dielectric Properties of Polymers" (Ed. Karasz, F. E.), Plenum, New York, 1972, 217.
15. North, A. M.; Pethrick, R. A.; Wilson, A. D. Polymer 1978, 19, 923.
16. Lilaonitkul, A.; Cooper, S. L. Macromolecules 1979, 12, 1146.
17. Pochan, J. M.; Crystal, R. G. "Dielectric Properties of Polymers" (Ed. Karasz, F. E.), Plenum, New York, 1972, 313.
18. North, A. M.; Pethrick, R. A.; Wilson, A. D. Polymer 1978, 19, 913.
19. Massa, D. J.; Schrag, J. L. J. Polym. Sci., A2 1972, 10, 71.
20. Böttcher, C. J. F.; Bordewijk, P. "Theory of Electric Polarization", Vol. II, 2nd ed., Elsevier, Amsterdam, 1978.
21. Vallance, M.; Faith, III, D. C.; Cooper, S. L. Rev. Sci. Instrum. 1980, 51, 1338.
22. Hyde, P. J. Proc. IEE 1970, 117, 1891.

23. van Beek, L. K. H. Progress in Dielectrics 1967, 7, 69.
24. Brown, Jr., W. F. J. Chem. Phys. 1955, 23, 1514.
25. Sillars, R. W. J. Inst. Elect. Engrs. 1937, 80, 378.
26. Fricke, H. J. Phys. Chem. 1953, 57, 934.
27. Saito, S.; Sasabe, H.; Nakajima, T.; Yada, K. J. Polym. Sci., A2 1968, 6, 1297.
28. Harrel, Jr., L. L. Macromolecules 1969, 2, 607.
29. Flory, P. J. "Polymer Chemistry", Cornell, Ithaca, 1953, 568.
30. Lilaonitkul, A.; Cooper, S. L. Rubber Chem. Technol. 1977, 50, 1.
31. Davidson, D. W.; Cole, R. H. J. Chem. Phys. 1951, 19, 1484.
32. Fong, F. K.; Smyth, C. P. J. Phys. Chem. 1963, 67, 226.
33. Maxwell, J. C. "Electricity and Magnetism", Vol. 1, Clarendon, Oxford, 1892, 452.

RECEIVED May 4, 1982.

An Automated Thermal Analysis System for Reaction Kinetics

A. F. KAH, M. E. KOEHLER, T. H. GRENTZER¹,
T. F. NIEMANN¹, and T. PROVIDER

SCM Corporation, Glidden Coatings and Resins Division, Strongsville, OH 44136

A DuPont Model 990 Thermal Analysis Console with Model 910 DSC accessory was interfaced to a minicomputer system by means of a microcomputer for automated data collection. A program to provide the analysis of reaction kinetics data by the single dynamic scan method for DSC kinetics was developed. Features of this program include a fit of the data to a single equation by multiple regression techniques to yield the reaction order, the energy of activation and the Arrhenius frequency factor. The rate constant $k(T)$ is then calculated and conversion data as a function of time and temperature can be generated at the operator's option.

The automation of the single dynamic DSC scan approach has provided an accurate, time efficient, routine method for obtaining quantitative reaction kinetics information for decomposition, polymerization and curing reactions.

The majority of work reported in the literature for obtaining reaction kinetics information from differential scanning calorimetry (DSC) has been devoted to isothermal studies which require a number of the thermograms over a range of reaction temperatures. In our previous work (1,2), we described the methodology involved in using a single dynamic DSC scan (one thermogram) to obtain reaction kinetics information on model systems such as the decomposition of 2,2-azo-bis-isobutyronitrile, the decomposition of calcium oxalate, and the reaction of phenylglycidyl ether with 2-ethyl-4-methylimidazole, as well as practical coatings systems

¹ Current address: Owens Corning Fiberglas Corp., Technical Center, Route 16, P.O. Box 415, Granville, OH 43023

such as high solids coatings, gel coat resins and powder coatings. In this work, we discuss the methodology used to automate the single dynamic scan method to provide, routinely, reaction kinetics information.

Data Acquisition System

Automation of the DSC was achieved by interfacing a DuPont Model 990 Thermal Analysis Console with Model 910 DSC accessory to a micro-mini computer system. Analog and digital signals from the instrument are interfaced to the microcomputer which is responsible for data collection and all real-time activities. At the completion of the experiment, data are transferred via a serial line to the minicomputer for storage, analysis, report generation and plotting. Details of the mini-microcomputer system and its organization and operation have been reported elsewhere (3,4).

The analog signals are taken from the recorder portion of the DuPont 990 console at points labeled as 'test point 1' on the amplifier printed circuit board for each channel. This yields a voltage proportional to the pen displacement and that is affected by the position of the sensitivity (attenuation) dial on the console, but is not affected by the zero offset controls. The actual gain and offset of the signal at this point are measured for each channel. Analog signals from the instrument are then further conditioned and scaled before passing them to the A/D converter. This is accomplished by means of instrumentation amplifiers followed by low pass active filters which are implemented on printed circuit boards designed in our laboratory.

Automated Instrument Analysis Process

There are four stages in an automated instrument analysis. These are shown schematically in Figure 1 of Chapter 13. In the first stage the instrument operator initiates the analysis by means of a dialog program on the minicomputer. An example of the dialog for the DSC operation is shown in Figure 1. The dialog asks a series of questions about the sample identification and parameters required for instrument operation and data analysis. When the dialog is complete the minicomputer sends all of the input data to the microcomputer. The microcomputer acknowledges that it received the data and turns on a status light at the instrument indicating that it is ready.

The second stage is data acquisition. This stage is initiated when the operator starts the instrument. For the DSC operation, data are collected on three analog channels corresponding to the two pens (Y and Y') on the DuPont 990 console and to the temperature axis. Data are collected on a time base using the microcomputer's crystal based real-time programmable clock.

During the third stage the microcomputer transmits the data it has collected and stored in its memory to the minicomputer. The minicomputer stores these data in data files on one of the disks.

The fourth stage is the data analysis and takes place in the minicomputer. This data reduction is done by FORTRAN programs. Reports and plots are generated at this time.

Data Analysis Methods

The basic assumption of the DSC kinetic method is that the rate of heat evolution from a reaction is proportional to the rate of the chemical reaction and hence, the total heat evolved up to any point during the reaction is proportional to the amount of reactants consumed.

Assuming that reagents are present in stoichiometric proportion and that there is only one slow step in the reaction mechanism, the general n^{th} order rate expression can be written in terms of concentration in logarithmic form yielding the following expression.

$$\ln k(T) = \ln \left\{ \frac{1}{C_0} \left(\frac{dC}{dt} \right) / \left(\frac{C_0 - C}{C_0} \right)^n \right\} \quad (1)$$

where C_0 is the initial concentration, C is the amount reacted at time, t , dC/dt is the rate of disappearance of reactants, n is the reaction order and $k(T)$ is the temperature dependent rate constant.

Rewriting equation (1) in terms of the observable variables obtained from the DSC experiment, we obtain

$$\ln k(T) = \ln \left\{ \frac{1}{\Delta H_0} \left(\frac{dH(t,T)}{dt} \right) / \left(\frac{\Delta H_0 - H(t,T)}{\Delta H_0} \right)^n \right\} \quad (2)$$

where ΔH_0 is the total heat of reaction, $H(t,T)$ is the heat evolved up to time, t , and temperature, T , and $dH(t,T)/dt$ is the time and temperature dependent heat flow shown diagrammatically in Figure 2.

By substituting the Arrhenius expression

$$\ln k(T) = \ln A - \frac{E}{RT} \quad (3)$$

into equation (2) and rearranging, we obtain our working equation.

$$\left[\ln \frac{1}{\Delta H_0} \left(\frac{dH(t,T)}{dt} \right) \right] = \ln A - \frac{E}{RT} + n \left\{ \ln \left[\frac{\Delta H_0 - H(t,T)}{\Delta H_0} \right] \right\} \quad (4)$$

```

DIA 30
Instrument No...23
JOB 5432 DSC REACTION KINETICS:23

Initials...MEK
1 Sample ID...AIBN IN DNBTH
2 Heating rate... 15
3 Air or Nitrogen (A or N)...N
4 Rerun (Y or N)...N
5 X Range <50>... 20
6 Y Range... .05
7 Y' Range... .1
8 Y Axis (Y, DY, T or EXT)<Y>...Y
9 Sample weight (ms)... 1
10 Pan: Regular, Hermetic, Liquid (R, H or L)<R>...L
11 Lid (Y or N)...N
12 Expected runtime in minutes... 20
    Maximum runtime is 30. min

Any errors? (0 or item number)...0

OK
>

```

Figure 1. Dialog for DSC reaction kinetics.

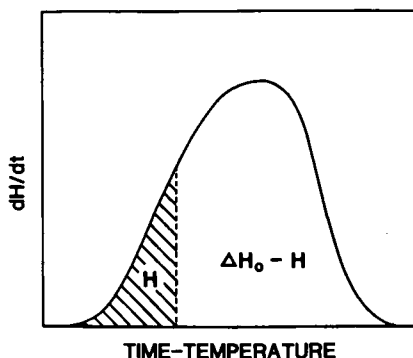


Figure 2. Observable variables for DSC single dynamic scan kinetics experiment.

which is of the form

$$Z = a + bx + cy \quad (5)$$

The data are fit to this expression by a multiple regression technique (5) to yield

n = Reaction order
E = Energy of activation
A = Arrhenius frequency factor.

The rate constant $k(T)$ is then calculated from equation (3).

To perform an analysis of reaction kinetics by the single dynamic scan method, the operator runs the program THERM as shown in Figure 3. The operator selects the appropriate Y channel (pen) for which the analysis is to be performed. The raw data for the temperature and for the selected Y channel are read from the raw data file.

A polynomial was fit to the calibration curve for the thermocouple by means of a minimization of the maximum deviation technique using the Nelder Mead sequential simplex minimization algorithm method.(5,6,7) The coefficients of this polynomial are stored in the analysis program and are used to convert thermocouple voltages to temperature values. Y values are converted to $dH(t,T)/dt$, the heat flow into and out of the sample in mc/sec. The operator selects a baseline for the analysis by entering the temperatures of the beginning and end points of the baseline. A plot is produced of the raw data with the operator selected baseline shown as illustrated in Figure 4.

The data are integrated by the trapazoidal method to give partial areas, $H(t,T)$, in mc. Integration over the entire thermogram provides the total heat of reaction ΔH_0 (mc). Due to the limited resolution of the temperature data, a linear interpolation is performed from the end points of the selected baseline to assign the proper temperature increment between data points on the time-temperature axis for the calculation of partial areas. This method avoids artifacts of zero areas when the temperature change between data points is less than the resolution of the A/D converter. The assumption is made that temperature is a linear function of time (an inherent assumption of the single dynamic scan method).

The operator may select the portion of the peak to be analyzed by entering the temperature limits in degrees. The default is to analyze the central 99% of the area under the peak eliminating 0.5% of the total area from each tail. This reduces spurious results due to small errors in the baseline selection.

The multiple regression is performed and a plot is made of $(Z_{exp} - Z_{calc})/Z_{exp}$ vs temperature as a check on the goodness of fit of the regression. An example is shown in Figure 5. A plot

```

>RUN LA:$THERM
  Job number ... 2883
  Which pen is to be used (L or R) R
  Define baseline in degrees centigrade,
    from 52.80 to 166.44
    Lower limit ... 70
    Upper limit ... 155
  99 % of area is between 86.84 and 147.48 C.
  Give editing limits in degrees C.
    Lower limit < 103.52 > ... 87
    Upper limit < 141.57 > ... 147

--- EXPERIMENTAL RESULTS

      1.0109 ORDER OF REACTION
      52.0114 HEAT OF REACTION, CAL/G
      31.4756 ENERGY OF ACTIVATION, KCAL/MOLE
0.286751E+16 ARRHENIUS FREQUENCY FACTOR
0.355922E+02 Ln(A)
      0.9999 CORRELATION

--- EDITING CONDITIONS

      BASELINE 70.00 TO 155.00 C.
      EDITED 87.00 TO 147.00 C.

      98.87 AREA PERCENT UNDER EDITED PORTION

Report only, Save plot files, Edit < Delete > S
Conversion calculations? Y
Give data for conversion table: end with control Z
  Temperature (Degrees C.) ... 100
  Maximum time (minutes) ... 60
97.5199 PERCENT CONVERTED AT 60.00 MINUTES
Give data for conversion table: end with control Z
  Temperature (Degrees C.) ... ^Z

Plot files available -----
DATA ( Raw data files with baseline)
NORM ( Normalized data and fraction converted)
ZCHECK ( Temp vs. (Z - Zcalc) / Z)
LIN ( 1/Temp vs. ln(K) )
CONVER ( Time ( sec) / fraction converted)

>

```

Figure 3. Operator interaction with program THERM.

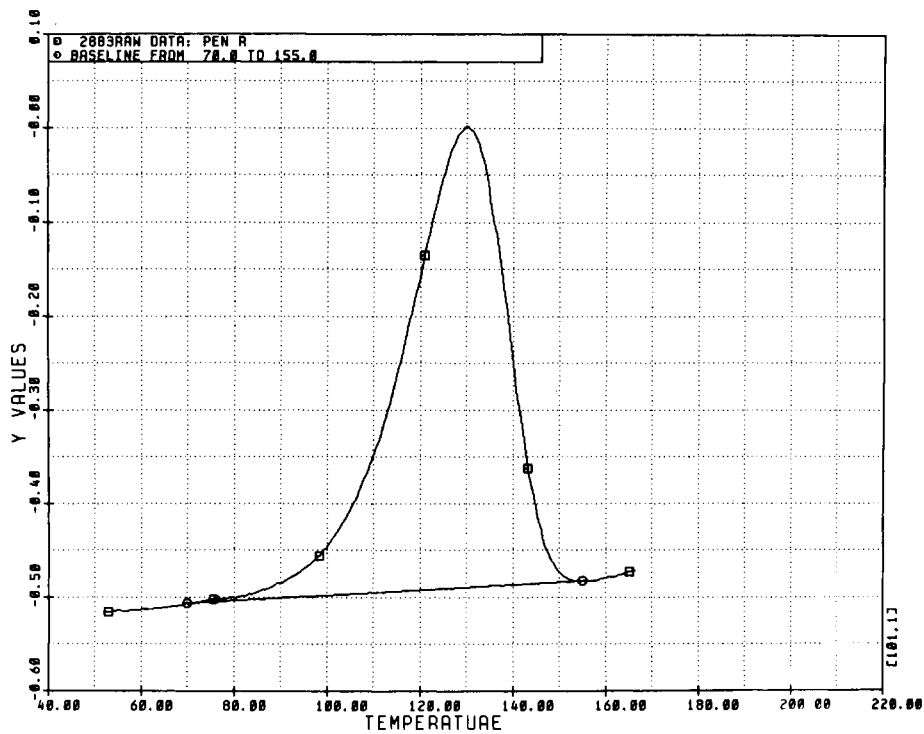


Figure 4. Raw data with operator selected baseline. Key: □, 2883 raw data, Pen R and ○, baseline from 70.0 to 155.0°C.

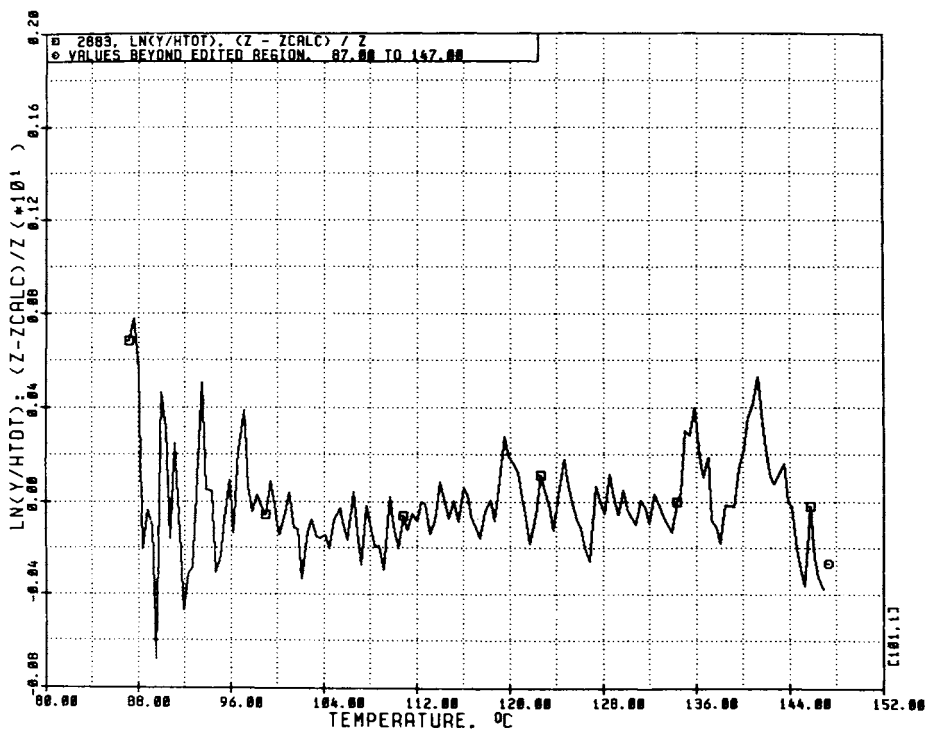


Figure 5. Normalized plot to check goodness of fit. Key: □, 2883, $\text{LN}(Y/HTOT)$, $(Z-ZCALC)/Z$ and ○, values beyond edited region 87.00 to 147.00°C.

of $\ln k(T)$ vs $1/T$ is produced for the 99% area limits with the least squares fit over the editing limits shown as illustrated in Figure 6. Finally, a normalized plot of the baseline corrected DSC curve with the integral curve showing the extent of the reaction as a function of temperature superimposed on it is produced as shown in Figure 7.

A report is printed showing identification information, experimental conditions, editing limits for the analysis and the kinetic and thermodynamic results of the analysis as shown in Figure 8. Plots of % conversion vs time at selected temperatures (Figure 10), as well as a table of the % conversion at specific times and temperatures (Table I), may be generated at the operator's option from the equations below.

$$\% \text{ conversion} = (1 - e^{-k(T)t}) \times 100\% \quad \text{for } n = 1 \quad (6)$$

and (7)

$$\% \text{ conversion} = 1 - [(n - 1) k(T)t + 1]^{1/1-n} \times 100\% \quad \text{for } n \neq 1$$

Conclusions

The automation of the single dynamic DSC scan approach has provided an accurate, time efficient, routine method for obtaining quantitative reaction kinetics information for decomposition, polymerization and curing reactions. Record-keeping of experimental conditions is more complete and accurate. In addition, automation has made it possible to examine in detail the effects of DSC heating rate and baseline selection upon the quantitative results as well as to assess carefully the validity of the kinetic model for specific reaction systems.

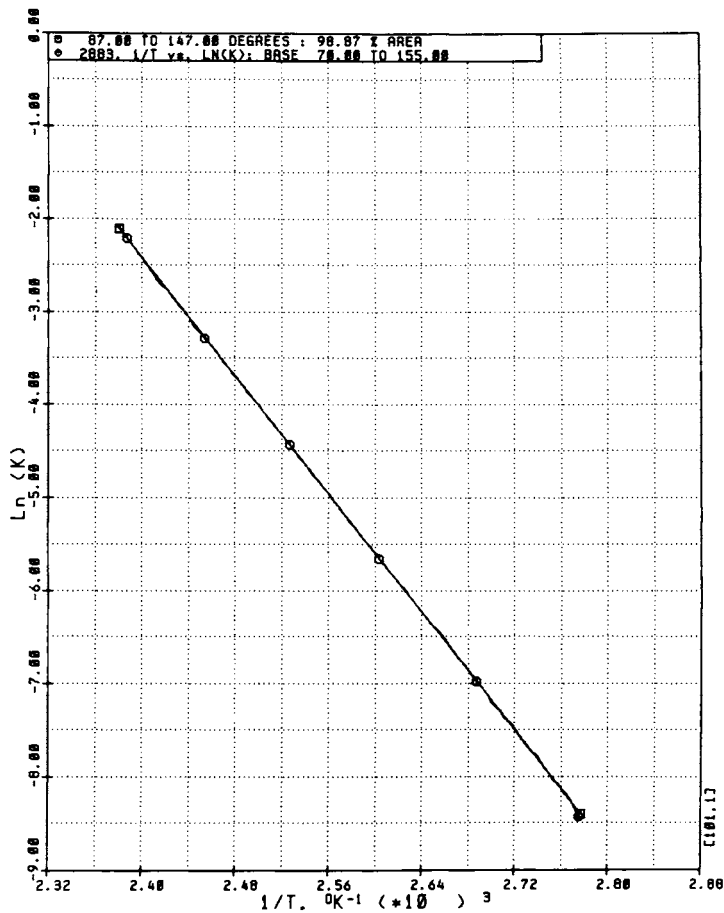


Figure 6. Plot of experimental $\ln k$ vs. $1/T$ and linear least squares fit. Key: \square , 87.00 to 147.00°C, 98.87% area and \odot , 2883. $1/T$ vs. $\ln k$, baseline from 0°C to 155.0°C.

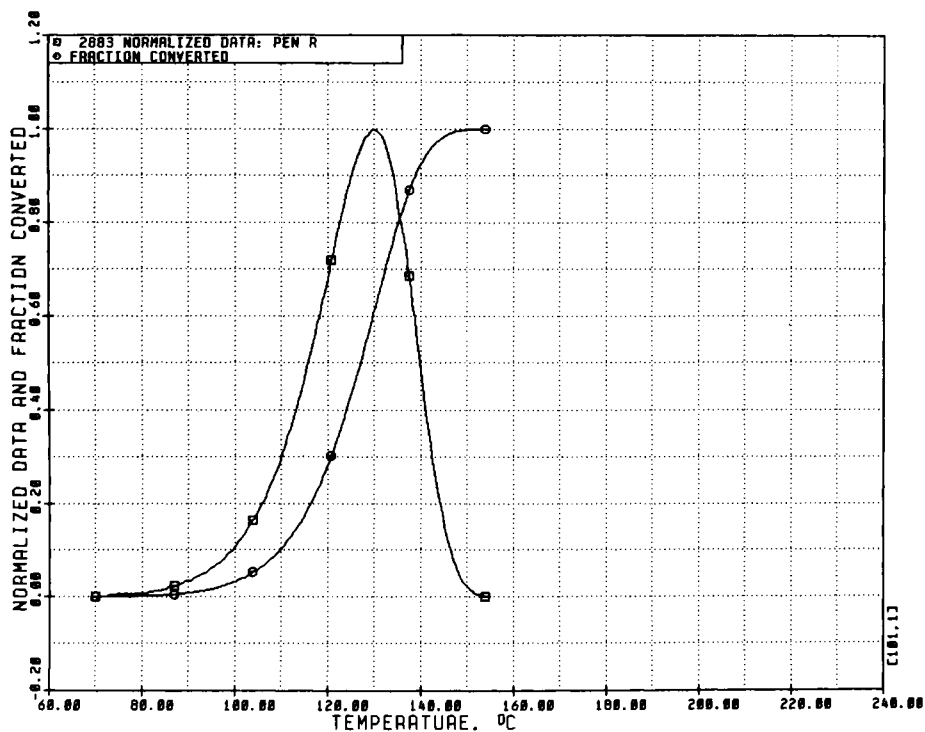


Figure 7. Normalized raw data and fractional conversion. Key: \square , 2883 normalized data, Pen R and \circ , fraction converted.

DIFFERENTIAL SCANNING CALORIMETER
REACTION KINETICS, 1 DYNAMIC SCAN

AIBN INDNBTH

```
-----  
JOB NUMBER      2883  
RUN NUMBER      1  
OPERATOR        SAK  
DATE            10-DEC-80  
TIME            14:31:10
```

--- EXPERIMENTAL RESULTS

```
1.0109  ORDER OF REACTION  
52.0114  HEAT OF REACTION, CAL/G  
31.4756  ENERGY OF ACTIVATION, KCAL/MOLE  
0.286751E+16  ARRHENIUS FREQUENCY FACTOR  
0.355922E+02  Ln(A)  
0.9999  CORRELATION
```

--- EDITING CONDITIONS

```
BASELINE      70.00 TO 155.00 C.  
EDITED        87.00 TO 147.00 C.  
  
98.87  AREA PERCENT UNDER EDITED PORTION
```

--- EXPERIMENTAL CONDITIONS

```
15.00  HEATING RATE, DEGREES C PER MINUTE  
1.00   SAMPLE WEIGHT, MILLIGRAMS  
1.0590 CELL CALIBRATION CONSTANT  
20.00  X SCALE SENSITIVITY, DEG/INCH  
R      RIGHT PEN USED  
0.05  Y SCALE SENSITIVITY, MCAL/SEC.IN  
N      SAMPLE RUN UNDER NITROGEN  
L      PAN TYPE: LIQUID DROP  
N      SAMPLE RUN WITHOUT PAN LID
```

Figure 8. Sample report from program THERM.

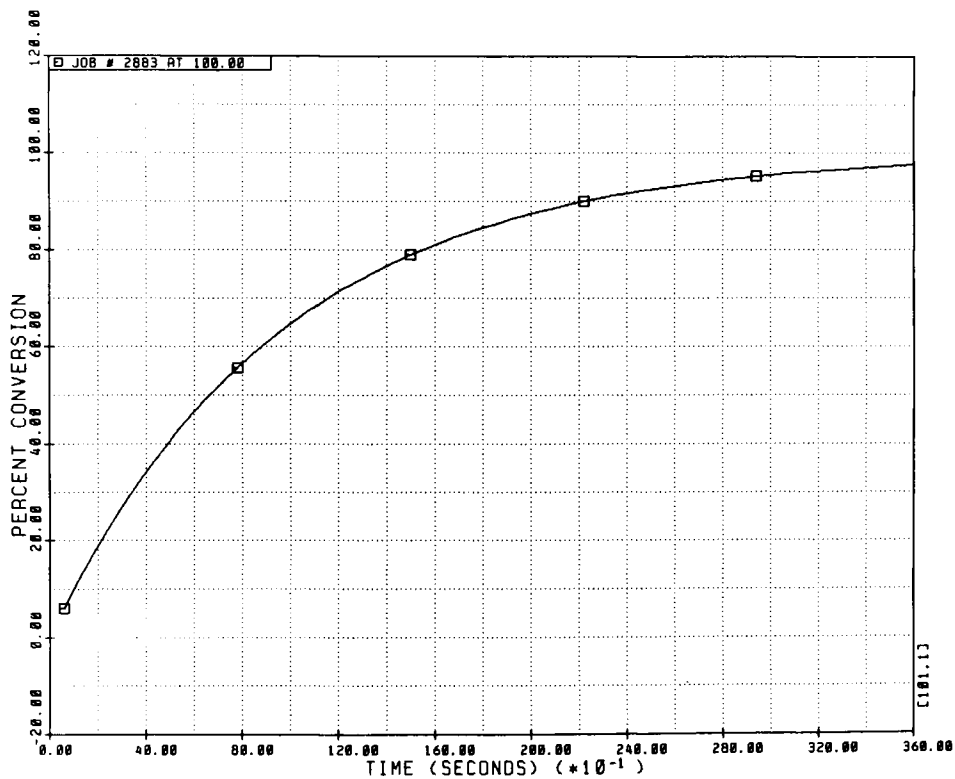


Figure 9. Plot of calculated % conversion at selected temperature. Job 2883 at 100.00°C.

Table I. Calculated % Conversion at Selected Temperature

JOB NUMBER	2883
RUN NUMBER	1
AIBN INDNBTH	

TEMPERATURE, C.	100.
REACTION CONSTANT	0.104795E-02
ORDER OF REACTION	1.0109
TIME IN SECONDS	PERCENT CONVERTED
120.	11.80963
240.	22.21032
360.	31.37335
480.	39.44600
600.	46.56050
720.	52.83055
840.	58.35830
960.	63.23162
1080.	67.52948
1200.	71.32011
1320.	74.66370
1440.	77.61395
1560.	80.21716
1680.	82.51490
1800.	84.54303
1920.	86.33378
2040.	87.91495
2160.	89.31152
2280.	90.54514
2400.	91.63493
2520.	92.59796
2640.	93.44899
2760.	94.20129
2880.	94.86630
3000.	95.45437
3120.	95.97438
3240.	96.43436
3360.	96.84124
3480.	97.20128
3600.	97.51987

Acknowledgement

The authors acknowledge the assistance of Dr. John J. Stansbrey with the numerical methods used in the treatment of data.

Literature Cited

1. Grentzer, T. H.; Holsworth, R.M.; Provder, T.; Kline, S. "Quantitative Reaction Kinetics by Differential Scanning Calorimetry", Proceedings of the Tenth North American Thermal Analysis Society Conference, (Oct. 26-29, 1980), Boston, Mass., 269.
2. Grentzer, T. H.; Holsworth, R. M.; Provder, T. "Quantitative Reaction Kinetics by Differential Scanning Calorimetry", ACS Organic Coatings and Plastics Preprints, 1981, 44, 673.
3. Niemann, T. F.; Koehler, M. E.; Provder, T. "Microcomputers used as Laboratory Instrument Controllers and Intelligent Interfaces to a Minicomputer Timesharing System"; in "Personal Computers in Chemistry", Lykos, P., Ed.; John Wiley and Sons: New York, 1981.
4. Kah, A. F.; Koehler, M. E.; Eley, R. R.; Niemann, T. F.; Provder, T. "An Automated Ferranti Shirley Viscometer", this volume.
5. Olsson, P. M.; Nelson, L. S. Technometrics 1975, 17, 45.
6. Smith, J. M. "Mathematical Modeling and Digital Simulation for Engineers and Scientists"; John Wiley and Sons: New York, 1977.
7. Olsson, D. M. J. Quality Technology 1974, 6, 53.

RECEIVED May 4, 1982.

Analysis of an Epoxy Curing Reaction by Differential Scanning Calorimetry

NICOLE LEVY

Bell Laboratories, Norcross, GA 30071

A composition and kinetic study was conducted of the curing of a bisphenol-A-diglycidylether resin (R) with triethylene-tetramine-phenol hardener (H) using the Mettler TA2000B thermal analysis system and associated software. At elevated temperatures, the highest crosslink density is obtained at mix ratios (expressed in equivalents) $H/R > 1.0$. At smaller mix ratios, a strong dependence of T_g on composition and degree of cure is observed. Analysis of T_g as function of degree of cure or mole fraction of converted epoxide groups shows that for the same degree of cure, the T_g 's for ambient and high temperature cure schedules differ. This behavior was interpreted to be the result of different rate determining curing reactions with different temperature dependencies. In the kinetic study, we used dynamic DSC and the nth-order equation used by the Mettler software. The calculated degrees of cure showed good agreement with measured values for low conversions. For high conversions, the predicted cure was ~10 to 15% lower than the measured degree of cure, but was linearly related to the measured cure. Thus, if a correction factor for conversions higher than 70% is used, the accuracy of the predicted conversion, obtained with the Mettler program and the nth-order equation, is sufficient for establishing optimum isothermal cure schedules.

0097-6156/82/0197-0313\$06.00/0
© 1982 American Chemical Society

The curing behavior of an epoxy system was investigated by dynamic differential scanning calorimetry (DSC). The epoxy resin (R) was a blend of bisphenol-A-diglycidylether (90%) and a monoepoxide (10%). The hardener (H) was a triethylene-tetramine-phenol-formaldehyde adduct containing 2% free phenol.

The purpose of the study was a) to determine the effect of relative resin/hardener composition and ambient and elevated temperature curing schedules on the glass transition temperature, T_g , and on the degree of cure of the epoxy system, and b) to evaluate the agreement between the calculated degree of cure using the nth-order kinetic equation (1.1) (1, 2, 3) and the measured degree of cure.

$$d\alpha/dt = k(1-\alpha)^n. \quad (1.1)$$

We have used in this work, the Mettler TA2000B thermal analysis system and the supplied Kinetic and Applied Kinetic Programs. This instrument and associated software is capable of analyzing on-line the nth-order equation (1.1).

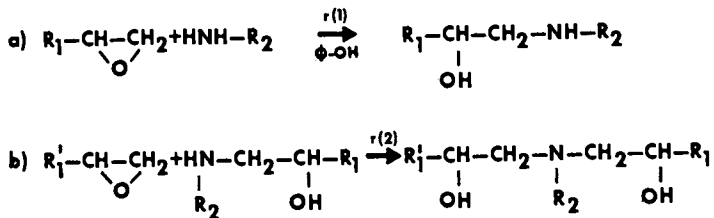
The applicability of equation (1.1) and the Mettler programs would be advantageous for rapid evaluation of the degree of cure. From the degree of cure as function of time at temperatures T , optimum curing ($>90\%$) schedules, as function of composition can be determined, to avoid partially cured epoxies which may be tacky below T_g and flow above T_g .

Experimental

Instrumental. The Mettler TA2000B thermal analysis system is equipped with an interface system, and Hewlett-Packard 9815 desk top calculator and 7225 plotter. Samples, weighing 5-10 mg, sealed in aluminum pans and under a nitrogen blanket, were heated in the calorimeter at a rate of 10 deg/min from -35 or 10 deg C to 180 deg C respectively, for specific heat and kinetic scans. Specific heat measurements were calibrated with alumina to an accuracy of $\pm 3\%$. Temperatures and enthalpies were calibrated with an Indium sample. The accuracies were ± 0.02 deg C and $\pm 2\%$ (Indium 28.5 J/g), respectively.

Sample Preparation. The epoxy system (Reicholdt Chemical Company), consisted of a resin Epotuf 37-128, with an epoxide equivalent weight of 197, and a hardener, Epotuf 37-614 with an amine hydrogen equivalent weight of 50 and containing $\sim 2\%$ free phenol. Samples containing 1 g resin (0.00508 equivalents) with corresponding equivalents of hardener to give H/R ratios ranging from 0.75 to 1.36 were cured as described below.

Analytical. For the evaluation of the rate controlling curing reactions



(a) and (b) (4, 5, 6) several cure schedules were used:

A) Ambient (25 deg C) temperature preparation for 0.1h followed by programmed heat-up to 180 deg C. This schedule results in complete cure (i.e., no reaction enthalpy can be measured in a subsequent scan). The enthalpy measured during the heat-up is $\Delta H(k)$. Since we assume that cure is negligible during the 0.1h after mixing, $\Delta H(k)$ corresponds to the maximum reaction enthalpy for each composition. T_g is measured during a second heat-up.

B) Ambient temperature cure for 20h. For measurement of the reaction enthalpy due to uncured epoxy, and measurement of T_g of the epoxy cured at ambient temperature, this schedule is followed by a programmed heat-up to 180 deg C. During this heat-up the composition is cured completely, and the enthalpy measured is $\Delta H(s)$.

C) Ambient temperature cure for intermediate times. As for schedule B) this cure schedule is followed by a heat-up to 180 deg C for measurements. The resulting enthalpy values are also noted as $\Delta H(s)$.

The heat of reaction, enthalpy ΔH , is proportional to the degree of cure or the number of reacted sites. The composition, expressed as ratio of equivalents of hardener to equivalents of resin, H/R, will affect the number of possible crosslinks. The composition with the most reacted epoxide groups will be that with the largest heat of reaction, $\Delta H(\text{max})$, since $\Delta H(\text{max})$ is proportional to the conversion of epoxide groups. We can now define, for schedule A and varying H/R, a relative degree of cure, $\Delta H(k)/\Delta H(\text{max})$, and, for schedule B (20h at ambient temperature), a reduced degree of cure, $1-\Delta H(s)/\Delta H(k)$. To allow comparison of the relative and reduced degree of cure, a normalized degree of cure is defined as $[1-\Delta H(s)/\Delta H(k)][\Delta H(\text{max})]$ or $[\Delta H(k)-\Delta H(s)]/\Delta H(\text{max})$.

The glass transition temperatures for different compositions and cure schedules were determined at $1/2\Delta C(p)$ from each programmed heat-up.

Kinetics. The kinetic evaluation of the reaction parameters is contained in the Kinetics and Applied Kinetics programs supplied by the Mettler Instrument Corporation described on p. 320.

Results and Discussion

Effect of Hardener/Resin Composition on Degree of Cure.

The relative degree of cure, $\Delta H(k)/\Delta H(\max)$, as function of composition, H/R, for samples cured with schedule A are reported in Figure 1. The maximum enthalpy of reaction was determined to be 342 ± 2 J/g from an average of three scans for samples with H/R = 1.13-1.16.

At H/R < 1.1 the relative degree of cure is proportional to H/R. At H/R > 1.1 the relative degree of cure is constant and the maximum attainable number of crosslinks are formed. Since a larger than stoichiometric quantity of hardener is necessary for maximum cure, the reactivity of the amine hydrogens in the hardener varies, ($r(1) \neq r(2)$), that is some hydrogens contribute only partially to the curing reaction (4,5).

Effect of Composition on T_g . The glass transition temperatures for samples cured with schedule A (fully cured) are shown in Figure 2. When comparing Figure 2 to Figure 1, we note that T_g goes through a maximum at H/R = 1.0, indicating that at this composition the highest crosslink density is attained. At H/R < 1.0 not all epoxides are reacted and thus a proportionally lower crosslink density and T_g are attained. At H/R > 1.0 T_g again decreases, as expected for a lower concentration of epoxide groups in the hardener rich mixture resulting in lower crosslink density.

Effect of Curing Time and Temperature on T_g and Degree of Cure. Samples having different H/R compositions were also cured with schedule B. The dependence of T_g on composition is shown in Figure 3 (open squares). The same samples were subsequently heated a second time in the calorimeter to determine the T_g 's (closed squares) of the now fully cured samples (no measurable reaction enthalpy). The T_g 's of these samples are the same as under schedule A (solid line).

From Figure 3 it is evident that T_g of the ambient temperature cured samples is less dependent on composition than on cure temperature.

The dependence of T_g on the degree of cure is shown in Figure 4a for schedule A (closed circles), schedule B (open squares) and for schedule B after heat-up (closed squares). For the latter samples $\Delta H(RT_{\text{cure}}) + \Delta H(s) = \Delta H(k)$ was assumed. The observation of different T_g 's for identical relative (schedule A) and normalized (schedule B) degrees of cure precludes the interpretation that both reactions (a) and (b) occur at all

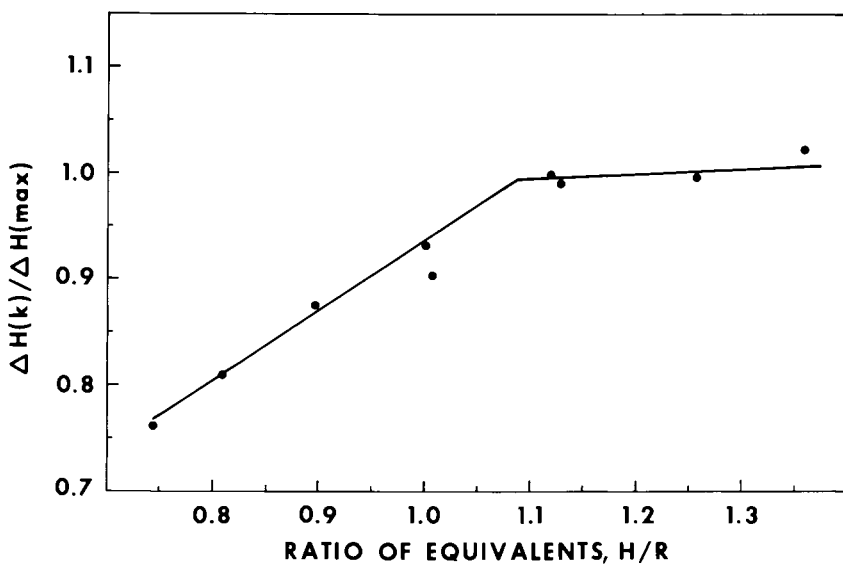


Figure 1. Relative degree of cure, $\Delta H(k)/\Delta H(\max)$, as function of composition.

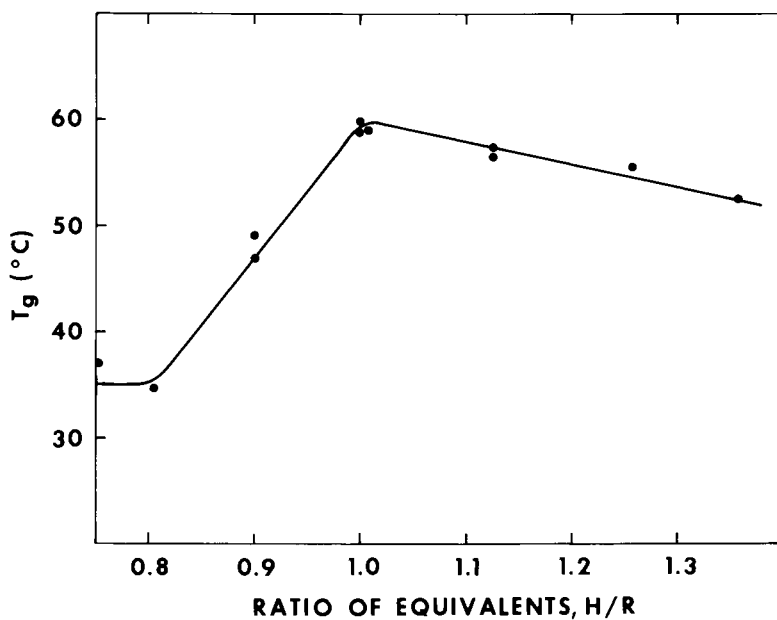


Figure 2. Dependence of glass transition temperature, T_g , on composition for samples cured with schedule A.

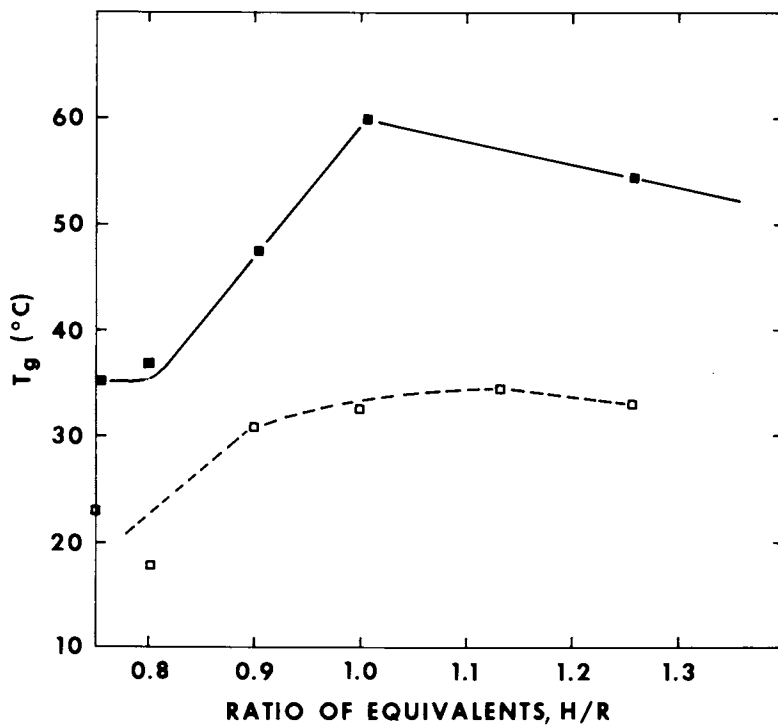


Figure 3. Dependence of glass transition temperature on composition of samples cured at ambient temperature and following subsequent heat-up. Key to cure schedule: —○—, A; □, B; and ■, B + heat-up to 180°C.

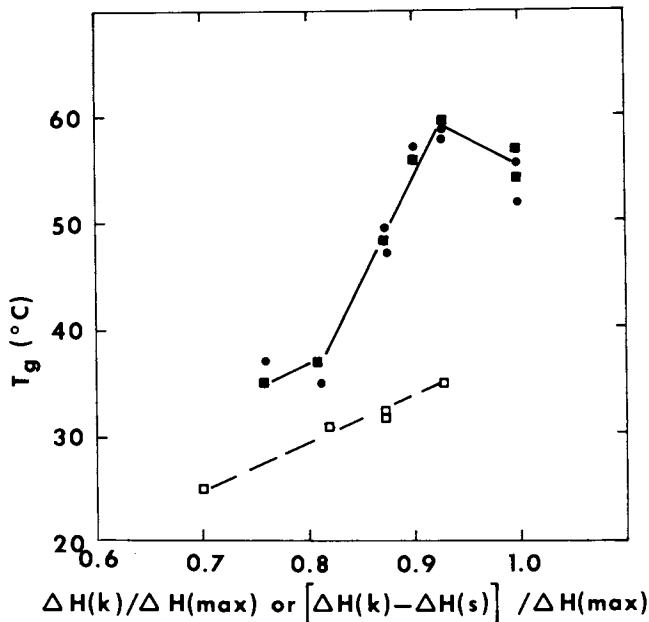


Figure 4a. Dependence of T_g on degree of cure. Key to cure schedule: ●, A; □, B; and ■, B + heat-up to 180°C.

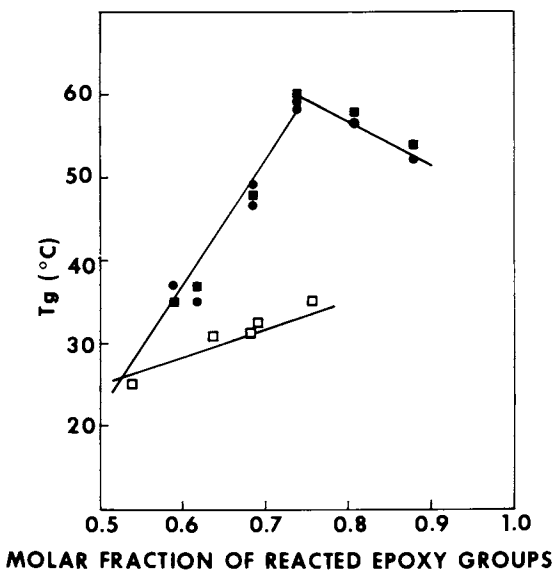


Figure 4b. Dependence of T_g on molar fraction of reacted epoxy groups. Key to cure schedule: ●, A; □, B; and ■, G + heat-up to 180°C.

temperatures, and that diffusion control inhibits complete reaction at room temperature. However, different activation energies or temperature dependencies for (a) and (b) would give rise to the results observed in Figures 3 and 4a.

When calculating the molar fraction of reacted epoxy groups using as heat of reaction per epoxy group 106 J/mole (5), a behavior similar to Figure 4a is observed in Figure 4b. In this case, for highly resin rich compositions only, both schedule A and B afford one single T_g , suggesting that for these compositions only reaction (a) occurs even at high temperature.

The lower T_g 's observed for samples cured with schedule B are consistent with the lower crosslink density expected for reactions of the epoxide groups with the primary amine (a). The higher T_g 's observed for samples cured with schedule A are consistent with the higher crosslink density, molecular weight and steric hindrance (7) expected in the products of reactions (b). The higher exotherm peak temperatures (130-135 deg C) for samples prepared with curing schedule B compared to samples cured with schedule A (~95 deg C) support this assignment. Further evidence for this mechanism will be presented in the following section.

Kinetic Model for Curing Reaction and Comparison Between Predicted and Measured Degree of Cure. We modeled the epoxy curing reaction for all H/R studied, using the n-th order rate equation (1.1) substituting for the rate constant k in (1.1) the expression from the Arrhenius equation in (3.4.1)

$$k=k(0)\exp(-E(a)/RT). \quad (3.4.1)$$

One can evaluate according to equation (3.4.2) the reaction parameters during programmed heat-up.

$$\ln d\alpha/dt=\ln k(0)+n \ln(1-\alpha)-E(a)/RT. \quad (3.4.2)$$

The programmed heat-up yields Figure 5. The exotherm is analyzed by measuring the fractional conversion $\alpha=\Delta H(\text{partial})/\Delta H(\text{total})$, and the rate of reaction $d\alpha/dt=dH/dt[1/\Delta H(\text{total})]$, where dH/dt corresponds to the heat flow at temperature T and $H(\text{total})$ is the total reaction enthalpy $\Delta H(s)$ or $\Delta H(k)$. It follows that $(1-\alpha)=\Delta H(\text{remaining})/\Delta H(\text{total})$. The Mettler Kinetics program evaluates the calorimetric data by multiple regression analysis to give the kinetic reaction parameters $E(a)$, $\ln k(0)$, and n. The statistical parameters for the regression equation indicate that 97.5-99.0% of the data are explained by the regression coefficients. The reaction parameters are summarized in Table I.

We notice from the parameters in Table I that under schedule A the reaction proceeds with $n \sim 2$, an apparent activation energy of 72-76 kJ/mole and a frequency factor of 19.0-21.0

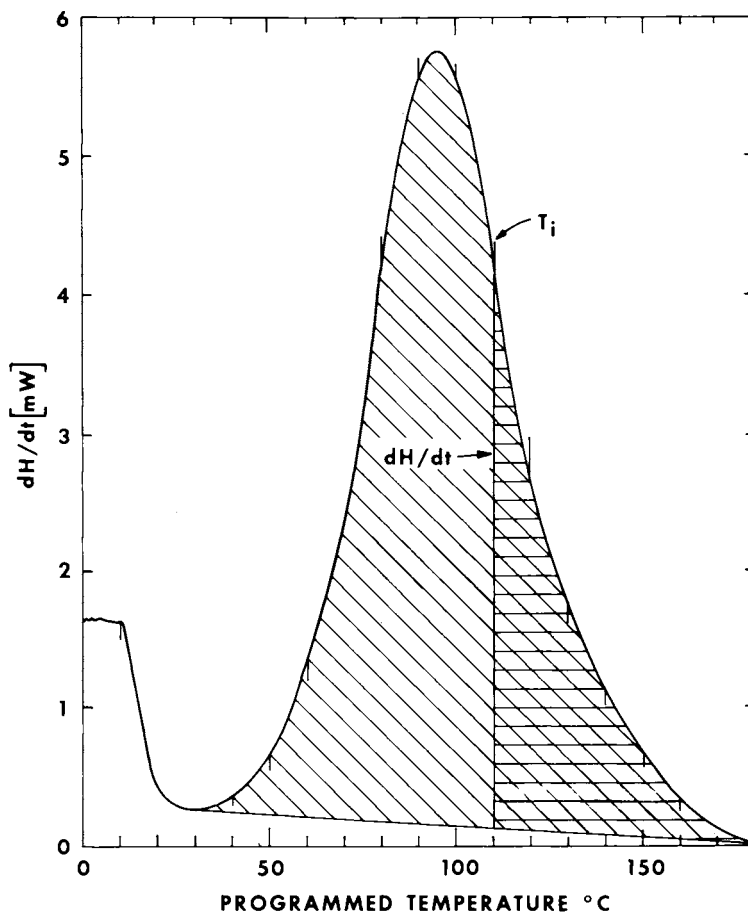

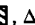


Figure 5. DSC-scan for composition $H/R = 1.13$, 5.41 mg, and $\Delta H = 339$ J/g.
 Key: , ΔH (total) and , ΔH (remaining) at T_i .

$$\Delta H \text{ (partial)} = \Delta H \text{ (total)} - \Delta H \text{ (remaining)}$$

Table I. Epoxy-System Curing Parameters. Continued on next page.

H/R	$\frac{\Delta H(k)}{\Delta H(max)}$	Schedule	Ambient Curing Time (h)	$1 - \frac{\Delta H(s)}{\Delta H(k)}$	$\Delta H(s)$ or $\Delta H(k)$ J/g	E(a) kJ/mole	$\xi n, k(O)$ l/sec	η
1.36	1.02	A	0.1	0	350	73.1	19.9	1.9
		C	1.25	24.2	266	83.2	23.5	3.0
		C	2.0	50.3	174	72.7	19.6	2.1
		C	27	94.8	18	103.4	27.7	1.7
1.26	1.00	A	0.1	0	342	72.7	19.6	1.9
		C	1.25	25.7	255	70.7	18.8	2.1
		C	120	98.0	8	66.6	15.6	1.0
1.13	0.99	A	0.1	0	339	72.7	19.6	2.0
		C	1.25	19.8	272	75.7	20.6	2.4
		B	21.0	93.4	23	78.3	19.1	1.4
1.12	1.00	A	0.1	0	342	75.1	20.4	2.1
		C	1.5@ 40°C	57.0	75	70.0	18.3	2.4
1.00	0.93	A	0.1	0	318	76.0	20.7	2.1
		C	1.25	22.3	247	82.0	22.9	3.1
		B	20.0	93.4	21	87.3	21.9	1.2
1.01	0.93	A	0.1	0	309	75.1	20.3	2.1
		C	1.25	19.4	249	77.3	21.9	2.7
		B	20	91.3	27	85.1	21.0	1.4

Table I. Continued. Epoxy-System Curing Parameters.

H/R	$\frac{\Delta H(k)}{\Delta H(max)}$	Schedule	Ambient Curing Time (h)	$1 - \frac{\Delta H(s)}{\Delta H(k)}$	$\Delta H(s)$ or $\Delta H(k)$ J/g	E(a) kJ/mole	$\dot{\Delta n}$ k(O) l/sec	\bar{n}
0.90	0.87	A	0.1	0	300	75.9	20.6	2.2
		C	1.25	21.5	234	85.7	23.7	3.3
		C	2.0	39.9	180	86.8	24.3	3.4
		B	21	93.4	20	96.9	24.6	1.1
0.81	0.81	A	0.1	0	278	-	-	-
		C	1.25	22.3	216	76.9	20.9	2.4
		C	2.0	37.2	174	76.3	20.6	2.6
		B	18.5	90.3	21	108	28.2	1.0
0.75	0.76	A	0.1	0	260	75.3	20.3	2.2
		C	1.25	21.9	203	76.2	20.7	2.4
		C	2.0	35.8	167	-	-	-
		C	29	92.7	19	120	32.5	1.2

l/sec. Under schedule B, the reaction of the residual epoxy proceeds with $n \sim 1.2$, a higher apparent activation energy of 85-108 kJ/mole and a higher frequency factor of 21-28 l/sec. These results together with the higher exotherm temperatures observed on heat-up after schedule B suggest that different temperature dependencies exist for room and high temperature reactions (6, 8), respectively.

Numerical integration of equation (3.4.2) using the Mettler program, yields the degree of conversion as function of time and temperature using the reaction parameters determined from the multiple linear regression analysis. Such a plot for $H/R = 1.13$ at 25 deg C, is shown in Figure 6 and corresponds to cure under schedule C for samples without internal heat generation (isothermal reaction).

Using this approach one can calculate the degree of cure from the reaction parameters obtained with negligible ambient cure (schedule A) and compare it to the measured degree of cure for thin samples cured with schedule C (in thin samples internal heat generation can be neglected). The degree of agreement would establish whether the nth-order equation is accurate. In Figure 7, the predicted degrees of cure for different compositions, are compared to the measured degrees of conversion, $1 - \Delta H(s) / \Delta H(k)$, obtained from heat-up according to schedule C. The line shown has unit slope. The agreement between the predicted and the measured values is within two percent for most compositions and thus acceptable. In Figure 8 the same comparison is made for samples cured with schedule B. The measured conversions are linearly related to the predicted results. Thus a linear equation can be used to calculate true (measured) conversions from the predicted values.

Conclusions

We have shown that for an epoxy system cured at elevated temperature, the highest crosslink density is obtained at mix ratios (expressed in equivalents) $H/R > 1.0$. At smaller mix ratios a strong dependence of T_g on composition and degree of cure is observed.

The same epoxy system, when cured at ambient temperature yields lower T_g 's than for similar degrees of cure attained at high temperature. This behavior suggests that two rate-determining curing reactions with different temperature dependencies take place.

The degree of cure, when modeled with the nth-order equation, showed good agreement with measured values for low conversions and short cure times. For long cure times and high conversions, the predicted conversion was ~10 to 15% lower than the measured degree of cure. Measured conversions however correlate linearly with predicted conversions. Taking this

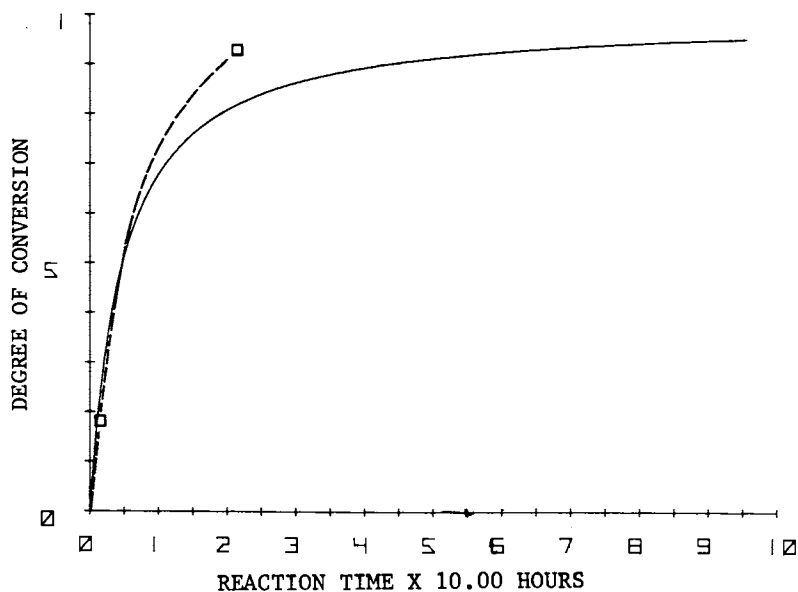


Figure 6. Calculated degree of cure at 25°C isothermal temperature for composition $H/R = 1.13$, $E(a) = 72.7$ kJ/mol, $\ln k(0) = 19.6$, and $\Delta H = 339$ J/g. Key: ---, measured degree of cure, $1 - \Delta H(S)/\Delta H(K)$, and —, calculated degree of cure.

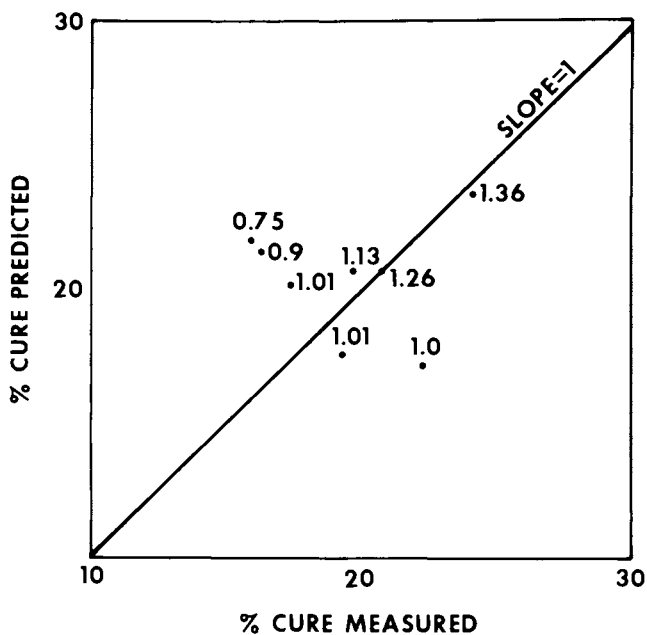


Figure 7. Comparison of predicted degrees of cure to measured degrees of conversion for different compositions. Conditions: schedule C, 1.25 h ambient cure.

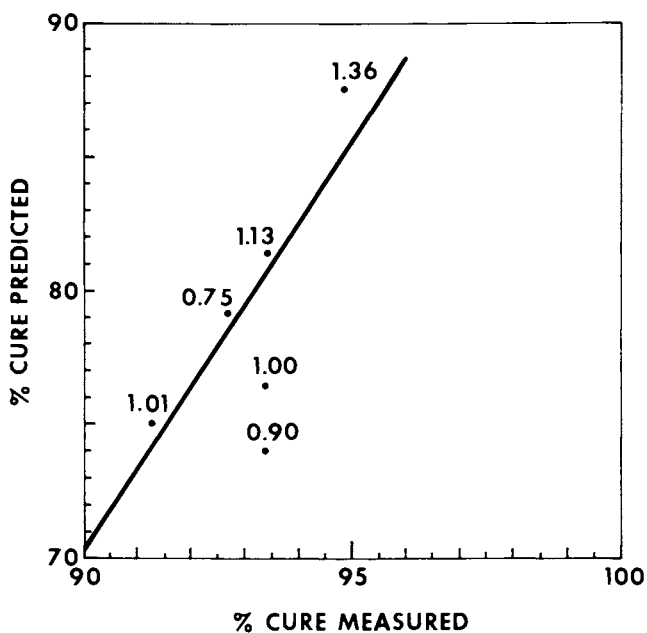


Figure 8. Comparison of predicted degrees of cure to measured degrees of conversion for different compositions. Conditions: schedule B, 20+ h ambient cure.

into consideration, optimum cure schedules under commercial conditions can be derived without resorting to more complex kinetic treatments (2, 9).

Acknowledgements

The author thanks Dr. R. Sabia for reviewing the manuscript.

Literature Cited

1. Barton, J. M.; Brit. Poly. J. 1979, 11, 117.
2. Barton, J. M.; Polymer 1980, 21, 603.
3. Allen, P. E. M.; Patrick, C. R.; "Kinetics and Mechanisms of Polymerization Reactions", Ellis Horwood, Chichester, 1974, Chap. 2.
4. Bokare, U. M.; Gandhi, K. S.; J. Poly. Sci. Poly. Chem. Ed. 1980, 18, 857.
5. Horie, K.; Hiura, H.; Sawada, M.; Mita, I.; Kambe, H.; J. Poly. Sci., 1970, Part A-1, 8, 1357.
6. Sacher, E.; Ann. Rep., Conf. Elec. Insul. Diel. Phenomena, 1971, 144.
7. Nielsen, L. E.; Mechanical Properties of Polymers and Composites, 1974, Vol. 1, Marcel Dekker Inc., New York.
8. Vlastaras, A. S.; Ann. Rep., Conf. Elec. Insul. Diel. Phenomena 1971, 249.
9. Prime, R. B.; Poly. Eng. and Sci. 1973, 14, 2067.

RECEIVED May 4, 1982.

Automated Torsion Pendulum: Control and Data Collection/Reduction Using a Desktop Computer

JOHN B. ENNS and JOHN K. GILLHAM

Princeton University, Department of Chemical Engineering,
Polymer Materials Program, Princeton, NJ 08544

A torsion pendulum interfaced with a desktop computer form an automated instrument for dynamic mechanical characterization of polymeric materials. The computer controls the initiation of the oscillations, collects the digitized data and calculates the shear modulus and loss modulus from the damped oscillations, utilizing one of four methods of analysis: 1) fitting the data points about the maxima and minima to a quadratic equation to obtain their times and amplitudes, from which the frequency and logarithmic decrement can be calculated; 2) fitting the data to a four-parameter equation of motion by a least squares technique; 3) fitting the data to a six-parameter solution to the equation of motion by a non-linear least squares technique; and 4) taking the Fourier transform of the data, which results in a maximum at the frequency of the oscillation whose amplitude is inversely proportional to the damping coefficient. The advantages and disadvantages of each method are discussed and the results of torsion pendulum and torsion braid analysis (TBA) experiments are compared.

The torsion pendulum has proven to be an important and versatile tool in the study of dynamic mechanical properties of materials. In our laboratory it has been applied primarily to polymers, although elsewhere it has been used with a wide variety of materials, ranging from liquids to metals and ceramics. The basis of its wide appeal lies in its fundamental simplicity: information about the complex modulus of the material under investigation is obtained by simply observing the decaying oscillations of the pendulum. After the pendulum is set in motion, it is permitted to oscillate freely at its resonant frequency while the amplitude of the oscillatory wave decays. In an unautomated system it is a

0097-6156/82/0197-0329\$07.00/0
© 1982 American Chemical Society

relatively simple but tedious task to calculate the shear modulus and the loss modulus from the period of the oscillation, its logarithmic decrement and the geometric constants of the system. The independent variable in the investigation of dynamic mechanical properties of a material is often temperature, but it can also be time, as in the case of chemically reactive or physically aging systems.

A variation of the torsion pendulum, torsional braid analysis (TBA), utilizes a supported specimen so that the dynamic mechanical properties of a sample can be monitored in the liquid as well as the solid states (1, 2). An inert multifilamented glass braid is impregnated with the sample (usually in its liquid state or in solution). The observed dynamic mechanical properties are relative due to the composite nature and complex geometry of the specimen.

The purpose of this paper is to describe an automated torsion pendulum controlled by a desktop computer, to discuss four separate methods of data analysis, and to compare the results of a torsion pendulum experiment and a TBA experiment using the same epoxy resin.

Instrumentation

A schematic diagram of the torsion pendulum is shown in Figure 1. Free oscillations are initiated by an angular step-displacement of the upper member of the pendulum. The response of the lower member is a damped wave at the natural frequency of the system, and therefore is related to the physico-mechanical properties of the specimen.

The damped oscillations are converted to an electrical signal by a non-drag optical transducer: light is passed through a pair of polarizers, one of which serves as the inertial mass of the pendulum, to a photo-detector. The temperature, humidity and gas (usually helium) surrounding the specimen are closely controlled.

The torsion pendulum has been interfaced with a digital desktop computer (Hewlett Packard 9825B) shown in the system diagram Figure 2 (3). The motors which align the specimen and initiate the waves are under computer control via the scanner (HP 3495A) and relays. At present the direction of the temperature scan and the status of the experiment (whether to hold, reverse, or terminate) at either of the temperature limits set by the programmer (Eurotherm Corp.) are under computer control as well, but the rate of temperature change and the limits are not. The amplified thermocouple and wave signals are digitized by a high speed digital voltmeter (HP 3437A) whose scan rate is programmable, and the scanner supervises the I/O activity. The computer calculates the frequency and damping parameters from the raw data and plots the dynamic mechanical properties of the specimen as a function of temperature and/or time. A photograph of the equipment is shown in Figure 3. A commercial version of the automated torsion pendulum/torsion braid analyzer is available from Plastics Analysis Instruments, Inc., P.O. Box 408, Princeton, New Jersey.

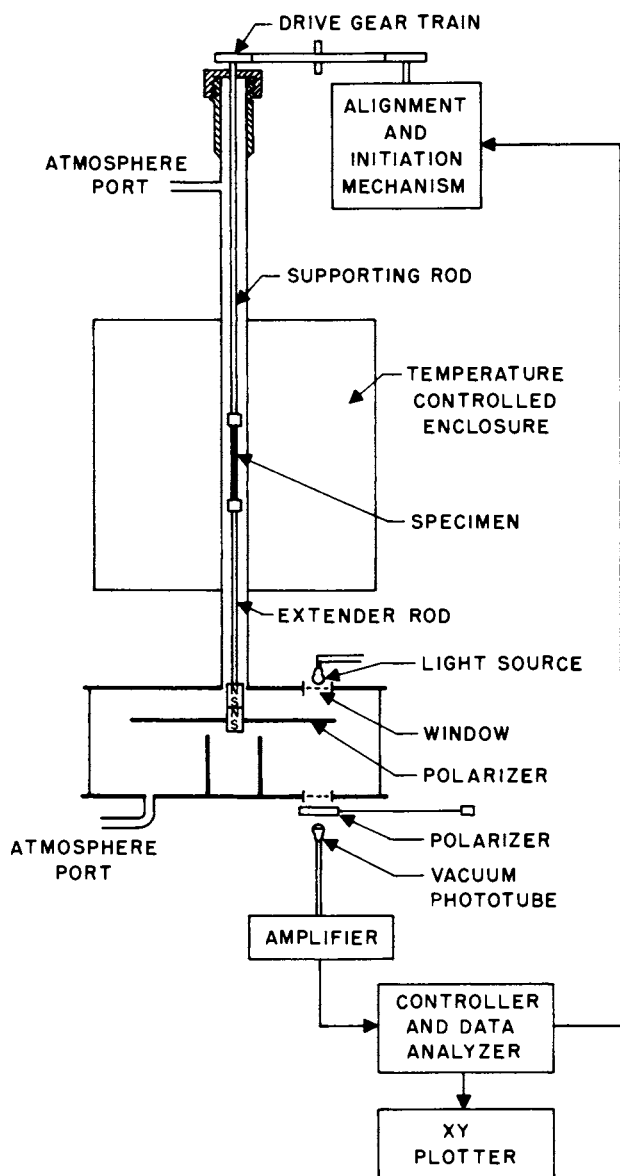


Figure 1. Schematic of an automated torsion pendulum.

An analog electrical signal is obtained from passing a light beam through a pair of polarizers, one of which oscillates with the pendulum. The pendulum is aligned for linear response and initiated by a computer that also processes the damped waves to provide the elastic modulus and mechanical damping data that are plotted on an *XY* plotter versus temperature or time.

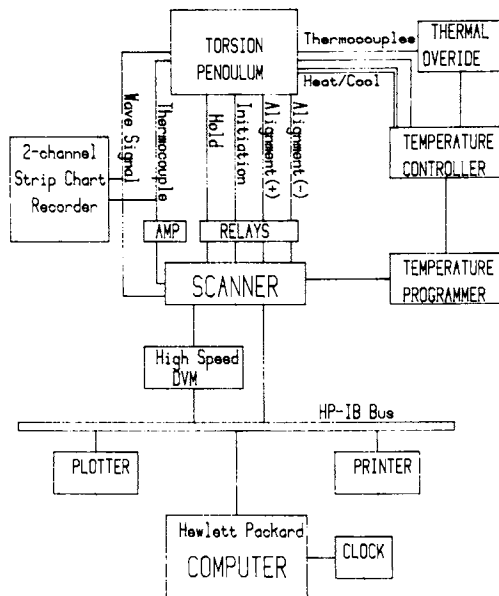


Figure 2. Automated torsion pendulum: system schematic for interfacing with a digital computer.

The torsion pendulum has been interfaced with a digital desktop computer (HP-9825B). The motors which align the specimen and initiate the waves are under computer control. The wave and amplified analog thermocouple signals reach the computer digitized via a digital voltmeter (HP-3437A). The scanner (HP-3495A) supervises the I/O activity. Upon receiving the digitized raw data the computer calculates the frequency and damping parameters, and plots the dynamic mechanical properties of the specimen as a function of temperature and time.

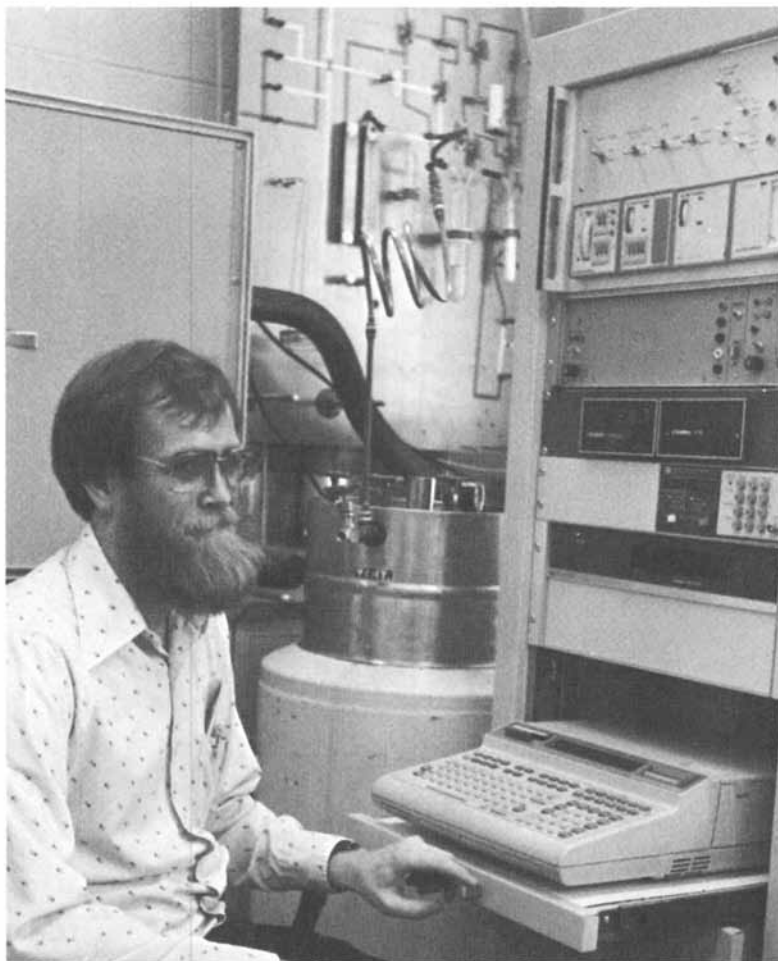


Figure 3. Automated torsion pendulum.

The pendulum is housed in the cabinet at the left; the oven is separated from the optical transducer by an insulated 3/4 inch horizontal aluminum plate. The temperature controller, digital voltmeter, scanner, and computer are in the rack at the right. The atmosphere control panel and liquid nitrogen container are shown in the background.

For each damped wave the computer goes through a control sequence, schematically represented in Figure 4. Since the specimen may twist due to an uneven distribution of thermal stresses, the alignment motor rotates the pendulum through a gear train to the same reference position at the start of each control sequence. To initiate the oscillations, a second motor rotates the pendulum a specified angular displacement against the tension of a spring. The pendulum is held in this cocked position until oscillations set up by the alignment and cocking procedure have decayed, at which time the clutch is disengaged and the pendulum swings back so as to oscillate about the reference position. The data are then collected and reduced. The temperature (or time, for isothermal runs) is measured with the specimen in the cocked position and again after the data are collected. After plotting the reduced data, the oscillation is monitored until it decays to within specified limits and the cycle repeats.

The data obtained from the torsion pendulum can be displayed in various modes (4): the shear modulus G' is given by

$$G' = KI \left(\frac{2\pi}{P} \right)^2 \left[1 + \left(\frac{\Delta}{2\pi} \right)^2 \right] \quad (1)$$

or by its approximation

$$\tilde{G}' \cong 4\pi^2 KI \left(\frac{1}{P} \right)^2 \quad (2)$$

where P is the period, Δ is the logarithmic decrement and K is a geometric constant. In a TBA experiment, where K is unknown, the relative rigidity [$\propto (1/P)^2$] is measured. Usually the logarithmic decrement term in equation (1) is negligible; only in the transition regions, where $\Delta > 0.6$, does it become greater than one percent. In Figure 5 both the shear modulus and its approximation are plotted (5, 6): the curves are indistinguishable except in the transition regions. The energy lost during the deformation can be displayed in a variety of ways (Figure 5): loss modulus

$$G'' = 4\pi KI\alpha/P \quad (3)$$

logarithmic decrement

$$\Delta \cong \pi \frac{G''}{G'} = \alpha P = \pi \tan \delta \quad (4)$$

and damping coefficient α . A shift is observed in the maximum by which the transition temperature is identified: for example, $T_g(G'') < T_g(\Delta) < T_g(\alpha)$ for a solid-to-rubber transition. (For a rubber-to-solid transition the shift occurs in the reverse order.)

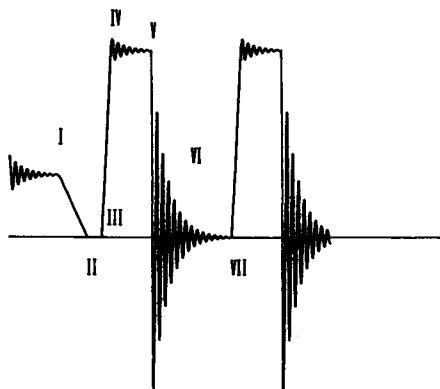


Figure 4. Automated torsion pendulum: control sequence. Key: I, previous wave decays, drift detected and correction begins; II, reference level of polarizer pair reached; III, wave initiating sequence begins. IV, decay of transients; V, free oscillations begin; VI, data collected; and VII, control sequence repeated.

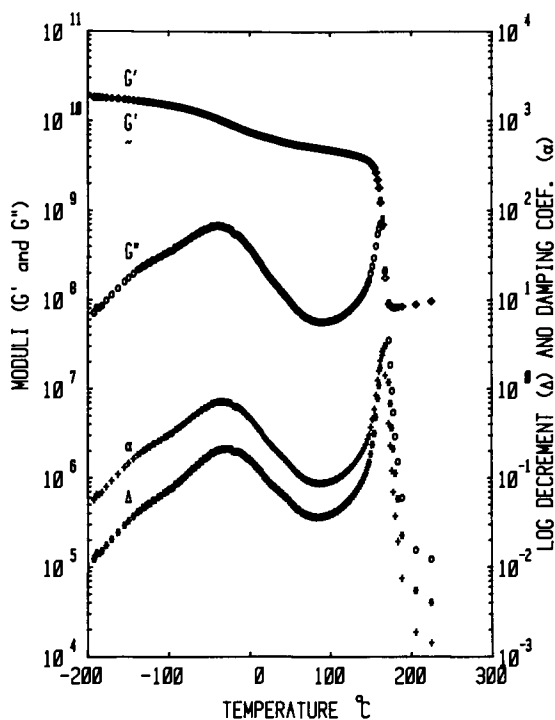


Figure 5. Dynamic mechanical spectrum (torsion pendulum) of a cured film of Epon 828/PACM-20. Both the shear modulus G' (\square) and its approximation G'_a (\diamond) are plotted on the upper curve; the lower three curves are loss modulus G'' (\circ), logarithmic decrement Δ (*), and damping coefficient α (+).

Software

An efficient algorithm is required to monitor the oscillatory wave signal in real time. The flow chart is shown in Figure 6. The algorithm is used to monitor the wave while waiting for it to decay (Figure 4: prior to I and between IV and V), and to collect the data (Figure 4: VI) for subsequent analysis. The routine will provide the approximate location of the extrema (peaks) in real time at a scan rate of up to 75 points per second. If a scan rate faster than 75 points per second is required, the maxima and minima are located after the data have been collected and before initiation of the next wave.

In order to digitize the signal efficiently, the scan rate (digitization rate) S , must be chosen to match the characteristics of the oscillations. The optimum scan rate is a function of the period (P) of the oscillation, the number of data points (N) collected per wave, the time required for the oscillations to decay to a specified limit, and the method of analysis used. The scan rate corresponding to 40 points per cycle ($S = 40/P$) provides an adequate representation of the oscillations for most data reduction methods (see later). A rough estimate of the period is obtained from the first quarter cycle after initiation, and the scan rate is adjusted accordingly. To locate the peaks, an interval consisting of $1 + 4R$ (where R is a function of scan rate, usually equal to 4) data points moves along as the data are acquired, and the local maxima and minima are located by determining whether the center datum point of the interval is greater than (for a maximum) or less than (for a minimum) both the first and last data points of that interval. As soon as this set of criteria is met the center datum point is stored: the next peak is then sought. The reason for using more than three consecutive data points is to insure that a noisy signal does not simulate a maximum or minimum. This method, although quite crude, is much faster than one which involves taking a derivative of the data to locate the peaks. After all the data points have been collected, an approximate determination of the peaks is made by searching for the maximum or minimum among the data points within each of the intervals in which a maximum or minimum was detected.

Data Reduction. The oscillatory motion of a freely moving torsion pendulum has been described by an equation of motion (4):

$$I \frac{d^2\theta}{dt^2} + \eta_{\text{dyn}} \frac{d\theta}{dt} + G_{\text{dyn}} \theta = 0 \quad (5)$$

where I is the moment of inertia, η_{dyn} is the dynamic viscosity, G_{dyn} is the elastic shear modulus, θ is the angular deformation, and t is the time. The solution is a damped sine wave:

$$\theta = \theta_0 \exp(-\alpha t) \cos(\omega t + \phi) \quad (6)$$

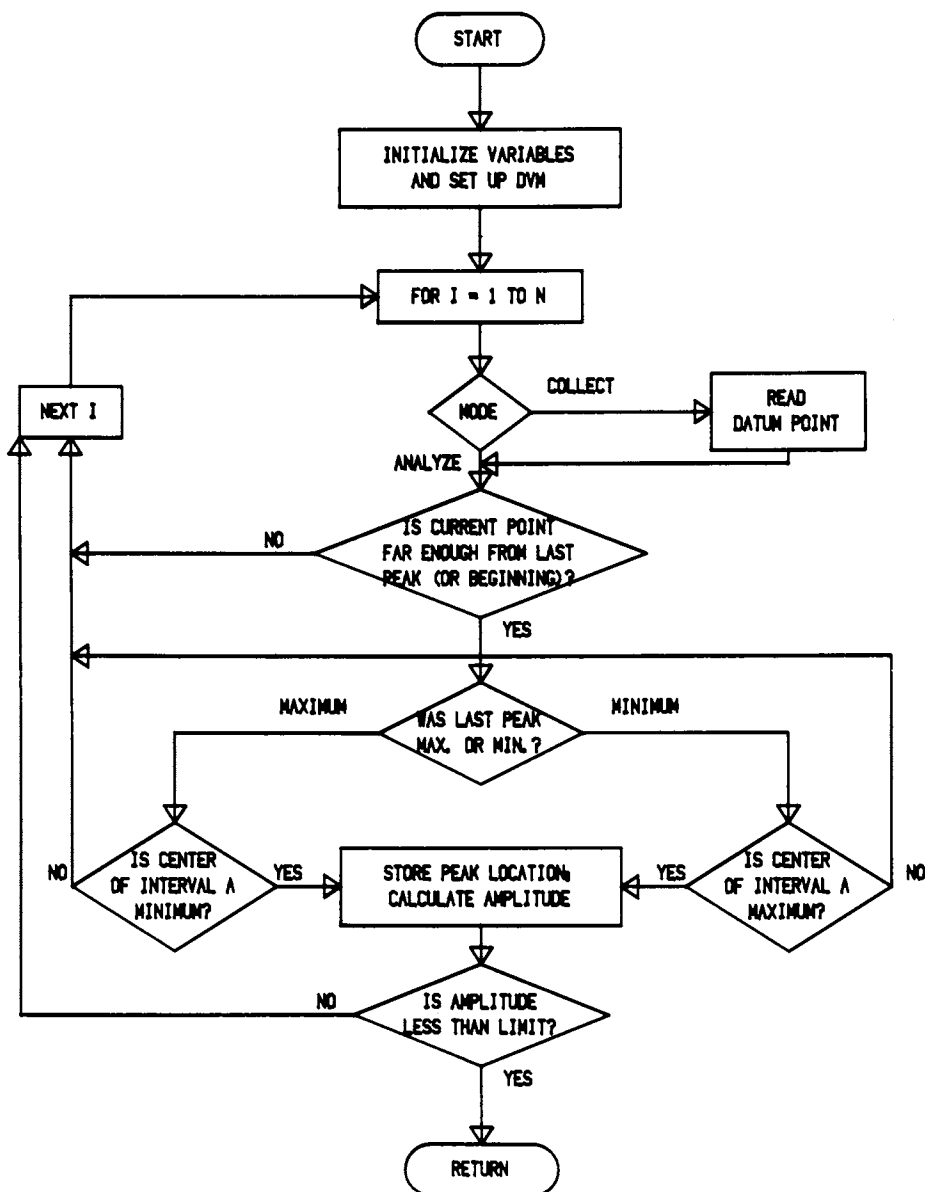


Figure 6. Flow diagram of data collection/peak-finding algorithm.

where θ_0 is a constant; α is the damping coefficient,

$$\alpha = \eta_{\text{dyn}}/2I \quad (7)$$

ω is the natural angular frequency (radians/sec),

$$\omega = \left[\left(\frac{G_{\text{dyn}}}{I} \right) - \left(\frac{\eta_{\text{dyn}}}{2I} \right)^2 \right]^{1/2} \quad (8)$$

and ϕ is a phase angle. The shear modulus, G' , and loss modulus, G'' , can be derived from information in the wave:

$$G' = KI(\omega^2 + \alpha^2) \quad (9)$$

and $G'' = 2KI\alpha\omega \quad (10)$

where K is a geometric constant.

Peak Finding Method. Since the approximate location of the peaks has already been determined, the data points about each peak are fitted to a quadratic equation

$$\theta = a + bt + ct^2 \quad (11)$$

by a least squares method. The optimum number of data points to be used in fitting the quadratic equation to the data has been determined to be those in the interval $\pm 0.2\pi$ (7). Since the data were obtained at a scan rate such that 40 points per cycle were collected, the number of points used for fitting a quadratic is $(0.4\pi/2\pi)40 = 8$; because the calculations require an odd number of data points, 9 data points are used. Linear least squares fitting of the experimental data points to the quadratic equation requires minimization of the summation of residuals

$$Q = \sum_{i=1}^n (f_i - \theta_i)^2 \quad (12)$$

where $f_i = a + bt_i + ct_i^2 \quad (13)$

and θ_i are experimentally observed data at times t_i . From the requirement that Q must be minimized,

$$\frac{\partial Q}{\partial A_k} = 2 \sum_{i=1}^n (f_i - \theta_i) \left(\frac{\partial f_i}{\partial A_k} \right) = 0 \quad (k = 1 \text{ to } 3) \quad (14)$$

where $A_1 = a$, $A_2 = b$, and $A_3 = c$;

this results in a set of three linear equations written in matrix form:

$$\begin{bmatrix} \sum_i 1 & \sum_i t_i & \sum_i t_i^2 \\ \sum_i t_i & \sum_i t_i^2 & \sum_i t_i^3 \\ \sum_i t_i^2 & \sum_i t_i^3 & \sum_i t_i^4 \end{bmatrix} \begin{bmatrix} A_1 \\ A_2 \\ A_3 \end{bmatrix} = \begin{bmatrix} \sum_i \theta_i \\ \sum_i t_i \theta_i \\ \sum_i t_i^2 \theta_i \end{bmatrix} \quad (15)$$

If the time-axis data are offset so that the central datum point is zero, the odd powered summations are identically equal to zero, thus simplifying the matrix. The solution to this set of equations provides the parameters of the quadratic equation. The best estimate of the peak position is obtained from the first derivative

$$\frac{d\theta}{dt} = b + 2ct = 0 \quad (16)$$

$$t_p = -\frac{b}{2c} \quad (17)$$

and

$$\theta_p = a + b\left(-\frac{b}{2c}\right) + c\left(-\frac{b}{2c}\right)^2 = a - \frac{b^2}{4c} \quad (18)$$

This procedure is performed for the first minimum and the following maximum, as well as for the last pair (the selection of which depends on the damping), and the period is calculated by dividing the elapsed time between the maxima by the number of cycles. The logarithmic decrement is obtained from the relation

$$\Delta = \left(\frac{2}{i-1}\right) \ln \left[\left(\frac{\theta_{i-1}}{\theta_i} \right) \right] \quad (i = 3, 5, 7 \dots) \quad (19)$$

where θ_i is the amplitude of the i th extremum.

Least Squares Method (8). A torsion pendulum specimen has a tendency to change its rotational orientation during the course of an experiment due to an uneven distribution of stresses caused by volume expansion and contraction. This results in a drift in the baseline of the wave signal which can be represented by

$$\theta = \theta_0 \exp(-\alpha t) \cos(\omega t + \phi) + Bt + C \quad (20)$$

where B is the drift coefficient and C is the offset. The corresponding differential equation can be written as

$$\frac{d^2\theta}{dt^2} + 2\alpha \frac{d\theta}{dt} + (\alpha^2 + \omega^2)\theta - C(\alpha^2 + \omega^2) - 2\alpha B - B(\alpha^2 + \omega^2)t = 0 \quad (21)$$

which may be simplified to

$$D = \frac{d^2\theta}{dt^2} + A_1 \frac{d\theta}{dt} + A_2\theta + A_3t + A_4 = 0 \quad (22)$$

A_k ($k = 1$ to 4) are the parameters fitted by a linear least squares analysis to determine

$$\alpha = \frac{A_1}{2} \quad (23)$$

and

$$\omega = [A_2 - \left(\frac{A_1}{2}\right)^2]^{1/2} = \frac{2\pi}{P} \quad (24)$$

The derivative values of θ at any point i are calculated numerically from a quadratic equation which uses five consecutive points to obtain the first and second derivatives:

$$\frac{d\theta}{dt} \Big|_i = \left(\frac{-2\theta_{i-2} - \theta_{i-1} + \theta_{i+1} + 2\theta_{i+2}}{10h} \right) \quad (25)$$

$$\frac{d^2\theta}{dt^2} \Big|_i = \left(\frac{2\theta_{i-2} - \theta_{i-1} - 2\theta_i - \theta_{i+1} + 2\theta_{i+2}}{7h^2} \right) \quad (26)$$

where h is the time interval between data points.

The linear least squares fitting of n experimental data points to the differential form of the equation of motion involves minimization of the summation

$$Q = \sum_{i=1}^n (f_i - D_i)^2 \quad (27)$$

where

$$f_i = \frac{d^2\theta}{dt^2} \Big|_i + A_1 \frac{d\theta}{dt} \Big|_i + A_2\theta_i + A_3t_i + A_4 \quad (28)$$

is calculated from experimental data and D_i is identically zero by definition. From the requirement that Q is minimized,

$$\frac{\partial Q}{\partial A_k} = 2 \sum_{i=1}^n f_i \left(\frac{\partial f_i}{\partial A_k} \right) = 0 \quad (k = 1 \text{ to } 4) \quad (29)$$

This set of linear equations can be written in matrix notation:

$$\begin{bmatrix} \sum_i \dot{\theta}_i^2 & \sum_i \dot{\theta}_i \theta_i & \sum_i \dot{\theta}_i t_i & \sum_i \dot{\theta}_i \\ \sum_i \dot{\theta}_i \theta_i & \sum_i \theta_i^2 & \sum_i \theta_i t_i & \sum_i \theta_i \\ \sum_i \dot{\theta}_i t_i & \sum_i \theta_i t_i & \sum_i t_i^2 & \sum_i t_i \\ \sum_i \dot{\theta}_i & \sum_i \theta_i & \sum_i t_i & \sum_i 1 \end{bmatrix} \begin{bmatrix} A_1 \\ A_2 \\ A_3 \\ A_4 \end{bmatrix} = \begin{bmatrix} -\sum_i \ddot{\theta}_i \dot{\theta}_i \\ -\sum_i \ddot{\theta}_i \theta_i \\ -\sum_i \ddot{\theta}_i t_i \\ -\sum_i \ddot{\theta}_i \end{bmatrix} \quad (30)$$

When this expression is solved for A_k , the values of α and ω are obtained (Equations 23 and 24).

Non-Linear Least Squares Method (9). Assuming that (from equation 20)

$$\theta = A_1 \exp(-A_2 t) \cos(A_3 t + A_4) + A_5 t + A_6 \quad (31)$$

where now $A_1 = \theta_0$, $A_2 = \alpha$, $A_3 = 2\pi/P$, $A_4 = \phi$, $A_5 = B$ and $A_6 = C$ is an adequate representation of the solution to the equation of motion of a torsion pendulum, the parameters A_k ($k = 1$ to 6) can be determined by fitting the data (θ_i , t_i ; $i = 1$ to n) to the solution.

If the values of the parameters A_k were known, it would be possible to evaluate

$$f_i = A_1 \exp(-A_2 t_i) \cos(A_3 t_i + A_4) + A_5 t_i + A_6 \quad (32)$$

for each t_i to obtain a set of "true" residuals

$$r_i = f_i - \theta_i \quad (i = 1 \text{ to } n) \quad (33)$$

A "true" residual would represent the difference between the actual function value at t_i and the empirical value θ_i . These "true" residuals cannot be calculated because the actual values of the parameters A_k are not known.

However, initial estimates of the parameters A_k^0 can be obtained from other methods, or a previous wave, and "computed" residuals can be calculated:

$$R_i = A_1^0 \exp(-A_2^0 t_i) \cos(A_3^0 t_i + A_4^0) + A_5^0 t_i + A_6^0 - \theta_i \quad (i = 1 \text{ to } n) \quad (34)$$

Improved estimates of the parameters A_k can be obtained by a differential correction technique based on least squares, provided that the estimates A_k° are sufficiently close to the actual values of the parameters A_k to lead to convergence of the method. This differential correction technique can be derived by first expanding the function about A_k° using a linear Taylor series expansion of the form

$$f(t_i, A_1, A_2, \dots, A_6) = f(t_i, A_1^{\circ}, A_2^{\circ}, \dots, A_6^{\circ}) + \frac{\partial f}{\partial A_1} (A_1 - A_1^{\circ}) + \frac{\partial f}{\partial A_2} (A_2 - A_2^{\circ}) + \dots + \frac{\partial f}{\partial A_6} (A_6 - A_6^{\circ}) \quad (35)$$

so that a relation between the r_i and R_i can be obtained. This relation can be found by evaluating the equation at each value of t_i and subtracting θ_i from both sides of the equation. Using the definitions

$$\delta A_k = A_k - A_k^{\circ} \quad (36)$$

and

$$\left. \frac{\partial f_i}{\partial A_k} = \frac{\partial f_i}{\partial A_k} \right|_{t = t_i, A_k = A_k^{\circ}} \quad (37)$$

the result can be written in the form

$$f(t_i, A_1, A_2, \dots, A_6) - \theta_i = f(t_i, A_1^{\circ}, A_2^{\circ}, \dots, A_6^{\circ}) + \left(\frac{\partial f_i}{\partial A_1}\right) \delta A_1 + \dots + \left(\frac{\partial f_i}{\partial A_6}\right) \delta A_6 - \theta_i \quad (i = 1 \text{ to } n) \quad (38)$$

The desired relation between the r_i and R_i can then be found by substituting the expressions for r_i and R_i :

$$r_i = R_i + \left(\frac{\partial f_i}{\partial A_1}\right) \delta A_1 + \dots + \left(\frac{\partial f_i}{\partial A_6}\right) \delta A_6 \quad (i = 1 \text{ to } n) \quad (39)$$

This relation can be used to compute, from A_k° , a set of parameters A_k that minimizes the sum of the squares of the "true" residuals r_i , i.e.,

$$Q = \sum_{i=1}^n r_i^2 = \sum_{i=1}^n [R_i + \left(\frac{\partial f_i}{\partial A_1}\right) \delta A_1 + \dots + \left(\frac{\partial f_i}{\partial A_6}\right) \delta A_6]^2 \quad (40)$$

The function Q has a minimum value when all of its partials with respect to the δA_k are simultaneously zero:

$$\begin{aligned} \frac{\partial Q}{\partial (\delta A_k)} = & 2 \sum_{i=1}^n \left(\frac{\partial f_i}{\partial A_k} \right) R_i + \left(\frac{\partial f_i}{\partial A_k} \right) \left(\frac{\partial f_i}{\partial A_1} \right) \delta A_1 + \dots \\ & + \left(\frac{\partial f_i}{\partial A_k} \right) \left(\frac{\partial f_i}{\partial A_6} \right) \delta A_6 = 0 \quad (k = 1 \text{ to } 6) \end{aligned} \quad (41)$$

Rearranging,

$$\begin{aligned} \delta A_1 \sum_{i=1}^n \left(\frac{\partial f_i}{\partial A_k} \right) \left(\frac{\partial f_i}{\partial A_1} \right) + \dots + \delta A_6 \sum_{i=1}^n \left(\frac{\partial f_i}{\partial A_k} \right) \left(\frac{\partial f_i}{\partial A_6} \right) = \\ - \sum_{i=1}^n \left(\frac{\partial f_i}{\partial A_k} \right) R_i \quad (k = 1 \text{ to } 6) \end{aligned} \quad (42)$$

Evaluating this equation for each k , and writing the result in matrix form, the normal equations are obtained:

$$\begin{bmatrix} \sum \left(\frac{\partial f_i}{\partial A_1} \right)^2 & \sum \frac{\partial f_i}{\partial A_1} \frac{\partial f_i}{\partial A_2} & \sum \frac{\partial f_i}{\partial A_1} \frac{\partial f_i}{\partial A_3} & \sum \frac{\partial f_i}{\partial A_1} \frac{\partial f_i}{\partial A_4} & \sum \frac{\partial f_i}{\partial A_1} \frac{\partial f_i}{\partial A_5} & \sum \frac{\partial f_i}{\partial A_1} \frac{\partial f_i}{\partial A_6} \\ \sum \frac{\partial f_i}{\partial A_2} \frac{\partial f_i}{\partial A_1} & \sum \left(\frac{\partial f_i}{\partial A_2} \right)^2 & \sum \frac{\partial f_i}{\partial A_2} \frac{\partial f_i}{\partial A_3} & \sum \frac{\partial f_i}{\partial A_2} \frac{\partial f_i}{\partial A_4} & \sum \frac{\partial f_i}{\partial A_2} \frac{\partial f_i}{\partial A_5} & \sum \frac{\partial f_i}{\partial A_2} \frac{\partial f_i}{\partial A_6} \\ \sum \frac{\partial f_i}{\partial A_3} \frac{\partial f_i}{\partial A_1} & \sum \frac{\partial f_i}{\partial A_3} \frac{\partial f_i}{\partial A_2} & \sum \left(\frac{\partial f_i}{\partial A_3} \right)^2 & \sum \frac{\partial f_i}{\partial A_3} \frac{\partial f_i}{\partial A_4} & \sum \frac{\partial f_i}{\partial A_3} \frac{\partial f_i}{\partial A_5} & \sum \frac{\partial f_i}{\partial A_3} \frac{\partial f_i}{\partial A_6} \\ \sum \frac{\partial f_i}{\partial A_4} \frac{\partial f_i}{\partial A_1} & \sum \frac{\partial f_i}{\partial A_4} \frac{\partial f_i}{\partial A_2} & \sum \frac{\partial f_i}{\partial A_4} \frac{\partial f_i}{\partial A_3} & \sum \left(\frac{\partial f_i}{\partial A_4} \right)^2 & \sum \frac{\partial f_i}{\partial A_4} \frac{\partial f_i}{\partial A_5} & \sum \frac{\partial f_i}{\partial A_4} \frac{\partial f_i}{\partial A_6} \\ \sum \frac{\partial f_i}{\partial A_5} \frac{\partial f_i}{\partial A_1} & \sum \frac{\partial f_i}{\partial A_5} \frac{\partial f_i}{\partial A_2} & \sum \frac{\partial f_i}{\partial A_5} \frac{\partial f_i}{\partial A_3} & \sum \frac{\partial f_i}{\partial A_5} \frac{\partial f_i}{\partial A_4} & \sum \left(\frac{\partial f_i}{\partial A_5} \right)^2 & \sum \frac{\partial f_i}{\partial A_5} \frac{\partial f_i}{\partial A_6} \\ \sum \frac{\partial f_i}{\partial A_6} \frac{\partial f_i}{\partial A_1} & \sum \frac{\partial f_i}{\partial A_6} \frac{\partial f_i}{\partial A_2} & \sum \frac{\partial f_i}{\partial A_6} \frac{\partial f_i}{\partial A_3} & \sum \frac{\partial f_i}{\partial A_6} \frac{\partial f_i}{\partial A_4} & \sum \frac{\partial f_i}{\partial A_6} \frac{\partial f_i}{\partial A_5} & \sum \left(\frac{\partial f_i}{\partial A_6} \right)^2 \end{bmatrix} \begin{bmatrix} \delta A_1 \\ \delta A_2 \\ \delta A_3 \\ \delta A_4 \\ \delta A_5 \\ \delta A_6 \end{bmatrix} = \begin{bmatrix} - \sum \frac{\partial f_i}{\partial A_1} R_i \\ - \sum \frac{\partial f_i}{\partial A_2} R_i \\ - \sum \frac{\partial f_i}{\partial A_3} R_i \\ - \sum \frac{\partial f_i}{\partial A_4} R_i \\ - \sum \frac{\partial f_i}{\partial A_5} R_i \\ - \sum \frac{\partial f_i}{\partial A_6} R_i \end{bmatrix} \quad (43)$$

where

$$\frac{\partial f_i}{\partial A_1} = \exp(-A_2 t_i) \cos(A_3 t_i + A_4) \quad (44)$$

$$\frac{\partial f_i}{\partial A_2} = -A_1 t_i \exp(-A_2 t_i) \cos(A_3 t_i + A_4) \quad (45)$$

$$\frac{\partial f_i}{\partial A_3} = -A_1 t_i \exp(-A_2 t_i) \sin(A_3 t_i + A_4) \quad (46)$$

$$\frac{\partial f_i}{\partial A_4} = -A_1 \exp(-A_2 t_i) \sin(A_3 t_i + A_4) \quad (47)$$

$$\frac{\partial f_i}{\partial A_5} = t_i \quad (48)$$

$$\frac{\partial f_i}{\partial A_6} = 1 \quad (49)$$

The solution, δA_k , of this set of normal equations is a first-order approximation of the changes in A_k required to obtain the parameters A_k . If any $|\delta A_k| > \epsilon$ (error limit), A_k is replaced by $A_k + \delta A_k$ and the entire differential-correction procedure is repeated using these new estimates.

Fourier Transform Method. Another method of data reduction is to take a fast Fourier transform (FFT) of the wave (10). As indicated in Figure 7, the Fourier transform of a damped sine wave with a single frequency is a single maximum in the frequency domain at the frequency of the oscillation. The amplitude (H) of the transformed data as a function of angular frequency (ω) is given by (11)

$$H = \frac{\theta_0 [\alpha^2 (\alpha^2 + \omega^2 + \omega_0^2)^2 + \omega^2 (\alpha^2 + \omega^2 - \omega_0^2)^2]^{\frac{1}{2}}}{(\alpha^2 + \omega^2 - \omega_0^2)^2 + (2\alpha\omega)^2} \quad (50)$$

where θ_0 is the initial amplitude, α is the damping coefficient, and ω_0 is the natural angular frequency of the oscillation. The amplitude of the peak is given by

$$H_{\max} = \left(\frac{\theta_0}{\alpha}\right) \left[\frac{\alpha^2 + \omega_0^2}{\alpha^2 + 4\omega_0^2}\right]^{\frac{1}{2}} \cong \frac{\theta_0}{2\alpha} \quad (\alpha \ll \omega_0) \quad (51)$$

from which α , the damping coefficient, is obtained.

Discussion. The four methods of data reduction were used to analyze the raw data of the same TBA specimen during a slow (0.25°C/min) temperature scan (Figure 8). A comparison of the spectra indicates that they all gave similar results over the range of period (0.3 to 1.8 sec) and logarithmic decrement (0.01 to 1.08) encountered in the experiment. (The automated torsion pendulum has been used to reduce data with a range of 0.1 to 15 sec. for the period, and 0.001 to 4.0 for the

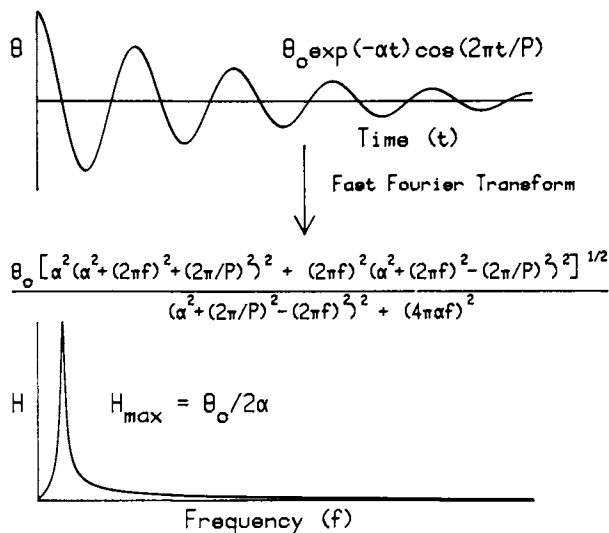


Figure 7. Fourier transform method. The Fourier transform of an exponentially damped sine wave of period P and damping coefficient α is a single maximum at the oscillation frequency whose amplitude is inversely proportional to the damping coefficient.

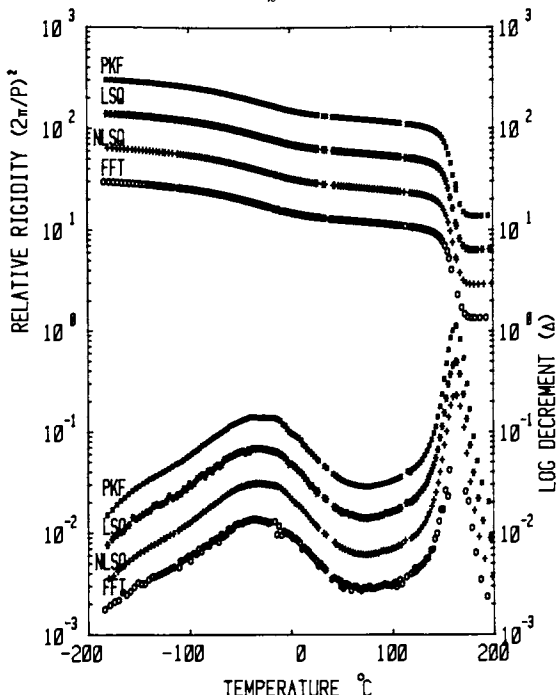


Figure 8. Dynamic mechanical spectrum (TBA) of Epon 828/PACM-20 in which the relative rigidity and logarithmic decrement have been calculated by four methods: \square , peak-finding [PKF]; $*$, linear least squares (LSQ); $+$, non-linear least squares (NLSQ); and \circ , fast Fourier transform (FFT). For clarity the LSQ, NLSQ and FFT data have been displaced vertically in equal increments from the PKF data.

logarithmic decrement). In Figure 8 there is no appreciable difference in the relative rigidity, but in the logarithmic decrement the non-linear least squares reduction method produces the smoothest results, followed by the peak-finding method. The linear least squares and Fourier transform methods have considerable scatter. The linear least squares method also results in a small systematic difference in the logarithmic decrement from the other three.

Although the peak-finding method is the simplest way of deriving the period and logarithmic decrement from the raw data, it has some limitations in that at least 2.25 cycles of oscillation are required in order to do the calculation. This is a problem when the system approaches critical damping conditions. It also is difficult to calculate the logarithmic decrement at very low damping (when the peak amplitude changes only slightly during the time data is collected) due to the resolution of the digitizing voltmeter. Of the four methods discussed, the peak finding method is the most sensitive to the scan rate, since the number of data points about each peak that are fitted to the three-parameter quadratic equation should be at least nine as discussed earlier. Therefore the scan rate, which depends on the estimate of the period, needs to be quite close to $40/P$, where P is the actual period. Also, a systematic error is introduced when this method is used, because the position of the peaks is a function of the damping as well as the period. As can be seen in Figure 9, the peaks shift to shorter times as the damping increases.

The least squares fitting method overcomes limitations of the peak finding method, but introduces some errors of its own. It is not as sensitive to the scan rate, as long as $S \gg 2/P$ (the Nyquist frequency), and its accuracy increases with increasing number of data points. It was found empirically (8) that the error was reduced if an integral number of cycles was used in the analysis. Some error is introduced due to the fact that first and second derivatives of the raw data have to be taken.

The use of the non-linear least squares method does not require any derivatives, but needs an initial estimation and takes more time to compute, since several iterations (usually 3 or 4) are necessary to reduce the difference between the estimated and calculated values of the damping coefficient to within 0.1%. But since this method only requires between 100 and 150 data points without a loss in accuracy compared to as many as 1000 for the peak-finding and least squares methods, the scan rate can be reduced as much as 90% and the time required for the calculations is reduced to the order of a minute.

The Fourier transform method requires a minimum of 1024 data points to provide enough resolution to calculate the damping coefficient. The FFT of 1024 data points takes approximately a minute with the HP 9825B computer, so this constitutes a practical limit in resolution due to computer memory size and time considerations. So as not to introduce error, the damped oscillations

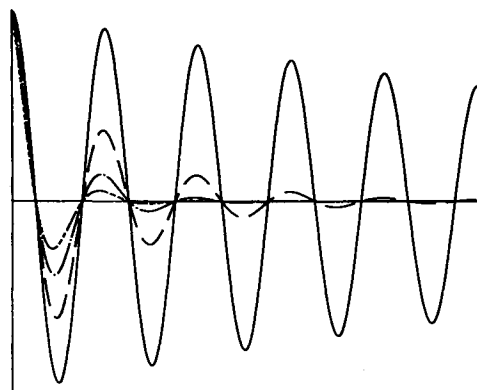


Figure 9. Damped sine wave. Error in measuring period by peak-finding method: the peaks of an exponentially damped sine wave of single frequency (0.5 Hz) shift to shorter times with increasing damping coefficient. Key to α values: —, 0.05; ---, 0.5; - · -, 1.0; ———, 1.5.

$$\text{Equation of motion: } I \frac{d^2\theta}{dt^2} + n_{dyn} \frac{d\theta}{dt} + G_{dyn}\theta = 0$$

$$\text{Solution: } \theta = \theta_0 \exp(-\alpha t) \cos(\omega t)$$

$$\text{Shear modulus: } G' = KI(\omega^2 + \alpha^2)$$

$$\text{Loss modulus: } G'' = KI\omega\alpha$$

$$\text{where } \omega = 2\pi/P, \alpha = \Delta/P, \text{ and } \Delta = \ln(\Lambda_n/\Lambda_{n+1})$$

American Chemical
Society Library
1155 16th St., N.W.
Washington, D. C. 20036

must not be truncated; therefore it is important to adjust the scan rate and the number of data points so that the entire wave is collected. The major problem with using the FFT method is the difficulty in obtaining accurate values of α ; the curve is Laurentian, and hence its amplitude at the maximum is difficult to obtain. One way around this is to use a curve fitting procedure, but then there is no advantage in using this method. Some alternatives may be to use a larger and faster computer, or a dedicated microprocessor such as the spectrum analyzer (HP 3582A), which can compute the FFT in real time. A practical feature of the FFT is in the display of the transformed data; any non-homogeneity of the signal due to other modes of motion will appear as secondary peaks, and so this method serves as an excellent way to monitor the oscillations.

Although comparison of the four methods shows that the smoothest reduced data for the given experiment were obtained using the non-linear least squares method, the ultimate quality depends on the quality of the sensor signals of the experiment. Published superior TBA spectra obtained using the linear least squares method (8), and the peak-finding method using an analog computer (2), were presumably the consequence of a better basic experiment than the one used in this report to compare (as in Figure 8) the data reduction methods.

Calibration

A calibration wire whose shear modulus is known can be used to determine the moment of inertia of the pendulum assembly, so that quantitative measurements of the dynamic mechanical properties of specimens can be made. The shear modulus of the calibration wire is obtained by measuring the period of oscillation of a simple torsion pendulum consisting of an aluminum rod suspended by the wire. The moment of inertia of this system is given by

$$I = m\left(\frac{r^2}{3} + \frac{\ell^2}{12}\right) \quad (52)$$

where m is the mass, r is the radius and ℓ is the length of the rod.

The shear modulus G' of a wire is given by

$$G' = \frac{8\pi LI}{R^4 P^2} \quad (53)$$

where L is the length and R is the radius of the wire. With the calibration wire (whose shear modulus was determined to be 9.789×10^{11} dyne/cm²) as a specimen in the automated torsion pendulum, the moment of inertia of the pendulum that was used routinely in the subsequent experiments was determined to be 138.7 g-cm². The shear modulus of a film of known dimensions can then be calculated

from the period and logarithmic decrement using the equation (4):

$$G' = \frac{4\pi^2 IL}{NP^2} \left(1 + \frac{\Delta^2}{4\pi^2}\right) - \frac{mga^2}{12N} \quad (54)$$

where N is a form factor:

$$N = \frac{ab^3}{3} (1 - 0.63 b/a) \quad (55)$$

a is the width, b is the thickness ($b < a/3$), L is the length, m is the mass supported by the specimen and g is the gravitational constant.

Comparison of Torsion Pendulum and TBA

A film of an amine-cured epoxy, Epon 828 (Shell)/PACM-20 (DuPont) with $T_{g\infty} = 166^\circ\text{C}$, was cured by heating it to 250°C in a helium atmosphere. The dynamic mechanical spectrum of this film is shown in Figure 5. For comparison, the corresponding spectrum of a specimen consisting of a multifilamented glass braid impregnated with the uncured resin and cured in the TBA apparatus by heating it to 200°C under helium atmosphere is shown in Figure 10.

It has been reported (12) that the shear modulus as measured by the torsion pendulum and TBA should differ only by a multiplicative constant below T_g and the logarithmic decrement should be identical. Although the spectra of Epon 828/PACM-20 obtained by torsion pendulum and torsional braid analysis show transitions at the same temperature (glass transition at 166°C and a secondary sub-glass transition at -28°C), the results indicate that the actual modulus and logarithmic decrement cannot be compared quantitatively. In Figure 11 the relative rigidity (TBA) has been shifted vertically for comparison with the torsion pendulum data; a vertical shift on a logarithmic scale is equivalent to multiplying by a constant. It is evident by comparing the curves in Figure 11 that there is only a qualitative correlation between them.

Conclusions

The automation of the torsion pendulum utilizing a desktop computer eliminates the tedious data analysis previously associated with that technique. Any one of four data reduction methods can be used; the experimental conditions will determine which is the optimum one to employ. The torsion pendulum technique provides quantitative values of shear modulus and logarithmic decrement and in the torsion braid mode provides a qualitative analysis of materials, especially in the liquid-to-solid transition region. In addition to providing the capability of using any one of four data reduction techniques, the computer has the advantage of storing the data on magnetic tape, where it is available to be

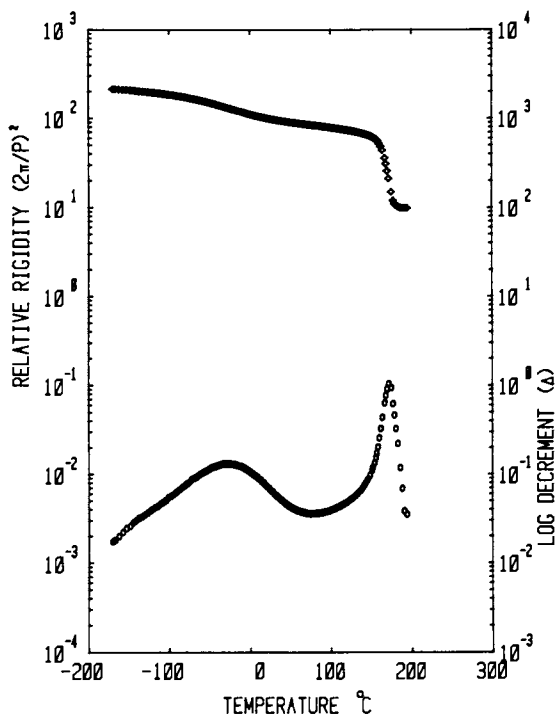


Figure 10. Dynamic mechanical spectrum (TBA) of a cured composite specimen (glass braid impregnated with Epon 828/PACM-20 resin). Key: \diamond , relative rigidity vs. T and \circ , log decrement vs. T .

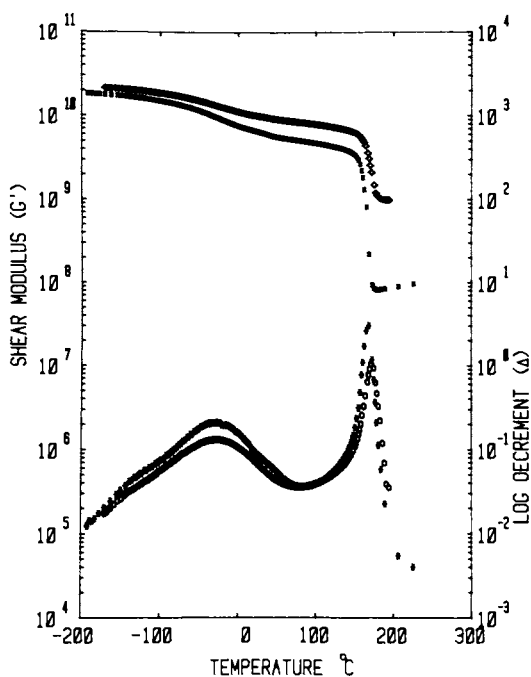


Figure 11. A comparison of torsion pendulum data obtained using a film [\square , shear modulus vs. T ; $*$, log decrement vs. T] and TBA data obtained using a supported specimen [\diamond , relative rigidity vs. T ; \circ , log decrement vs. T].

accessed for further computation or to be plotted in whatever mode is most suitable. Since the computer is easily programmable, the software can readily be adapted to consider other variables or to control the experiment in other ways.

Acknowledgment. This research was partially supported by the Office of Naval Research.

Literature Cited

1. Gillham, J. K. AIChE Journal, 1974, 20, 1066.
2. Gillham, J. K. "Torsional Braid Analysis (TBA) of Polymers", in Developments in Polymer Characterization-3, J. V. Dawkins, Ed., Applied Science Publishers: London, 1982. Ch. 5.
3. Enns, J. B.; Gillham, J. K.; Doyle, M. J. ACS Div. Organic Coatings and Plastics Chemistry, Preprints, 1980, 43, 669.
4. McCrum, N. G.; Read, B. E.; Williams, G. Anelastic and Dielectric Effects in Polymeric Solids, John Wiley and Sons, Ltd: London, 1967.
5. Enns, J. B.; Gillham, J. K.; Small, R. ACS Polymer Division, Preprints, 1981, 22, 123.
6. Enns, J. B. Ph.D. Thesis, Princeton University, 1982.
7. Solomon, James, "Development of a Data Reduction Scheme for Torsional Braid Analysis: Curve Fitting by Least Squares". Senior Thesis, Dept. of Chemical Engineering, Princeton University, Princeton, NJ, April 1976.
8. Gillham, J. K.; Stadnicki, S. J.; Hazony, Y. J. Appl. Polymer Sci., 1977, 21, 40.
9. McCalla, T. R. Introduction to Numerical Methods and Fortran Programming. John Wiley & Sons, Inc.: New York, 1967.
10. Ackroyd, M. H. Digital Filters. Butterworths: London, 1973.
11. Champeney, D. C. Fourier Transforms and Their Physical Applications. Academic Press: New York, 1973.
12. Hartman, B; Lee, G. F. J. Appl. Polymer Sci., 1977, 21, 1341.

RECEIVED May 4, 1982.

Advanced Thermal Analysis System (ATHAS) Polymer Heat Capacity Data Bank

UMESH GAUR¹ and BERNHARD WUNDERLICH

Rensselaer Polytechnic Institute, Department of Chemistry, Troy NY 12181

Heat capacity is the key thermodynamic property of a material. It is well enough understood to permit, when determined over a wide range of temperature, the connection between macroscopic thermodynamic properties and microscopic structure and motion. Through the knowledge of heat capacity the other thermodynamic functions, namely enthalpy, entropy, and Gibbs energy can be derived.

$$H - H_0 = \int_0^{T_1} C_p dT + \Delta H_1 + \int_{T_1}^{T_2} C_p dT + \Delta H_2 \dots \quad (1)$$

$$S = \int_0^{T_1} \frac{C_p}{T} dT + \frac{\Delta H_1}{T_1} + \int_{T_1}^{T_2} \frac{C_p}{T} + \frac{\Delta H_2}{T_2} \dots \quad (2)$$

$$G - H_0 = H - TS \quad (3)$$

In these equations $T_1, T_2 \dots$ represent equilibrium first order transition temperatures and $\Delta H_1, \Delta H_2 \dots$ the corresponding equilibrium transition enthalpies. H_0 is the enthalpy of the material analyzed at 0 K.

Heat capacity theory permits a correlation with the chemical structure of the repeating unit (1-3). In the solid state, only vibrational contributions need to be considered (skeletal and group vibrations). For an approximate discussion of the skeletal vibrations, the molecule is considered to be a string of structureless beads of the given formula weight. For linear macromolecules with similar backbones, the geometry and force constants are similar so that intramolecular skeletal vibrations are fixed by the mass of the structureless bead. The intermolecular vibrations of linear macromolecules have quite low

¹ Current address: Personal Products, Division of Johnson & Johnson, Milltown, NJ 08850

frequencies and are few in number. They are usually excited already below 50 K so that their detailed frequencies must be known only for the heat capacities below 50 K. Due to the large differences in frequency and geometry of the group and skeletal vibrations, the group vibrations can be considered largely uncoupled from the skeletal vibrations, and thus are only chemical structure dependent. The same group will give the same heat capacity contribution in any molecule. Thus, all contributions to heat capacities of linear macromolecules, except the intermolecular skeletal vibrations, are dependent on the chemical structure only, and are additive. Based upon the above hypothesis, a chemical structure based heat capacity prediction scheme for polymers and copolymers was developed in our laboratory (2). To test the addition scheme a heat capacity data base was established in 1967. The heat capacity addition scheme could predict the heat capacity of carbon backbone polymers and copolymers within 5% (2). However, to further extend the addition scheme to more complicated polymers containing hetero chain atoms and large side groups, and to rigid backbone polymers in the solid state as well as in the liquid state, a much larger heat capacity data base representing very many types of repeat unit was needed.

Heat capacities of polymer are complicated by physical and chemical structural changes, namely by changes in crystallinity, crystal structure, morphology, tacticity, molecular weight and copolymer unit content. Furthermore the picture can be complicated by changes in mechanical, thermal and possibly electrical history of the polymer.

The microscopic structure of polymers is primarily identified by the crystal structure and the crystallinity of the sample. It can produce significant changes in the heat capacity (especially at very low temperature and in the temperature region between the glass transition and the melting temperature). Most heat capacity studies do not contain data on the variation in macroscopic structure. For this type of analysis, measurements are needed on a large number of samples of differing crystallinities. Thus, there exists besides extensive new measurements, a need for the collection of all measured data in a data bank to most efficiently correlate heat capacities with the microscopic structure and to extrapolate the heat capacity data to the limiting structures of the molecules. Only on the basis of a large volume of critically analyzed data can the detailed structure dependence be derived.

The glass transition of polymers is easily characterized by thermal analysis. A sharp increase in heat capacity on unfreezing over a narrow temperature region is observed. At

present two empirical rules exist for estimation of this heat capacity change:

$$\text{Wunderlich's rule (4) } \Delta C_p = 11.3 \text{ JK}^{-1} (\text{mol bead})^{-1} \quad (4)$$

$$\text{and Boyer's rule (5) } \Delta C_p T_g = 15 + 0.04 T_g \text{ cal g}^{-1} \text{ K}^{-1} \quad (5)$$

where a bead is defined as a molecular grouping which can be considered a rigid bead in the molecule. In the recent past we have found many exceptions to both the rules (3,6). Most of the deviations were for polymers containing large aromatic groups, which contribute almost twice as much to the heat capacity increase as smaller beads such as CH_2 -. This creates the need for a large, critically evaluated data base for heat capacity changes at the glass transition. As for the heat capacity itself, considerable changes in glass transition temperature, temperature range, and detailed heat capacity values (hysteresis) are observed for samples for non-standard thermal and mechanical histories.

The first order phase transitions, primarily identified with the melting transition, make up the final thermal characterization of a material. Equilibrium heats of transition and transition temperatures are needed to use eqs. 1-3 for a full-range thermal characterization. A larger discussion of the interpretation and prediction of melting temperatures has been given recently (7). In brief, quite frequently the heat of fusion per large atom in a macromolecule (such as C, O, N, but exclude H) is 2.4 (+0.3) kJ/mol and the entropy of fusion per flexible main chain segment (such as CH_2 -, O-, C_6H_4 -, $\text{CH}=\text{CH}$ -, CO-NH -, etc.) is 9.5 (+1.4) J/(K mol). These + quantities are linked by the melting temperature.

$$T_m = \frac{\Delta H_f}{\Delta S_f} \quad (6)$$

The error limits given in ΔH_f and ΔS_f are derived from a critical evaluation of about 40 different macromolecules (7). As in heat capacities and glass transitions, extension of the description of macromolecules is possible (necessary) when considering the normally present non-equilibrium states. Partial crystallization, small crystal sizes, impurity and copolymer content, and straining of molecules from the random coil conformation are the major effects to be considered. The changes of heats of transition and temperatures of transition and their use to characterize the non-equilibrium state have been given an initial critical survey (7).

In this paper our efforts are directed towards the establishment of a heat capacity data bank which are detailed. Of necessity, the initial steps are directed towards the equilibrium properties. Extensions to include glass transitions,

melting transitions, and ultimately also solid-solid and mesophase transitions are in various stages of planning. A final step must be the extension of the data bank to non-equilibrium properties.

The Polymer Heat Capacity Data Bank

To address our efforts towards correlating the macroscopically measured heat capacity data to their microscopic origin, the data base started in the 1960's was updated and computerized about five years ago (8). The data bank is now incorporated within ATHAS, Advanced Thermal Analysis, a laboratory for research and instruction. The data bank maintains a collection of more than 500 publications on heat capacities of polymers which includes all measurements ever reported. The publication list is updated every six months. From each publication the following information is retrieved:

1. polymers studied
2. temperature range studied
3. thermal history and sample characterization
4. experimental technique used and claimed uncertainty
5. accuracy of representation of data.

Based upon the above information, the publication is then critically assessed for quality and reliability of the heat capacity data. Judgments for evaluating the quality of heat capacity data are based upon the following:

- a) characterization of the samples used for heat capacity measurements
- b) experimental technique used and reported uncertainty
- c) representation of data, and
- d) visual comparison of data with other investigations.

The principles followed in selecting acceptable data are, briefly, as follows:

- a) Purity and morphological characterization of the samples are examined. Data on uncharacterized, commercial plastics are considered unreliable. The key characterization parameter useful for our analysis, besides molecular weight and thermal history, is the crystallinity of the sample. Crystallinity calculated from density measurement is preferred over its determination from the heat of fusion, X-ray and IR spectroscopy. Crystallinity determination from enthalpy and the heat capacity change at the glass transition are considered least reliable.

- b) The experimental aspects are examined for each measurement. The reliability of the measuring technique, as determined from results on standard calibration materials, is considered important. Below 100 K, adiabatic calorimetric results are in general considered more reliable than differential scanning calorimetric measurements. From 200 to 350 K, depending upon the sophistication of the instrument and averaging procedures used, the differential scanning calorimetry and adiabatic calorimetry data may be considered equally good. Above 350 K, in certain cases, due to metastability of the samples, differential scanning calorimetry results are often preferred over adiabatic calorimetry.
- c) Heat capacity data represented only by small graphs which cannot be read accurately are not considered reliable. Tabulated data are considered more reliable than graphical data. If raw heat capacity data points are reported by investigators, their data are curve fitted and the heat capacity function obtained is preferred over the tabulated and graphical values.
- d) If any measurement shows obvious, significant deviations from other data sets of comparable samples, the data are questioned. Such discrepancies are usually several standard deviations and indicate systematic errors.

The acceptable heat capacity data are stored on magnetic tape in temperature intervals of 0.1 K up to 1 K, 0.2 K to 2 K, 1 K to 10 K, 2 K to 20 K, and 5 K to 30 K. At temperatures higher than 30 K, intervals of 10 K are used. If the data are not reported in the temperature intervals desired by us, the data are interpolated. The spline function technique is used to determine the interpolated heat capacity at desired temperature. If unsmoothed data have been reported by the authors, the data are smoothed by curve-fitting prior to storage.

A Hewlett-Packard calculator (minicomputer) of type 9821A, equipped with magnetic tape deck and interfaced with thermal line printer HP 9866B and plotter HP 9862A is the data handling system. Computer programs have been developed to govern interpolation, curve fitting, data storage, tabulation and plotting of the heat capacity data. Programs have also been developed for assistance in comparison and critical assessment of the data and to further analyze the data to determine the best heat capacity values. Subroutines have been written to correlate the heat capacity data and the morphological properties to determine the heat capacity of completely amorphous and completely crystalline linear macromolecules. A detailed listing of these

programs and the instructions for their operations are given in reference 8.

Results

The data bank contains in over 800 tables all information on the heat capacity of polymers. These acceptable heat capacity data have been computer processed, to derive for the first time a comprehensive set of recommended data. At present, recommended data are available for 96 polymers. These recommended data are summarized in the table below. They are being discussed in nine successive papers in the Journal of Physical and Chemical Reference Data (1981/82). The first two papers have already been published (9, 10).

Publication	No. of Polymers	Manuscript Pages
1. Selenium	1	81
2. Polyethylene	1	91
3. Polypropylene	1	62
4. Polystyrene	1	52
5. Polyoxides	12	150
6. Acrylic Polymers	15	95
7. Other Carbon Backbone Polymers	24	170
8. Polyesters and Polyamides	10	120
9. Aromatic and Inorganic Polymers	31	103

The recommended data are, whenever possible, extrapolated to the limiting macroconformation to determine the heat capacity of the crystalline and amorphous states. In cases where low temperature data are available, the thermodynamic functions; entropy, enthalpy and Gibbs energy have also been calculated.

The recommended heat capacity data are currently being analyzed in terms of chemical structure, structure of the polymers in the glassy, crystalline and molten states. The data are further being analyzed to study the effect of branching, molecular weight and tacticity on the heat capacity of polymers. Comprehensive tabulation of heat capacities of various structural units are being prepared and will be available in the near future.

From the recommended data, a compilation of heat capacity changes at the glass transition has been made. These data are

being analyzed in terms of the hole theory of the glass transition to possibly develop an addition scheme for ΔC_p at T_g .

Future of the Polymer Heat Capacity Data Bank

The polymer heat capacity data bank is, as outlined in the Introduction, is only the first step towards the establishment of a comprehensive Thermal Properties Data Bank. Presently we are expanding our efforts to include glass transition temperatures, melting temperatures and heats of fusion. In the planning stage are specific volume, compressibility, and thermal conductivity data banks, as well as the expansion to non-equilibrium properties.

Based on the structure-related addition schemes for the thermal properties, it should, for example, be possible to quantitatively generate differential scanning calorimetry curves for polymers, copolymers and their mixtures. With easy access to the data bank, it should be possible for thermal analysts to compare their newly measured DSC curves with the computer generated standard curves for on-line analysis of macromolecules.

This improvement of the Data Bank to computer handling is presently being tested and discussed. Our goal is to transfer the Data Bank to the RPI IBM 3033 computer which should be accessible in the future through computer networks such as TELENET. The data management is presently explored using the SPIRES system (Stanford Public Information Retrieval System). A brief outline of the development stages of this effort is as follows:

1. Input Block

To find the needed polymer we are exploring extensive lists of synonyms, source and structure based names, and name-structure correlations so that entry into the data bank is possible from every recognizable description of the macromolecule. The finally chosen polymer will be characterized by its repeating unit formula (for addition schemes), a system number (arbitrary for data search), and the best name (for report output).

Out of this block the user would enter the Data Bank proper. We envision four interacting data banks of which we have chosen the Heat Capacity Data Bank for

closer scrutiny and initial development. The other three data banks are the PVT-Data Bank, Transition Data Bank, and Thermal Conductivity Data Bank. Their interaction becomes clear from eqs. 1 to 3 which illustrates the need of transition data. Changes from C to C_V which are needed for comparison of experimental and calculated data illustrate heat capacity and PVT-data bank interaction.

2. Heat Capacity Data Bank

A. Recommended Data

The recommended data, as developed above, form subblock A of the Heat Capacity Data Bank. They can be retrieved as such, or they can be searched for their base (i.e., detailed references and data tables) and also for additional, non-used data (detailed references and data tables as well as reasons for exclusion - see, for example Refs. 9 and 10). If there are no recommended data, or only insufficient recommended data are available or if information on prediction schemes is requested, block B of the Heat Capacity Data Bank is entered.

B. Prediction Schemes

This subblock of the Heat Capacity Data Bank contains empirical as well as theoretical prediction calculations of the heat capacity which are continuously updated. Based on the chemical structure (back-bone, side-chain) as well as on the physical state (glass, crystal, mesophase, liquid, semicrystalline, equilibrium, history), a heat capacity is retrieved. The Prediction Scheme subblock can also be searched for its base, i.e., the precise assumptions which go into the prediction, with documentation to the literature.

C. Calculation Block

The final subblock of the Heat Capacity Data Bank involves programs for needed calculations in the thermal analysis field. The simple stages involve data treatment for input and output, calculation of derived functions as given, for example, in eqs. 1 to 3. Further stages include the data analysis in form of Debye and Tarasov Θ -temperatures and group vibration frequencies, a stage already completed (11). Self-

adaptive integration routines and self-generation of the various heat capacity tables have been developed. Calculation routines for liquid heat capacities and history effects are similarly contemplated.

Overall then, the data bank would represent an up-to-date knowledge of thermal data of macromolecules. Since the computer storage permits constant updating, it will always remain current. Naturally, a series of easy extensions of such a system are possible. The extensive reference lists covering all aspects of thermal analysis can be accessed separately and used for literature searches. Furthermore, our interest in teaching offers the incorporation of instructional blocks into the data banks ranging from simple "how to do" to basic theory. Audio courses have already been developed in these areas (12) and presently computer coupled teaching is explored.

Although some of the future just outlined seems to be far future, we feel that this course of action is the next needed step in the development of thermal analysis.

Appendix

A typical example of computer processing of literature data to yield the recommended data. Figures 1, 2, and 3 are computer plots of all literature data on trigonal, glassy and molten selenium. The final computer reduced recommendation data are shown in figure 4.

Twenty-three investigations have been reported in the literature on the heat capacity of selenium. Although the heat capacity of over forty samples have been measured, only 13 of the 23 investigations containing data on 20 samples had acceptable data. Unacceptable data for trigonal selenium could be easily eliminated due to large systematic deviations. For glassy selenium the data close to the glass transition regions showing deviations were discarded. In the molten state, due to complications of ring-chain equilibrium, data measured in our laboratory on cooling (shown as \square) and the adiabatic calorimetry data (shown as +) were preferred over all other measurements which were differential scanning calorimetry data of lesser precision (9).

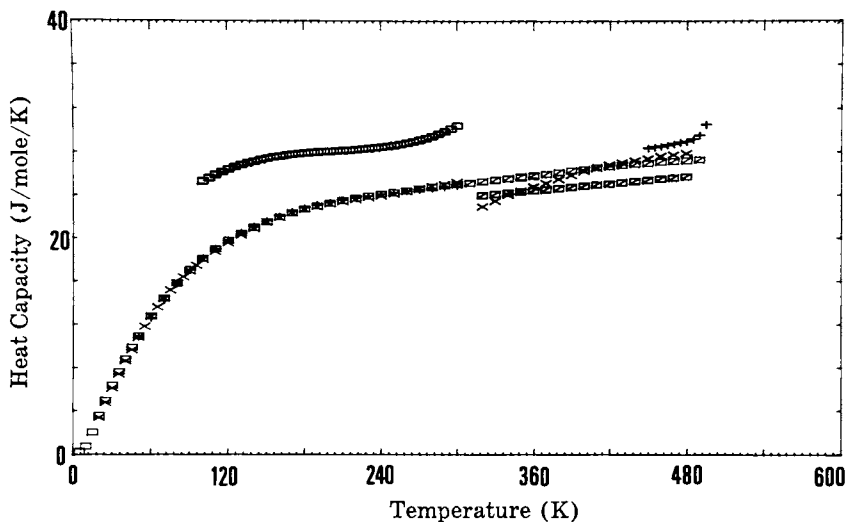


Figure 1. Computer plot of all literature data on trigonal selenium. Key: \square , data measured in this laboratory and $+$, adiabatic calorimetry data. See Ref. 9 for further explanation.

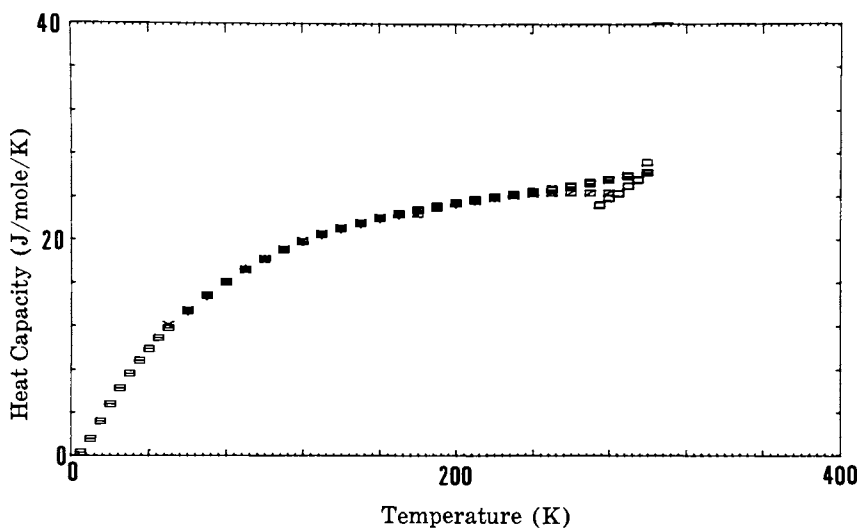


Figure 2. Computer plot of all literature data on vitreous selenium. Key: \square , data measured in this laboratory and $+$, adiabatic calorimetry data. See Ref. 9 for further explanation.

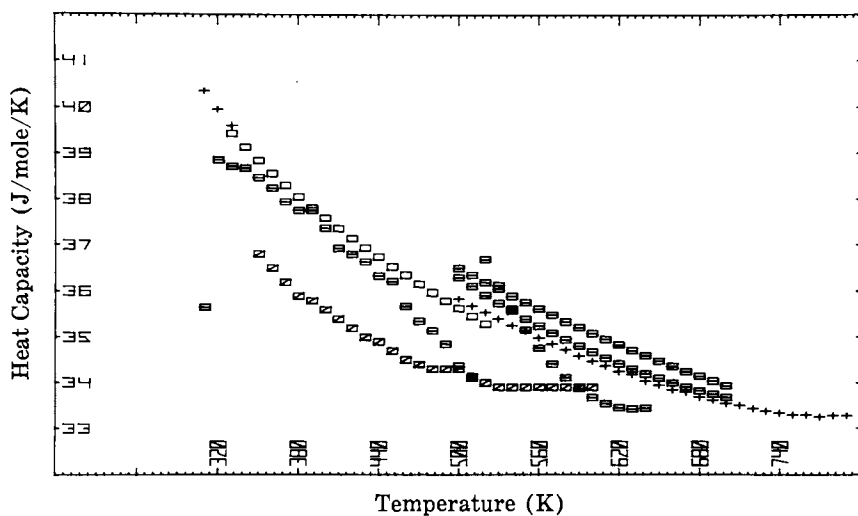


Figure 3. Computer plot of all literature data on liquid selenium. Key: \square , data measured in this laboratory and $+$, adiabatic calorimetry data. See Ref. 9 for further explanation.

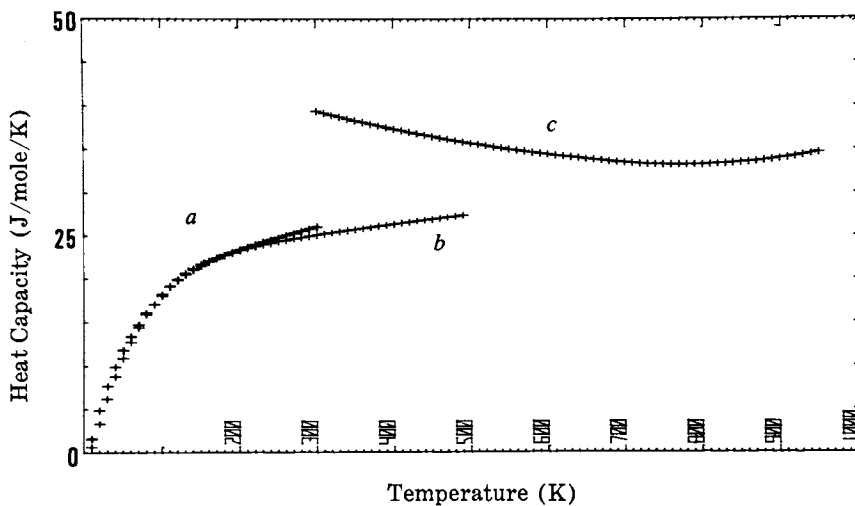


Figure 4. Final computer reduced recommendation data on selenium. Key: a, vitreous; b, trigonal; and c, liquid.

Acknowledgements

This work has been supported by the Polymers Program of the National Science Foundation, Grant Number DMR 78-15279.

Literature Cited

1. B. Wunderlich and H. Baur, *Adv. Polymer Sci.*, 7, 151 (1970).
2. B. Wunderlich and L. D. Jones, *J. Macromol. Sci.* B3, 67 (1969).
3. U. Gaur and B. Wunderlich, *Polymer Div. Am. Chem. Soc. Preprints* 20, 429 (1979).
4. B. Wunderlich, *J. Phys. Chem.* 64, 1052 (1960).
5. R. F. Boyer, *J. Macromol. Sci.-Phys.* B7, 487 (1973).
6. R. C. Bopp, U. Gaur, R. P. Kambour, and B. Wunderlich, to be published.
7. B. Wunderlich, "Macromolecular Physics, Vol. 3, Crystal Melting." Academic Press, New York, 1981.
8. U. Gaur, Ph.D. Thesis, Rensselaer Polytechnic Institute (1979).
9. U. Gaur, H.-C. Shu, A. Mehta, and B. Wunderlich, *J. Phys. Chem. Ref. Data*, 10, 89 (1981).
10. U. Gaur and B. Wunderlich, *J. Phys. Chem. Ref. Data*, 10, 119 (1981).
11. Yu. V. Cheban, S.-F. Lau, and B. Wunderlich, *Colloid Polymers Sci.* to be published 1982.
12. B. Wunderlich, Rensselaer Audio Courses in Thermal Analysis and Polymers. For information contact the author or the Office of Continuing Study, Rensselaer Polytechnic Institute, Troy, N.Y. 12181; Telephone (518) 270-6442.

RECEIVED May 17, 1982.

Computerized Viscoelastic Master Plots for Vibration Damping Applications

RICHARD P. CHARTOFF and JOHN L. GRAHAM

University of Dayton, The Center for Basic and Applied Polymer Research,
Dayton, OH 45469

Using a computerized data reduction scheme that incorporates a generalized WLF equation, dynamic mechanical data for two different polymers were correlated on master curves. The data then were related to the vibration damping behavior of each material over a broad range of frequencies and temperatures. The master curves are represented on a novel reduced temperature nomograph which presents the storage modulus and loss tangent plots simultaneously as functions of frequency and temperature.

The data reduction procedure cited is particularly useful in treating resonant vibration measurements where frequency varies during a scan over a range of temperatures. Normally to obtain a master curve using such instruments, data must be obtained for several samples having different shapes and sizes. However, using the procedure discussed only a single scan over a range of temperatures is required in order to obtain a master curve. Viscoelastic data for polymethylmethacrylate obtained independently with a resonant vibration instrument and a constant frequency instrument are shown to be equivalent.

Vibration Damping Considerations. The necessity for absorbing vibrational energy occurs whenever a structural unit has the possibility of being excited mechanically or acoustically to vibration modes having very high amplitudes. In the most critical situations such as in aircraft systems this can lead to structural fatigue and failure. Practical solutions to damping

0097-6156/82/0197-0367\$06.00/0
© 1982 American Chemical Society

these vibrations usually involve application of high damping materials to selected areas. Frequently these materials are polymers.

The ability of a polymer to effectively dissipate energy as part of a structure can be related to its linear viscoelastic properties. These are measured by dynamic mechanical analysis. A polymer has maximum potential for damping vibrations in the temperature and frequency range covered by the transition region where properties change from glassy to rubbery behavior as shown in Figure 1.

In order to be effective the polymer must be applied to a structure in a configuration that will assure that sufficient energy is dissipated. Usually it is applied to a metal substrate in film form either as a free layer or with its surface constrained by metal foil or a second metal plate. The dominant mode of deformation in a free layer is tensile while the dominant mode in a constrained layer is shear.

Theories for free layer(1, 2, 3) and constrained layer(4) damping indicate that free layer treatments give maximum damping in the low temperature side of the transition region, while constrained layers perform most efficiently in the high temperature end of the transition zone.

Viscoelastic Master Curves. In order to evaluate whether a given material is suitable for a particular damping application we need to know its viscoelastic properties over a broad range of temperature and frequency. However, in most instances we can measure these quantities only over a limited range of temperature or frequency. The data are then extended to other temperatures and frequencies by using the time-temperature-superposition procedure(5, 6) to form viscoelastic master curves that correlate the data and extend its utility.

A drawing of some typical master curves is presented in Figure 2 where modulus and loss tangent data are displayed as a function of reduced frequency. The simulated data represent points taken at five temperatures over a limited frequency range and then superposed using the temperature shift values, a_T , given in the insert on the diagram. The diagram also contains a number of oblique temperature lines and a frequency scale on the right-hand side. These will be explained in a subsequent paragraph.

When presented in this way in terms of reduced frequency, the master curve is rather cumbersome to use because frequency cannot be read from the plot directly. It must be determined for a particular temperature using an auxiliary plot (or table) of a_T vs. T values.

The Reduced Temperature Nomograph

Construction and Use of the Nomograph. The calculation of modulus and loss tangent values as a function of frequency at a

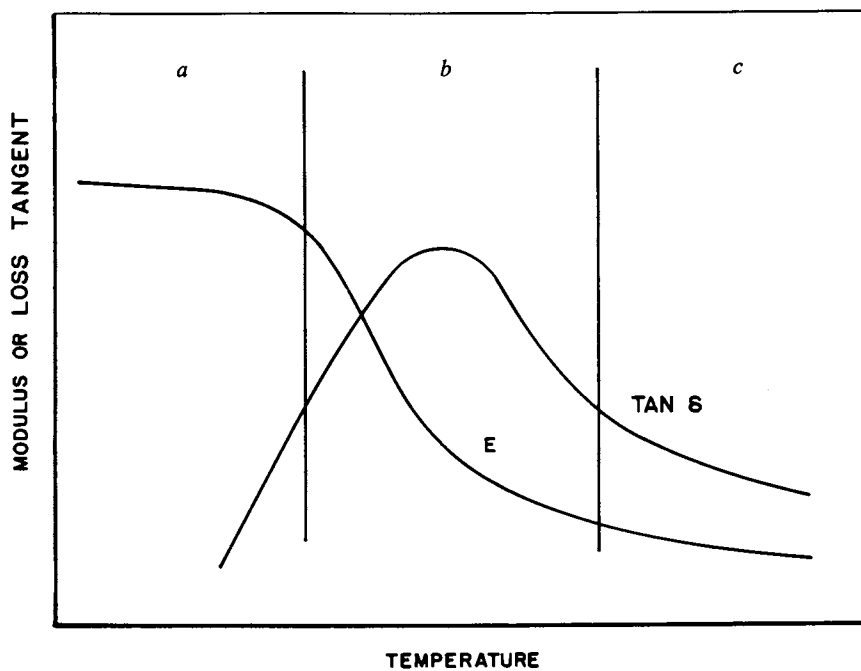


Figure 1. Typical dynamic mechanical modulus and loss tangent data as a function of temperature. Key: a, glassy region; b, transition region; and c, rubbery region.

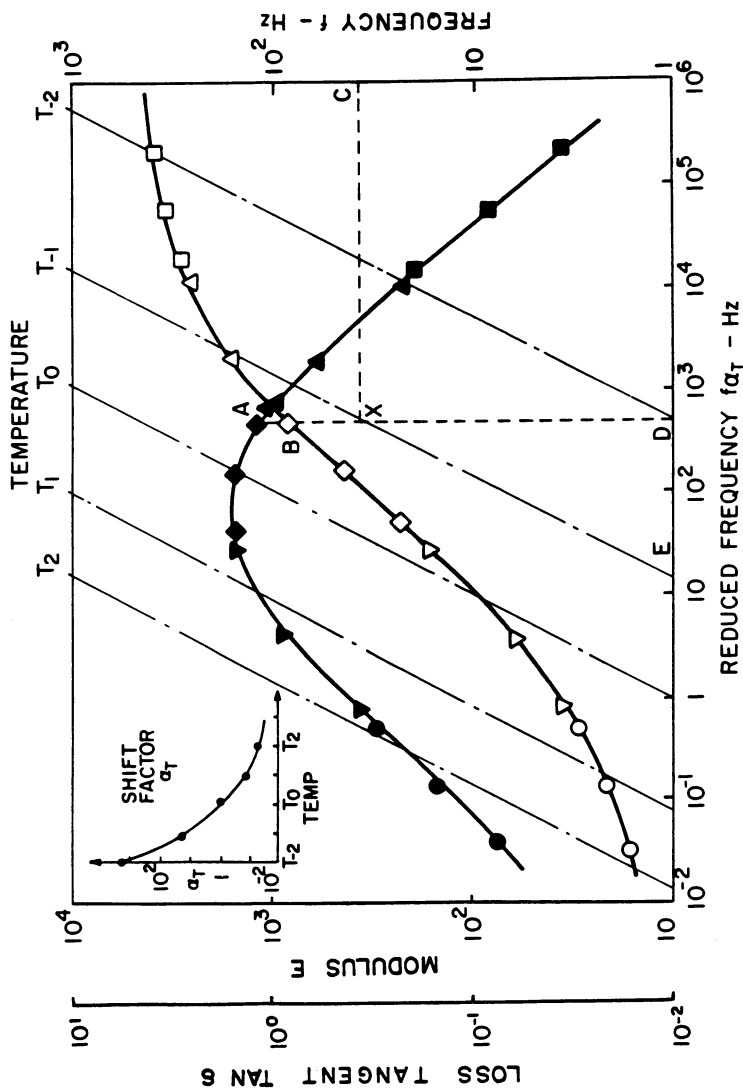


Figure 2. Viscoelastic master curves represented on reduced temperature nomograph. Key: solid symbols, modulus values and open symbols, loss tangent values. Insert at upper left shows the shift factor function, a_T , used for data reduction.

constant temperature, T_i , can be simplified considerably by defining an auxiliary function, $f_{ja_{T_i}}$, where a_{T_i} is the value of a_T at temperature T_i . A novel procedure was developed by Jones(7) for applying this function by plotting it directly onto the reduced frequency master curve in order to facilitate the direct reading of data for selected frequencies.

Following this procedure, a master curve is converted to a nomograph by plotting $f_{ja_{T_i}}$ as a function of f_j using the same abscissa as for the plots of modulus and loss tangent vs. fa_T . An auxiliary frequency scale is constructed as the ordinate on the right side of the figure(7). The values of $f_{ja_{T_i}}$ form a set of oblique lines, each point of which defines the reduced frequency value at T_i corresponding to frequency f_j . Thus points along the abscissa where $f=1.0$ Hz represent values of a_T itself. A shift one decade upward on the frequency scale to $f=10.0$ Hz represents values of $10 a_T$, etc. From this, values of E' and $\tan \delta$ at temperature T_i can be determined using the master curves of E' and $\tan \delta$ vs. fa_T .

To illustrate the use of the nomograph, assume that we wish to find the value of E' and $\tan \delta$ at T_{-1} and some frequency f (point C) of Figure 2. The intersection of the horizontal line $f = \text{constant}$, line CX, with $f_{ja_{T_{-1}}}$, line EX, defines a value of fa_T at (f, T_{-1}) , point D, of about $4 \cdot 10^2$ Hz. From this value of fa_T it follows from the plots of E' and $\tan \delta$ that $E' = 10^3 \text{ N/m}^2$, point B, and $\tan \delta = 1.2$, point A.

Data Reduction Procedure. The nomograph lends itself readily to reduction of viscoelastic data and is particularly convenient for computerized procedures. If one selects the proper position for T_0 and the interval ΔT between T_0 and T_1, T_2 , etc., then the grid of lines can be used to place the test data in position. This is done by calculating fa_T with assumed values of a_T vs. T . The appropriate values of a_T vs. T used in our laboratories were derived by experiment on an extensive series of polymers and ceramics and fit the generalized WLF expression(7):

$$\log_{10} a_T = \frac{-12(T-T_0)}{291.7 + (T-T_0)} \quad \text{Equation 1}$$

In practice the computerized data reduction procedure consists of the series of steps listed in Table I. For both multimodal resonant frequency data and constant frequency dynamic taken at several different frequencies, the correct value of the reference temperature (T_0) is that which reduces the scatter of the modulus and loss tangent data to fit a smooth curve. The initially assumed value of T_0 is taken as the temperature corresponding to the loss tangent maximum or T_g . If this value of T_0 does not give satisfactory superposition, the assumed value of T_0 is adjusted to a slightly higher value and the procedure is repeated until a satisfactory superposition is achieved. Previous

TABLE I
SUMMARY OF COMPUTATION STEPS IN REDUCTION OF
VISCOELASTIC DATA

- Compile raw data
- Calculate modulus and $\tan \delta$ values
- Compile and list processed data
- Edit data
- Graph modulus vs. temperature and $\tan \delta$ vs. temperature
- Estimate T_0 values from $\tan \delta$ vs. T
- Construct reduced variables plot of data using the generalized a_T vs. T data
- Inspect for data superposition
- Repeat procedure using different T_0 values until superposition is satisfactory
- Curve fit to data if desired

experience has indicated that a T_0 value equal to $T_g + 50^\circ\text{C}$ gives good results with equation 1. This is the value of T_0 used to reduce single mode resonant frequency data obtained with the DuPont dynamic mechanical analyzer as discussed below.

A detailed discussion of the calculation scheme and the computer program for generating nomographs is presented in reference (8). The calculation proceeds with $E'(T, f)$ being converted to $E'(fa_T)$ using equation 1 and the assumed value of T_0 . The nomograph is constructed and the data are plotted for the assumed value of T_0 . The process is repeated for other values of T_0 and the correct value is selected when scatter in the data is minimized. The correct T_0 value (for minimum data scatter) can be identified by visual inspection or statistically by least squares fitting the data for the various T_0 values and selecting the T_0 value that minimizes the residuals(9). Sub-routines for fitting curves to the experimental data are included in the computer program for data reduction(8).

Examples of Data Reduction

An example of experimental data correlated and reduced by the procedure described is presented in Figure 3. These data represent the master curves for a cured fluorosilicone polymer and were taken with two separate instruments operating in different frequency ranges. The two instruments are (1) a resonant dwell vibrating beam apparatus covering the frequency range of 60-5 K-Hz and (2) a DuPont 981 dynamic mechanical analyzer (DMA) covering the 5-50 Hz range. The solid line curves are the "best fit" for the resonant beam data.

Several points are worth noting based on Figure 3. First of all, the nomograph master curves are in excellent means for comparing data that were taken for different frequency ranges

with separate instruments. Second, the validity of using the master curves to extrapolate low frequency data (such as those from the DMA) to much higher frequencies is confirmed. Finally, since both instruments are resonant vibration instruments where the measurement frequency varies as the material's modulus varies, the nomograph is seen to be an effective way of representing viscoelastic data in a form that is fully equivalent to constant frequency data taken on other types of instruments.

This final point is illustrated more clearly in Figure 4 where viscoelastic data from the DMA instrument are related on a nomograph plot to those from a Rheovibron DDV-II instrument. The polymer is a commercial sample of poly-methylmethacrylate, PMMA. The Rheovibron data from 3.5, 11, 35, and 110 Hz are superposed on the nomograph along with the resonant frequency DMA data using a T_0 value of 175°C for this sample of PMMA. If some other T_0 value is selected, the various curves do not superpose adequately as indicated by the separate curves in Figure 5 for $T_0 = 0^\circ\text{C}$. As the T_0 value selected approaches the required value the separate curves will begin to merge until superposition is achieved.

Thus the data reduction procedure cited compensates for a basic problem with correlating resonant vibration measurements, that frequency varies during a scan over a range of temperatures. In order to obtain master curves using such a technique, data must be obtained for several samples having different shapes and sizes. However, using the procedure discussed a single scan over a range of temperatures is sufficient for obtaining the master curves.

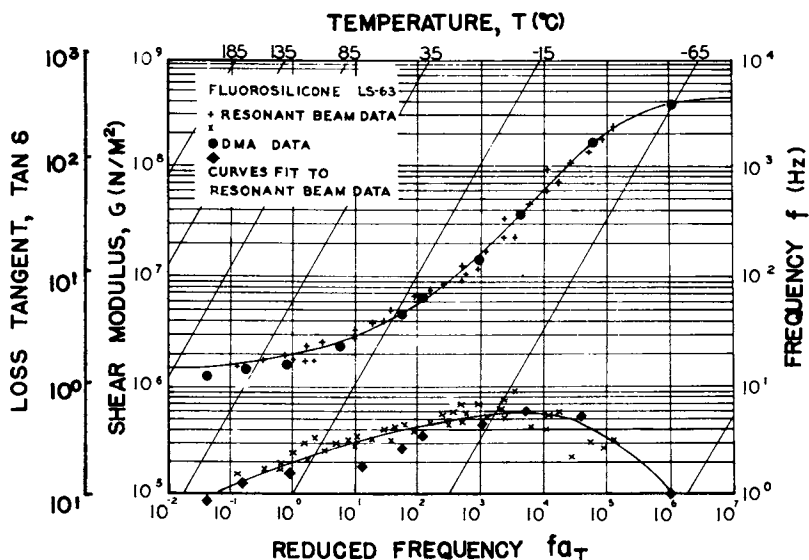


Figure 3. Reduced temperature nomograph for a fluorosilicone polymer. Data taken by both resonant beam and DMA instruments. Key: upper curve, modulus and lower curve, loss tangent.

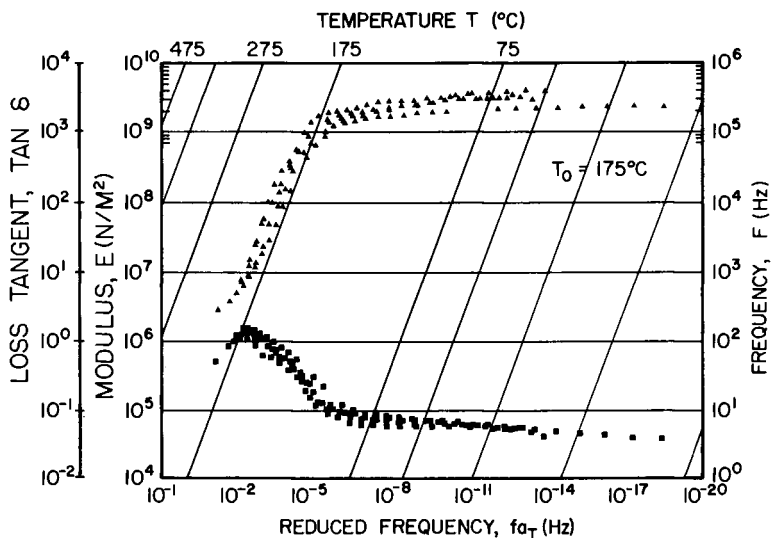


Figure 4. Reduced temperature nomograph showing that rheovibron and DMA data for PMMA superpose into single master curves when $T_0 = 175^\circ\text{C}$; DMA points are center on each plot. Key: \blacktriangle , modulus curve and \blacksquare , loss tangent.

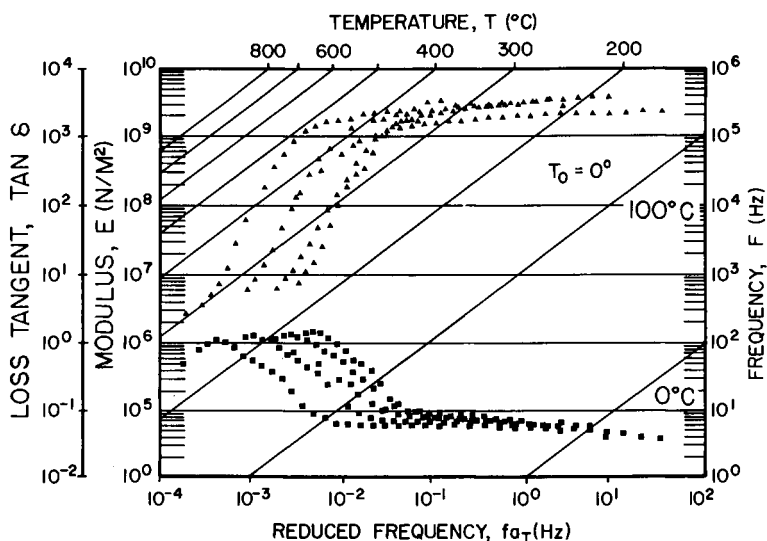


Figure 5. Reduced temperature nomograph for PMMA data of Figure 4 plotted with $T_0 = 0^\circ\text{C}$. The data do not superpose; from left to right data are 110 Hz, 35 Hz, DMA, 11 Hz and 3.5 Hz. Key: \blacktriangle , modulus and \blacksquare , loss tangent.

Acknowledgements

The authors wish to thank Messrs. Daniel Miller, David McCann, and Mark [redacted] 11 for their assistance in obtaining data and [redacted] in nomograph form. Mr. Michael Drake and Dr. David Jones provided valuable background information and stimulating discussions on the use of viscoelastic data reduction schemes for various types of materials.

Literature Cited

1. Oberst, H.; Frankenfield, K. Acoustics, 1952, 2, (Akustische Beih. 4), 181.
2. Oberst, H. Ber. Ver. Deuts. Ing., 1956, 8, 100.
3. Oberst, H. Proc. 3rd Int. Cong. Acoustics, ed. L. Cremer, Elsevier, Amsterdam, 1962, p. 352.
4. Kerwin, E. M. J. Acoust. Soc. Amer., 1959, 31, 952.
5. Tobolsky, A. V.; Andrews, R. D. J. Chem. Phys., 1945, 13, 3.
6. Ferry, J. D. J. Amer. Chem. Soc., 1950, 72, 3746.
7. Jones, D. I. G. Shock and Vibration Bull., 1978, 48(2), 13.
8. King, Jr., C. S. University of Dayton Research Institute Technical Report, UDR-TR-78-49, May 1978.
9. Rogers, L. C.; Nashif, A. Shock and Vibration Bull., 1978, 48(2), 23.

RECEIVED May 11, 1982.

Application of the Computer to Degradation Kinetics of Poly(vinyl Halides)

JOSEPH D. DANFORTH

Grinnell College, Grinnell, IA 50112

Computer programs have been used to correlate the degradation kinetics of poly(vinyl halides) assuming a kinetic model that is based on the zipper mechanism. Best fit values of the parameters of the kinetic model allow reproduction of a degradation with an error that is usually less than 0.6% per point.

A program for simulating runs makes it possible to study the expected behavior of single samples and their mixtures for arbitrarily assigned values of the parameters of the kinetic model. The parameters which are primarily responsible for the shapes of the rate vs time degradation curves are k_1 , the fraction of chains started per sec, and k_2 , the fraction of a started chain unzipping per sec.

Poly(vinyl chloride), poly(vinyl fluoride) and poly(vinylidene chloride) degrade thermally by acceleratory reactions forming hydrogen halide as a volatile product (1). Depending upon the sample and the conditions, the number of hydrogen halide measurements for a typical run may vary from twenty to over two-hundred. Each measurement represents the hydrogen halide peak formed during a sample interval which is 60, 90, or 120 seconds. The cumulative sum of peak areas to time, t , divided by the total peak area gives the fraction decomposed, α , at that time. Experimental α - t curves are compared with theoretical curves to obtain best fit values of the kinetic parameters.

The storage of data for hundreds of runs and the calculation of α at the maximum rate represent conventional applications of the computer to the handling of large amounts of data and complex calculations. Programs for obtaining best fit values of parameters for several kinetic models and for simulating α - t data represent unique applications of the computer to degradation kinetics and will be described.

0097-6156/82/0197-0377\$06.00/0
© 1982 American Chemical Society

The Program for Obtaining Best Fit Values of Kinetic Parameters

An algorithm described by Powell (2) was modified for application to the specific problems of degradation kinetics. The computer used in this work was a PDP-11/70, Digital Equipment Corp. For calculating best fit values of parameters for several kinetic models, a run number was designated to call from storage the observed hydrogen halide peak areas which had been recorded as a function of time. One of two kinetic equations designated as "first order" ($F = k_3 e^{-k_1 t}$) (3) and "constant percentage" ($F = C = \alpha_\infty$) (4) were normally used. Additional equations that have been used for the correlation of other acceleratory reactions are available in the function section of the program and new equations can be added when desired.

The two kinetic models that effectively correlate data for the degradation of vinyl polymers were developed on the basis of the zipper mechanism and differ only in the approximations used to account for the premature termination of zip chains. Although the equations are complex in appearance (3), they are based on the relatively simple assumptions of the zipper mechanism. Chains are initiated as a certain fraction of chains per second, k_1 , and unzip at a certain fraction of a started chain per second, k_2 . The relative values of k_1 and k_2 establish the amount of S-character in the acceleratory α -t curves and influence the value of α at which the maximum rate appears. The parameters, k_3 (first order equation) and α_∞ (constant percentage equation) are necessary to account for the incomplete loss of hydrogen halide when degradation ceases. For complete degradation $k_3 = 0$ and $\alpha_\infty = 1$ and the two equations are identical. A fourth parameter, t_s , represents a time shift which allows the theoretical curve to be moved to the right or left along the time axis but does not alter the shape of the calculated or observed α -t curve. When hydrogen halide retention is less than 20%, the two models give best fit values of k_1 and k_2 that are in reasonable agreement.

After the equation for fitting has been specified, the operator has the option of entering initial estimates for k_1 , k_2 , k_3 (or α_∞) and t_s . If no best estimate for one or more of the parameters is made, the computer makes its own best estimate(s). For any one or more best estimate there is an option for fixing the estimated value(s) and obtaining best fit values of the remaining parameters.

After parameter estimates have been made, the operator specifies whether best fits are to minimize the sum of the squares of the percentage differences (normalized chis) or the absolute differences (unnormalized chis) between alpha, data and alpha, calculated. Unnormalized chis were usually specified because they gave the best agreement of calculated and data α -t curves over the entire range of a degradation. Normally, two digit precision was specified for the fitting process. The range of alpha values over which the best fit was to be obtained was then

entered. Limited ranges of alpha were useful for eliminating induction periods.

At this point in the program the screen displays the options and parameter estimates for verification. After verification the data are processed and pertinent results are shown on the terminal as illustrated in Table I.

TABLE I. Sample Printout of a Typical Run

50.1 mg	#4 at 230°C	60 sec interval
First Order Kinetics (Equation 1)		
	Initial Guesses	Best Fit Values
For k_1	0.002271	0.002278
For k_2	0.0008962	0.0008958
For k_3	0.4300	0.4375
For t_s	35 sec	33.7 sec
Unnormalized Chis	two digit precision	
Error per fit point %	0.333	
Error per data point, %	0.328	

After the data of Table I are shown the following options are available:

Do you want a printout of α -t values at your terminal? Do you want a hard copy of all run data printed at the central printer? Do you wish to fit the data to greater precision? Do you wish to continue?

In the normal operation of the program best estimates of k_2 and t_s are made from the raw data and k_1 and k_3 (or α_∞) are estimated from previous knowledge. For runs with induction periods t_s is the time at which the acceleratory reaction begins and k_2 is the reciprocal of the time after the acceleratory reaction begins required to attain the maximum rate of hydrogen halide production. The best fit values obtained by the computer are then used as estimates for a repeat computer fit at two digit precision until, as shown in Table I, there is little difference between estimates and best fit values. When these repeated fits are obtained and the values of k_2 and t_s are not significantly different from the values estimated from the raw data, a hard copy is obtained for the permanent data file. The hard copy repeats the data of Table I and prints as a function of time: alpha, data; alpha, calc.; $\Delta\alpha$ per interval, data; and $\Delta\alpha$ per interval, calc. The range of alpha over which the fit was made is set apart by dotted lines in the printout.

The best fit parameters for most runs gave calculated α -t curves that were practically indistinguishable from the corresponding data curves (3). Although four parameters were used, two of them are limited in the values they may have by the data.

Simulation of Runs for Single and Mixed Samples of Poly(vinyl-chloride)

Calculated values of the change of alpha per interval for fixed values of parameters are proportional to peak areas of actual runs and can be used as raw data for simulating runs. A simulated run with single values of the parameters, as would be expected, gives best fit values of the assigned parameters to two digit precision.

Figure 1 shows simulated peaks at 60 sec intervals for certain assigned values of k_1 and k_2 under conditions of complete degradation at infinite time ($k_3=0$). When $k_1(0.0005) \ll k_2(0.01)$ as shown in the lower simulation there is a sharp increase to a maximum rate at 180 sec and then the rate decreases logarithmically with time as would be expected for a first order reaction.

When $k_1(0.01) \gg k_2(0.0005)$ as shown in the middle simulation, the rate of degradation remains constant from about 400 sec. to 2000 sec. and represents zero order kinetics over most of the degradation. At relative values of k_1 and k_2 of 1 to 20 and 20 to 1 the initial and final portions of these degradations are characteristic of acceleratory reactions. When ratios are 1 to 100 and 100 to 1, the acceleratory characteristics are not seen and the reactions are truly first order and zero order. The upper simulation shows a typical acceleratory reaction in which $k_1 = k_2 = 0.0008$. An alpha-time plot for the data of the upper simulation gives the typical S-shaped curve of an acceleratory reaction.

Thus, first order kinetics and zero order kinetics appear as special cases of the more general kinetics which have been derived on the basis of the zipper mechanism. The zipper model does not invoke the steady state assumption but allows the number of producing sites to increase during the acceleratory period as more zip chains start production and to decrease during the deceleratory period as more chains are terminating than are starting.

For simulating runs representing mixed samples a program was written that allowed the assignments of k_1 , k_2 and k_3 for one to ten samples at their designated mole fractions. The α -t values were calculated for each sample using the "first order" model. At each time the sum of the product of each alpha value times its mole fraction gave the value of alpha for the mixture. The $\Delta\alpha$ per interval values corresponded to the peak areas that would be expected for the mixture. Using this program simulated α -t curves and $\Delta\alpha$ per interval-time curves for mixtures of samples were printed for inspection. It was shown that a sample having a distribution of chain lengths (various k_2 's) around an average value, as would be expected for actual samples, gave a k_2 value corresponding closely to the weighted average of the arbitrarily assigned values.

Similarly, a limited distribution of starting characteristics (k_1) for samples of a given chain length gave the assigned value

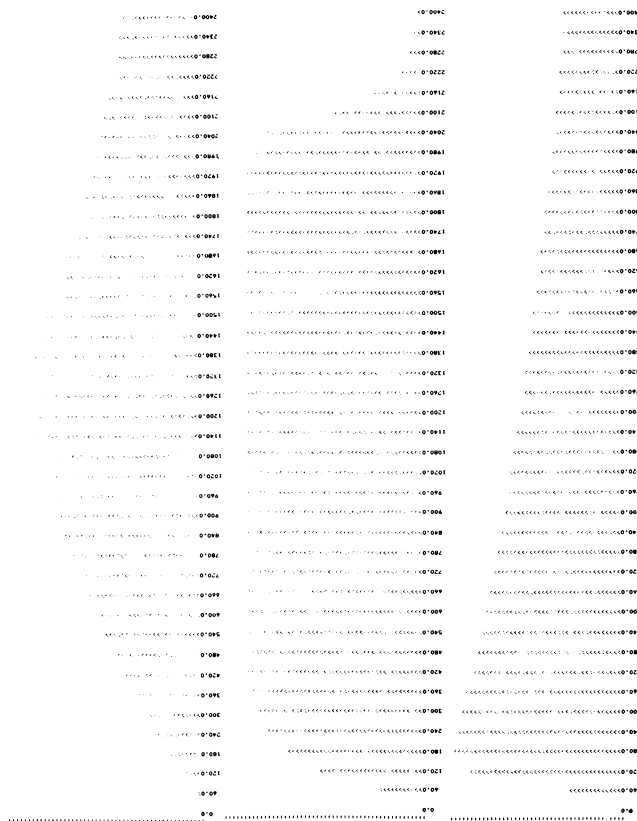


Figure 1. Photograph of computer simulated peaks at 60 s intervals. Key: upper simulation, $k_1(0.0008) = k_2(0.0008)$; middle simulation, $k_1(0.0100) \gg k_2(0.0005)$; and lower simulation, $k_3(0.0005) \ll k_2(0.0100)$.

of k_2 and a weighted average of k_1 . When both k_1 and k_2 were allowed to vary evenly around an average value, the best fit program gave k_1 and k_2 values that were close to their weighted averages. Although the simulations for samples of single valued parameters could be fit with 0.0% error per fit point, the mixed samples were fit with approximately 0.5% error per fit point. Runs using the data of actual samples were normally fit with an error per fit point less than 0.6%. Thus, the best fit program gave good fits and meaningful values of parameters for simulated runs in which there were modest variations of chain length and starting characteristics within the sample.

Figure 2 shows simulations of peak vs time using best fit values for two actual samples, having degrees of polymerization, 684 (upper simulations) and 1272, (middle simulation), and for a mixture of equal weights of these samples (lower simulation). The simulated runs for the individual samples and their mixtures correspond in shapes to those observed for the actual samples. Before simulation it had been erroneously expected that the mixture would exhibit two clearly defined maxima corresponding to those of the individual samples. However, only a single maximum was observed. The error per fit point for this simulation was about five times the error observed for runs in which k_1 and k_2 values were evenly distributed around an average value. Thus, mixed samples of widely differing characteristics gave acceleratory curves but these curves were not effectively fit by single valued parameters.

Simulations for single samples and mixed samples have been useful in the better understanding of the limiting characteristics of the kinetic model and of the influence of the starting characteristics and the zip rate on the kinetic patterns of single and mixed samples.

The storage of voluminous run data in a readily available form and the obtaining of best fit values of kinetic parameters have been useful in the better understanding of the degradation kinetics of poly(vinyl halides).

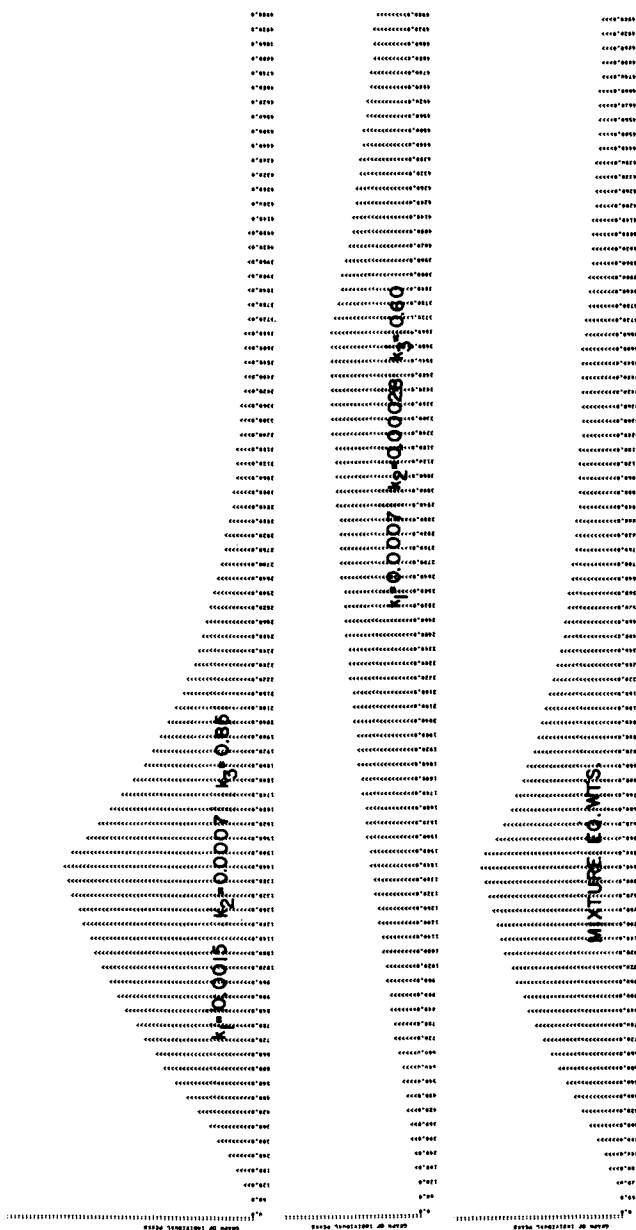


Figure 2. Photograph of computer simulated peaks at 60 s intervals. Key: upper simulation, degree of polymerization = 1272; and lower simulation, mixture of equal weights.

Acknowledgement

Acknowledgement is made to the donors of the Petroleum Research Fund, administered by the ACS, for support of this work.

Acknowledgement is also made to students, John Bloom and Joel Spiegel, for modification of existing programs and for the development of new programs that were applicable to the study of degradation kinetics.

Literature Cited

1. Danforth, J. D., U.S.-Japan Symposium on Polymer Chemistry, Palm Springs, Cal., Nov. 1980.
2. Powell, M.J.D., The Computer Journal 1964, 7 (2), 155-162.
3. Danforth, J. D., Bloom, J., Spiegel, J., J. Macro. Sci., CH, Part A, 1981, 17(6).
4. Danforth, J. D., and Takeuchi, T., J. Polym. Sci. Polym. Chem. Ed. 1973, 11 2083-90.

RECEIVED May 19, 1982.

Prediction of Polymer Solution Properties from a Model of Chain Conformations and Interactions

WITOLD BROSTOW and M. ANTONIETA MACIP

Drexel University, Department of Materials Engineering, Philadelphia, PA 19104

JERZY S. SOCHANSKI

University of Quebec, Department of Physics, Trois-Rivieres, Quebec, Canada G9A 5H7;
and World Open University, Division of Physics, Orange, CA 92667

A model of chain conformations in solution has been studied numerically on a computer. The polymer chains less than fully flexible were considered. Each chain was represented by relatively rigid groupings of base units called compact bundles, intercalated with sequences of base units called extended bundles. Several parameters characterizing the chains were varied. Thus, consequences of the model were found from the point of view of the exchange interaction energy, polymer concentration, number of segments in a bundle, molecular mass and temperature. Experimental evidence supporting conclusions from our model as well as the model itself is reviewed.

Computers are used to study polymeric materials, to provide better processing of these materials, and also to make possible better use of the products. In the present work we study consequences of a model of chain conformations in solution. The computer is used to find out how varying a parameter characterizing the chain affects the chain conformations, behavior and properties. Several parameters describing the chain are so varied in turn. The study at the molecular level is related to macroscopic behavior of polymer-containing liquid phases.

Many properties of polymer solutions are well explained in terms of the freely-jointed-chain model. The present work constitutes a part of a program of study of polymer chains in solution which are partially rigid (or partially flexible). Given the success of the freely-jointed-chain approach, we would like to explain first why our problem is important. Therefore, the pertinent experimental evidence is discussed in the following section. Only afterwards we define the model and report our computations.

0097-6156/82/0197-0385\$06.00/0
© 1982 American Chemical Society

Experimental Information

Experimental evidence concerning non-uniform and less-than-fully flexible macromolecules in solution comes from various quarters. We shall now briefly review a number of elements of this evidence.

A key fact has been pointed out in 1956 by Flory (1): values of configurational dimensions of polymer molecules in dilute solutions are often approximately twice those calculated assuming free rotation about all single bonds. This has been for Flory a point of departure for a theoretical study; we shall discuss his work further in the following section.

An experimental study of chain conformations has been conducted by Aharoni (2-5) by the use of electron microscopy. The importance of direct observations such as Aharoni's has been already pointed out elsewhere (6, 7). He has found that polymeric chains consist of regions of high density separated by regions of lower segmental density. This has been observed in amorphous materials obtained by forced and very fast drying of solutions, so that the chain structure prevalent in solution has been preserved. The instantaneous shape and segmental density of individual chain molecules are neither symmetrical nor Gaussian. However, for macromolecules studied by Aharoni both the shape and segmental density become spherical and Gaussian when averages are taken over all angles and/or large populations of chains.

Necessarily chain conformations are reflected in solution properties such as viscosity. In a series of papers Utracki and his colleagues (8-11) have studied Newtonian viscosities of polymer solutions; they have also studied polymer melts, and nonpolymeric liquid phases, organic as well as inorganic ones. The aim of the work was to construct a corresponding states principle for viscosity η in function of temperature T and concentration c . Some of the $\eta(T)$ as well as some $\eta(c)$ curves have shown changes of slope. A tentative explanation of the discontinuities has been provided (10) in terms of changes of chain conformations with concentration. Utracki also (10) notes earlier evidence (8, 9) concerning possible structural transitions caused by temperature changes, in single component liquids as well as in solutions. It is very interesting that some curves of viscosity vs. a concentration-dependent parameter defined by Utracki (10) are straight lines, while other such lines exhibit inflection points. We shall return to this finding later on, in terms of our computation results.

Further, if there is a conformational change reflected by viscosity, we can expect that it will be reflected also in other macroscopic properties of the solution. Forsman and Poddar (12) have studied viscosity of stereoisomers of poly (1, 4-dichloro-2,3-epoxybutane) in a series of solvents: dimethylformamide, dimethylacetamide, cyclohexanone and benzene. They have found abrupt changes in slope in the viscosity vs. concentration

curves, similar to those observed by Utracki for other systems. At the same time, Poddar and Forsman (13) have studied dilute solutions of the same polymer in a number of solvents by the methods of light scattering, osmometry and gel permeation chromatography. They have found evidence that an ordered structure in solution is disrupted by strong polymer + solvent interactions. Poddar and Forsman assume a parentage relationship between chain conformations in the solid state and in solution: since the solid polymer is helical, they believe that the ordered structure in solution has the helical block conformation. Further, in a third paper from the same series, Poddar and Forsman (14) say that the more ordered structure involves higher stiffness - precisely the problem with which we are concerned in this work.

Price and Fukutani (15) have studied poly (*tert*-butyethylene oxide) in the crystalline phase and in solution by NMR, and also the crystals by x-rays. They have concluded that the molecules in solution are either rigid helices or exist as helical blocks. The latter structure has been confirmed by Doddi, Forsman and Price (16) by osmometry, viscometry and light scattering; it is the same structure as in the solid state. Once again we have the problem of chain rigidity in solution, and also a parentage relationship between a chain structure in solid and in a liquid phase.

While we are concerned mainly with solutions, it is interesting that the parentage relationship appears also in the other possible passage of a solid polymer into a liquid phase, namely by melting. Already in 1945 Charlesby (17) pointed out the existence of what he called the memory effect in polyethylene films: orientation was preserved even after prolonged heating above the melting point. Much later Kamel and Charlesby (18,19,20) reported NMR spin-spin relaxation (T_2) spectra for solid and molten polymers, including copolymers. In spectra of the melts they have found three components: one called T_{2L} corresponding to relatively short and highly mobile chains which are present sometimes; a second called T_{2S} representing the entangled network (the amorphous component before melting); and a third component called T_{2X} , from relatively dense well-packed regions resulting from melting of crystalline domains. It appears that both key methods of producing polymer-containing liquid phases, that is dissolution and melting, produce comparable results. Thus, a coherent overall picture emerges.

Finally, there is no reason why partial rigidity in solution should be limited to very long chains. Oligomeric molecules of alkynes have interesting properties pointed out by Kehiaian (21), related to differences in rigidity: 3-hexyne is more rigid than 1-hexyne. Enthalpies of mixing H^E of both these compounds have been measured by Wilhelm, Inglesse, Grolier and Kehiaian(22). These authors note the importance of geometric packing for the thermodynamic properties of solutions. Indeed, since rigidity affects packing and thus distances between interacting units

(polymer segments and solvent molecules) we can explain (23) the differences in properties of pure hexynes such as molar volume, enthalpy of vaporization and normal boiling point. Moreover, on the basis of the same approach we predict (23) that H^E vs. concentration curves of binary mixtures of 1-hexyne should lie above the analogous H^E curves of 3-hexyne with the same second component; this is precisely what Wilhelm and his colleagues (22) have found experimentally.

Model

The model is based on experimental observations, including those enumerated in the preceding section. The generality of the phenomena we want to treat is related to the following fact: completely flexible polymer chains in solution are well known to exist; at the same time fully rigid macromolecules are known too (liquid crystals); therefore, it is only reasonable to expect that a whole gamut of intermediate situations occurs in the nature.

As noted above, the first study of the problem of partial chain flexibility has been done by Flory (1) - one more problem in polymer science which he was the first to tackle. Flory has assumed the existence of a favorable arrangement of a number of consecutive base units. The configurational free energy of this arrangement differs by an amount ϵ from other possible sequences. Apparently, these other arrangements do not have to be all identical; thus ϵ represents an average value. Flory points out that the stiffness of the chain is involved. He places the chains and solvent molecules on a lattice, a convenient although not a necessary step.

To pursue the problem it is convenient to introduce some terminology. Instead of a phrase "a favorable arrangement of a number of consecutive base units" we shall use the name compact bundle; it is relatively more rigid. Other arrangements of monomeric units will be called extended bundles. Thus we have two kinds of units constituting a polymer chain, to be denoted by symbols c and e . We introduce the symbol N_{ce} for the number of pairs of nearest neighbor bundles such that one of them is compact and the other extended. N_{cc} and N_{ee} are defined analogously.

We ought to note that the word "bundle" has already been used by Pechhold and collaborators (24) with a quite different meaning. We are forced to appropriate this word since the otherwise very rich English language does not seem to have enough words to describe a set of connected monomeric units within a chain. A number of different meanings has been ascribed to the word "segment". Words like "submolecule", "supersegment" or even "blob" have been used too. Also, Schelten and Stamm (25) have found experimentally by diffuse neutron scattering in polyethylene melts that "bundles" corresponding to the Pechhold concept do not exist in nature.

To describe a polymer chain in solution, we need more parameters. Consider a system of N_1 monomer plus N_2 polymer molecules. Each polymeric molecule contains \underline{r} base units, and also consists of \underline{b} bundles. Since the bundles are either compact or extended, we have, in obvious notation,

$$b_c + b_e = b \quad (1)$$

The terminology we have adopted shows that both kinds of bundles are on equal footing. As Rice and his colleagues (26) did in a somewhat similar situation, we assume that the number of segments \underline{r}_b in a compact bundle (akin to their "helical section") is the same as in an extended bundle. Therefore

$$br_b = r \quad (2)$$

If bundles are not of the same length, and a distribution of bundle sizes exists, then r_b is an average parameter.

The quantities N_{yy} , defined above can be further elucidated with an example. For instance, denoting each compact bundle by c and each extended one by e , in the sequence

$$cccccccccc \quad (3)$$

we have $b = 10$, $b_c = 6$, $N_{ce} = 2$, $N_{cc} = 4$ and $N_{ee} = 3$.

The solution is characterized by a coordination number \underline{z} ; among other things, this takes care of the excluded volume problem. In general, z depends on temperature and density and is obtainable from diffractometric measurements via an integration of the pair radial distribution function $g(R)$. In this way each polymer segment has \underline{z} nearest neighbors, and so has each monomer molecule. We define (23) as ζ the number of nearest neighbor sites which are occupied by segments directly connected to a given segment. In a chain without branches and without cycles, disregarding the end-of-chain effects, the average value of ζ for the chain is 2. At a segment at which branching occurs, where we have, say, $\zeta = 4$, there are also two values of $\zeta = 1$ at the end of the two branches, and the average of $\zeta = 2$ is preserved. On the other hand, in molecules containing cycles, an average value for the chain of $\zeta > 2$ results.

According to our definitions, each polymer segment has $z - \zeta$ external nearest neighbors with which it interacts. Consider a segment in a compact bundle surrounded by compact bundles. Denote by $(z - \zeta)v_m$ the average number of interactions with other

polymer segments (nonnearest neighbors in the same chain or in other chains). The remainder, that is $(z - \zeta)(1 - v_m)$ is the number of interacting pairs of our segment with its nearest neighbor solvent molecules. Take now a segment in a compact bundle surrounded by extended bundles. Such a segment is also an average representative, since in a compact bundle we might have half of the segments adjacent to an extended bundle and another half adjacent to a compact bundle. (The procedure we use is equivalent to breaking all compact bundles into halves, and then reassembling the halves adjacent to other compact bundles separately from the halves adjacent to extended bundles). Now we denote by $(z - \zeta)v_t$ the average numbers of interactions of such a segment with other polymer segments (indexes m and t denote "middle" and "terminal", since we are dealing with location in a string of compact bundles). Analogously, for a segment in an extended bundle we denote by $(z - \zeta)v_e$ the average number of interactions with other polymer segments.

As for intermolecular and intersegmental interactions, there are three types of them: 1-1, 1-2 and 2-2. Following Flory (27, 28) we define the average interaction energy $u_{yy'}$ per pair $y-y'$ by

$$u_{yy'} = - \frac{\eta_{yy'}}{v} \quad (4)$$

where v is the segment volume. Except for an improbable case of a pressure so high that the repulsion becomes dominant, $\eta_{yy'}$ represents an attractive interaction. Then $u_{yy'}$ is a positive quantity.

The model thus has been defined in terms of polymer chain structure, solution structure, and interactions. Now statistical mechanics can be applied to it. We use the partition function devised by Flory (27, 28). For simplicity, instead of the entire system, we study a subsystem containing one polymer molecule plus its share of N_1/N_2 monomer molecules. The partition function of the subsystem has the same form as that for the entire system (27,28) that is

$$Q = Q^{\text{comb}} Q^{\text{fv}} Q^{\text{c}} \quad (5)$$

The combinatorial factor Q^{comb} is related to the fraction of the three-dimensional space taken by polymeric chains and the other part taken by the solvent and is independent of the compactness (or otherwise) of the chain. The free volume factor Q^{fv} depends on the experimental values of molar volume V (or segmental volume v), of isobaric expansivity α and of isothermal compressibility κ_T . The configurational (or interactional, or potential

energy) factor Q^C involves a certain number of ways, call it Ω , of realizing a configuration with a prescribed number b_c of compact bundles and with b_e extended bundles. The result can be simply written as

$$Q^C = \sum_{b_c, b_e, N_{ce}} \Omega e^{-\frac{U^C}{kT}} \quad (6)$$

The exponential term represents the usual Boltzmann factor: U^C is the configurational energy obtained from summation of all possible kinds of interactions in the subsystem; k is the Boltzmann constant, and T the thermodynamic temperature. The complete expression for U^C is displayed elsewhere (23). From combinatorics we have

$$\Omega = \frac{b_c! b_e!}{\left(b_c - \frac{N_{ce}}{2}\right)! \left(b_e - \frac{N_{ce}}{2}\right)! \left[\left(\frac{N_{ce}}{2}\right)!\right]^2} \quad (7)$$

There exists relations between the quantities b_c , b_e , N_{cc} , N_{ee} and N_{ce} . Namely, since the maximum number of partitions in a row of m objects is $m - 1$, we have

$$N_{cc} + N_{ee} + N_{ce} = b - 1 \approx b \quad (8)$$

Neglecting again unity for sufficiently long chains, we have also

$$2N_{cc} + N_{ce} = 2b_c \quad (9a)$$

$$2N_{ee} + N_{ce} = 2b_e \quad (9b)$$

In view of relations (8) and (9), we have for a given value of b two independent variables, for instance b_c and N_{ce} . An appropriate statistical mechanical procedure is now to extremize the partition function (5) in turn with respect to b_c and N_{ce} . Details of the procedure are described in the first of our papers on the present topic (23). If the polymer concentration in solution is not very high, all $z - \zeta$ external interactions of a segment in an extended bundle are directed towards solvent molecules, and characterization of such segments in terms of a v_e parameter is not necessary. Since our treatment is not significantly affected by specific values of v -type parameters, an assumption made in (23) and repeated here is $v_e = 0$.

With the solvent represented by index 1 and the polymer by 2, we have three parameters characterizing pair interaction energies; η_{12} , η_{11} and η_{22} . This is still relatively complex, so we

now introduce one parameter characterizing the energetic situation in solution. Similarly as Flory (27,28) we define

$$X_{12} = \frac{z(\eta_{11} + \eta_{22} - 2\eta_{12})}{2v^*{}^2} \quad (10)$$

where v^* is the segmental hard-core (incompressible) volume. Thus X_{12} represents the difference between the average energy density of mixed interactions (polymer + solvent) and the half of the arithmetic sum of pure interactions (polymer + polymer and solvent + solvent).

By using (10), the final equations obtained in (23) can be rewritten as

$$\ln \frac{b_c \left(b - b_c - \frac{N_{ce}}{2} \right)}{(b - b_c) \left(b_c - \frac{N_{ce}}{2} \right)} + \frac{\beta r_b (z - \zeta) v^*{}^2}{zv} \left[v_m - 2 \left(\frac{\frac{N_{ce}}{2}}{b_c + \frac{N_{ce}}{2}} \right) (v_m - v_t) \right] X_{12} = 0 \quad (11)$$

$$\ln \frac{\left(b_c - \frac{N_{ce}}{2} \right) \left(b - b_c - \frac{N_{ce}}{2} \right)}{\left(\frac{N_{ce}}{2} \right)^2} - \frac{2\beta r_d (z - \zeta) v^*{}^2}{zv} \left(\frac{b_c}{b_c + \frac{N_{ce}}{2}} \right)^2 (v_m - v_t) X_{12} = 0 \quad (12)$$

Here $\beta = (kT)^{-1}$.

Computations

We have been using computers in supposedly more sophisticated applications, such as representation of the pair radial distribution function $g(R)$ (29), construction of the Voronoi diagram (30), simulation of light scattering in polymer solutions (31) or Monte Carlo simulation of a fluid with central force fields (32). The present application is anything but sophisticated: we are solving a system of two equations, (11) and (12), in two unknowns: b_c and N_{ce} . And yet, without a computer this could not have been accomplished. We can see from the parameters featured in Eqs. (11) and (12) the number of factors affecting the configuration of a polymeric chain in solution. The equations are anything but linear.

We note that an increase in, say, $v_m - v_t$ in Eq. (12) can be compensated by a simultaneous decrease of, for instance, v^* .

This is the reason why we have made calculations in series. In each series X_{12} was varied, while other parameters kept constant.

The computer used was an IBM 370/168 belonging to the UNI-COLL Corporation of Philadelphia. Typically, a solution was accepted when the r.h. sides of Eqs. (11) and (12) became $0(E-9)$ or $0(E-10)$. A number of such series computations have been performed; some of them are reported elsewhere (33) and some in the following section.

Results and Discussion

Before discussing computer-generated solutions, let us quote results from a special case considered in (33). For $X_{12} = 0$ and taking into account the chain dynamics for, say, $b = 25$ our model suggests the following conformations:



Similar configurations should be formed in favorable solvents, that is when, other things being equal, X_{12} is small and positive.

As noted above, we have generated quite a few pairs of solutions of Eqs. (11) and (12). Because of space limitations we can show here only a few. Some further results obtained are reported elsewhere (33). Figure 1 shows the results of one such series in which X_{12} underwent variations. The series is instructive as well as typical. Values of b_c and N_{ce} were obtained from simultaneous solutions of Eqs. (11) and (12) for each X_{12} . The chain contained 6000 segments, each bundle $r_b = 10$ segments. Other parameters were: $z = 6$; $\zeta = 2$; $v_m = 0.200$; $v_t = 0.100$; $v = 1.08 \text{ cm}^3\text{g}^{-1}$; $v^* = 0.90 \text{ cm}^3\text{g}^{-1}$; $T = 300.0 \text{ K}$. The broken line represents $N_{ce}/2$ vs. X_{12} , in $\text{J}\cdot\text{cm}^{-3}$ (note that given Eqs. (4) and (10) X_{12} has the dimensions of pressure and not energy; it is the interchange energy density). The continuous line represents the changes of the b_c/b fraction with X_{12} .

Some conclusions from the computations made, including those shown here and reported in a related paper (33) can be summarized as follows:

i) An increase in X_{12} leads ultimately to conversion of all bundles into compact ones. Thus, the fraction b_c/b goes symbatically with X_{12} . This is one of the aspects of the behavior such that the curve shown in Figure 1 is typical;

ii) Calculations of polymer chain surfaces by structural schemes such as the Bondi scheme (34) produce generally values larger than those derived from thermodynamic properties of solutions (35,36). The reason for this is that structural schemes have been constructed without realizing the existence of compact

bundles. Segments in these bundles expose their surfaces less, and this is reflected in thermodynamic properties such as excess functions of mixing;

iii) For a given positive value of X_{12} , an increase in polymer concentration produces a decrease of N_{ce} and a higher value of b_c/b . Thus, higher concentration favors lower pervaded volume and smaller radius of gyration, R_g . An exception to this is a region close to $(b_c/b) = 1$ when relative stiffness of the chain is high.

iv) Our results provide a basis for the hydrodynamic volume model of Rudin and collaborators (37,38,39). The Rudin model has led to successful predictions (39) of effects of solvent and concentration on elution volumes in gel permeation chromatography;

v) An increase in molecular mass M produces a proportional increase of b , b_c , b_e and N_{ce} . Thus, b_c/b remains the same, a fact used to advantage in the treatment of mechanical degradation in flow (see below, also (40));

vi) As seen in Figure 1, sufficiently negative values of X_{12} convert the chain into a fully extended one. It should be noted, however, that positive X_{12} s prevail for typical polymers in solution (28);

vii) Our scan of the literature data, including the extensive set of Abe and Flory (41) indicates that in general X_{12} decreases when temperature increases. Therefore, our model implies that an increase in T produces less compactness (lower b_c/b) and higher pervaded volume.

viii) Our results and those obtained by Mark and collaborators (42-45) on effects of flexibility of polyoxides $[(CH_2)_y-O]_r$ in their unperturbed states upon their properties are in agreement and also mutually complementary;

ix) The conformational changes with concentration are slow for low values of X_{12} and relatively quite fast for higher X_{12} values (that is in less favorable or worse solvents). This is the reason for the two kinds of viscosity vs. a concentration-dependent parameter curves found by Utracki (10); some with and some without an inflection point. The same explanation applies to the results of Forsman and collaborators (12,13,14).

Polymer Conformations in Flow

The phenomenon of drag reduction (DR) in flow by dissolution of small amounts of certain polymers has an immense field of applications (46), including petroleum pipelines and fire-fighting. However, DR is complicated by mechanical degradation

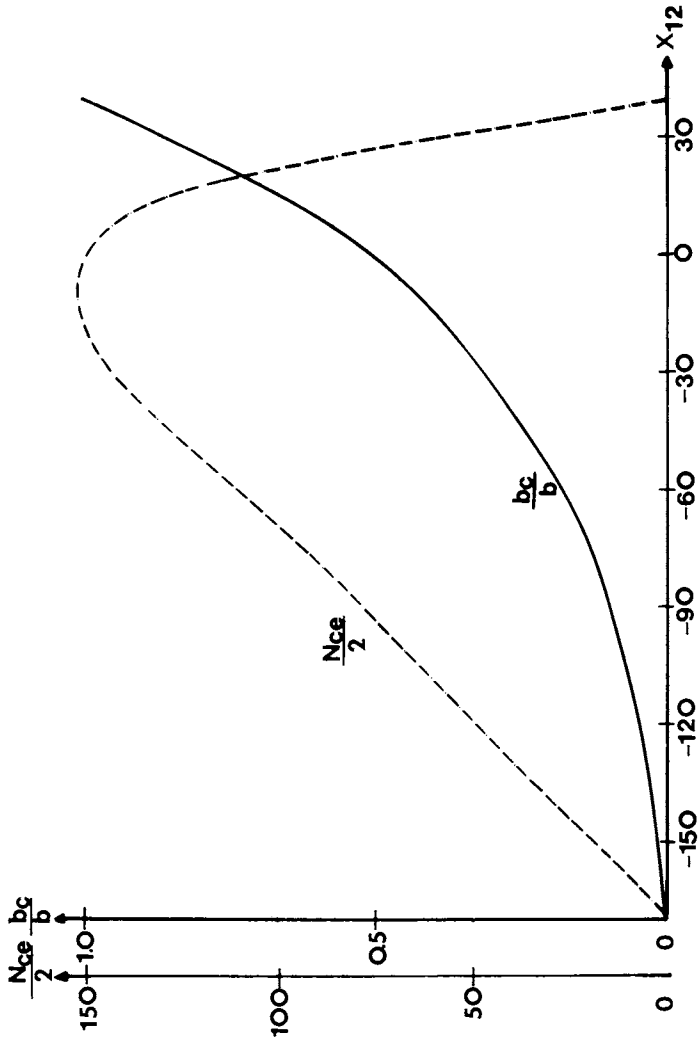


Figure 1. Plots of $N_{ce}/2$ and b_c/b vs. the interchange energy density x_{12} (J/cm^3).

in flow (MDF) (47,48). Various attempts to explain and treat quantitatively DR and MDF failed; in fact, several experimental findings have been labelled as contrary to expectations (49). We can trace this failure to two reasons. First, chain conformations and interactions at molecular and segmental level have not been appropriately taken into consideration. Second - again - the existence of compact bundles has not been realized. While the model we are studying has been constructed essentially in equilibrium terms, its extension to DR and MDF (40) turned out to be successful. To conclude this paper, let us enumerate some of the phenomena related to DR and MDF, explained in terms of the model proposed in (23) and on the basis of our calculations:

i) In less favorable solvents (higher X_{12}) we have higher b_c/b ; see conclusion i) in the preceding Section. More compactness produces less chain flexibility, and therefore more MDF:

ii) Because of the same factor, that is high b_c/b , in poor solvents we have less pervaded volume, and therefore less DR:

iii) The bond cleavage depends on the number and distribution of compact bundles in the chain. Therefore - exactly as the experiments tell us - the cleavage neither occurs at random nor does it take place exactly at the midpoint of the chain;

iv) An increase of M (see conclusion v) above) produces a slight increase of the undegradable molecular weight M_∞ . This conclusion has yet to be tested experimentally, with data more accurate than those presently available;

v) Since MDF depends principally on intermolecular interactions, it is independent of solvent viscosity at a given shear stress. Once again, this is precisely what the experiment tells us.

Acknowledgments

Financial support provided to one of us (M.A.M.) by Dean Otto W. Witzell and Professor Jack Keverian of Drexel University is gratefully acknowledged. Dean Richard E. Woodring has kindly provided us with computer time. Colleagues who have discussed this work are too numerous to name, but comments of all of them are appreciated.

Literature Cited

1. Flory, P. J. Proc. Royal Soc. A 1956, 234, 60.
2. Aharoni, S. M. Polymer 1978, 19, 401.
3. Aharoni, S. M. J. Macromol. Sci. Phys. 1978, 15, 635.
4. Aharoni, S. M. Macromolecules 1978, 21, 677.

5. Aharoni, S. M.; Kramer, V.; Vernick, D. A. Macromolecules 1979, 12, 265.
6. Brostow, W. "Science of Materials"; Wiley: New York, 1979.
7. Brostow, W. "Introducción a la ciencia de los materiales"; Editorial Limusa: México, D.F., 1981.
8. Utracki, L. A.; Simha, R.; Eliezer, N. Polymer 1969, 10, 43.
9. Utracki, L. A. J. Macromol. Sci. Phys. 1974, 10, 477.
10. Utracki, L. A. J. Macromol. Sci. Phys. 1980, 18, 731.
11. Utracki, L. A.; Simha, R. J. Rheol. 1981, 25, 329.
12. Forsman, W. C.; Poddar, S. K. preprint from the University of Pennsylvania, Philadelphia, 1981.
13. Poddar, S. K.; Forsman, W. C. preprint from the University of Pennsylvania, Philadelphia, 1981.
14. Poddar, S. K.; Forsman, W. C. preprint from the University of Pennsylvania, Philadelphia, 1981.
15. Price, C. C.; Fukutani, H. J. Polymer Sci. A-1 1968, 6, 2653.
16. Doddi, N.; Forsman, W. C.; Price, C. C. J. Polymer Sci. Phys. 1974, 12, 1395.
17. Charlesby, A. Proc. Phys. Soc. 1945, 57, 510.
18. Kamel, I.; Charlesby, A. J. Polym. Sci. Phys. 1981, 19, 803.
19. Kamel, I.; Charlesby, A. in Proc. 3rd Int. Meeting Radiation Processing, Tokyo, 1980.
20. Kamel, I.; Charlesby, A. preprint from Dept. of Physics, Royal Military College of Science, Shrivenham, England, 1981.
21. Kehiaian, H. V. in Thermochemistry and Thermodynamics, MTP International Review of Science, vol. 10, H.A. Skinner, editor; Butterworth: London, 1972; p. 121.
22. Wilhelm, E.; Inglese, A.; Grolier, J.-P. E.; Kehiaian, H. V. Monatsh. Chem. 1978, 109, 235.
23. Brostow, W. to be published.
24. Pechhold, W. R. Colloid Polym. Sci. 1980, 253, 269.
25. Schelten, J.; Stamm, M. Macromolecules 1981, 14, 818.
26. Rice, S. A.; Wada, A.; Geiduschek, E. P. Disc. Faraday Soc. 1958, 28, 1246.
27. Flory, P. J. J. Am. Chem. Soc. 1965, 87, 1833.
28. Flory, P. J. Disc. Faraday Soc. 1970, 49, 7.

29. Brostow, W.; Sochanski, J. S. Phys. Rev. A 1976, 13, 882.
30. Brostow, W.; Dussault, J.-P.; Fox, B. L. J. Comput. Phys. 1978, 29, 81.
31. Brostow, W.; McEachern, D.; Perez-Gutierrez, S. J. Chem. Phys. 1979, 71, 2716.
32. Bose, T. K.; Brostow, W.; Sochanski, J. S. Phys. Chem. Liquids 1981, 11, 65.
33. Brostow, W.; Macip, M. A.; Sochanski, J. S. in preparation.
34. Bondi, A. J. Phys. Chem. 1964, 68, 441.
35. Eichinger, B. E.; Flory, P. J. Trans. Faraday Soc. 1968, 64, 2035.
36. Brostow, W. Macromolecules 1971, 4, 742.
37. Rudin, A. J. Polymer Sci. A-1 1971, 9, 2587.
38. Rudin, A. J. Polymer Sci. A-1 1972, 10, 217.
39. Rudin, A.; Wagner, R. A. J. Appl. Polymer Sci. 1976, 20, 1483.
40. Brostow, W. in preparation.
41. Abe, A.; Flory, P. J. J. Am. Chem. Soc. 1965, 87, 1838.
42. Takahashi, Y.; Mark, J. E. J. Am. Chem. Soc. 1976, 98, 3756
43. Abe, A.; Mark, J. E. J. Am. Chem. Soc. 1976, 98, 6468.
44. Mark, J. E. J. Chem. Phys. 1977, 67, 3300.
45. Mark, J. E. Acc. Chem. Res. 1979, 12, 49.
46. Zakin, J. L. J. Rheol. 1980, 24, 523.
47. Virk, P. J. Am. Inst. Chem. Engrs. J. 1975, 21, 625.
48. Bearman, N. S. Ann. Rev. Fluid Mech. 1978, 10, 47.
49. Hunston, D. L.; Zakin, J. L. Polymer. Eng. Sci. 1980, 20, 517.

RECEIVED May 6, 1982.

Mathematical Treatment of the Emulsification of Benzene and Styrene in Aqueous Hexadecyltrimethylammonium Bromide-Cetyl Alcohol Mixtures

Y. J. CHOU¹, M. S. EL-AASSER, and J. W. VANDERHOFF

Lehigh University, Emulsion Polymers Institute and Departments of Chemistry and Chemical Engineering, Bethlehem, PA 18015

Styrene or benzene "mini-emulsions" of 0.1-0.3 μ m diameter were prepared at 63° using aqueous hexadecyltrimethylammonium bromide-cetyl alcohol mixtures; the most stable emulsions, formed at 1:3-1:1 molar ratios, contained crystalline, rodlike particles of hexadecyltrimethylammonium bromide and cetyl alcohol, 1-2 μ m in length and 0.1-0.2 μ m in diameter. Conductometric titration of these optimum systems with styrene or benzene gave a near-linear leg descending to an inflection point followed by another near-linear leg ascending to a second inflection point and a near-constant or slowly-decreasing leg thereafter. The descending leg was interpreted as solubilization of the oil in micelles or crystalline complex, the ascending leg as emulsification to form tiny droplets which grew by coalescence and diffusion, and the near-constant or slowly decreasing leg to droplet growth by diffusion. The conductometric titration curves were expressed by an exponential step function in terms of the initial conductance, the conductances at both inflection points, a solubilization constant, an emulsification constant, and a droplet growth constant. Iterative computer solution of this mathematical model gave a reasonable fit of the different experimental titration curves, and the calculated parameters were correlated with the hexadecyltrimethylammonium bromide and cetyl alcohol concentrations, to give the distributions of the emulsifier as solute emulsifier, micellar emulsifier, and emulsifier in the crystalline complex. The correlation of emulsion stability with the presence of the crystalline, rodlike particles allowed a prediction of emulsion stability. Finally, a three-dimensional

¹ Current address: Avery International, 325 N. Altadena Drive, Pasadena, CA 91107.

plot of conductance as a function of added benzene and cetyl alcohol concentration at a given hexadecyltrimethylammonium bromide concentration was calculated by computer curve-fitting and used to visualize the conductance surface at any desired angle.

The emulsification of oil in water using ionic oil-in-water emulsifiers in concentrations of 0.5-5.0% based on dispersed phase with conventional agitation gives fluid, opaque "macroemulsions", i.e., emulsions with average droplet sizes of ca. $1\mu\text{m}$ or greater. Similarly, the emulsification of oil in water using mixtures of ionic oil-in-water emulsifiers with fatty alcohols in certain molar ratios and in concentrations of 10-50% based on dispersed phase gives transparent or translucent viscous "microemulsions", i.e., emulsions with average droplet sizes of $0.1\mu\text{m}$ or smaller. The use of similar ionic emulsifier-fatty alcohol mixtures in concentrations of 0.5-5.0% based on dispersed phase gives fluid, opaque "mini-emulsions", i.e., emulsions with average droplet sizes of $0.1-0.3\mu\text{m}$. Thus the emulsification of styrene in water using sodium lauryl sulfate alone gives average droplet sizes of $1\mu\text{m}$ or greater while the emulsification in aqueous sodium lauryl sulfate-cetyl alcohol mixtures with simple stirring gives average droplet sizes of ca. $0.2\mu\text{m}$ (1). Similar results were obtained with the corresponding hexadecyltrimethylammonium bromide-cetyl alcohol mixtures (2). The application of this emulsification technique to polymer solutions using ionic emulsifier-fatty alcohol or ionic emulsifier-n-alkane mixtures gives latexes with average particle diameters in the range $0.1-0.2\mu\text{m}$ (3-7).

The mechanism of this mini-emulsion emulsification process was investigated by the conductometric titration of aqueous hexadecyltrimethylammonium bromide-cetyl alcohol mixtures with benzene or styrene combined with transmission electron microscopic examination of the morphology of the mixed emulsifiers and the styrene droplets formed (2,8). Figure 1 shows that the titration curves with and without cetyl alcohol are quite different: that for hexadecyltrimethylammonium bromide alone comprises a near-linear decrease to an inflection point V_0 followed by a second near-linear decrease of much smaller slope; that for the hexadecyltrimethylammonium bromide-cetyl alcohol mixture of 1:1 molar ratio comprised a lower initial conductance and a short near-linear decrease to an inflection point V_1 , an increase to a second inflection point V_2 , and a very slow decrease or constant region. The form of the titration curve with cetyl alcohol varied according to the hexadecyltrimethylammonium bromide-cetyl alcohol molar ratio. Figure 2 shows the conductometric titration curves for hexadecyltrimethylammonium bromide-cetyl alcohol ratios of 1:0.33 to 1:6. These curves show that, with increasing proportion of

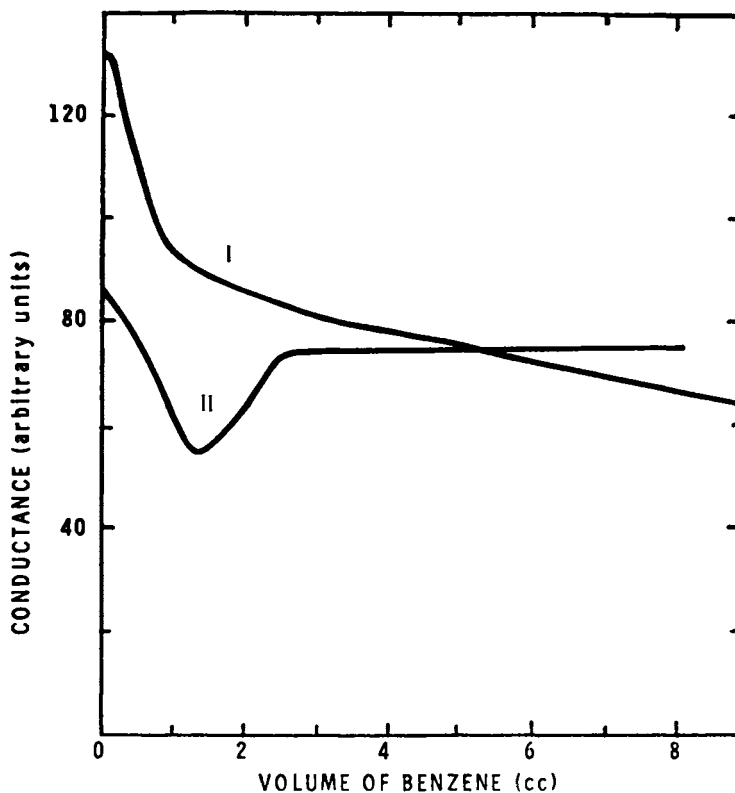


Figure 1. Conductometric titration at 63°C of 25 cc water containing 0.15 g hexadecyltrimethylammonium bromide and 0.10 g cetyl alcohol (1:1 molar ratio) with benzene at a constant rate of 1 cc/min. Key: I, no cetyl alcohol; II, 0.10 g cetyl alcohol. (Reproduced, with permission, from Ref. 2. Copyright 1980, Plenum Press.)

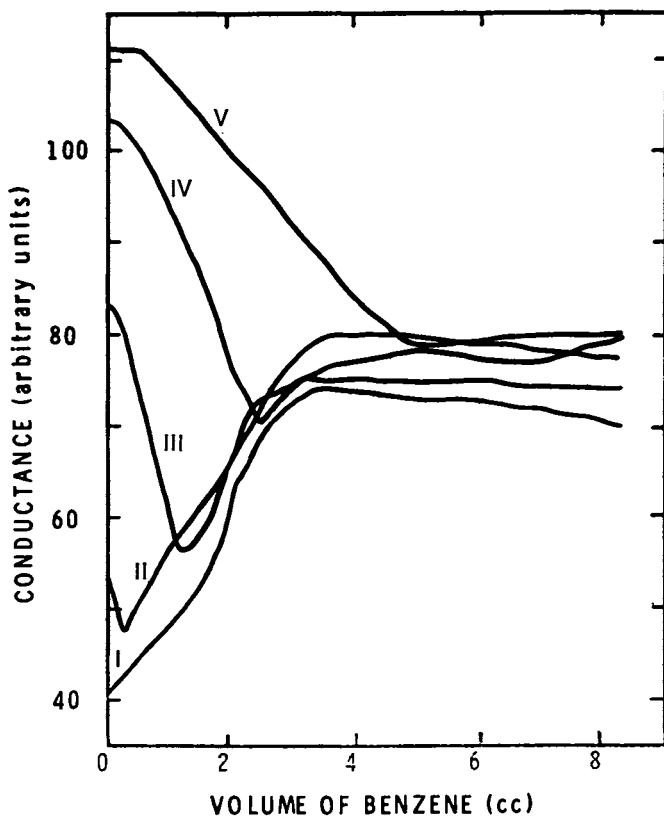


Figure 2. Conductometric titration at 63°C of 25 cc water containing 0.15 g hexadecyltrimethylammonium bromide and varying quantities of cetyl alcohol with benzene at a constant rate of 1 cc/min. Hexadecyltrimethylammonium bromide-cetyl alcohol molar ratios: I, 1:6; II, 1:3; III, 1:1; IV, 1:0.5; and V, 1:0.33. (Reproduced, with permission, from Ref. 2. Copyright 1980, Plenum Press.)

cetyl alcohol, the initial conductance decreased, the slope of the descending leg increased, and the inflection point V_1 occurred at a smaller volume of benzene titrant; for the 1:6 molar ratio, the descending leg was not observed at all. The slopes of the ascending legs between inflection points V_1 and V_2 were about the same, as were the slopes beyond the inflection point V_2 .

The electron microscopic investigation showed that rodlike particles 1-2 μm in length and 0.1-0.2 μm in diameter were formed at hexadecyltrimethylammonium bromide-cetyl alcohol ratios of 1:3 to 1:1 (Figure 3). These rodlike particles showed an electron diffraction pattern (Figure 4) that was not shown by either hexadecyltrimethylammonium bromide or cetyl alcohol alone. Moreover, heating these particles in the transmission electron microscope showed transitions near the melting points of both cetyl alcohol and hexadecyltrimethylammonium bromide.

Measurement of the styrene droplet sizes showed that the initial droplet sizes were relatively large (ca. 0.5 μm) but decreased greatly to ca. 0.1 μm as the conductance decreased to the inflection point V_1 , then increased by coalescence to the inflection point V_2 and increased slowly thereafter, principally by growth. The rodlike particles, which were observed before the titration, began to disappear during the decrease in conductance to the inflection point V_1 and disappeared completely before the inflection point V_2 was reached.

The purpose of this paper is to propose an interpretation of the foregoing results, to develop a mathematical model which uses the capability of the computer to establish the parameters that are important in the emulsification process, to predict the shape of the conductometric titration curves, and, finally, to visualize the conductometric titration curves as three-dimensional conductance-oil volume-cetyl alcohol concentration plots.

Interpretation of the Conductometric Titration Curves

In the aqueous mixed emulsifier system, the hexadecyltrimethylammonium bromide exists in one of three forms: (i) solute molecules in the aqueous phase; (ii) micelles of aggregated molecules; (iii) crystalline complex with cetyl alcohol. The conductance of these three forms should decrease in the order: solute molecules > micellar molecules >> crystalline complex. The cetyl alcohol does not contribute to the conductance.

The characteristic conductometric titration curve can be divided into three stages: (i) an initial near-linear descending leg decreasing to the inflection point V_1 ; (ii) a near-linear leg ascending to the inflection point V_2 ; (iii) a slowly decreasing or constant near-linear leg.

The initial descending leg is interpreted as the solubilization process. If micelles are present, the added oil will be solubilized. Also, the added oil may be solubilized in the hexadecyltrimethylammonium bromide-cetyl alcohol complex. That the sol-

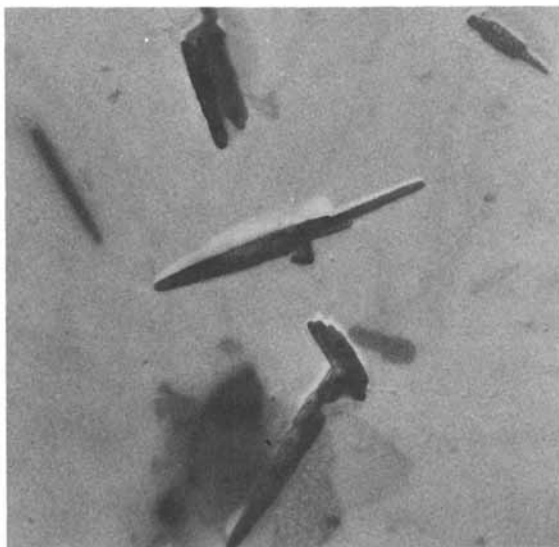


Figure 3. Transmission electron micrograph of diluted hexadecyltrimethylammonium bromide-cetyl alcohol (1:1 molar ratio) mixed emulsifier system showing rodlike particles. (Reproduced, with permission, from Ref. 2. Copyright 1980, Plenum Press.)

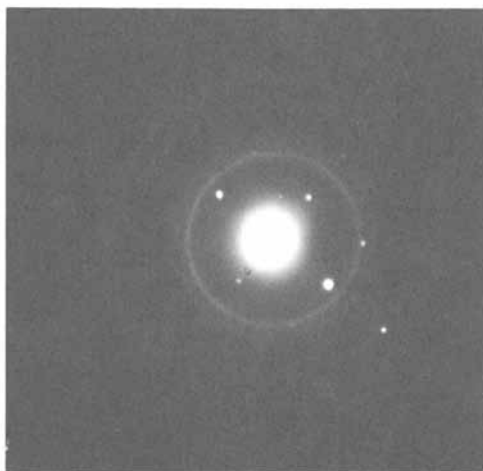


Figure 4. Selected-area transmission electron microscope diffraction pattern of the rodlike particles of hexadecyltrimethylammonium bromide-cetyl alcohol (1:3 molar ratio) produced by 100 KV electron beam. (Reproduced, with permission, from Ref. 2. Copyright 1980, Plenum Press.)

ubilization is not instantaneous is shown by the presence of both relatively large styrene droplets and the crystalline rodlike particles. This stage terminates at the inflection point V_1 where the volume of oil added is just equal to the amount that can be solubilized in the micelles or complex.

The following ascending leg is interpreted as the emulsification process. The volume of oil added is greater than can be solubilized in the micelles or complex and therefore is emulsified, first as very fine droplets that grow in size by coalescence and probably also by swelling by added oil. At the same time, the crystalline rodlike particles disappear, either by disruption from internal swelling or disintegration and reformation of the complex on the surface of the styrene droplets. This particle growth by coalescence and swelling continues up to the second inflection point V_2 .

The second slowly decreasing leg is interpreted as the particle growth process in which the number of styrene droplets is approximately constant and the added styrene diffuses through the aqueous phase and swells these droplets further.

Mathematical Model of the Conductometric Titration Curves

The three stages of the conductometric titration curve were expressed as an exponential step function with the requisite parameters.

$$F = P(1)e^{-P(2)V} [U(V)-U(V-V_1)] + P(3)e^{P(4)(V-V_1)} [U(V-V_1)-U(V-V_2)] + P(5)e^{P(6)(V-V_2)} [U(V-V_2)] \quad (1)$$

where F is the conductance, $P(1)$ the initial conductance, $P(2)$ the solubilization constant, $P(3)$ the conductance at the end of the solubilization stage, $P(4)$ the emulsification constant, $P(5)$ the conductance at the end of the emulsification stage, $P(6)$ the particle growth constant, V the volume at a given time t , $U(V)-U(V-V_1)$ the step function when V is less than V_1 , $U(V-V_1)-U(V-V_2)$ the step function when V is between V_1 and V_2 , $U(V-V_2)$ the step function when V is greater than V_2 , and V_1 and V_2 the volumes at the inflection points.

This equation was solved by iterative computer regression analysis (9) using the data of the conductometric titration of 0.6% aqueous hexadecyltrimethylammonium bromide solutions with the different hexadecyltrimethylammonium bromide-cetyl alcohol molar ratios shown in Figure 2. Table I gives the results of this analysis.

Table I
Regression Analysis of Conductometric
Titration Data using Equation 1

Molar Ratio HTAB:CA*	P(1)	P(2)	P(3)	P(4)	P(5)	P(6)
1:6.00	---	---	3.98×10	2.11×10^{-1}	7.42×10	-9.07×10^{-3}
1:3.00	5.39×10	3.85×10^{-1}	4.99×10	1.61×10^{-1}	8.03×10	-7.24×10^{-3}
1:1.00	8.67×10	3.44×10^{-1}	6.06×10	9.42×10^{-2}	7.52×10	-3.98×10^{-3}
1:0.50	1.08×10^2	1.61×10^{-1}	7.33×10	2.48×10^{-2}	7.99×10	1.11×10^{-3}
1:0.33	1.14×10^2	7.29×10^{-2}	7.68×10	6.37×10^{-3}	7.87×10	1.73×10^{-3}

*hexadecyltrimethylammonium bromide-cetyl alcohol

Figures 5-9 compare the calculated curves with the experimental curves for hexadecyltrimethylammonium bromide-cetyl alcohol ratios of 1:0.33, 1:0.5, 1:1, 1:3, and 1:6, respectively. The fit between the calculated and experimental curves is reasonably good, and the characteristic parameters of each curve are defined.

Discussion

The parameters P(1) and P(2) define the solubilization stage. In the absence of micelles, there is no solubilization of the oil phase. Therefore, in this case, there are no values of P(1) and P(2), e.g., as for the 1:6 hexadecyltrimethylammonium bromide-cetyl alcohol molar ratio.

The parameter P(1) represents the initial conductance. Table II compares the experimental and calculated values of this parameter.

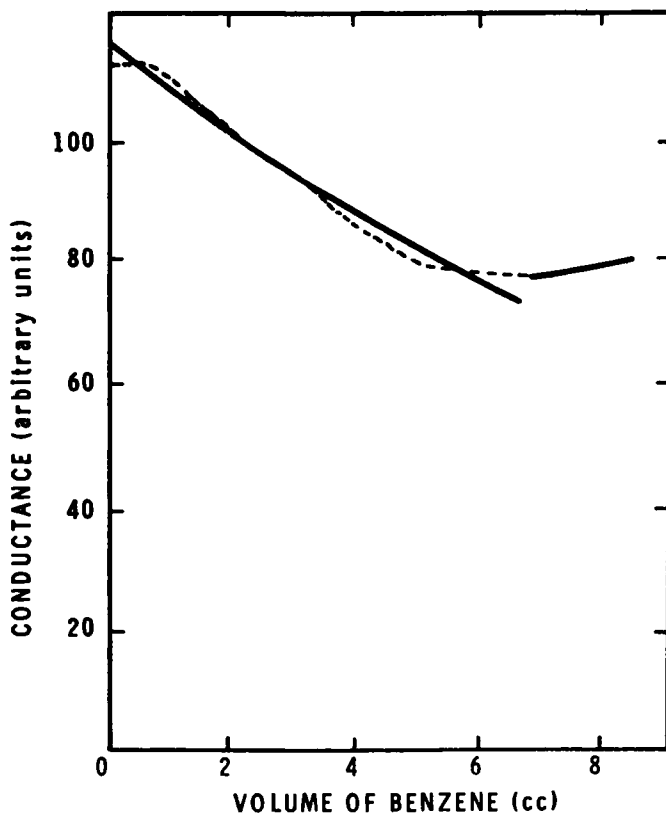


Figure 5. Conductometric titration at 63°C of 25 cc water containing 0.15 g hexadecyltrimethylammonium bromide and 0.033 g cetyl alcohol (1:0.33 molar ratio) with benzene at a constant rate of 1 cc/min. Key: ---, conductometric titration curve; and —, calculated using Equation 1.

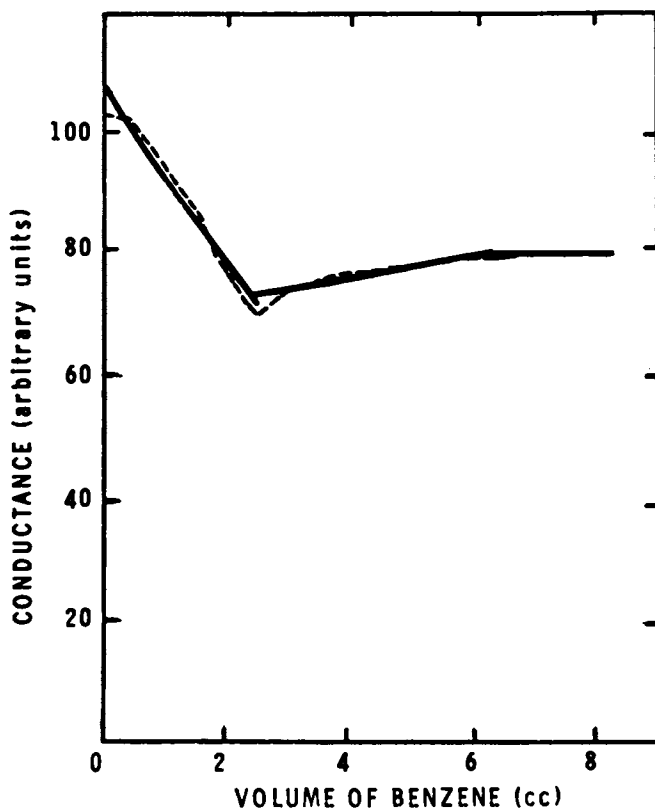


Figure 6. Conductometric titration at 63°C of 25 cc water containing 0.15 g hexadecyltrimethylammonium bromide and 0.050 g cetyl alcohol (1:0.5 molar ratio) with benzene at a constant rate of 1 cc/min. Key: ---, conductometric titration curve; —, calculated using Equation 1.

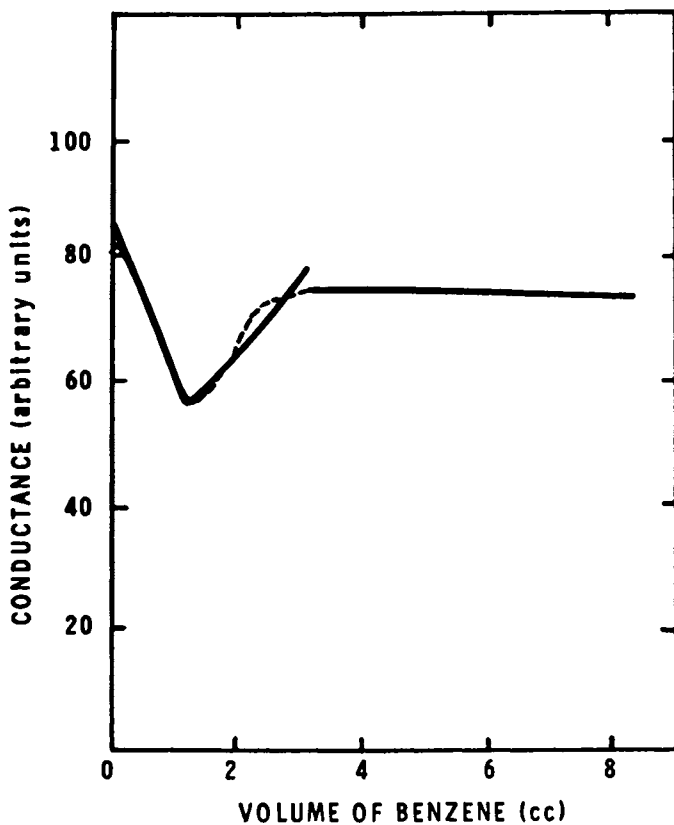


Figure 7. Conductometric titration at 63°C of 25 cc water containing 0.15 g hexadecyltrimethylammonium bromide and 0.10 g cetyl alcohol (1:1 molar ratio) with benzene at a constant rate of 1 cc/min. Key: ---, conductometric titration; —, calculated using Equation 1.

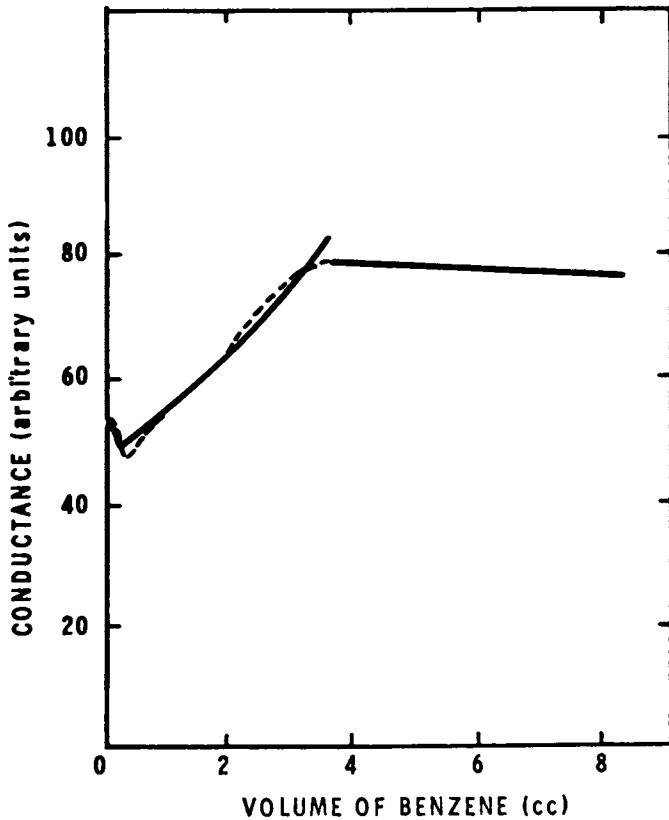


Figure 8. Conductometric titration at 63°C of 25 cc water containing 0.15 g hexadecyltrimethylammonium bromide and 0.30 g cetyl alcohol (molar ratio 1:3) with benzene at a constant rate of 1 cc/min. Key: ---, conductometric titration; —, calculated using Equation 1.

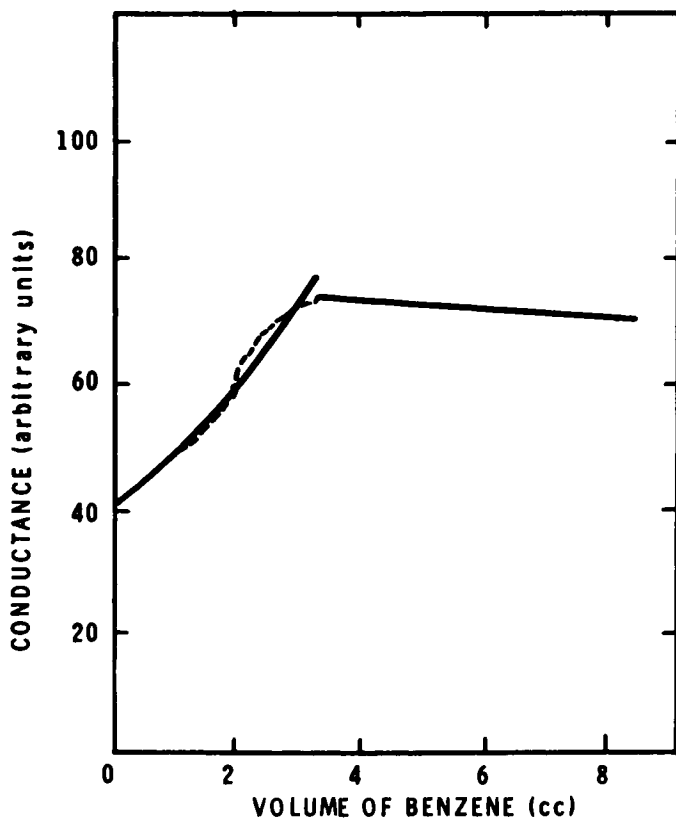


Figure 9. Conductometric titration at 63°C of 25 cc water containing 0.15 g hexadecyltrimethylammonium bromide and 0.60 g cetyl alcohol (1:6 molar ratio) with benzene at a constant rate of 1 cc/min. Key: ---, conductometric titration; —, calculated using Equation 1.

TABLE II
Comparison of Experimental and Calculated Values of P(1)

Molar Ratio HTAB:CA	Initial Conductance	
	Experimental	Regression Analysis
1:0.33	110.5	114.4
1:0.50	103.1	107.9
1:1.00	83.0	86.7
1:3.00	53.1	53.9
1:6.00	41.0	----

 The agreement between the calculated and the experimental values is good.

According to the proposed model, the descending leg of the conductometric titration curve represents the solubilization process. With decreasing hexadecyltrimethylammonium bromide-cetyl alcohol molar ratio, the initial conductance decreases and the descending leg becomes shorter and disappears at the 1:6 ratio. Assuming that the crystalline rodlike particles are non-conducting, the conductance is attributed principally to the solute hexadecyltrimethylammonium bromide molecules. The descending leg is attributed to the solubilization of the oil in the micelles. Since the total amount of hexadecyltrimethylammonium bromide in the mixed emulsifier system is known, its concentration in the crystalline rodlike particles can be obtained by subtracting the concentration of solute and micelle molecules from the total emulsifier concentration.

The conductance of the bromide counterion associated with the emulsifier micelles is $4.212 \times 10^3 M$ divided by the conductance readout (8). The concentration of hexadecyltrimethylammonium bromide in the micelles at a 1:3 molar ratio is $(53.1 - 41.0) / 4.212 \times 10^3$ or $2.87 \times 10^{-3} M$. The total concentration of hexadecyltrimethylammonium bromide in the system is $(0.15 / 364.6)(1000 / 25)$ or $1.65 \times 10^{-2} M$. The solute and micellar hexadecyltrimethylammonium bromide concentrations are subtracted from the total concentration to give the concentration in the crystalline rodlike particles. Table III gives these concentrations for the hexadecyltrimethylammonium bromide-cetyl alcohol ratios of 1:6 to 1:0.33.

TABLE III
Distribution of Hexadecyltrimethylammonium Bromide
in the Mixed Emulsifier System

Molar Ratio HTAB:CA	Concentration, M		
	Solute	Micelles	Rodlike Particles
1:6.00	8.28×10^{-4}	0	1.56×10^{-2}
1:3.00	8.28×10^{-4}	2.87×10^{-3}	1.28×10^{-2}
1:1.00	8.28×10^{-4}	9.97×10^{-3}	5.66×10^{-3}
1:0.50	8.28×10^{-4}	1.47×10^{-2}	9.35×10^{-4}
1:0.33	8.28×10^{-4}	1.65×10^{-2}	-8.65×10^{-4}

The actual solute and micellar concentrations of hexadecyltrimethylammonium bromide should be lower than the calculated values because the rodlike particles and micellar aggregates are assumed to be non-conducting. The negative value calculated for the concentration in rodlike particles for the 1:0.33 hexadecyltrimethylammonium bromide-cetyl alcohol molar ratio is essentially zero. Figure 2 shows that the benzene conductometric titration curve for the 1:0.33 hexadecyltrimethylammonium bromide-cetyl alcohol ratio is very close to that for the same concentration of hexadecyltrimethylammonium bromide without cetyl alcohol (Figure 1).

The parameter $P(2)$, the solubilization constant, has a finite value when micelles are present in the mixed emulsifier system. The smaller the value of $P(2)$, the smaller the concentration of micellar hexadecyltrimethylammonium bromide and the better the balance between the hexadecyltrimethylammonium bromide and cetyl alcohol in the crystalline rodlike particles.

It is assumed that the optimum hexadecyltrimethylammonium bromide-cetyl alcohol ratio for the formation of perfect crystals also corresponds to the formation of the highest-stability emulsions. The measurement of emulsion stability by ultracentrifugation (8) showed that emulsions prepared with a 1:3 hexadecyltrimethylammonium bromide-cetyl alcohol molar ratio showed the best stability. Therefore, the rodlike particles formed in this system should have the highest crystallinity, which was confirmed by electron diffraction measurements in the transmission electron microscope (2). The ratio $P(2)/P(2)_b$, where the subscript b denotes the system of highest crystallinity, has values of 0.894, 0.419, and 0.189 for hexadecyltrimethylammonium bromide-cetyl alcohol molar ratios of 1:1, 1:0.50, and 1:0.33, respectively, relative to a value of 1.000 for the 1:3 ratio.

The slope of the descending leg of the titration decreases and the value of V_1 increases with increasing hexadecyltrimethyl-

ammonium bromide-cetyl alcohol ratio. The parameter V_1 is related to the time period during which solubilization occurs and therefore increases when more micelles are present. The decrease in the slope of the descending leg is attributed to the poorer crystallinity of the rodlike particles formed with excess hexadecyltrimethylammonium bromide. As the oil is added to the system, the rodlike particles disintegrate more readily, releasing small concentrations of hexadecyltrimethylammonium bromide to the aqueous phase continuously.

The parameter $P(3)$ represents the conductance at the end of the solubilization stage. Table III shows that the concentration of hexadecyltrimethylammonium bromide in the crystalline rodlike particles increases with increasing cetyl alcohol concentration. Therefore, this parameter represents the number of crystalline rodlike particles in the system prior to emulsification.

The parameter $P(4)$, the emulsification constant, is related to the number of crystalline rodlike particles available to stabilize the very small emulsion droplets formed during the emulsification process. The higher the cetyl alcohol concentration at a given hexadecyltrimethylammonium bromide concentration, the more crystalline rodlike particles are generated, but the degree of crystallinity is better related to the parameter $P(2)$ than to $P(4)$.

The parameter $P(5)$ represents the conductance at the end of the emulsification process and the beginning of the particle growth process; its values are nearly constant.

The parameter $P(6)$, the particle growth constant, is related to the number of crystalline rodlike particles. The larger the number of these rodlike particles, the smaller the value of $P(6)$. This parameter is also related to the retardation effect on the conductance.

Extension and Verification of the Mathematical Model

To confirm the validity of the mathematical model, two series of conductometric titrations were carried out: (i) the hexadecyltrimethylammonium bromide concentration was decreased to 0.4% at 1:1 and 1:3 hexadecyltrimethylammonium bromide-cetyl alcohol ratios and increased to 0.8% at the 1:3 molar ratio (Figure 10); (ii) the hexadecyltrimethylammonium bromide-cetyl alcohol molar ratio was increased to 1:7 at 0.6% hexadecyltrimethylammonium bromide (Figure 11).

Figure 10 shows that varying the hexadecyltrimethylammonium bromide concentration at the same hexadecyltrimethylammonium bromide-cetyl alcohol ratio changed the conductometric titration curve. For 0.4% hexadecyltrimethylammonium bromide at the 1:3 molar ratio, the conductometric titration curve showed no initial descending leg, suggesting that this system contained no emulsifier micelles. In comparison, the conductometric titration curve for 0.6% hexadecyltrimethylammonium bromide-cetyl alcohol at the

same 1:3 molar ratio (Figure 2) showed a small initial descending leg, suggesting that this system contained a small number of micelles. For 0.8% hexadecyltrimethylammonium bromide at the 1:3 molar ratio, the length of the initial descending leg was even greater. Table IV compares the distributions of hexadecyltrimethylammonium bromide between micelles, solute molecules, and rodlike particles for these systems.

TABLE IV
Distribution of Hexadecyltrimethylammonium Bromide
in the Mixed Emulsifier System

% HTAB	Molar Ratio HTAB:CA	Concentration, M		
		Solute	Micelles	Rodlike Particles
0.4	1:3	8.28×10^{-4}	0	1.06×10^{-2}
0.6	1:3	8.28×10^{-4}	2.87×10^{-3}	1.28×10^{-2}
0.8	1:3	8.28×10^{-4}	7.60×10^{-3}	1.35×10^{-2}
0.4	1:1	8.28×10^{-4}	4.34×10^{-3}	5.72×10^{-3}
0.6	1:1	8.28×10^{-4}	9.97×10^{-3}	5.66×10^{-3}

These results show that, at a given hexadecyltrimethylammonium bromide-cetyl alcohol molar ratio, the concentration of hexadecyltrimethylammonium bromide in the micelles increases with increasing emulsifier concentration while that in the rodlike particles is about the same or increases only slightly. For 0.4% hexadecyltrimethylammonium bromide at the 1:3 molar ratio, there are no micelles, which explains the absence of a descending leg in the titration curve; moreover, the concentration of emulsifier in the rodlike particles is slightly less than at 0.6% and 0.8% emulsifier at the same molar ratio. In these latter cases, the concentration in micelles increases with increasing emulsifier concentration, while that in the rodlike particles is about the same or increases only slightly. For 0.4% hexadecyltrimethylammonium bromide at the 1:1 molar ratio, micelles are observed and the concentration in that form increases with increasing emulsifier concentration; however, the concentration in rodlike particles is about the same for both 0.4% and 0.6% hexadecyltrimethylammonium bromide. Furthermore, the concentration of emulsifier in rodlike particles is consistently smaller for the 1:1 molar ratio than for the 1:3 molar ratio; apparently, the greater proportion of cetyl alcohol results in the incorporation of more emulsifier in the rodlike particles.

The foregoing experimental results were also analyzed using the regression Equation 1 described earlier.

TABLE V
Regression Analysis of Conductometric Titration
Data using Equation 1

Molar Ratio							
% HTAB:	CA	P(1)	P(2)	P(3)	P(4)	P(5)	P(6)
0.4	1:3	----	----	3.26×10	1.03×10^{-1}	6.24×10	2.87×10^{-2}
0.6	1:3	5.39×10	3.85×10^{-1}	4.99×10	1.61×10^{-1}	8.03×10	-7.24×10^{-3}
0.8	1:3	7.30×10	5.99×10^{-1}	3.22×10	1.63×10^{-1}	8.20×10	-2.42×10^{-2}
0.4	1:1	5.97×10	3.98×10^{-1}	3.73×10	9.10×10^{-2}	7.20×10	1.57×10^{-2}
0.6	1:1	8.67×10	3.44×10^{-1}	6.06×10	9.42×10^{-2}	7.52×10	-3.98×10^{-3}

The results of Table V are consistent with those of Table IV. The values of P(1) were in reasonable agreement with the initial conductances of the titration curves, and the values of P(2) increased with increasing emulsifier concentration at the 1:3 molar ratio, and decreased slightly at the less efficient 1:1 ratio (there are no values of P(1) and P(2) for 0.4% emulsifier at the 1:3 molar ratio because of the absence of a descending leg). At both the 1:3 and 1:1 molar ratios, the values of P(2) were smaller for the 0.6% emulsifier than for the 0.8% and 0.4% emulsifier, respectively, which suggests a better balance between the hexadecyltrimethylammonium bromide and cetyl alcohol in the rodlike particles, despite the increase in micellar emulsifier with increasing emulsifier concentration.

The values of P(3) were in reasonable agreement with the conductances at the inflection point V_1 for the samples containing 0.6% emulsifier, but significantly lower than the experimental conductances for the samples containing 0.4% and 0.8% emulsifier (that for the 0.4% emulsifier at the 1:3 molar ratio, which contained no micelles was in good agreement with the initial conductance), perhaps because the titration curves of Figure 10 are more rounded at this inflection point than those of Figure 2; extrapolation of these curves to a sharp endpoint would give lower experimental values. The values of P(4) increased slowly with increasing emulsifier concentration at a given molar ratio in much smaller proportion than the increase in emulsifier concentration. These values suggest that the number of crystalline rodlike particles available to stabilize the very small emulsion droplets is more dependent on the hexadecyltrimethylammonium bromide-cetyl alcohol molar ratio than on the emulsifier concentration, being significantly smaller for the 1:1 ratio than for the 1:3 ratio.

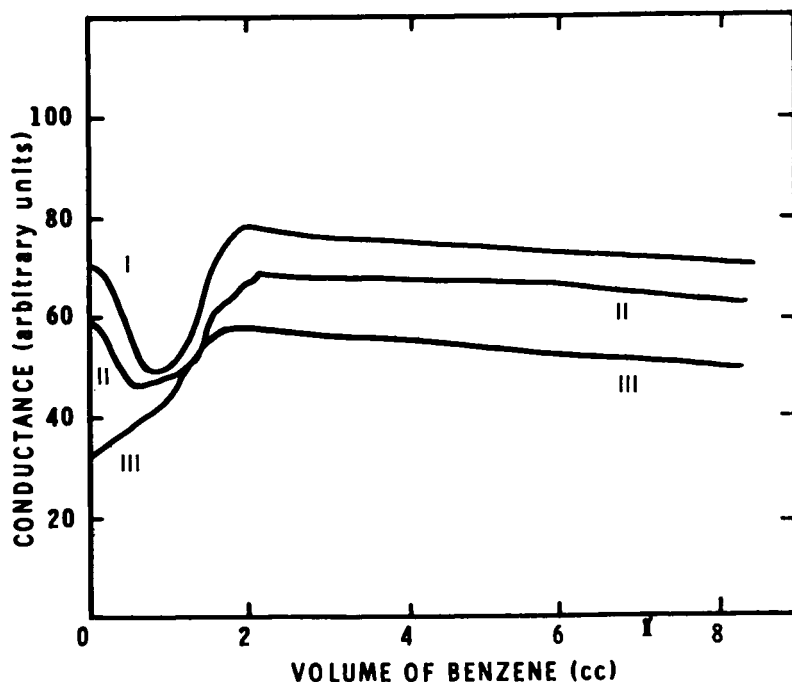


Figure 10. Conductometric titration at 63°C of 25 cc water containing 0.20 or 0.10 g hexadecyltrimethylammonium bromide and varying amounts of cetyl alcohol with benzene at a constant rate of 1 cc/min. Key: I, 0.20 g hexadecyltrimethylammonium bromide and 0.40 g cetyl alcohol (1:3 molar ratio); II, 0.10 g hexadecyltrimethylammonium bromide and 0.067 g cetyl alcohol (1:1 molar ratio); and III, 0.10 g hexadecyltrimethylammonium bromide and 0.20 g cetyl alcohol (1:3 molar ratio).

The values of P(5) were in reasonable agreement with the conductances at the inflection points V_2 , being about the same or slightly smaller. The values of P(6) were positive only for the 0.4% emulsifier at the 1:3 and 1:1 molar ratios. The negative values for the 0.6% emulsifier at 1:3 and 1:1 molar ratios and 0.8% emulsifier at 1:3 molar ratio are equal to zero within experimental error. These values suggest that the number of crystalline rodlike particles is greater for the 0.6% and 0.8% emulsifier than for the 0.4% emulsifier.

Figure 11 shows that the conductometric titration curves for 0.6% hexadecyltrimethylammonium bromide were essentially the same for molar ratios of 1:6 and 1:7. In both cases, the absence of a descending leg suggests that no micelles were present. Therefore, a further increase in the cetyl alcohol concentration resulted in an increase of that incorporated into the rodlike particles, which diminishes the crystallinity but gives no significant change in the conductometric titration curve.

Thus both of these extensions of the changes in the conductometric titration curves resulting from a change in emulsifier and cetyl alcohol concentrations were consistent with the proposed mathematical model.

Three-Dimensional Conductance-Oil Volume-Cetyl Alcohol Plots

The complex variation of the conductance with added oil volume at a given hexadecyltrimethylammonium bromide concentration was shown by a three-dimensional conductance-oil volume-cetyl alcohol concentration plot. The conductometric titration curves of Figure 2 were fitted using various equations. The best fit was obtained with the following expression.

$$F = A_0 + \sum_{n=1}^6 \{A_n X + B_n / X + A_n X^2 + B_n / X^2 + \dots + A_n X^6 + B_n / X^6\} \quad (2)$$

where X is the volume of added benzene, and A_0 , $A_1 \dots A_6$, and $B_1 \dots B_6$ are coefficients. The first part of Equation 1 expresses the oscillating part of the conductometric titration curve and the second part, the decaying part. Figure 12 compares the conductometric titration curve for 0.6% hexadecyltrimethylammonium bromide at 1:3 hexadecyltrimethylammonium bromide-cetyl alcohol molar ratio (Figure 2) with the fitted curve. The agreement between experimental and calculated curves is excellent; the three parts of the conductometric titration curve are fitted by Equation 2 using thirteen coefficients.

Table VI gives the values of these thirteen coefficients for the conductometric titration curves of Figure 2 and 0.6% hexadecyltrimethylammonium bromide at molar ratios of 1:0.33, 1:0.50, 1:1, 1:3, and 1:6.

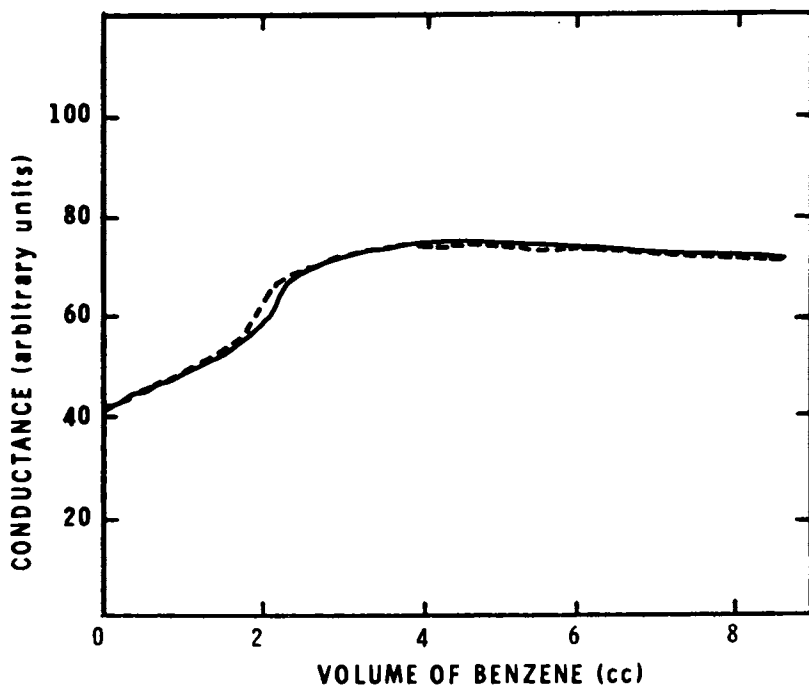


Figure 11. Conductometric titration at 63°C of 25 cc water containing 0.15 g hexadecyltrimethylammonium bromide and 0.60 or 0.70 g cetyl alcohol with benzene at a constant rate of 1 cc/min. Key: ---, 0.60 g cetyl alcohol (molar ratio 1:6) and —, 0.70 g cetyl alcohol (molar ratio 1:7).

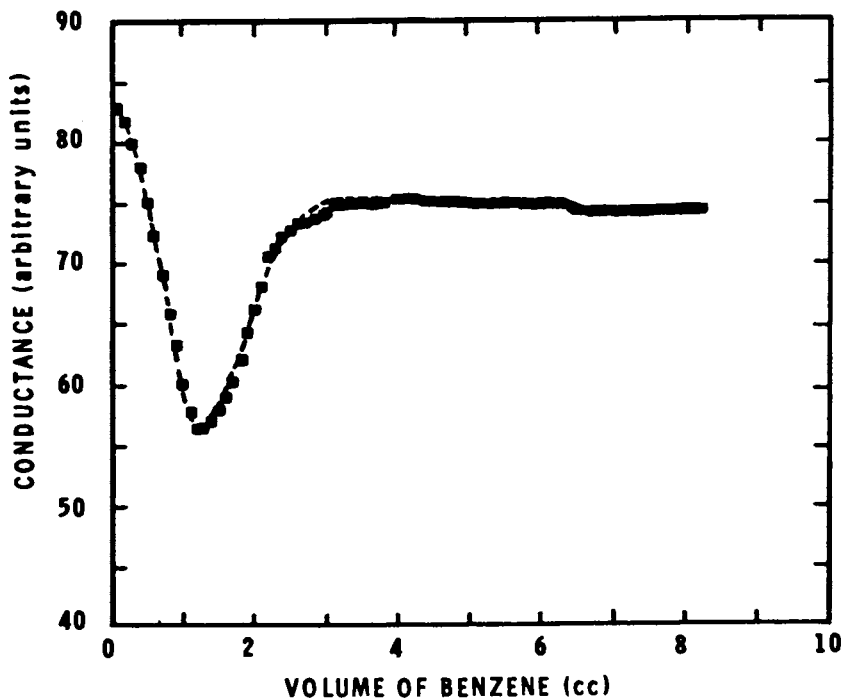


Figure 12. Conductometric titration at 63°C of 25 cc water containing 0.15 g hexadecyltrimethylammonium bromide and 0.30 g cetyl alcohol (molar ratio 1:3) with benzene at a constant rate of 1 cc/min. Key: ■, experimental curve and ---, calculated using Equation 2.

TABLE VI
Coefficients of Equation 2 for Conductometric
Titration Curves of Figure 2

Co- effi- cient	Molar Ratio HTAB:CA				
	1:6	1:3	1:1	1:0.50	1:0.33
A ₀	-1288.8	250.49	-2924.4	3097.8	-6.3251
A ₁	727.69	-218.39	1788.1	-1903.4	36.704
A ₂	-219.6	126.88	-627.84	708.03	-3.9731
A ₃	38.297	-37.271	131.93	156.44	-2.1492
A ₄	-3.7978	5.8106	-16.279	20.138	0.67757
A ₅	0.19637	-0.46015	1.0857	-1.392	-0.071166
A ₆	-0.0040359	-0.014581	-0.030164	0.039874	0.0026112
B ₁	1408.0	-65.353	2887.3	2837.1	160.41
B ₂	-870.49	-23.786	-1630.5	1624.1	-113.21
B ₃	313.83	24.789	543.70	-554.99	44.035
B ₄	-63.701	-7.4121	103.52	108.5	-9.3678
B ₅	6.5860	0.9416	10.187	-10.929	0.99793
B ₆	-0.2612	-0.042428	-0.39016	0.42607	0.040321

The three-dimensional plots were constructed in a rectangular box with the volume of added benzene forming the X-axis, the cetyl alcohol concentration of the Y-axis, and the conductance the Z-axis. The coefficients given in Table VI were used to calculate the conductance at a given cetyl alcohol concentration for each 0.4 cc added benzene from 0 to 8.0 cc, to give twenty values of the conductance. This calculation was repeated for twenty-three cetyl alcohol concentrations ranging from 1:0.25 to 1:6 molar ratios, i.e., over the range shown in Figure 2. Equation 2 was then used to fit the variation of conductance with the five different cetyl alcohol concentrations of Figure 2 at each of the twenty benzene concentrations over the range 0.0-8.0 cc. The coefficients obtained, analogous to those of Table VI, were used to calculate the conductance at each of the twenty benzene concentrations for each of twenty-three increments of cetyl alcohol concentration re-

presented by variation of the molar ratio over the range 1:0.25-1:6.00 taken every 0.25 unit of cetyl alcohol ratio. These results gave 460 conductance values as a function of volume of added benzene and cetyl alcohol concentration. These 460 points were arranged in a three-dimensional plot in the rectangular box, and the points were connected to form the three-dimensional structure. This box with the three-dimensional plot was then rotated horizontally and tilted vertically to obtain the best view of the structure.

Figure 13 shows the three-dimensional plot viewed from a horizontal angle of 250° and a vertical angle of 65° . This view shows that the descending leg of the conductometric titration curve diminished with increasing cetyl alcohol concentration until it disappeared. Beyond the disappearance of the descending leg, the titration curve changed only slightly upon further addition of cetyl alcohol.

Figure 14 shows the three-dimensional plot viewed from a horizontal angle of 30° and a vertical angle of 5° . This view shows the deep valley formed by the inflection point V_1 and its disappearance with increasing cetyl alcohol content. Moreover, the region beyond the inflection point V_2 is shown as a broad, relatively flat plateau. Thus the three-dimensional plot on the rectangular box can be tilted at any angle desired to show the specific features of interest.

Furthermore, the lines connecting the conductance curves at each benzene concentration can be omitted to give the family of conductometric titration curves corresponding to each cetyl alcohol concentration. Figure 15 shows these conductometric titration curve viewed from a horizontal angle of 275° and a vertical angle of 50° ; the range in which the descending leg disappears can be seen clearly.

Summary

The conductometric titration of aqueous hexadecyltrimethylammonium bromide-cetyl alcohol mixtures with benzene allows determination of the mechanism of emulsification. However, the shapes of the conductometric titration curves are complex: the most stable systems show a near-linear descending leg followed by a near-linear ascending leg followed by a near-linear near-constant region; the less stable systems, a near-linear ascending leg followed by a near-linear near-constant region. These conductometric titration curves have been fitted by a mathematical model using an iterative computer technique. This mathematical model gives the distribution of the hexadecyltrimethylammonium bromide as solute emulsifier, micellar emulsifier, and combined in crystalline rodlike particles with the cetyl alcohol, as well as the relative number and crystallinity of the rodlike particles. The emulsification to form 0.1-0.3 μm emulsion droplets is attributed to these rodlike particles so that the determination of their emulsifier

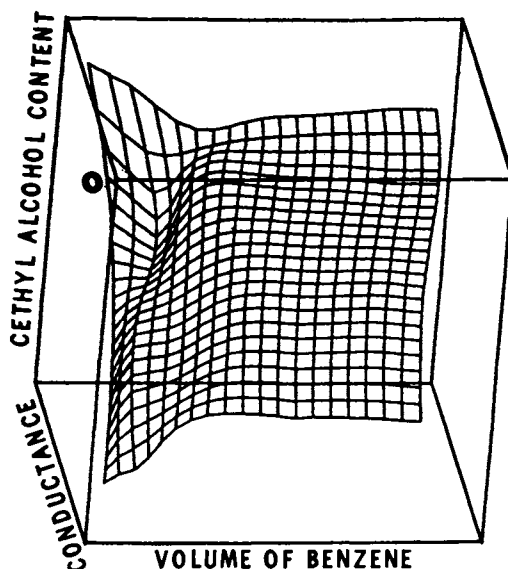


Figure 13. Three-dimensional conductance-benzene volume-cetyl alcohol concentration plot calculated using Equation 2 for conductometric titration at 63°C of 25 cc water containing 0.15 g hexadecyltrimethylammonium bromide and varying concentrations of cetyl alcohol with benzene at a constant rate of 1 cc/min viewed at a horizontal angle of 250° and a vertical angle of 65° .

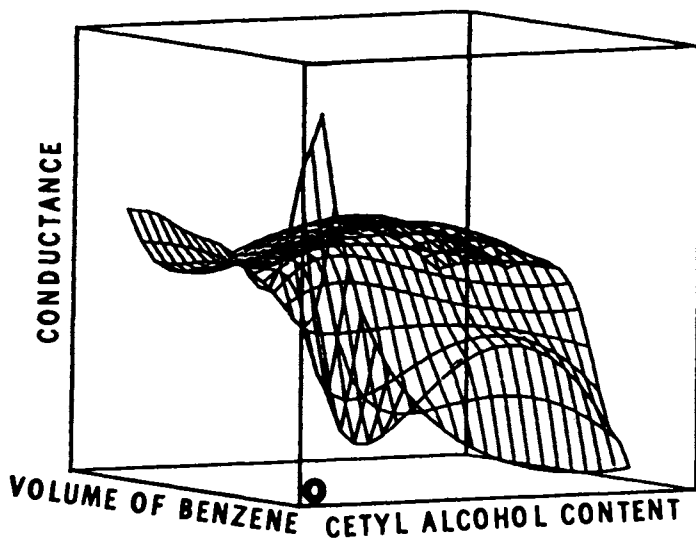


Figure 14. Three-dimensional conductance-benzene volume-cetyl alcohol concentration plot calculated using Equation 2 for conductometric titration at 63°C of 25 cc water containing 0.15 g hexadecyltrimethylammonium bromide and varying concentrations of cetyl alcohol with benzene at a constant rate of 1 cc/min viewed at a horizontal angle of 30° and a vertical angle of 5° .

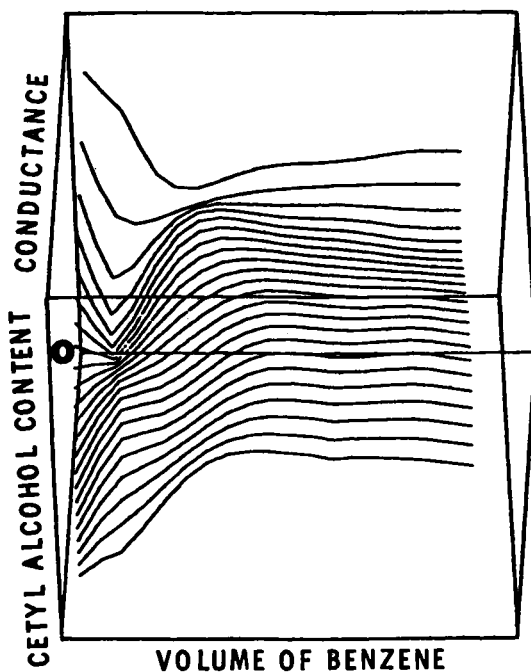


Figure 15. Three-dimensional plot of family of conductometric titration curves calculated using Equation 2 for titration at 63°C of 25 cc water containing 0.15 g hexadecyltrimethylammonium bromide and varying concentrations of cetyl alcohol with benzene at a constant rate of 1cc/min viewed at a horizontal angle of 275° and a vertical angle of 50° .

content allows prediction of relative emulsion stability. Furthermore, a three-dimensional plot of conductance as a function of added volume of benzene and cetyl alcohol concentration at constant hexadecyltrimethylammonium bromide concentration allows visualization of the conductance surface at any desired angle.

Literature Cited

1. Ugelstad, J., El-Aasser, M. S., Vanderhoff, J. W. J. Polymer Sci., Polymer Letters Ed. 1973, 11, 503-13.
2. Chou, Y. J., El-Aasser, M. S., Vanderhoff, J. W. J. Dispersion Sci. Tech. 1980, 1, 129-50; ibid. in "Polymer Colloids II", R. M. Fitch, ed., Plenum Press, New York, 1980, p. 599-618.
3. Vanderhoff, J. W., El-Aasser, M. S., Hoffman, J. D., U.S. 4,070,323 (to Lehigh University), Jan. 24, 1978.
4. Vanderhoff, J. W., El-Aasser, M. S., Ugelstad, J., U.S. 4,177,177 (to Lehigh University), Dec. 4, 1979.
5. El-Aasser, M. S., Misra, S. C., Vanderhoff, J. W., Manson, J. A. J. Coatings Tech. 1977, 49(635), 71-8.
6. El-Aasser, M. S., Vanderhoff, J. W., Poehlein, G. W. Preprints Organic Coatings Plastics Chem. 1977, 37(2), 92-7.
7. El-Aasser, M. S., Hoffman, J. D., Manson, J. A., Vanderhoff, J. W. Preprints Organic Coatings Plastics Chem. 1980, 43, 136-41.
8. Chou, Y. J. Ph.D. Dissertation, Lehigh University, 1978, p. 156-186.
9. Marquardt, D. W. J. Soc. Ind. Appl. Math. 1963, 11, 431-41.

RECEIVED May 4, 1982.

Computer Methods for Finding Solvent Blend Replacements and for Predicting Water/Cosolvent Evaporation at Any Humidity

ALBERT L. ROCKLIN

Shell Development Company, Westhollow Research Center, Houston, TX 77001

Reformulation of coatings to cut solvents costs, accommodate shortages, and comply with regulations can be improved by computer simulation. Efficient optimization requiring the balancing of a large number of variables is easily handled by computer whereas it may be impossible by hand methods. The chemist does not have to be a computer expert to use a simulation program. Computer programs can be designed by programming experts for anyone who can use a typewriter. Two examples are given of previously described solvents programs that are convenient to operate and that have proved to be very useful. Of interest in water reducible systems is a program for predicting evaporation rate and solvent balance during evaporation of blends of water with any number of dissolved cosolvents at any humidity. For conventional solvent blends there is a program which finds lowest cost replacements having properties specified by the chemist.

Rising prices, solvent shortages, and environmental restrictions on solvent emissions are putting an increasing strain on the coatings industry. Formulations employing traditional solvent blends which had been developed after years of trial and error may now be found to be too expensive or based on unavailable or discontinued solvents or in violation of pollution control regulations. To stay in business, manufacturers have to reformulate or embrace new technology such as water-borne, high solids, or powder. Whichever route is chosen, optimization is difficult because of the large number of variables that must be taken into account. The traditional method of laboriously measuring the effect of each variable one at a time over a significant range is cumbersome, expensive, and impractical. This is where computers can help. Computer simulations of various aspects of coatings

0097-6156/82/0197-0427\$06.00/0
© 1982 American Chemical Society

behavior permit a rapid survey of the effects of changing one or more variables. Since lengthy calculations are no longer an obstacle, combinations of variables can be explored efficiently for optimum effects. Though optimization must be arrived at through actual testing and measuring, the computer simulation can show the coatings technologist where an appropriate place is to start the experiments. It can also reveal important trends that might be overlooked in a conventional experimental program.

The computer is no substitute for skill, expertise, experience, or judgment. It is a tool that, if used properly, can greatly increase the effectiveness of a technologist. Yet there are two obstacles that stand in the way of effective computer utilization - fear of computers and domination by non-chemist computer experts. Chemists unfamiliar with computers tend to be afraid of them because they think that effective use requires an advanced knowledge of computer languages. This is not so. The fact is that just as a person need not be an expert mechanic or automotive engineer to be able to drive a car skillfully, so does the chemist not have to be a programming or computer language expert to use a computer to advantage. Very little skill is required to operate a program. Those described in this paper can be run with ease after just a few minutes of instruction. Nor is computer skill required in designing a program to do a certain job. If the chemist knows what the job is, for example calculation of vapor pressures, all that is needed is to give the appropriate equations to a skilled programmer, along with instructions as to how the chemist prefers to enter data and have results printed out. The program can then be written to the chemists taste. But this is where the second problem can arise. Frequently, visionary computer experts will initiate programs after only brief contact with chemists. Those programs are written from the computer expert's point of view, not the chemist's, and so may be unpopular because they have the wrong flavor. Worse still, in many organizations computer departments go farther than merely helping the chemists with their computer problems. They exercise complete control over access to and use of the company computer facilities. All computer operation must be funnelled through a designated person. This stifling procedure discourages productive and imaginative use of the computer by those very persons for whom the programs were written. It shuts them off from those features that make interactive computer operation so attractive - immediacy and flexibility. It is as if chemists were not allowed to do their own weighings, these being performed on request by the keeper of the balances!

In this paper, I discuss two examples of computer programs that perform calculations that are impossible by hand methods. Both have been published previously but are presented here to illustrate the power of the computer in solving practical problems. Both perform calculations using data from a computerized data file of individual solvent properties. The first predicts evaporation

behavior of aqueous solvent blends containing any number of dissolved cosolvents at any humidity. Its value can be appreciated when it is realized that humidity has a strong effect on the drying time and solvent balance of a water reducible coating, with consequent effects on the quality of the film produced. The second computer method selects minimum cost solvent blend replacements that will comply with chosen specifications. This can help lower cost, circumvent shortages, and comply with pollution control regulations.

Evaporation Program

The evaporation program (1) uses a repetitive procedure for predicting solvent evaporation in the Shell Evaporimeter as it would be measured by ASTM D3539. The first step calculates the time to evaporate a small portion of the blend at a constant rate determined by the initial composition. Following this, a new composition is computed and the process repeated using the new composition to calculate a new rate. At each step, the evaporation rate is calculated by adding up the rates of the individual components at their concentrations in the blend. The method takes into consideration the effect of evaporative cooling on evaporation rate and adjusts the rates of the individual components according to the actual temperature of the blend as it evaporates. Activity coefficients are calculated at that temperature by the UNIFAC (2-4) group method. Humidity is accommodated by applying a linear correction factor to the water evaporation rate.

These concepts are incorporated in the following equation which computes the total mass rate of evaporation at each step as the sum of the evaporation contributions of each component:

$$r(t) = \sum_{i=1}^n x_i(t) \gamma_i(t, T_{sol}) r_i^{\circ} (T_{sol}/T_{min_i})^{1/2} \quad (1)$$

where $r(t)$ = total rate of evaporation from solution at time t , in grams/sec of the n components.

$x_i(t)$ = mole fraction of component i in the blend at time t .

$\gamma_i(t, T_{sol})$ = activity coefficient of component i at time t at the actual temperature of the blend during evaporation.

T_{sol} = actual temperature of the evaporating blend.

r_i° = rate of evaporation (g/s) of pure i , at its actual evaporation temperature (T_{min}) as measured by ASTM D3539 at 25C.

The term $(T_{sol}/T_{min})^{1/2}$ is a temperature correction (5) to r_i° to account for the fact that each solvent is evaporating at solution temperature (T_{sol}) rather than at the temperature at which it evaporates as a pure solvent (T_{min}).

For the water component of the blend, the evaporation rate term in Equation 1 is multiplied by the linear humidity correction factor $(1-RH/100)$ as follows:

$$r_{H_2O} = (1-RH/100) \times_{H_2O} Y_{H_2O} (t, T_{sol}) r_{H_2O}^0 (T_{sol}/T_{min})^{1/2} \quad (2)$$

where RH is relative humidity of the ambient air surrounding the evaporating blend and r_{H_2O} is the evaporation rate of water from the blend.

The program is easy to use. No computer programming training is required. Using a simple terminal with a telephone connection to the central computer, the chemist enters the composition of the blend and the relative humidity in response to sequential questions as they appear at the terminal. Figure 1 illustrates a typical data entry sequence. The computer asks the questions one at a time and the chemist enters the appropriate response after the = : prompt. The first group asks general questions. Which calculations are to be done, and in what form will the data be entered? The second group asks specific questions. What is the composition of the blend, and at what relative humidity will it be evaporating? The question sequence and all operational and readout features involving chemist/computer interaction were designed by the chemist for the convenience of the chemist, in cooperation with a computer programmer who then wrote the program. Figure 2 shows the printouts of the predicted evaporation curves for an aqueous blend evaporating at 15% and at 75% RH. The computer shows that the blend will take three times as long to evaporate at the higher humidity.

The fate of cosolvents can be predicted quite closely. Figure 3 shows the change in composition of a four component blend as it evaporates, first at 40% RH, then at 65% RH. The calculated values come very close to values obtained by GC analysis of the blend during evaporation.

The above examples show how a computer program can predict the properties of a solvent blend. This can be a valuable tool for a coatings technologist who is designing a coating and would like to know ahead of time what will be the properties of a solvent blend that is under consideration.

Solvent Blend Replacement Program

The solvent blend replacement program (6) does a different job. It calculates the composition of the cheapest organic solvent blend that will have properties specified by the chemist. Solvent blend replacement is based on the generally applicable principle that if the solvent portion of a conventional formulation is replaced by a new blend of different composition but having the same solvent properties as the old blend, the new coating will perform the same as the old. To use the program to

```
***** SHELL SOLVENT EVAPORATION PROGRAM *****  
  
TYPE 1 FOR EVAPORATION TIME PLOT, 2 FOR TABLE = :1  
TYPE 1 FOR SOLVENT BALANCE; OTHERWISE TYPE 2 = :1  
  
NOTE THAT ONLY THE FIRST FIVE SOLVENTS WILL BE PLOTTED.  
IF WATER IS SIGNIFICANT, IT WILL APPEAR AS THE FIRST SOLVENT.  
TYPE 1 FOR VOL 2 FOR WT FRACTIONS = :2  
  
NO. OF LISTED SOLVENTS (0=END RUN) = :4  
SOLVENT NOS. = :78,48,26,79  
WT.FRACTIONS = :.7,.1,.1,.1  
RELATIVE HUMIDITY (ENTER 0. IF HUMIDITY NOT CONSIDERED) = :50.  
TYPE 1 TO PROCEED, 2 IF UNLISTED SOLVENTS, 3 IF WRONG DATA = :1
```

Figure 1. Data entry section.

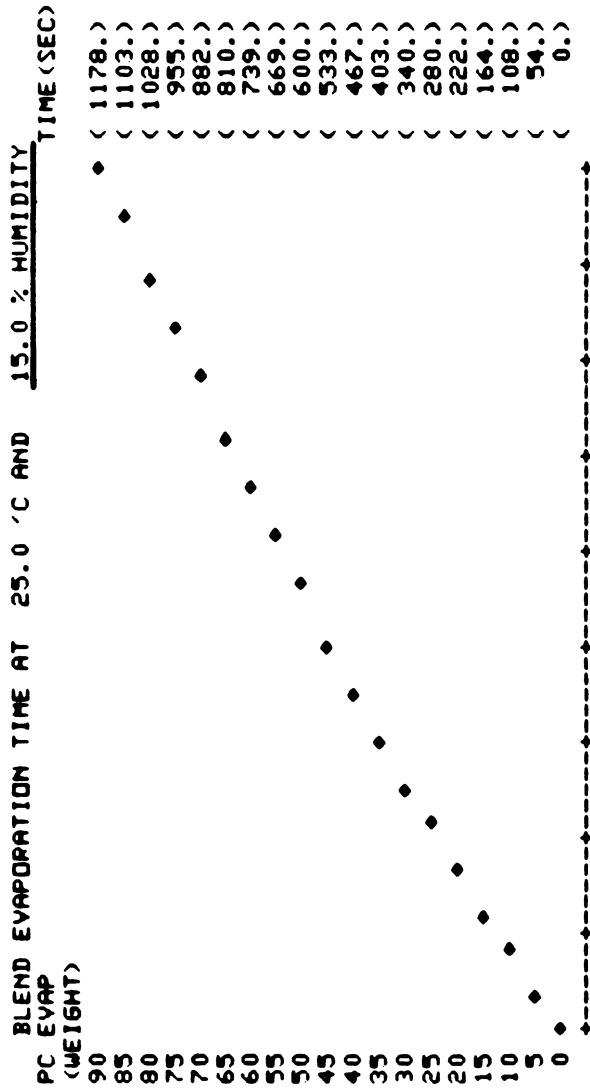


Figure 2a. Computed evaporation curve at 15% humidity for a solvent blend composed of 70% w water and 10% w each of 2-butoxyethanol, dimethylformamide, and 4-methoxy-4-methyl-2-pentanone. 90% evaporation time = 1178 at 25°C.

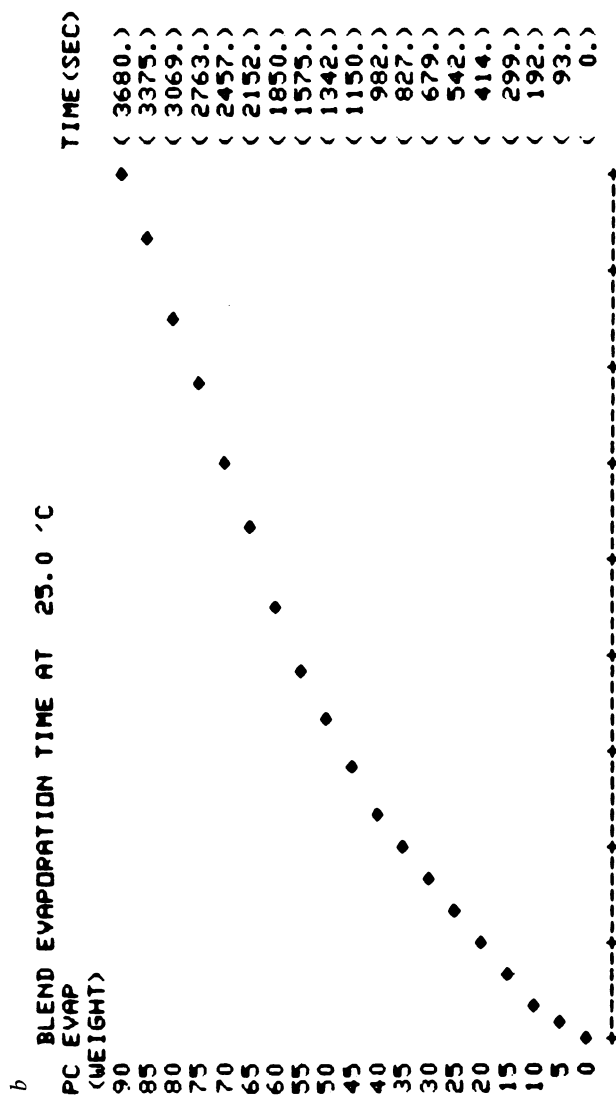


Figure 2b. Computed evaporation curve at 75% humidity for a solvent blend composed of 70% w water and 10% w each of 2-butoxyethanol, dimethylformamide, and 4-methoxy-4-methyl-2-pentane. 90% evaporation time = 3680 s.

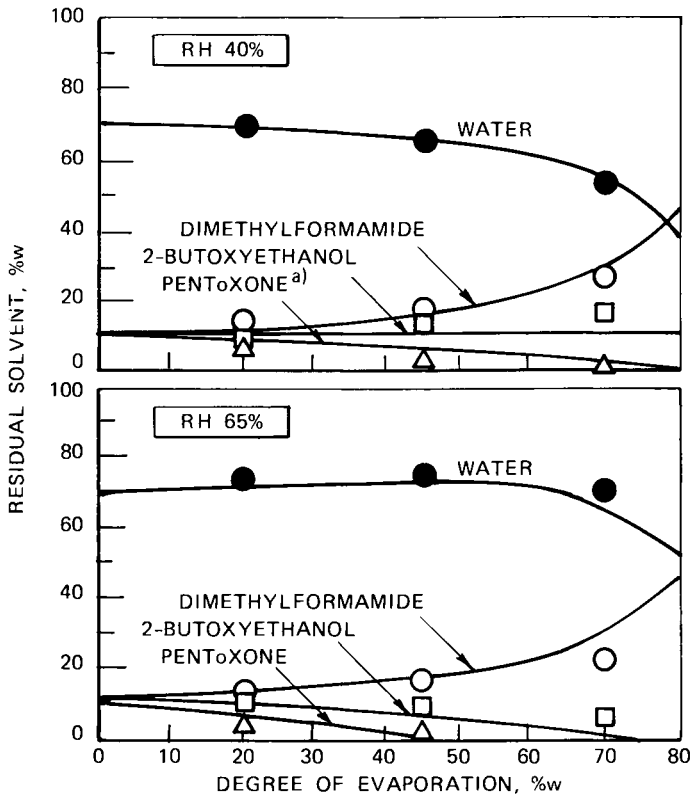


Figure 3. Comparison of calculated solvent balance (lines) with observed concentrations (points) on evaporation of 4-component blend at two humidities. (Reproduced, with permission, from Ref. 1. Copyright 1980, Federation of Societies for Coatings Technology)

^{a)} 4-methoxy-4-methyl-2-pentanone; PENTOXONE is a registered trademark of Shell Chemical Company.

advantage, the chemist must know which solvent properties are important to coatings performance and understand their effect.

The first step is to calculate the properties of the original blend. This is done by the previously described computer program. For an organic solvent blend, that program not only calculates evaporation characteristics but also calculates solution parameters. Solubility parameter, polarity, and hydrogen bonding affect the capacity of the blend to dissolve a resin; evaporation rate affects the drying rate of the coating whereas solvent balance during drying will affect film quality. Not all the properties of the original must be repeated in the substitute. The chemist decides which parameters to select and which values to specify, then chooses a group of up to fifteen solvents from which the replacement might be made. The computer will call on only those solvents that are needed to satisfy the parameter values at the lowest price. Computer flexibility of choice can be increased by designating the specified value of each parameter as either a minimum or a maximum instead of one to be met exactly. For example, a blend can be constrained to have a viscosity no greater than 0.6 cps and a solubility parameter no less than 8.3. Since each parameter or constraint is represented in the program by a linear equation, the computer selection of an optimum solvent blend is nothing more than the solution to a set of simultaneous equations in as many variables as there are constraints. The job would be impossible by hand but is easy for the computer.

Table I shows a typical replacement blend. As expected, the Rule 66 blend is more expensive than the non-exempt original, but its properties are at least as good, and in some respects better. In particular, the replacement gives a lower viscosity at higher solids. To some extent, this offsets the higher solvents price because less solvent is needed to obtain application viscosity.

In this example, the substitute is not an exact match for the original. It rarely has to be. If the computer calculated blend seems inappropriate, the chemist can tinker with the parameter specifications, impose more or delete some constraints, or change the panel of solvents candidates until the calculated blend appears reasonable. A large number of options can be explored in a very short time.

Conclusion

These two computer programs illustrate the value of applying computer methods. The chemist need not shy away from complicated calculations. By surveying logical proposals via computer simulation, the chemist can be far more efficient and selective in designing an experimental optimization program. In these examples the predictions are based on readily available technology and the calculations are straightforward, but they are so lengthy that it is impossible to do them by hand. Without the computer the calculations would not be done at all, and the chemist would have

Table I. PROPERTIES OF NON-EXEMPT NITROCELLULOSE LACQUER SOLVENT BLEND AND ITS RULE 66 EXEMPT REPLACEMENT.

Solids Composition, pbw		
RS 1/4 Second Nitrocellulose (Dry)	10	
Non-Drying Coconut Alkyd	10	
Dioctyl Phthalate	4	
	Non-Exempt	Exempt
Solvent Composition, %v	<u>Blend</u>	<u>Replacement</u>
n-Propyl Acetate	14.0	-
Isobutyl Acetate	26.0	-
n-Butyl Acetate	-	25
Methyl Isobutyl Ketone	-	7
Amyl Acetate	-	14
n-Butyl Alcohol	4.8	-
Ethyl Alcohol	-	15
Xylene	27.6	6
Toluene	27.6	-
VM&P Naphtha EC	-	29
	<u>100.0</u>	<u>100</u>
Solvent Properties		
Cost, Cents/Gallon	206	231
Specific Gravity, 25/25C	0.864	0.814
Estimated Evaporation Time, sec ^a), 25C	348	322
Solubility Parameter	8.83	8.92
Fractional Polarity	0.048	0.102
Hydrogen Bonding Index (Shell)	4.99	2.45
Estimated Viscosity, cps, 25C	0.65	0.69
Determined Viscosity, cps, 25C	0.62	0.66
Lacquer Properties		
Viscosity at Application Solids, cps, 25C	55	42
Application Solids, %w	17.8	20.4
Blush Resistance, % Relative		
Humidity at 80F (27C)	84	82
Flow on Glass (10 = Best)	2	5-6
Film Thickness, Mils	1.4	1.5
Tukon Hardness, KHN ₂₅		
4 Hours Air Dry	3.2	2.4
24 Hours Air Dry	5.2	5.0
Print Resistance, 18 Hours		
Film Thickness on Maple (Mils)	3.0	3.0
1 psi	No Print	No Print
2 psi	Very, Very Slight Print	
5 psi	Very Slight Print	

a) On Shell Thin Film Evaporometer by ASTM D3539.

(Reprinted with permission, from Ref. 6. Copyright 1970, Federation of Societies for Coatings Technology.)

to fall back on slower, and much less adequate, approximations. The computer is a wonderful tool but it has no opinions, imagination, or intelligence. All it can do is calculate accurately and rapidly. It knows nothing about chemistry but it can be an enormous help to a resourceful chemist by opening up the possibility of performing complex calculations that would never have been considered seriously.

Literature Cited

1. Rocklin, A. L.; Bonner, D. C. Journal of Coatings Technology, 52, No. 670, 27-36 (1980).
2. Fredenslund, A.; Jones, R. L.; Prausnitz, J. M. AIChEJ., 21, 1086(1975).
3. Fredenslund, A.; Gmehling, J.; Rasmussen, P. "Vapor-Liquid Equilibria Using UNIFAC," Elsevier, Amsterdam, 1977.
4. Skjold-Jorgensen, S.; Kolbe, B.; Gmehling, J.; Rasmussen, P. Ind. Eng. Chem. Proc. Des. Dev., 18, 714 (1979).
5. Gardner, G. S. Ind. Eng. Chem., 32, 226 (1940).
6. Walsham, J. G.; Edwards, G. D. Journal of Paint Technology, 43, No. 554, 64 (1971).

RECEIVED May 4, 1982.

Design and Analysis of an Acrylonitrile-Butadiene-Styrene (ABS) Pipe Compound Experiment

M. H. WILT and G. F. KOONS

United States Steel Corporation, Research Center, Monroeville, PA 15146

Selected blends of styrene-acrylonitrile copolymer (30 to 55%), a styrene-butadiene copolymer grafted with styrene and acrylonitrile (45 to 70%), and a coal-tar pitch (0 to 25%), were prepared. Physical properties of the experimental blends were determined and statistical techniques were used to develop empirical equations relating these properties to blend composition. Scheffé canonical polynomial models and response surfaces provided a thorough understanding of the mixture system. These models were used to determine the amount of coal-tar pitch that could be incorporated into ABS compounds that would still meet ASTM requirements for various pipe-material designations.

A significant reduction in cost could be achieved if appreciable quantities of coal-tar pitch could be incorporated into ABS for the production of a satisfactory pipe compound. Because of the availability of trained plastics and mathematics personnel at the U. S. Steel Research Laboratory, an interdisciplinary approach was made to the problem. Before any blending was done, an appropriate experiment was designed to obtain a maximum output of information with a minimum amount of experimentation. This paper reports the results and analysis of the experimentation.

Materials and Experimental Work

For this study the materials shown in Table I were used.

0097-6156/82/0197-0439\$06.00/0
© 1982 American Chemical Society

Table I
Blend Components

Styrene-butadiene copolymer - 19 percent SAN; 81 percent graft grafted with styrene and acrylonitrile	
Styrene-acrylonitrile copolymer (SAN)	- \bar{M}_n 64,600, \bar{M}_w 179,800; percent AN 27.5
Coal-tar pitch prills	- S.P. 112°C

Blends were produced in a small Banbury mixer. About 3 lb of dry-blended material was added to the Banbury. After the flux point, blends were run for two more minutes and dumped. Conditions were speed No. 2, 30 psi on the ram, and a dump temperature of 310°F. Test specimens were molded on a 3-oz Van Dorn injection-molding machine; front, middle, and rear zones were 500, 485, and 470°F, respectively. The mold temperature was 160°F; the molding cycle was typical for ABS. Test methods were ASTM Standard Procedures.

Experimental Design

The major consideration in selecting the experimental region for this study was that it include compositions that could be expected to produce acceptable pipe compounds. A second consideration was that the region be comprehensive enough to include blends containing pitch in excess of the maximum amount that could be acceptably added to pipe compounds. In other words, if the experiment was to indicate the maximum tolerable amount of pitch, then some blends containing unacceptable amounts also had to be studied.

The experimental region, shown by the ternary diagram in Figure 1, contained blends ranging from 45 to 70 percent graft, 30 to 55 percent SAN, and up to 25 percent pitch. This region is only a portion of all the possible combinations of the three components.

A mathematical transformation was made to convert the absolute amounts of each element to their relative amounts within the subregion studied. These relative amounts are called pseudo-components (1). For example, the blend consisting of 45 percent graft, 30 percent SAN, and 25 percent pitch contains the maximum amount of pitch and minimum amounts of the other constituents. If X_1 , X_2 , and X_3 represent the relative amounts of each component, the pitch vertex can be labeled $X_1 = 0.0$, $X_2 = 0.0$, and $X_3 = 1.0$ (Figure 2).

* See References.

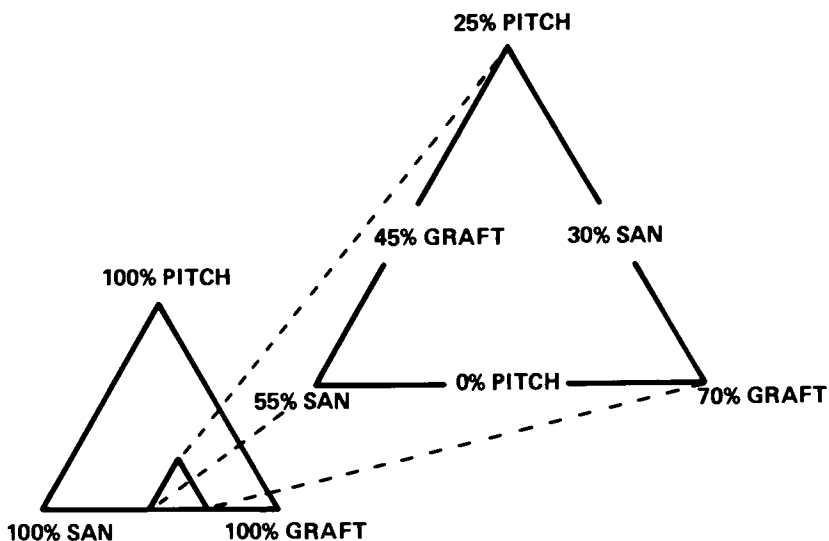


Figure 1. Schema showing experimental blends and resultant Izod values.

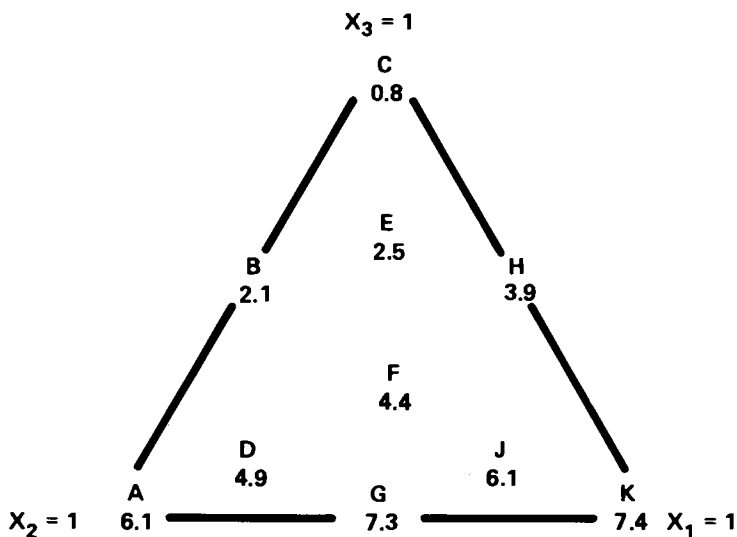


Figure 2. Schema of experimental region. Blend indicated by letters and measured Izod indicated by numbers.

$$X_1 = (\text{GRAFT} - 0.45) / 0.25; X_2 = (\text{SAN} - 0.30) / 0.25; X_3 = \text{PITCH} / 0.25$$

Results and Discussion

The Izod impact, deflection temperature under load (DTUL), and yield strength (YS) of each experimental blend were determined. The results are presented in Table II.

Figure 2 also shows the Izod impact results. There were obvious and anticipated synergistic effects operative within the system. For example, consider the blends that contained no pitch; as graft initially replaced SAN, the Izod changed from 6.1 to 7.3 ft-lb/inch of notch. However, after a certain amount of graft was added, additional replacement of SAN by graft had virtually no effect on the Izod impact value.

Empirical models were used to relate the changes in composition to resultant changes in properties. The form of the model used is the special cubic which was developed by Scheffé (2).

$$Y = \beta_1 X_1 + \beta_2 X_2 + \beta_3 X_3 + \beta_{12} X_1 X_2 + \beta_{13} X_1 X_3 + \beta_{23} X_2 X_3 + \beta_{123} X_1 X_2 X_3 + \epsilon$$

where Y is the property of interest; X's are the pseudocomponent amounts of graft, SAN, and pitch, respectively; β 's are the coefficients that describe the effects of the components; and ϵ denotes the error term. The following equations resulted from the model-fitting procedure:

$$\text{Izod} = 7.39 X_1 + 6.08 X_2 + 0.72 X_3 + 2.54 X_1 X_2 - 5.31 X_2 X_3$$

$$\text{DTUL} = 202.3 X_1 + 211.8 X_2 + 182.9 X_3 - 22.8 X_1 X_3 - 22.2 X_2 X_3$$

$$\text{YS} = 4367.2 X_1 + 6087.5 X_2 + 5071.5 X_3 + 1440.0 X_1 X_3 + 586.0 X_2 X_3$$

For each equation, two statistics that describe the adequacy of the equations were calculated—the adjusted coefficient of determination (3) (adjusted R^2) and the standard error of estimate (SEE). The adjusted R^2 denotes the proportion of the variability observed in the property that was explained in the terms of the equation. The SEE is a measure of the unexplained variability that still existed after the significant effects were taken into account, Table III.

Table II
Properties of ABS - Pitch Blends

Composition and Properties	Blend										
	A	B	C	D	E	F	G	H	J	K	
Graft, %	45.0	45.0	45.0	50.0	50.0	53.5	57.5	57.5	60.0	70.0	
SAN, %	55.0	42.5	30.0	45.0	35.0	38.0	42.5	30.0	35.0	30.0	
C.T. Pitch, %	0.0	12.5	25.0	5.0	15.0	8.5	0.0	12.5	5.0	0.0	
Izod Impact, ft-lb/in.	6.1	2.1	0.8	4.9	2.5	4.4	7.3	3.9	6.1	7.4	
DTUL, °F (264 psi)	213	191	183	202	186	197	204	188	192	205	
Yield Strength, psi	6080	5740	5065	5615	5385	5410	5280	5080	5035	4350	

Table III

Adequacy of Regression Equations

<u>Yield Strength</u>	<u>Adjusted R²</u>	<u>SEE</u>
Izod	0.996	0.14 ft-lb/in. of notch
DTUL	0.880	3.4°F
Yield Strength	0.994	37 psi

A convenient way of depicting the effects of composition on a particular property is through use of a response surface (4). A response surface is a topographical-like map that shows compositional regions in which similar properties can be expected. Figures 3 through 5 depict response surfaces for Izod, DTUL, and yield strength, respectively.

These response surfaces were used to determine compositions that could be used to produce several types and grades of rigid ABS pipe compound. For example, Type 4, Grade 1 pipe must satisfy the minimum requirements shown in Table IV.

Table IV

Requirements of Type 4, Grade 1 Pipe Compound

<u>Property</u>	<u>Specification</u>
Izod	>1 ft-lb/in. of notch
DTUL	>190°F
Yield Strength	>5000 psi

These restrictions define a region within the pseudocomponent system where the properties can be expected to simultaneously satisfy all three specifications. From a practical point of view, the region should be conservatively defined because each regression equation is subject to a degree of error. Assuming 0.2 ft-lb/inch of notch, 5°F, and 50 psi provide satisfactory safety margins, the region of possible blends is as shown in Figure 6.

The actual choice within this region may depend upon economic or other considerations. If the choice is solely dependent upon maximizing the amount of pitch in the blend, it appears that, in terms of pseudocomponents, 0 percent graft and approximately 60 percent SAN and 40 percent pitch would be the selected blend. In absolute terms, this translates to about 45 percent graft, 45 percent SAN, and 10 percent pitch. The maximum amounts of pitch for other pipe grades are shown in Table V.

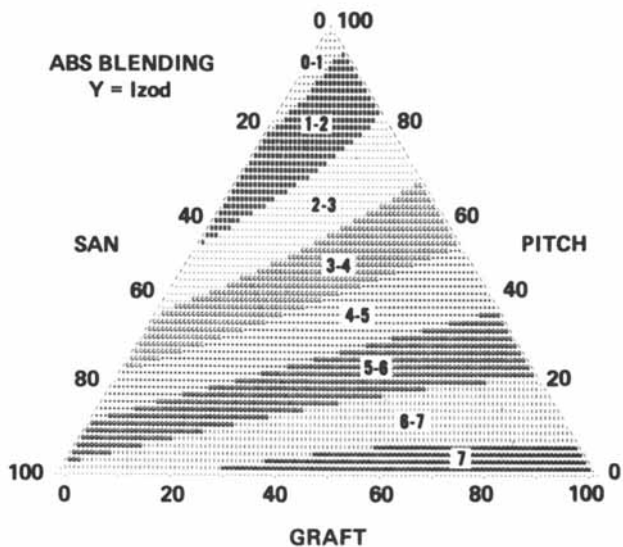


Figure 3. Response surface—predicted Izod for compositions in experimental region.

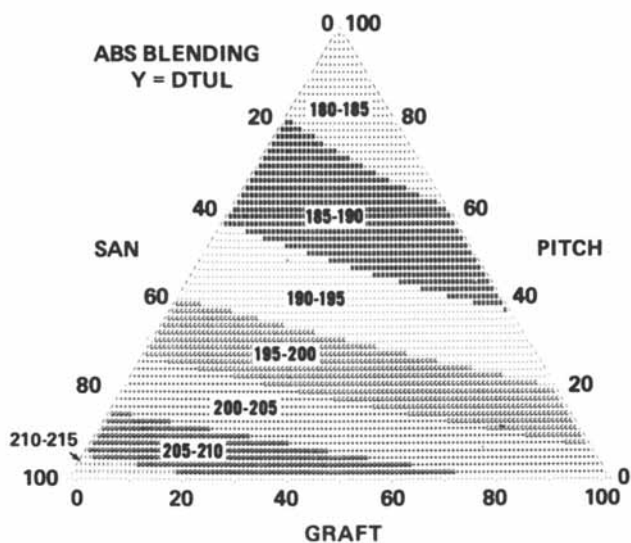


Figure 4. Response surface—predicted DTUL for compositions in experimental region.

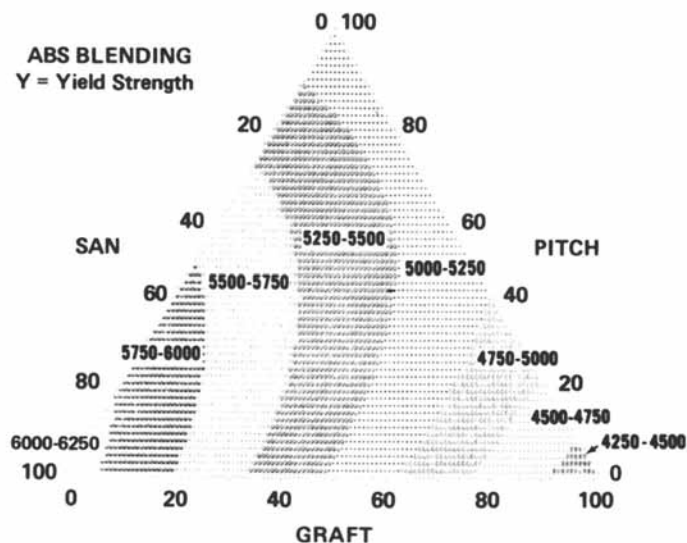


Figure 5. Response surface—predicted yield strength for compositions in experimental region.

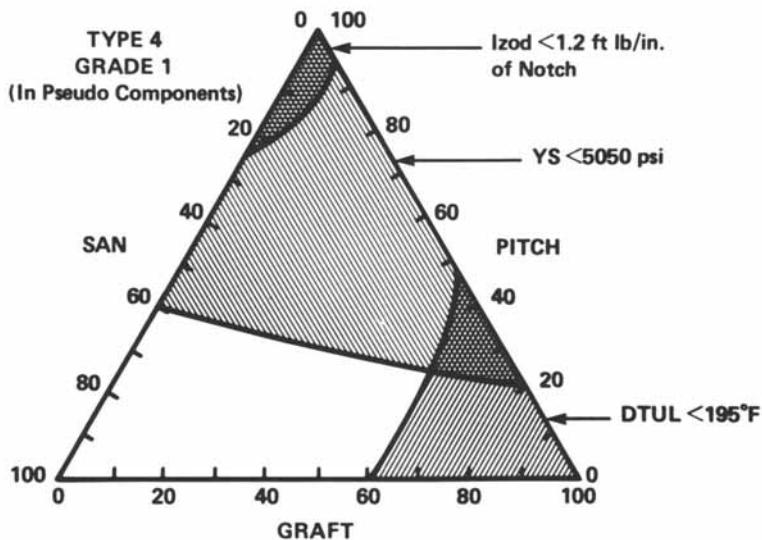


Figure 6. Blends within experimental region suitable for Type 4 Grade 1 ABS pipe compound.

Table V

Allowable Pitch Content of ABS Pipe Compounds

<u>Pipe Material Designation</u>	<u>Izod,ft-lb/in. of notch</u>	<u>DTUL, °F</u>	<u>Yield Str,psi</u>	<u>Maximum Pitch,%</u>	<u>Limiting Factor</u>
Type 1, Grade 1	3	180	4000	16	Izod, DTUL
Type 1, Grade 2	6	180	4500	5	Izod
Type 1, Grade 3	3	220*	7000*	-	*
Type 2, Grade 1	4	200	7000*	-	*
Type 4, Grade 1	1	190	5000	10	DTUL

* Did not achieve within the experimental region.

Conclusion

An experiment was designed to determine the amount of coal-tar pitch that could be incorporated into ABS pipe compounds. Ten selected blends were prepared and critical physical properties determined. Statistical techniques were used to develop empirical equations relating the resultant properties to blend composition. Scheffé canonical polynomial models and response surfaces provided a thorough understanding of the mixture system. These models were used to determine the amount of coal-tar pitch that could be incorporated into ABS compounds that would still meet ASTM requirements for various pipe-material designations.

Acknowledgment

The blending and testing work was supervised by V. M. DiNardo and L. E. Carlisle, Jr., respectively.

It is understood that the material in this paper is intended for general information only and should not be used in relation to any specific application without independent examination and verification of its applicability and suitability by professionally qualified personnel. Those making use thereof or relying thereon assume all risk and liability arising from such use or reliance.

American Chemical
Society Library
1155 16th St., N.W.

Literature Cited

1. Kurotori, J. S., Experiments with Mixtures of Compounds Having Lower Bounds, *Industrial Quality Control*, Vol 22, (1966), 592-596.
2. Scheffé, H., Experiments With Mixtures, *Journal of Royal Statistical Society, Series B*, Vol. 20, (1958), 344-360.
3. Marquardt, D. W. and Snee, R. D., Test Statistics for Mixture Models, *Technometrics*, Vol. 16, No. 4, (1974), 533-537.
4. Koons, G. F. and Heasley, R. H., Response Surface Contour Plots for Mixture Problems, *Journal of Quality Technology*, Vol. 13, No. 3, (1981), 207-214.

RECEIVED May 4, 1982.

INDEX

A

- ABS pipe-compound experiment,
design and analysis 439-447
- Absorption behavior
polystyrene in solution 166, 170-177
vibrational energy, computerized
viscoelastic master plots for
vibration damping
applications 367-368
- Acceleratory reactions of poly-
(vinyl halides) 377-383
- Acid, isocyanate, reaction simulation
using CSMP 67-68
- Acrylonitrile-styrene copolymer,
design and analysis of blends 439-447
- Activation energy, automated thermal
analysis 301
- Addition rate of monomers to propa-
gating chain 93
- Additivity, Beer's law 152-154, 161,
163, 166, 171
- Adiabatic calorimetry data vs. differ-
ential scanning calorimetry
data 359, 363-365
- Advanced thermal analysis, heat
capacity data bank 355-365
- AIBN—*See* Azobisisobutyronitrile
- Alcohol, cetyl
and hexadecyltrimethylammonium
bromide, emulsification of ben-
zene and styrene 399-424
three-dimensional conductance-
volume-concentration plots 418-422
- Algorithm
data acquisition, capillary
rheometer 244-246
Nelder Mead sequential simplex
minimization 301
- Amine-cured epoxy resin, automated
torsion pendulum vs. torsional
braid analysis 349-350
- Analysis
ABS pipe-compound experiment 439-447
and automated capillary rheometer
measurement 243-248
copolymer composition 103
- Analysis (*continued*)
regression, of conductometric titra-
tion, hexadecyltrimethylammo-
nium bromide-cetyl alcohol
mixed emulsifier system 41
residual monomer 101-103
spectrometric 103
torsional braid 330, 332, 350-357
- Analytical model, interfacial
polarization 284-285
- Analyzer, dynamic mechanical 372-374
- Anionic polymerization of styrene
initiated by *n*-butyllithium 3-11
- Anionic surfactants, polystyrene
swelling 200-206
- Apparatus, resonant dwell vibrating
beam 372
- Apparent shear rate, capillary
rheometer measurement 244
- Application
computer to degradation kinetics of
poly(vinyl halides) 377-383
continuous poly(vinyl acetate)
emulsion polymerization
reactors for reaction system
design 209-220
morphology studies, polarization in
thermoplastic elastomers 277-295
- Aqueous hexadecyltrimethylammo-
nium bromide-cetyl alcohol
mixtures, emulsification of ben-
zene and styrene, mathematical
treatment 399-424
- Areas, hydrogen halide peak, com-
puter program for degradation
kinetics of poly(vinyl halides) 378-383
- Aromatic groups, heat capacity data .. 357
- Arrhenius frequency factor, automated
thermal analysis 301
- ATHAS—*See* Advanced thermal
analysis
- Attraction, model of solution chain
conformations and interactions .. 390
- Automation
capillary rheometer measurement
and analysis 243-248

Automation (*continued*)

Ferranti-Shirley viscometer	223-239
thermal analysis system reaction	
kinetics	297-305
torsion pendulum	329-352
Average properties model	88-90
Average sequence length	177 <i>t</i>
Average sequence length mean of	
distributions	92
Axisymmetric formulations	266
Azobisisobutyronitrile (AIBN)	124
Azeotropic composition, styrene-	
methylacrylate copolymers	132

B

Balance, solvent of a water-reducible	
coating	427-437
Ball and chain model	28-29
Bank, polymer heat capacity data	355-365
Batch thermally initiated bulk	
styrene polymerization	21-25
B-centered pentad fractions	143
Beer's law mass detection	152
Benzene, mathematical treatment of	
emulsification in aqueous hexa-	
decyltrimethylammonium bro-	
mide-cetyl alcohol mixtures	399-424
Bimodal distribution, high density	
polyethylene molecular weight	
distribution analysis	60
Binary copolymerization	88-89
Biquadratic basis functions, mixed	
interpolation isoparametric	
rectangles	256
Bisphenol-A-diglycidylether resin	
curing reaction	313-326
Blend replacements, solvent	427-437
Blends, molecular weight distribution	
analysis	45-63
Block copolymer, segmented	
polyurethanes	277-295
Block, calculation, heat capacity	
data	362-363
Bondi scheme, model of chain solution	
conformations and interactions	393-394
Boyer's rule	357
Braid, multifilamented glass	330, 350-357
Branching effects, long chain,	
prediction	209-220
Bulk styrene polymerization, thermally	
initiated	21-25
Bundles, model of chain solution	
conformations and inter-	
actions	385-396
Butadiene copolymer grafted with	
styrene and acrylonitrile, design	
and analysis of blends	439-447

2-Butoxyethanol, solvent system	
evaporation	432-433
Butterworth filtering, fourth-order	280
<i>n</i> -Butyllithium initiation, polymeriza-	
tion of styrene	3-11

C

Calculation block, heat capacity	
data bank	362-363
Calculations, structural features of	
terpolymers, programs	137-149
Calibration, automated torsion	
pendulum	348-349
Calorimetry	
differential scanning data, vs.	
adiabatic data	359, 363-365
differential scanning, epoxy curing	
reaction	313-326
Canonical polynomial models,	
Scheffe, ABS pipe compounds	439-447
Capillary pressure, curvature-	
dependent	258
Capillary rheometer measurement	
and analysis	243-248
<i>N</i> -Carboxy anhydride polymerization	
using CSMP, simulation of	
kinetics	67
<i>N</i> -Carboxyl anhydride (NCA)	79-81
Casson analysis, shear stress vs.	
shear rate	227-228
CCD— <i>See</i> Copolymer composition	
distribution	
Cetyl alcohol, three-dimensional	
conductance-volume-concentra-	
tion plots	418-422
Chain, 3iP, computer approximations	
of premature termination	378-380
Chain conformations and interactions	
model	385-396
Chain flexibility	385-396
Chain length, distribution, simulation	
of poly(vinyl halides)	
kinetics	378-383
Chain length dependent determination,	
computational aspects of free	
radical polymerization kinetics	27-42
Chain propagation, radical, peroxide-	
initiated styrene polymerization	14-25
Chain stiffness	385-396
Characterization techniques	102 <i>t</i>
Chain transfer, to monomer and	
solvent, styrene polymerization	14
Chloride, vinyl polymers, com-	
puterized degradation kinetics	377
Chromatograph, gel permeation,	
copolymerization of styrene with	
methyl acrylate	126

- Chromatography
 gas, residual monomer
 determination 132, 134f
 gel permeation 110-111
 size exclusion, SAN copolymers .. 151-181
 Chromophore, SAN copolymers 166
 Closed loop control, styrene
 polymerization 6-8
 Coal-tar pitch, design and analysis
 of blends 439-447
 Coating, water-reducible, drying time
 and solvent balance 427-437
 Columns, SEC 110-111
 Combinatorial factor, model of chain
 solution conformations and
 interactions 390-392
 Compact bundles, model of chain
 solution conformations and inter-
 actions 385-396
 Composition behavior assumptions 89-90
 Composition distributions 89-90
 Composition, copolymer, function of
 retention volume 173, 178-181
 Composition, copolymer, styrene and
 methyl acrylate 127, 129f, 131f
 Composition hardener/resin, effect
 on degree of cure 316
 Comprehensive models 93
 Compressibility, isothermal, model of
 chain solution conformations
 and interactions 390
 Compressibility, nonisothermal
 polymer flows 267
 Computations, model of chain solution
 conformations and inter-
 actions 390-392
 Concentration, polymer, model of
 chain solution conformations
 and interactions 386, 393-396
 Concentration, solute and micellar,
 hexadecyltrimethylammonium
 bromide emulsifier systems 399-424
 Concentration, solvent blends and
 evaporation 429-434
 Condensation
 N-carboxy anhydride
 polymerization 79
 self-promoted polyaddition, use
 of CSMP 79-81
 Schulz-
 Zimm model 47-48, 55f, 58f, 62f
 Conductance-oil volume-cetyl alcohol
 plots, three-dimensional 418-422
 Conductometric titration curves, hexa-
 decyltrimethylammonium bro-
 mide-cetyl alcohol mixed emulsi-
 fier systems 401-424
 Cone-plate viscometer 223-239
 Configurational dimensions, polymer
 molecules in dilute solutions .. 388-396
 Conformations, model of polymer
 solution properties 385-396
 Constant
 particle growth hexadecyltrimethyl-
 ammonium bromide-cetyl
 alcohol mixed emulsifier
 system 414
 rate, computer program for
 degradation kinetics 378-380
 Continuous flow stirred tank reactors
 (CSTR's), oscillations 209-220
 Continuous loop reactor 24f
 Continuous poly(vinyl acetate) emul-
 sion polymerization reactor,
 dynamic model 209-220
 Continuous system modeling program
 (CSMP) 75-84
 Continuous thermally initiated bulk
 styrene polymerization 21-25
 Control, automated torsion
 pendulum 329-352
 Control, closed loop, styrene
 polymerization control 6-8
 Control analysis, styrene polymeriza-
 tion using *n*-butyllithium
 initiation 4
 Control strategy
 copolymerization of styrene with
 methyl acrylate 119-124
 reactors 87, 111-112
 Controlled semi-batch solution
 copolymerization of styrene with
 methyl acrylate 117-134
 Controller transfer function matrix,
 styrene polymerization control 8
 Conversion
 dependency, vinyl polymerization
 kinetics 29-32
 low and high, refractive index of
 SAN copolymers 154, 161-166
 predicted, Mettler program 313-326
 rate, continuous stirred tank reactor
 styrene polymerization 21, 218
 Coordination number, model of chain
 solution conformations and
 interactions 389-393
 Copolymer
 analysis 103
 composition
 distribution (CCD) 90-99, 101
 function of retention
 volume 173 78-181
 styrene and methyl
 acrylate 127, 129f, 131f
 film analysis, IR spectroscopy .. 185-196

- Copolymer (*continued*)
- fractionation 108
 - styrene-butadiene, grafted with styrene and acrylonitrile, design and analysis of blends 439-447
- Copolymerization equation 88-89, 99-100
- Copolymerization, styrene with methyl acrylate 117-134
- Cosolvent/water evaporation at any humidity 427-437
- Cost of solvent, solvent blend replacement 427-437
- p*-Cresol-formaldehyde 79-81
- Crystal structure of polymers, heat capacity data 356-358
- Crystalline stability, application of polarization morphology 287
- CSMP—*See* Continuous system modeling program
- CSTR's—*See* Continuous flow stirred tank reactors
- Cumulative overall 89-90
- Cured, epoxy resin amine-, automated torsion pendulum vs. torsional braid analysis 349-350
- Curing reaction
- epoxy, differential scanning calorimetry 313-326
 - quantitative reaction kinetics 297
- Curves
- conductometric titration, hexadecyltrimethylammonium bromide-cetyl alcohol mixed emulsifier system 401-424
 - viscoelastic 368
- D**
- Damped resonant frequency 279
- Damping applications, vibrations, viscoelastic master plots 367-374
- Damping parameters, automated torsion pendulum 330-350
- Data acquisition
- automated torsion pendulum 329-352
 - Ferranti-Shirley viscometer 224
 - modified Gottfert capillary rheometer 243
 - thermal analysis 298
- Data analysis
- Ferranti-Shirley viscometer 227
 - thermal analysis 299-305
- Data bank, polymer heat capacity, pressure-volume-temperature, and thermal conductivity 355-365
- Data entry sequence, solvent system evaporation 430-431
- Data reduction
- automated torsion pendulum 336-348
 - viscoelastic master plots for vibration damping applications 367-374
- Data storage, parameter calculation for kinetic models 377-383
- Dead polymer chain formation 32, 35-37
- Decomposition, quantitative reaction kinetics 297
- Decoupling in steady-state, styrene polymerization control 7-8, 11
- Deflection temperature under load (DTUL), styrene blends 442-447
- Deformation energy of loss modulus .. 335
- Degradation, mechanical, model of chain solution conformations and interactions 393
- Degradation kinetics of poly(vinyl halides) 377-383
- Degree of polymerization, simulation of poly(vinyl halides) kinetics 382, 383f
- Density, interchange energy, polymer + solvent 392-393
- Depolarization currents, dielectric spectroscopy of polyurethanes 292
- Design
- ABS pipe-compound experiment 439-447
 - optimal multiple reactor system 209-220
- Detectors, mass, assumptions for use in spectroscopy 152
- Detection
- UV, polystyrene latexes 200
- Deviatoric stresses 266-267
- Dielectric constant and hypochromic effects 170
- Dielectric spectroscopy 279-284, 290-292
- Differential composition distributions 89-90
- Differential equations
- CSMP 65-84
 - least squares data reduction for automated torsion pendulum 339-344
 - styrene polymerization kinetics 14-21
- Differential scanning calorimetry vs. adiabatic calorimetry data 359, 363-365
- epoxy curing reaction 313-326
- Diffraction pattern, transmission electron micrograph, hexadecyltrimethylammonium bromide-cetyl alcohol 401-404
- Digitization rate, automated torsion pendulum 336-337

- Dimensions, configurational, polymer molecules in dilute solutions 388-396
- Dimer, self-condensation of 2,4-dimethylol-4-methylphenol, rate constants 75*f*
- Dimethylformamide, solvent system evaporation 432-433
- Dispersity index, copolymerization of styrene with methyl acrylate 122*t*
- Disproportionation, copolymerization of styrene with methyl acrylate 123*t*
- Disproportionation, vinyl polymerization kinetics 32, 35-37
- Distribution of chain length, simulation of poly(vinyl halides) kinetics 378-383
- Distribution function, pair radial, model of chain solution conformations and interactions 389, 392
- Distribution placements, monomer or sequence, unconditional probabilities 139-145
- Distribution
- copolymer composition 89-99, 101
 - frequency-dependent electric-field, application to morphology 278-295
 - molecular weight 87, 90, 93-99, 101
 - monomer unit, simulation using CSMP 82-84
 - sequence length 87, 90-93, 101
- Distributive properties model 93
- Double bond polymerization, terminal 210
- Double-beam IR spectrophotometer, film analysis 186
- Down-channel extruder drag flow, nonisothermal polymer flows 268-270
- Drag reduction (DR), conformations in flow 394-396
- Drop volume method 200
- Drying time of a water reducible coating 427-437
- DTUL—*See* Deflection temperature under load
- Dyads, structural calculations 137-149
- Dynamic mechanical analyzer (DMA) 372-374
- Dynamic mechanical modulus data, glassy to rubbery region, viscoelastic master plots 368-369
- E**
- Elastomers, thermoplastic, polarization 277-295
- Electrical polarization, morphological heterogeneities 277-295
- Electron micrograph, transmission, hexadecyltrimethylammonium bromide-cetyl alcohol mixed emulsifier system 401-404
- Electron microscopy, polystyrene latexes 200
- Element, isoparametric penalty 265-276
- Element mesh, finite, nonisothermal polymer flows 272*f*
- Element method, Galerkin finite, roll coating 251
- Emulsifiers
- ionic oil-in-water, mathematical model of benzene and styrene emulsions 399-424
 - sodium dodecyl sulfate 203-205
- Emulsion polymerization reactor, dynamic model, continuous poly(vinyl acetate) 209-220
- Energy
- absorption, vibrational, computerized viscoelastic master plots for vibration damping applications 367-368
 - activation, automated thermal analysis 301
 - balance 122
 - deformation, loss modulus 335
 - density of mixed interactions of polymer + solvent 392-393
 - exchange interaction, model of chain solution conformations and interactions 385-396
 - interfacial and mixing 198-199
 - potential, model of chain solution conformations and interactions 390-392
- Enthalpy
- equilibrium transition 355
 - molar 121-122
- Entry flow streamlines, nonisothermal polymer flows 272*f*
- Epimerization reaction 73-79
- Epoxy curing reaction, differential scanning calorimetry 313-326
- Epoxy resin, amine-cured, automated torsion pendulum vs. torsion braid analysis 349-350
- Equation
- differential, least squares data reduction for automated torsion pendulum 339-344
 - validity, of copolymerization 99-100
- Equation of motion, automated torsion pendulum 336, 338, 341
- Equilibrium first order transition temperatures, heat capacity data 355
- Equilibrium swelling of latex particles with monomers 197-206
- Equilibrium transition, enthalpy 355
- Error in variables methods (EVM) 98-99
- Ethyl methacrylate, monomer 40, 42*f*
- Evaporation at any humidity, water/cosolvent 427-437

- EVM—*See* Error in variables methods
- Exchange interaction energy, model of solution conformations and interactions 386–396
- Expansion, linear Taylor series 342
- Expansivity, isobaric, model of solution conformations and interactions 390–392
- Exponential distribution, Schulz-Zimm model 47–48, 55f, 58f, 62f
- Extended bundles, model of solution conformations and interactions 385–396
- Extinction coefficient, SAN copolymer 170–177
- F**
- Factor
- Arrhenius frequency, automated thermal analysis 301
- combinatorial, model of chain solution conformations and interactions 390–392
- free volume, model of chain solution conformations and interactions 390–392
- Fast Fourier transform (FFT) method 345–348
- Ferranti-Shirley viscometer, automated 223–239
- Film analysis, IR spectroscopy 185–196
- Film, nip flow in roll coating 251–263
- Filtering, fourth-order Butterworth 280
- Finite element formulation, polymer melt flow simulation 254–276
- First order kinetics, program for parameter estimation 379t
- First order transition temperatures, equilibrium, heat capacity data .. 355
- Flexibility, chain 385–396
- Flory distribution model 47, 56f, 57f, 61f
- Flory-Huggins equation 198–199
- Flow
- conformations, drag reductions 394–396
- nonisothermal polymer, modeling 265–276
- Flow rate
- change in response to reaction temperature 130f
- roll coating 252
- Flow stirred tank reactors, continuous 209–220
- Fluid bulk modulus, nonisothermal polymer flows 267
- Fluid compressibility, nonisothermal polymer flows 267
- Fluid, shear-thinning results 261–263
- Fluoride-vinyl polymers, degradation kinetics 377
- Fluorosilicone polymer reduced temperature nomograph 374f
- FORTTRAN and CSMP 66
- Fourier transform method, data reduction for automated torsion pendulum 345–348
- Fourth-order Butterworth filtering 280
- Fractionation 108
- Fractionation gel permeation chromatography 50–63
- Free energy of mixing 199
- Free radical polymerization
- kinetics 88–101
- chain length dependent termination, computational aspects 27–42
- styrene 21–24
- Free surface representation 252
- Free volume factor, model of chain solution conformations and interactions 390–392
- Free volume model 100
- Frequency-dependent electric-field distribution, application to morphology 278–295
- Frequency factor, Arrhenius, automated thermal analysis 301
- Frequency parameters, automated torsion pendulum 330–350
- FT—*See* Fourier transform method
- Function
- chain length dependence 33f
- pair radial distribution 389, 392
- partition 390
- process transfer, styrene polymerization control 6
- G**
- Galerkin finite element method, roll coating 251
- Gauss-Legendre numerical integration 268
- Gas chromatography, residual monomer determination 132, 134f
- Gel effect
- free radical polymerization kinetics, chain length dependent termination 27–42
- interpretation and termination reactions 100
- Gel permeation chromatography 110–111
- copolymerization of styrene with methyl acrylate 126
- molecular weight distribution analysis 50–63
- Gel pores 110–111
- Generation reactor, tubular seed 214
- Gibbs-Thomson equation 198–199
- Glass braid, multifilamented 330, 350–357
- Glass transition of polymers, heat capacity data 356–358

- Glassy selenium, heat capacity data 363-364
- Gottfert capillary rheometer, modified, data acquisition system 243
- GPC—*See* Gel permeation chromatography
- Gravity effects, roll coating 251-263
- H**
- Halide-vinyl polymers, degradation kinetics 377
- Hardener, triethylene tetramine-phenol, epoxy curing reaction 313-326
- HDPE—*See* High density polyethylene
- Heat balance 122
- Heat capacity data bank 355-365
- Heat generation, internal, nonisothermal polymer flows 267-268
- Heat of reaction per epoxy group 320
- Heterogeneity
 microstructure, and copolymer properties 99
- morphological, electrical polarization 277-295
- Hexadecyltrimethylammonium bromide-cetyl alcohol mixtures, aqueous, emulsification of benzene and styrene 399-424
- High conversion terpolymer structure 143
- High density polyethylene 52
- Humidity, water/cosolvent evaporation 427-437
- Hydrodynamic volume model 394
- Hydrogen halide peak areas, degradation kinetics of poly(vinyl halides) 378-383
- Hydrophilic systems, swelling phenomena 197-206
- Hydrostatic stress, nonisothermal polymer flows 267
- Hypochromic effect, methyl methacrylate and polystyrene 170
- I**
- I-mer radicals 28-29
- Incompressible volume, segmental hard-core, model of solution conformations and interactions .. 392
- Inertia, moment of, automated torsion pendulum 348-349
- Inertial forces, Reynolds number .. 254-255
- Infrared spectroscopy—*See* IR
- Initiation
 N-carboxy anhydride polymerization 79
- copolymerization of styrene with methyl acrylate 123*t*
- efficiency, peroxide in styrene polymerization 14-25
- potassium persulfate 200, 218
- rate, in styrene polymerization, viscosity effect 4
- Input block, heat capacity data bank 261-262
- Intramolecular skeletal vibrations .. 355-358
- Instrument analysis process, Ferranti-Shirley viscometer 225-227
- Integration
 Gauss-Legendre numerical 268
- Runge-Kutta 77
- Interactions, model of chain solution properties 385-396
- Interchange energy density, model of chain solution conformations and interactions 393
- Interface
 data acquisition system to modified Gottfert capillary rheometer .. 243
- minicomputer to thermal analysis system 297-305
- Interfacial energy 198-199
- Interfacial tension, latex 197-206
- Intermolecular interactions, model of chain solution conformations and interactions 390-396
- Intermolecular vibrations of linear macromolecules 355-358
- Internal heat generation, nonisothermal polymer flows 267
- Ionic emulsifier-fatty alcohol, mathematical model of benzene and styrene emulsions 399-424
- IR
 spectrophotometer, double-beam, film analysis 186
- spectroscopy
 copolymer film analysis 185-196
- SAN copolymers 150-153
- software 185-196
- Isobaric expansivity, model of solution conformations and interactions 390-392
- Isocyanate-acid reaction simulation using CSMP 67-68
- Isoparametric penalty elements .. 265-276
- Isoparametric rectangles, mixed interpolation, nine-node biquadratic basis functions 256
- Isothermal compressibility, model of solution conformations and interactions 390

- Isothermal cure schedules, optimum,
Mettler software313-326
- Isothermal polystyrene reactor 3-11
- Izod impact, styrene blends442-447
- J**
- J-mer radicals28-29
- K**
- Kinetics
N-carboxy anhydride polymeriza-
tion simulation using CSMP .. 67
- copolymerization reactions88-101
- curing reaction 320-324
- Mettler software313-326
- parameters378-380
- polymer modification reaction
simulation using CSMP 82
- poly(vinyl halides) degradation 377-383
- styrene polymerization simulation ..13-25
- terminal double bond
polymerization 211
- thermal analysis system297-305
- L**
- Language, computer—*See* Software
- Laplace transform, process transfer
function, styrene polymerization
control 6
- Latex mathematical model of benzene
and styrene emulsions 399-424
- Latex particles with monomers, equi-
librium swelling197-206
- Lattice strains, applications of
polarization morphology 287
- Least squares method, data reduction
for automated torsion
pendulum338-348
- Light scattering, molecular weight
determination107-108
- Light scattering photometer,
polystyrene latexes 200
- Linear least squares, automated
torsion pendulum .. 338-341, 345-348
- Linear macromolecules, intermolec-
ular vibrations 355-358
- Linear Taylor series expansion 342
- Linearity, Beer's law152-154, 161,
163, 166, 171
- Liquid phase, model of chain
conformations and inter-
actions 385-396
- Liquid selenium, heat capacity
data 363, 364f
- Logarithmic distribution, Wesslau
model48-49, 53f, 59f, 63f
- London forces and extinction
coefficient 170
- Long chain approximation (LCA) 90
- Long chain branching effects,
prediction209-220
- Lorenz-Lorenz equation, validity 163
- Loss modulus, calculation for auto-
mated torsion pendulum 329-352
- Loss tangent data, glassy to rubbery
region, viscoelastic master
plots368-369
- Low density polyethylene, noniso-
thermal polymer flows268-269
- Lubrication approximation at liquid/
gas interface, roll coating 254
- M**
- Macromolecules
linear, intermolecular vibrations 355-358
- non-uniform, model of solution
conformations and inter-
actions386-388
- thermal data 355-365
- Macroscopic behavior, chain confor-
mations and interactions 385-396
- Mass detectors, spectrophotometers,
assumptions for use 152
- Mass, molecular, model of solution
conformations and inter-
actions394-396
- Mathematical model
copolymerization of styrene with
methyl acrylate121-124
- emulsification of benzene and
styrene in aqueous hexadecyl-
trimethylammonium bromide-
cetyl alcohol mixture399-424
- styrene polymerization kinetics13-25
- vinyl polymerization kinetics27-42
- Matrix, styrene polymerization model 7t
- MDF—*See* Mechanical degradation
in flow
- Mechanical analyzer, dynamic372-374
- Mechanical degradation in flow model
of solution conformations and
interactions 394
- Mechanical modulus, dynamic, glassy
to rubbery region, viscoelastic
master plots368-369
- Mean of distributions, average
sequence lengths 92
- Melt flow, simulation, finite element
formulation265-276
- Melt viscosity, capillary rheometer
measurement 244
- Melting transition357-358

- Method**
- data analysis, Ferranti-Shirley viscometer 227
 - Fourier transform, data reduction for automated torsion pendulum 345-348
 - Galerkin finite element, roll coating 251
 - least squares, data reduction for automated torsion pendulum 338-341, 345-348
 - Nelder Mead sequential simplex minimization algorithm 301
 - nonlinear least squares, data reduction for automated torsion pendulum 341-348
 - peak finding, data reduction for automated torsion pendulum 338-339, 345-348
 - Savitsky-Golay, shear rate and viscosity 236
 - trapazoidal, automated thermal analysis 301
 - 4-Methoxy-4-methyl-2-pentanone, solvent system evaporation 432-433
 - Methyl methacrylate 40, 41*f*
 - hypochromic effect 170
 - swelling of polymethyl methacrylate latex particles 203-206
 - Methyl acrylate, copolymerization with styrene 117-134
 - Mettler thermal analysis system 313-326
 - Micellar concentrations, hexadecyltrimethylammonium bromide-cetyl alcohol emulsifier systems 399-424
 - Micelles, hexadecyltrimethylammonium bromide-cetyl alcohol mixed emulsifier system 404-424
 - Micrograph, transmission electron, hexadecyltrimethylammonium bromide-cetyl alcohol mixed emulsifier system 401-404
 - Microscopic structure of polymers, heat capacity data 356-358
 - Microstructure heterogeneity and copolymer properties 99
 - Mini-computer
 - heat capacity data bank 359-360
 - interface to Ferranti-Shirley viscometer 223-239
 - interface to thermal analysis system 297-305
 - Mini-emulsions, mathematical model of benzene and styrene emulsions 399-424
 - Mixing, energy 198-199
- Model**
- average properties 88-90
 - chain conformations and interactions in solution 385-396
 - conductometric titration curves, hexadecyltrimethylammonium bromide-cetyl alcohol mixed emulsifier system 405-406
 - copolymerization of styrene with methyl acrylate 121-124
 - copolymerization reactions 88-101
 - equilibrium swelling of latex particles with monomers 197-206
 - Flory distribution 47, 51*f*, 56*f*, 57*f*
 - free-volume 100
 - hydrodynamic volume 394
 - kinetic
 - curing reaction 320-324
 - parameters 378-380
 - styrene polymerization
 - kinetics 13-25, 19-21
 - vinyl polymerization kinetics 27-42
 - Model, multi-component 45-63
 - nonisothermal polymer flows 265-276
 - particle property 210
 - Scheffe canonical polynomial, ABS pipe compounds 439-447
 - Schulz-Zimm distribution 47-48, 55*f*, 58*f*, 62*f*
 - statistical, copolymerization
 - reactors 90-93
 - styrene polymerization using *n*-butyllithium initiation 3-11
 - Wesslau distribution, multi-component models 48-49, 53*f*, 59*f*, 63*f*
 - zipper 378-383
 - Modified Gottfert capillary rheometer, data acquisition system 243
 - Modulus, dynamic mechanical, glassy to rubbery region, viscoelastic master plots 368-369
 - Modulus, shear and loss, calculation for automated torsion pendulum 329-352
 - Molar enthalpy 121-122
 - Molar extinction coefficient 177*t*
 - Molecular mass, model of solution conformations and interactions 394-396
 - Molecular weight
 - averages, prediction 209-220
 - determination 103-106
 - light scattering 107-108
 - distribution (MWD) 87, 90, 93-99, 101
 - analysis 45-63
 - termination rate constant 32-42

- Molecular weight (*continued*)
 poly(vinyl acetate) emulsion
 polymerization reactors ...209-220
 retention volume, function ...173, 178-181
 set point change, styrene
 polymerization4, 6, 8-10
 styrene polymerization ...21-25, 126, 133;
 undegradable model of chain solu-
 tion conformations and inter-
 actions 396
- Moment of inertia, automated torsion
 pendulum348-349
- Monitoring wave signal, real time, for
 automated torsion pendulum 336
- Monodisperse polystyrene and poly-
 methyl methacrylate latex,
 swelling198-206
- Monomer
 chain transfer, styrene
 polymerization 14
 methyl acrylate117-134
 methyl and ethyl methacrylate40-42
 mutual solubility with polymer,
 vinyl polymerization27-42
 ratio variation with reaction time
 in a batch reactor125-126
 reactivity ratios118-119
 self-condensation of 2,4-dimethylol-
 4-methylphenol, rate constants 75*f*
 sequence distribution placements,
 unconditional probabilities 139-145
 triads, modified polymer, simula-
 tion using CSMP 82-84
 unit distribution, simulation
 using CSMP82-84
 vinyl polymerization kinetics29-42
- Motion, equation, automated torsion
 pendulum336, 338, 341
- Motten selenium, heat capacity
 data363, 364*f*
- MULT and RATIO software,
 comparison193-194
- Multi-component models
 Flory distribution model 47, 56*f*, 57*f*, 61*f*
 Schulz-Zimm distribution
 model47-48, 55*f*, 58*f*, 62*f*
 Wesslau distribution
 model48-49, 53*f*, 59*f*, 63*f*
- Multifilamented glass braid ...330, 350-357
- Multiple regression technique, auto-
 mated thermal analysis 301
- MWD—*See* Molecular weight,
 distribution
- N**
- Navier-Stokes system 254
- NCA—*See* *N*-Carboxy anhydride
- Near IR spectroscopy, SAN
 copolymers150-153
- Nelder Mead sequential simplex
 minimization algorithm method ... 301
- Newtonian fluid252, 256, 258
- Nip flow in roll coating251-263
- Nitrile group absorption 173
- NMR 109
- Nomograph, reduced temperature ...368-374
- Nondrag optical transducer330-331
- Nonionic surfactants 204*t*
- Nonisothermal polymer flows265-276
- Nonlinear least squares method, data
 reduction for automated torsion
 pendulum341-348
- Nonlinear polymerization reactor,
 styrene polymerization control .. 11
- Nonlinear regression analysis, molec-
 ular weight distribution45-63
- Normalization factor, calculations of
 terpolymer structure141-142
- Nonuniform macromolecules, model
 of solution conformations and
 interactions386-396
- Nuclear magnetic resonance—*See*
 NMR
- O**
- Oil-in-water emulsifiers, ionic, mathe-
 matical model of benzene and
 styrene emulsions399-424
- Optical transducer, nondrag330-331
- Optimal multiple reactor system
 design209-220
- Optimization
 hexadecyltrimethylammonium
 bromide-cetyl alcohol ratio,
 emulsifier systems399-424
- isothermal cure schedules, Mettler
 software313-326
- solvent blends427-437
- styrene polymerization control 6, 8
- Order, reaction, automated thermal
 analysis 301
- Organic solvent blend, evaporation 435
- Oscillations, continuous flow stirred
 tank reactors209-220
- Osmometry 106
- P**
- Pair radial distribution function,
 model of solution conformations
 and interactions389, 392
- Parameter
 CSMP for evaluation73-79

- Parameter (*continued*)
- consequences for chain conformations, behavior, and properties 385-396
 - epoxy curing reactions 320-323
 - frequency and damping, automated torsion pendulum 330-350
 - kinetic models, data storage 377-383
 - Particle generation rate, vinyl acetate polymerization 211
 - Particle growth constant, hexadecyltrimethylammonium bromide-cetyl alcohol mixed emulsifier system 414
 - Particle property model 210
 - Particle size development of poly(vinyl acetate) emulsion polymerization reactors 209-220
 - Particle size distribution and viscosity 219
 - Particle size, latex 197-206
 - Particle-water interfacial tension 198
 - Partition function, model of solution conformations and interactions .. 390
 - Peak areas
 - data reduction for automated torsion pendulum 338-339, 345-348
 - hydrogen halide, computer program for degradation kinetics of poly(vinyl halides) 378-383
 - poly(vinyl halides) degradation kinetics 380-383
 - Penalty elements, isoparametric 265-276
 - Pendulum, automated torsion 329-352
 - Pentads, structural feature calculations 138
 - Performance function, styrene polymerization control 6, 8
 - Permittivity plots, application of polarization morphology 287, 289f
 - Peroxide-initiated suspension polymerization styrene 21-24
 - Phase, liquid, model of chain conformations and interactions 385-396
 - Photometer, light scattering, polystyrene latexes 200
 - Pipe-compound experiment, ABS, design and analysis 439-447
 - Piston velocity 243, 246
 - Pitch content of ABS pipe compounds 447t
 - Pitch, coal-tar, design and analysis of blends 439-447
 - Plots, three-dimensional conductance-oil volume-cetyl alcohol 418-422
 - Plots, viscoelastic master, vibration damping applications 367-374
 - Plotting, automated thermal analysis 298
 - Poly(vinyl halides), computer application to degradation kinetics of 377-383
 - PMMA—*See* Poly(methyl methacrylate)
 - Polarization
 - interfacial, analytical model 284-285
 - thermoplastic elastomers 277-295
 - Pollution control regulations, solvents 427-437
 - Polyaddition with condensation, self-promoted, CSMP 79-81
 - Polycondensation reaction simulation, CSMP 68, 73-79
 - Polydispersity index with reaction time in semi-batch reactor 120-122, 127-129
 - Polyester, spectra interpretation 286-290
 - Poly(ethyl methacrylate) 40, 42f
 - Polyethylene
 - high density 52
 - low density, nonisothermal polymer flows 268-269
 - Polymer epimerization reactions 73-79
 - Polymer flow, nonisothermal 265-276
 - Polymer heat capacity data bank 355-365
 - Polymer modification reaction simulation, CSMP 82-84
 - Polymer solution properties, model of chain conformations and interactions 385-396
 - Polymer spectra, interpretation 285-292
 - Polymerization degree against reaction time in batch reactor 125-129, 131f
 - Polymerization kinetics
 - free radical, chain length dependent termination, computational aspects 27-42
 - poly(vinyl halides) 382, 383f
 - quantitative 297
 - styrene, simulation 13-25
 - Polymers, crystal structure, heat capacity data 356-358
 - Poly(methyl methacrylate) 40, 41f
 - latex particles, swelling 203-206
 - reduced-temperature nomograph 372-374
 - Polynomial models, Scheffe canonical, ABS pipe compounds 439-447
 - Polystyrene
 - absorption behavior 166, 170-177
 - hypochromic effect 170
 - refractive index 161-166
 - Polystyrene latex particles with styrene, swelling 200, 203
 - Polystyrene reactor, isothermal 3-11
 - Polyurethane, spectra interpretation 286-290
 - Poly(vinyl acetate) emulsion polymerization reactor, continuous 209-220
 - Potassium persulfate initiation 200, 218

- Potential energy factor, model of solution conformations and interactions 390-392
- Precision, computer program for best fit values in degradation kinetics 379
- Prediction schemes, heat capacity data bank 362
- Pressure, normalized, nonisothermal polymer flows 273f
- Pressure profile, nip flow in roll coating 258, 261
- Pressure-volume-temperature, data bank 355-365
- Probabilities
- copolymerization 90-93
 - styrene-centered triads, extinction coefficient 170
 - unconditional, monomer or sequence distribution placements 139-145
- Process transfer function, styrene polymerization control, Laplace transform 6
- Production rate set point change, styrene polymerization 4, 6, 8-10
- Programs for calculations of terpolymer structure 137-149
- Propagation
- N*-carboxy anhydride polymerization 79
 - copolymerization of styrene with methyl acrylate 123f
 - free-radical polymerization kinetics 30
 - and terpolymer structure 139-145
- Properties
- heat capacity data bank 355-365
 - polymer solution, model of chain conformations and interactions 385-396
- Proton NMR, composition determination of styrene with methyl acrylate copolymer 125
- Pure interactions, model of solution conformations and interactions .. 392
- R**
- Radial distribution function, pair . 389, 392
- Radical
- chain propagation, peroxide-initiated styrene polymerization 14-25
 - i*-mer and *j*-mer 28-29
 - structural features of terpolymers 139-145
- Random distribution, Flory model 47, 56f, 57f, 61f
- Rate, scan, automated torsion pendulum 337
- Rate, water evaporation, solvent systems at various humidities .427-437
- Rate constant
- degradation kinetics 378-380
 - monomer and dimer, self-condensation of 2,4-dimethylol-4-methylphenol 75f
 - terminal double bond polymerization 211
 - termination rate 27
- Rate constants for interconversion units 82
- RATIO and MULT software, comparison 193-194
- Ratio
- optimum hexadecyltrimethyl ammonium bromide-cetyl alcohol emulsifier systems 399-424
 - reactivity, structural features of terpolymers 137-145
 - swelling 200
- Reactor configurations, comparison 215f
- Reactor design 111-112
- Reaction
- acceleratory, of poly(vinyl halides) 377-383
 - epoxy curing, differential scanning calorimetry 313-326
 - heat of, per epoxy group 320
 - termination, and gel effect interpretation 100
 - zero and first order, simulation of degradation kinetics of poly(vinyl halides) 380-383
- Reaction engineering, copolymerization of styrene with methyl acrylate 117-134
- Reaction kinetics, automated thermal analysis system 297-305
- Reaction parameters, epoxy curing reactions 320-323
- Reaction rate, termination rate constant 27
- Reactivity ratios 98-100
- monomer 118-119
- structural features of terpolymers 137-145
- Reactor
- continuous flow stirred tank, oscillations 209-220
 - continuous loop 24f
 - continuous poly(vinyl acetate) emulsion polymerization, dynamic model 209-220
 - control strategies 87
 - isothermal polystyrene 3-11
 - tubular seed generation 214
- Reactor design 111-112

- Reactor design, optimal multiple ..209-220
 Reactor train, soap levels 214
 Real time monitoring, wave signal,
 for automated torsion pendulum 336
 Recombination, vinyl polymerization
 kinetics32, 35-37
 Reduced temperature nomograph ..368-374
 Reducible coating, water, drying time
 and solvent balance427-437
 Reduction scheme, data, viscoelastic
 master plots for vibration damp-
 ing applications367-374
 Reduction, drag, conformations in
 flow394-396
 Refractive index measurements,
 SAN copolymers154, 161-166
 Regression analysis of conductometric
 titration data, hexadecyltri-
 methylammonium bromide-cetyl
 alcohol mixed emulsifier
 system401-424
 Regression equations, adequacy, ABS
 pipe compounds 444*f*
 Regulations of solvents427-437
 Relative humidity (RH), solvent
 system evaporation 430
 Replacements, solvent blend427-437
 Repulsion, model of chain solution
 conformations and interactions .. 390
 Residual monomer analysis101-103
 Residuals, summation, automated tor-
 sion pendulum338-341
 Resin, amine-cured epoxy, automated
 torsion pendulum vs. torsional
 braid analysis349-350
 Resin, hardener/, composition on
 degree of cure 316
 Resole polycondensation 68
 Resonant beam data, vibration damp-
 ing applications371-374
 Resonant dwell vibrating beam
 apparatus 372
 Response surface-predicted Izod,
 ABS pipe compounds444-447
 Reversible polymer modification
 reactions, simulation using CSMP 82
 Reynolds number 254
 RH—*See* Relative humidity
 Rheometer measurement, automated
 capillary and analysis243-248
 Rheovibron data, computerized visco-
 elastic master plots373-374
 Rigid solutions, partially, model of
 chain conformations and inter-
 actions385-396
 Roll coating, nip flow251-263
 Rubber-to-solid transition, automated
 torsion pendulum 335
 Runge-Kutta integration method 77
- S**
- Savitsky-Golay method, shear rate
 and viscosity 236
 Scheffe canonical polynomial
 models, ABS pipe com-
 pounds439-447
 Scheme, Bondi, model of chain solu-
 tion conformations and inter-
 actions 393
 Schulz-Zimm distribution
 model47-48, 55*f*, 58*f*, 62*f*
 Scan rate, automated torsion
 pendulum 337
 SEC—*See* Size exclusion
 chromatography
 Segmental hard-core (incompressible)
 volume, model of solution con-
 formations and interactions 392
 Segments of bundles, model of chain
 solution conformations and inter-
 actions385-396
 Selectivity equation 88-89
 Selenium, heat capacity data363-365
 Self diffusion coefficients28-29
 Self-condensation, 2,4-dimethylol-4-
 methylphenol 75*f*
 Self-promoted polyaddition with
 condensation, use of CSMP79-81
 Separation techniques, gel permeation
 chromatography 50-63
 Sequence length
 average, mean of distributions 92
 UV absorption of styrene containing
 copolymers170-181
 Sequence length determination 108
 Sequence length distribution,
 unconditional probabilities ...139-145
 Sequence length distribution
 (SLD) 87, 90-93, 101
 Sequential simplex minimization algo-
 rithm method, Nelder Mead 301
 Shear modulus calculation for auto-
 mated torsion pendulum325-329
 Shear rate experiment, build-up of
 structure 223
 Shear rate step 236
 Shear stress
 capillary rheometer measurement .. 244
 model of solution conformations
 and interactions 396
 Shear stress contours, nonisothermal
 polymer flows 273*f*
 Shear stress vs. shear rate, Casson
 analysis 227-228
 Shear-thinning rheology, roll
 coating251-263

- Shortage of solvents 427-437
- Signal digitization, automated
torsion pendulum 336
- Simulated peaks, poly(vinyl halides)
degradation kinetics 380-383
- Simulation
copolymerization of styrene with
methyl acrylate 125, 127
nip flow in roll coating 251-263
poly(vinyl chloride) degradation
kinetics 380-383
prediction water/cosolvent evapora-
tion at any humidity 427-437
solvent blend replacement 427-437
styrene polymerization kinetics 13-25
- Size exclusion chromatography
(SEC) 101-102, 109-111
- Size exclusion chromatography of
SAN copolymers 151-181
- Skeletal vibrations, intramolecular 355-358
- SLD—See Sequence length
distribution
- Soap levels, reactor train 214
- Sodium dodecyl sulfate emulsifiers 203-205
- Software
automated torsion pendulum 336
comparison of MULT and
RATIO 193-194
copolymerization of styrene with
methyl acrylate 126
CSMP 66-84
heat capacity data bank 359-360
IR spectroscopy 185-196
Mettler thermal analysis system 313-326
- Solid content in a controlled and
uncontrolled semi-batch
reactor 132f
- Solid-to-rubber transition, automated
torsion pendulum 335
- Solubilities
mutual monomer-water 199
mutual monomer and polymer,
vinyl polymerization 27-42
- Solubilization process, hexadecyltri-
methylammonium bromide-cetyl
alcohol mixed emulsifier
system 399-424
- Solute concentrations, hexadecyltri-
methylammonium bromide
emulsifier systems 399-424
- Solutions
dilute, configurational dimensions
of polymer molecules 388-396
partially flexible, model of chain
conformations and inter-
actions 385-396
polystyrene, absorption
behavior 166, 170-177
- Solutions (*continued*)
properties, polymer, model of chain
conformations and inter-
actions 385-396
- Solvent
blend replacements 427-437
chain transfer, styrene polym-
erization 14
interactions, model of chain solu-
tion conformations and inter-
actions 392-396
packing, SEC 110-111
SAN copolymer, refractive index .. 167f
transfer, copolymerization of
styrene with methyl acrylate .. 123f
vinyl polymerization kinetics 29-42
viscosity, model of chain solution
conformations and inter-
actions 396
- Solvent balance of a water reducible
coating 427-437
- Specific volumes, low and high
conversion copolymers 169f
- Spectra, polymer, interpretation 285-292
- Spectrometer, dielectric 279-284
- Spectrometric analysis 103
- Spectrophotometer
assumptions for use as mass
detectors 152
double-beam IR, film analysis 186
UV 151-181
- Spherulites, application of polariza-
tion morphology 287
- Spring relaxation, shear stress
data 228-236
- Stability, crystalline, application of
polarization morphology 287
- Stanford Public Information Retrieval
System (SPIRES) 261-263
- Stationary state hypothesis (SSH) 90
- Statistical models 90-93
- Steady-state conditions, styrene
polymerization using *n*-butyl-
lithium initiation 5t, 6-8
- Stiffness of chain 385-396
- Stoichiometric coefficient 121
- Storage
automated thermal analysis 298
data, parameter calculation for
kinetic models 377-383
- Stress, hydrostatic, nonisothermal
polymer flows 267
- Stress, shear, model of solution con-
formations and interactions 396
- Stresses, deviatoric 266-267
- Structure
model of chain solution conforma-
tions and interactions 390-396

- Structure (*continued*)
- terpolymers, programs for
 - calculations 137-149
 - Structure based names, heat capacity
 - data bank 361-362
 - Structure of polymers
 - crystal, heat capacity data 356-358
 - microscopic, heat capacity data 356-358
 - Styrene
 - copolymerization with methyl
 - acrylate 117-134
 - emulsification, in aqueous hexadecyltrimethylammonium bromide-cetyl alcohol mixtures, mathematical
 - treatment 399-424
 - polymerization
 - kinetics 13-25
 - n*-butyllithium initiation 3-11
 - sequence lengths by UV 153
 - Styrene acrylonitrile copolymers
 - size exclusion chromatography 151-181
 - and styrene-butadiene copolymer, design and analysis of
 - blends 439-447
 - Styrene-centered triads, probabilities,
 - extinction coefficient 170
 - Summation of residuals, automated
 - torsion pendulum 338-341
 - Surfactants, anionic, nonionic, and polymeric 197-206
 - Swelling
 - equilibrium, latex particles with
 - monomers 197-206
 - hexadecyltrimethylammonium bromide-cetyl alcohol mixed emulsifier system 405-424
 - ratios 200
 - Synonyms, source and structure based
 - names, heat capacity data
 - bank 261-262
 - Systems simulation 8, 11
- T**
- Tangent data, loss, glassy to rubbery
 - region, viscoelastic master
 - plots 368-369
 - Tank reactors, continuous flow
 - stirred, oscillations 209-220
 - Taylor series expansion, linear 342
 - TBA—*See* Torsional braid analysis
 - Temperature
 - contours, nonisothermal polymer
 - flows 275f
 - effect, epoxy curing
 - reactions 316, 318-320
 - equilibrium first order transition,
 - heat capacity data 355
 - Temperature (*continued*)
 - model of solution conformations
 - and interactions 386, 394-396
 - nomograph, reduced 368-374
 - shift values, computerized visco-
 - elastic master curves 368-369
 - solvent system evaporation 429-430
 - under load, deflection, styrene
 - blends 442-447
 - Tension, interfacial, latex and
 - particle-water 197-206
 - Tensor V, rate of deformation 266
 - Terminal conversion 89-90
 - Terminal double bond polymerization 210
 - Terminal model reactivity ratios 143
 - Termination, chain length dependent,
 - computational aspects of free
 - radical polymerization kinetics 27-42
 - Termination combination, copolymerization of styrene with
 - methyl acrylate 123f
 - Termination rate constant 27
 - Termination rate constant, molecular
 - weight distribution 32-42
 - Termination reaction and gel effect
 - interpretation 100
 - Termination of zip chains, premature,
 - computer approximations 378-380
 - Ternary polymer solution 199
 - Terpolymers, structural
 - calculations 137-149
 - Tetrads, structural calculations 137-149
 - Theory, heat capacity 355-358
 - Thermal analysis, heat capacity
 - data 355-365
 - Thermal analysis system reaction
 - kinetics, automated 297-305
 - Thermal conductivity
 - data bank 355-365
 - nonisothermal polymer flows 267-268
 - Thermal convection, nonisothermal
 - polymer flows 268
 - Thermal degradation kinetics,
 - parameter estimation 377-383
 - Thermal flux, nonisothermal polymer
 - flows 268
 - Thermally initiated butyl polymerization of styrene, batch and
 - continuous 21-25
 - Thermodynamic model, swelling of
 - polystyrene and polymethyl
 - methacrylate latexes 197-206
 - Thermodynamic results, automated
 - thermal analysis 305
 - Thermodynamics, heat capacity
 - data bank 355-365
 - Thermoplastic elastomers,
 - polarization 277-295

- Three-dimensional conductance-oil
 volume-cetyl alcohol plots 418-422
- Three-dimensional formulations 266
- Time, drying, water reducible
 coating 427-437
- Titration curves, conductometric,
 hexadecyltrimethylammonium
 bromide-cetyl alcohol mixed
 emulsifier system 401-424
- Torsion pendulum, automated 329-352
- Torsional braid analysis (TBA) 330, 332,
 350, 357
- Transducer, nondrag optical 330-331
- Transient-response spectrometer 290-292
- Transition temperatures, equilibrium
 first-order, heat capacity data 355
- Transition, solid-to-rubber, automated
 torsion pendulum 335
- Translational diffusion controlled
 termination 28-29
- Transmission electron micrograph,
 hexadecyltrimethylammonium
 bromide-cetyl alcohol mixed
 emulsifier system 401-404
- Trapazoidal method, automated
 thermal analysis 301
- Triads, structural calculations 137-149
- Triethylene tetramine-phenol hardener,
 epoxy curing reaction 313-326
- Trigonal selenium, heat capacity
 data 363-364
- Tubular seed generation reactor 214
- Two-dimensional flows 255
- U**
- Ultraviolet spectrophotometers and
 spectroscopy—*See* UV
- Unconditional probabilities, monomer
 or sequence distribution
 placements 139-145
- Uncontrolled semi-batch solution
 copolymerization of styrene with
 methyl acrylate 117-134
- Undegradable molecular weight,
 model of chain solution conformations
 and interactions 396
- Universal Calibration, size exclusion
 chromatography 110-111
- UV spectroscopy
 composition determination of
 styrene methyl acrylate
 copolymer 125
- detection, polystyrene latexes 200
- SAN copolymers 166, 170
- spectrophotometers 151-181
- V**
- Validity of copolymerization
 equations 99-100
- Velocity field, nonisothermal
 polymer flows 272f
- Velocity, piston 243, 246
- Vibrating beam apparatus, resonant
 dwell 372
- Vibration, intramolecular and
 intermolecular 355-368
- Vibration damping applications,
 viscoelastic master plots 367-374
- Vinyl acetate polymerization,
 terminal double bond 210
- Vinyl acetate/vinyl chloride copoly-
 mers, software for copolymer
 film analysis 185-196
- Vinyl polymer, Schulz-Zimm
 model 47-48, 55f, 58f, 62f
- Vinyl polymerization, mutual solubility
 of monomer and polymer 27-42
- Viscoelastic master plots, vibration
 damping applications 367-374
- Viscometer, automated Ferranti-
 Shirley 223-239
- Viscosity
 and Casson analysis 223
- melt, capillary rheometer
 measurement 244
- model of chain solution conforma-
 tions and interactions 386, 394-396
- non-Newtonian 261
- and particle size distribution 219
- shear stress at constant RPM 228
- and styrene polymerization kinetics 19-25
- Viscous free surface flow
 problems 253-256
- Vitreous selenium, heat capacity
 data 363-364
- Volume, segmental hard-core (incom-
 pressible), model of chain solu-
 tion conformations and
 interactions 392
- Volume model, hydrodynamic 394
- Volume-cetyl alcohol, three-dimen-
 sional plots 418-422
- Volumetric dilation, nonisothermal
 polymer flows 267
- Volumetric flow rate, capillary
 rheometer data 243
- W**
- Water reducible coating, drying time
 and solvent balance 427-437

- Water/cosolvent evaporation at any
 humidity in water reducible
 systems 427-437
- Wave signal real time monitoring for
 automated torsion pendulum 336
- Weight fraction, styrene polymers 18, 21-25
- Wesslau distribution model, multi-
 component 48-49, 53f, 59f, 63f
- Wire, calibration, automated torsion
 pendulum 348-349
- Wunderlich's rule 357
- Y**
- Yield strength
 ABS pipe compounds 446f
 styrene blends 442-447

Z

- Zero and first order reaction, simula-
 tion of degradation kinetics of
 poly(vinyl halides) 380-383
- Zero-shear viscosity 19-25
- Ziegler type polymerization, molecular
 weight distribution 52
- Zip chains, computer approximations
 of premature termination 378-380
- Zipper mechanism, degradation
 kinetics of poly(vinyl
 halides) 377-383